Thesis in joint-supervision
between

UNIVERSITY OF LILLE

Doctoral School of Science of Matter, Radiation and Environment

and

"GHEORGHE ASACHI" TECHNICAL UNIVERSITY OF IAȘI

Doctoral School of the Faculty of Chemical Engineering and Environmental Protection

Domain: Biological function engineering, Chemical engineering

PhD Dissertation

LAYERED DOUBLE HYDROXIDES AND THEIR COMPOSITES: DESIGN, SYNTHESIS AND SPECIFIC APPLICATIONS

by

Elena-Florentina GROSU

Reviewers:	Horia IOVU	Professor	Polytechnic University of Bucharest
	Vanessa PREVOT	Research Director	University Clermont Auvergne
	Catherine SARAZIN	Professor	University of Picardy Jules Verne
President	Teodor MĂLUȚAN	Professor	"Gheorghe Asachi" Technical University of Iasi
Thesis Supervisors:	Gabriela CARJA	Professor	"Gheorghe Asachi" Technical University of Iasi
	Rénato FROIDEVAUX	Professor	University of Lille

5th of April 2019

Acknowledgments

A dream you dream alone is only a dream,
A dream you dream together is reality
John Lennon

This manuscript presents the research results obtained in different laboratories from Romania, France and Belgium, during my four years of PhD. I am thankful to a number of coordinators, colleagues and friends, due to their constant supervision, help and encouragements in exploring my creativity, in obtaining relevant results and finally in publishing them.

First of all, I want to thank to both my PhD supervisors: Professor Gabriela Carja from Gheorghe Asachi Technical University and Professor Renato Froidevaux from Lille University, France. I am very grateful to Professor Gabriela Carja for the opportunity to start a PhD under her supervision. Furthermore, I want to thank her for all advices, for her patience and understanding, and for her implication in becoming a competitive researcher. Moreover, is important to mention that, without her connections in the scientific world, this work could not be possible. I am thankful to Professor Renato Froidevaux for his constant support, especially during the last year, and for his positive feedback and constructive discussions regarding the research. Additionally, I am grateful for all his efforts in finding financial support during my stages at Lille University.

I am very grateful to the members of the jury: Prof. Vanessa Prevot, Prof. Catherine Sarazin, Prof. Horia Iovu and Prof. Teodor Măluțan for their time and reflections regarding the work presented in my thesis manuscript.

I would like to acknowledge Professor Pegie Cool and dr. Elena Seftel form Antwerp University, Belgium, for their supervision and support during my six months Erasmus stage.

A very important role in my formation was played by my colleagues Magda and Kalim. I thank them for their enthusiasm, elegance and clarity in explaining methods and giving advices, which maintained me focused on the research.

Special acknowledgements are for those I never met, but they had an important implication in this work, by performing different material characterizations, that I could not do. I am also greateful to all the persons working in the administration offices, who helped me during the last four years.

I have in my mind many moments when I felt discouraged. The challenges and the good moments of this PhD would be meaningless without the presence of my dear friends and colleagues Diana, Mihaela and Simona, who gave me confidence and a lot of encouragements.

Acknowledgments

I would like to acknowledge the support and love of my family, and especially to my little sister who is such a surprising person. Some thoughts and feelings are flying to those who will never read this, but they played an important role in becoming the person I am today.

Finally, I dedicate this success to that person who was behind me in the last ten years and filled my life with love and happiness. Your love makes me a better human being.

Abstract / Résumé

Abstract

Exploring the nano scale features of the matter and combining together different materials, novel composites with enhanced features can be fabricated, for their further utilization in biomedicine, catalysis, engineering, electronics, biotechnology and others. The anionic clays, also called layered double hydroxides (LDHs) are a category of hydrotalcite composites which possess high compositional variety, able to self-assembly. When used in presence of biological systems, they act as soft materials, with no significant effect over the constituent biomolecules. In this context, the thesis subject deals with the design of nanostructured composites LDHs type, for their further physicochemical characterization and utilization in photocatalysis, biomedicine and biochemistry. The first part of this work approaches the fabrication of self-assembled nanoparticles (NPs) as Au, In, Ag, and Ga on ZnLDHs materials by using co-precipitation, followed by reconstruction or impregnation synthesis methods. The applied characterization techniques proved that the novel materials have a hydrotalcite structure, they are crystalline and after reconstruction, the initial structure is recovered. The nanomaterials NPs/LDHs showed high photo-response activity when irradiated under simulated solar light and they were able to photodegrade organic pollutants as phenol, p-nitorphenol, acetophenone and diclofenac. The enhancement of hybrids performance, compared with their parent materials, is a consequence of the formation of surface separation between dispersed NPs and clay surface, which leads to recombination rate decrease. The second part of this thesis investigates the interactions between the LDHs or Au/LDHs based materials and Horseradish Peroxidase (HRP) enzyme. The results proved that the LDHs products resulted after clay calcination at 550 °C are capable to immobilize the enzyme via adsorption, with layered structure reformation. The kinetic data showed that only the materials without AuNPs retain the enzyme activity, while those with AuNPs in their structure are enzymatically inactive. The concept of photo-enzymatic degradation of phenol under solar irradiation and in presence of HRP/LDH biohybrid was also confirmed. The result was expressed as the synergetic effect between the enzymatic and the photocatalytic degradation. Furthermore, it was demonstrated that HRP can mediate the gold release from Au/LDH surface through HRP-AuNPs complex formation. In a separate study the nicotinamide adenine dinucleotide (NADH) cofactor was regenerated from NAD^+ in presence of Au/LDH, solar light and using flavin mononucleotide (FMN) as an electron mediator. At a pH value of 8, the NADH regeneration was total in a time interval of two hours. In the last section of this work, the interactions between Au/LDHs materials and hepatitis B virus (HBV) were investigated. The cytotoxicity data have been demonstrated that the LDHs materials had no significant influence over cells viability. Remarkably, the Au/LDHs formulations have shown that they can inhibit the HBV proliferation. The parent LDHs materials manifest a modest antiviral activity.

Keywords: LDHs, NPs/LDHs, HRP, immobilization, HRP/LDH, organic pollutants, photodegradation, photo-enzymatic degradation NADH regeneration, HBV.

Résumé

Explorer les caractéristiques à l'échelle nanométrique de la matière et la combiner avec d'autres matériaux, permettent la fabrication de nouveaux objets avec des fonctionnalités améliorées, pour une utilisation potentielle dans le domaine biomédical, la catalyse, l'ingénierie, l'électronique, la biotechnologie, etc… Les argiles anioniques, également appelées des Hydroxydes Doubles Lamellaires (HDL), constituent une catégorie de matériaux hydrotalcite qui possèdent une grande variété de compositions et une capacité d'auto-assemblage. Lorsque ces HDL sont utilisés en présence de systèmes biologiques, ils agissent comme des matériaux *soft*, sans effet significatif sur les biomolécules constitutives. Dans ce contexte, le sujet de thèse porte sur la conception de matériaux HDL nanostructurés, leur caractérisation physico-chimique et leur utilisation en photocatalyse, biomédecine et biochimie. La première partie de ce travail aborde la fabrication de nanoparticules auto-assemblées (NP) sous forme de matériaux Au, In, Ag et Ga sur ZnHDLs en utilisant la co-précipitation suivie par une étape de reconstruction/imprégnation. Les techniques de caractérisation utilisées ont montré que les nouveaux matériaux avaient une structure hydrotalcite, qu'ils étaient cristallins et que, après reconstruction, la structure initiale était récupérée. Les nanomatériaux NP/HDL ont montré une activité de photodéposition élevée lorsqu'ils étaient irradiés sous une lumière solaire simulée et étaient capables de photodégrader des polluants organiques tels que le phénol, le p-nitrophénol, l'acétophénone et le diclofénac. L'amélioration des performances des matériaux hybrides néoformés, par rapport à leurs matériaux d'origine, est une conséquence de la formation d'une séparation superficielle entre les NP dispersés et la surface d'argile, ce qui conduit à une diminution du taux de recombinaison. La seconde partie de cette thèse étudie les interactions entre les matériaux ayant pour base HDL ou Au/HDL et l'enzyme Peroxydase de raifort (HRP). Les résultats ont montré que les produits HDL résultant de la calcination de l'argile à 550° C sont capables d'immobiliser l'enzyme par adsorption, avec reformage de la structure en couches. Les données cinétiques ont montré que seuls les matériaux sans AuNPs conservent l'activité de l'enzyme, alors que ceux contenant les AuNPs dans leur structure sont « enzymatiquement » inactifs. Le concept de dégradation photo-enzymatique du phénol sous irradiation solaire et en présence de biohybride HRP/HDL a également été confirmé. Le résultat a montré un effet synergique de la dégradation enzymatique et photocatalytique. De plus, il a été démontré que HRP peut influencer la libération de particules d'Au de la surface des Au/HDL lors de la formation de complexes HRP-AuNPs. Dans une seconde étude, le cofacteur nicotinamide adénine dinucléotide (NADH) a été régénéré à partir de NAD^+ en présence de Au/HDL, de lumière solaire et en utilisant de la flavine mononucléotide (FMN) comme médiateur électronique. À une valeur de pH égale à 8, la régénération du NADH était totale dans un intervalle de temps de deux heures. Dans la dernière partie de ce travail de thèse, les interactions entre les matériaux Au/HDL et le virus de l'hépatite B (VHB) ont été étudiées. Les données de cytotoxicité ont montré que les matériaux HDL n'avaient pas d'influence significative sur la viabilité des cellules. De manière remarquable, les formulations Au/HDL ont montré qu'elles peuvent inhiber la prolifération du VHB. Les HDL bruts manifestent une activité antivirale modeste.

Mots clés: HDL, NP/HDL, HRP, immobilisation, HRP/HDL, polluants organiques, photodégradation, dégradation photo-enzymatique, régénération du NADH, VHB.

Table of contents

Table of Contents

Table of contents

SECOND SECTION: Original Research

Table of contents

Table of contents

Introduction

People didn't created the nano world, nature did! Nature has got there first and spent 3.8 billion years finding clever ways to use nanoscale. Now, if we understand the nature nano secrets, we can use them to imitate all the extraordinary things that nature made.

The nanotechnology and the nanomaterials are relatively new research directions, intensively approached in the last years, due to their significant potential applications in biology, physics, chemistry, medicine and engineering.

An important class of nano structured materials is the anionic clays. Generally named layered double hydroxides, these materials have been studied since the XIX century. They are extremely versatile and their general formula favors the incorporation in their structure of a high number of cations. Furthermore, they own the unique property of *structural memory effect,* which allows the fabrication of nanostructured self-assemblies based on LDHs. Due to their specific properties, the anionic clays have been found as perfect candidates to be used in catalysis, biomedicine, electrochemistry, photocatalysis, enzyme immobilization and others.

Considering the features that the LDH composites possess, the main objectives of this work has been the synthesis of LDHs precursors, with different chemical composition and with different ratio between the M^{2+}/M^{3+}, for their further utilization in the fabrication of self-assembled nanoparticles (NPs) on LDHs type materials. Via thermal treatment, derived mixed oxides had been also fabricated. The resulted nanocomposites had been used in organic pollutant photodegradation, enzyme immobilization and biomedical use.

The thesis manuscript has two main sections: the *State of the Art* and the *Original Research.*

The *State of the Art* section is displayed on the **Chapter 1**. This chapter includes the general information about the LDHs materials, as synthesis methods, specific properties, characterization tehniques and recent results obtained regarding the utilization of LDHs based materials in photocatalysis, biomedicine and enzyme immobilization.

The *Original Research* has three chapters. **Chapter 2** approaches the synthesis of novel and highly photo-resposive LDHs based materials, for organic pollutants photodegradation purpose. NPs/ZnLDHs (NPs = Au. Ag, In, Ga) based nanocomposites have been fabricated combining the co-precipitation with the reconstruction methods. All the materials have been physico-chemical characterized by using XRD, FTIR, UV-Vis, TG, EDX, XPS. Further, the composites have been used in the photodegradation of different aqueous solution of phenol, p-nitrophenor, acetophenone or diclofenac. The chapter conclusions underlines that the synthetized materials are extremely efficient in solar pollutant degradation and the introduction in their structure of noble elements had a beneficial impact on their photocaltalytic activity.

In **Chapter 3** have been investigated the ability of ZnAlLDH, Au/ZnAlLDH and their calcined derivatives to immobilize the Horseradish Peroxidase (HRP). The resulted materials have been used in enzymatic reactions. It was also studied the ability of HRP to mediate the gold release from Au/ZnAlLDH. Furthermore, the HRP photo-activation and NADH photo-regeneration by using solar irradiated Au/ZnAlLDH composite was as well approched.

Introduction

The research results regarding LDHs materials for biomedical purpose have been presented in **Chapter 4**. Formulations type Au/ZnAlLDH, Au/MgAlLDH and Au/MgFeAlLDH have beed synthesized and physico-chemical characterized. The resulted hybrids have been tested against hepatitis B virus (HBV).

Last part was dedicated for the general conclusions and perspectives. In the end, an overview of the research activity was presented.

Abreviations and Symbols

Abbreviations

LDH	Layerd Double Hydroxide	LC-MS	Liquid Chromatography–Mass Spectrometry
NPs	Nanoparticles	p-nPN	p-nitrophenol
MMO	Mixtures of Mixed Oxides	HRP	Horseradish Peroxidase enzyme
TGA	Thermogravimetric Analysis	ABTS	2,2'-azino-bis(3-ethylbenzothiazoline-6-sulphonic acid
XRD	X-Ray Diffraction	$ABTS_{oxd}$	Oxidized form of ABTS
FTIR	Fourier-Transform Infrared Spectroscopy	$ABTS_{red}$	Reduced form of ABTS
Enz	Enzyme	cat	catalase
DTA	Differential Thermal Analysis	NAD^+	Oxidized form of Nicotinamide Adenine Dinucleotide
DTG	First derivative *of a* mass loss curve	NADH	Reduced form of Nicotinamide Adenine Dinucleotide
SEM	Scanning Electron Microscopy	FMN	Flavin Mononucleotide
TEM	Transmission Electron Microscopy	HBV	Hepatitis B Virus
EDX	Energy-Dispersive X-ray Spectroscopy	HepG2.2.2.15	Hepatic cell type
XPS	X-ray Photoelectron Spectroscopy	SVP	Subviral Particles
UV-Vis	UV-Vis Spectroscopy	DCF	Diclofenac
e^-	Electron	h^+	Hole
ELISA	Enzyme-Linked Immunosorbent Assay	ICP	Inductively Coupled Plasma
MTS	Cell Proliferation Colorimetric Assay Kit	SDS-PAGE	Sodium-Dodecyl Sulfate-Polyacrylamide Gel Electrophoresis
Lg	Light	Ly	Lysine
CB	Conduction Band	BCA	Bicinchoninic Acid

Abreviations and Symbols

VB	Valence Band
HRTEM	High Resolution Transmission Electron Microscopy
EXAFS	Extended X-Ray Absorption Fine Structure
SPR	Surface Plasmon Resonance
Ph	Phenol
p-NP	p-nitrophenol
fcc	face-centered cubic
XANES	X-ray Absorption Near Edge Structure
AcPh	Acetophenone
g-C_3N_4	CN
R	Reconstruction
I	Impregnation
DRIFT	Diffuse Reflectance Infrared Fourier Transform Spectroscopy
TOC	Total Organic Carbon

Symbols

n	Interlamellar anion charge
M^{II}	Divalent cation
M^{III}	Trivalent cation
Zn	Zinc
Al	Aluminum
Fe	Iron
Au	Gold
y	Interlamellar water molecules.
λ	Radiation wavelength
E_n	Photone energy in excitated state
A	Absorbance
ε	Molar absorption coefficient
l	Length of the solution that light
V_i	initial rate of product formation
[S]	substrate concentration
[P]	Product concentration
$A\%$	Percentage absorbance
k	Shape factor, generally equal with 0.9
n	Diffraction order
d	Interplanar distance
θ	Incident angle of the X-ray
h	Planck constant
ν	photon frequency
$\Delta\sigma$	Disorder in the neighbor distance
E_K	Kinetic energy of the photoelectron
E_B	Binding energy of the photoelectron
$T\%$	Percentage transmittance
T	Transmittance
A^{n-}	Iinterlamelar anion molecules
$\bar{\upsilon}$	Radiation wavenumber
I_0	Intensity of incident radiation
I	Intensity of transmitted radiation
Cr	Chromium
ν	Stretches vibration
δ	Deformation vibrations
ΔE	Transition energy
E_0	Photon fundamental enery
Ag	Silver
c	Speed of light in vacuum
N	Coordination number
a, c	Unite cell parameters
α	Absorption coefficient
c	Sample concentration

Abreviations and Symbols

K_M	Michaelis-Menten constant
V_{max}	Maximum reaction rate
$V_{max\ specific}$	Specific maximum velocity
R	Distance to neighboring atom

List of figures

List of Figures

List of Figures

List of Figures

List of Figures

List of Figures

List of Figures

List of Figures

List of Figures

List of Figures

List of Tables

List of Tables

State of the Art

Science knows no country, because knowledge belongs to humanity, and is the torch which illuminates the world.

Louis Pasteur

1. Layered double hydroxides, nanocomposites based on layered double hydroxides and their derived mixtures of mixed oxides

This first chapter presents general aspects about the layered double hydroxides (LDHs). Starting from LDHs materials, nanocomposites containing nanoparticles (NPs) dispersed on LDHs surface (NPs/LDHs) can be designed and further used in specific applications. Through thermal treatment, the LDHs and their hybrids can be precursors for the derived mixtures of mixed oxides (MMO) synthesis. Furthermore, these materials can be used as supports for biomolecules immobilization, as enzymes (Enz), leading to biohybrid type Enz/LDHs. Theoretical information about the LDHs, NPs/LDHs, Enz/LDHs and MMO synthesis, their characterization and particular application in photocatalysis, enzyme-catalysis and biomedicine are presented.

1.1. Layered double hydroxides

1.1.1. Layered double hydroxides structure

Layered double hydroxides (LDHs) are a nanocomposite class also called anionic clays, whose organization is based on the structure of brucite [$Mg(OH)_2$], in which a part of divalent cations have been replaced by trivalent cations [1]. These materials are investigated due to their special properties and they have technological importance in catalysis, separation technology, optics, medical science and nanocomposite material engineering [2].

First natural LDH material was discovered in Sweden around 1842 by Hochstetter, being a combination between magnesium and aluminum, also called hydrotalcite [3]. Further, more than 40 other natural anionic clays had been discovered and they were generally named as hydrotalcites [4]. During the time, hydrotalcites group was intensely approached and in 1915, Manasse determined the correct formula for the hydrotalcite [3,5], while in 1942, Feitknecht started to synthetize different anionic clay structures and he called them *double sheet strucures* [3].

As expressed above, the LDHs structure is based on that of brucite. For a better understanding of hydrotalcite minerals, brucite structure has to be first approached. In figure 1.1 can be observed that in a brucite sheet, the magnesium cations are surrounded octahedrally by hydroxyl anions, forming an octahedral unite. This octahedral unite, will form neutrally charged infinite sheets. These layers are overlapping one another, being connected together via hydrogen bonds [3,5]. The basal spacing between lamellas is approximately 0.48 nm [6].

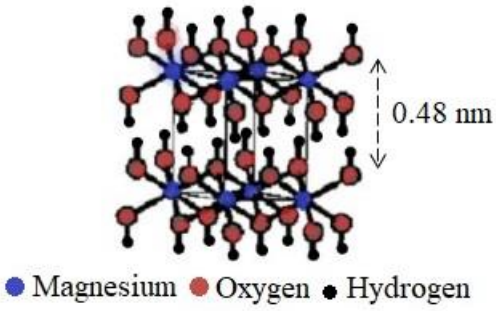

Figure 1.1: Schematic representation of brucite structure [5].

In case of hydrotalcite minerals, a fraction of Mg cations are replaced by a trivalent one, leading to formation of positively charged layers. Because the entire LDHs structure has a neutral charge, the positive lamellas are contrabalanced by anions, which are placed in the interlayer space (figure 1.2) [7]. In the interlayer space are also placed water molecules which are connected to anions and layers via hydrogen bonds. The general formula of layered double hydroxides is expressed below [5]:

$$[M^{II}_{1-x}M^{III}_{x}(OH)_2]^{x+}[A^{n-}]_{x/n} \cdot yH_2O$$

where:

- M^{II} represents the divalent cation (Mg^{2+}, Ca^{2+}, Zn^{2+}, etc);
- M^{III} represents the trivalent cation (Al^{3+}, Cr^{3+}, Fe^{3+}, Co^{3+}, etc);
- A^{n-} represents the interlamelar anion molecules (Cl^-, CO_3^{2-}, NO^{3-}, etc);
- *n* represents the interlamellar anion charge;
- *x* represents the molar ratio between $[M(III)/M(II) + M(III)]$;
- *y* represantes the interlamellar water molecules [5].

An important aspect which has to be mentioned is the cations radius. The radii of the involved structural ions must have appropriate values. Sometimes, large radius can be incompatible with the brucite-like sheet. As a consequence, the octahedral coordination is destroyed and a new coordination is formed with one water molecule from the interlayer domain [8].

From the general formula of LDHs nanomaterials can be remaked the high compositional diversity of these structures. Even if the formula implies only the presence of divalent and trivalent cations, during the time in brucie-like sheet, monovalent and tetravalent cations were introduced. In a review article published by Basu and coworkers, were presented the metals used in LDHs structures. In figure 1.3 it can be observed that many different types of metals were used to obtain synthetic anionic clays [6].

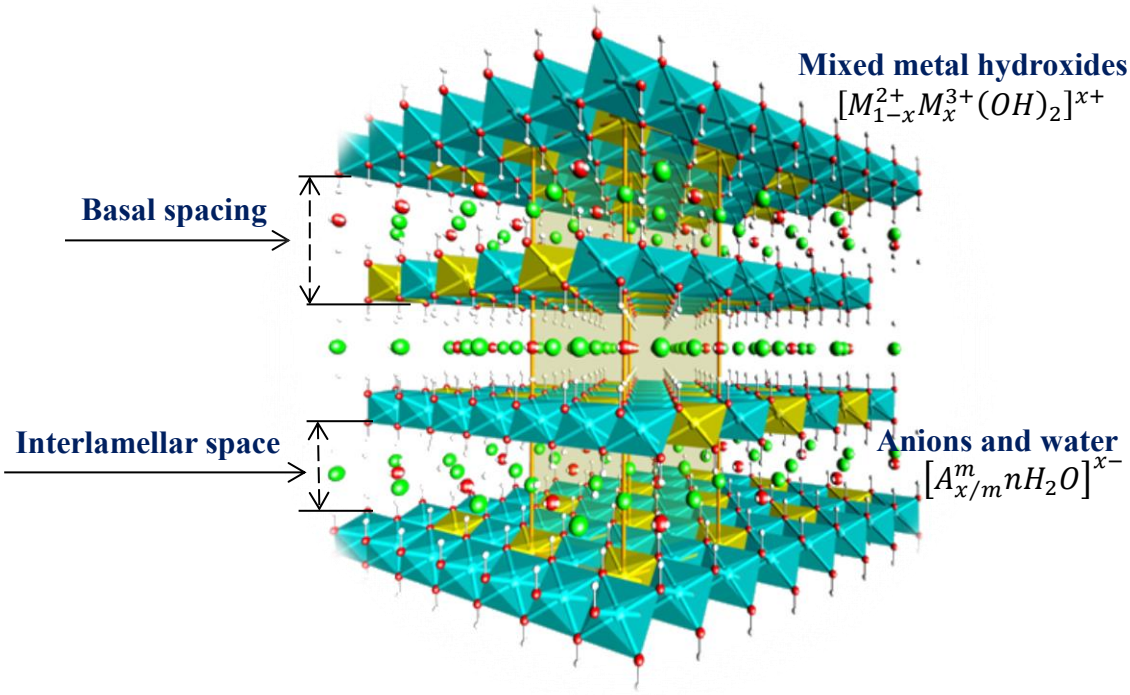

Figure 1.2: Schematic representation of layered double hydroxide structure [7].

One important characteristic of LDHs nanocomposites is their ability to incorporate in the interlamellar space different anions molecules. Distinct negatively charged species were introduced in the structure of the anionic clays during the initial synthesis or after, via ionic exchange. Some examples of anions can be [3,6]:

- *organic anions*: acids (adipic, succinic, sebacic, oxalic, chlorocinnamic), carboxylates, phosphates, alkyl sulphates;
- *anorganic anions*: F^-, Cl^-, I^-, Br^-, OH^-, $(ClO_4)^-$, $(NO_3)^-$, $(ClO_3)^-$, $(IO_3)^-$, $(CO_3)^{2-}$, $(SO_4)^{2-}$, $(WO_4)^{2-}$, $(CrO_4)^{2-}$, $[Fe(CN)_6]^{3-}$, $[Fe(CN)_6]^{4-}$, $[SiO(OH)_3]^-$;
- *heteropolyacides:* $(PMo_{12}O_{40})^{3-}$, $(PW_{12}O_{40})^{3-}$;
- *lamellar species*: $(Mg_2Al(OH)_6)^+ \cdot [Mg_3(OH)_2/Si_3AlO_{10}]^-$.

Related with anions nature, it has to be mentioned that they will chance the basal spacing of the LDH material, proportional with their dimension. In figure 1.4 is expressed the way how the interlayer space varies in function of the negatively charged species [8].

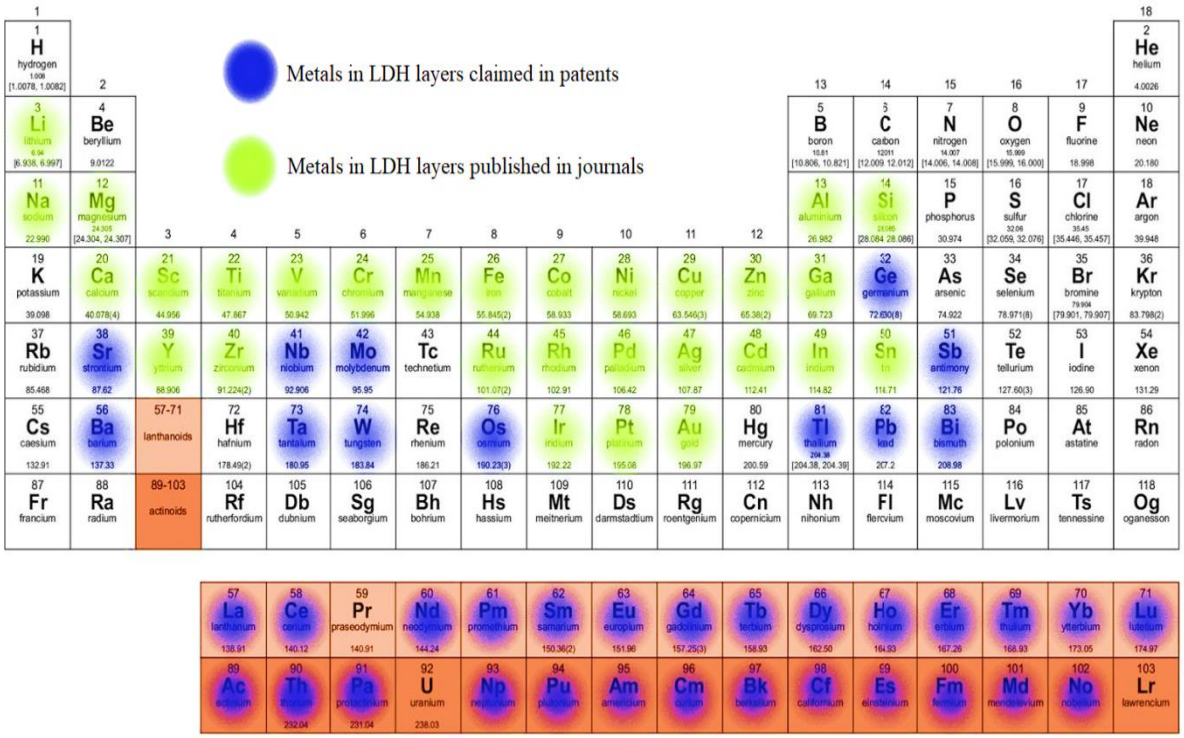

Figure 1.3: Metals used to obtain synthetic layered double hydroxides [6].

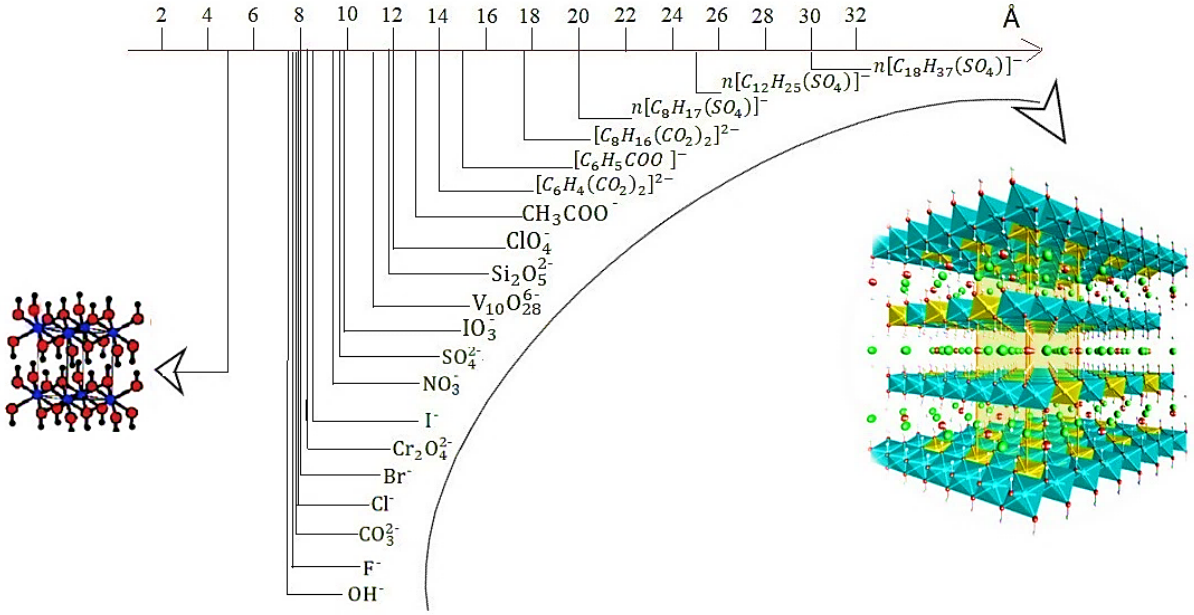

Figure 1.4: Basal spacing evolution in function of anion nature [8].

The LDHs materials present different affinities for the anionic molecules. Because the carbonate anion has the highest selectivity for these nanocomposites, the synthesis has to be

carry out in an inert atmosphere [5], if another anion, different from CO_3^{2-}, has to be incorporate in the material structure.

From the figure 1.4 can be observed that the interlayer space increases with the complexity of the anion molecules.

1.1.2. Layered double hydroxides specific properties

Layered double hydroxides had paid researchers attention due to their specific and controllable properties. Having a high compositional diversity, these anionic clays can be designed for their utilization in particular applications. Thus, varying some synthesis parameters, or using different methods of synthesis, one LDH material can have in the end a different porosity, shape or textural features compared with a LDH having the same composition, but obtained via a distinct way [9]. The fundamental properties of LDHs are the following:

- Ionic exchange capacity;
- Basic properties;
- Catalytic properties;
- Mixed metal oxide formation;
- Structural memory effect;
- Morphological and textural properties;
- Magnetic properties;
- Optical properties;
- Semiconductor properties;
- Photocatalytic properties.

a) ***Ionic exchange capacity***

The ionic exchange capacity of LDHs nanocomposites is directly correlated with their structure. Because the interlamellar space is connected to the metallic layers via electrostatic forces and hydrogen bonding [5], these nanomaterials own good exchange abilities. However, the practical exchange capacities (1-1.5 meq/g) is approximatively 50 % smaller that the theoretical one (3.3 meq/g). The exchange selectivity increases proportionally with anion charge density. An important parameter which might affect the exchange is the pH value of solution, which can favor or block the processes [10]. In a study published by Li and Ma had been shown which is the ionic exchange order for some mono- and divalent anions (figure 1.5) in case of NiAlLDHs [11]. From figure 1.5 can be concluded that the LDHs materials have a high affinity for multiple charged anions. Also, the anionic clays containing in their structure $(NO_3)^-$ or Cl^- are recommended as good precursors in ionic exchange processes [10].

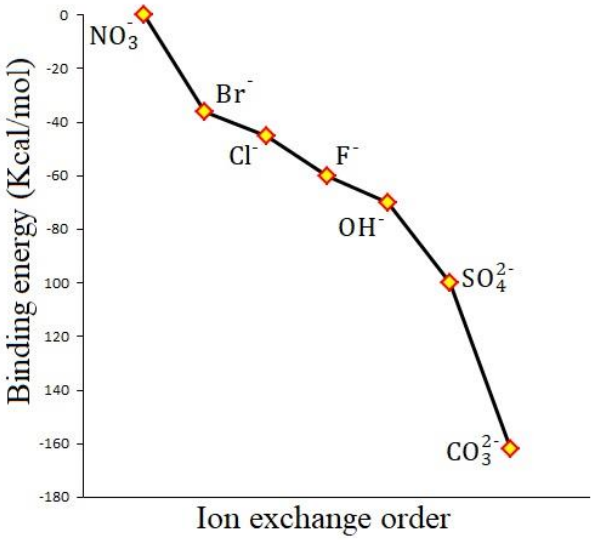

Figure 1.5: Binding energy for interlayer anions in case of NiAlLDH [11].

b) ***Basic properties***

Compared with their calcined derivatives, the fresh LDHs nanocomposites have lower basic properties. However, a difference in basicity can be observed between different anionic clays. For example, the aniconic clays based on Mg and Al are more basic then ZnAlLDH or ZnCrLDH [10,12].

c) ***Catalytic properties***

Layered double hydroxides and their derivatives were used in polymerization, condensation, oxidation, ethanolysis of propylene oxides [10,12], transesterification [13], and others catalytic processes. The main characteristic that makes these materials to be good candidates for catalysis use are their chemical and structural properties, as high surface area, good dispersion of structural metals, good thermal and mechanical stability, basic properties and also the possibility of doping with different metals or other species [14].

d) ***Mixed metal oxide formation and structural memory effect***

The thermal treatments of anionic clays can lead to a homogeneous nanocomposite formed by metal oxide and spinel-like phase, denoted mixed metal oxides (MMO). Furthermore, this method replaces with success the traditional ways of obtaining $M^{II}O/M^{II}M_2^{II}O_4$. In many cases, the resulted LDHs calcination product has superior properties compared with similar materials obtained via a different method [15–17].

The heating imposes a progressive weight loss and structural modifications. Under a continuous heating, in a given temperature range, the LDHs materials can suffer reversible or permanent modifications, in a temperature dependent manner. For instance, a heating up to 200 °C has no significant impact on lamellar structure, while a heating temperature up to 550 °C

allows the structural reconstruction of the initial LDHs. More increase of temperature will lead to a more difficult or impossible recover of the lamellar structure [5].

The structural memory effect of LDHs is their particular ability to rebuild the lamellar structure of the fresh material, when the LDH was thermal treated at a temperature up to 500 °C. In these conditions, if the resulted mixed oxide is added to a salt solution, the lamellar structure will be reformed [5,8].

e) Morphological and textural properties

Layered double hydroxides can have distinct morphological and textural properties, these features being controlled via synthesis. Using the conventional preparation methods, the LDHs can be obtained as powders, spheres, films, 1 D, 2 D LDH nanocomposites, nanoscrolls, etc. In figure 1.6 are presented LDHs images analyzed with electronic microscopy instruments [9,18,19].

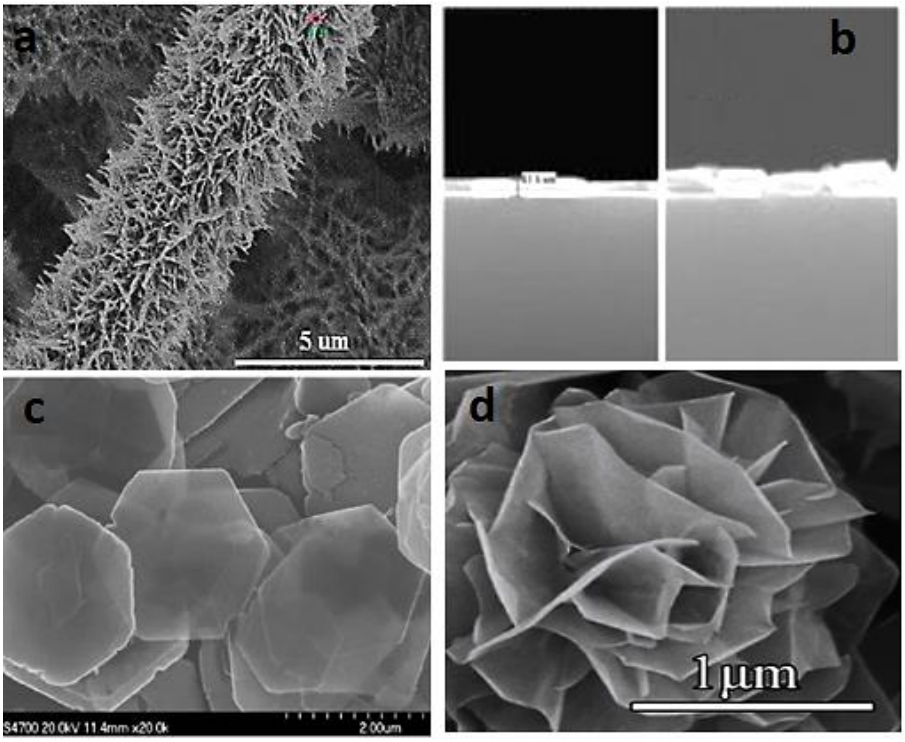

Figure 1.6: SEM images of different LDHs structures: (a) nanoscrolls; (b) 1 D and 2 D LDHs; (c) LDHs hexagonal platelets; (d) LDHs nanoflowers [9,18,19].

f) Magnetic properties

Some LDHs nanocomposites, in function of their structural metals, can exhibit magnetic properties. Thus, the usual anionic clays like MgAlLDH, ZnAlLDH, can be mixed with

magnetic particles, or, more efficient for the magnetic features, is the direct synthesis of magnetic LDHs, using salts which contain cations as Fe, Co, Ni [20,21].

g) ***Optical properties***

The anionic clays are able to absorb light. Some of them, like ZnAlLDH, MgAlLDH present absorption only in the UV region of the spectrum [22,23]. Others, like ZnCrLDHs, FeLDHs or LDHs containing Au, Ag, Pt exhibit also the ability of absorbing visible irradiation [20,24–26]. The principle that underlines the optical properties of materials is their characteristic to be formed by atoms. The atoms electrons can vibrate at specific frequency. If the electrons of a material will interact with a light wave with the same frequency, the light energy will be absorbed and further transformed in vibrations. Forward, the vibrational motion is converted to thermal energy, and in this way, the light is never released in its initial form. Thus, because the particular capacity of atoms to have distinct natural frequencies, they will absorb the light in a selective manner [27].

h) ***Semiconductor and photocatalytic properties***

The anionic clays posse semiconducting properties and due to this characteristic they can act as excellent photocatalysts in water depollution, water splitting, water oxidation, CO_2 reduction and other processes which involve LDHs activation by irradiation [28]. When a semiconductor material is excited by an appropriate source, it can generate, because of the electron transition from valence band to the conduction band, electron-hole pair which will initiate oxidation reactions [6,29]. Notable catalytic performances were reported for the hybrid formulation between different nanoparticles and Zn, Ni, Cr, Mg layered double hydroxides. Thus, G. Chen *et. al*., using specific synthesis methods, have obtained Pt/ZnTiLDHs structures and they used them successfully in rhodamine B photodegradation [30]. Furthermore, catalysts like ZnCrLDH, ZnTiLDH, ZnCeLDH, Ce/ZnSnLDH, Ce/ZnTiLDH, Ti/MgAlLDH, were used for the photogedradation of aqueous solution of phenol or methyl orange, or in the CO_2 photocatalytic reduction and oxygen photocatalytic generation [31–35].

1.1.3. Layered double hydroxides synthesis methods

Many methods were used for LDHs formulation synthesis and in general, in function of the required composite properties, can be used preferential synthesis ways. The factors which influence the properties of the obtained catalyst are the pH (influence the crystallinity, the unite cell parameters) [36], the temperature (influences the cation stoichiometry), salt solution concentrations (gives the ration between the cations), athmospheric condition of maturation

(controls the nature of the interlayer anions). In figure 1.7 are presented the most important methods for anionic clays preparation.

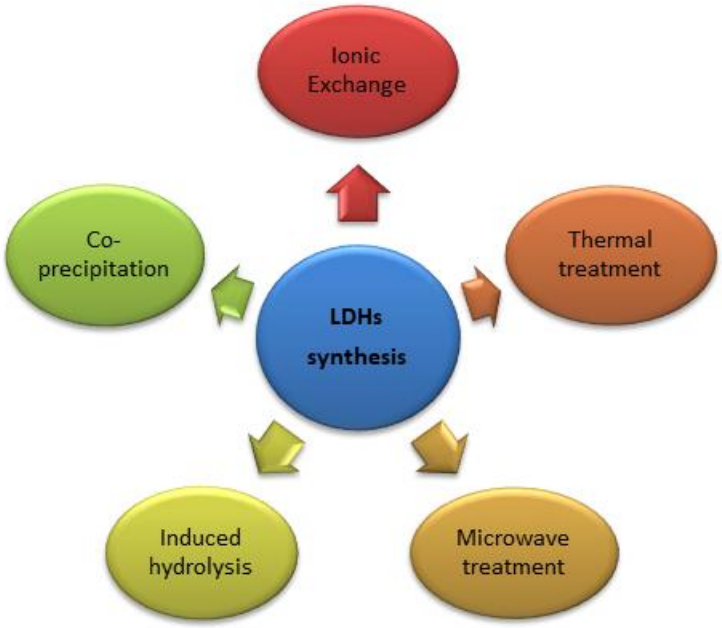

Figure 1.7: Layered double hydroxides synthesis methods [36].

a) ***Direct co-precipitation method***

The coprecipitation is the most used LDHs synthesis technique [37]. This method implies the addition of a base solution to salt mixtures, containing the metal cations, generally M (II) and M (III), and the anion which will be incorporated in the material structure. Regarding the way how the precipitation is made, three different methodes can be discussed:

- Titration with NaOH and/or $NaHCO_3$ denotted secvential precipitation or the pH increasing method;
- The low supersaturation at constant pH, when the pH value is controlled by the simultaneous slow addition of precipitation agents (NaOH and $NaHCO_3$ and the metal solution salt; with this method can be obtained anionic calys with a good homogeneity and with well defined crystals.
- The high supersturtion at constant pH, when the precursor salts and the prcipitation agents are added very fast [3].

In particular, layered double hydroxides with a high homogeneity can be obtained via low supersaturation co-precipitation at constant pH. The LDHs materials obtained through this method are well crystallized, with small particles dimensions, high surface area and high pores diameter [8]. The precipitation pH will influence the structural, textural and chemical properties of the material. Generally, the co-precipitation involves de next steps, expressed in figure 1.8.

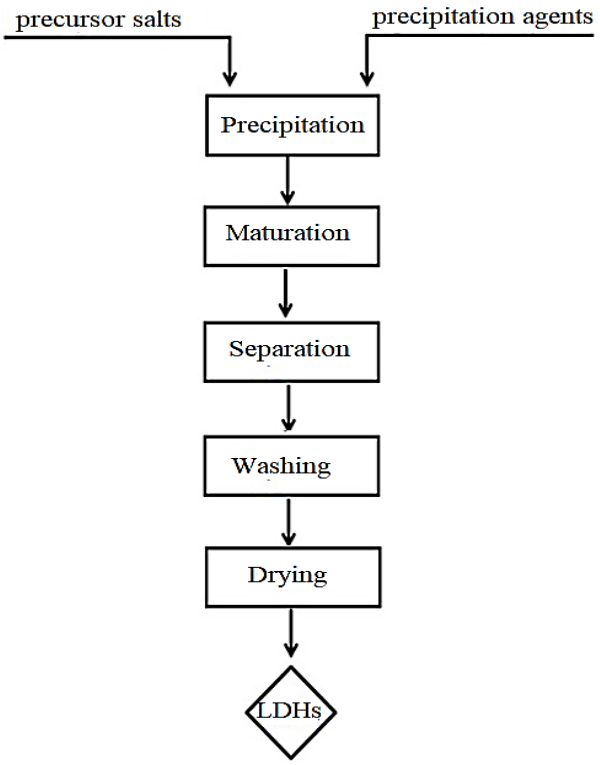

Figure 1.8: The main steps in LDHs preparation using co-precipitation method.

The salts and precipitation agents solutions are prepared in bidistilated water and added in the same time, keeping the pH at a constant value, which was fixed before starting the synthesis. The next step, maturation is made under continuously stirring. The maturation time can control the further properties of the LDH material. Abderrazek et al. prepared ZnAlLDH materials at different aging times (1, 2, 4, 12, 24 h). The materials characterization via XRD, FTIR and TG, show that the LDH resulted after 24 h maturation time has the best crystallinity [38]. The separation of the precipitate can be made through filtration or centrifugation, followed by several washings steps designed to remove the base excess and the impurities. The drying is made at a temperature up to 100 °C.

*b) **Ionic exchange method***

The ionic exchange method is mostly applied when the coprecipitation can not be used [3]. In this method the original anion of the layered structure is replaced by another anion (figure 1.9). For the exchange reaction, the LDH is mixed with a precursor solution containing the new anion and stirred together. To increase the exchange rate, the solution can be sonicated.

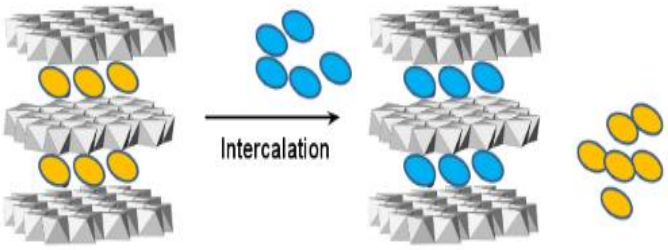

Figure 1.9: Schematic representation for the layered double hydroxides preparation by using the ionic exchange method.

1.1.4. Physico-chemical characterization of the layered double hydroxides

Different techniques as X-Ray Diffraction (XRD), Fourier-Transform Infrared Spectroscopy (FTIR), Thermogravimetric Analysis (TG), Scanning Electron Microscopy (SEM), Transmission Electron Microscopy (TEM), Energy-Dispersive X-ray Spectroscopy (EDX), X-ray Photoelectron Spectroscopy (XPS), UV-Vis Spectroscopy (UV-Vis) were used for the structural, chemical, Physico, morphological, optical and thermal characterization of LDHs nanomaterials [39]. The necessity of using these characterization techniques is not only to confirm and to understand the structure and the properties of the analyzed materials, but also to find a correlation between synthesis method, structure and properties. The main goal is to find the optimal condition in designing the best materials for particular application.

*a) **X-ray Diffraction (XRD)***

The solid materials can be as follow:

- crystalline, when the atoms are regularly arranged, and the crystal is formed by the repetition of a volume element, denoted elementary cell (the elementary cell is described by three axes: a, b, c and the angles between axes: alpha, beta and gamma);
- amorphous, when the atoms are irregularly arranged.

The X-rays are electromagnetic radiations similar to light, with much smaller wavelengths (10^{-5} Kx si 10^{2} Kx (1Kx = 1,00202 Å ; 1 Å =10^{-10} m) and much larger energies, having a signifiant capacity of matter penetration.

X-Ray diffraction is an analysis used to investigate crystalline solides. It is a non-destructive analysis, offering informations about the structural defects, particles dimensions and the composition of phases. The diffraction take place at the interaction between the radiation and a periodic system, when consecutive interferences, at particular angles are produced [40]. The crystalline struture of a material is defined as the repetition of the atoms plans which form the structure. When an X-ray beam interacts with the atoms, some of the X-rays are

transmitted, others are absorbed or reflected, while some of them are diffracted. The materials possess different abilities to diffract the X-Ray, even if they have the same chemical composition. For instance, for three different materials, but which are chemically identical (glass, quartz and cristobalite), the XRD spectra are distinct (figure 1.10). The glass is an amorphous material, while the quartz and the cristobalite are crystalline materials [41].

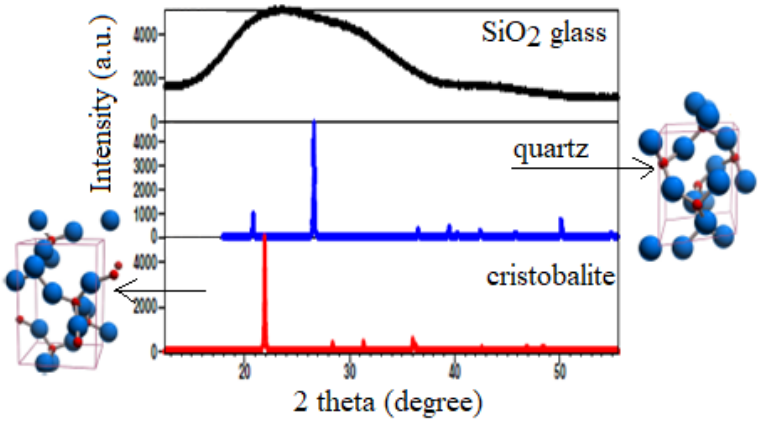

Figure 1.10: XRD spectra for glass, quartz and cristobalite [41].

As it can be seen from the figure 1.10, an XRD spectrum expresses the dependence between the intensity and the diffraction angle. So, using the diffracted rays, the distance between the atom plans can be calculated with the help of Bragg's law (eq. 1.1):

$$n\lambda = 2d \sin\theta \quad (1.1)$$

Where:

- n represents the diffraction order;
- λ represents the incident X-ray wavelength;
- d represents the interplanar distance;
- θ represents the incident angle of the X-ray [41].

A very simple procedure for solids XRD analysis was developed simultaneously in Europe and the USA, when Hull, Debye and Scherrer designed a powder-diffraction analysis room. Their method implied the utilization of a small quantity of sample prepared as a very fine powder, bonded on a rotating glass support. While the sample is continuously rotated along the axes of the cylindrical chamber, it is crossed by the incident X-ray. The diffracted radiation is projected on a film placed on the interior surface of the cylinder (figure 1.11) [42].

Regarding the layered double hydroxides, the XRD analysis gives information about crystallinity, interlayer anion nature, nanoparticles dimension, confirming in the same time the structure of the material. The etalon of the anionic clays is considered to be the natural hydrotalcite. The XRD spectra of LDHs materials presents some particularities, close to the one of hydrotalcite (figure 1.12), with intense and symmetric reflections at small angles, assigned for (003), (006) and (009) plans and with less intense and asymmetric reflections, at higher angles, attributed to (015), (018) and (110) plans [43].

From a LDHs X-Ray diffraction spectrum can be calculated the lattice parameters of the material, *a* and *c*. The lattice parameter *a*, calculated as $2d_{(110)}$, shows the distance between the

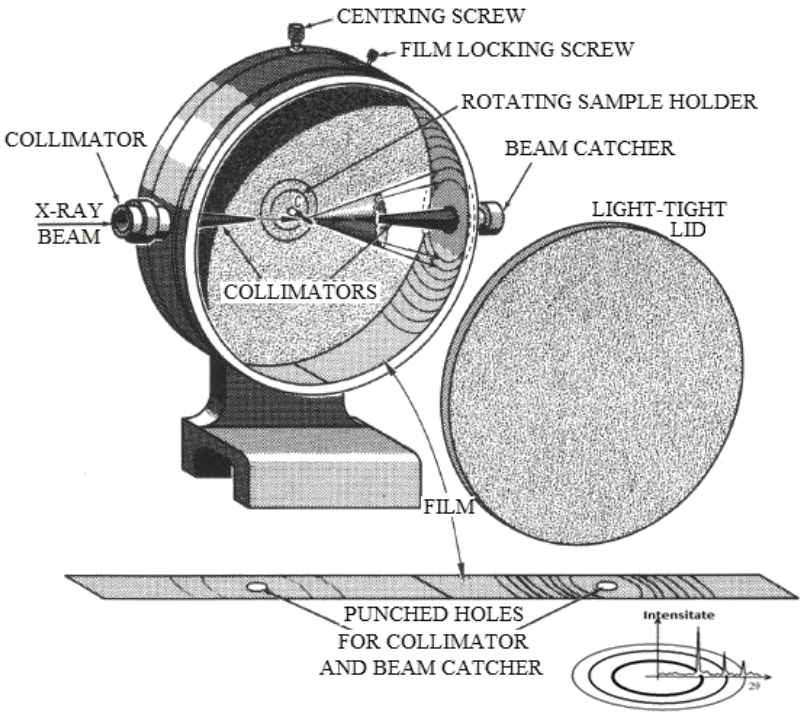

Figure 1.11: Powder diffraction Hull/Deby-Scherrer camera [42].

structural cations of the LDH. The value of this parameter is different in function of the nature of the metals from the brucite layers, and it can confirm the successful incorporation of a new metal in the nanocomposite. The lattice parameter *c*, calculated as $3d_{(003)}$, indicates the nature of the interlayer anions. Also, the value of c can indicate a modification of anions orientation, generally for the large anions, as the organic ones [5]. In case of the NPs/LDHs hybrids, the identification of the dispersed nanoparticles on LDHs can be possible only if their concentration is higher than 4%.

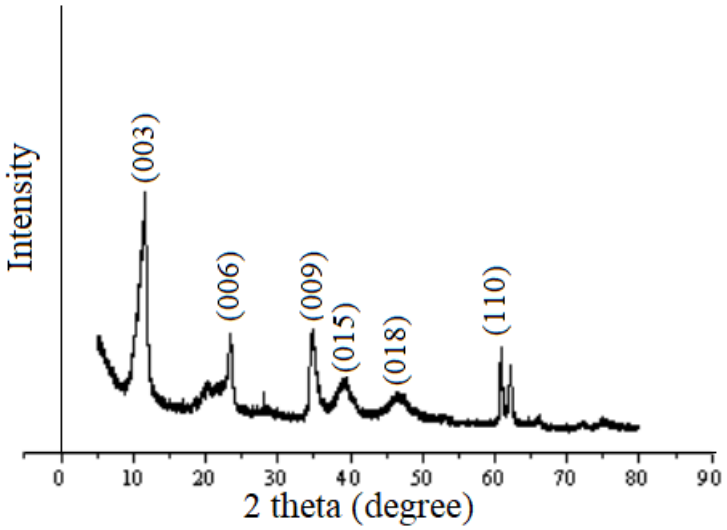

Figure 1.12: The XRD spectrum of hydrotalcite [43].

The XRD analysis allows the determination of crystals dimension, using the Scherrer equation (eq. 1.2), which says that the peak width (β) is inversely proportional with the crystallite size (D).

$$D = \frac{k \cdot \lambda}{\beta \cdot \cos\Theta} \tag{1.2}$$

- k – is the shape factor, generally equal with 0.9
- λ – is the X-ray wavelength
- Θ - is the Bragg angle [44].

b) *X-ray Photoelectron Spectroscopy (XPS)*

The XPS analysis is a sensitive technique used for the surface investigation of a material. It gives qualitative information about the specimen as its chemical composition, and the chemical and the electronic state of the constituent elements of the material. The XPS spectra are obtained when the material is irradiated with an X-Ray beam of electrons. The energy of the photon, hν, can be absorbed by one electron of the sample atom, which will be emitted through sample with a particular kinetic energy. In the absence of any inelastic collisions, the emitted photoelectron conserves its kinetic energy until it leaves the material. With the help of an electrostatic analyzer, the kinetic energy of the photoelectron can be experimentally measured. The kinetic energy (E_K) of the photoelectron is in direct relationship with the binding energy (E_B) of the electron of the sample atom, as follow (eq 1.3):

$$E_B = h\nu - E_K \quad (1.3)$$

This equation 1.3 allows the identification of the atom which emitted the photoelectron, because the binging energy is particular for each atom, being like a print [45].

The X-Ray photoelectron spectroscopy can be used for the analysis of a large number of materials like polymers, inorganic materials, ceramics, semiconductors, bio-materials, oils, woods and others.

Normally, XPS technique can detect all the elements which own an atomic number equal with three or higher.

Regarding the detection limit, usually the XPS instruments detect parts per thousand. However, it is possible to detect parts per million, but for this, special condition are required, as a long time for the data collection, or high concentration at top surface [46].

The most important components of an XPS apparatus (figure 1.13) are the X-Ray source, ultra-high vacuum (UHV) chamber, an electron energy analyzer, sample chamber, an electron collection lens, nickel-iron magnetic field screening, and an electron detector system.

An XPS spectrum is a graphical representation of the detected electrons number in function of the binding energy assigned to the detected electrons. Each electron produces a characteristic set of peaks, at a particular energy binding, allowing the identification of each element present in the sample. The peaks which form the spectrum corresponds to electrons configuration, while the number of the detected electrons is directly correlated with the quantity of element present in specimen [45].

In figure 1.14 are presented the XPS full spectrum NiTiLDH and the high resolution XPS spectrum of Ni2p, Ti2p and O1s. The material was synthetized by the R. Chowdhury and G Bhattacharyya and used for the removal of the organic dye under visible light irradiation. The full XPS spectrum confirms the presence of the metals with oxygen vacancies. It was identified the presence of Cl2p, C1s, N1s, Ti2p, O2p [47].

The high resolution spectrum of Ni2p (see figure 1.14 b) reveals characteristic peaks between 854-870 eV. The peak around 854 eV is assigned to the Ni^{2+} cations within NiO phase, while the peak at 857 eV is assigned to Ni^{2+} cations in the composite oxide structure. Between 871.6 and 885 eV is represented the $Ni2p_{1/2}$ region. The metallic Ni(0) was also detected at 873.2, suggesting a reduction of the Ni^{2+} ions on the LDH surface [47].

The high resolution spectrum of the Ti2p (figure 1.14-c) shows at the 455.2 and 461.5 eV the presence of two asymmetric peaks attributed to the $Ti2p_{3/2}$ and $Ti2p_{1/2}$ states of Ti. Besides the Ti^{4+} species, Ti^{3+} was also observed at 457.9 and 463.8 eV, assigned to the $Ti2p_{3/2}$ and $Ti2p_{1/2}$ peaks [47].

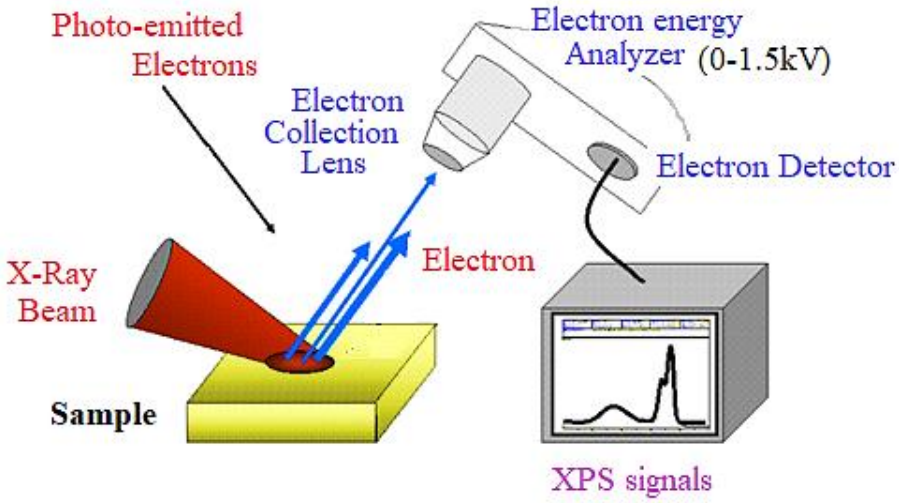

Figure 1.13 Basic components of XPS apparatus [46].

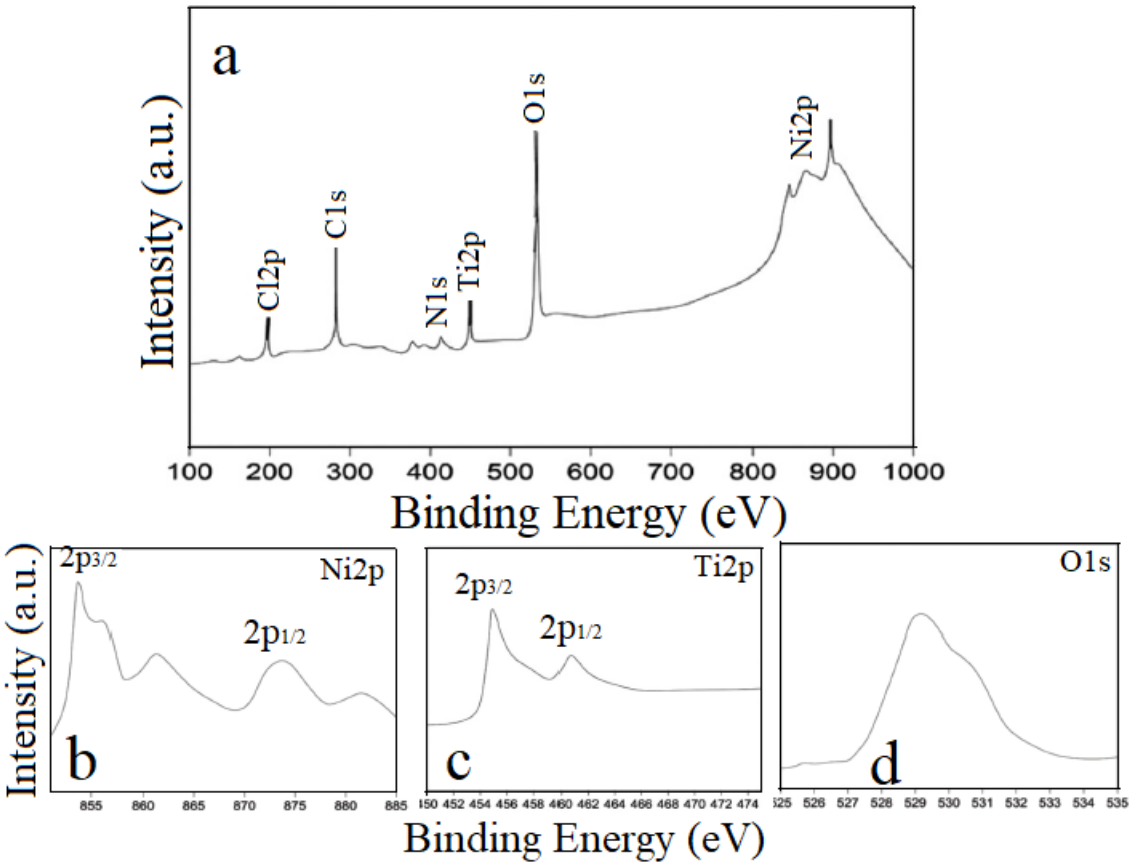

Figure 1.14: XPS spectra of NiTiLDH: a) full spectrum, and the high resolution spectra of b) Ni2p, c) Ti2p, d) O1s [47].

For the O1s, the high resolution XPS spectrum reveals the presence of two distinct surface oxygen species (figure 1.14 d). The peak around 529.6 eV can be attributed to the

lattice oxygen linked to the metal cations structure, while at a binding energy of 530.8 eV it can be assigned to the surface oxygen, including the oxygen species of the OH groups [47].

c) IR Spectroscopy with Fourier Transform (FTIR)

Infrared spectroscopy with Fourier Transform is a technique which gives information about the chemical bonds from a material, and it is used particularly for the nondestructive analysis of the solids and thin films. Liquids and gases can be also analyzed, but in the most of the situations, for a complete characterization of the sample, complementary analyses are required [48].

The IR spectrum is a graphical representation of the absorption curve of the IR radiation in function of the wavenumber or wavelength. The IR radiation absorption spectra are obtained because of the capacity of the molecules to vibrate at particular frequency. Mostly, the IR spectrum is expressed as percentage transmittance (T%) or absorbance (A%) in function of wavenumber. The relationship between the wavelength (λ) and wavenumber ($\bar{\upsilon}$) is given by the next relation (eq. 1.4):

$$\bar{\upsilon} = \frac{1}{\lambda} \tag{1.4}$$

The percentage transmittance/absorbance are defined as (eq 1.5, 1.6)

$$T(\%) = \frac{I}{I_0} \cdot 100 \tag{1.5}$$

$$A(\%) = \frac{I_0 - I}{I_0} \cdot 100 \tag{1.6}$$

where I_0 and I are the intensity of incident radiation and the intensity of transmitted radiation.

The IR spectrometry is based on the intensity modification of IR radiation, as a consequence of its interaction with the specimen. This modification is possible because the molecule is able to absorb only certain energy quanta. In other words, the sample absorbs the radiation selectively and this takes place only at specific wavenumbers, in function of the nature of chemical bonds present in the molecule. When the energy is absorbed, the chemical bond increases its vibrational energy level. The energy absorption leads to the appearance on IR spectrum of absorption bands. Each band corresponds to the vibration of a certain binding from the irradiated molecule. Generally, a binding from a molecule can vibrate in two ways (figure 1.15):

- stretches vibration, *v*, which take place along the bond;
- deformation vibrations**,** δ, when the angle between two bindings is deformed [48].

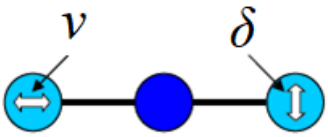

Figure 1.15: The two types of vibrations of a polar covalent bond involved in IR absorption.

The apparatus used in IR spectroscopy with Fourier Transform have as principle components the radiation source, the interferometer, sample compartment, detector, amplifier, convertor and a computer (figure 1.16). The IR source, generate the light beam, which is passed through the interferometer, it reaches the sample, and after transmitted to the detectors. The obtained signal is amplified and sent to a computer where the Fourier transform mathematical mechanism is applied to the raw data [48].

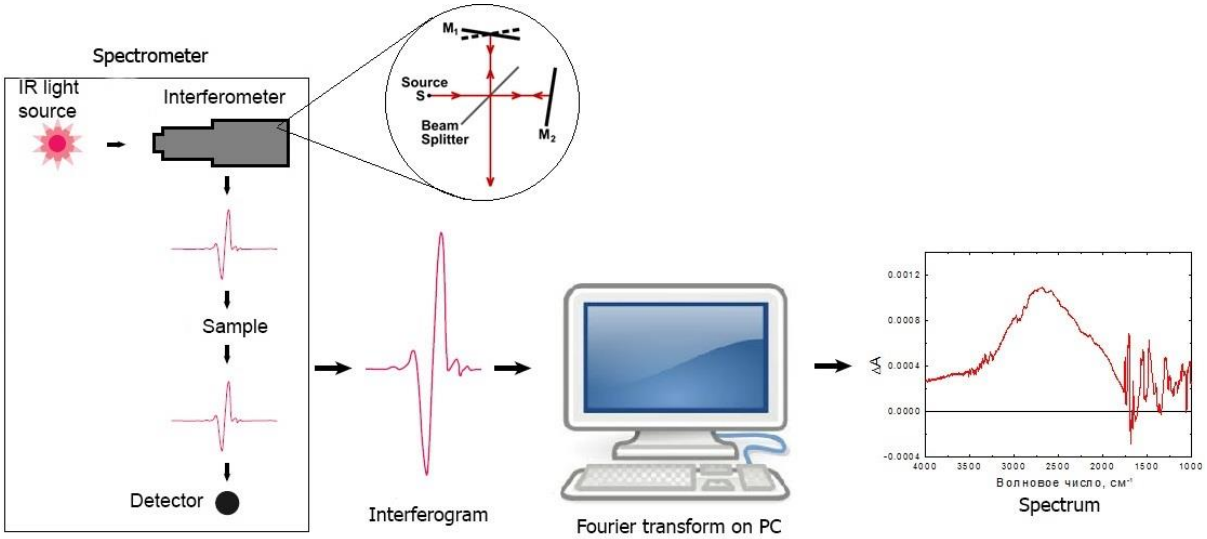

Figure 1.16: The block scheme of IR spectrometer with Fourier Transform [49].

The main difference between an IR and a FTIR spectrometer is the presence of the interferometer component in case of the FTIR instrument. This component has in its structure a beam splitter and two perpendicular mirrors; one mirror is movable (M1), and the other one is stable. The beam splitter will separate the radiation in half. One half is transmitted to the stationary mirror and the other part, reflected to the movable one. When the divided beams hit the mirrors, they are reflected back, and recombined by the beam splitter [49].

FTIR analyze is a useful tool for LDHs materials characterization because it offers information about the nature of the bindings formed between the anions and the brucite-like lamella. Furthermore, the anions present, in function of their type, different absorption bands, and with this characterization can be verified if after synthesis, the desired anions were incorporated in the material structure. Additionally, the FTIR analyze can give information about how different treatments, as calcination, affected the initial structure of the material.

The IR spectra of MgAlLDH and ZnCrLDH (figure 1.17) show the characteristic vibration bands which are particular to the layered double hydroxides, with absorption band

around 3450 cm^{-1}, associated with O-H binding, from metal-hydroxyl groups, followed by another absorption peak at 1635 cm^{-1} assigned to interlayer water. Also, the signal for CO_3^{2-} is

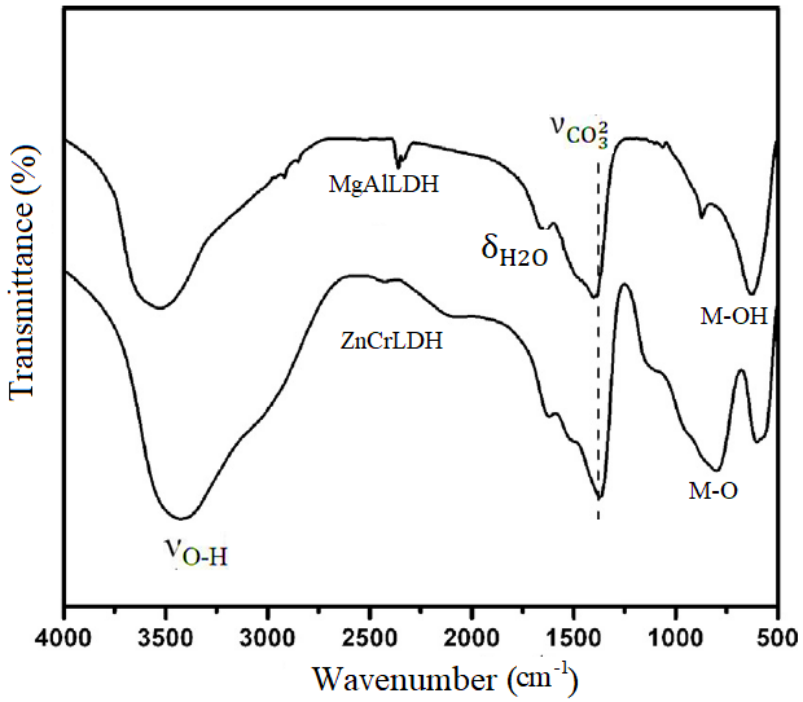

Figure 1.17: FTIR spectra of MgAlLDH and ZnCrLDH [50].

present around 1384 cm^{-1}. At lower wavenumbers, 500-800 cm^{-1} can be noticed the absorption bands characteristic to metal-oxygen (M-O) and metal-hydroxyl (M-OH) [50].

*d) **Photoresponsive characteristics studied by UV-Vis spectroscopy***

The optical analysis methods are based on the interaction of the electromagnetic radiation with the atoms or molecules of the specimen. As a consequence of these interactions, absorption, emission and diffusion phenomena take place, which can be experimentally measured. These methods give qualitative, quantitative and structural information about the analyzed sample, and they are nondestructive analysis techniques [51].

The chemical species (atoms and molecules) are stable only at particular values of the energy. The stationary state having the lowest energy is denoted *fundamental state* (E_0), and the rest of the stationary states with higher energies, are named *excited state* (En). The transition of chemical species for a stationary state to another one can be possible with the absorption or the emission of particular quantity of energy, as illustrated in figure 1.18 [51].

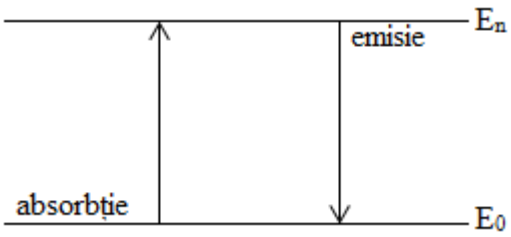

Figure 1.18: Schematic representation of electromagnetic radiation adsorption/emission phenomena [51].

From figure 1.18 can be observed that through energy absorption, the atoms or molecules are passing to a superior energy state, while when emission take place, the chemical species return to an inferior energy state. The energy difference of the involved stationary state is named *transition energy* and it depends on radiation wavelength or frequency (eq 1.7):

$$\Delta E = E_n - E_0 \tag{1.7}$$

The image of each transition between two discrete energy levels gives a *spectral line*, characterized by the radiation wavelength (λ) and frequency (ν) (eq. 1.8, 1.9):

$$\nu = \frac{\Delta E}{h} \tag{1.8}$$

$$\lambda = \frac{c}{\nu} = \frac{c \cdot h}{\Delta E} \tag{1.9}$$

where *c* is the speed of light in vacuum and *h* is Plank constant. The totality of the spectral lines which correspond to the transitions between the energy states, ordered in function of the radiation wavelength or frequency, forms the *spectrum* of the sample [51].

The *UV-Vis absorption spectroscopy* is a method based on the ability of the sample, whatever its aggregation state is, to absorb electromagnetic radiations from ultraviolet-visible domain. The UV-Vis absorption spectrum is a graphical representation of the quantity of the absorbed radiation, in function of the radiation wavelength or frequency. The quantitative law of the UV-Vis spectroscopy is the Lambert-beer law (eq. 1.10):

$$A = \varepsilon \cdot l \cdot c \tag{1.10}$$

where: *A* is the absorbance; ε is the *molar absorption coefficient and l is* the length of the solution that light passes through; *c* is the sample concentration. During the time different spectrometers were designed, but the most used is the double-beam spectrometer, whose schematic representation is presented in figure 1.19.

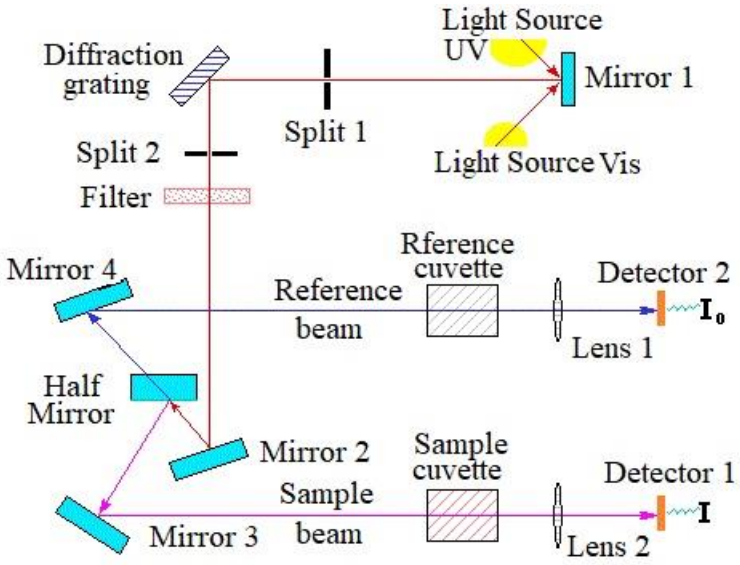

Figure 1.19: Schematic representation of double-beam UV-Vis spectrometer [52].

The UV-Vis spectrometer principle of operation involves the separation of a beam of light into its component wavelengths using a diffraction grating. Each single wavelength beam is reflected by mirror 2 to a half mirror which will split the beam in two similar beams, with the same intensity. One beam will reach at mirror 4, it will be reflected, and will pass through the reference cuvette. The other beam will be reflected by mirror 3 and the beam will pass through sample cuvette. The resulted intensities after the interaction between the light and sample/reference are measured by detectors and compared. Generally, the reference is considered to have a very small capacity of absorbing light, and for this reason its intensity is denoted I_0. The intensty of the ligth that will cross the sample is denoted with *I.* Normally, if a sample compound, at a specific wavelength, does not absorb the light, $I = I_0$. Then, when the compound absorbs, the intensity is smaller than I_0 and the difference $I_0 - I$ is represented as a wavelength function. The absorbance is calculated as $A = \log I_0/I$. The absorbance can be expressed also as transmittance, which is $T = 1/A = I/I_0$ [52].

The LDHs optical properties are investigated to confirm their capacity to absorb the electromagnetic radiation and to prove the presence of different cations in the material structure. This analysis can be made for the fresh nanomaterial, after LDHs synthesis, but also for the materials formed via different treatments applied to these, like reconstruction and calcination. The analysis of the materials obtained after calcination and reconstruction is important because in this way can be investigated how these two treatments affect the initial optical properties of the material. Thus, having information about the physico-chemical properties of these formulations can be anticipated and understood their behavior in the applications for which they were designed. In figure 1.20 are presented the diffuse reflectance UV-Vis spectra for three ZnLDHs materials: ZnCeLDH, ZnTiLDH, ZnCrLDH. May be observed that ZnCeLDH and ZnTiLDH present absorption only in ultraviolet region of the spectrum, with the most intense bands at 280 nm (ZnCeLDH) and 304 nm (ZnTiLDH).

Contrawise, ZnCrLDHs has three absorption maxima, two in the visible region (410 nm and 570 nm) and one in the UV, around 210 nm [32] . These results can indicate that ZnCrLDHs is a material which can be used in application initiated by visible light.

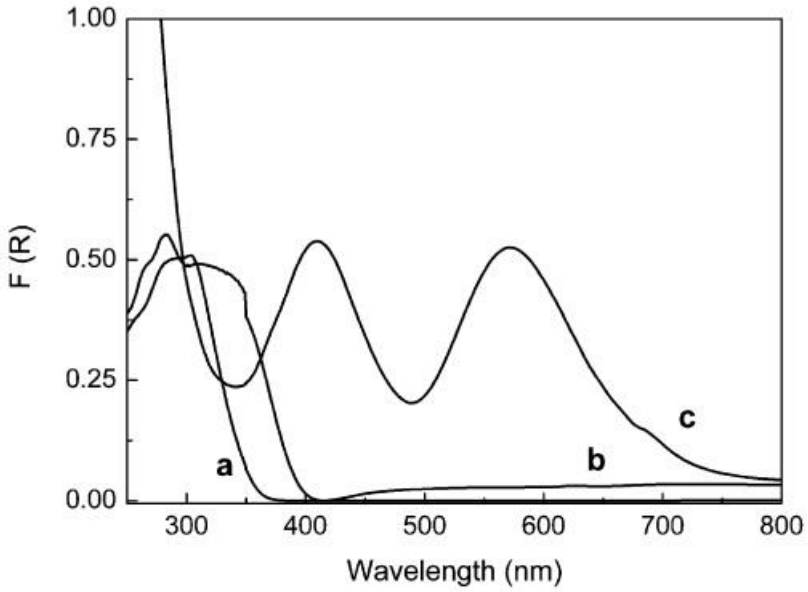

Figure 1.20: UV-Vis diffuse reflectance spectra for three ZnLDHs materials: a) ZnTiLDH, b) ZnCeLDH, c) ZnCrLDH [32].

Textural properties studied by SEM/TEM analyses

The electronic microscopy appeared as a solution for the optical microscopy limitations, becoming one of the most preformat and versatile technique for nanomaterials characterization [53].

At the beginning of XX century was discovered that the accelerated electrons can behave in the same way like the light. Possessing the propriety of moving in a straight line, the electrons have wavelengths with 100.000 smaller than those of the light. Furthermore, it was noticed that the role played by the glass lens, can be also played by electric and magnetic fields, in case of the use of electrons. So, starting from these characteristics, in 1931 first transmission electronic microscope was designed [54]. The electronic microscopes use instead of light an electrons beam, and for the particles focalization, electromagnetic lens are used.

When an electrons beam hits the sample, different signal are produced, as expressed in figure 1.21. In function of the collected signal, textural, morphological, and compositional information can be obtained.

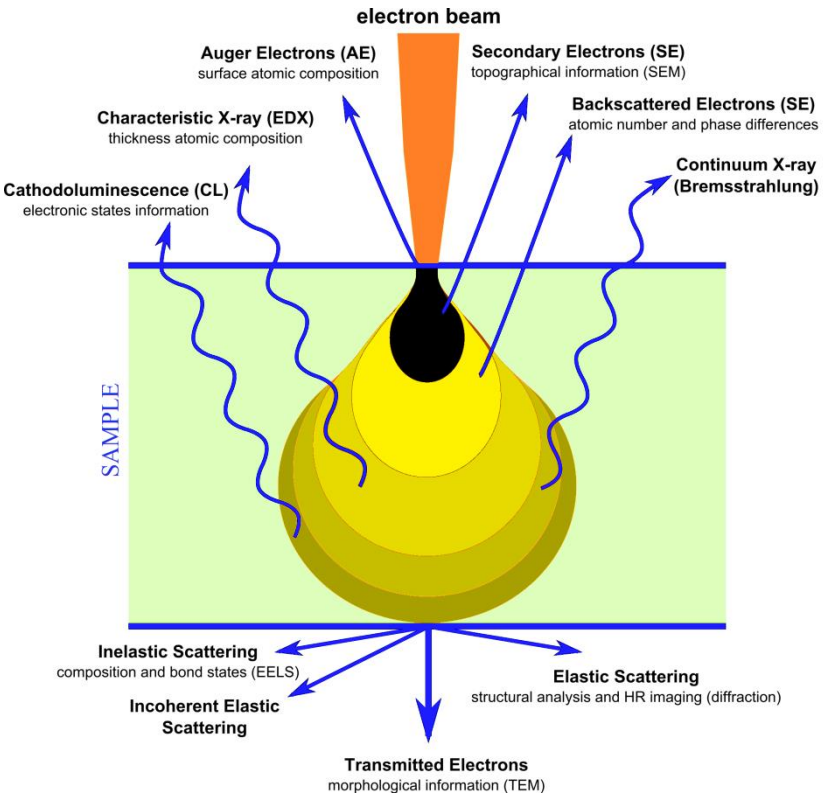

Figure 1.21: Signals produced at the interaction of electronic beam with sample [55].

e) Scanning electron microscopy (SEM)

This type of electronic microscopy uses an electrons beam which possesses a high energy, to generate signals at the surface of the solid sample. Figure 1.21 reveals the formation at the top of the specimen of secondary and backscattered electrons which are captured and used in sample analysis.

The components of an electronic microscope are: electron source (tungsten filament, field emission gun or solid state crystal) lenses, scanning coil, sample chamber, detectors (figure 1.22). The electron source is placed in the top of the instrument and it has the role to generate the required electrons for the SEM analyze. The electromagnetic lenses control the electrons path to the sample. The sample room is the space where the specimen is placed and fixed in order to be examined. The detectors collect the electrons coming from the sample (only secondary and backscattered electrons) and convert them in analytical signal, which can be easily interpreted by the researcher. At the end of analyze, a 2D image with information about

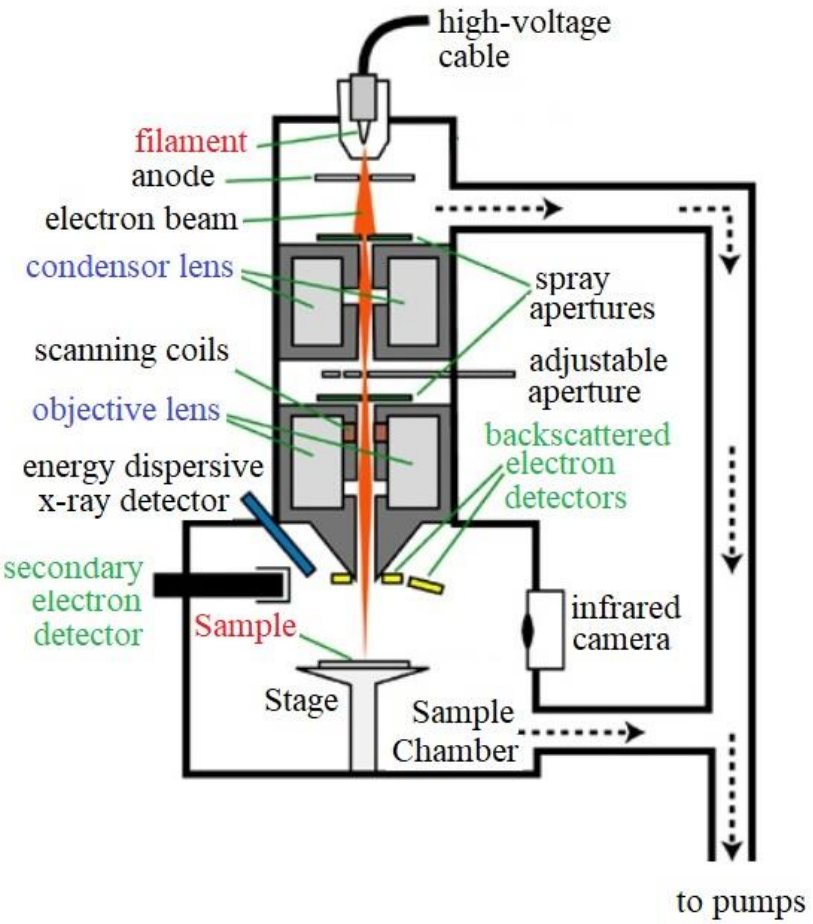

Figure 1.22: Scanning electron microscope components [56].

.

the material surface, shape, particles dimension, orientation and agglomeration grade is obtained. Being a versatile and powerful technique, SEM analyses is used for the investigation of large number of materials, including layered double hydroxide nanocomposites. Many researchers used SEM technique for the surface analysis of fresh, calcined and reconstructed LDHs nanocomposites [57,58].

Figure 1.23 presents the SEM images of MgAlLDH obtained via hydrothermal method. It can be observed that the material is formed from micrometric hexagonal platelets which overlap one on other. This is the typical morphology of the layered double hydroxides [9]. However, in function of the synthesis conditions and the used regents, the morphology of the composite can be modified. X. Wang and co-workers obtained MgAlLDH with globular agglomerated crystals, by intercalating in the material structure chromium complexes [59].

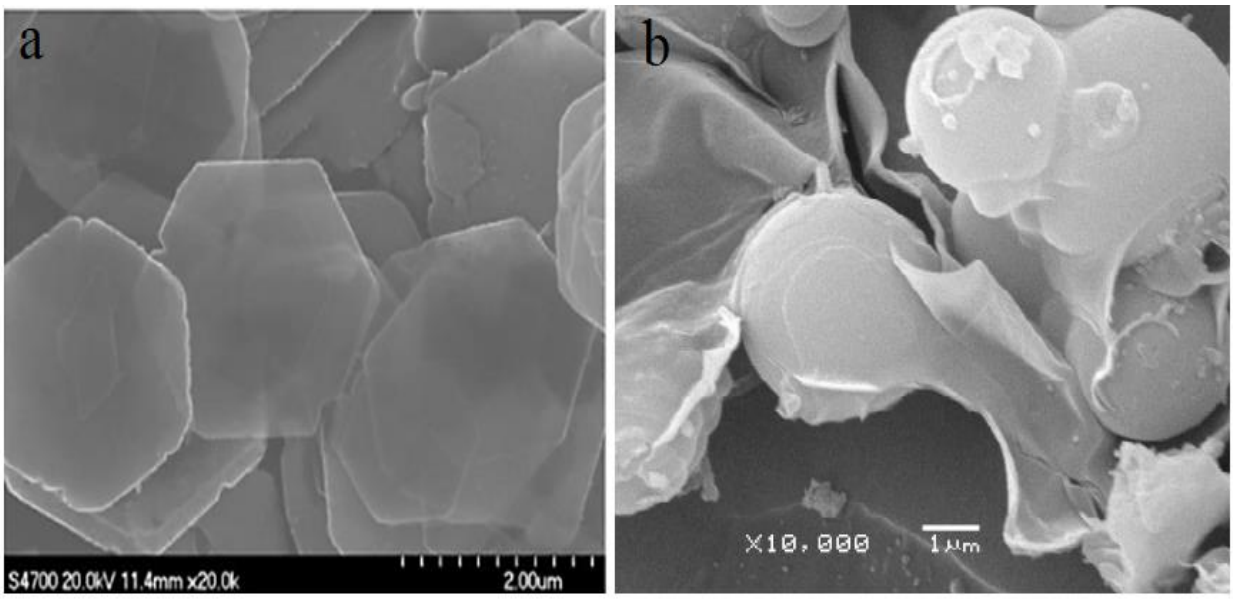

Figure 1.23: Different morphologies for the MgAlLDH material; a) hexagonal platelets, b) globular crystals.

f) Transmission electron microscopy (TEM)

Transmission electron microscopy is a technique in which the electrons are transmitted through an ultrathin specimen (< 100 nm) to form an image. As discussed above, when the electrons hit the sample, they are affected in different ways. Some of them are total or partial absorbed by the specimen, others are scattered, and others are passing through the sample without any changes. The transmitted electrons, in function of their interaction with the sample, continue to move inside of the microscope column, with different energies values. When these electrons will come across to a fluorescent screen, they will be detected and further a 2D image of the sample will be obtained. The image is formed by darker areas assigned to the regions with high electrons absorption, and brighter areas attributed to low electrons absorption regions [60].

The transmission electron microscope (figure 1.24) is composed by a vertical cylinder with electron source, vacuum, electromagnetic lens, sample holders and detectors.

The electrons are emitted by a cathode, being accelerated by an anode, and after they are passed through an aperture in the vacuum chamber. The electron beam is controlled by the electromagnetic lens.

The TEM analysis gives information about the shape and particles dimension, nanoparticles dispersion on a surface, and also about the material composition and crystalline structure. TEM analysis is very useful for NPs/LDHs investigation.

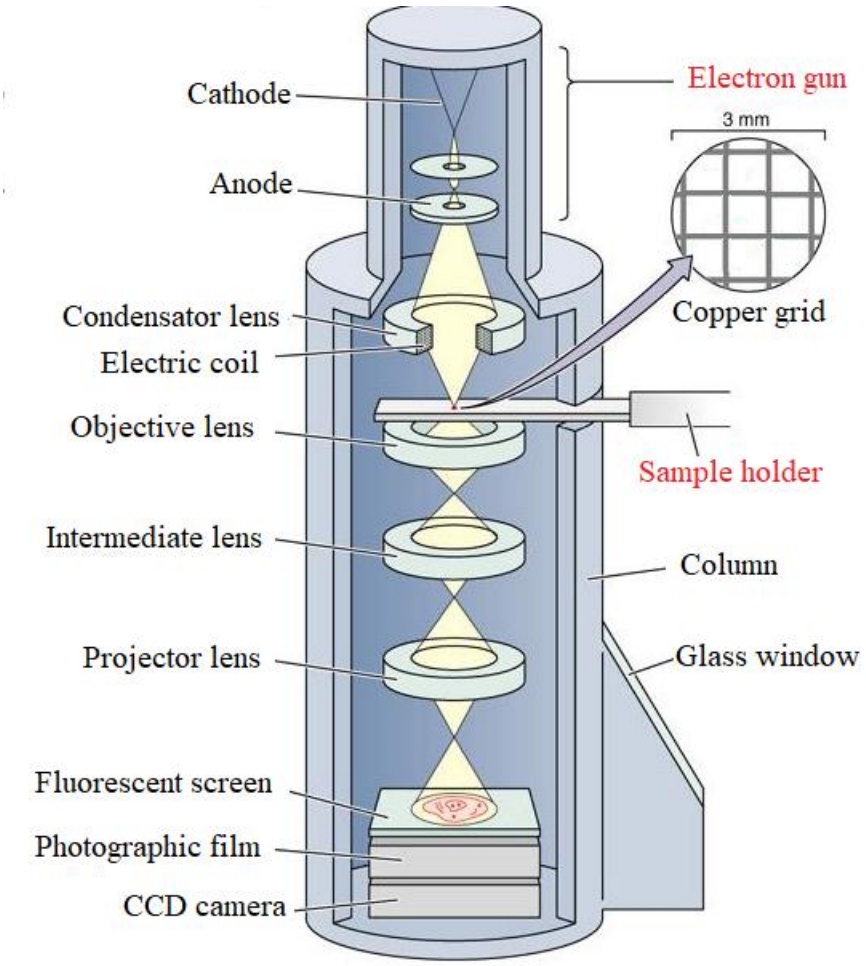

Figure 1.24: Transmission electron microscope main components [61].

The TEM analyze of a CoAlLDH before and after applying the delamination under microwave procedure shows that the material retains its hexagonal to circular platelets morphology, having diameters between 50-200 nm (see figure 1.25 a-b) [62].

Ultra-thin CoNiLDH with a 2D nanostructure was obtained by using an ethylene glycol-water homogenous system. The TEM, the high resolution TEM images (HRTEM) and the SAED (selected area electron diffraction) of the material confirm that the method can be used to obtain LDH with thin nanosheets morphology. The SAED revealed that the diffraction rings have a low intensity, underlining that the material has a low crystallinity [63].

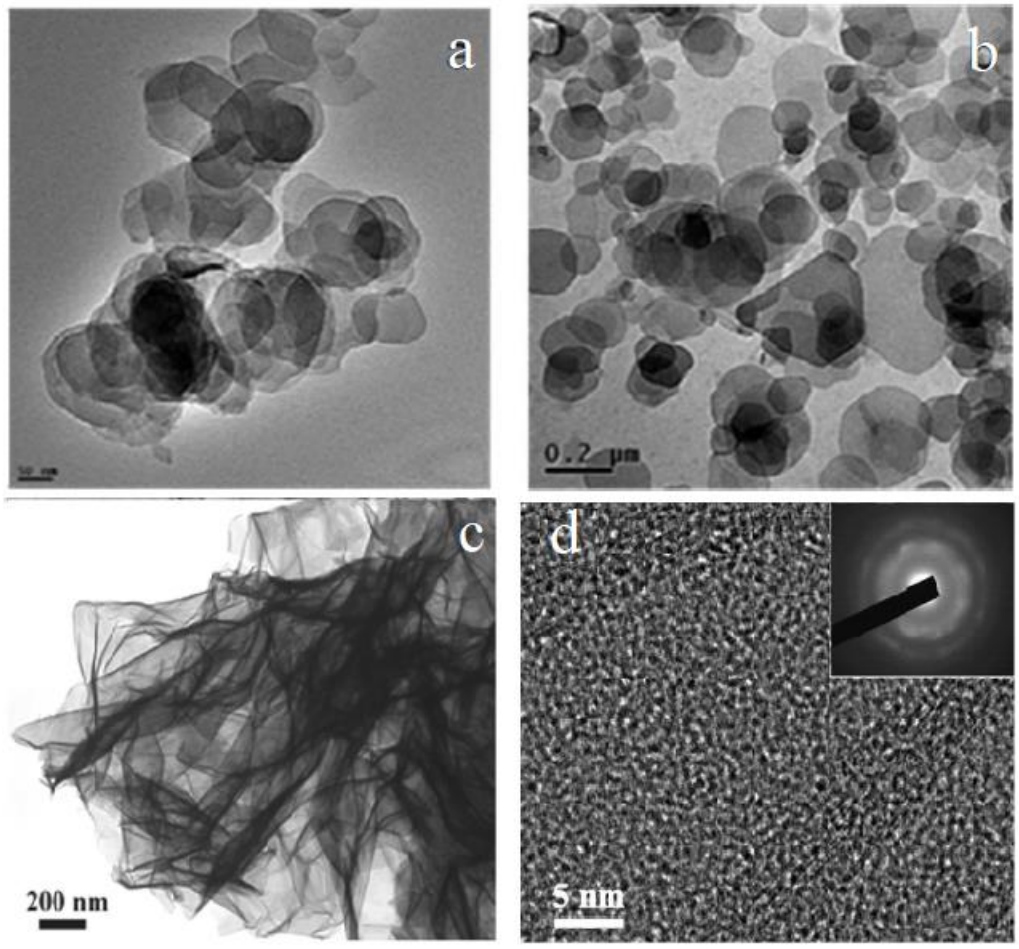

Figure 1.25: TEM images of CoAlLDH a) before and b) after delamination under microwave; c) TEM and d) HRTEM of CoNiLDH; the insert is the SAED of CoNiLDH [62,63].

g) Elemental composition studied by EDX

The verification of the elemental composition of materials can be realized with the utilization of energy-dispersive X-ray spectroscopy (EDX). With this analysis can be confirmed the composition of a compound and the percentage ratio between the elements, and also its purity.

The EDX uses X-Rays for the hitting of the specimen, with the purpose of obtaining an emission X-Ray spectrum, which offers information about the constituent elements of the solid. Each element possesses its own emission X-Ray spectrum. The elements with an atomic number between 4 and 92 can be determined with this type of investigation, but not all type of EDX instruments are able to analyze elements with $Z < 10$. The qualitative analysis supposes the identification of the spectral lines, while the quantitative one implies the measurement of the line intensity [64].

The EDX analysis systems are attached to the instruments used in the electronic microscopy, as SEM, TEM [64]. In this case, TEM or SEM apparatus are equipped with detectors capable to capture the characteristic X-Ray, which are further used in the elemental analyze.

Figure 1.26 presents the TEM imagine (a) and the correspondent EDX spectrum (b) of ZnAlTiLDH. It may be noticed from figure 1.26 b that all the elements of the material were detected [65]. This is an indication that, after the synthesis, all the elements were incorporated in the material structure and also that the resulted composite has a high purity because no other additional elements were remarked.

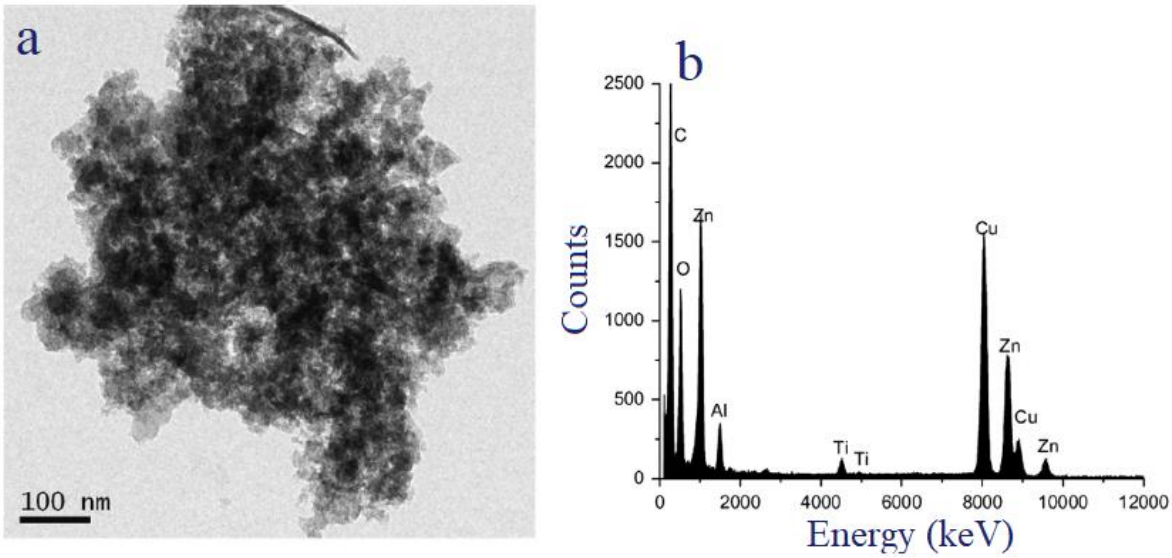

Figure 1.26: TEM imagine and EDX spectrum of ZnAlTiLDH [65].

h) ***Thermogravimetric analysis (TGA/DTG)***

The thermogravimetric analysis (TGA) measures weight modification of a sample as a function of temperature or time; the analyis is carried out in an inert atmosphere. When a material is the subject of a thermal treatment, it suffers mass losses which may be caused by Physico phenomena like: gas adsorption or desorption, phase transformation (vaporization, sublimation) or chemical phenomena like decomposition or chemisorption.

To obtain supplementary information and to simplify the results interpretation, the TGA can be accompanied by the differential thermal analysis (DTA). Furthermore, first derivative *of a* mass loss *curve* (DTG) may be used to appreciate easily the moment of the weight loss.

The differential thermal analysis gives information about the phase transformation and the process which take place. So, in function of the peaks orientation, the processes can be exothermic (adsorption, crystallization, oxidation, chemisorption) or endothermic (reduction, desorption, melting).

The main components of an instrument used in thermogravimetric analysis (figure 1.27)

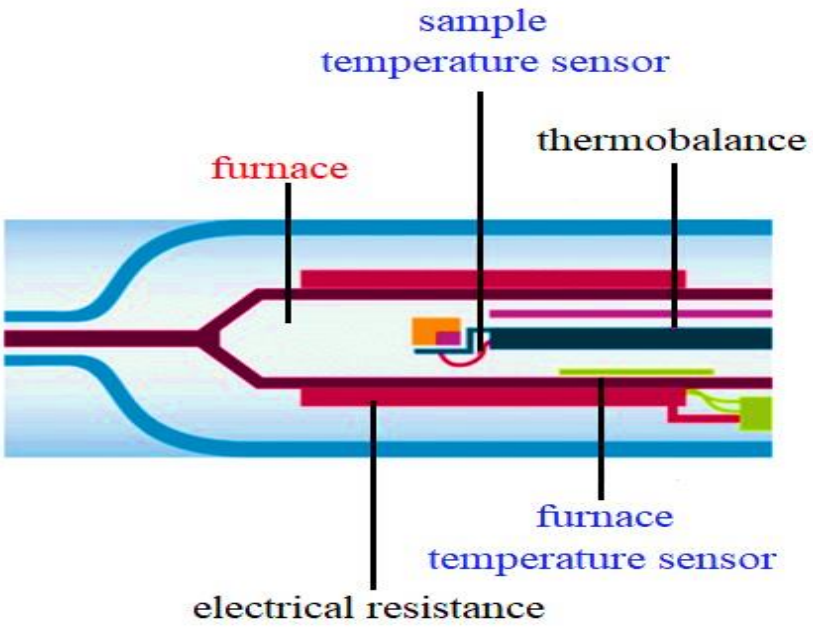

Figure 1.27: Main components of an instrument used in thermogravimetric analysis [66].

are the microbalance (1-100 mg), the reference and the sample crucibles, furnace, furnace controller, inert atmosphere generator, recording device [66].

In case of the LDHs nanocomposites, the TGA gives information about the temperature values when the material losses the physisorbed water, the interlayer water, and also the temperature values when the lamellas are dehydroxylated and the interlayer anions are removed.

Figure 1.28 presents the TGA/DTG (a) and TGA/DTA curves for ZnAlLDH. Three degradation steps can be observed from figure 1.28 a of the TGA curve. First stage of the thermal degradation is attributed to the interlayer water removal from the LDH structure (32-175 °C). The next step corresponds to the dehydration of the clay (175-230 °C), and the third stage may be assigned to the decomposition of the anions in the interlayer (230-460 °C). The DTG curve also presents three peaks at 137, 254 and 228 °C corresponding to the removal of interlayer water, layers dehydration and anions decomposition.

The DTA curve of ZnAlLDH expressed in figure 1.28 b shows that the mass losses take place via endothermic transformation. The peak which appears around 141 °C can be attributed

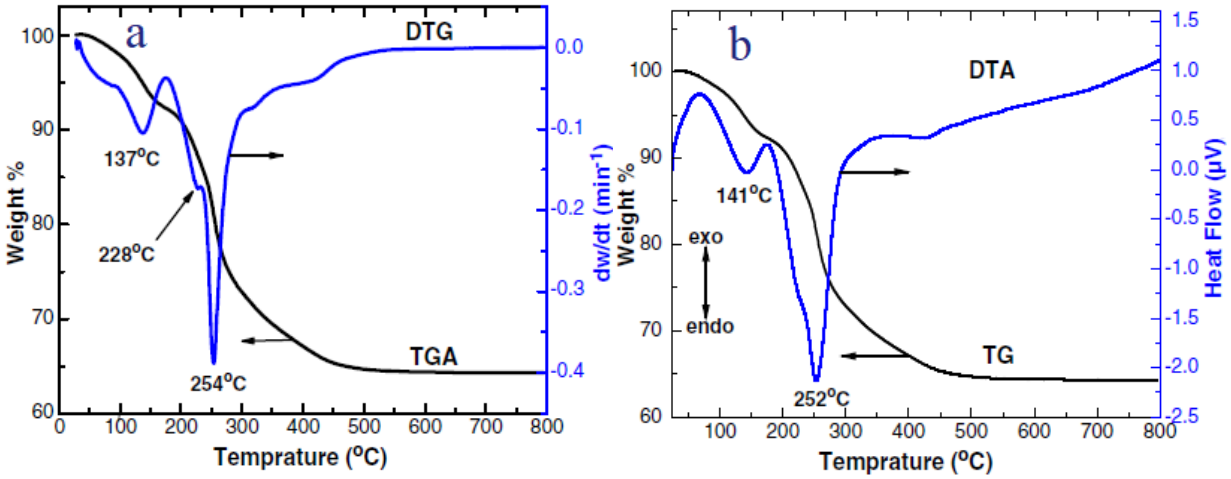

Figure 1.28: TGA/DTG (a) and TGA/DTA curves for ZnAlLDH [22].

to the physisorbed and interlayer water removal. The next intense peak, at 252 °C corresponds to lamellas dehydroxylation and anions decomposition [22].

1.1.5. **Specific applications of LDHs in photocatalysis and nanomedicine**

Layered double hydroxides can be used in many applications including gens and drug delivery, biotechnology, biomedicine, biology, catalysis, cosmetics, biosensing devices design, environmental remediation and others. These anionic clays can be used in such large areas of interest because they possess advantages like high phisico-chemical stability, low toxicity and a good biocompatibility with different types of biomolecules, they are able of self-assembly and structure recovery in particular condition [67].

a) ***Specific applications of LDHs in photocatalysis***

Photocatalysis is a branch of catalysis which uses for the initiation of reaction the electromagnetic radiation and a particular catalyst. The layered double hydroxides can be used in photocatalysis because their semiconductor properties. In figure 1.29 is shown how semiconductors, in presence of an appropriate energy source (electromagnetic radiation, temperature) can generate charge carriers type *electron-holes*, which will be further used in redox species formation [68].

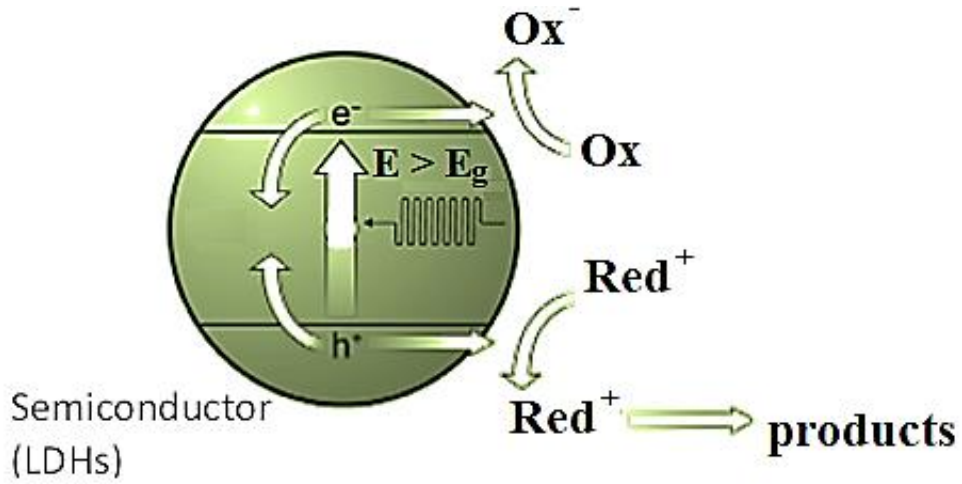

Figure 1.29: Redox species generation by a semiconductor material in presence of an appropriate energy source [68].

Important studies were focused on the utilization of materials like TiO_2, ZnO, SnO_2 in photocatalytic processes. Results have shown that these materials have a low catalytic performance, because of the high rate of charge carrier recombination [69].

The hydrotalcites, being semiconductor nanocomposites, have paid attention to researcher for their utilization in light driven applications. A relevant aspect in photocatalysis is to design materials able to generate a positive response under solar or visible irradiation. This aspect is important because the solar light, which is a free and cost less energy source, is composed by 92-95 % visible light. For this reason, in the LDHs structure were introduces transitional metals, capable to induce an absorbance shift to the red zone of the spectrum [70,71].

ZnFeAlLDHs with different ratio between the metallic cations were synthetized via co-precipitation method and used in the photodegradation of the 2,4-diclorophenoxyacetic acid under UV irradiation. Results have shown that the materials are able to remove the pollutant. Furthermore, their photoactivity enhances with the increase of the Fe^{3+} content. After 6 h of irradiation the photocatalytic performance was between 72-86% pollutant removals. The initial ratio between the 2,4-diclorophenoxyacetic acid and the catalysts was 1.35 mmol/g [72].

P.R Chowdhury and K.G. Bhattacharyya have synthetized through the hydrothermal method a NiTiLDH and they tested in the visible light driven methylene blue photodegradation. They made a full study, testing the influence of the parameters as pH and catalyst concentration on the reaction velocity. Their results are given in the figure 1.30. It might be observed that the performance increases with the increase of catalyst content, till a maximum is reached. For a catalyst contend of 15 mg, all the methylene blue is photodegraded in 75 minutes. At different pH values, the NiTiLDH material showed the highest photoresponse at a value of 11.

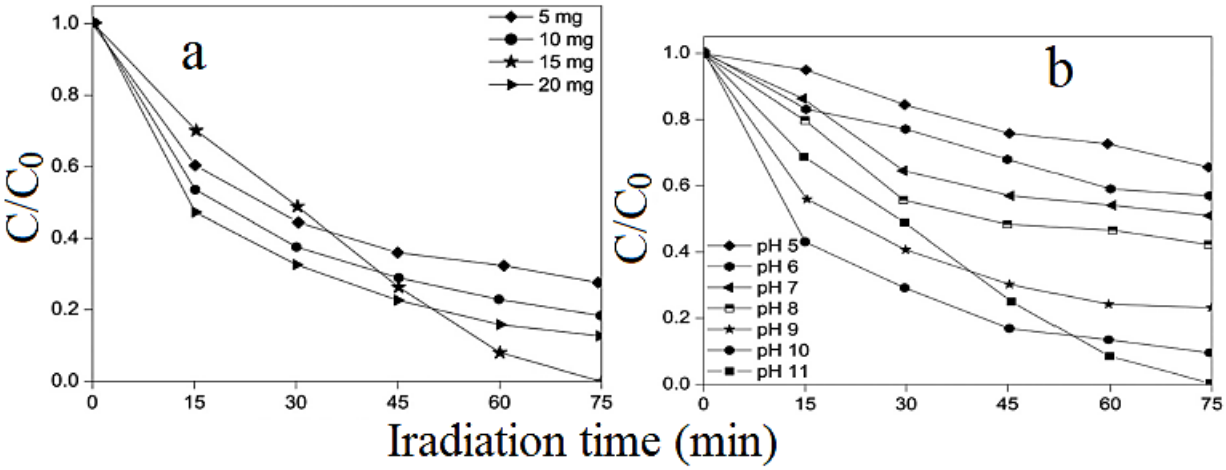

Figure 1.30: The effect of a) catalyst concentration at pH=11 and pollutant concentration=0.3 mg/L and of b) pH for a catalyst content=15 mg and a pollutant concentration 0.3 mg/mL on reaction performance

Furthermore, the decrease of pH at values of 5 or 6 has a drastically effect on the catalyst activity. This can be explained by a competitive adsorption on LDH surface between the H^+ ion and the pollutant [47].

In optimal conditions of pH and catalyst concentration, different concentrations of dye have been tested. Also the stability of the NiTiLDH was investigated. The results are given in the figure 1.31. As suspected, the increase of the pollutant quantity, leads to a decrease of the catalyst efficiently. The catalyst performance over five repetitive cycles proves that the material is stable and it can be used many times without a significant loss of activity [47].

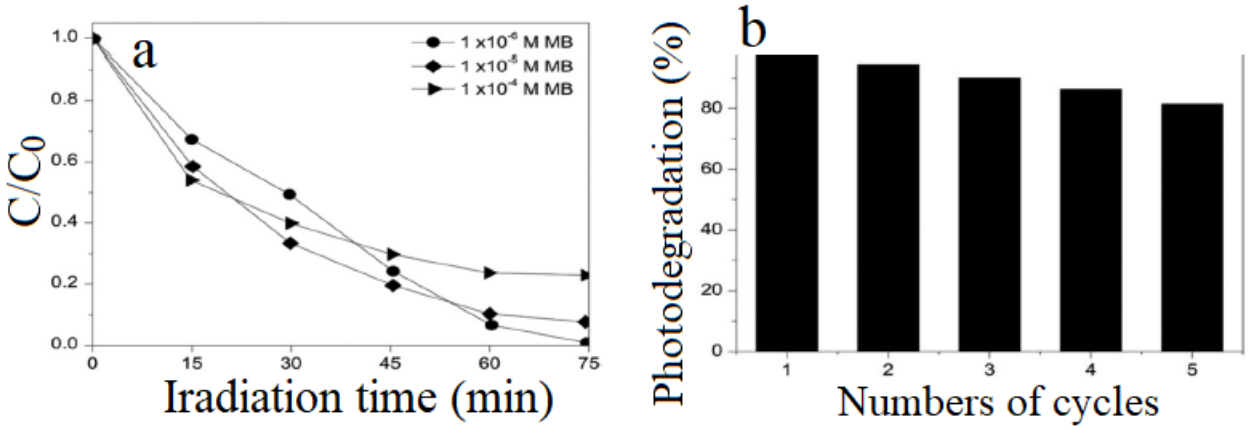

Figure 1.31: The effect of methylene blue initial concentration on photodegradation reaction; ph = 11; catalyst content =15 mg, total reaction volume 200 mL [47].

A similar study made for the photodegradation of methylene blue has shown a poor activity of the NiFeLDH [73] in the degradation of this pollutant. Y Zhao and co-workers have

synthetized a group of LDH materials type MCr-X-LDH, were M = Cu, Ni, Zn and X = NO_3 or CO_3. They used the prepared materials for the photodegradation of sulforhodamine-B and congo red pollutants under visible light. Their results have proven that the materials with carbonate anions in their structure are less preformat than those with the nitrate anions. The photocatalytic performances for this group of catalysts were between 5-98 % for the sulforhodamine-B removal (5% for NiCr-CO_3-LDH and 98 % for CuCr-NO_3-LDH) and between 20-90 % for congo red removal (20 % for ZnCr-CO_3-LDH and 90 % for CuCr-NO_3-LDH) [74].

Other LDHs materials used in photodegradation are listed in table 1.1.

Table 1.1: LDHs materials used in photodegradtion of different organic pollutants.

LDHs formulations	**Pollutant**	**Reference**
MgAl	methylene blue methyl orange formaldehyde;	[50]
ZnTi	rhodamine B, phenol, methylene blue O2 generation,	[30] [34] [69] [32]
ZnFe,	rhodamine B,	[75]
FeTi	*rhodamine B*	[75]
ZnCe	O2 generation	[32]
ZnCr	orange II, O2 generation	[76] [32]
MgAlTi	methylene blue, 2, 4 diclorophenol	[77] [78]

BiZnTi	indigo carmine	[79]
MgZnAl	Acid 2, 4 dichlorophenoxiacetat,	[23]
ZnAlTi	rhodamine B	[65]
	methylene blue	[71]

b) ***Specific applications of LDHs in biomedicine***

In *vivo* studies have shown that LDHs materials as ZnAlLDH and MgAlLDH possess a good biocompatibility with the living tissue. Recently, LDHs materials were implanted in rats muscles. No inflammation was observed after 28 day from implantation. Furthermore, the tissue reconstruction was observed [80]. In a similar study which was made this time on rabbits, have been proved that the implantation of the specimen middle ear has no negative impact on the animals health. The material was slowly dissolved and adsorbed by the living tissue [81].

The main direction on layered double hydroxides utilization in biomedicine is the drug delivery. Having a high ability to incorporate in their structure large molecules, they are highly recomandated for this application. Additionally, they can enhance the pharmaceutical solubility without affecting its therapeutic activity [82].

Dejbbi and co-workers obtained via ionic exchange and co-precipitation methods two materials based on MgAlLDH containing berberine chloride. The release of the drug from the support surface was carried out at 7.4 value of pH and 37 °C. The result shows that the release is more efficient from a hybrid obtained via co-precipitation (87%). In vitro tests made on pathogen bacteria have proven that the hybrids have inhibitory effect on pathogen proliferation [83].

Via an anionic exchange method, the diclofenac was successfully intercalated between the interlayer space of the ZnAlLDH. 84% from the intercalated drug quantity was released after 600 minutes [84].

Efavirnez (EFZ), a drug used as inhibitor for the Human Immunodeficiency Virus, has adsorbed on CaAlLDH. The EFZ molecules are characterized by a poor solubility in water. However, when released from the clay's surface, the EFZ solubility increases with 558 % compared to the drug alone, after two hours. The cytotoxicity experiments proved that CaAlLDH has no negative effect on cells viability [85]. Vitamin C was also adsorbed in CaAlLDH and successfully released in phosphate buffer, pH 7.4 [86].

Other drugs which were combined with LDHs are given in table 1.2.

Table 1.2: Drugs adsorbed or intercalated on/into LDHs structure.

LDHs	Drug	Observation	Reference
ZnTiLDH	Ibuprofen,	release study	[87]
ZnAlLDH	2-mercaptobenzothiazole	anti-microbial activity study	[88]
	Isonicotinic acid hydrazine	anti-tuberculosis therapy, high biocompatibility of LDH, increase of drug activity	[89]
MgAlLDH	Norfloxacin	drug release study,	[90]
	doxorubicin	anticancer therapy,	[91]
	Pirenoxine sodium	in *vitro/vivo* drug release, ocular drug delivery.	[92]
	Amoxicillin	textural properties study	[93]
	5-fluorouracil	Anticancer therapy.	[94]
	Methotrexate	in *vivo* studies on mice, antitumoral therapy for osteosarcoma	[95]
	Pifithrin-α-l	in *vivo* release study, good osteoinductivity	[96]
	Raloxifene hydrochloride	in *vivo* drug release study, high biocompatibility, anticancer therapy.	[97]

The LDHs materials have been hosts also for organic molecules as DNA [98]. Materials like ZnFeLDH, MgAlLDH, MgFeLDH, ZnAlLDH have been used as DNA delivery matrix for mammalian cell transfections. The cytotoxic tests carried out in vitro have proven that these materials have a low toxicity for the cervical cancer cells, embryonic kidney and hepatocellular carcinoma [99].

Besides these application listen above, the LDHs materials can be used also in cosmetics, especially in sunscreen formulations [100]. Li and collaborators recently intercalated into ZnTiLDH material the cinnamic acid. After the evaluation of the optic properties of the resulted material, was remarked that the LDH has an enhanced ability of UV absorption. Further, the complex was used in the preparation of a cosmetic cream. The formulations with and without ZnTi-cinnamic acid were tested to evaluate the UV absorption capacities. The results indicated that an increase of UV absorption was remarked for the final product, containing LDH [101].

1.2. Nanocomposites based on layered double hydroxides

The layered double hydroxides can be precursors for the preparation of nanocomposites where on the clay surface are dispersed different metallic or oxide nanoparticles. The resulted materials, generally denoted as NPs/LDHs can express enhanced properties comparted with

their parent materials and due to this aspect their synthesis and further utilization in specific application are extremely attractive.

1.2.1. Nanocomposites type NPs/LDH synthesis methods

The NPs/LDHs materials can be obtained by two main methods: the reconstruction and the impregnation.

a) ***The reconstruction method***

The calcined layered double hydroxides own the ability to reform their initial layered structure when the metal oxides resulted after the thermal treatment are rehydrated in a salt solution containing the anion which will be incorporated between layers. The method leads to the formation of dispersed nanoparticles on LDHs structure (NPs/LDH). In figure 1.32 is

Figure 1.32: The NPs/LDHs nanocomposites synthesis by using the structural memory effect of the layered double hydroxides.

presented the reconstruction method. In the LDHs reconstruction process, temperature has an important role. When the initial clay was calcined at 550 °C, the total reformation of the layered structure was obtained after 24 h of rehydration. The augmentation of the calcination temperature to 750 °C, increases the time of the total recover of the initial structure, while a temperature up to 1000 °C drives only to a partial reconstruction [5]. The reconstruction method is indicated in the synthesis of LDHs nanocomposites intercalated with large dimensions anions [5].

b) ***The impregnation method***

The NPs/LDHs structures can be obtained through the direct addition of LDHs materials to a salt solution (see figure 1.33 b). Also, different nanoparticles dispersed on LDHs surface can be obtained via coprecipitation method, when the LDHs precursors as the salts

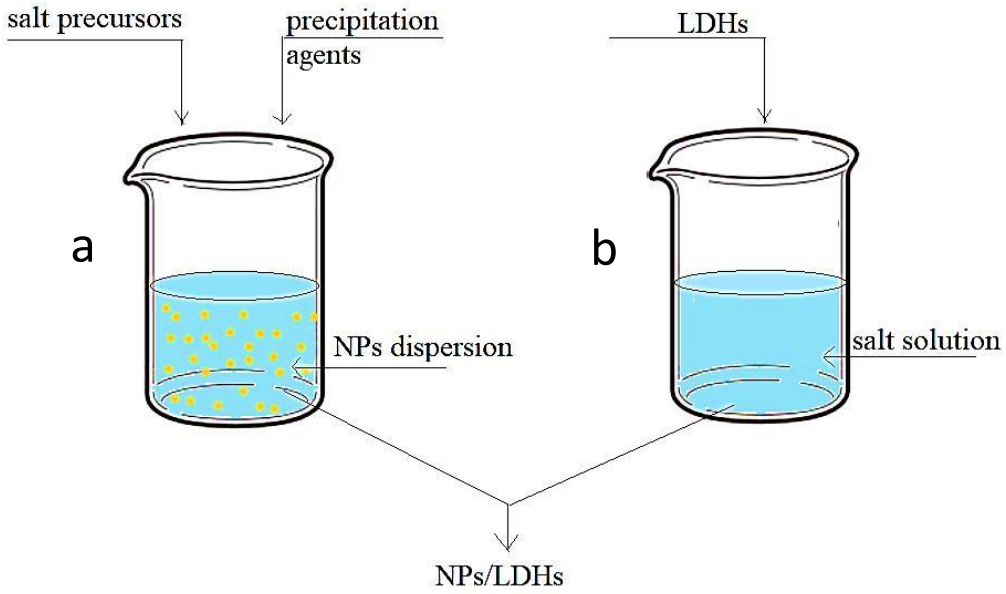

Figure 1.33: The NPs/LDHs nanocomposites synthesis by using the impregnation methods.

solution and the precipitation agents are added drop by drop to a solution containing dispersed nanoparticles [102,103] (see figure 1.33 a). The direct contact between two solutions containing the dispersed LDH and the dispersed NPs can lead also to NPs/LDH formulations [104]. Usually, the resulted solutions are stirred between 24-48 h before recovering the solid. As well, the anionic exchange method can be used for the NPs/LDHs nanocomposite preparation [105].

1.2.2. Physico-chemical characterization of the NPs/LDHs formulation

For the physico-chemical characterization of the NPs/LDHs formulations can be used the same techniques as in case of the layered double hydroxide. In the following are presented the particularities of the NPs/LDHs nanocomposites evaluated by using XRD, XPS, FTIR, UV-Vis, SEM, TEM, EDX and TG/DTG instruments.

a) ***X-ray Diffraction (XRD)***

In figure 1.34 are presented the XRD patterns for different Ag/ZnTiLDHs formulations. The hybrids were obtained via impregnation route, by adding the LDH matrix to solutions with different contents of $AgNO_3$. All the resulted materials present the characteristic diffraction peaks assigned to the basal reflection (003), (006), (009) plans, and non basal reflection (012)

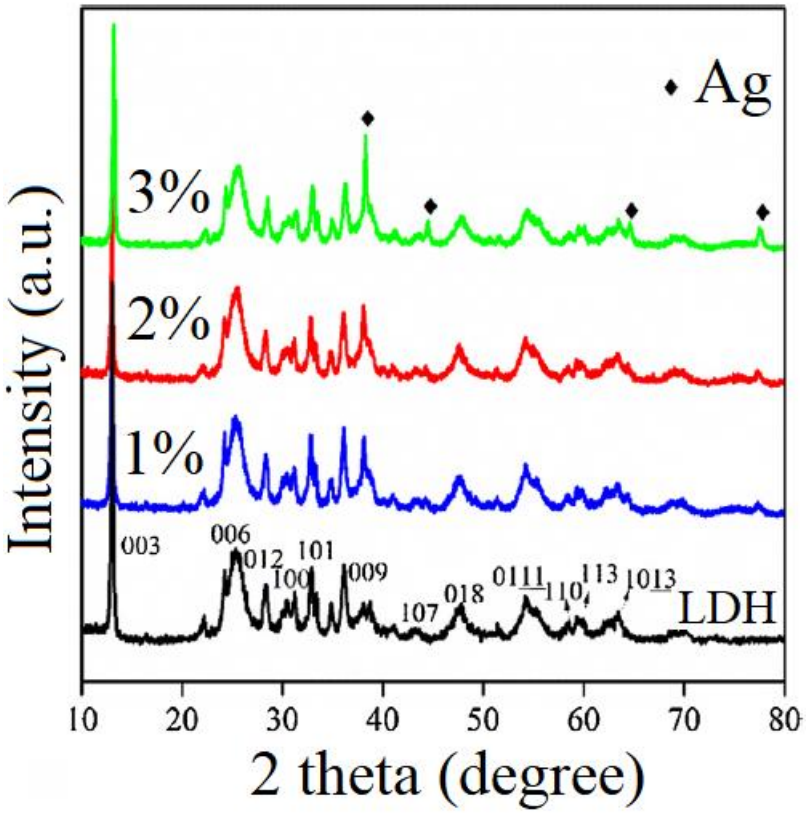

Figure 1.34: XRD patterns of different materials type Ag/ZnTiLDH [25].

(110 and (113) plans which might be attributed to the LDH phase. The introduction of the Ag on the clay surface has no effect on the crystal structure of the LDH. The presence of the AgNPs on the ZnTiLDH is confirmed by the reflections which appear at 2Θ = 38°, 44°, 64.5° and 77.5°and they are typical for the cubic phase of Ag [25].

b) ***X-ray Photoelectron Spectroscopy (XPS)***

In figure 1.35 are presented the XPS spectra for graphene (GO) and GO/NiAlLDH. The graphene XPS full spectrum (figure 11 a) reveals that GO has in its composition mainly C and O, these two components being certified by the presence of O1s, C1s and O KLL peaks at 532.5, 284.5 and 976.5 eV. The carbon C1s high resolution XPS spectrum (figure 11 b) presents three important peaks at 284.5, 286.6 eV and 288.4 eV assigned to C-C, C-O and O-C=O species [106].

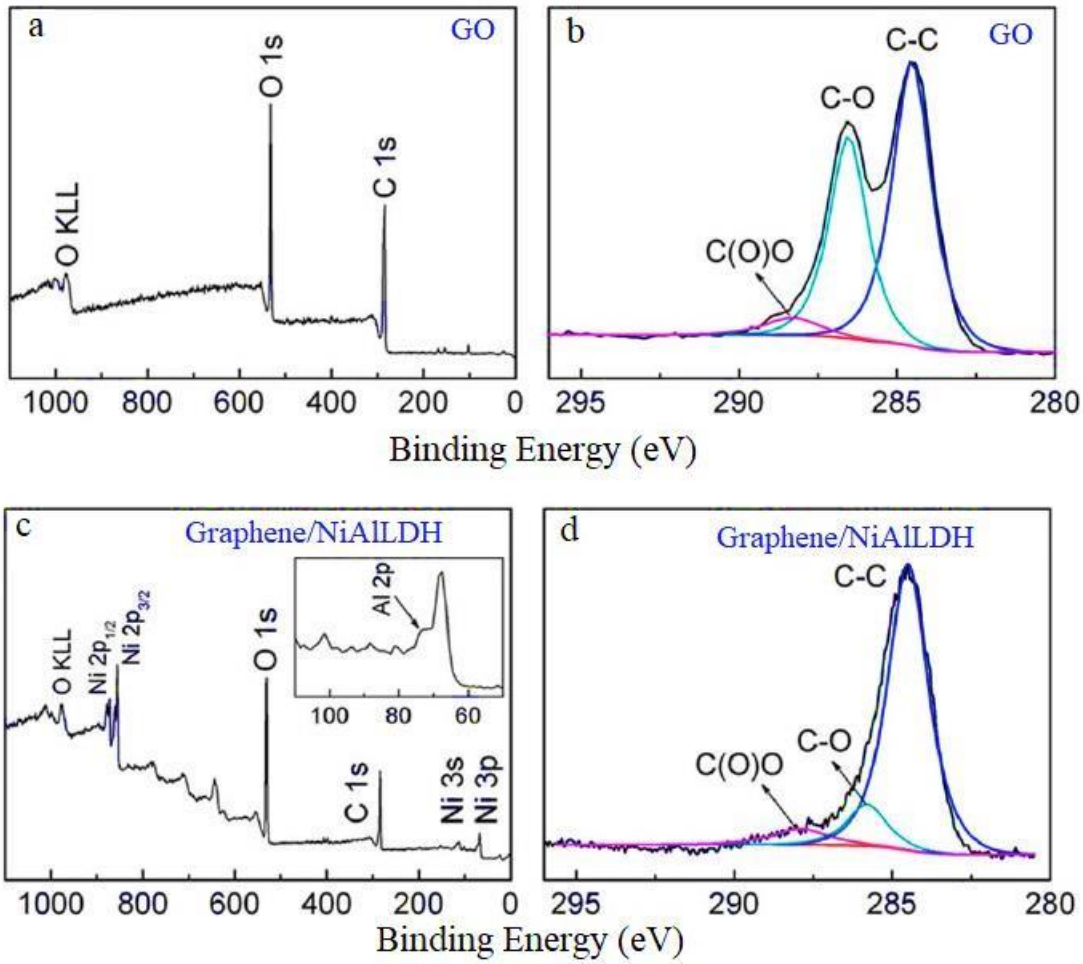

Figure 1.35: (a) XPS full spectrum of GO, (b) XPS high resolution spectrum of C1s from GO, (c) XPS full spectrum of the graphene/NiAl LDH, and (d) XPS high resolution spectrum of C1s from graphene/NiAl LDH nanowires [106].

Regarding the XPS spectrum of the hybrid nanocomposite, GO/NiAlLDH, it shows that the graphene is present in the nanomaterial structure, and beside the characteristic peaks of GO (C1s and O1s), at 73, 856, and 873 eV (figure 1.35 c) are detected the representative signals for Al2p, $Ni2p_{3/2}$, and $Ni2p_{1/2}$ pointing the presence of NiAlLDH into the nanohybrid structure. By comparing the spectra of C1s expressed in figure 1.35 b and d, can be easily noticed that in figure 1.35 d the intensity of C-O and O-C=O decreases, showing that the amount of groups containing oxygen decreases also because of the thermal reduction of graphene [106].

c) IR Spectroscopy with Fourier Transform (FTIR)

A hybrid material type Ag/MgAlLDH was obtained by the simple addition of biogenic AuNPs dispersion to a MgAlLDH gel, followed by the mixture stirring during 2 h at room temperature. Further, the resulted solid was recovered via centrifugation, washed many times and dried. The biogenic AgNPs were obtained by the addition of $AgNO_3$ to a fungal

biomaterial. In figure 1.36 are presented the FTIR analyses for the LDH, AgNPs and Ag/LDH. It might be observed that the FTIR spectrum of the Ag/MgAlLDH presents characteristic vibration bands for both AgNPs and MgAlLDH. Thus, the peak at 1369 cm^{-1} is assigned to the vibration mode of the carbonate anions, while the biogenic AgNPs presence is indicated by the peaks around 963 cm^{-1}, 1060 cm^{-1} and 1031 cm^{-1} which are characteristic for the vibration mode of the trans-ethylenic moiety and for the N-H mode of the free amino groups of bio-

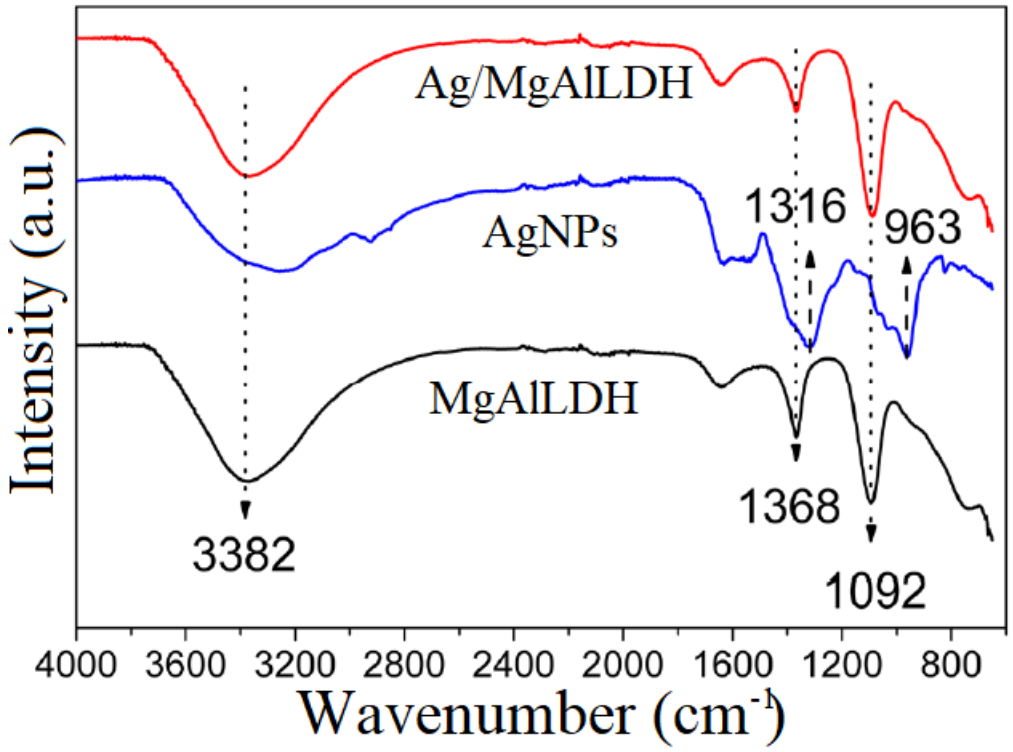

Figure 1.36: FTIR spectra for MgAlLDH, AgNPs, Ag/MgAlLDH [107].

macromolecules. The FTIR data confirms that the biogenic AgNPs were adsorbed on the clay surface [107].

*d) **Photoresponsive characteristics studied by UV-Vis spectroscopy***

Recently, Z. Wang and colleagues have prepared a complex hybrid type Au-Pd/MgAl. To obtain this complex, firstly was obtained the LDH matrix, and after, combining the impregnation route with the reduction method, the final nanomaterial was obtained. Via impregnation route, were also synthetized the simple Au/LDH and Pt/LDH materials.

The nanocomposites optical properties were investigated by UV-Vis spectroscopy. The UV-Vis spectra of the initial LDH material and its hybrids are presented in figure 1.37. It might

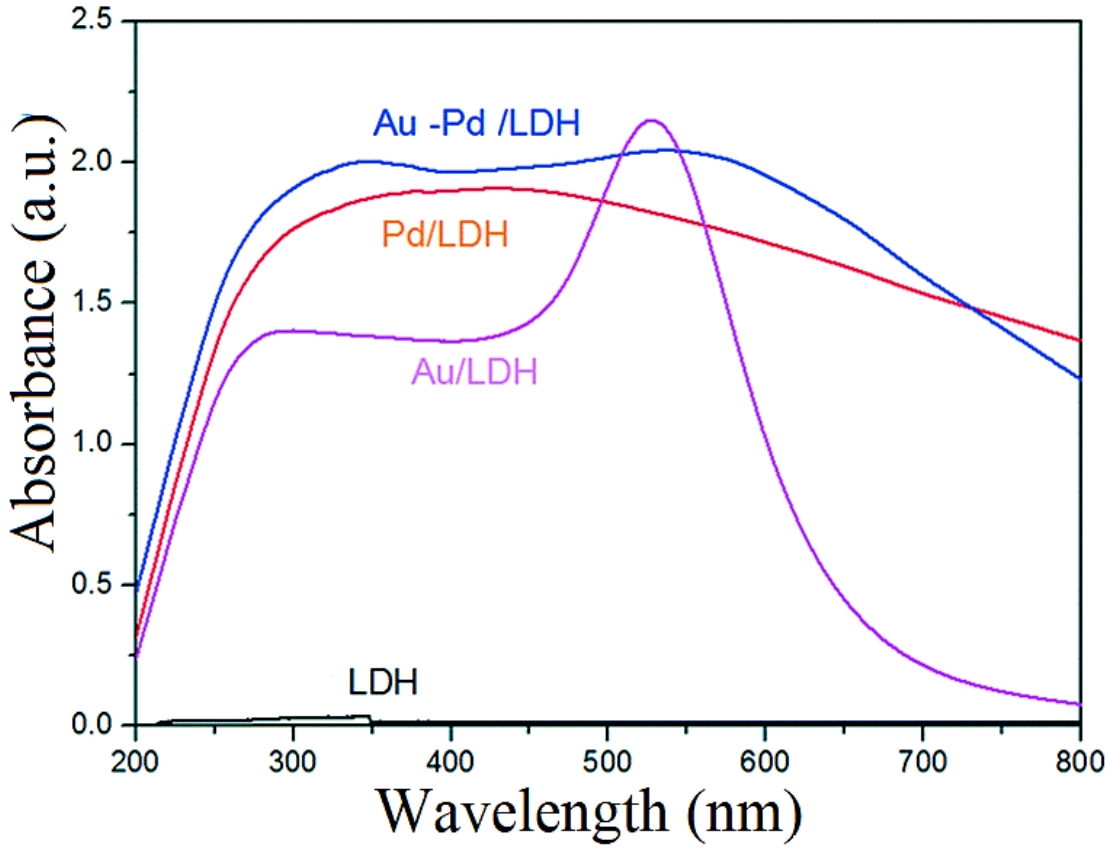

Figure 1.37: UV-Vis spectra of LDH, Au/LDH, Pd/LDH and Au-Pd/LDH [26].

be observed that the MgAlLDH has very low absorption ability above 400 nm. Alter the metal nanoparticles loading on the clay surface, the nanomaterials present a highly enhancement of the visible light absorption. The absorption edge around 520 nm for the Au/LDH material can be assigned to the AuNPs, while the edge at 330 nm in case of Pt/LDH can be attributed to the PtNPs. For the Au-Pt/LDH absorption edges characteristic to both AuNPs and PtNPs can be remarked in case of the blue line spectrum [26].

e) ***Scanning electron microscopy (SEM)***

Fan and co-workers have prepared, by using light reduction and anion exchange methods, a Ag/AgBr/CoNiLDH type nanocomposite. Firstly, the CoNi-BrLDH was obtained. Secondly, using a solution of $AgNO_3$ the Br anion was exchanged with the nitrate anion, and dispersed AgBr nanoparticle were formed on the LDHs surface. The Ag/AgBr/LDH material was obtained after the light reduction. The SEM images presented in figure 1.38 show the

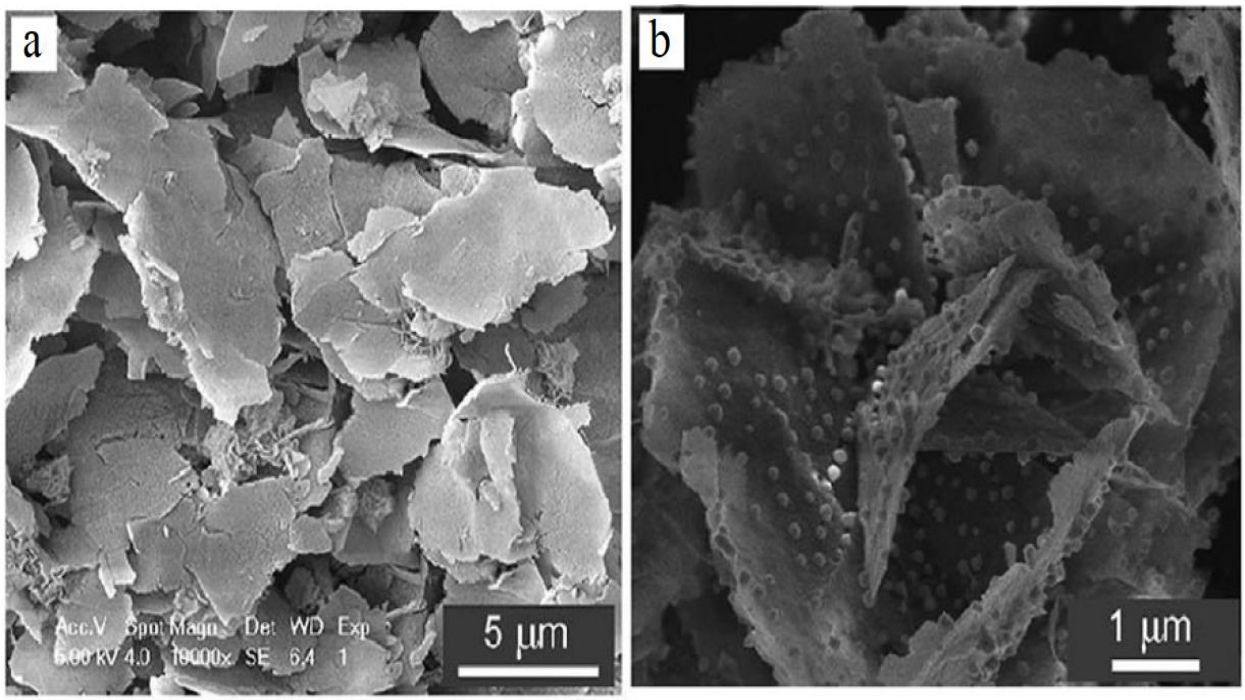

Figure 1.38: SEM images of a) CoNiLDH and Ag/AgBr/CoNiLDH [105].

morphologies of the parent CoNiLDH and the Ag/AgBr/CoNiLDH. It can be easily observed that after the anionic exchange and the light reduction, nanoparticles of Au/AgBr with diameters between 50-150 nm are remarked on larger surface, which might be assigned to the LDH matrix [105].

f) Transmission electron microscopy (TEM)

The TEM analysis gives information about the shape and particles dimension, nanoparticles dispersion on a surface, and also about the material composition and crystalline structure. TEM analysis is very useful for NPs/LDHs investigation. Lu and co-workers [108] have prepared a TiO_2/CuMgAlLDH nanocomposite. To investigate the TiO_2 nanoparticles presence on the LDHs surface TEM instrument was used. In figure 1.39 a-d, TEM images of TiO_2/CuMgAlLDH are given. From figure 1.39 a and b, can be remarked the presence of TiO_2 on LDH matrix, with nanoparticles dimensions have between 2 and 6 nm (figure 1.39 b). From figure 1.39 d, which presents a magnification of selected region from figure 1.39 c, the planes which correspond to the (012) reflection of CuMgAlLDH and the (021) reflection of TiO_2 can be observed [108].

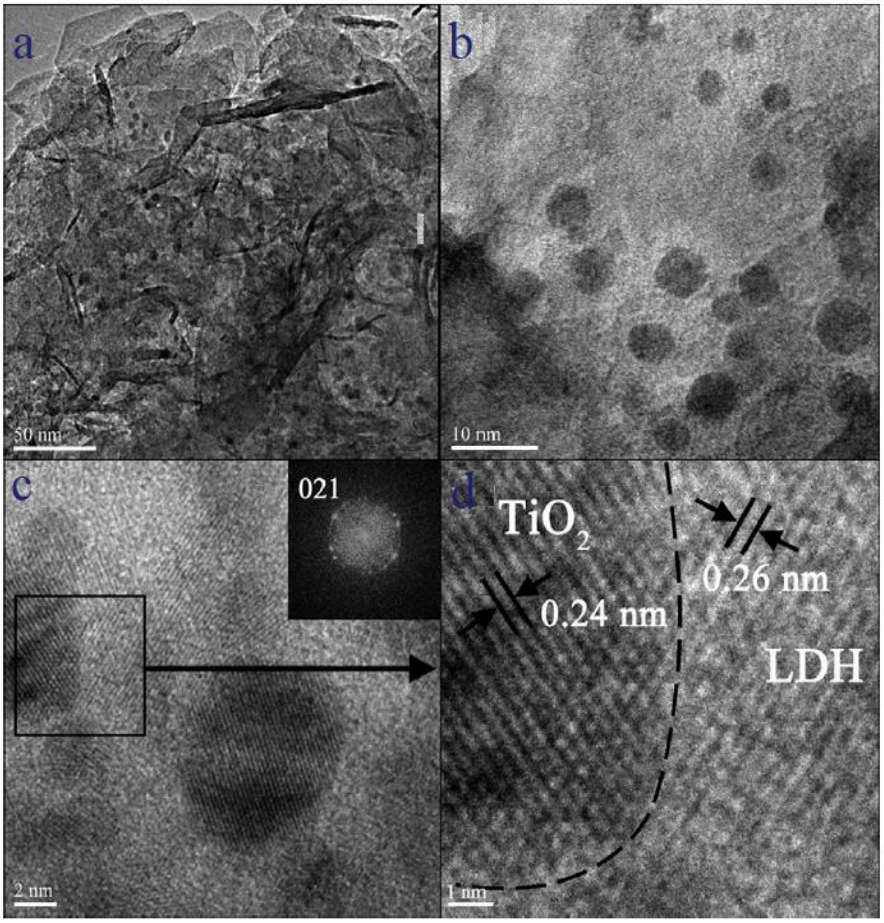

Figure 1.39: TEM images of a), b) TiO_2/CuMgAlLDH and HRTEM of c) TiO_2/CuMgAlLDH and d) magnification of a selected section of c [108].

*g) **Elemental composition studied by EDX***

Fe_3O_4 nanoparticles dispersed on MgAlLDH matrix were obtained by impregnation method. For this, the Fe_3O_4NPs have been dispersed in a 1:1 *vol* water-methanol solution. To this dispersion, the precipitation agents and de precursor salts were added. After 24 h of the maturation, the solid was magnetically separated, washed with alcohol and water and dried at 60 °C. The elemental composition (figure 1.40) was investigated by using an EXD instrument. The spectrum of the Fe_3O_4/MgAlLDH shows that all the elements used at the material synthesis are present in the final nanocomposite [109].

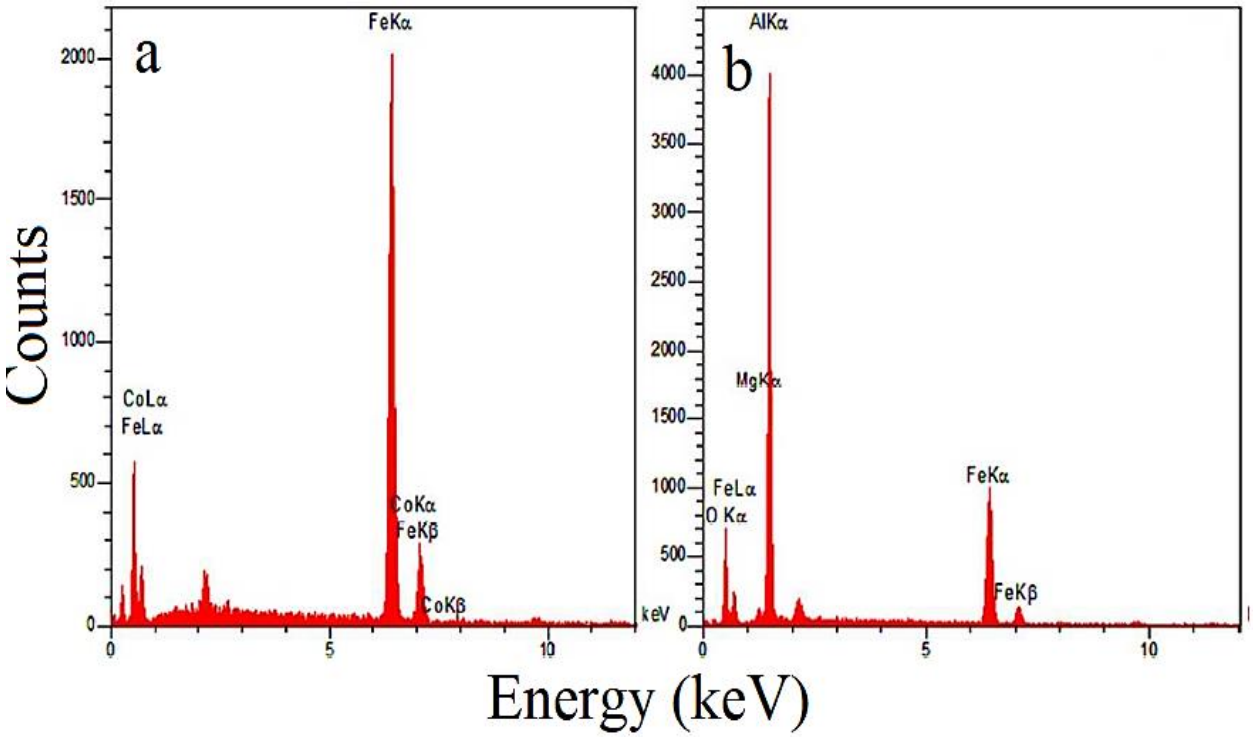

Figure 1.40: EDX spectrum of a) Fe_3O_4NPs and b) Fe_3O_4/MgAlLDH [109].

h) ***Thermogravimetric analysis (TGA)***

The material Fe_3O_4/MgAlLDH whose synthesis and elemental composition was presented in the previous section was further investigated by using the thermogravimetric analysis. Figure 1.41 presents the TG curves for MgAlLDH and Fe_3O_4/MgAlLDH.

The TG curve for MgAlLDH indicates two important mass losses, between 50-800 °C. The first loss, in a range between 30-260 °C has a value of 9 % and it is assigned to the water molecules removal. The second mass loss of 8.5 % take place in a range between 260-800 °C and it is characteristic to the layered matrix collapse [109].

For the nanocomposite material, Fe_3O_4/MgAlLDH, the first weigh loss (3%) happens in a range of 50-250 °C and it is characteristic to water removal, including the physisorbed and the interlayer water. Further, 12 % of mass is lost between 250-550 °C as a consequence of the layered structure collapse. A third weight loss (5%) is remarked at 550-800 °C which is assigned to the metal oxide and spinel phase formation [109].

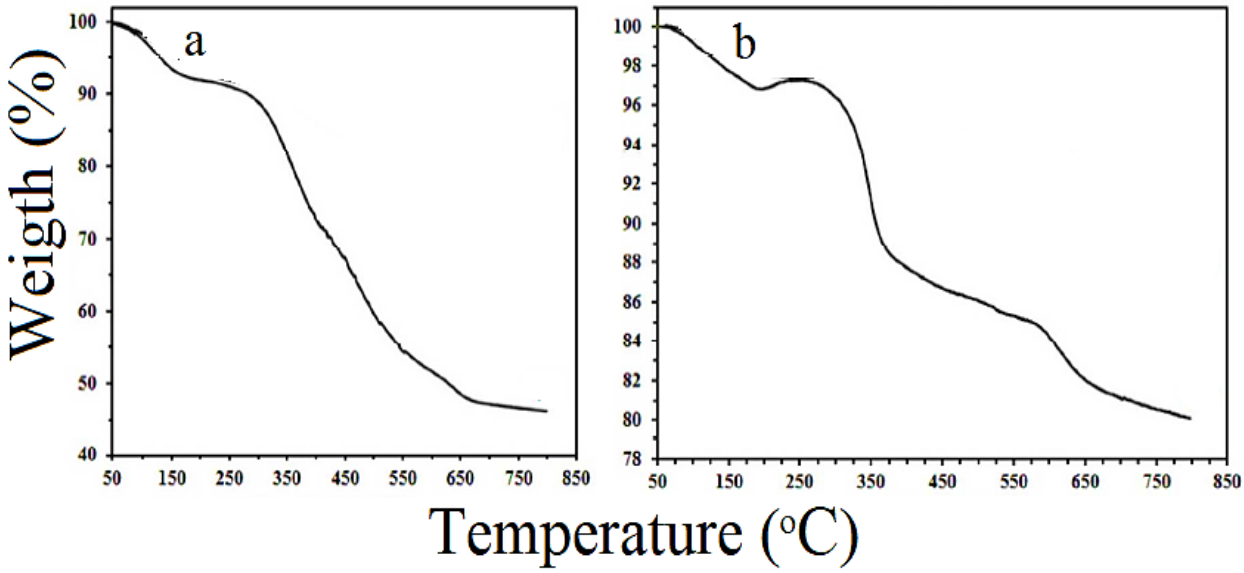

Figure 1.41: TG curves for the a) MgAlLDH and b) Fe_3O_4/MgAlLDH [118].

1.2.3. Specific applications of NPs/LDHs in photocatalysis and nanomedicine

a) *Specific applications of NPs/LDHs in photocatalysis*

The usual LDHs materials, eg, MgAlLDH, ZnAlLDH, have a large band gap, and for this reason their photocatalytic performances are reduced. Thus, Ingram and De Oliveira, in two separate studies, proved that combinations between two semiconductor materials can solve the issue of a high rate of recombination [68,110]. In this context, to increase the LDHs catalytic activity, on clay surface can be dispersed different photo-responsive nanoparticles via reconstruction or impregnation.

The general photodegradation mechanism for a combination of two semiconductors is presented in figure 1.42. In this case, the photoinduced electron of the first semiconductor is transferred from the valence band to the conduction band, where it can move freely. The surface separation formed between the semiconductors will behave as electrons trap and as a consequence, the recombination rate is decreased [68,110].

Starting from this point, the dispersion of different nanoparticles on the LDHs surface had paid the researchers attention. For instance, Y. Zhu prepared Ag/ZnTiLDH type formulation with different contents of AgNPs on the LDH. The nanocomposite formulations were tested in the solar photodegradation of the Rhodamine B (RhB). Their obtained results are presented in figure 1.43. It can be observed that 60 minutes of irradiation can produce cca 15 %

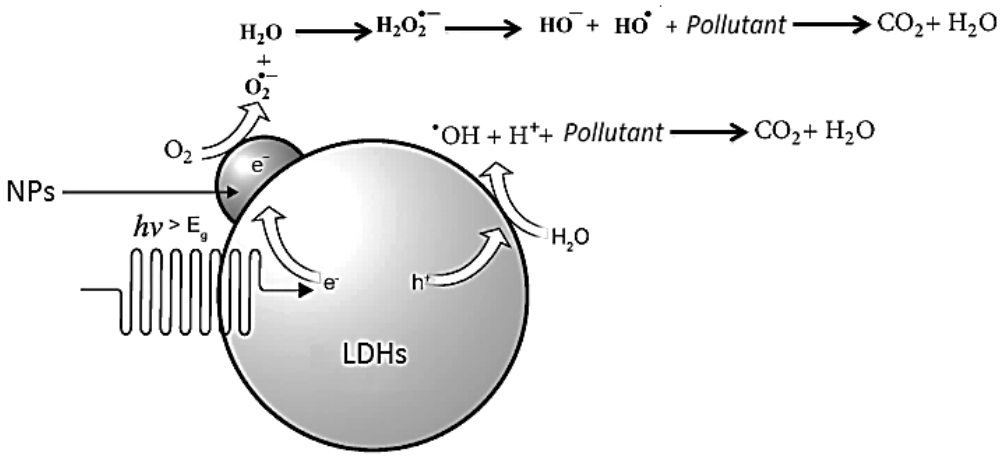

Figure 1.42: Photodegradation general mechanism involving a two semiconductors material [68].

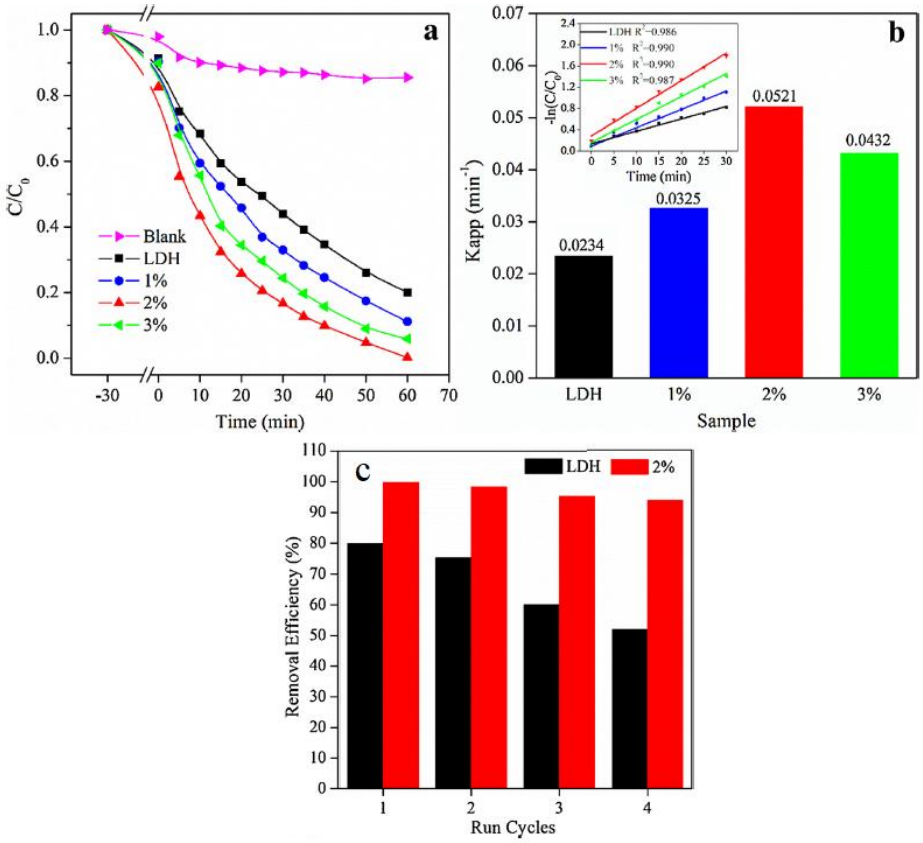

Figure 1.43: Photocatalytic results obtained for the solar photodegradation of RhB by using Ag/ZnTiLDH: a) degradation kinetics, b) apparent rate constant; insert pseudo-first order kinetics, c) RhB removal efficiency over 4 run cycles using Au/ZnTiLDH, 2% AgNPs [25].

of RhB pholtolysis. However, when the catalysts are present in the system, a fast decrease of pollutant concentration was observed (see figure 1.43 a). The pollutant removal was dependent on the silver content dispersed on catalysts surface. The higher photodegradation performance

was obtained with the Au/ZnTi containing 2% of silver. The kinetic results expressed by the values of the rate constant k_{app} are in good agreement with the decrease of the RhB concentration. They show that the most preformat system is that containing 2% of AgNPs, which presents a k_{app} 2.2 times higher than that of the parent LDH. In figure 1.43 c can be observed that the Ag/ZnTiLDH has a robust structure, being able to retain more than 90 % from its initial performance, while ZnTiLDH losses about 50 % of activity over 4 repetitive runs [25].

A complex and efficient photocatalyst was obtained by J. Sun and co-workers. They firstly obtained the ZnCr-Cl-LDH through co-precipitation method. Afterwards, the LDH material was dispersed in absolute alcohol and to this solution was added the $AgNO_3$ solution drop by drop. In the end a hybrid type Ag/AgCl/ZnCrlLDH was obtained. The materials were used in the visible light photodegradation of the Rhodamine B (RhB), using a 300 W xenon lamp, a solution of 25 mg/L RhB and 0.1g/L catalyst. In figure 1.44 are presented the obtained

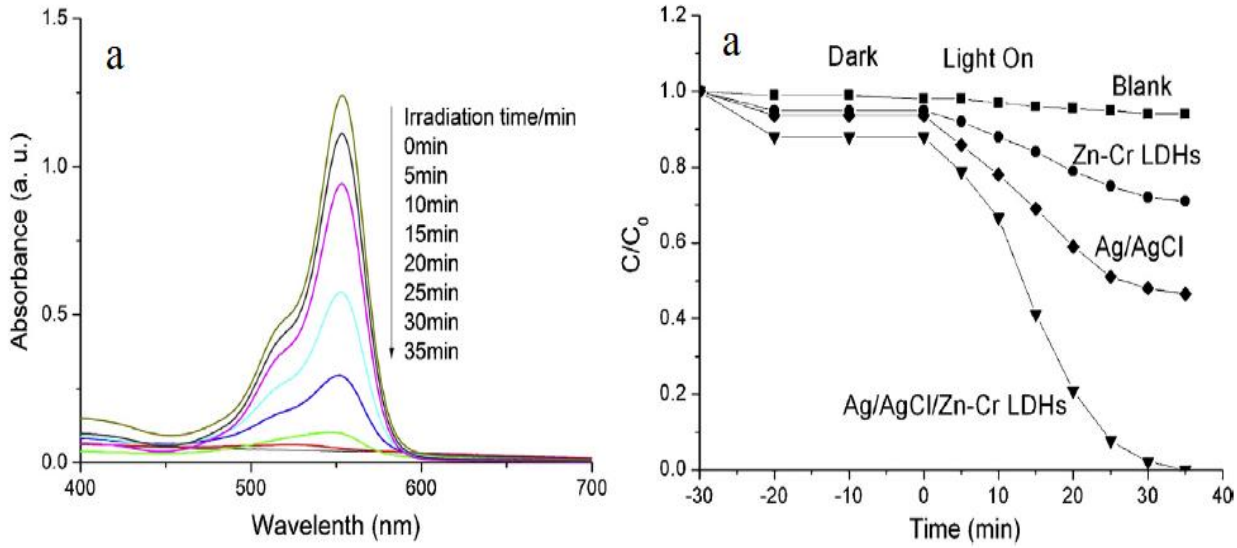

Figure 1.44: a) UV-Vis spectra profiles of RhB during photodegradation in presence of Ag/AgCl/ZnCr and b) the variation of the RhB concentration at different reaction times [111].

results for this study. They show that as separate elements, the LDH and Ag/AgCl complex are able to remove less than 50 % from the initial concentration of the pollutant. However, the hybrid shows significant enhancement of the photoresponsive activity as can be observed from the figure 1.44 b. The pollutant concentration decreases fast, and after 30 minutes of irradiation, almost all the RhB was removed from the system [111].

Other NPs/LDHs nanocomposites used in photocatalysis are listed in table 1.3.

Table 1.3: NPs/LDHs formulation used in organic pollutant photodegradation.

LDHs formulations	Pollutant	Reference
Nb/ZnAl,	congo red,	[112]
Cu/ZnAl	nylosan navy;	[113]
Ti/ZnAl	rhodamine B	[1]
Ti/ZnAl,	methylene blue	[114] [115] [116]
Ti/MgAl,	phenol; methylene blue, Dimethyl phthalate	[117] [118] [119]
Ti/MgAl,	methyl orange	[35];
ZnFeAl, Fe/ZnFeAl	phenol, 2,4 dinitrophenol	[120]
ZnTi, Ce/ZnTi	phenol	[34]
Ti/ZnFe	methylene blue, phenol	[114]
CuMgAlTi, Ti/CuMgAlTi	methylene blue	[108]
CuZnAl, Ti/CuZnAl	methylene blue, phenol	[114]
CuZnFeTi, Ti/CuZnFeTi	methylene blue, phenol	[114]
ZnSn, Ce/ZnSn	Phenol	[33]

b) *Specific applications of NPs/LDHs in biomedicine*

The NPs/LDHs materials can play important roles in biomedical applications. Combining the advantages of two or many nanoparticle in a single nanocomposite, a multiple function material can be obtained.

D Marcato and *al*. have synthetized AgNPs in presence of fungi, starting from $AgNO_3$. MgAlLDH was prepared via co-precipitation route. Both components were contacted for 2 h, and after separation, washing and drying, Ag/MgAlLDH hybrid was obtained. The prepared materials were tested against *Escherichia coli* and *Staphylococcus aureus*. For this, between 0-250 µg/mL of solid were used for the determination of the antibacterial activity. The cytotoxic activity was tested by using a lung fibroblast cell line, derived from a hamster [107].

The results have shown that the simple LDH has no inhibitory effect on the microbial activity of the tested microorganisms. However, the AgNPs and the Ag/MgAl present inhibitory effect at the same minimum concentrations. The cytotoxic effect (see figure 1.45) shows that the MgAlLDH and the Ag/MgAlLDH have a small effect on the viability of the cells, while the biogenic AgNPs present at a maximum concentration, a decrease of cells

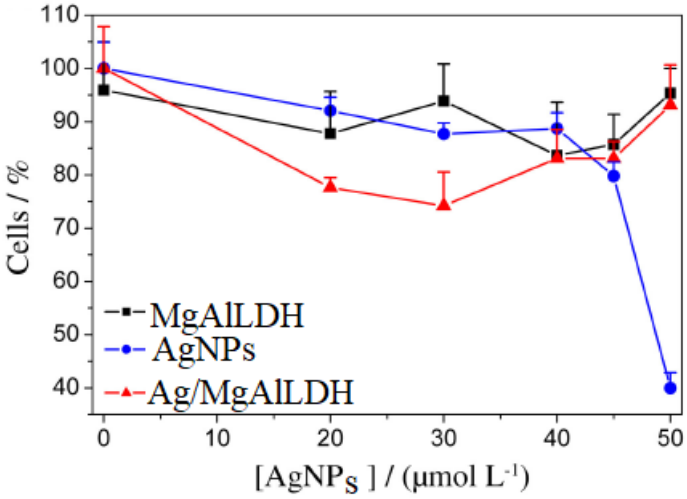

Figure 1.45: Cytotoxic effect on the cells proliferation in presence of MgAlLDH, AgNPs and Ag/MgAlLDH.

proliferation with 50 %. This is a clear indication that the presence of LDH matrix retains the inhibitory effect against the bacteria, but it decreases the cytotoxic effect of the nanoparticles [107]. Formulation type Ag/LDH were also used against Gram Positive *S. aureus* and Gram-negative *E. coli*. The hybrid formulation has a strong antimicrobial effect against these bacteria [121].

A complex hybrid based on ZnO/ZnAlLDH incorporated in waterborne polyurethane (WPU) was obtained by W-D Zhang and *al.* Firstly the ZnAlLDH matrix was prepared via co-precipitation method. Afterwards, the ZnO/ZnAlLDH was obtained by refluxing method, contacting the clay with $Zn(NO_3)_2$, and in the end the hybrid was incorporated in the WPU

matrix. The resulted composite showed a high antimicrobial activity against Gram-positive *Escherichia coli* and Gram negative *Staphylococcus aureus* [122].

Other formulation as SiO_2/LDH and Fe_3O_4/doxifuridine-LDH, ferrite-LDH, have been investigated and they have shown potential for drug release, magnetic drug targeting and magnetic arthritis therapy [123].

1.3. Metal mixed oxides derived from layered double hydroxides

1.3.1. Metal mixed oxides derived from LDHs-synthesis methods

The LDHs based materials can be excellent precursors for the mixtures of metal oxides formation (MMO). Thus, a LDHs material, or its hybrid formed after reconstruction (NPs/LDHs), under an appropriate temperature can lead to the formation of a homogeneous phase, containing metal oxides and spinel phases. In figure 1.46 are presented the main steps in

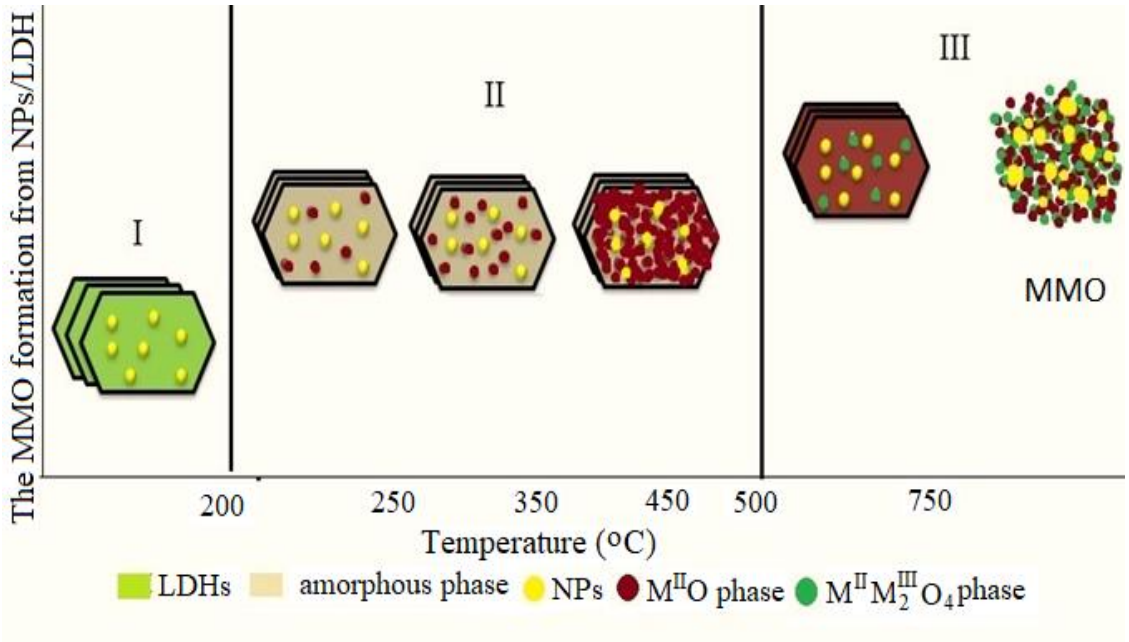

Figure 1.46: Schematic representation of MMO formation [17].

metal oxide/spinel mixtures synthesis starting from a NPs/LDHs material. The process is characterized by three stages: firstly, at a temperature up to 200 °C, the physisorbed water removal and the LDH take place, with the preservation of the layered structure of the material. In the second step, at 250 °C, the interlayer water is released. Between 250-500 °C, the layers dihydroxylation and the LDH carbonate ion removal take place, when the layered structure is destroyed. Also, this stage is characterized by the apparition of an amorphous phase and metal

oxide phase. With the increase of the temperature, the metal oxide will be homogeneously dispersed in the amorphous oxide phase, which up to 500 °C will decrease to almost zero. The last step implies the formation of the spinel oxide ($M^{II}M^{III}_2O_2$), dispersed in the $M^{II}O$ phase [17].

1.3.2. Physico-chemical characterization of the metal mixed oxides derivatives

The effect of the thermal treatment on the LDHs structure and the MMO formation can be investigated by using the characterization techniques as XRD, XPS, FTIR, UV-Vis, TEM, SEM, EDX.

a) X-ray Diffraction (XRD)

Metal mixed oxides derivatives were obtained by S. Thomas and V Kamath by calcination at 800 °C of freshly prepared ZnGaLDH. The structural characteristics of the obtained MMO were investigated by XRD analyze. The XRD pattern of the material is presented in figure 1.47 and it shows the clear formation of the $ZnO/ZnGa_2O_4$ nanocomposite. In this new material, the spinel-like phase is homogeneously dispersed into the ZnO phase. The peaks are sharp underlining a high crystallinity of the material. The presence of the spinel-phase is indicated by the less intense reflections, while the ZnO presents more intense peaks [124].

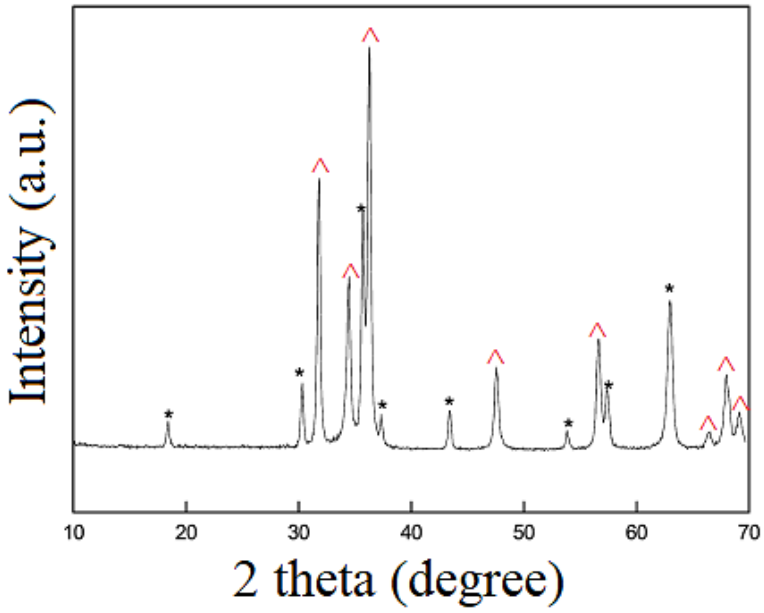

Figure 1.47: XRD pattern of ZnGaLDH calcined at 800 °C; * $ZnGa_2O_4$, ^ ZnO [124].

b) *X-ray Photoelectron Spectroscopy (XPS)*

B. Hu and collaborators have prepared via co-precipitation route the ZnAlLDH. The obtained clay was calcined at 550 °C and used in the absorption of Cr (IV) from aqueous solution. Further, the material was calcined at 900 °C and used in the photodegradation of methyl orange. The XPS spectrum of the ZnAlCr-900 nanocomposite is shown in figure 1.48.

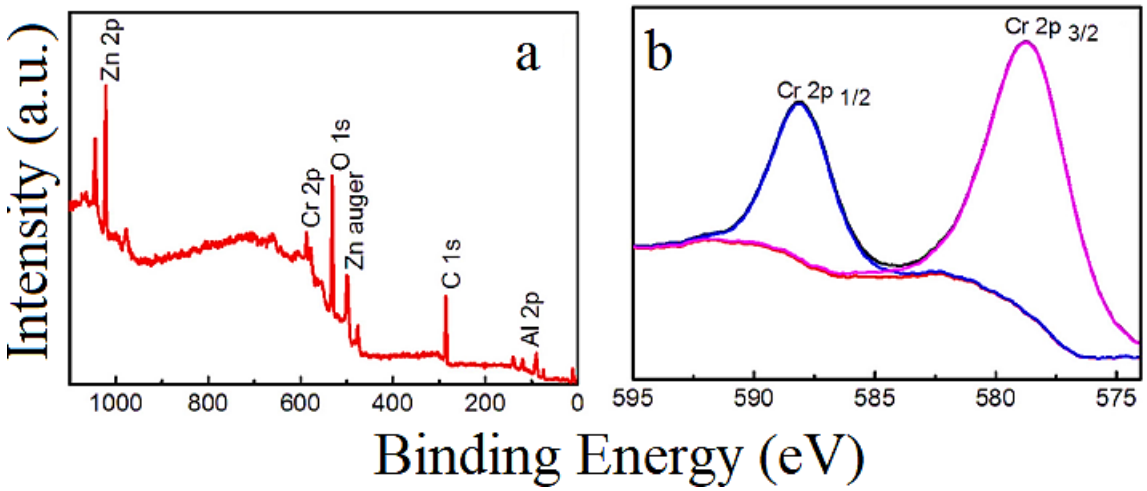

Figure 1.48: a) XPS spectrum of ZnAlCr-900 and b) high resolution XPS spectrum of Cr2p.

It might be observed that the material surface is composed by O, Zn, Cr, Al and C. The carbon is suggesting the presence of some impurities. The high resolution spectrum of Cr2p with peaks centered around 579 and 588 eV reveals the presence of Cr(IV), confirming that the valence of this cation is not depending on the formation ZnO and $ZnAl_2O_4$ [125].

c) *IR Spectroscopy with Fourier Transform (FTIR)*

The FTIR analyze of the MMO confirms the presence of the metal oxides and the spinel like phase in the material structure. After the thermal treatment at a high temperature, the anions and the water molecules are removed from the material. In figure 1.49 is presented the FTIR spectrum of the ZnAlLDH calcined at 800 °C. It might be noticed that the vibration bands assigned to O-H groups, watere molecules and the interlayer anion are not present on the spectrum, and intense peaks between 750-400 cm^{-1} can be remarked and attributed to the MMO [126].

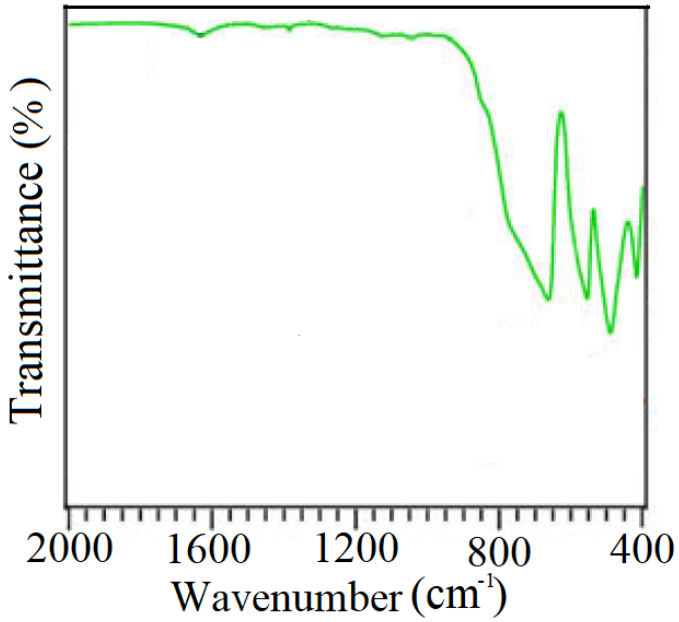

Figure 1.49: FTIR spectrum of ZnAlLDH calcined at 800 °C [126].

d) ***Photoresponsive characteristics studied by UV-Vis spectroscopy***

Generally, the calcination process can modify the optical properties of the LDHs materials. In figure 1.50 are presented the UV-Vis spectra of the ZnFeLDH, and ZnFeLDH calcined at 550 and 700 °C. The fresh material presents a small absorption of the light, and a calculated band gap of 2.45 eV. The calcined products present an improved ability to absorb

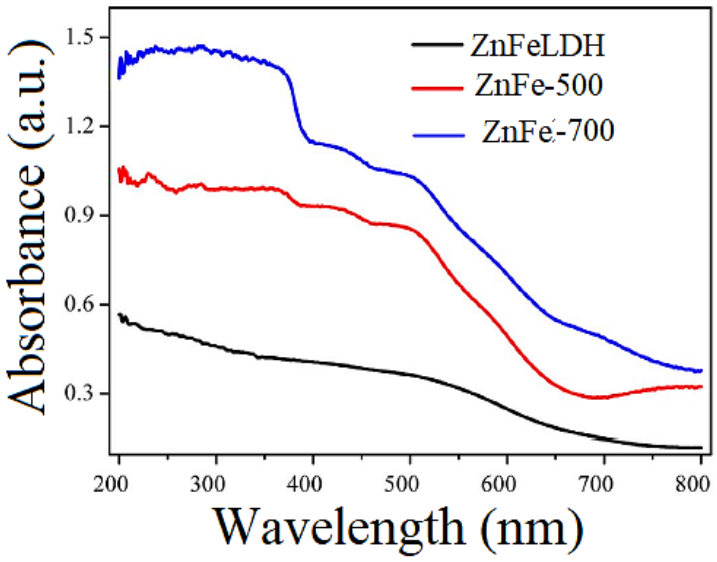

Figure 1.50: UV-Vis spectra of the ZnFeLDH, ZnFe-500 and ZnFe-700 [127].

both UV and visible light, especially the material calcined at 700 °C. A decrease of band gap

was noticed after the calcination, to 2.34 eV for ZnFe-550 and 2.26 eV for ZnFe-700. Based on this results, it is expected that in a photocatalytic process, the calcined materials to show the highest performance [127].

*e) **Textural properties studied by SEM/TEM analyses***

In figure 1.51 are expressed the textural and the morphological properties of the ZnAlCr-900 material, whose synthesis and XPS analyze were presented previously. The SEM images presented in figure 1.51 a and b show that the composites retains the lamellar structure

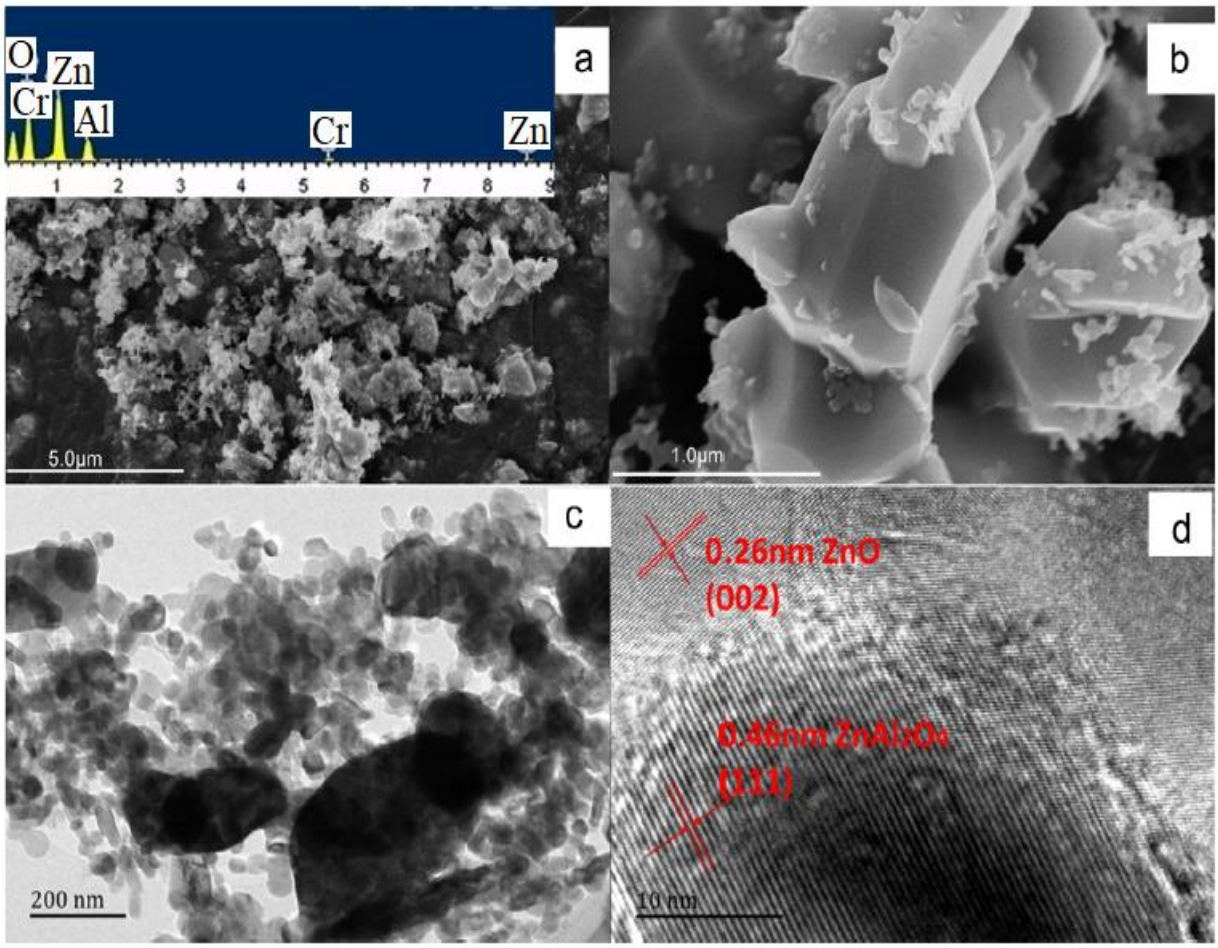

Figure 1.51: a), b) SEM images, c) TEM images, d) HRTEM images of ZnAlCr-900; insert of a) EDX spectrum [125].

of its ZnAlCrLDH precursor, but large aggregates with a diameters of 1 μm are formed. The formation of spinel phase in the continuous network of the metal oxide nanoparticles might involve a direct interaction/contact between these two phases. In the insert of figure 1.51 is presented the EDX spectrum of the material. It can be observed that after the thermal treatment, the calcined product is composed by O, Zn, Al and Cr. The TEM images (figure .1.51 c, d)

reveal that both $ZnAl_2O_4$ and ZnO phases have a high crystallinity. The high resolution TEM imagine shows the lattice fringes of the phases which can be identified as the (002) plane of the ZnO phase with a spacing value of 0.26 nm, and (111) facets of $ZnAl_2O_4$ phase with spacing value of 0.46 nm. From figure 1.51 d might be also observed that the spinel phase is dispersed in the ZnO phase [125].

1.3.3. Specific applications of MMO in photocatalysis and nanomedicine

a) Specific applications of MMO in photocatalysis

Another simple and low cost method to obtain combinations between two or many semiconductors is to use LDH or NP/LDHs as precursors. Starting from these composites, via thermal treatment, heterojunction nanostructures can be obtained, between oxides and spinel phases. These features of the LDHs materials make them to be important photocatalysis, and as it was previously expressed, the combination of two semiconductors can be a manner to decrease the recombination rate of the charge carriers involved in the photocatalytic process.

CeO_2 nanoparticles dispersed on the ZnTiLDH surface were obtained by combining the co-precipitation with the reconstruction method. The resulted material, denoted as CeO_2/ZnTiLDH was tested in the pholtodegradation of phenol, under UV irradiation. Together with the fresh materials, the calcined products at 600 and 750 °C were also tested. The obtained results are given in figure 1.52. It might be observed that during the irradiation under UV light

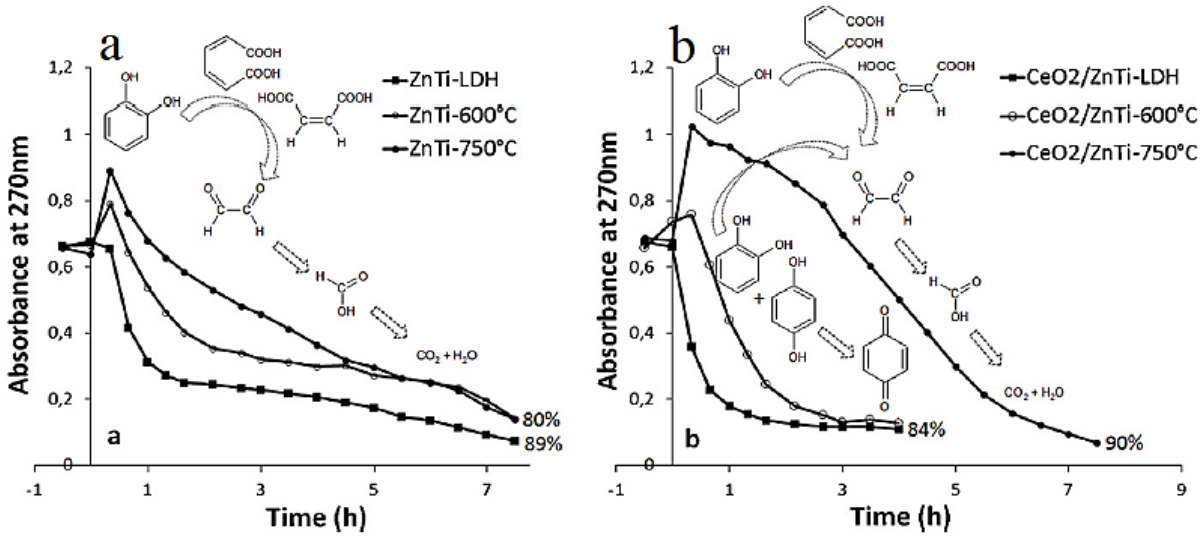

Figure 1.52: Photodegradation of phenol under UV irradiation by using ZnTiLDH, ZnTi-600 and ZnTi-750 and b) CeO_2/ZnTiLDH, CeO_2/ZnTi-600 and CeO_2/ZnTi-750 [34].

the absorbance decreases gradually in time. The best catalysts considering the photodegradation percentages reported to the irradiation time are the calcined hybrids. The fresh materials and

the calcined one, ZnTi-600 and ZnTi-750, lead to a total degradation between 80-90 % in 7 h, while the CeO_2/ZnTi-600 and CeO_2/ZnTi-750 materials lead to 84 % photodegradation in 4 h [34].

Mixed metal oxides obtained by thermal treatment of ZnFeLDH at 550 and 700 °C were used for the methylene blue and tetracycline photodegradation under visible light. The results have shown that the calcined product present a superior performance for the photodegradation of both organic pollutants [127]

MgZnInLDH was prepared by co-precipitation and after calcined at 300, 500 and 800 °C. The obtained materials were tested in the visible light photodegradation of the methylene blue. The pollutant can be degraded only by light in a proportion of 36 %. However, the presence of the catalysts in the system increases the methylene blue removal, and the most preformat catalysts are the calcined one. Their performance enhances with the calcination temperature increase, the MgZnInLDH calcined at 800 °C being able to degrade the entire pollutant amount in 5 h [128].

b) *Specific applications of metal oxides and MMO in biomedicine*

The metal oxides resulted after the LDHs calcination around 500 °C can be used for the intercalation of different drugs in the material structure, and further investigated for the drug release and therapeutic activity [129].

Fe_2O_3/MgAlLDH was prepared by adding drop by drop the salts solution and the precipitation precursors to a methanol dispersion containing Fe_2O_3 nanoparticles. The obtained material was calcined at 500 °C and used to incorporate the DFUR anticancer agent. The drug release was investigated in free or under magnetic field. Without magnetic field, 96 % of the DFUR is released from the LDH matrix in 200 minutes, while under the stimulation of magnetic field, 93% of the drag is released in 560 minutes. This behavior indicates that the drug release can be controlled by the magnetic field, having promising utilization in magnetic drug targeting [130].

ZnAlDLH with silver incorporated in its structure was obtained via co-precipitation rout as described by G Mishra. The XRD and TEM analyses have proven that the AgNPs were deposited on the LDH surface. The obtained material was thermal treated at 800 °C and its antimicrobial activity against *Escherichia coli* and *Staphylococcus aureus* was tested. For comparison, the simple ZnAlLDH and the uncalcined Ag/LDH were also tested. The results have shown that the simple LDH had no inhibitory effect, while the thermal treated material, which is a combination between the spinel phase, ZnO and Ag_2O, presented the highest antibacterial activity [131].

In a review published in 2014 by X. Bi, others pharmaceuticals incorporated in LDHs materials by using metal oxides were mentioned. For instance, drugs as camptothecin, ibuprofen, naproxen, fenbufen, fluribiprofen, indomethacin, mefenamic acid, 5-fuorouracil,

doxifluridine, camptothecin were adsorbed on metal oxides resulted from the calcination of MgAlLDH, ZnAlLDH, MgFeAlLDH and used for the drug release investigation [132].

1.4. Biocomposites based on layered double hydroxides

Layered double hydroxides are materials able to incorporate in their structure large biomolecules as enzymes. The enzymes are biological catalysts involved in different processes which take place in the living systems. The enzyme utilization has its origin in the ancient times, when their nature and properties were not known, being used especially in food processing actives. What is special to these active proteins is their ability to operate under mild conditions. Furthermore, they possess very high substrate specificity, leading to the formation of certain products. The enzymes are able to catalyze reactions in their free state or attached to a surface [133]. However, being expensive materials, because of their extraction and purification, and relatively unstable, the enzymes utilization at an industrial level imposes their immobilization on different surfaces.

The immobilized enzymes are that enzymes localized on a particular surface, with retention of their activity. A consequence of immobilization is the reduction of operational costs, and the increase of enzyme utilization number, repetitively and continuously [134]. In addition, after the attachment on a surface, the enzyme thermal and mechanical stability can increase. Another strength of immobilization is the possibility to stop the reaction at determined moments, and because the possibility to separate the solid from the reaction system, the product contamination with enzymes is avoided [135].

The enzyme immobilization represents an important aspect not only for their industrial utilization, but also for a number of applications in diagnostics, therapeutics, biosensors, and bioaffinity chromatography [133].

1.4.1. Enzyme structure and properties

Enzymes are catalysts able to speed the velocity of a chemical reaction without the implication of a supplementary additive. Generally, the enzymes are proteins which possess in their structure an active site. The active site is involved in the catalytic process, being the area where the substrate binds with the protein. The enzymes are protein macromolecules with a tridimensional structure and they are built from amino acids. The amino acids sequence forms a linear chain named primary structure (figure 1.53 A). The amino acids can bind with each other via hydrogen bond resulting the secondary structure (Figure 1.53 B). The secondary structure can be presented as α-helix or β-sheet (anti-parallel sheet or parallel sheet). Because of 2D linear chain folding-up in the secondary structure, the enzyme can fold-up further to a tridimensional structure, the tertiary one (figure 1.53 C).

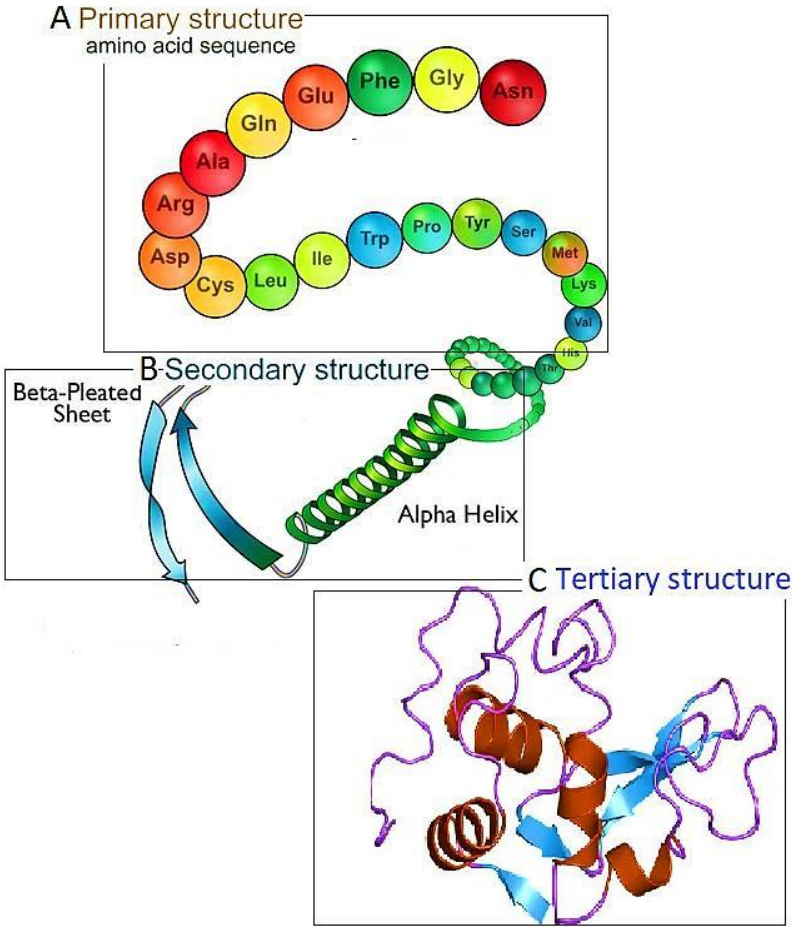

Figure 1.53: Enzyme primary (A), secondary (B) and tertiary (C) structure.

The enzymes can be classified in six main classes: oxidoreductase, transferase, hydrolase, lyases, isomerases and ligases.

Optimal operational condition of enzymes

Enzyme activity is depending on factors as temperature, pH and reaction medium. All these factors can increase or can decrease the enzyme performance. Each enzyme has its optimal reaction conditions.

Generally, for the classic reactions, the temperature increase, increases the speed of the process. In case of enzyme, the temperature increase enhances the number of collisions which take place between the active centrum of enzyme and the substrate molecules, and as a consequence the velocity of reaction increases. However, the enzymes do operate at an optimal temperature. Being proteins, they are altered by extreme temperature values, when the H-bonds can break. In function of their origin, the enzymes optimal temperatures can variate. For instance, the human body enzymes can be used with good performances in a temperature range

between 35 to 40 °C. Other active proteins, as the ones from thermophilic bacteria, can operate at higher temperature, between 65 to 80 °C (see figure 1.54 A) [136].

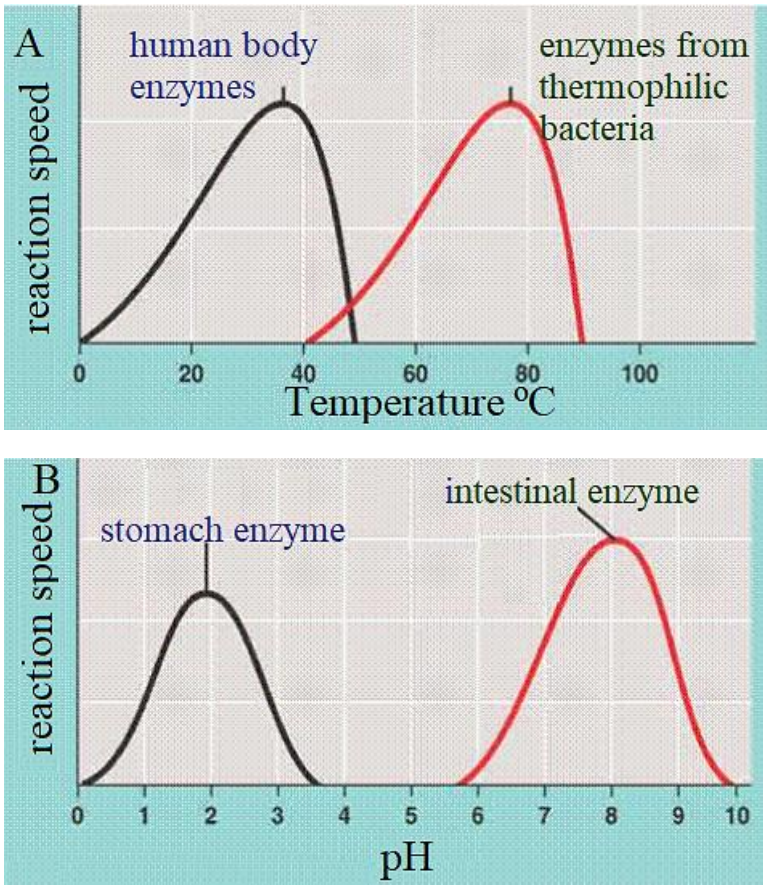

Figure 1.54: Effect of A) temperature and B) pH on enzymes reaction rate [136].

As well as the temperature, the pH is another important factor which influences the enzyme performance. Most of the enzymes remain active in a pH range between 6 to 8, and their pH stability is depending on the system where they are working. For example, an enzyme from stomach will operate at optimal pH of 2, while the one from the intestine will have an optimal pH around 8 (figure 1.54 B). The extreme pH values, as very low or very high, can destroy the H bonds in the protein because of the high concentration of H^+, respectively OH^- ions. As a consequence of this fact, the substrate cannot bind properly to the active site of the enzyme and its activity decreases or can stop [136].

Another important factor which influences the enzyme performance is the substrate concentration. For a given enzyme concentration, the concentration enhancement, will saturate progressively the active site of the enzme, till the maximal rate of reaction will be reached The increase of substrate concentration has no effect on the reaction rate, after the rate reaches its maximum value (see figure 1.55 a). The reaction rate can be also increased with the increase of the enzyme quantity (figure 1.55 b), when the substrate is in excess [136].

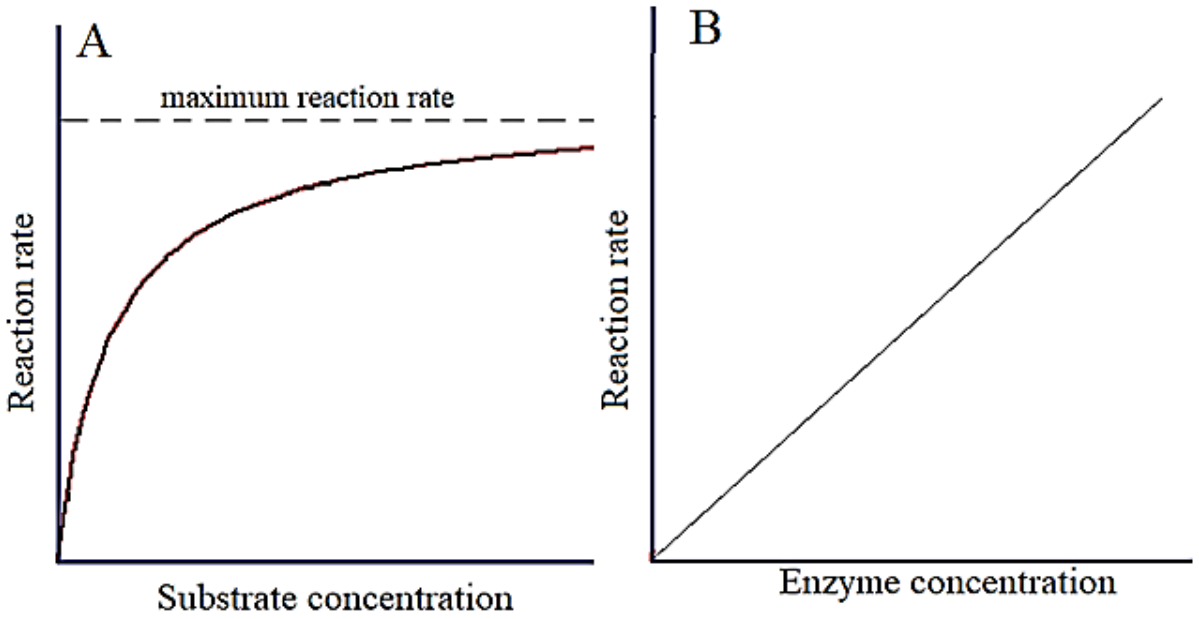

Figure 1.55: Reaction rate variation in function of A) substrate concentration and B) enzyme concentration [136].

Enzymatic reaction

The enzymatic reactions is often characterized by a high specificity degree. Typically, the majority of enzymes enzyme can catalyze only a single type of reaction, which means that it will accept only certain substrates. When an enzyme will meet an appropriate substrate, they bind in a reversible way, forming an enzyme-substrate active complex (ES). Further, the enzyme catalyzes the reaction, an enzyme-product is formed, the products are released in the system and the enzyme returns to its initial form (see eq. 1.11). For each reaction step, association (k_1, k_{cat}) and dissociation (k_{-1}) constants are assigned for the complex formation [137].

$$E + S \underset{k_{-1}}{\overset{k_1}{\rightleftarrows}} ES \xrightarrow{k_{cat}} E + P \qquad (1.11)$$

The enzyme-substrate complex can be formed in two different ways. According to the simplistic Emil Fisher model, the enzyme and substrate are complementary and they fit perfectly, without any supplementary modification. This is the *lock-key model*. The second proposed complex formation is the one of Daniel Koshland (figure 1.56), which says that the enzyme and the substrate do not fit like a key and a lock, but the active site of the enzyme reshaped continually as a consequence of enzyme interaction with the substrate. This is the *induced fit model* [138].

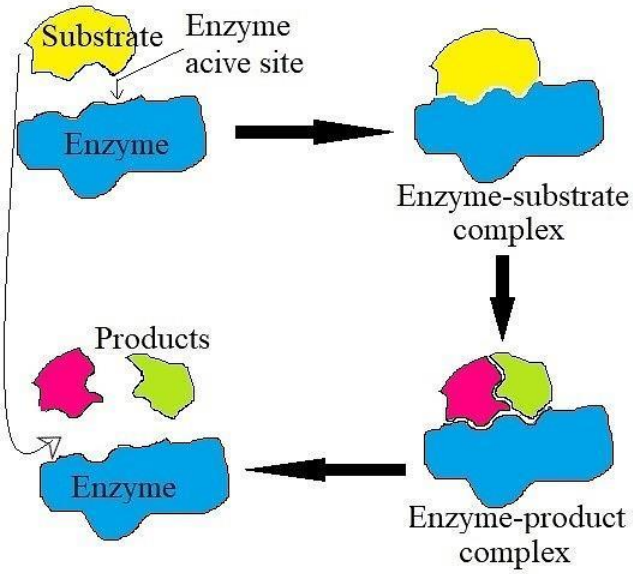

Figure 1.56: Daniel Koshland induced fit model.

The kinetics of an enzymatic reaction can be evaluated by Michaelis-Menten relation (eq. 1.12). This equation describes the rate of products formation, in an enzymatic process, without any secondary inhibition processes [137].

$$V_i = \frac{d[P]}{d\tau} = \frac{V_{max} \cdot [S]}{K_M + [S]} \tag{1.12}$$

V_i is the initial rate of product formation;
[S] is the substrate concentration;
[P] is product concentration;
K_M is Michaelis-Menten constant;
V_{max} is the maximum reaction rate [137].

The graphical representation of equation 1.12 drives to Michaelis-Mentin plot (figure 1.57). According with this, the K_M constant can be defined as the substrate concentration for which the reaction speed is a half from the maximum reached rate. Because of the maximum velocity cannot be exactly calculated from Michaelis-Mentin plot, the linearization of equation 1.12 is mandatory [137] for the determination of the kinetic parameters, V_{max}, K_M and $V_{max\ specific}$. The maximum specific rate, $V_{max\ specific}$, represents the maximum velocity reported to the enzyme quantity used for the catalytic reaction.

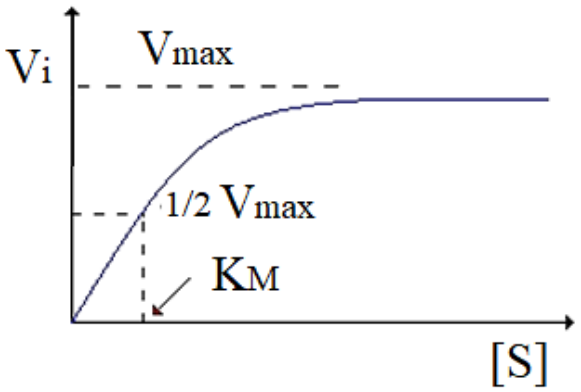

Figure 1.57: Michaelis-Mentin graphical representation [137].

One of the most used linear representations of equation 1.12 is the Lineweaver-Burk relation (eq. 1.13).

The graphical representation of equation 1.13 allows the determination of V_{max} and $K_{M.}$

$$\frac{1}{V_i} = \frac{K_M}{V_{max}} \cdot \frac{1}{[S]} + \frac{1}{V_{max}} \qquad (1.13)$$

as expressed in figure 1.58.

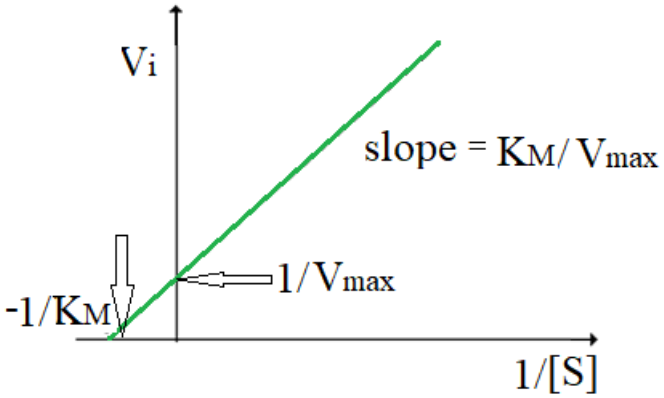

Figure 1.58: Graphical representation of Lineweaver-Burk equation [137].

Some substances can induce a decrease of enzyme performance, and the process is called enzyme inhibition. The inhibition can be competitive, noncompetitive and uncompetitive. The competitive inhibition takes place when the substrate and the inhibitor are in competition for the active centrum of the enzyme. In case of noncompetitive inhibition, the inhibitor binds on other site of the enzyme, named allosteric site, and this linkage, can block or change the active centrum of enzyme, and as a consequence, the enzymatic activity decreases,

or can stop. Uncompetitive inhibition happens when the inhibitor binds to the enzyme-substrate complex and this phenomenon take place usually when the reaction occurs with several substrate or products [139].

1.4.2. Enzyme immobilization methods and supports

a) Enzyme immobilization methods

At the beginning of XX century, Nelson and Griffin proved that an adsorbed enzyme on a solid support (active carbon) can have the same enzymatic activity as the native one. In 1949, Micheel and Ewers immobilized a physiological active protein, and two years later, in 1951, Campbell attached the albumin on diazotized p-aminobenzylcellulose. The first enzyme immobilization, with the purpose of enzymatic performance enhancement, was done in 1953 by Grubhofer and Schleith. They immobilized enzymes like *diastase*, *pepsin*, *ribonuclease* on diazotized polyaminopolystyrene resin. In the next years, the enzyme immobilization paid the attention of many scientists and many studies on physico-chemical properties of the attached active proteins were done. The attached enzyme on a support was denoted generally immobilized, but others terms can be used to express the same fact: fixed enzyme, water-insoluble enzyme, matrix-supported enzyme or trapped enzyme [140].

The enzymes are able to bind to a surface due to some of their functional groups as animo and carboxyl groups, phenolic groups, the imidazole group of histidine, the hydroxyl groups from threonine and serine [140]. Because the enzymes are sensitive biomolecules, their immobilization must be carry out under mild conditions. Some of the reasons of the immobilization of this biocatalysts are:

- the possibility to reuse the enzymatic material many times;
- the possibility to stop the reaction just by removing the supported enzyme from the system;
- the products are not unpurified with enzymes [135].

The immobilization methods can be reversible and irreversible, which means that after immobilization, the enzyme can be or not removed from the support, with the retention of its activity. The main enzyme supporting techniques are the next (figure 1.59):

- enzyme binding on water-insoluble supports, like glass, synthetic polymers, polysaccharides derivatives, via adsorption, covalent or ionic linkage;
- enzyme crosslinking using bi- or multifunctional reactive like glutaraldehyde, hexamethylene diisocyanate;
- enzyme entrapment in a matrix of a semipermeable gel or inside of a polymer membranes.

The enzyme immobilization on a solid support is one of the most used irreversible techniques. The involved enzyme groups in the immobilization are the amino, carboxylic,

phenolic groups, groups which do not play an important role in catalytic performance. The enzyme catalytic activity after a covalent linkage on a solid support depends on the immobilization conditions, support shape, dimensions and nature.

The covalent coupling has to be done without losses of enzyme activity and without destruction of its active site. For this reason, the covalent binding is more difficult to be realized compared with adsorption and ionic linkage. However, this method leads to extremely powerful bond between the biocatalyst and support [141,142]. Because in the formation of the biohybrid has to participate only those groups without value in the enzymatic reaction, protection methods can be used to avoid the implication of the active site in the immobilzation process. One of these methods can involve the enzyme immobilization in presence of a substrate or of a competitive inhibitor.

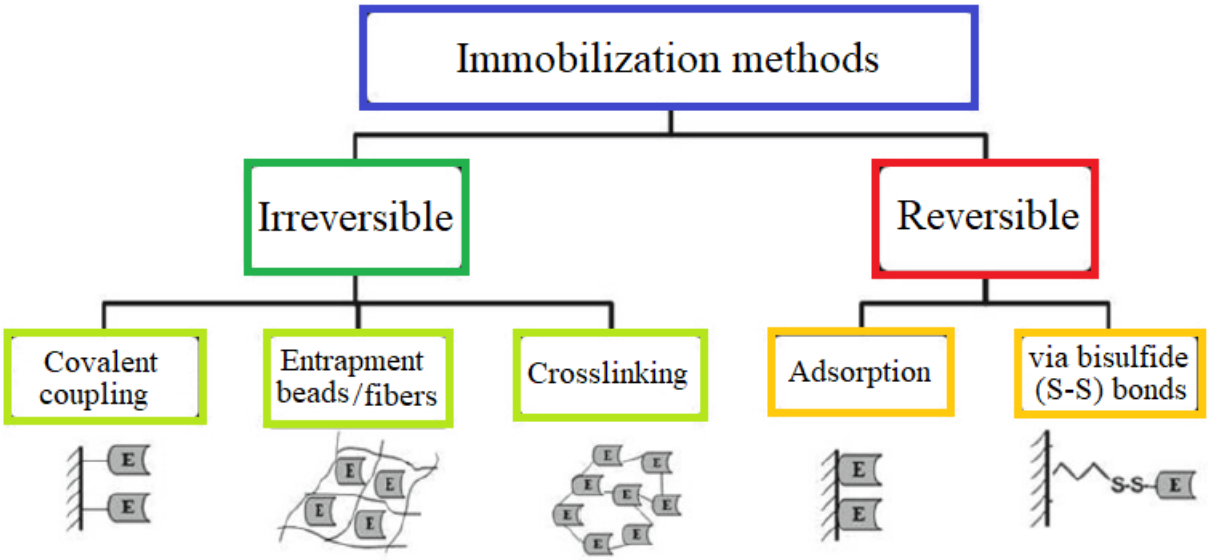

Figure 1.59: The most important methods of enzyme immobilization [133].

The covalent binding can be realized with the implication of different bonds:

- support-N=N–enzyme;
- support-CO-NH—enzyme;
- support-CH_2-NH-enzyme,
- support-CH_2-S–enzyme;
- support-CH=N–enzyme;
- support-CNH-NH–enzyme;
- support-SS–enzyme;
- support-O$(CH_2)_2$N=CH $(CH_2)_3$CH=N-enzyme [141].

Enzyme **crosslinking** is a free support immobilization method involving the utilization of bi- or multifunctional materials which lead to the reticulation of enzymes. This technique is an expensive one and usually the crosslinked enzyme suffers a decrease of activity because

some of the biomolecule will act as a support. Generally, this method can be used for the stabilization of the adsorbed biomolecules, to prevent their leaking from the solid surface. The most used reagent is glutaraldehyde [142].

The **reversible** enzyme immobilization methods are carried out in mild conditions. They are attractive techniques because allow the loading of fresh enzyme when the initial ones losses their activity. The **direct physical adsorption** of enzymes on different supports is made via hydrogen bonds, van der Waals forces or hydrophobic interactions. The procedure is simple and cost effective, is not involving additional reactive and the immobilization is made under gentile conditions, with high enzyme activity retention. However, because the adsorption take place via weak bonds, enzyme desorption can happen as a result of temperature or pH variation, ionic strength, or because of the simple presence of the substrate. Another disadvantage is the fact that the adsorption is not specific, and other molecules can link to the surface, changing the enzyme properties [142].

b) Supports in enzyme immobilization

The support characteristics can have an important influence on the catalytic performance of the immobilized enzymes. There are some significant aspects which have to be considerated when a support has to be chosen for a further utilization in enzyme immobilization:

- Functional groups: influence the enzyme operational stability on support; usually, the immobilization methods involve the nucleophilic attack of enzyme's amino groups on the activate functional groups of the substrate.
- Permeability and support surface area: a large surface area (>100 m^2g^{-1}) and a large porosity are undesirable because the enzyme and the substrate can easily to penetrate the support; pores dimension around 30 nm are a good parameter for enzyme immobilization for most of the supports;
- Support hydrophobicity and hydrophilicity can influence the strength and the type of the non-covalent interaction with the enzyme, and also the adsorption and the substrate/product distribution and availability;
- Support insolubility is mandatory to avoid enzyme losses and product contamination;
- Mechanical stability: in case of biohybrid utilization in a stirred reactor, the support must be mechanically stable;
- Support resistance against microorganisms action;
- Support regeneration: it is important especially for the expensive supports [143].

Supports can be, according to their chemical composition, organic (chitosan, collagen, cellulose, pectin, starch, carrageenan etc.) and inorganic (zeolite, ceramics, celite, silica, activated carbon, charcoal, anionic clays) and in function of the origin of material, they are natural or synthetic.

1.4.3. Enzyme-LDHs biocomposites

Enzyme-LDHs biocomposites - synthesis methods

The enzyme-LDHs biocomposites (Enz/LDHs) can be obtained via adsorption or via co-precipitation. During the synthesis, it is important that the temperature and the pH to be chosen in the operational range of the enzyme.

a) **Co-precipitation method**

The Enz/LDHs synthesis via co-precipitation method involves the simultaneously addition of an enzyme solution, precipitation agent and salts solution, followed by maturation, hybrid separation, which is further washed, and dried at an appropriate temperature. To avoid the intercalation of other anions between lamella, the synthesis must be done under an inert atmosphere. The co-precipitation can be also carried out by adding the precipitation agents and the salt solution to an enzymatic solution [83].

b) **Adsorption**

The Enz/LDHs biohybrids can be obtained as well via adsorption. In this case, in an enzymatic solution is dispersed the fresh LDH material or the calcined LDH. The mixture is kept under moderate stirring, to avoid enzyme foaming; the enzyme quantity in solution is monitored to know when the adsorption is ended. The product is washed to remove the non-adsorbed protein, and dried at room temperature [144].

Physico-chemical characterization of the Enz/LDHs biocomposites

An important step in enzyme immobilization is the phisico-chemical characterization analysis of the resulted biocomposite. The used techniques have to confirm the enzyme presence on the chosen support and the properties of the new biomaterial.

a) ***X-ray Diffraction (XRD)***

XRD analysis of the immobilized enzyme usually gives information about how the immobilization process affected the support structure. However, in function of support, the protein presence can be also confirmed. For instance, in case of the anionic clays, the enzyme can be adsorbed on solid surface, or intercalated between lamella (figure 1.60).

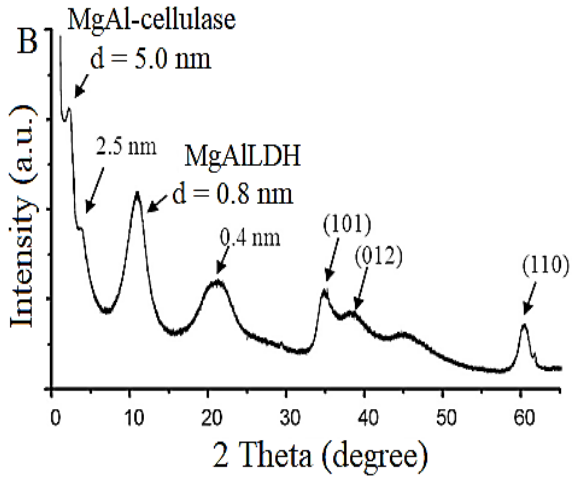

Figure 1.60: XRD pattern of MgAl-cellulase (B) [145].

When intercalation takes place, the XRD pattern of the LDH-enzyme material can be used for enzyme immobilization confirmation. As it was discussed in a previous chapter, the LDHs anions can be identified by calculating the interlayer distance corresponding to (003) peak. In case of MgAl-cellulase material, this distance was calculated from the first intense peak. So the value of the basal spacing increases from 0.8 nm (MgAlLDH) to 5 nm for MgAl-cellulase, proving that the enzyme was successfully intercalated between clay lamella [145].

b) IR Spectroscopy with Fourier Transform (FTIR)

FTIR analyze (see figure 1.61) is an useful technique when working with immobilized enzyme, which can be used to confirm the enzyme binding to a support. As for the simple

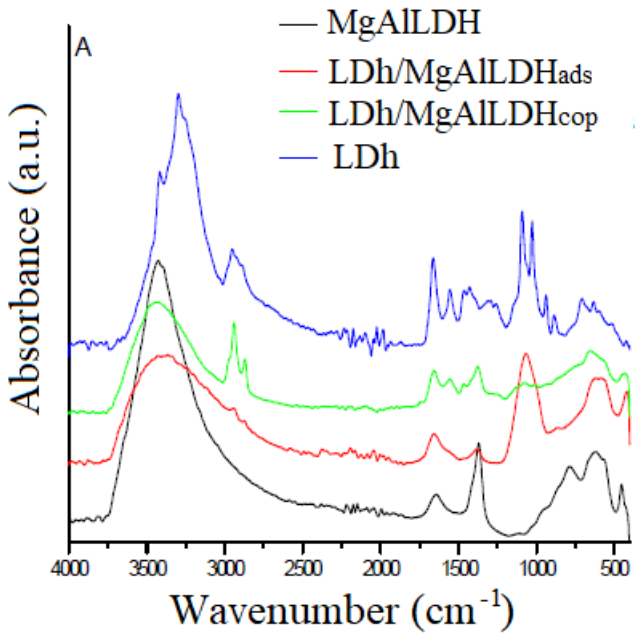

Figure 1.61: FTIR spectra for MgAlLDH, LDh/MgAlLDH$_{ads}$, LDh/MgAlLDH$_{cop}$, LDh.

LDHs, the FTIR analyze of Enz/LDHs gives information about the functional groups present in the material structure. Supplementary functional groups will be present on a FTIR spectrum in case of a Enz/LDH biohybride. In figure 1.61 are presented the spectra for lactate dehydrogenase (LDh), MgAlLDH and LDh/MgAlLDH obtained by co-precipitation and adsorption. The LDh characteristic adsorption bands can be remarked around 2900, 1550, 1100 and 950 cm^{-1} and they are assigned to the $–NH_2$ amide groups, the aromatic groups, C-N or C-C binding and C-H binding of the aromatic groups present in the enzyme structure. These signals are identical for both free and immobilized enzyme, indicating that the immobilization succeeded. Besides this peaks, the characteristic vibration pf the LDH matrix are also present. Can be identified the signals of the hydroxyl groups O-H at 3400 cm^{-1}, the signals for the carbonate anions at 1360 cm^{-1}, of the water molecules at 1640 cm^{-1} and those characteristic to M-O and O-M-O stretching modes in an range between 850-440 cm^{-1} [83].

c) Scanning electron microscopy (SEM)

N. Zou and J. Plank reported the successful intercalation of cellulase into MgAl-NO_3LDH matrix. The intercalation was confirmed via scanning electron microscopy and the chemical composition of the new material was verified by EDX measurements. Figure 1.62 A

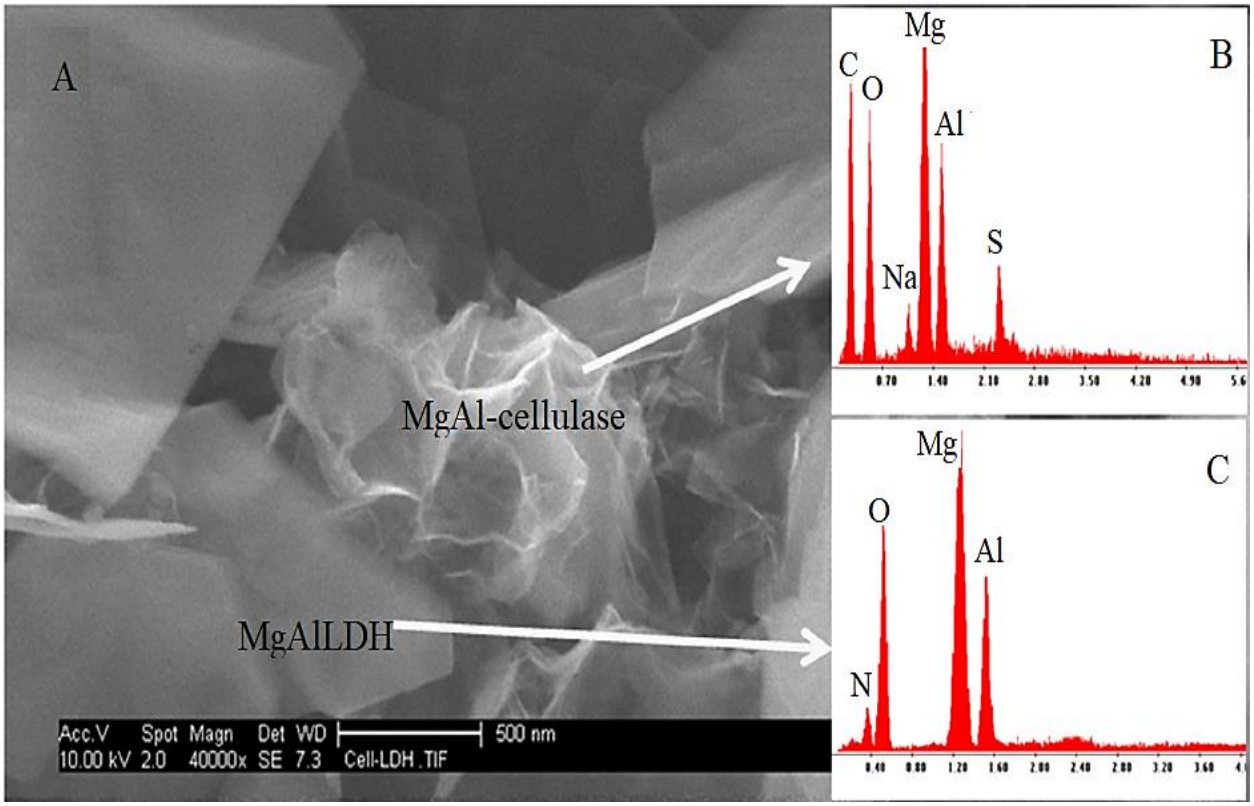

Figure 1.62: SEM imagine of MgAl-cellulase material (A) and EDX analysis for MgAl-cellulase particles (B) and MgAlLDH (C) [145].

shows the presence of cellulase as inter-grown nanofoils, with flower aspect and with a

thickness of cca. 20 nm. This morphology is typical for anionic clays incorporating large molecules. The EDX measurements were done on the same sample, but in different areas. Such, it can be easily observed from figure 1.62 B that the nanofoils belong to the biohybride, due to the high carbon content, while the large hexagonal platelets are characteristic to clay matrix (figure 1.62 C).

d) Transmission electron microscopy (TEM)

M.A. Dejbbi and co-workers were synthetized via co-precipitation method and adsorption biohybrides between LDHs nanomaterials and lactate dehydrogenase (LDh). The influence of immobilization process on LDH morphology was investigated via transmission electron microscopy (TEM). Figure 1.63 shows the TEM images for MgAlLDH, LDh/MgAlLDH$_{ads}$ and LDh/MgAlLDH$_{cop}$. The fresh MgAlLDH has a typical hydrotalcite structure, formed by hexagonal platelets [83].

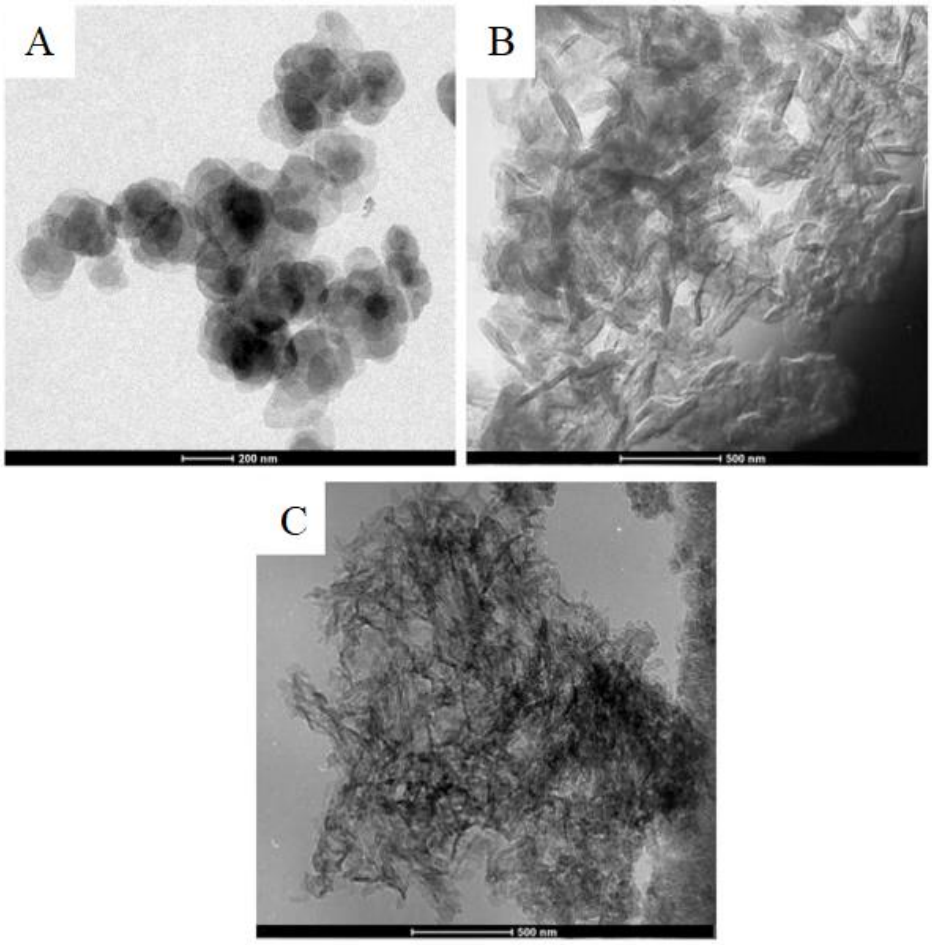

Figure 1 63: TEM images for A) MgAlLDH, B) LDh/MgAlLDH$_{ads}$, C) LDh/MgAlLDH$_{cop}$.

When the LDh is adsorbed on LDH surface (see figure 1.55 B), a small change of TEM occurs, as a result of enzyme aggregation on solid surface. The coprecipitation leads to dense aggregates of enzyme on LDH surface (see figure 1.64 C) [83].

e) Thermogravimetric analysis (TGA)

MgAlLDH modified with glutamic acid was prepared by Cordova and Borges and further used to immobilize the laccase enzyme via adsorption protocol. The obtained materials were denoted as MgAlLDH-G and MgAlLDH-GL. The thermal stability of the obtained materials was investigated by using the thermogravimetric analyze (figure 1.64). The TG curve of the free enzyme shows that the protein starts to lose weight around 230 °C. The copper content from the laccase enzyme is insufficient to be detected by this measurement, since in the enzyme structure are only four active centers containing cooper. The modified LDH material, MgAlLDH-G, in a range between 30-850 °C losses 48.3% of its initial mass, while the

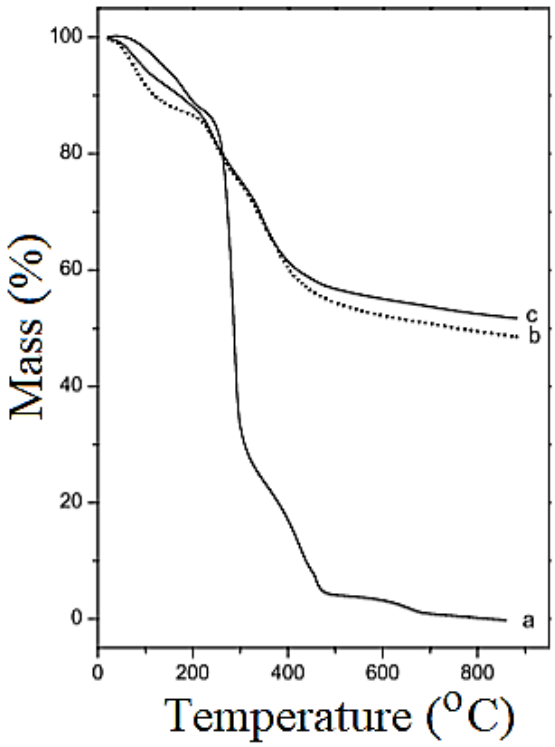

Figure 1.64: TG curves for a) free laccase, b) MgAlLDH-G, c) MgAlLDH-GL [146].

biomaterial, MgAlLDH-GL, losses in the same range 51.5%. This additional mass loss is a clear indication of enzyme presence on the materials surface, which, when immobilized it adds organic matter to the initial material [146].

Specific applications of LDHs based materials in enzyme immobilization

a) Specific applications of LDHs in enzymes immobilization

A new class of hybrid materials can be designed by combining different biomolecules with the inorganic supports. Layered double hydroxides, besides their intensively utilization in catalysis, photocatalysis, separation, optics and others, were approached also in enzyme immobilization, especially for the biosensor design and biocatalysis. Properties like: variable anionic exchange capacities, low toxicity, adjustable textural and morphological properties controlled by synthesis, variable chemical composition of the layer and interlayer space, and also the ability to incorporate large molecules in their structure, make the LDHs composites to be attractive materials for the enzyme immobilization [147].

Recently, Y. Ding and co-workers have used MgAlLDH material to adsorb on its surface the dextranase enzyme. They showed that the protein presence on the materials surface affected clay's crystalline structure. The interaction between the support and enzyme were hydrophobic and electrostatic [148]. Previously, CoAlLDH was obtained via co-precipitation method. The obtained material had been deposited on electrodes and after the tyrosinase enzyme was auto-assembled on the modified electrode. The biosensor was used for the detection of polyphenols. The results have shown that a robust and sensitive biosensor was obtained, which could be used many time without significant loss of performance [149].

Phenol oxidase and ZnAlLDH were together spread on a glass electrode, which was after dried at the room temperature. The biosensor was tested in the detection of catechol. The results showed that the biosensor has a good affinity to substrate, high storage stability and a sensitivity of cca 7800 $mA/M/cm^2$ [150]. For phenols detection, another enzyme was used for biosensor fabrication. Horseradish peroxidase (HRP) was immobilized on the CoAlLDH and afterwards the biohybrid was attached to a glass carbon electron. The biosensor was used in 2-clorophenol and H_2O_2 detection. The biosensor sensitivity was 678 μA/μmol/l and the limit of detection was 0.002 μmol/L [151].

Besides the immobilization of enzymes on LDHs for biosensing purpose, these biohybrids were used also in biocatalysis. Fructose-6-phosphate aldose was immobilized on MgAlLDH and tested in the sugar analogues synthesis. The activity of the biohybride was comparable with the one of the free enzyme, with only 10 % of activity loss [152]. Yeast transketolase was adsorbed on ZnAlLDH and MgAlLDH surface. The enzyme presence on the materials surface induces an important amorphization, with a high decrease of crystallinity. The enzymatic reaction was carried out L-erythrulose and D-ribose-5-phosphate as substrates. The determined kinetic parameters have similar values for the free and supported enzyme [153].

It is interesting to note that on the same LDHs materials can be immobilized many enzyme in the same time. R Mahdi presented for the first time the immobilization of four distinct enzymes (dihydroxyacetone kinase pyruvate kinase, triosephosphate isomerase and

fructose-6-phosphate aldolase) on MgZnAlLDH. The biohybrid was successfully used in the d-fructose-6-phosphate synthesis [154].

b) Specific applications of NPs/LDHs in enzyme immobilization

The hybrids nanomaterials obtained by combining different organic or inorganic nanoparticle with LDHs matrix started also to pay attention for enzyme immobilization. However, the number of studies made on NPs/LDHs is considerable smaller from that involving simple LDHs composite.

Wang and co-workers have fabricated a H_2O_2 biosensor by supporting on a glass carbon electrode (GCE) a biohybride material containing HRP attached on a mixture of CoFeLDH and carbon nanodots (C-Dots). The biosensor shows its maximum performance at a pH value of 7 and it has superior analytical performances in terms of detection limit and selectivity compared with CoFeLDH/GCE, C-Dots/GCE, C-Dots/CoFeLDH/GCE formulations (see table 1.4) [155].

Table 1.4: Analytical performance of the tested sensors and biosensors based on HRP-LDH.

Electrode type	Linear range (µM)	Limit of detection (µM)	Sensitivity (mA mM^{-1} cm^{-1})
C-Dots/GCE	1.0-3.5	0.55	0.055
CoFeLDH/GCE	1.0-6.0	0.68	0.061
C-Dots/CoFeLDH/GCE	0.5—7.5	0.46	0.12
HRP/C-Dots/CoFeLDH/GCE	0.1-23.1	0.04	0.47

This study clearly indicates that biohybrid materials obtained between enzymes and NPs/LDHs nanocomposites can lead to formulations with enhanced performances. Chitosan-LDH matrix was used also as a support for the enzyme immobilization. The fabricated material was used as cholesterol biosensors. The obtained nanohybrid had a high analytical performance, good stability, and high sensitivity. [123].

c) Specific applications of metal oxides in enzyme immobilization

The LDH materials can be also used as precursors for supports in enzyme immobilization. The layered double oxides (LDO) resulted after the clay calcination at a

temperature up to 550 °C have a large surface area and comparing with the fresh LDHs, they present less diffusion resistance. Furthermore, they are porous materials and they have both basic and acid sites [156].

The first time when the LDO were used in enzyme immobilization was in 2001 when L. Ren and co-workers have shown that the penicillin G acylase can be adsorbed on MgAlLDH calcined at 550 °C. The resulted product had presented an increase of the resistance for the acid medium [157].

J. Zhu immobilized the acid phosphatase enzyme on MgAlLDH calcined at 500 °C. Compared with the fresh material, the calcined LDH present a higher ability to adsorb the enzyme on its surface. Furthermore, the thermal treated material retains 88 % from the residual activity, while the uncalcined composite only 80 %. 60 % of activity is retained after six consecutive runs, for both materials. An increase of enzyme thermal stability was observed for the acid phosphatase supported on MgAlLDH calcined at 500 °C [144].

MgAlLDH calcined at 500 °C was also used as a support for the immobilization of bromelain. The maximum absorption amount was 157 mg/g. An increase of storage and thermals stability was observed for the immobilized enzyme. The authors also released the enzyme from the support. They succeeded to release about 70 % of the initial adsorbed enzyme. The released enzyme retains 81 % of its initial activity [156].

1.5. Conclusions

This first chapter was dedicated to the *State of the Art*, where the most important general aspects regarding the synthesis, characterization and the utilization of the LDH materials have been discussed and analyzed. The LDH composites, also denoted as anionic clays, can be obtained by using a large number of synthesis methods. However, the most used, according to the literature, are the co-precipitation used for the fabrication of the precursor matrix, and the reconstruction, when nanocomposites type NPs/LDH are obtained, by exploring the unique propriety of the hydrotalcite materials called *structural memory effect.*

The physico-chemical characterization of these composite and nanocomposites involves many techniques which give information about the structure and the crystallinity (XRD), chemical composition (EDX), surface chemical state (XPS), the nature of the functional groups (FTIR), the optical and thermal properties (UV-Vis and TG), and also about their texture and morphology (TEM, SEM).

Regarding their applications, the LDH based materials, due to their features, can be used in fields as biology, medicine, catalysis and photocatalysis, electrochemistry, sensing and biosensing. This chapter presented also the most recent studies involving anionic clays and their derivatives in application as pollutant photodegradation, enzyme immobilization and their utilization in biological systems.

In the photocatalytic applications, different performant heterostructures like Nb/ZnAlLDH, Cu/ZnAlLDH, Ti/ZnALDH, ZnFeAlLDH, Ce/ZnSnLDH etc were fabricated,

characterized and successfully used for the photodegradation of congo red, nylosan navy, rhodamine B, methylene blue, phenol, 2,4-dinitrophenol, etc. When used in presence of biological systems, is important to mention that the LDH materials behave as soft composites, they are highly biocompatible, manifesting a minimal negative effect over the normal cells. For this reason, the anionic clays have been used may times as carriers for drugs. Furthermore, the results of the recent studies show that different formulation based of LDHs can be used as antimicrobial, antitumoral or anticancer agents.

The synthesis of bioconjugates type Enz/LDHs can be carried out by using the co-precipitation, when the enzyme is added in the same time with the precursor metal salts, or by using the direct absorption, when can be used the fresh LDH or its calcined derivative. The physco-chemical characterization can be performed on the same instruments mentioned above. The studies made on this topic show that the main utilization of these biocomposites is in biosensing and in enzymatic catalysis.

SECOND SECTION

Original Research Results

There comes a point in your life when you need to stop reading other people's books and to write your own.

Albert Einstein

2. LDHs, NPs/LDHs and their derived mixed oxides for solar photodegradation of organic pollutants

The increase of environmental problems, the energy shortages and the increasing demand for water, have determined that the solar photodegradation of different substances as aromatic compounds, dyes, pharmaceuticals and personal care products to become an important research topic all over the world. The semiconductor photocatalysts are able to generate advanced oxidation reactions under irradiation. For this reason, they can be used in processes like water photolysis, photo-decomposition or photo-oxidation of dangerous compounds, artificial photosynthesis and others. Considering these aspects and all the features of layered double hydroxides, in this chapter will be presented original results obtained by using LDHs, NPs/LDHS and MMO composites in solar photodegradation of pollutants as phenol, p-nitrophenol, acetophenone and diclofenac.

2.1. Generalities

Environment problems as pollution, global warming, resources shortage and energy are demanding a constant research focused in finding the best ways for consume and waste management and also in designing materials and processes for the removal of the existent pollutants.

Water pollution is a real issue all over the world. The world population is growing every year, and in the same time the water consumption is increasing also. More than 2 million tons of waste materials are discharged in the fresh waters daily and because of the unsafe water, 2.2 millions of persons die every year. On the other hands, the ecosystem is altered and fauna is in a significant danger [158–160].

Phenols and their derivatives compounds are an important source of pollution. They are effluents of some industries like iron, wood, plastic, steel, dye, resins, pulp and paper. It was proven that the phenols can be toxic for the living organism even if they are in small quantities [161]. Phenol safety file classifies it as a hazardous material, with harmful effects on skin (numbness, convulsion, coma, and death) and eyes (pain, severe deep burns, and loss of Vision). By inhalation and ingestion, phenol can cause headache, vomiting, unconsciousness, abdominal pain, diarrhea and sore throat [162]. When phenols are discharges in nature, they accumulate in soil and water, and further in plants, animals and fish. In this way, phenols can be integrated by humans and their health will be affected [161].

The limit concentrations of phenol in waste water, imposed by Environmental Protection Agency and the Central Pollution Control Board, are 0.001 mg/L, while in the industrial effluent in a range of 0.1 and 5 mg/mL [161]. In this context, methods like photodegradation [33], adsorption, polymerization, biological degradation, extraction, advanced oxidation methods, electro and photo-Fenton processes were used for phenolic compounds removal [161].

Acetophenone is an aromatic ketone used in cosmetics, as flavoring agent in food, tobacco, catalysts for olefins polymerization and as a solvent for resins and plastics synthesis [163]. It was found that acetophenone can irritate the skin, the eyes, the nose and the troth, can cause headache, nausea and the exposure at high concentration can affect the nervous system. Till now, no information was published about the carcinogenic effect or the effect on the reproductive system in humans [163,164]. However, tests made on rats show that the acetophenone can induce congestion of liver, kidney and lungs via inhalation [164]. The European Union imposes a maximum concentration of acetophenone in drinking water of 0.1 mg/L, while of phenol is 0.005 mg/L [165].

Acetophenone was found in drinking water and air [166]. By inhalation or ingestion of polluted air and water the population can be easily exposed. Furthermore, even if the acetophenone do not present a high risk, some of its halogenate derivatives are extremely toxic and harmful for the environment [167]. Because the waste water is a complex system containing may others compounds, acetophenone has to be removed before its release in the municipal water, to avoid the interaction with other compound which may lead to its halogenate derivatives. Since now, the acetophenone was biodegraded using a bacterium named *Aromateleum aromaticum* [167], via pulsed corona discharges [166] and photodegradation.

Diclofenac (DCF) is an anti-inflammatory drug with an annual consumption of 940 tons and with a concentration detected in wastewater, aquatic environment and drinking water up to 21.6 μg/L. Being a stable molecule, it is resistant to biodegradation and it cannot be degraded only by the solar light [168]. Recently, it was introduced in the first watch list of substances to be considerate in all the member states of Europe [169]. It was found that the DCF can affect the hepatic gene expression in fish [170].

Photodegradation can be used in pollutants removal as a promising replacement for traditional methods as adsorption, filtration, ultrafiltration and others. Generally, the photodegradation system involves a catalyst, an irradiation source and a pollutant. When the catalyst is irradiated by light, the electrons from the valence band are transferred in the conduction band of the material, where they can move freely. The electron-hole pair will generate redox species which participate to the photodegradation of the pollutant (see eq. 2.1-2.5).

$$\text{Catalyst} + h\nu \rightarrow \text{Catalyst}\,(e_{CB^-} + h_{VB^+}) \quad (2.1)$$

$$\text{Catalyst}\,(h_{VB^+}) + H_2O \rightarrow \text{Catalyst} + OH^{\bullet} + H^+ \quad (2.2)$$

$$OH^{\bullet} + \text{Pollutant} \rightarrow \text{Degradation products} \quad (2.3)$$

$$\text{Catalyst}\,(e_{CB^-}) + O_2 \rightarrow \text{Catalyst} + O^{\bullet -} \quad (2.4)$$

$$O^{\bullet -} + \text{Pollutant} \rightarrow \text{Degradation products} \quad (2.5)$$

The irradiation source can be the UV, the visible or the solar light. Because the solar light is a free and cost-less source of energy, the tendency is to develop materials for solar or visible light driven processes.

The photocatalytic performance of the synthesized materials had been evaluated in the solar degradation of pollutants as phenol, p-nitrophenol, acetophenone and diclofenac. As a general protocol, in a 100 mL pollutant solution with a concentration of 25 mg/L, was dispersed 0.1 g catalyst (1g catalyst/L solution pollutant). Because the adsorption-desorption equilibrium is an important step in a photodegradation process, firstly the system was stirred in the dark till no modification of the UV-Vis profile was observed. After the equilibrium was established, the first sample was taken and denoted *0 min*, and the irradiation was turn on. The sampling was done at determinate times and the pollutant concentration was monitored by UV-Vis measurements, after the solid was removed by centrifugation. A blank test, without the catalyst, was also performed in order to verify if the organic compound can be degraded only by light.

The irradiation was provided by a solar simulator (Model US 800, Unnasol, Germany). The experimental device is presented in figure 2.1. It involves the solar lamp, a water recycling reactor and a stirrer.

The photodegradation reaction was monitored by recording the UV-Vis spectra profiles following different absorption peaks, in function of the pollutant nature.

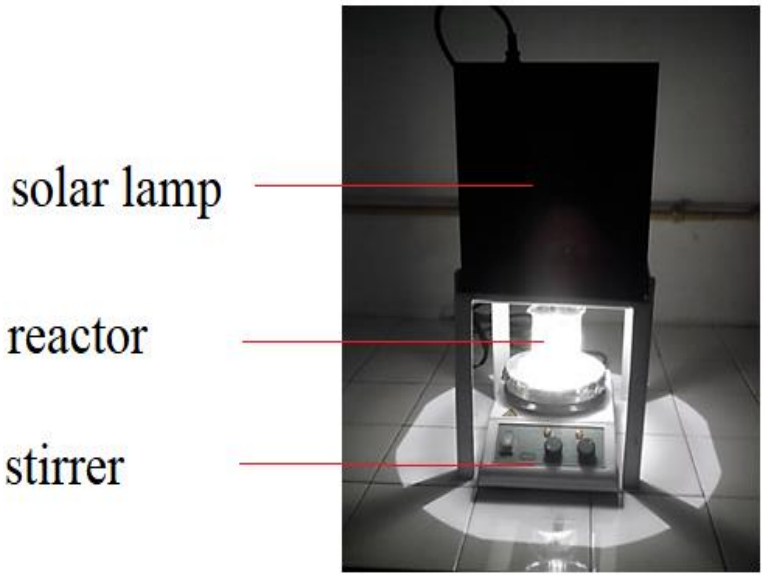

Figure 2.1: The photocatalytic experimental device.

2.2. Nanoparticles of gold and silver on ZnAlLDH with a Me^{2+}/Me^{3+} ratio=2/1; 3/1; 4/1 and ZnGaLDH with a Me^{2+}/Me^{3+} ratio=2/1 for the solar photodegradation of phenol, p-nitrophenol and acetophenone

2.2.1. Introduction

Nobel nanoparticles (AuNPs) have paid attention in the catalysis field since Bond et al. proved in 1979 that the hydrogenation reaction of alkyne and alkene can be catalyzed by Au/SiO_2 [171]. Later, in two separately studies, Haruta et al [172], and Hutchings et al. [173] confirmed that the gold nanoparticles can be successfully used in catalysis, for acetylene hydrochlorination [173] and low-temperature CO oxidation [172]. Starting with these discoveries, the free and supported AuNPs were intensely approached in heterogeneous catalysis applications [171]. The relevance of this topic is clearly underlined by the large amount of publications related with AuNPs in catalysis. In other words, more than 2800 publications are appeared between 1980 and 2016 [171], presenting the results of reactions catalyzed by formulations containing AuNPs e.g. oxidation of alcohols, oxidation of trialkylsilanes to silanols, hydrogenation of nitro groups, H_2O_2 synthesis, degradation of toluene, propanol, methanol [174], photocatalysis, cross coupling, nucleophilic addition, and much more [175].

The supported gold on solids might be a good direction since the supports can lead to AuNPs stabilization at different oxidation state as Au^0, Au^+ and Au^{3+} [174]. Furthermore, the support can influence the nanoparticles dispersion on its surface. Also, the combination between a semiconductor support and AuNPs can solve the high rate recombination of charge-carriers, extremely important when the hybrids are designed for photocatalytic processes [175]. Additionally, the utilization of AuNPs in photocatalysis is highly recommended because nobel metals are able to generate surface plasmon resonance responses (SPR). SPR can be defined as the response produced by the collective vibrations of surface free electrons under electromagnetic irradiation [176,177].

Generally, the supported noble nanoparticles can be obtained via two main protocols: the direct adsorption and the deposition-precipitation. Deposition-precipitation leads to a larger amount of NPs on support compared with the adsorption method. However, the deposition is dependent on the zero potential charge of the support, the optimal value being 5 [174]. The support and the protocol for the nanoparticles attachment have to be chosen taking into consideration the NPs stability on the carrier. For this reason, different ligands can be used, or the NPs can be introduced inside of polymeric or inorganic matrix [174]. An easy, economic and free of supplementary organic compounds addition, is to use the self-assembly and the structural memory effect of the anionic clays, to obtain highly dispersed nanoparticles on their surface. The layered double hydroxides are able to recover their layered structure when the metal mixed oxides formed by calcination are rehydrated in a particular salt solution [178]. After the rehydration process, on the LDH surface self-assembled nanoparticles will be obtained. Considering this, in this section will be prepared LDHs materials via co-precipitation method, and via reconstruction, Au/LDHs and Ag/LDHs nanocomposited will be prepared.

2.2.2. Synthesis and physico-chemical characterization of ZnAlLDHs with a Me^{2+}/Me^{3+} ratio of 2/1; 3/1; 4/1 and ZnGa (2/1) materials and their derived mixed oxides.

Synthesis

The ZnAlLDHs composites with the cationic ratio of 2, 3 and 4 were prepared via co-precipitation method, at a constant pH of 9 [3]. The standard protocol involved firstly, the preparation of three solutions containing the precursor salts. The salt solutions were formed by 0.1 or 0.15 or 0.2 moles of $Zn(NO_3)_2*6H_2O$ (Sigma Aldrich, ≥99%) and 0.05 moles of $Al(NO_3)_3*9H_2O$ (Sigma Aldrich, ≥99%). The precipitation solution was made from Na_2CO_3 and NaOH, and the final concentration was 1M. The precipitation was carried out drop by drop, under vigorous stirring, at a temperature of 45 °C and keeping the pH at a value of 9. The maturation step had a 24 h duration and the temperature was about 45 °C. After maturation, the product was washed several times with bidistilated water and dried at 60 °C. The samples were

denoted ZnAl(2/1), ZnAl(3/1) and ZnAl(4/1). The derived mixed oxides were obtained by applying a 750 °C temperature during 12 h to appropriate amounts of fresh ZnLDHs. ZnGa(2/1) composite was obtained by following the same steps like in case of ZnAlLDHs, but for this material the salts solution was prepared 0.04 moles of $Zn(NO_3)_2*6H_2O$ and 0.02 moles of $Ga(NO_3)3*xH_2O$ (Sigma Aldrich, ≥99%).

Physico-chemical characterization

To confirm that the hydrotalcite structure was obtained, the LDHs matrixes were physico-chemically characterized. The XRD data were obtained with Shimadzu X-ray 6100 diffractometer with monochromatic light (λ=0.1541 nm), performing at 40 kV and 30 mA over a 2θ range from 4 to 80°. The optical properties of the materials were investigated by using a V650 JASCO spectrophotometer with an integrating sphere. The TG-DTG curves were obtained with PerkinElmer Diamond Thermogravimetric/Differential Thermal Analyzer. FTIR analysis was carried out on a PerkinElmer FTIR Spectrum 100 spectrometer.

The XRD spectra of the fresh sample show that the clay structure was obtained, and after calcination the MMO were formed (see figure 2.2). The ZnLDHs have a high crystallinity,

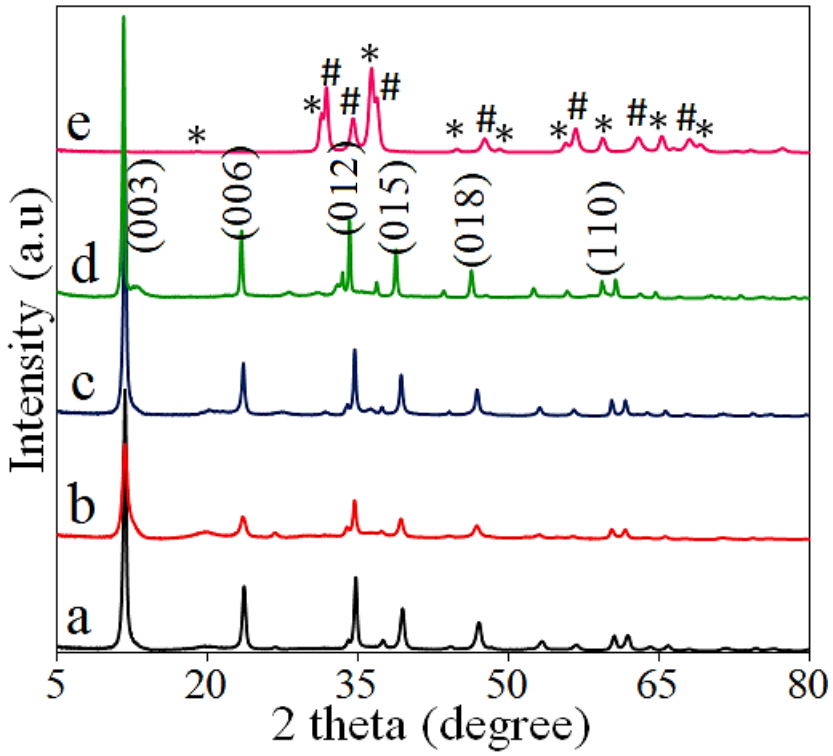

Figure 2.2: XRD spectra of a) ZnAl(2/1), b) ZnAl(3/1), c) ZnAl(4/1), d) ZnGa(2/1) and e) ZnAl(2/1) 750, $*ZnAl_2O_4$, #ZnO.

with intense x-ray diffraction peaks, at 2Θ = 11.7, 23.6, 34.7, 39.4 and 60.4, and they can be assigned to the basal (003), (006), (012) and non-basal (015), (018), (110) diffraction planes.

Using the diffraction angle assigned to (003) plane, the interlayer distance was calculate and its value is 0.75, underlining that the interlayer anion is CO_3 [3]. After calcination, it might be observed that the lamellar structure is destroyed, and a mixture of ZnO and spinel-like phase is obtained [124].

The UV-Vis profiles of the fresh and calcined LDHs materials are given in figure 2.3. It might be observed that the absorption capacity of the uncalcined samples extends to visible region of the spectrum [23]. After the thermal treatment at 750 °C, the absorption profiles suffer a significant modification, with a shift to the blue area of the spectrum. The presence of two shoulders around 200 and 270 nm, assigned to spinel-phase and an adsorption edge at 360 attributed to ZnO can be also observed [179].

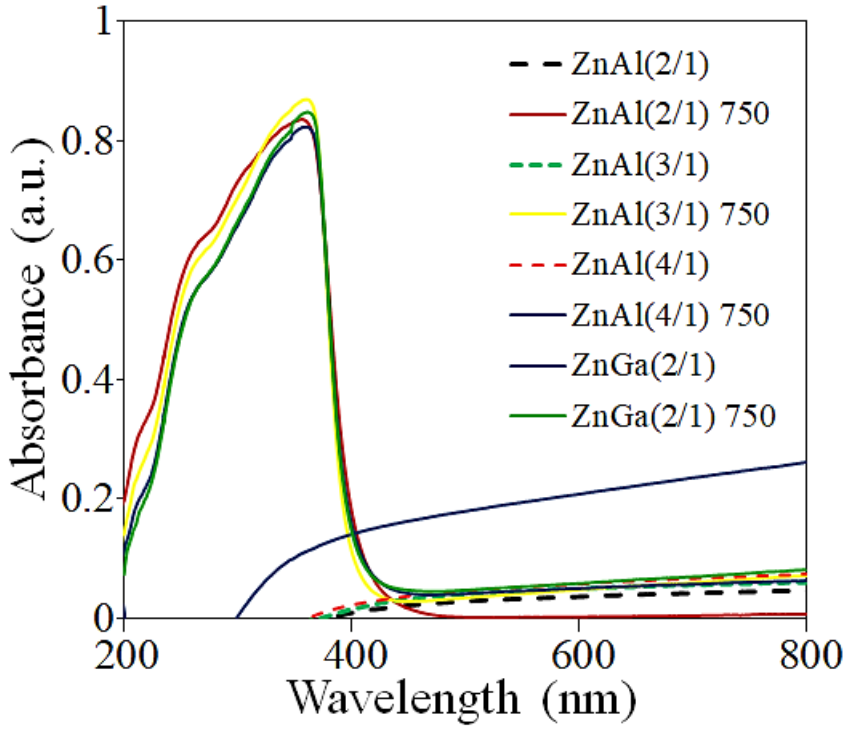

Figure 2.3: UV-Vis spectra for ZnAlLDH materials and their derived mixed oxides

In order to investigate the thermal stability of the synthetized materials, the thermogravimetric analysis was performed. The analysis, beside the information about sample stability, gives indication about the moment when the metal oxides are formed without lamella destruction. The TG-DTG curves and the FTIR spectra are listed in figure 2.4 and figure 2.5. The TG-DTG curves have a profile which is characteristic to hydrotalcite materials, with three important weight losses (figure 2.4). First mass loss is assigned to physisorbed and interlayer water removal and it takes place around 100-200 °C for ZnAlLDHs (figure 2.4 a-c) and 100-170 °C for ZnGa(2/1). Next weight loss happens from 200 to 280 °C for ZnAlLDHs and 170 to 240 for ZnGa(2/1) and it is attributed to layers dehydroxilation. The carbonate anions removal

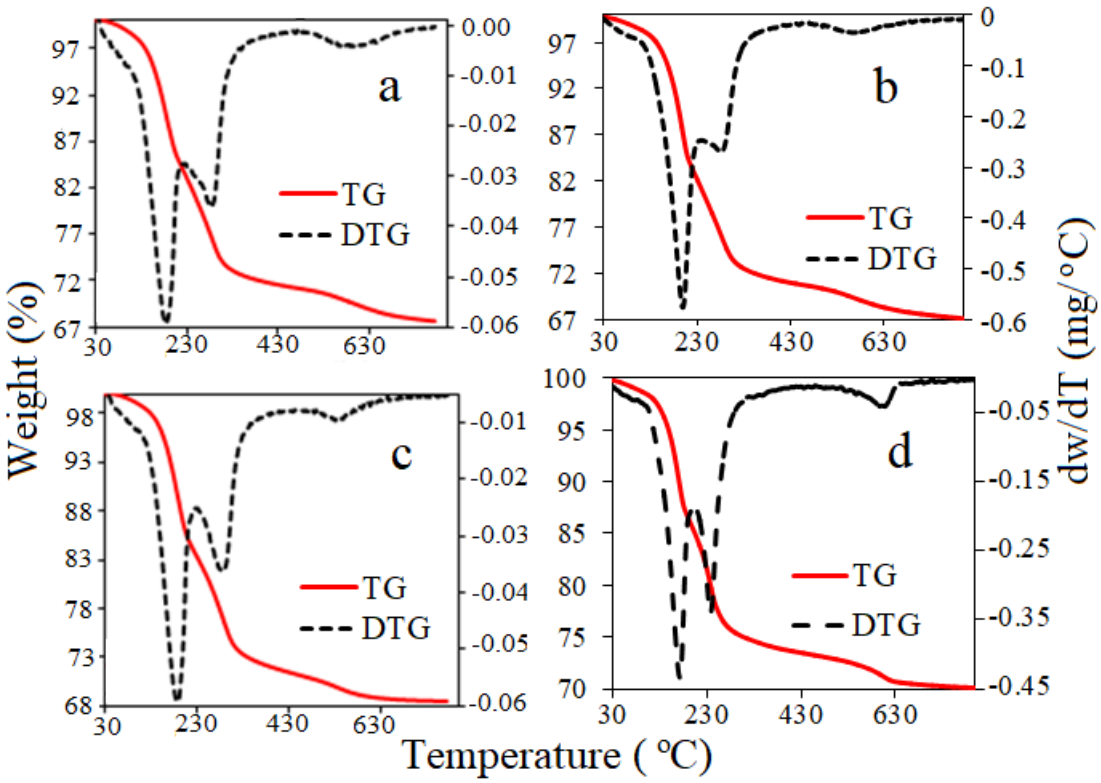

Figure 2.4: TG-DTG curves for a) ZnAl(2/1), b) ZnAl(3/1), c) ZnAl(4/1), d) ZnGa (2/1) materials.

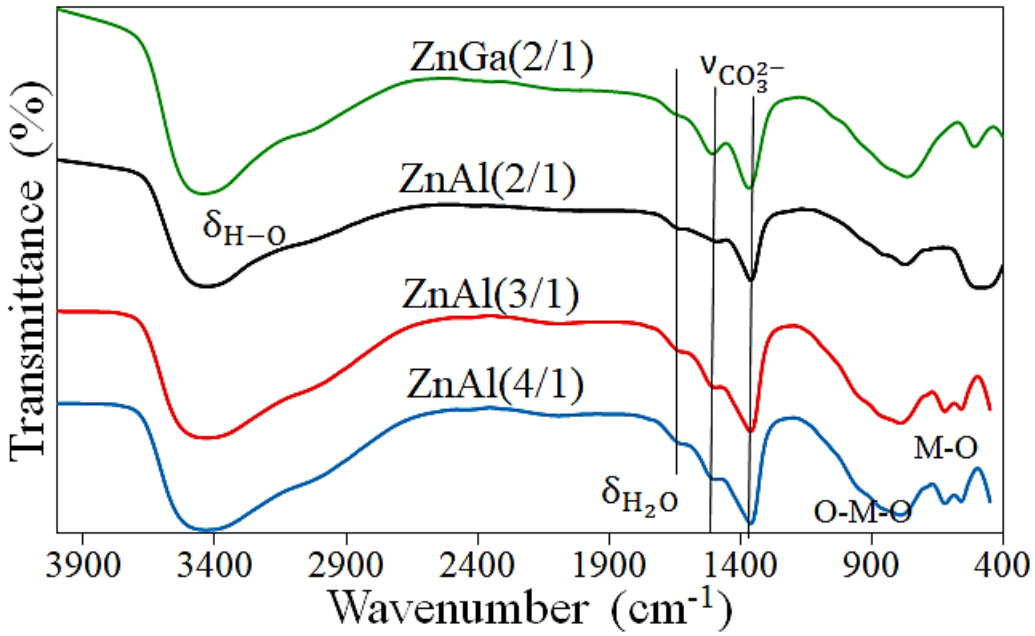

Figure 2.5: FTIR spectra of ZnAlLDHs and ZnGa(2/1).

takes place between 280-560 °C for ZnAl(2/1) and 240-600 °C for ZnGa(2/1). The moment of LDH structure destruction, followed by mixed oxide lattice formation is pointed by the endothermic peak from 560 °C for ZnAlLDHs and 600 °C for ZnGa(2/1). A total mass loss between 30-33 % was observed for the investigated materials [22]. The FTIR spectra (figure 2.5) show typical vibration bands of hydrotalcite materials. For all the LDHs an intense absorption band can be observed around 3450 cm^{-1} and it might be assigned to O-H groups from the brucite layer and the physisorbed water. The H-O-H bending vibration, assigned to the interlayer water is represented by an absorption peak around 1630 cm^{-1}. For all the LDHs materials the interlayer anion is CO_3^{2-} and the symmetric and antisymmetric stretching modes appear around 1360 cm^{-1}, 1500 cm^{-1}, respectively. Between 800-400 cm^{-1} can be observed the characteristic signals for M-O-M and M-O [50].

2.2.3. Synthesis and physico-chemical characterization of Au/ZnAlLDHs with a $Me^{2+}/Me3^{+}$ ratio=2/1; 3/1; 4/1 and Ag or Au/ZnGa(2/1) materials and their derived mixed oxides.

In a general description, the self-assembled materials containing Au or Ag on ZnLDHs were obtained via reconstruction method, by using the structure memory effect property of layered double hydroxides. Furthermore, impregnated ZnAlLDHs were synthetized through different protocols as they will be described forward.

a) **Synthesis and physico-chemical characterization of Au/ZnAl(2/1) LDHs**

Synthesis

Nanomaterials containing supported AuNPs on anionic clays was obtained via reconstruction route [3,180] by using ZnAl(2/1) matrix. Three samples containig 1,2 g of ZnAl(2/1) were calcined at 500 °C for 8 h. After calcination, when the calcined materials reached the temperature of 200 °C, the powders have been added to 250 mL aqueous solutions containing 0.1 g or 0.3g gold acetate (>99.9%, AlfaAesar). The mixtures were stirred at the room temperature for 3 h, afterwards they have been centrifuged and dried at 80 °C. The samples were denoted as Au/ZnAl(2/1)-R-1 (0.1 g gold acetate) and Au/ZnAl(2/1)-R-2 (0.3 g gold acetate).

Separately, after the addition of calcined ZnAl(2/1) into 250 mL aqueous solution containing 0.1g of Au(III) acetate, the dispersion was stirred under solar simulated irradiation (Model US 800, Unnasol, Germany) during 20 minutes. The product was named as Au/ZnAl(2/1)R-3-Lg. As a comparison, 0.24 g of fresh ZnAl(2/1) were mixed into 250 mL

aqueous solution with 0.02g content of Au(III) acetate. The dispersion was mixed under solar irradiation during 20 minute. After 3 h of stirring at room temperature, the solid was removed, washed with a solution of water: ethanol (1:1 vol. %) and dried under vacuum at 16 °C. The product was named Au/ZnAl(2/1)-Lg.

Two other samples were obtained via impregnation route [180]. One of the samples was synthetized by $HAuCl_4$ (>99.9%, AlfaAesar) impregnation followed by liquid reduction. For this, 0.42 g ZnAl(2/1) were added to 10 mL of aqueous solution containing 0.044 g $HAuCl_4$. The dispersion was mixed for 12 h at room temperature, followed by solid separation and washing with deionized water. In the end, the solid was dried under vacuum at 16 °C for 24 h. The obtained material was further put into 10 mL of dehydrated toluene (> 99.5%, Wako Pure Chemical) and to this mixture, 0.0126 g of $NaBH_4$ were added. The resulted dispersion was mixed during 10 minutes, afterwards 3 mL of ethanol (> 99.5%, Wako Pure Chemical) were added. After 6 h of stirring at the room temperature, the precipitate was separated, washed with a solution of deionized water: ethanol (1:1 vol. %) and dried under vacuum at 16 °C for 24 h. The sample was denoted as Au/ZnAl(2/1)-I- $NaBH_4$. For the second impregnated hybrid, 0.3 g of ZnAl(2/1) was added to 10 mL of deionized water and sonicated during10 minutes. Into this resulted dispersion, were added the aqueous solution of $HAuCl_4*4H_2O$ (0.031g in 20 mL water), L-lysine (0.036 g in 4 mL) (98%, Sigma–Aldrich Chemie) and $NaBH_4$ (0.026 g in 2 mL). The pH was adjusted at a value of 9.5 by adding diluted HCl (Wako Pure Chemical). After 1 h of mixing, the solution was left without stirring for the next 24 h. In the end, the solid was filtered, washed with a solution of deionized water : ethanol (1:1 vol. %) and dried at 60 °C for 12 h. The material was named Au/ZnAl(2/1)-I-Ly [181].

Physico-chemical characterization

The X-ray diffraction measurements were performed on D8 ADVANCE diffractometer (Bruker), at a Bragg angle (Θ) of 2Θ= 3◦–60; scan step of 0.01, scan rate of 5 s per step. The measurements were done at 40 kV and 40 mA using Cu K_α emission and a nickel filter. The UV-Vis absorption profiles were performed on a V650 JASCO spectrophotometer with an integrating sphere which was used for the diffuse reflectance measurements. XANES and EXAFS spectra were done in a transmission mode on beamline NW10A in the Photon Factory Advanced Ring. The obtained data were performed using an XDAP package. TEM analysis was also performed on a Model H-7650, Hitachi performing at 100 kV.

The XRD spectra of the ZnAl(2/1), Au/ZnAl(2/1)-R-1, Au/ZnAl(2/1)-R-2, Au/ZnAl(2/1)-R-3-Lg, Au/ZnAl(2/1)-I-$NaBH_4$, Au/ZnAl(2/1)-I-Ly are presented in figure 2.6. The XRD patterns show the characteristic peaks for hydrotalcite materials, attributed to (003), (006), (101), (009), (104), (015), (107), (018). (100) diffraction planes. For Au/ZnAl(2/1)-R-1 and Au/ZnAl(2/1)-R-3-Lg the ZnO signals at 2Θ = 31.9° and 36.4° (marked with #) are observed, suggesting that the layered structure of the initial material was not totally recovered [22,179]. For Au/ZnAl(2/1)-R-2, Au/ZnAl(2/1)-R-3-Lg materials, at 2Θ = 38.3° appeared a peak which was assigned to metallic gold crystals (marked with &) [182].

The optical properties of Au/ZnAl(2/1)LDHs are shown in figure 2.7. In the spectra of Au/ZnAl(2/1)-R-1, Au/ZnAl(2/1)-R-2 and Au/ZnAl(2/1)-R-3-Lg, the absorption peaks at 539 nm, 540 nm and 547 nm appears due to AuNPs surface plasmon resonance (SPR). For these SPR responses were reported dispersed AuNPs on LDHs matrix with particles size of 2.9-3.4 nm [178]. The reconstruction under solar light induced a red shift for Au/ZnAl(2/1)-R-3-Lg, compared with Au/ZnAl(2/1)-R-1, suggesting a quantum size effect of AuNPs.

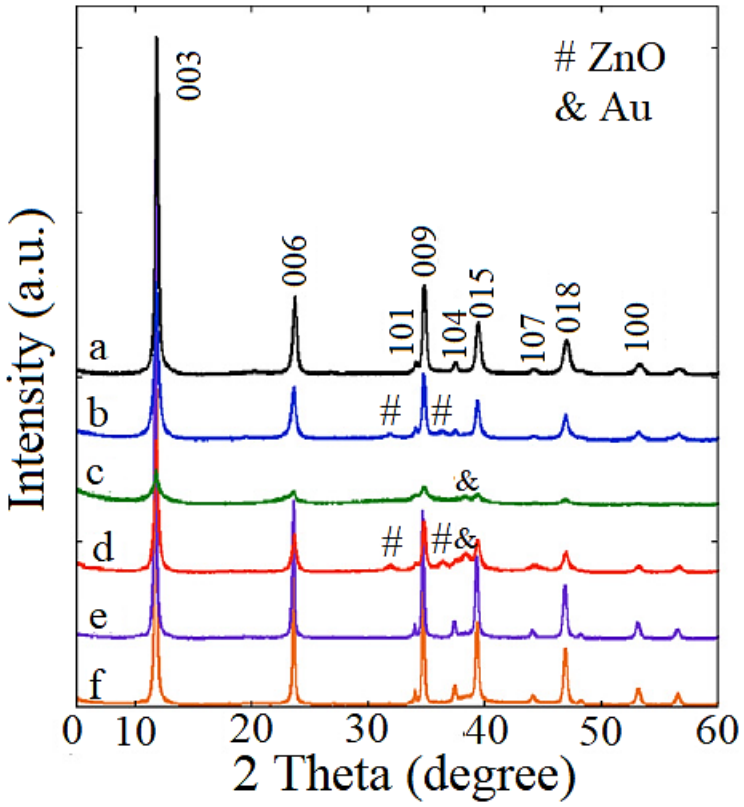

Figure 2.6: XRD pattern for a) ZnAl(2/1), b) Au/ZnAl(2/1)-R-1, c) Au/ZnAl(2/1)-Rec-2, d) Au/ZnAl(2/1)-R-3-Lg, e) Au/ZnAl(2/1)-I-$NaBH_4$, and f) Au/ZnAl(2/1)-I-Ly.

The calculated band gap values based on Davis-Mott equation (equation 2.1; where α-absorption coefficient, h Planck constant, ν light frequency, n =1/2, 3/2, 2, and 3) [183] are 5.7 eV for ZnAl(2/1), 3.1eV for Au/ZnAl(2/1)-R-1, 2.5 eV for Au/ZnAl(2/1)-R-2 and 2.6 eV for Au/ZnAl(2/1)-R-3-Lg. This decrease can be attributed to the presence of small amounts of metal oxide or spinel phases combined with AuNPs. For the impregnate samples, the typical absorption edge around 400 nm did not appear. These samples have the AuNPs SPR located at 536 nm for Au/ZnAl(2/1)-I-$NaBH_4$ and 537 nm for Au/ZnAl(2/1)-I-Ly. The UV-Vis spectrum for Au/ZnAl(2/1)-Lg had a AuNPs SPR with a small absorption broad at 552 nm.

$$\alpha \cdot h\nu^{\alpha}\left(h\nu - E_g\right)^n \qquad (2.1)$$

Au L_3-edge XANES spectra for Au/ZnAl(2/1) nanocomposites are presented in figure 2.8. For

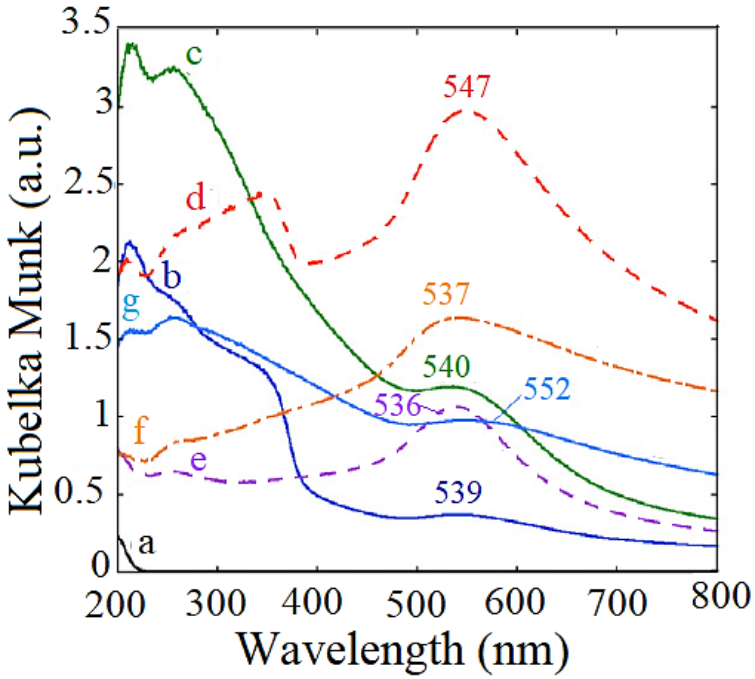

Figure 2.7: UV-Vis absorption spectra of for a) ZnAl(2/1), b) Au/ZnAl(2/1)-R-1, c) Au/ZnAl(2/1)-R-2, d) Au/ZnAl(2/1)-R-3-Lg, e) Au/ZnAl(2/1)-I-$NaBH_4$, f) Au/ZnAl(2/1)-I-Ly,

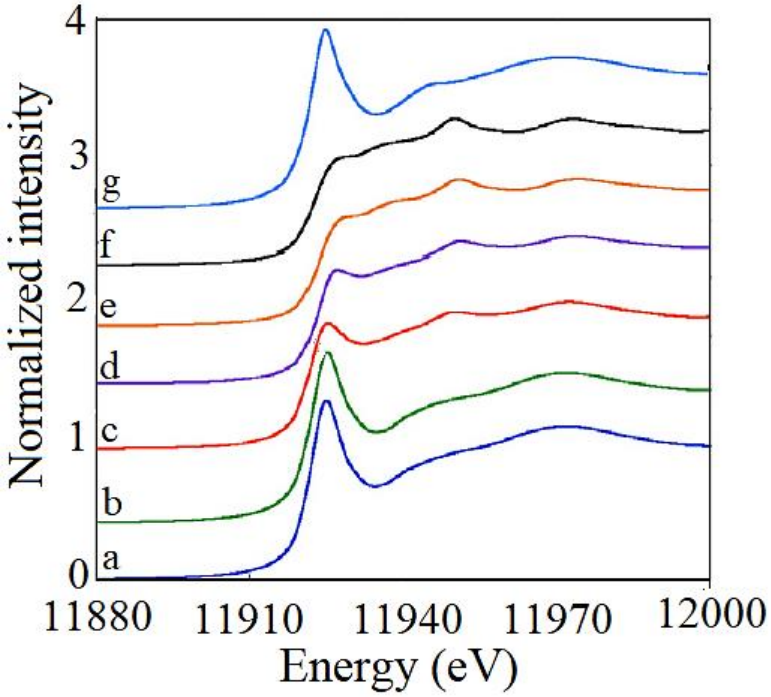

g) Au/ZnAl(2/1)-Lg.

Figure 2.8: Normalized Au L3-edge XANES spectra for a) Au/ZnAl(2/1)-R-1, b) Au/ZnAl(2/1)-R-2, c) Au/ZnAl(2/1)-R-3-Lg, d) Au/ZnAl(2/1)-I-NaBH4, e) Au/ZnAl(2/1)-I-Ly, f) Au metal foil, and g) Au_2O_3.

comparison, the spectra of Au_2O_3 and of Au metal foil are also given. It might be observed that the XANES profile of Au/ZnAl(2/1)-R-1 (a), Au/ZnAl(2/1)-Rec-2 (b) are similar to Au_2O_3 spectrum (g), while the impregnated sample Au/ZnAl(2/1)-I-Ly (e) is more similar with the spectrum (f) assigned to Au metal foil. However, for the Au/ZnAl(2/1)-R-3-Lg (c) and Au/ZnAl(2/1)-I-$NaBH_4$ (d), the Au L_3-edge spectra appears as a combination between spectra g and f, suggesting that in these two materials the sold sites are a mixture of Au^0 and Au^{3+}. The presence of the Au^0 in the impregnated samples might be a consequence of $NaBH_4$ or/and lysine utilization, while in case of reconstructed sample Au/ZnAl(2/1)-R-3-Lg, this presence might be attributed to the effect of the solar light.

Au-L_3 edge EXAFS and their associate Fourier transform (figure 2.9) were used to

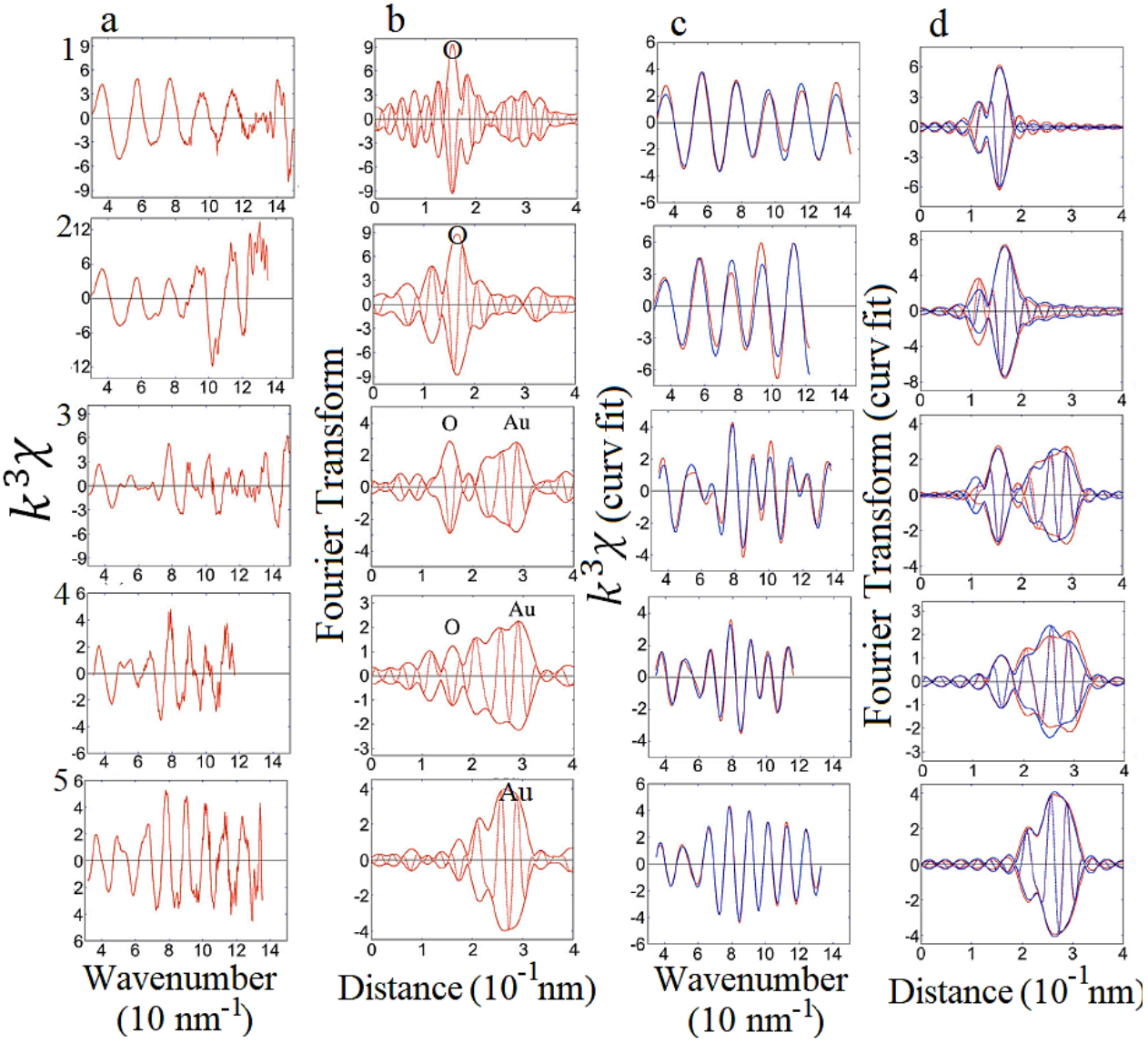

Figure 2.9: a) k^3-weighted EXAFS oscillation for Au/ZnAl(2/1)-R-1 (1), Au/ZnAl(2/1)-R-2 (2), Au/ZnAl(2/1)-R-3-Lg (3), Au/ZnAl(2/1)-I-$NaBH_4$(4), and Au/ZnAl(2/1)-I-Ly (5). b) associated Fourier transform, c) best-fit results in k-space and d) in R-space.

investigate the AuNPs coordination environment in Au/ZnAl(2/1)LDHs. In the Fourier transform, the peaks from 0.16 nm and 0.28 nm have been curve-fit to the parameters of Au-O and Au-Au interatomic pairs. In table 2 are presented the best-fit results. In figure 2.9 c and d, the red line is for the obtained experimental data, while with the blue lines are represented the calculated data.

The coordination number, N, for Au-O and Au-Au in the model samples Au_2O_3 and Au metal were 4 and 9, respectively. However, the values for N in case of Au/ZnAl(2/1)-R-3-Lg were 1.6 for Au-O and 12 for Au-Au, being smaller than for the models. The other two reconstructed samples have closer values to that of Au-O in Au_2O_3, suggesting that the reconstruction under solar irradiation leads to a decrease of coordination number. In a previous study made by L. Wang, it was proved that a decrease of N value can be the indication of strong interaction between the layered material and NPs. The AuNPs particle size based on N value assigned to Au-Au are given in table 1.1 [184]. The mean particle size for AuNPs according with N(Au-Au) in case of light reconstructed sample and the impregnated one are 9, 11.3, 11.8 nm (see table 2.1) [185].

Table 2.1: Results of curve-fit analysis for Au L3-edge EXAFS for Au/ZnAl(2/1)LDHs.

Specimen	**Au-O**	**Au-Au**
	R (nm)	
	N	
	$\Delta\sigma$ (10^{-5} nm^2)	
Au/ZnAl(2/1)-R-1	0.197 (±0.001)	
	3.7 (±0.9)	
	0.8 (±0.1)	
Au/ZnAl(2/1)-R-2	0.204 (±0.002)	
	3.7 (±0.3)	
	0.3 (±0.1)	
Au/ZnAl(2/1)-R-3-Lg	0.195 (±0.002)	0.2888 (±0.0004)
	1.6 (±0.1)	9.0 (±1.2)
	0.1 (±0.4)	0.3 (±0.1)
Au/ZnAl(2/1)-I-$NaBH_4$	0.199 (±0.005)	0.287 (±0.001)

	0.3 (±0.2) 0.1 (±0.5)	11.3 (±0.6) 0 (±0.1)
Au/ZnAl(2/1)-I-Ly		0.287 (±0.001) 11.8 (±0.7) 0.18 (±0.04)
Au_2O_3	0.2013 4 -	
Au metal		0.28884 12 -

The particles size distribution and TEM images and are given in figure 2.10 and 2.11.

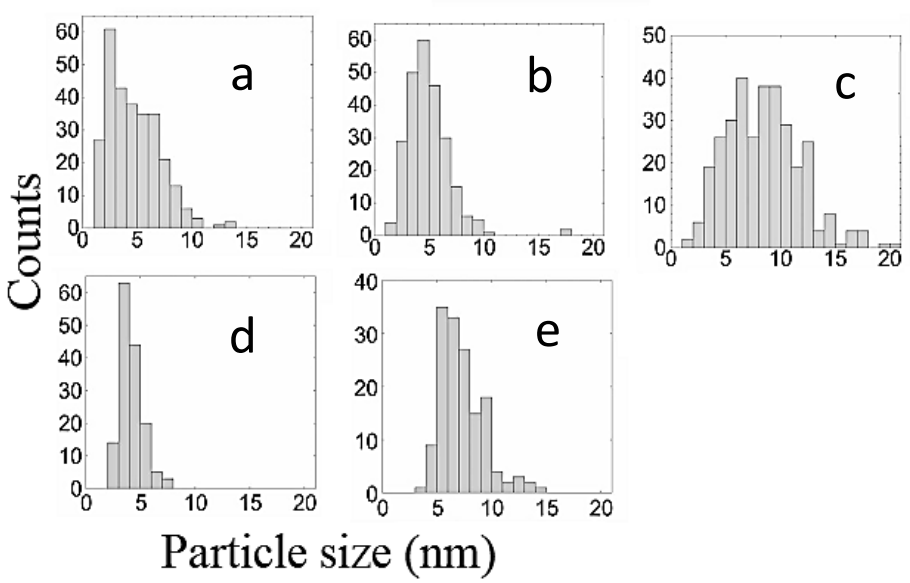

Figure 2.10: Particle size distribution for a) Au/ZnAl(2/1)-R-1, b) Au/ZnAl(2/1)- R-2 , c) Au/ZnAl(2/1)-R-3-Lg, d) Au/ZnAl(2/1)-I-$NaBH_4$, and e) Au/ZnAl(2/1)-I-Ly.

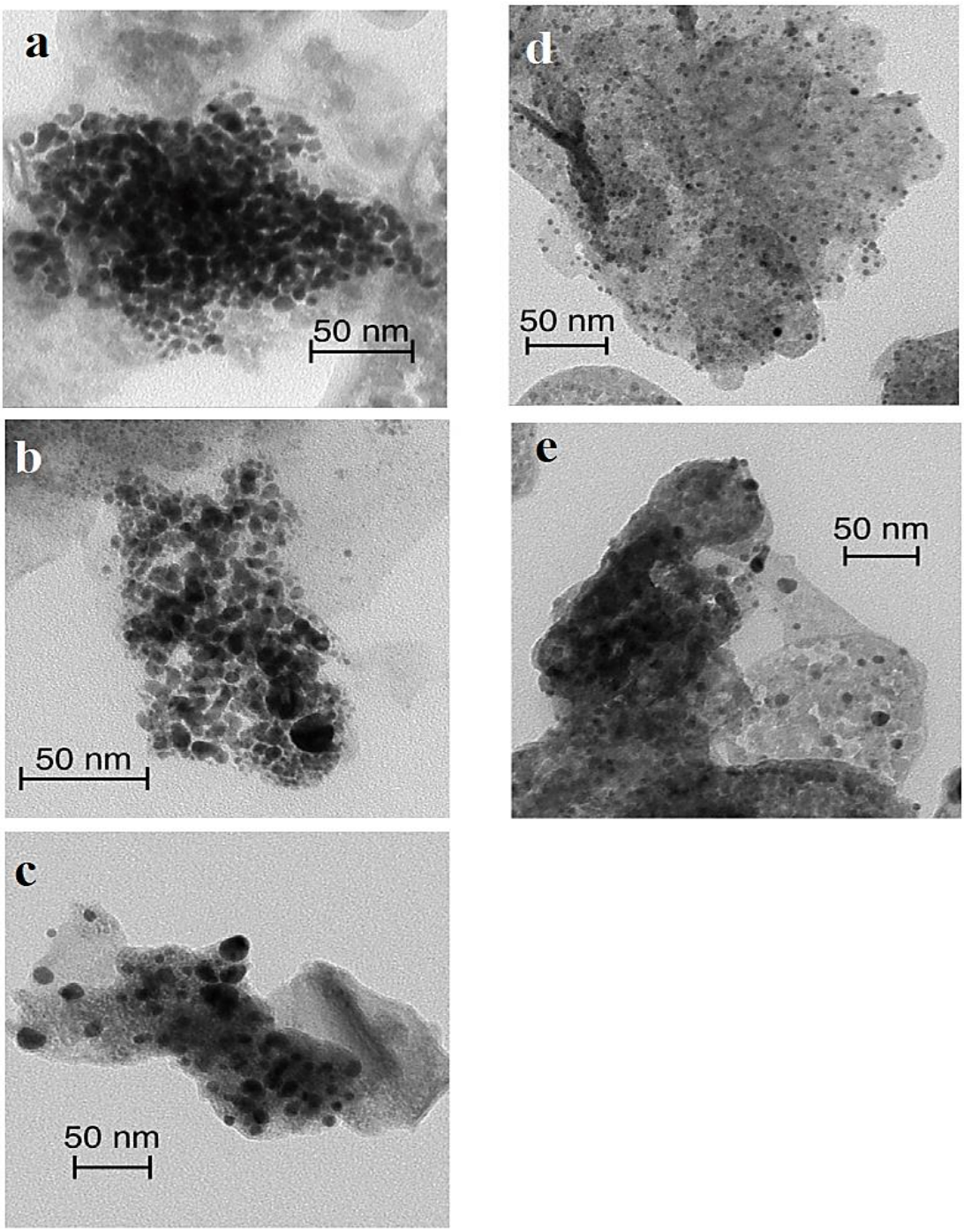

Figure 2.11: TEM images for a) Au/ZnAl(2/1)-R-1, b) Au/ZnAl(2/1)-R-2, c) Au/ZnAl(2/1)-R-3-Lg, d) Au/ZnAl(2/1)-I-$NaBH_4$, and e) Au/ZnAl(2/1)-I-Ly.

It might be observed that the AuNPs have a spherical shape, and they are well dispersed on ZnAl(2/1)LDH. The Au/ZnAl(2/1)-R-1 and Au/ZnAl(2/1)-R-2 samples have a predominate size of 4.7 nm and 4.9 nm, respectively. For the solar reconstructed sample, Au/ZnAl(2/1)-R-3-Lg, an increase of size to 8.5 nm was noticed.

b) Synthesis and physico-chemical characterization of Au/ZnAlLDHs with a Me2+/Me3+ ratio=2/1; 3/1; 4/1

Synthesis

Nanomaterials containing AuNPs supported on ZnAlLDHs were obtained through reconstruction route [3] using ZnAl(2/1), ZnAl(3/1) and ZnAl(4/1) layered double hydroxides. Au/ZnAl(2/1)LDHs were synthetized as follows: different amounts of ZnAl(2/1) were calcined at 470 °C; they were added to 200 mL deionized water solution with different quantities of Au (III) acetate; thus, the powders resulted after the calcination of 2.1 g, 2.1 g, 1 g and 1 g ZnAl(2/1) were added to 200 mL deionized water solutions containing 0.1 g, 0.2g, 0.12 g and 0.35 g of Au(III) acetate. The resulted suspensions, except the one with 0.12 g Au (III) acetate, were stirred for 7 h at the room temperature, afterwards they were centrifuged and dried at 80 °C. The mixture containing 0.12 g of gold acetate was firstly mixed under simulated solar light during 2 h, and another 5 hours without irradiation. The samples were denoted as: Au/Zn2Al(2.1_0.1), Au/Zn2Al(2.1_0.2), Au/Zn2Al(1_0.12)-Lg and Au/Zn2Al(1_0.35). Following the same protocol as for the ZnAl(2/1), were obtained the Au/ZnAl(4/1)LDHs. They were named as Au/Zn4Al(2.1_0.1), Au/Zn4Al(2.1_0.2), Au/Zn4Al(1_0.12)-Lg and Au/Zn4Al(1_0.35). In the brackets is expressed the ratio between the LDH and the gold content used at the nanocomposite fabrication. The samples reconstructed under solar light were calcined at 750 °C during 12 h.

Separately, 3.5 g of ZnAl(3/1) were calcined at 525 °C and added to 200 mL of deionized water solution containing 0.5g of $HAuCl_4$. The suspension was mixed 24 h at the room temperature, and then the solid was removed and dried at 80 °C.

Physico-chemical characterization

The structure and the optical properties of the materials were performed by using a PerkinElmer FTIR Spectrum 100 spectrometer and a V650 JASCO spectrophotometer with an integrating sphere.

As it was described above, the Au/ZnAlLDHs materials from this group were obtained via reconstruction route, following the rehydration of calcined ZnAlLDHs in deionized water

solution of gold acetate. FTIR analysis was made in order to confirm the recovering of the initial structure of the material. As it can be observed from figure 2.12, the spectra profiles of

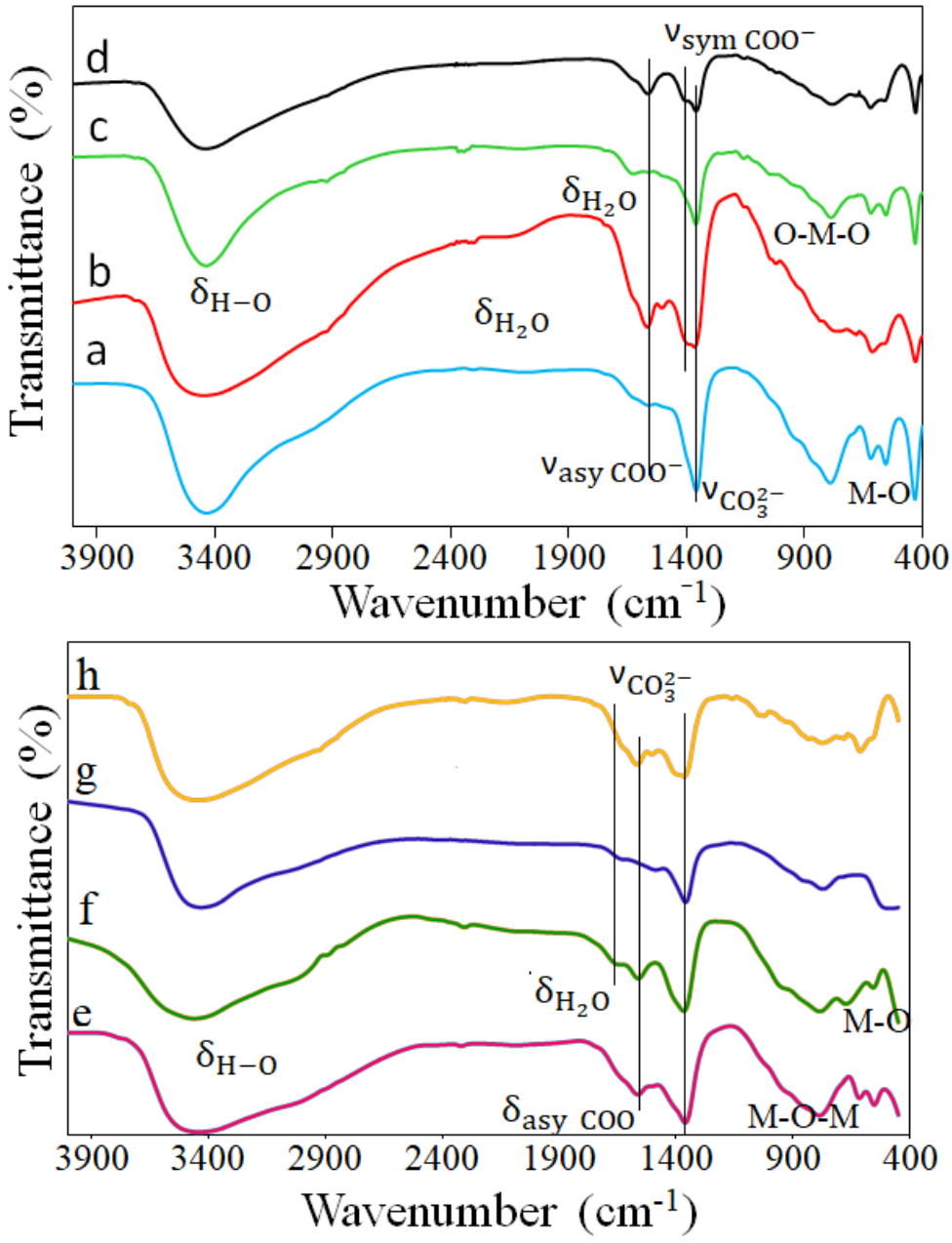

Figure 2.12: Spectra for a) Au/Zn2Al(2.1_0.1), b) Au/Zn2Al(2.1_0.2), c) Au/Zn2Al(1_0.12)-Lg d) Au/Zn4Al(1_0.35) e) Au/Zn4Al(2.1_0.1), f) Au/Zn4Al(1_0.12), g) Au/Zn4Al(2.1_0.12)-Lg and h) Au/Zn4Al(1_0.35).

Au/ZnAlLDHs are characteristic for hydrotalcite materials, underlining that the layered structure of the materials was recovered during the rehydration process. Besides the typical absorption bands around 3450 cm^{-1}, 1630 cm^{-1}, 1502 cm^{-1} and 1360 cm^{-1} which are assigned to

O-H stretching of hydroxyl groups of LDHs, H-O-H bending vibration of interlayer water molecules and the symmetric and antisymmetric bending vibrations of CO_3^{2-}[50], the presence of signals which have been attributed to acetate anion were recorded. Thus, two absorption bands at 1564 cm^{-1} and 1410 cm^{-1} might be observed, and assigned to the antisymmetric and symmetric stretching modes of COO^- anions [186]. The presence of the CO_3^{2-}shows the high affinity of the anionic clays for this ion.

The optical properties were investigated by using UV-Vis spectroscopy. In figure 2.13, 2.14 are given the UV-Vis spectra for Au/Zn2AlLDHs and Au/Zn4AlLDHs. As for the first group of materials, which has been already presented, the adsorption peaks of Au/ZnAlLDHs appear due to the SPR of AuNPs. Furthermore, it can be noticed that the reconstruction under solar irradiation leads to an intense of SPR response for Au/Zn2Al(1_0.12)-Lg and Au/Zn4Al(1_0.12)-Lg, compared with the classic reconstructed samples. The increase of the gold quantity and also the increase of the Me^{2+}/Me^{3+} from 2 to 3 and 4, induces a red shift of SPR peaks. Peculiarly, the materials with the highest gold quantity, Au/Zn2Al(1_0.35) and Au/Zn4Al(1_0.35) present a small SPR response. The absorption peaks corresponding to AuNPs are centered between 526 and 565 nm. The calcined samples present a shift of SPR to the red region of the spectrum underlining that the AuNPs dimensions increased or they have formed aggregates on the ZnO network [187,188].

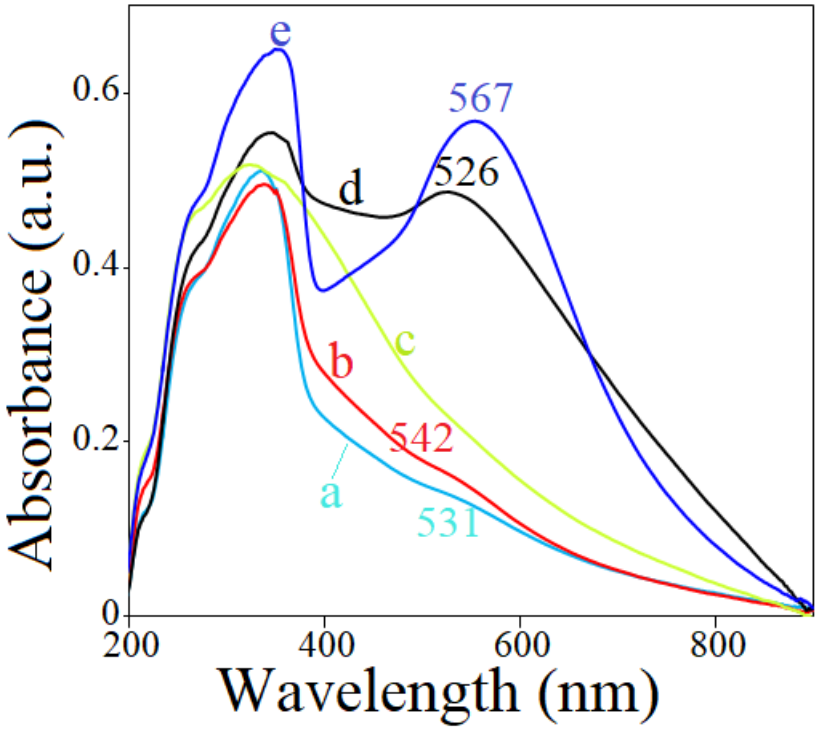

Figure 2.13: UV-Vis spectra of a) Au/Zn2Al(2.1_0.1), b) Au/Zn2Al(2.1_0.2), c) Au/Zn2Al(1_0.35), d) Au/Zn2Al(1_0.12)-Lg, e) Au/Zn2Al(1_0.12)-Lg-750.

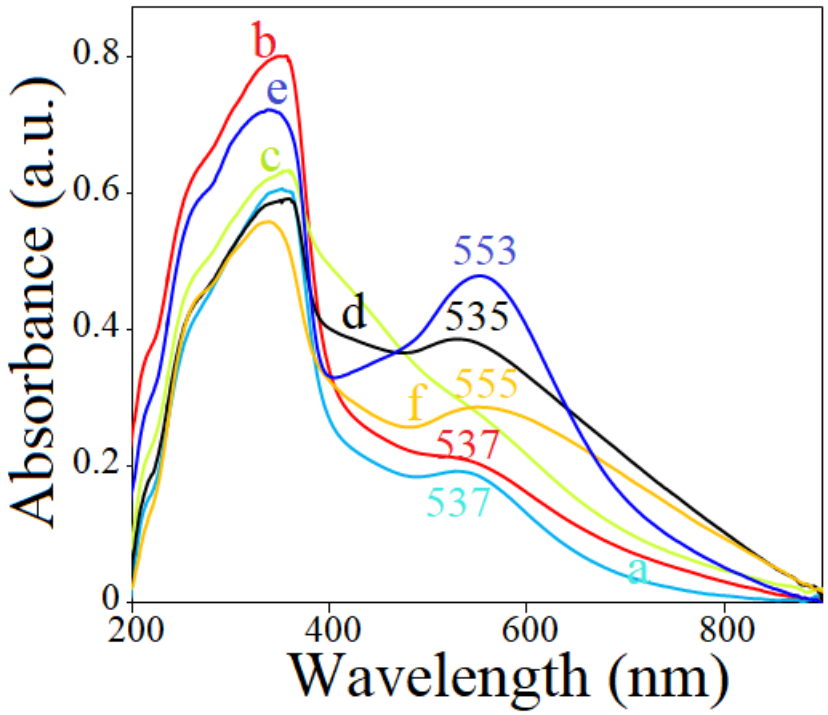

Figure 2.14: UV-Vis spectra of a) Au/Zn4Al(2.1_0.2), b) Au/Zn4Al(2.1_0.1), c) Au/Zn4Al(1_0.35), d) Au/Zn4Al(1_0.12)-Lg, e) Au/Zn4Al(1_0.12)-Lg-750, f) Au.ZnAl(3/1).

c) Synthesis and physico-chemical characterization of Ag or Au/ZnGa(2/1)

Synthesis

AuNPs and AgNPs on ZnGa(2/1) layered double hydroxides were obtained via reconstruction route [3]. Thus, 2.5 g ZnGa(2/1) were calcined at 500 °C and after cooling the powders till 400 °C , it was added to 150 mL of deionized water solution containing 0.3 g of Au(III) acetate. The resulted suspension was mixed at the room temperature during 24 h, afterwards the solid was removed by centrifugation and dried at 90 °C. For the fabrication of AgNPs dispersed on LDH, 1.5 g of ZnGa(2/1) were calcined at 500 °C, and when the power temperature decreasedat of 400 °C, it was added to 150 mL deionized water solution containing 0.35 silver sulfate (> 99.99 Sigma Aldrich). The mixture was stirred at the room temperature for 24 h, and then the solid was removed and dried at 90 °C. The samples were denoted as Au/ZnGa(2/1) and Ag/ZnGa(2/1).

Physico-chemical characterization

X-ray patterns were obtained with a PANalytical X'Pert PROMPD diffractometer. A V650 JASCO spectrophotometer with an integrating sphere was for the optical properties investigation, while the FTIR measurements were performed on a PerkinElmer FTIR Spectrum 100 spectrometer.

For the self-assembled AuNPs and AgNPs on ZnGa(2/1) LDH, the structure of the new hybrids shows a good crystallinity (figure 2.15), with intense peaks characteristic to the hydrotalcite composite. The diffraction peaks appear at 2Θ = 11.7°, 23.5°, 33.9°, 34.7°, 37.3°, 39.3°, 44.1°, 46.9°, 53.1°, 56.5°, 60.2°, 61.7°, 65.6° and they were assigned to (003), (006), (101), (012), (104), (015), (107), (018), (1010), (0111), (110), (113), (116) [189].

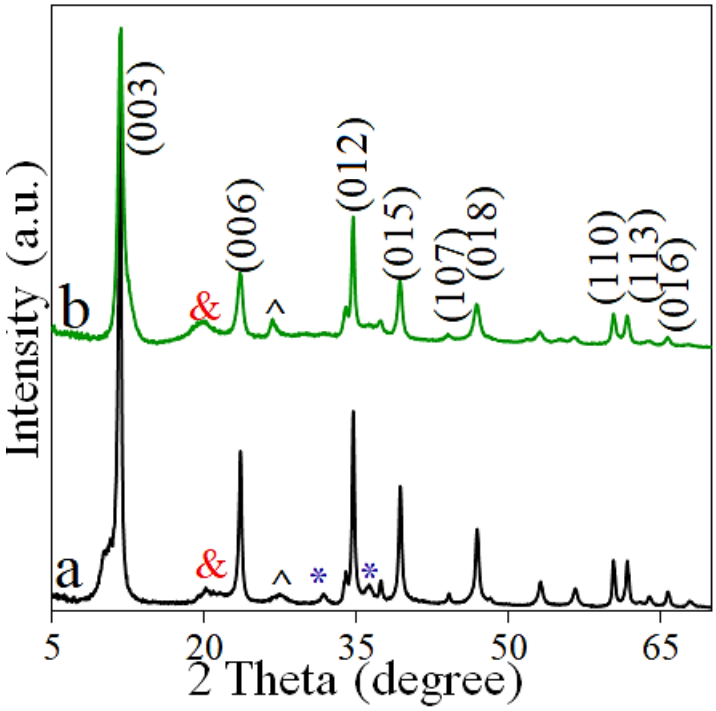

Figure 2.15: XRD patterns of a) Ag/ZnGa(2/1) and b) Au/ZnGa(2/1); (&) -β-Ga_2O_3, (^) α-GaO(OH), (*) ZnO.

The obtained UV-Vis spectra are given in figure 2.16 and they present absorptions bands centered around 534 nm for the Au/ZnGa(2/1) and a large absorption broad for the Ag/ZnGa(2/1) centered around 450 nm, proving the existence of AuNPs and AgNPs on LDH surface [178,190].

The anions nature into the interlayer space was evaluated by FTIR measurements. For both NPs/ZnGa(2/1) materials, the spectra (figure 2.17) are typical for the layered composites with the presence of an intense band around 3450 cm^{-1} assigned to the O-H stretching vibration, followed by the characteristic peak of the interlayer water molecules, at 1630 cm^{-1} and two other absorption at 1360 cm^{-1}, 1500 cm^{-1}attributed to symmetric and antisymmetric stretching modes of CO_3^{2-}respectively. Between 800-400 cm^{-1} can be observed the characteristic signals for M-O-M and M-O [50]. Because the high affinity of layered double hydroxides for the

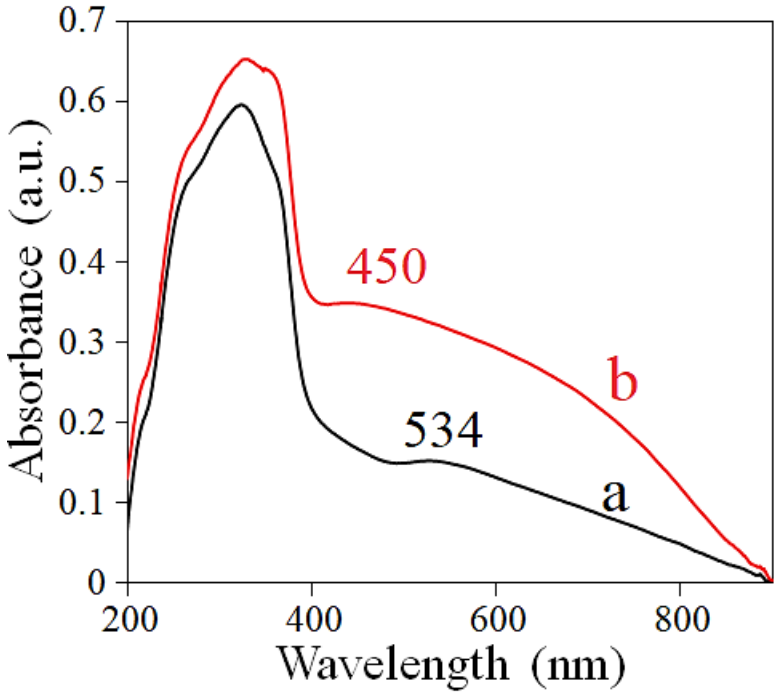

Figure 2.16: UV-Vis adsorption spectra for a) Au/ZnGa(2/1) and b) Ag/ZnGa(2/1).

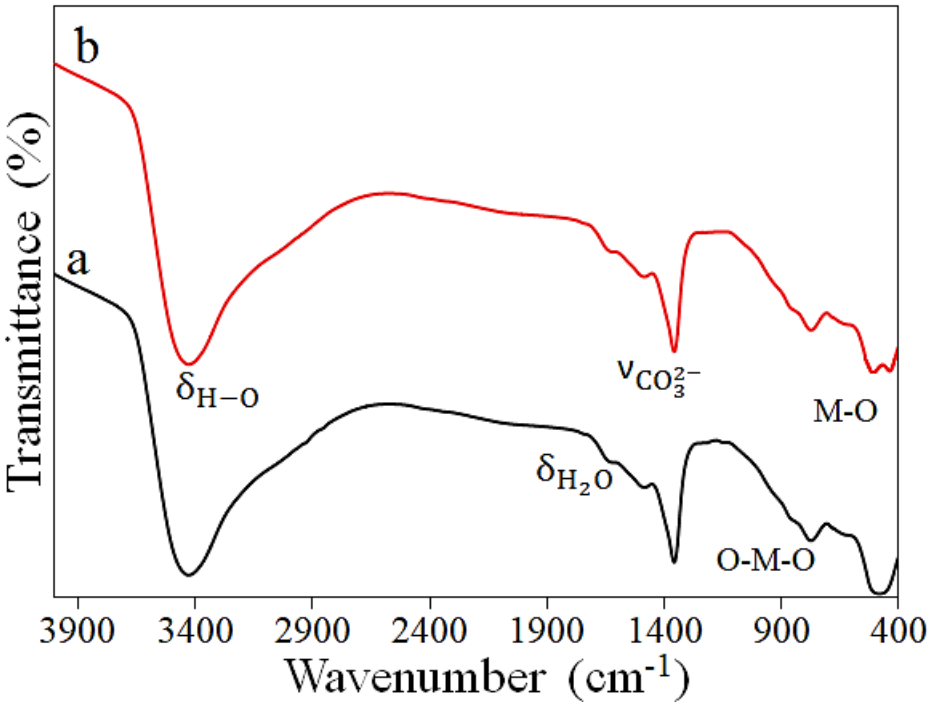

Figure 2.17: FTIR spectra for a) Au/ZnGa(2/1) and b) Ag/ZnGa(2/1).

carbonate anion, the intercalation of distinct anions between the interlayer space can be possible in the most of the situations only under an inert atmosphere. For this reason, during the reconstruction, the acetate and the sulfate anions were not incorporated in the material structure.

2.2.4. Au/ZnAl(2/1)LDHs self-assembly for phenol solar photodegradation

The photocatalytic performance of the ZnAl(2/1) and Au/ZnAl (2/1) was tested in the solar photodegradation of the 25 mg/L phenol solution using the protocol and the experimental device presented at the Generalities section. The blank test had shown that phenol is a very stable molecule, with no significant photolysis.

From figure 2.18 might be observed that for all the catalysts, the characteristic phenol absorbance at 270 nm decreases during the time, the less efficient material being ZnAl(2/1) with 7.6 % phenol photodegradation. For the rest of the nanomaterials, the influence of the AuNPs on LDH surface can be established from photocatalytic performance. UV-Vis absorption spectra reveal that the phenol is degraded via two major pathways. First mechanism involves the direct oxidation of the aromatic ring, followed by the ring opening, when o-benzoquinone and muconic acid are formed. The second mechanism takes place via indirect ring cleavage, when intermediate compounds as p-benzoquinone or hydroquinone are formed [34]. The pure compound UV-Vis spectra presented in figure 2.18-h can be used for photodegradation compound identification. The photodegradtion pathways are dependent on catalyst type. Thus, the reconstructed samples, Au/ZnA(2/1)-R-1, Au/ZnAl(2/1)-R-2, Au/ZnAl(2/1)-R-3-Lg degrade the pollutant via hydroxylated phenolic intermediates, with the formation of a degradation compound identified as p-benzoquinone, which has an absorption peak at 248 nm. The ZnAl(2/1) and the impregnated samples, Au/ZnAl(2/1)-I-$NaBH_4$, f) Au/ZnAl(2/1)-I-Ly, showed that the pollutant degradation follows both direct and indirect mechanism. To appreciate more precisely the peaks intensity corresponding for aromatic ring, p-benzoquinone and phenol, the spectra profiles were deconvoluted by using the four Gaussian peaks (see equation 2.6).

$$f(x) = a_1 \exp\left\{-\left(\frac{x-197}{b_1}\right)^2\right\} + a_2 \exp\left\{-\left(\frac{x-210}{b_2}\right)^2\right\} + a_3 \exp\left\{-\left(\frac{x-248}{b_3}\right)^2\right\} + a_4 \exp\left\{-\left(\frac{x-270}{b_4}\right)^2\right\} \quad 2.6$$

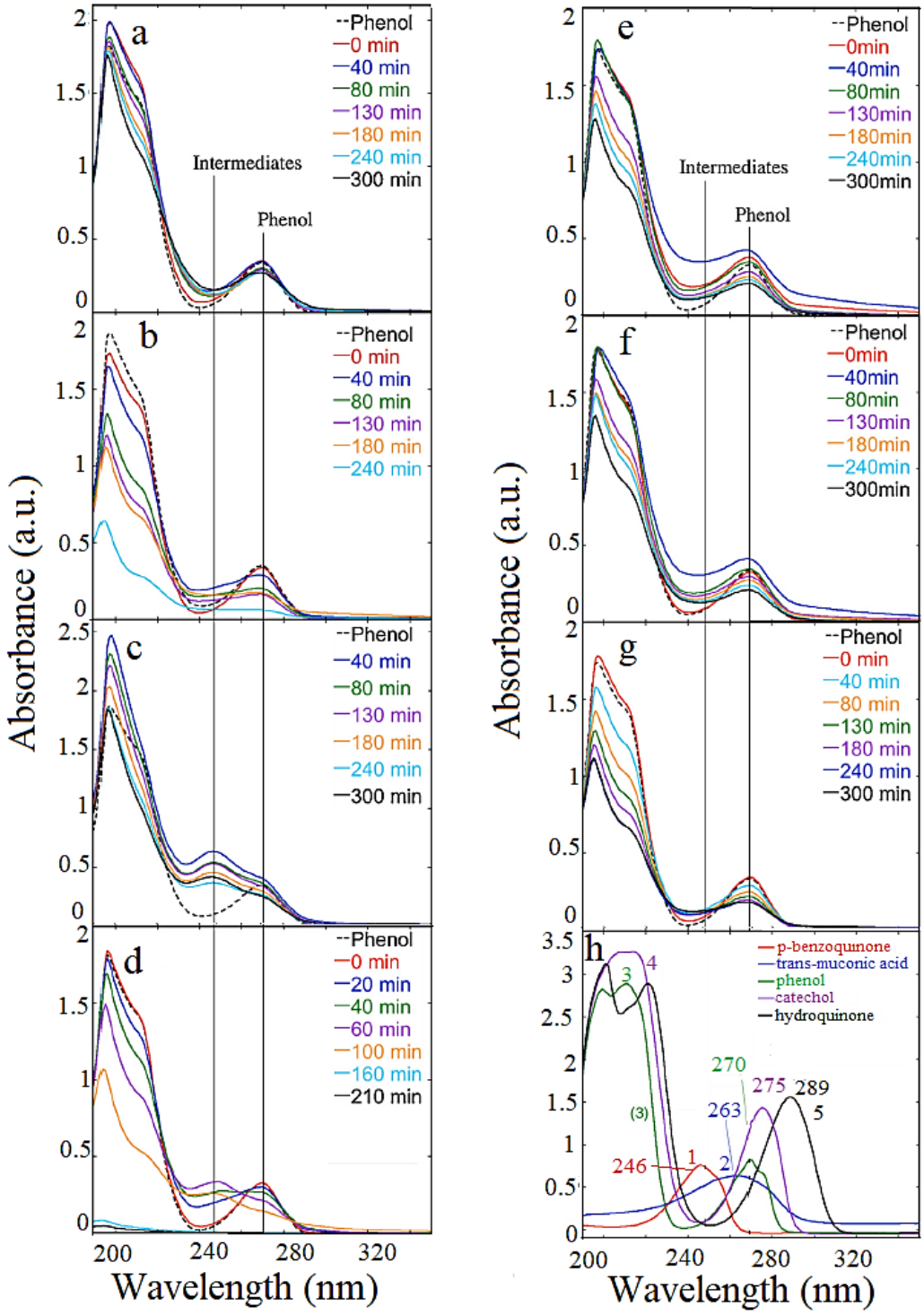

Figure 2.18: a) ZnAl(2/1), b) Au/ZnAl(2/1)-R-1, c) Au/ZnAl(2/1)-R-2, d) Au/ZnAl(2/1)-R-3-Lg, e) Au/ZnAl(2/1)-I-$NaBH_4$, f) Au/ZnAl(2/1)-I-Ly, g) Au/ZnAl(2/)-Lg, h) p-benzoquinone, trans,trans-muconic acid, phenol, catechol and hydroquinone

Where a and b are the absorbance, respectively the peaks width in nm. Figure 2.19 presents the absorbance evolution for phenol (A) and p-benzoquinone (B) based on Gaussian deconvolution. The phenol concentration has a continuous decrease during the time, while p-benzoquinone absorbance at 248 nm firstly increases as a proof of its formation, afterwards, the absorbance decreases, as a consequence of its degradation. The hydroquinone corresponding peak at 288 was not observed, which means that it was fast converted in p-benzoquinone. For the reconstructed samples, the maximum of p-benzoquinone is reached after 40-60 min. The Au/ZnAl(2/1)-R-3-Lg catalyst was the most preformat according with peak evolution expressed in figure 2.19-A-d. For Au/ZnAl(2/1)-R-2 material it was observed a fluctuant evolution of absorbance. During the 4 h, the absorbance at 248 nm reaches a maximum and a minimum; afterwards, it starts to increase again. An explanation of this fact can be a balance of the phenol photodegradation rates and the redox equilibrium between p-benzoquinone and hydroquinone. This evolution is also expressed in figure 2.20. For the impregnate samples, it was observed an enlargement of the absorption around 270 nm, suggesting the formation of compounds which have the maximum absorption peak close to that of phenol, as catechol (276 nm) and muconic acid (260 nm). Taking this into consideration, the proposed mechanism (figure 2.21) involves additionally, besides the indirect ring opening through p-benzoquinone, which takes place in the first 20-40 min, the phenol oxidation to catechol, which is further converted to o-benzoquinone and muconic acid.

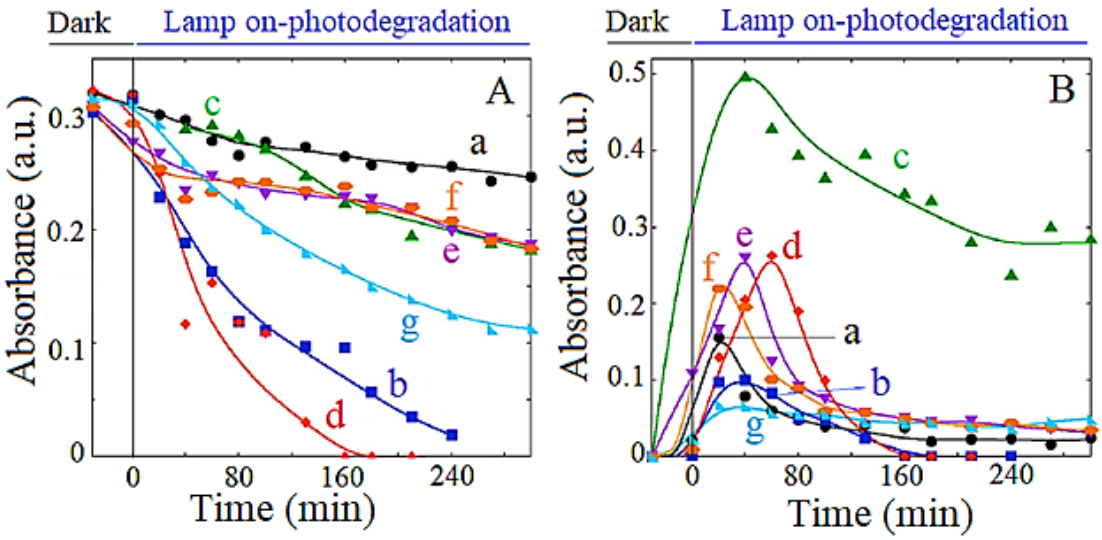

Figure 2.19: Absorbance evolution at 270 nm and 248 nm for (A) phenol and (B) p-benzoquinone based on Gaussian deconvolution; a) ZnAl(2/1), b) Au/ZnAl(2/1)-R-1, c) Au/ZnAl(2/1)-R-2, d) Au/ZnAl(2/1)-R-3-Lg, e) Au/ZnAl(2/1)-I-$NaBH_4$, f) Au/ZnAl(2/1)-I-Ly, g) Au/ZnAl(2/1)-Lg.

The performance in phenol photodegradation after 160 min is presented in figure 2.22. It might be observed that the solar reconstructed sample, Au/ZnAl(2/1)-R-3-Lg, is the most efficient

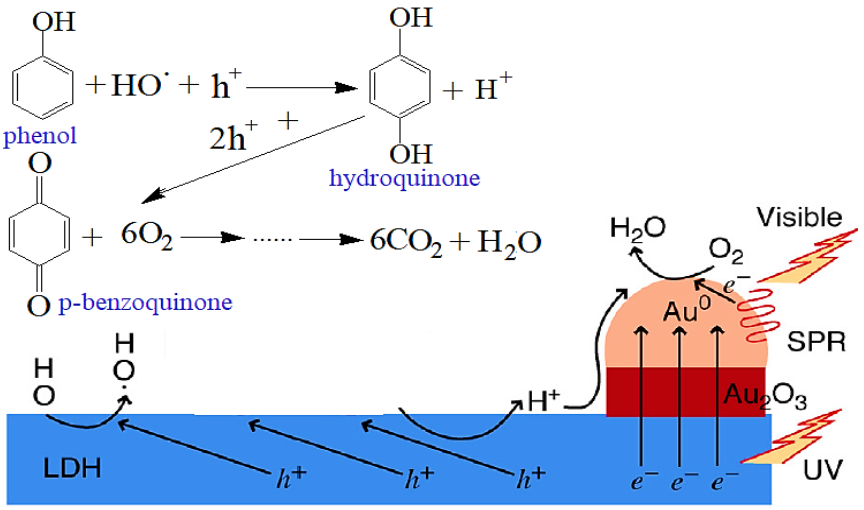

Figure 2.20: Phenol photodegradation in presence of solar irradiation and Au/ZnAl(2/1) reconstructed samples

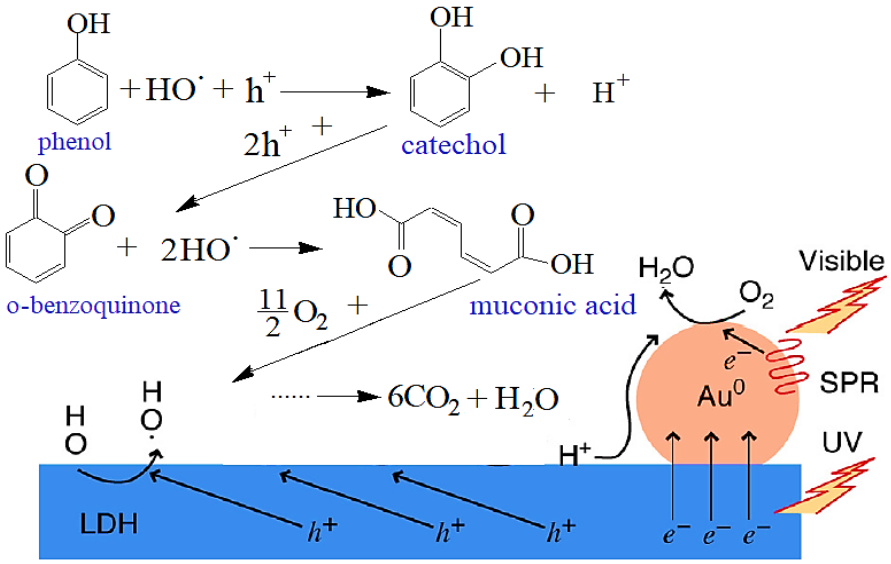

Figure 2.21: Phenol photodegradation in presence of solar irradiation and Au/ZnAl(2/1) impregnated samples

material, with total phenol degradation. The rest of the reconstructed sample presented a smaller photo-response compared with the Au/ZnAl(2/1)-R-3-Lg. Furthermore, samples withthe same content in ZnAl(2/1) and AuNPs (Au/ZnAl(2/1)-R-1, Au/ZnAl(2/1)-R-3-Lg and Au/ZnAl(2/1)-Lg) have different state of AuNPs: mix between Au^0 and Au^{3+} for Au/ZnAl(2/1)-R-3-Lg and only Au^{3+} for Au/ZnAl(2/1)-R-1 and Au/ZnAl(2/1)-Lg. The results prove that a mixtures between gold with different oxidation state can have a beneficial influence on the photocatalytic performant. In addition, the increase of the gold content causes a decrease of materials activity. This behavior was previously reported [191]. Also, the impregnation of LDH with AuNPs leads to less efficient materials, with only 23 % (Au/ZnAl(2/1)-I-Ly) and 26 % (Au/ZnAl(2/1)-I-$NaBH_4$) of phenol degradation. To complete the results expressed in figure 2.19, HPLC measurements were performed (Shim-pack VP-ODS column). Unfortunately, the calibration of p-benzoquinone was difficult and for this reason, no conclusive results were obtained.

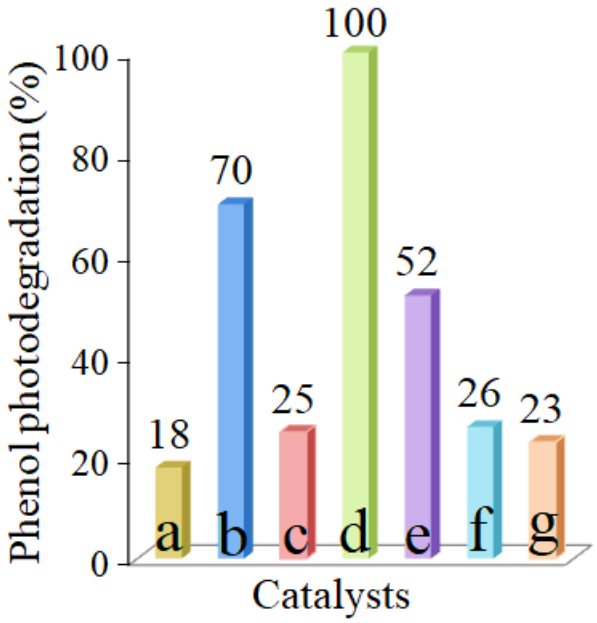

Figure 2.22: Photocatalytic performance of a) ZnAl(2/1),) Au/ZnAl(2/1)-R-1, c) Au/ZnAl(2/1)-R-2, d) Au/ZnAl(2/1)-R-3-Lg, e) Au/ZnAl(2/1)-Lg, f) Au/ZnAl(2/1)-I-$NaBH_4$, g) Au/ZnAl(2/1)-I-Ly.

For the best catalyst, Au/ZnAl(2/1)-R-3-Lg, the stability was tested. To do this, six tests were performed (see figure 2.23). After each test, the material was recovered and used again in the next test. After the 5 consecutive utilization, Au/ZnAl(2/1)-R-3-Lg nanomaterial retains 73 % of its initial activity. Before the sixth use, the material was solar irradiated during 1 h. An increase in activity from 73 % to 81 % was observed. The increase can be explained by the charge transfers which take place in the mixed phases of AuNPs and ZnAl(2/1) in the presence of the UV-visible irradiation.

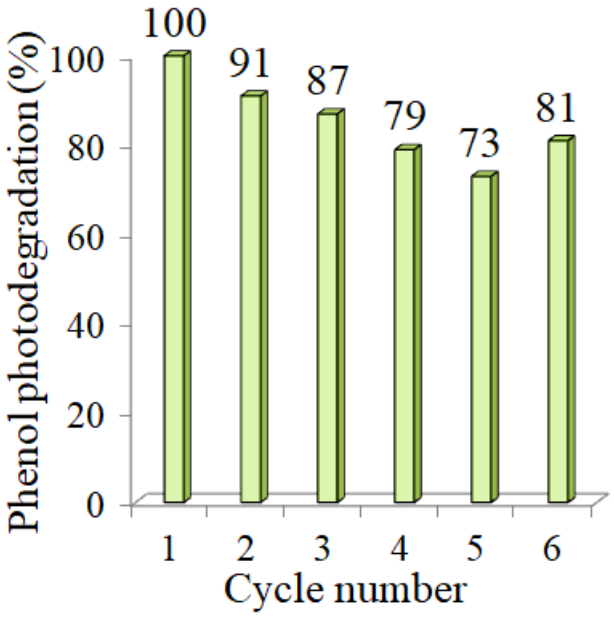

Figure 2.23: Au/ZnAl(2/1)-R-3-Lg photocatalytic activity during 6 successive cycles.

It was suspected that the loss of activity is related to potential AuNPs leaching. To investigate this, after each cycle, the catalyst was removed, and the supernatant was mixed with a new phenol solution. No further degradation of pollutant was noticed, proving that no /or insignificant losses of Au/NPs took place. The UV-Vis spectra of the supernatant do not present particular signals for the AuNPs.

In this section it was shown that the self-assembled AuNPs can be successfully used in phenol solar light driven photodegradation. The different routes of synthesis, reconstruction and impregnation, lead to Au/ZnAl(2/1) materials with different properties which performed the pollutant degradation via distinct pathways. Furthermore, the reconstructed sample, Au/ZnAl(2/1)-R-3-Lg, in which the AuNPs are a mixt of Au^0 and Au^{3+} presents the highest photo-response with a total phenol degradation in 160 minutes, while ZnAl(2/1) degraded only 18 % in the same time. Additionally, the Au/ZnAl(2/1)-R-3-Lg presents a high stability with the retention of 81 % of the initial activity after six consecutive utilizations. Compared with other LDHs materials used in the phenol degradation, our photocatalysts present an increase of photoresponse. For instance, M. Suares-Quezada and al. have prepared ZnAlCeLDHs and the resulted materials were calcined at 400 °C and tested for the UV phenol degradation. Comparing their best catalyst with our best Au/LDH, our material is able to degrade more that 99 % of phenol in 160 minutes of solar irradiation, while in their case only 90 % of pollutant was removed in 4 h [192]. Furthermore, these materials are more efficient that the previous materials obtained by our group. For example, Ce/ZnTiLDH photodegraded 90 % of phenol in 8 h by using a powerful UV lamp (700 W) [34]. Furthermore, Ti/MgAlLDH photodegraded 90 % of pollutant in 4.5 h [193]. However, our material have comparable performance with Ag/AgCl/$ZnSn(OH)_6$ which removed in 120 minutes, under visible irradiation, 90 % of phenol

[194], the initial concentration of pollutant being 2.5 times smaller than the one used in our case. Considering this, it can be concluded that the AuNPs self-assembly on LDHs materials assisted by solar light can lead to highly photo responsive materials, which can be successfully used in organic compounds photodegradation.

2.2.5. Au/ZnAlLDHs with a Me^{2+}/Me^{3+} ratio of 2/1; 4/1 for (phenol + p-nitrophenol) solar photodegradation

The photocatalytic activity of the ZnAlLDHs and Au/Zn2Al(1_0.12)-Lg, Au/Zn2Al(1_0.12)-Lg-750, Au/Zn4Al(1_0.12)-Lg and Au/Zn4Al(1_0.12)-Lg-750 nanomaterials (their synthesis and characterization was presented in chapter 2.2.3) was tested for the solar photodegradation of pollutant solution containing phenol (Ph) and p-nitrophenol (p-NP). For this, in 100 mL of phenol solution, with total concentration of 50 mg/L pollutants (25 mg/L Ph + 25 mg/L p-NP), were added 0.1 g/L of catalyst. After the adsorption-desorption equilibrium was established, the first sample was taken and denoted *0 min*, and the irradiation was turn on. The sampling was done at determinate times and the pollutants concentration was monitored by UV-Vis measurements, after the solid was removed by centrifugation. A blank test, without the catalyst, was also performed in order to verify if the organic compounds can be degraded only by the light. The results have shown that pollutants mixture is a very stable system, its photolysis being negligible. The experimental device was described in section 2.1.

This study presents, for the first time, the photocatalytic performance of self-assemble AuNPs on ZnAlLDH and their derived mixed oxides obtained by thermal treatment during 12 h at 750 ° in degrading a pollutants system containing phenol and p-nitrophenol. During the adsorption-desorption equilibrium it was observed that the p-nitrophenol was reduced to p-nitrophenolat anion and the original absorption peak was shifted from 317 nm to 400 nm. Thus, the photocatalytic studies were investigated considering the absorbance measured at wavelength of 400 nm. In the dark, after the reduction of p-nitrophenol, very small pollutant absorption was observed. In the case of the blank tests, no photodegradation was noticed. Thus, photodegradation was monitored by two peaks centered at 270 nm and 400 nm which are corresponding for phenol and p-nitrophenolat anion. When the solar irradiation lamp is turned ON, the photodegradation begins and the absorption peaks at 270 nm and 400 nm decrease with reaction time (see figure 2.24). However, for the fresh sample, ZnAl(2/1) and ZnAl(4/1) it was observed firstly an increase of absorbance at 400 nm and after it reaches a maximum, it decreases slowly. The increase can be associated with the slow p-nitrophenolat anion formation, while the decrease can be assigned to its photodegradation. Furthermore, these two materials present the smallest photo-response, with less than 10 % phenol and p-nitrophenolat ion removal.

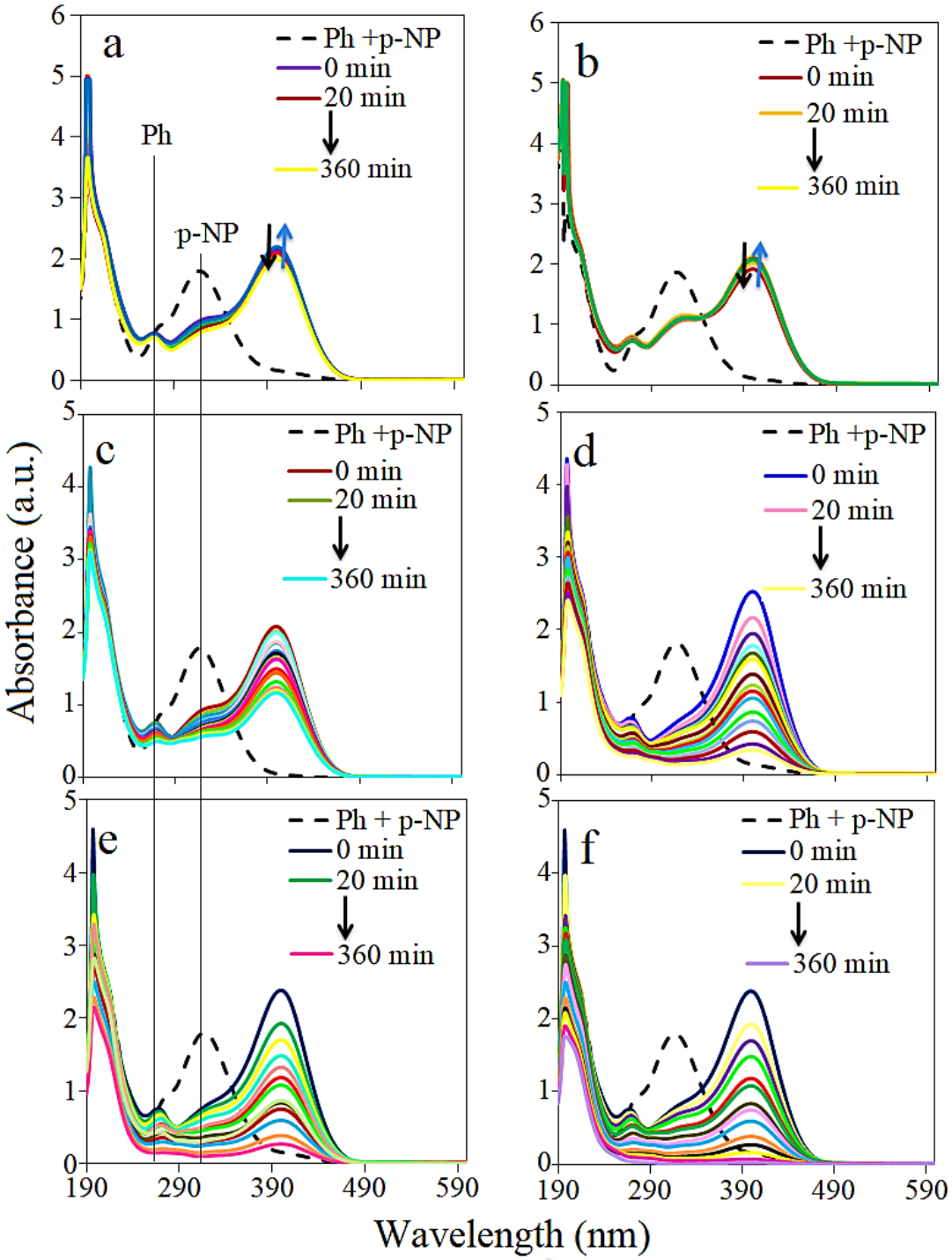

Figure 2.24: UV-Vis spectral profiles of Ph+ p-NP for a) ZnAl(2/1), b) ZnAl(4/1), c) Au/Zn2Al(1_0.12)-Lg, d) Au/Zn4Al(1_0.12)-Lg, e) Au/Zn2Al(1_0.12)-Lg-750, f) Au/Zn4Al(1_0.12)-Lg-750.

The evolution in time for this processes initiated by our catalysts and their photocatalytic performance are presented in figure 2.25. It can be observed that the absorbance

decreases gradually for the reconstructed and calcined samples and after 360 minutes of irradiation Au/Zn4Al(1_0.12)-Lg-750 catalyst photodegrades 99 % of the initial concentration of p-nitrophenolat ion and 96 % from the initial concentration of phenol (see figure 2.26).

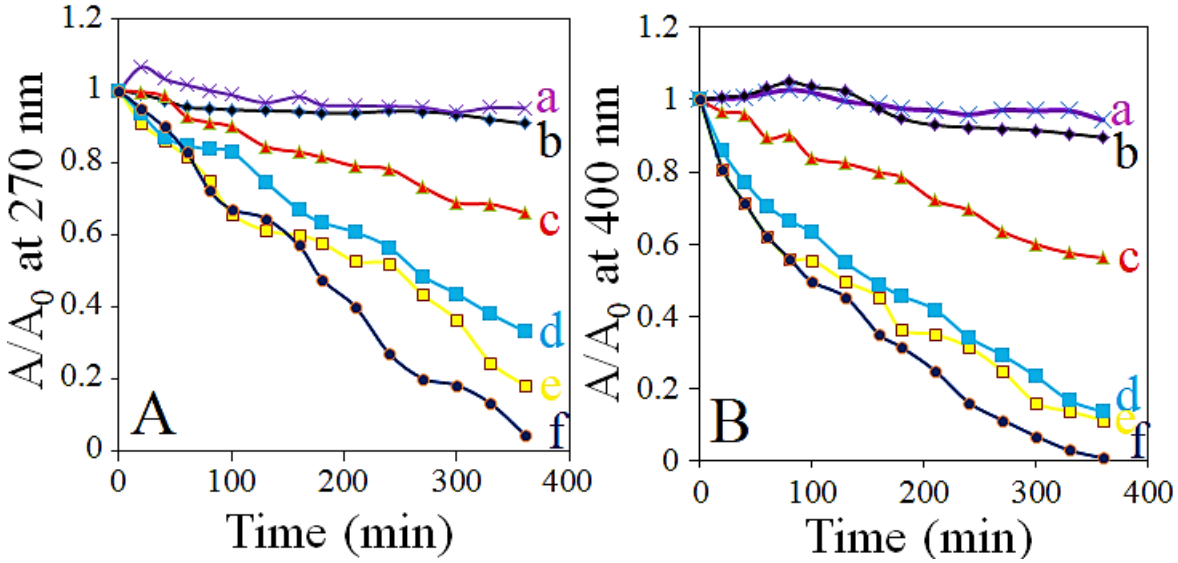

Figure 2.25: Normalized absorbance evolution at A) 270 nm and B) 400 nm for a) ZnAl(2/1), b) ZnAl(4/1), c) Au/Zn2Al(1_0.12)-Lg, d) Au/Zn4Al(1_0.12)-Lg, e) Au/Zn2Al(1_0.12)-Lg-750, f) Au/Zn4Al(1_0.12)-Lg-750.

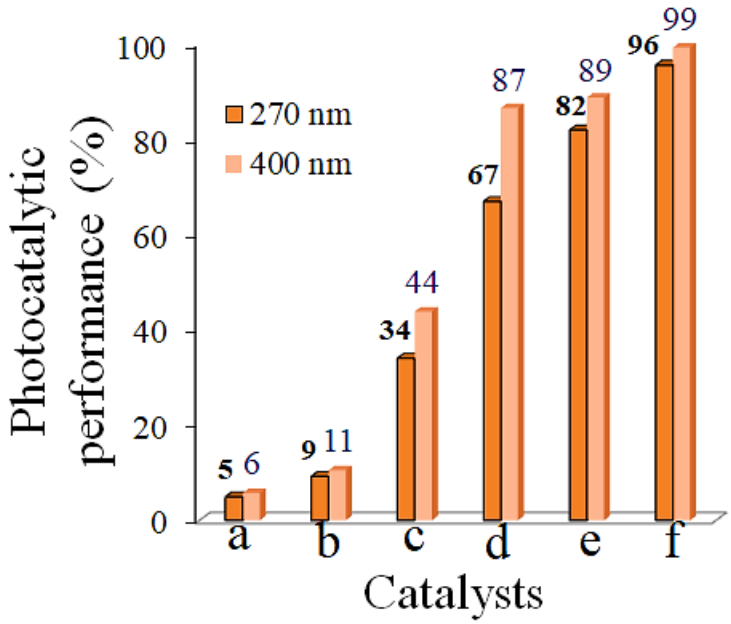

Figure 2.26**:** The photocatalytic performance at 270 nm and 400 for a) ZnAl(2/1), b) ZnAl(4/1), c) Au/Zn2Al(1_0.12)-Lg, d) Au/Zn4Al(1_0.12)-Lg, e) Au/Zn2Al(1_0.12)-Lg-750, f) Au/Zn4Al(1_0.12)-Lg-750.

The photodegradation reactions follow a pseudo-first-order kinetic. The apparent rate constants (k_{app}) were determinated from the slope of –ln(A) vs t plots, where A value represents the normalized absorbance at 400 nm or 270 nm, at different time intervals. The results shown in table 2.2 demonstrate that the photoresponsive activity of the samples increases this order: freshly LDHs < reconstructed samples < calcined samples. This behavior demonstrates that the deposition of AuNPs on LDHs materials improves the catalytic efficiency of the layered systems. Furthermore the increase of Zn content in the LDHs structure, increases the activity of the system. For the same content of gold, the solar reconstructed sample Au/Zn4Al(1_0.12)-Lg presents an increase of activity with approximately 50% compared with Au/Zn2Al(1_0.12)-Lg (see figure 2.26 and table 2.2). After the thermal treatment a significant increase of activity (more than 50 %) was recorded for the Au/Zn2Al(1_0.12)-Lg-750, compared with uncalcined

Table 2.2: The apparent constants for the phenol + p-nitrophenol photodegradation reactions.

Catalyst	Ph photodegradation k_{app} (x 10^{-3} min^{-1})	p-NP photodegradation k_{app} (x 10^{-3} min^{-1})
ZnAl(2/1)	0.2	0.2
ZnAl(4/1)	0.3	0.4
Au/Zn2Al(1_0.12)-Lg	1.2	1.7
Au/Zn4Al(1_0.12)-Lg	2.9	5
Au/Zn2Al(1_0.12)-Lg-750	3.9	5.5
Au/Zn4Al(1_0.12)-Lg-750	7.2	10.9

sample. X. Zhao and collaborators investigated the preparation of mixed oxide from LDHs through a thermal process. The catalysts were used in the photodegradation of methyl orange and also its UV-blocking properties were tested. They demonstrated that the coupling between the metallic oxides and the spinel phase can decrease the recombination rate of charge carriers leading to an enhancement of photo-responsive activity [17,179]. Thus, the increase of performance for the Au/ZnAlLDHs thermal treated samples can be a result of the material composition, which contains AuNPs, but also metal oxides and spinel-like phase, which can enhance the photo-response.

The photodegradation of phenolic pollutants involves two steps: firstly, phenol and p-nitrophenol are oxidized to highly toxic quinones like hydroquinone, and benzoquinone, 4-nitrochatechol followed by the opening of the aromatic ring with the formation of biodegradable aliphatic acids like oxalic acid [195,196].

As far as we know, the solar photodegradation of a mixture of Ph + p-NP was not investigated before. In a study published by S. Islam and al., 4g/L TiO_2 material was able to degrade under UV irradiation 90 % of p-NP in 2 h, starting from an initial pollutant

concentration of 14 mg/L [197]. In our case, the total pollutant concentration from the system was 50 mg/L and the catalyst concentration was 1 g/L. In another study, 20 mg/L p-NP was 100 % photodegraded by a UV lamp, in a time range of 60-90 minutes, by using 0.4 g/L Fe-TiO_2 catalyst [198]. However, considering the previous studies on the separately removal of these two compounds, whose results are comparable with the one obtained in our study [192,193,197], we believe that our materials are promising photocatalysts for the removal of different pollutants from the same systems.

2.2.6. Au/ZnAlLDHs with a Me^{2+}/Me^{3+} ratio of 2/1; 3/1; 4/1 for acetophenone solar photodegradation

The photocatalytic activity of the ZnAlLDHs, Au/Zn2AlLDHs: Au/Zn2Al(2.1_0.1), Au/Zn2Al(2.1_0.2), Au/Zn2Al(1_0.35), Au/Zn2Al(1_0.12)-Lg and Au/Zn4AlLDHs: Au/Zn4Al(2.1_0.2), Au/Zn4Al(2.1_0.1), Au/ZnAl(3/1), Au/Zn4Al(1_0.35), Au/Zn2Al(1_0.12)-Lg nanomaterials (their synthesis and characterization was presented in chapter 2.2.3.2) was tested for the solar photodegradation of acetophenone. The experimental protocol and devices were presented in the section 2.1.

In figure 2.27 are listed the UV-Vis profiles of acetophenone solar photodegradation in presence of the investigated materials. For all the catalysts, it was recorded a decrease of absorbance at 245 nm during the time. For the blank test, carried out without the addition of catalysts, the results showed a photodegradion yield of 51% (see figure 2.28 A-a). For some catalysts, such as ZnAl(2/1), ZnAl(3/1), ZnAl(4/1), Au/Zn2Al(2.1_0.1), Au/Zn2Al(2.1_0.2) and Au/Zn2Al(1_0.35) (see figure 2.27 a-e, g) an increase of the peack at 245 nm was observed, and it was assigned to the hyperchromic effect of these materials on acetophenone light absorption. The Au/Zn2AlLDHs samples present a small increase (8-26 %) of the photocatalytic performance, compared with the blank test. However, the solar reconstructed sample, Au/Zn2Al(1_0.12)-Lg, is able to remove 99 % of acetophenone in 130 minutes. From UV-Vis spectra presented in figure 2.13 can be noticed that the Au/Zn2Al(1_0.12)-Lg material presents the highest SPR effect, while for the rest of the catalysts, this effect is rather weak. This behavior can explain the low photo-response of these samples. Furthermore, the increase of the gold content it seems to have no beneficial effect for the enhancement of catalysts performance. In this case, the excesive deposition of AuNPs might lead to nanoparticles active site shielding on LDH surface.This effect was observed previously in case of TiO_2 doped with Bi [191] or g-C_3N_4 doped with Ag_3PO_4 [199].

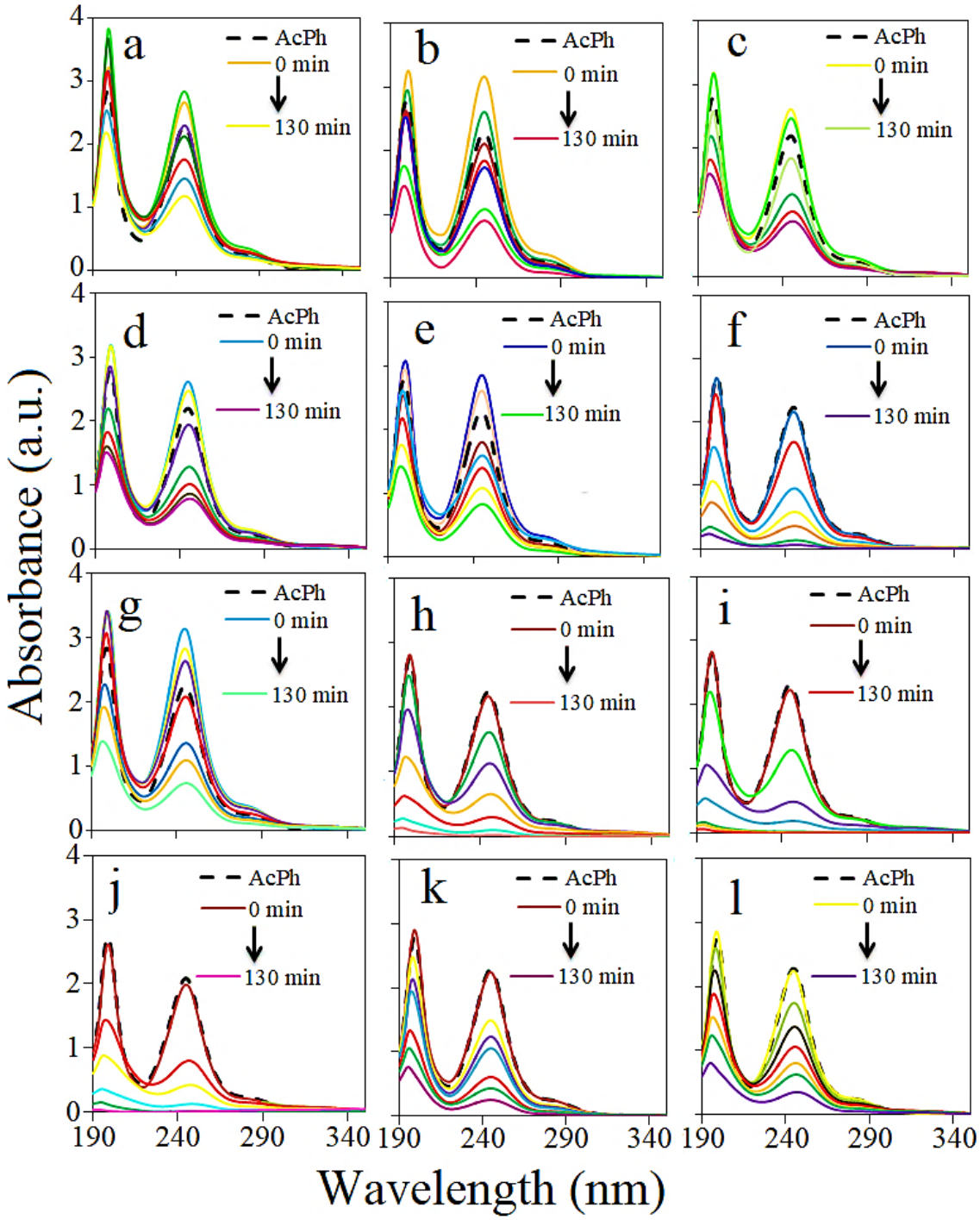

Figure 2.27: UV-Vis spectra profiles for acetophenone photodegradation for: a) ZnAl(2/1), b) ZnAl(3/1), c) ZnAl(4/1), d) Au/Zn2Al(2.1_0.1), e) Au/Zn2Al(2.1_0.2), f) Au/Zn2Al(1_0.12)-Lg, g) Au/Zn2Al(1_0.35), h) Au/Zn4Al(2.1_0.2), i) Au/Zn4Al(2.1_0.1), j) Au/Zn4Al(1_0.12)-Lg k) Au/Zn4Al(1_0.35), l) Au/ZnAl(3/1).

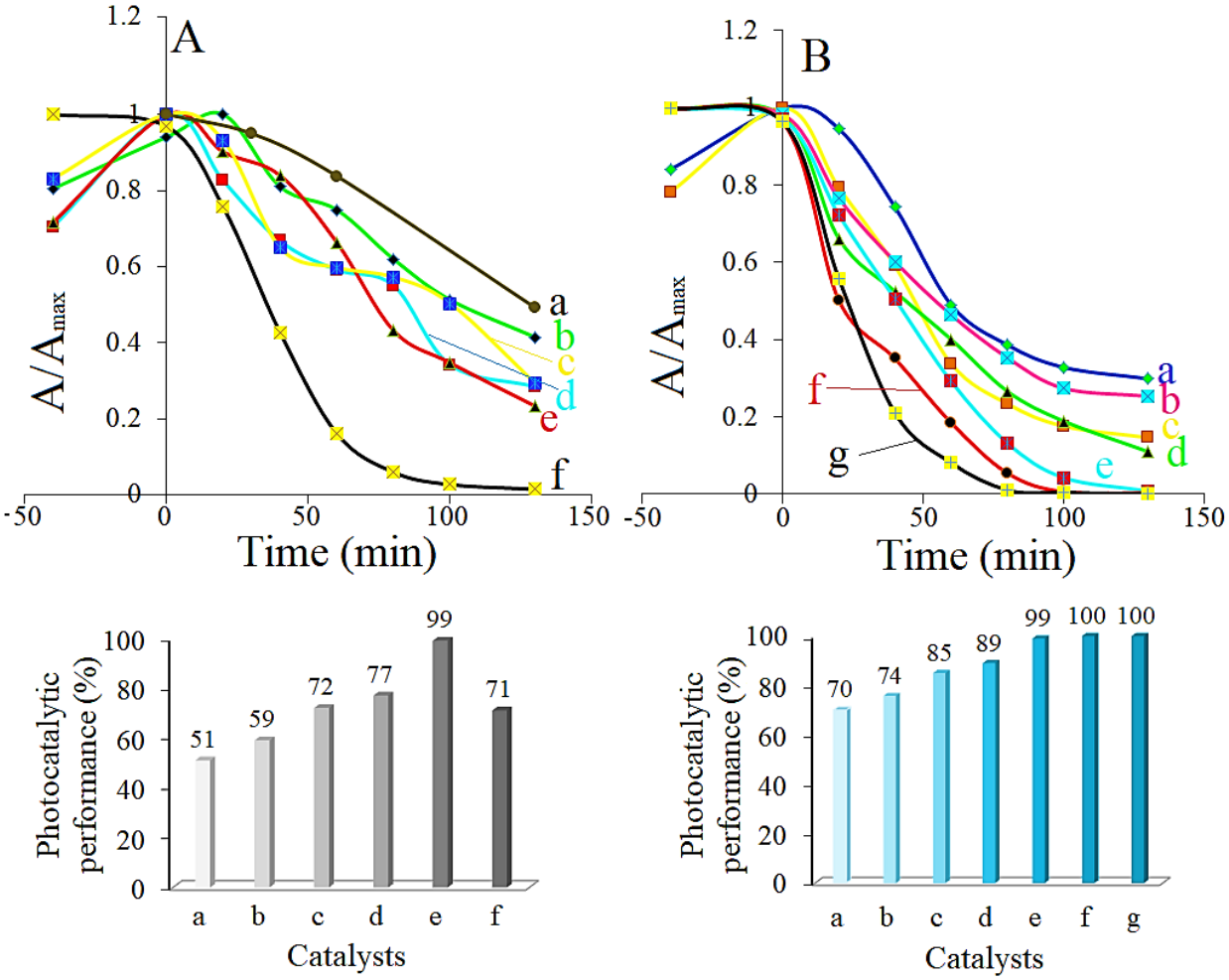

Figure 2.28: Normalized absorbance evolution and photocatlytic performance for: A) a) blank b) ZnAl(2/1), c) Au/Zn2Al(2.1_0.1), d) Au/Zn2Al(1_0.35) e) Au/Zn2Al(2.1_0.2), f) Au/Zn2Al(1_0.12)-Lg and B) a) ZnAl(3/1), b) ZnAl(4/1), c) Au/ZnAl(3/1) d) Au/Zn4Al(1_0.35), e) Au/Zn4Al(2.1_0.1), f) Au/Zn4Al(2.1_0.2), g) Au/Zn4Al(1_0.12)-Lg.

The increase of Zn^{2+} content induces an increase of performance from 59 % for ZnAl(2/1) to 70 % for ZnAl(3/1) and 73 % for ZnAl(4/1). The AuNPs self-assembled on ZnAl(4/1)LDH have best performance in acetophenone solar photodegradation, with a total pollutant removal. The difference in photocatalytic activity between the reconstructed sample on ZnAl(2/1) and ZnAl(4/1) can be explained firstly by the Zn^{2+} content in the LDH, but also by the SPR effect which is more intense for the Au/ZnAl(4/1)LDHs (see figure 2.13 and 2.14). The fastest degradation was obtained with Au/Zn4Al(1_0.12)-Lg sample (see figure 2.27-j and figure 2.27-h). These results show that the reconstruction carried out under solar light enhances the photo-response of the material. The presence of AuNPs on ZnAl(3/1) increases the activity from 70 % for ZnAl(3/1) to 85% for Au/ZnAl(3/1) (see figure 2.28 B-a and c).

The photodegradation reactions follow a pseudo-first-order kinetic. The apparent rate constants (k_{app}) were determinate from the slope of –ln(A) vs t plots, where A value represents the normalized absorbance at 245 nm. The half-life times $t_{1/2} = 0.693/k_{app}$ were also calculated. The apparent constants rates (k_{app}) and the half-life time $t_{1/2}$ are listed in table 2.3.

Table 2.3: Kinetic results for the solar photodegradation of acetophenone.

Catalyst	k_{app} (x 10^{-3} min^{-1})	$t_{1/2}$ (min)
ZnAl(2/1)	6.9	100.4
A/Zn2Al(2.1_0.1)	8.7	79.6
Au/Zn2Al(1_0.35)	9.7	71.4
Au/Zn2Al(2.1_0.2)	11.8	58.7
Au/Zn2Al(1_0.12)-Lg	35.3	17.3
ZnAl(3/1)	10.7	64.7
ZnAl(4/1)	11.1	62.4
Au/ZnAl(3/1)	16.3	42.5
Au/Zn4Al(1_0.35)	16.5	42
Au/Zn4Al(2.1_0.1)	36.5	18.9
Au/Zn4Al(2.1_0.2)	46.7	14.8
Au/Zn4Al(1_0.12)-Lg	59.9	11.5
Blank	5.7	121.6

It might be observed that the increase of the Zn^{2+} content induces a decrease of the $t_{1/2}$ from 100.4 minutes (ZnAl(2/1)) to 64.7 and 62.4 minutes for ZnAl(3/1) and ZnAl(4/1), respectively. Additionally to this decrease can be added the decrease induced by the AuNPs presence on the LDHs surface. The best catalysts, Au/Zn4Al(1_0.12)-Lg presents a $t_{1/2}$ six times smaller compared with ZnAl(4/1), and 10 times smaller if compared with the blank tests.

As far as we know, till now the LDHs materials were not used in the photodegradation of acetophenone. However, recently, S. Soltan et al. have fabricated a catalyst type TiO_2-SO_2 and they used in the UV photodegradation of the 10 mg/L acetophenone solution. Their catalyst was able to degrade 95 % of pollutant in 2 h [200]. A similar result was obtained by E. Amereh and S. Afshar using TiO_2 supported on NaX zeolite. They removed in 3 h 98 % from the initial solution of acetophenone (30 mg/L) by using an UV lamp [201]. The simple TiO_2, with a concentration of 3g/L, photodegradated 70 % from the initial concentration of acetophenone (30 mg/L) in 4 h of sunlight exposure [202]. Our results present an increase of activity, considering the fact that the process was carried out under solar irradiation and the solar irradiation has only between 5-8 % of UV component.

2.2.7. Au or Ag on ZnGa(2/1)LDH for solar photodegradation of acetophenone

The photocatalytic activity of the ZnGa(2/1)LDH, Au/ZnAl(2/1) and Ag/ZnAl(2/1) materials (their synthesis and characterization was presented in chapter 2.2.3) was tested for the solar photodegradation of acetophenone. The experimental protocol and device were presented in the section 2.1.

In figure 2.29 are presented the UV-Vis spectra profiles for acetophenone photodegradation (a-c) and the normalized absorbance evolution at 450 nm (d). After the

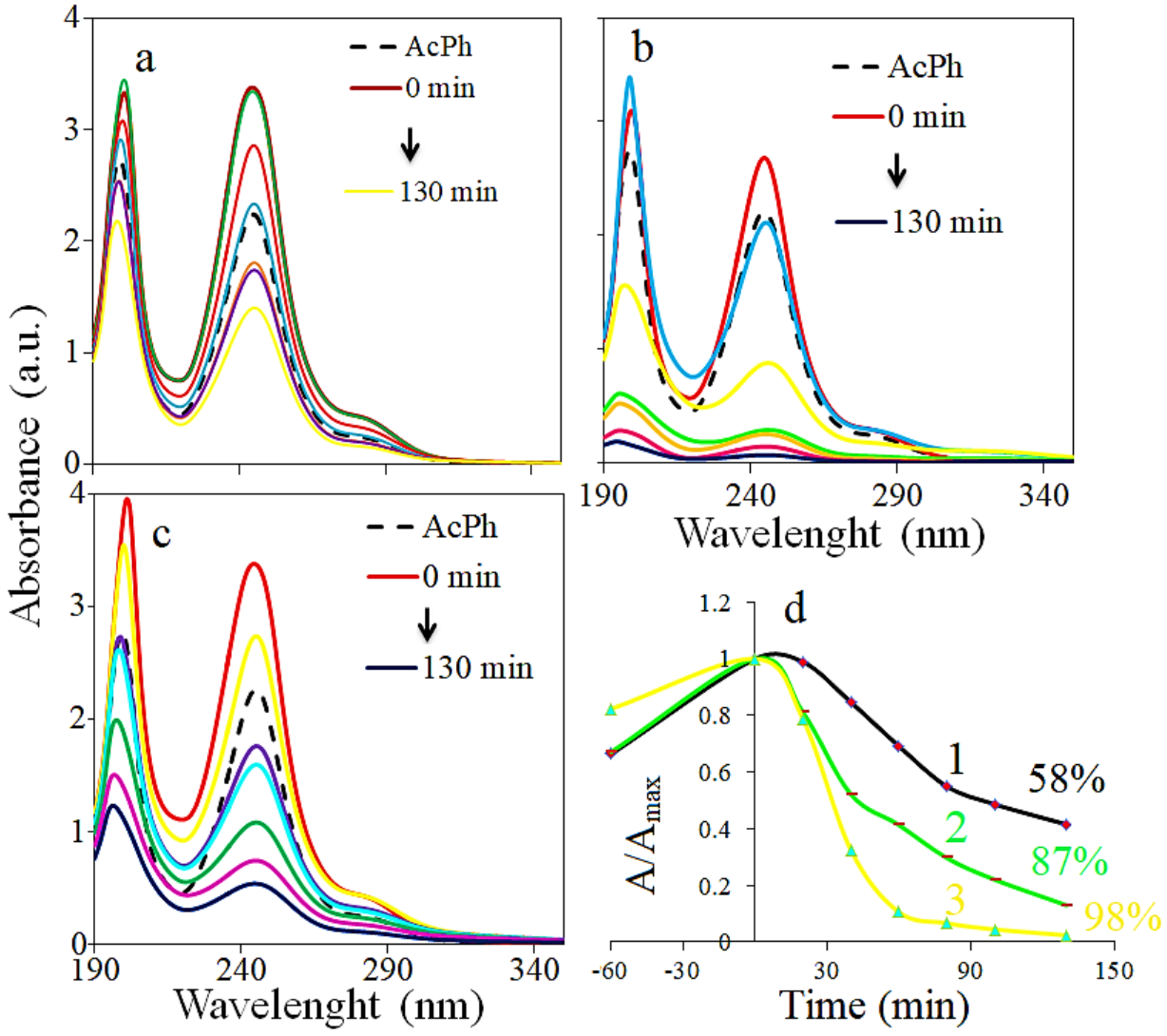

Figure 2.29: UV-Vis spectra profiles for acetophenone photodegradation for a) ZnGa(2/1), b) Au/ZnGa(2/1) and c) Ag/ZnGa(2/1) and d) the normalized absorbance evolution for 1) ZnGa(2/1), 2) Ag/ZnGa(2/1) and 3) Au/ZnGa(2/1).

adsorption-desorption equilibrium, an increase of absorbance at 245 nm was noticed. This

behavior can be attributed to the hyperchromic effect of the LDHs materials on acetophenone UV light absorption. However, after the solar lamp is turned on, for all the catalysts a decrease of absorbance was observed. As expected, the ZnGa(2/1)LDH has the lowest performance, with a 58 % acetophenone degradation in 130 minutes (see figure 2.29 a and d-1). The presence of AgNPs and AuNPs on ZnGaLDH induces an increase of activity in acetophenone photodegradation from 58 % (ZnGa(3/1) to 87 % for Ag/ZnGa(2/1)LDH and 98 % for Au/ZnGa(2/1)LDH. The difference of performance between Ag/LDH and Au/LDH can be explained by the strongest SPR effect in case of AuNPs reconstructed on ZnGa(3/1) (see figure 2.16).

The photodegradation reactions follow a pseudo-first-order kinetic. The apparent rate constants (k_{app}) were determinate from the slope of –ln(A) vs t plots, where A value represents the normalized absorbance at 245 nm. The half-life times $t_{1/2} = 0.693/k_{app}$ were also calculated. The apparent rates constants (k_{app}) and the half-life time $t_{1/2}$ are listed in table 2.4. The results show that the presence of AuNPs and AgNPs on LDHs surface induces a 4, respectively 2 times decrease of the $t_{1/2}$ comparing with the parent LDH. These results are comparable with those obtained for the previous group of NPs/ZnAl(2/1). However, a small increase of activity was observed for the ZnGa(2/1)LDH. The presence of AuNPs on the LDHs surface induces a higher increase of activity, compared with the nanocomposite containing AgNPs, due to a stronger SPR effect presented by Au/ZnGa(2/1) (see figure 2.16).

Table 2.4: Kinetic results for the solar photodegradation of acetophenone.

Catalyst	k_{app} **(x 10^{-3} min^{-1})**	$t_{1/2}$ **(min)**
ZnGa(2/1)	7.6	91.2
Au/ZnGa(2/1)	31.1	22.3
Ag/ZnGal(2/1)	15.8	43.9
Blank	5.7	121.6

In figure 2.30 is presented the proposed mechanism for the solar photodegradation of the acetophenone. According with the data which have been already published, the acetophenone degradation pathway can involve the formation of compounds as acetyl-phenol, phenylethanol, phenol and toluene [166,167], which can be further oxidized to water and carbon dioxide.

As it was presented in the previous subchapter, the acetophenone has been photodegraded by using mainly materials based on TiO_2 [200-202]. We present here for the first time the utilization of NPs/ZnGaLDHs materials for the solar decomposition of this pollutant. Our LDHs nanocomposites have shown kinetics comparable or higher than those presented in the studies made on the same subject.

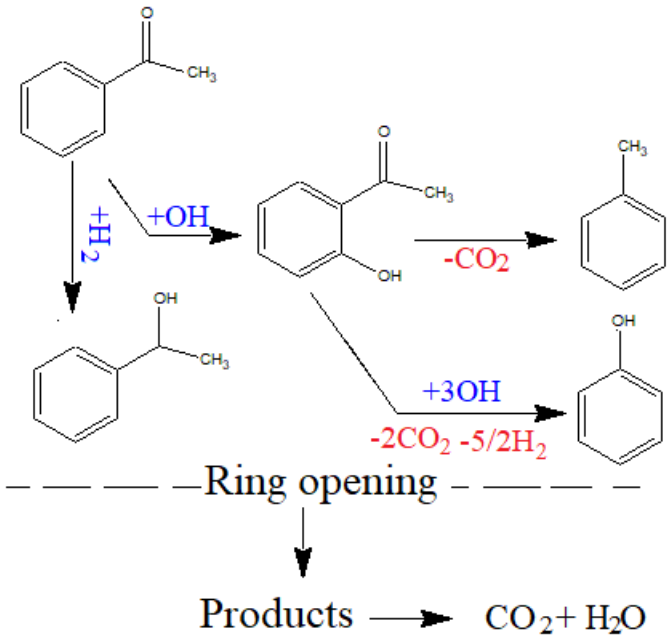

Figure 2.30: Proposed mechanism for acetophenone solar photodegradation and in presence of ZnGaLDHs.

2.3. ZnLDHs and their formulation type ZnLDHs-C_3N_4 with a LDH Me^{2+}/Me^{3+} ratio=2/1; 3/1 for the solar photodegradation of diclofenac.

2.3.1. Introduction

An important challenge in the fabrication of photoresponsive materials is to equilibrate the balance between performances, precursors availability and costs. In this context, the tendency is to replace from the structure of the catalyst, the expensive elements like Pt, Pd, with inexpensive ones like Co, Ni, Cu, Zn [203]. In recent years many efforts were focused on the synthesis of different materials containing Co [204]. Thus, materials based on Co and others elements such as Mg, Al, Ni, Cu, Li, Mn, Mo, C_3N_4, Pd and Pt, were used in applications like organic pollutant photodegradation and hydrogen production under visible light, electrodes and solar cells fabrication, alcohols synthesis from synthesis gas, benzene oxidation [203,205–212].

Graphitic carbon nitride (g-C_3N_4) is a metal-free polymeric semiconductor with photocatalytic properties, good thermal and chemical stability [213], simple fabrication from inexpensive precursors (such as urea or melamine) [214], and with good optical and electronical properties. However, under light irradiation, a fast recombination of electron-hole

charge carriers occurs in the g-C_3N_4 , and as a consequence, its utilization in processes driven by visible light irradiation is limited. Therefore, in order to overcome this inconvenient, the polymeric catalyst may be combined with other metallic semiconductor materials. From different strategies applied for the enhancement of the photocatalytic activity of g-C_3N_4, a notable enhancement of its photoresponsive properties under visible light were obtained when the g-C_3N_4 was coupled with Ag [213], $Bi_2O_2CO_3$, BiOCl [215], Fe_2O_3 [216], ZnO [217], Au/CdS [218], NiFeLDH [103]. These hybrids were used in the water oxidation, CO_2 conversion into fuel or dyes photodegradation.

As highlighted above, Zn-containing LDH materials proved to be good candidates in water remediation under light stimulation. On the other hand, Co is considered to have the highest activity from non-noble metals [211] and it was already introduced in some LDHs nanocomposites. In these conditions, a new layered double hydroxide containing both Co and Zn can lead to the formation of a nanocomposite with enhanced properties.

In this section, complex novel catalysts type ZnAlLDH-C_3N_4 and ZnCoAlLDH-C_3N_4 have been obtained by combining the co-precipitation with reconstruction or impregnation. The photocatalytic activity of the prepared materials was tested in the photodegradation of diclofenac under solar, UV and visible irradiation.

2.3.2. Synthesis and physico-chemical characterization of ZnLDHs, their derived mixed oxides and ZnLDHs-C_3N_4 formulations.

The ZnLDHs as ZnAl(2/1), ZnCoAl(2/1), ZnAl(3/1) and ZnGa(3/1) materials were obtained by co-precipitation method, following the steps presented in figure 1.8. The hybrid formulation containing g- C_3N_4 were obtained by using two different routes: the reconstruction and the impregnation. The resulted materials were characterized by using UV–Vis spectroscopy (UV-Vis), X-ray Diffraction (XRD), Energy Dispersive Spectroscopy (EDX), Diffuse Reflectance Infrared Fourier Transform Spectrometry (DRIFT), TG/DTA analysis.

The UV-Vis spectra were measured on a V650 JASCO spectrophotometer with an integrating sphere. X-ray patterns were obtained with a PANalytical X'Pert PROMPD diffractometer equipped with a Cu Kα radiation filtered; measurements were performed in the 2θ mode by using a bracket sample holder with a scanning speed of 0.04 °/4 s in continuous mode. The DRIFT spectra were performed on a Nicolet 6700 FTIR spectrophotometer, equipped with a mid-IR source (400 to 4000 cm^{-1}), with a KBr-beamsplitter, a Ne/He laser and a Michelson interferometer. A thermobalance model Mettler Toledo TGA/SDTA851 was used for the TG/DTG measurements.

a) Synthesis and physico-chemical characterization of ZnAl(2/1)LDH, ZnCoAl(2/1)LDH, their derived mixed oxides and their formulations with g-C_3N_4.

Synthesis

ZnAl(2/1) and ZnCoAl(2/1) layered double hydroxides were prepared by the co-precipitation method at constant pH [3]. So, ZnAl (Zn^{2+}/Al^{3+}= 2/1) was prepared by the slow addition of an aqueous solution of 0.1 moles of $Zn(NO_3)_2.6H_2O$ (Sigma Aldrich, ≥99%) and 0.05 moles of $Al(NO_3)_3.9H_2O$ (Sigma Aldrich, ≥99%), to an aqueous solution of 1 M $NaOH/Na_2CO_3$ in such a way that the pH remains constant at value of 9 during precipitation, using an automatic titration system. For the synthesis of ZnCoAl ($Zn^{2+}/Co^{2+}/Al^{3+}$= 2/1) was used a similar protocol, except that, in this case, the salts solution contain 0.075 moles of $Zn(NO_3)_2$*$6H_2O$ (Sigma Aldrich, ≥99%), 0.025 moles of $CoSO_4$*$7H_2O$ (Sigma Aldrich, ≥99%) and 0.05 moles $Al(NO_3)_3$*$9H_2O$ (Sigma Aldrich, ≥99%).The resulting precipitates were stirred for 24 h at 50°C. The final materials were recovered by filtration, washed several times with bidistilled water, dried at 80 ^{0}C and denoted as ZnAl(2/1) and ZnCoAl(2/1). Co-precipitation was carried out by using an automatic titration system (TrioLine 7800, SI Analytics) which is presented in figure 2.31.

The hybrid composites between the as-synthesized ZnAl(2/1) and ZnCoAl(2/1) and the graphitic carbon nitride (g-C_3N_4) were prepared by the so-called reconstruction method based on the unique memory effect property of the LDH-type materials, as well as via impregnation route. In a standard procedure, 1.25g of ZnAl(2/1) or ZnCoAl(2/1) calcined at 550°C for 7 h was added, when their temperature decreased to 400 °C, to an aqueous solutions containing 0.1 g of g-C_3N_4, and kept under vigorous stirring for 24 h at room temperature. The obtained solids were recovered by centrifugation and dried at 80 ^{0}C. The obtained materials were denoted as ZnAl-CN-R, and ZnCoAl-CN-R, respectively. Secondly, when the impregnation method was used, the same quantities of LDHs supports and g-C_3N_4 used for reconstruction were separately dispersed in a 1:1 solution of ethanol:water, sonicated for 1 h, then both solutions were mixed together for 48 h under magnetic stirring at room temperature and under argon atmosphere. The obtained samples were centrifuged, dried at 80 ºC and denoted as ZnAl-CN-I, and ZnCoAl-CN-I, respectively. The derived mixtures of mixed oxides were obtained by calcination of fresh ZnAl(2/1), ZnCoAl(2/1) layered double hydroxides at 750ºC for 7 hours. They were denoted ZnAl-750, ZnCoAl-750.

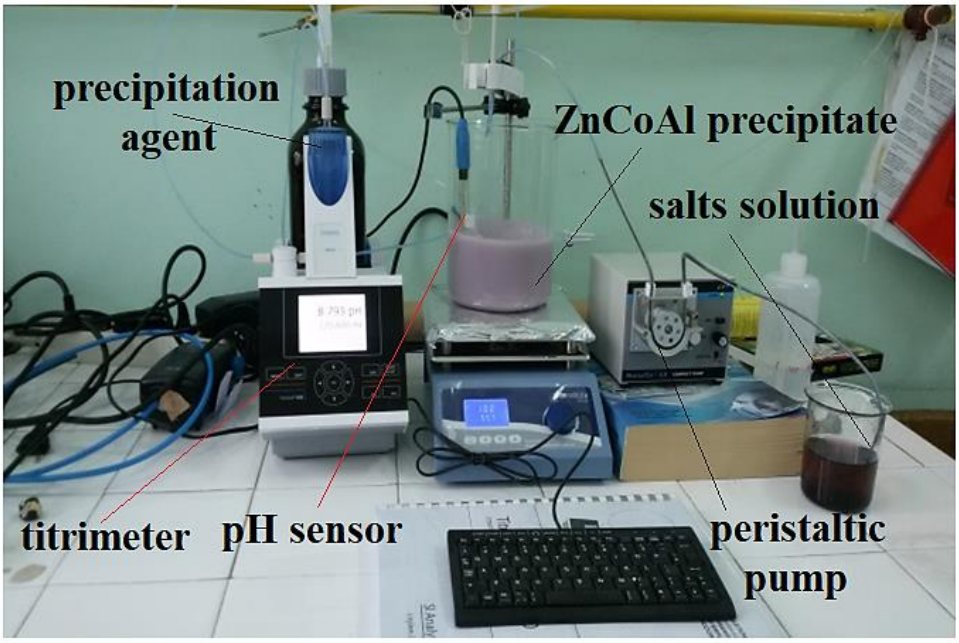

Figure 2.31: Titration system used for the ZnLDHs synthesis.

The graphitic carbon nitride was prepared from melamine, by calcination at 530 ^{0}C, for 5 hours.

Physico -chemical characterization

The structure of the samples was investigated using X-ray Diffraction analysis. The XRD patterns of fresh samples, the hybrid formulations containing graphitic carbon nitride, as well as their calcined samples are shown in figure 2.32. The XRD patterns reveal the characteristic lamellar structure of hydrotalcite-like clay with intense basal diffraction peaks around 11.7 ^{0}, 23.6 ^{0}, 34.7 ^{0}, indexed as (003), (006), (012) planes, and less intense diffraction nonbasal peaks about 39.3 ^{0}, 49.6 ^{0}, 60.6 ^{0} assigned to (015), (018), (110) planes [3]. The aspect of the diffraction peaks shows that the samples have a good crystallinity [219] and no other phases are present. For the ZnCoAl-CN-R was observed that the reconstruction was not total. The calculated interlayer distance, according with the (003) diffraction angle from 11.7°, is 0.76 nm for ZnCoAl-CN-R and 0.75 nm for the rest of catalysts, indicating the presence of carbonate anions CO_3^{2-} in the interlamellar region [3]. For the graphitic carbon nitride two commune peaks can be observed about 27.2° and 13.2°, indexed to (100) and (002) diffraction planes, being characteristic for the reflection of conjugated aromatic system, [215]. For the reconstructed and impregnated samples, the presence of g-C_3N_4 can be confirmed by XRD technique only in case of the reconstructed materials by the presence of a small peak around

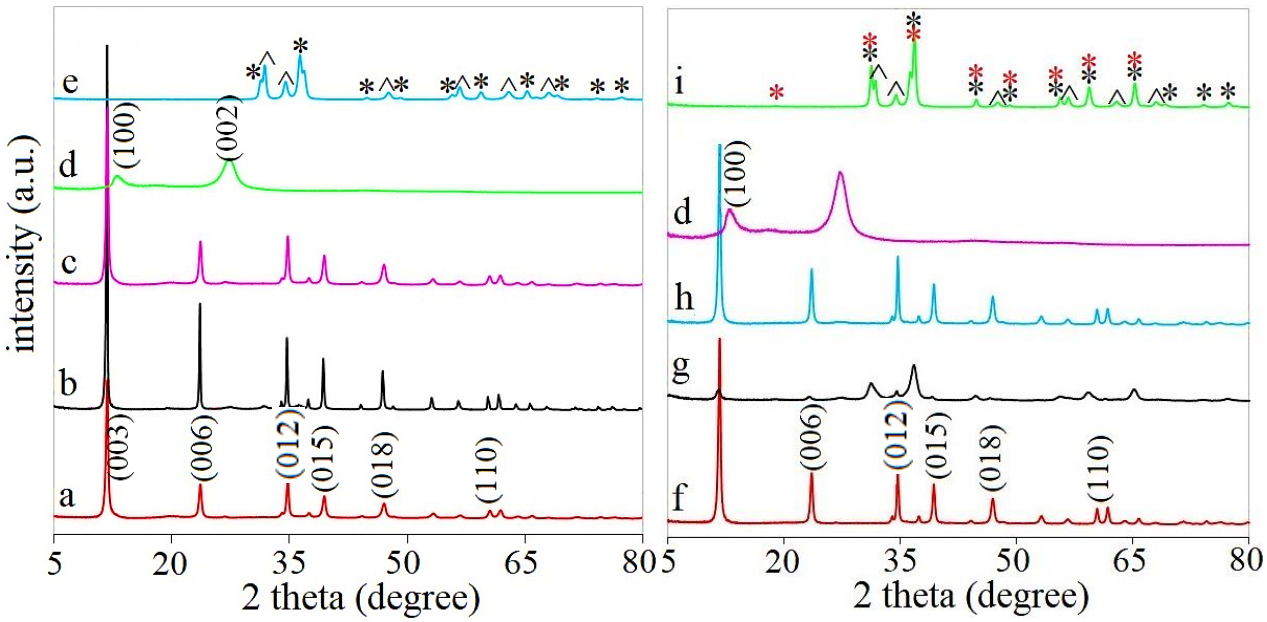

Figure 2.32: The X-ray diffraction patterns of the a) ZnAl(2/1), b) ZnAl-CN-R, c) ZnAl-CN-I, d) g-C3N4, e) ZnAl-750, f) ZnCoAl, g) ZnCoAl-CN-R, h) ZnCoAl-CN-I, i) ZnCoAl-750; (*) $ZnAl_2O_4$, (*) $CoAl_2O_4$; (^) ZnO.

27.5°. For the impregnated nanocomposites, the g-C_3N_4 phase can not be detected by using the XRD analysis, and this fact may be correlated with the small amount of g-C_3N_4 present in the hybrid structure [103]. After the thermal treatment at 750ºC the layered structure collapse with the concomitant formation of homogeneous mixtures containing spinel phases ($ZnAl_2O_4$ and $CoAl_2O_4$) and metallic oxides (ZnO, CoO). The lattice parameters, crystallites size, calculated by Scherrer equation and the M^{2+}/M^3 calculated from the EDX data are given in Table 2.5.

The presence of g-C_3N_4 on LDHs surface was confirmed by the EDX measurements. As it ca be observed from figure 2.33, in case of ZnCoAl-CN-R, beside the elements like Co, Zn, Al O, which are characteristic for the ZnCoAl(2/1), C and N are also present in the material composition proving that the hybridization between LDHs and of g-C_3N_4 has succeeded.

In order to confirm the reformation of the lamellar structure after the reconstruction step in the presence of the graphitic phase, the formation of LDH-C_3N_4 hybrids respectively, the DRIFT analysis was performed for the obtained samples. The DRIFT spectra (figure 2.34) show the presence of the characteristic vibration bands assigned to the layered double hydroxides. In this regard, broad absorption bands associated with the O-H stretching modes of hydroxyl groups of LDHs and the physisorbed water [1] can be observed between 3000 – 3500 cm^{-1} range. Further, a small broad shoulder around 1640 cm^{-1} might be attributed to H-O-H bending vibration of the interlayer water molecules connected to the interlayer anions

Table 2.5: Chemical composition and lattice parameters for the studied catalysts.

Sample	*M^{2+}/M^3	**Crystal size (nm)	Lattice parameters (Å)	
			a	*c*
ZnAl(2/1)	1.75	18.9	3.056	22.5
ZnAl-CN-I	1.51	21.5	3.058	22.5
ZnAl-CN-R	1.47	42.7	3.067	22.5
ZnCoAl(2/1)	1.8	25.8	3.064	22.5
ZnCoAl-CN-I	1.49	23.5	3.064	22.5
ZnCoAl-CN-R	1.48	14.2	3.076	22.8

* the molar ratio obtained by EDX; the initial M^{2+}/M^3 ratio from synthesis was equal with 2 for all the catalysts; **crystal size calculated with Scherrer equation; $a = 2d_{110}$ and $c = 3d_{003}$ are the unit lattice parameter.

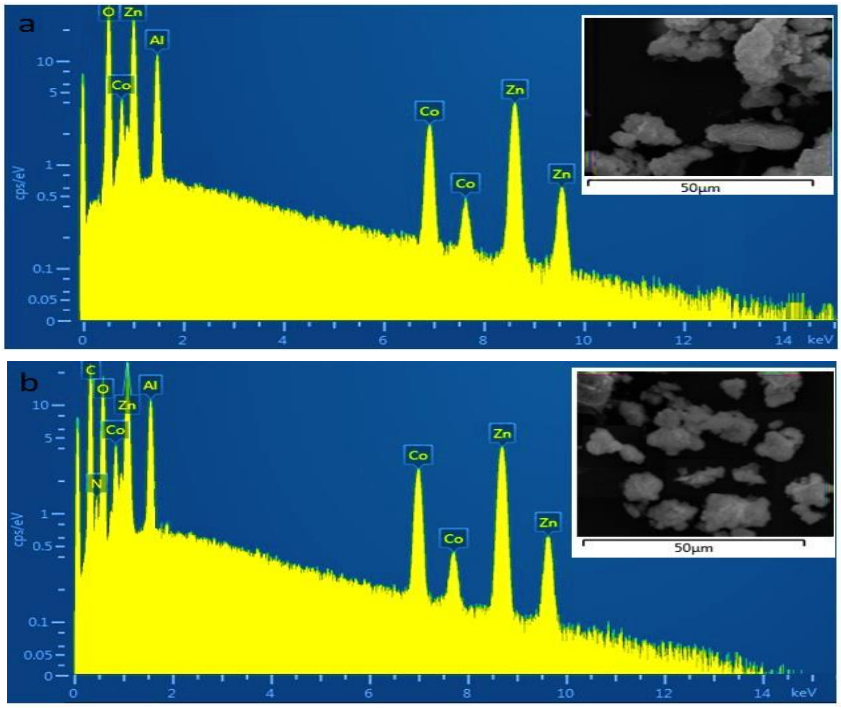

Figure 2.33: EDX spectra for a) ZnCoAl(2/1) and b) ZnCoAl-CN-R; insert: corresponding SEM images.

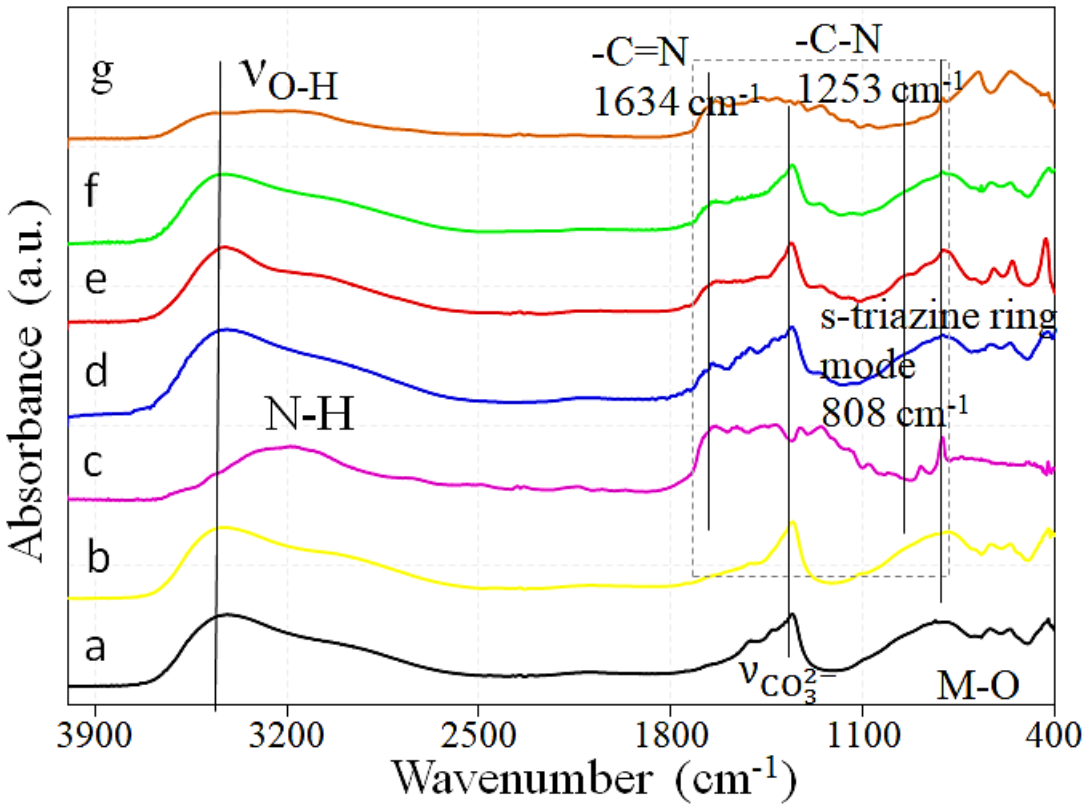

Figure 2.34: DRIFT spectra of a) ZnAl(2/1), b) ZnCoAl(2/1), c) g-C_3N_4, d) ZnAl-CN-I, e) ZnAl-CN-R, f) ZnCoAl-CN-I, g) ZnCoAl-CN-R.

molecules via hydrogen bonds [1]. The interlayer CO_3^{2-} anions are identified in all the obtained samples by the appearance of the intense vibration band at 1360 cm^{-1} and less intense at 1510 cm^{-1} corresponding to the symmetric and antisymmetric bending vibrations [220]. The corresponding vibrations bands for the M-O and O-M-O bonds (M = Zn, Co, Al), are observed in the low region of wavenumber between 800 cm^{-1} and 400 cm^{-1} [22]. For the hybrid formulations obtained via reconstruction and impregnation routes in presence of graphitic carbon nitride, new vibration bands appear which confirm the formation of a new nanocomposite. The typical vibration modes of g-C_3N_4 are around 3200 cm^{-1} being attributed to the stretching vibration of the N-H linkage as well as between 1640 cm^{-1} - 1254 cm^{-1} assigned to the particular stretching vibrations modes of C=N and C-N heterocycles [216]. The absorption band at 810 cm^{-1} is characteristic to the vibration mode of the s-triazine ring [221].

The UV-Vis Diffuse Reflectance Spectroscopy was further used to investigate the optical properties of the as-synthetized materials. In figure 2.35 can be observed that the absorbance of the initial semiconductors, ZnAl(2/1) and ZnCoAl(2/1) extends to the visible light region, and the presence of the Co^{II} in the structure of the LDH can be confirmed by an

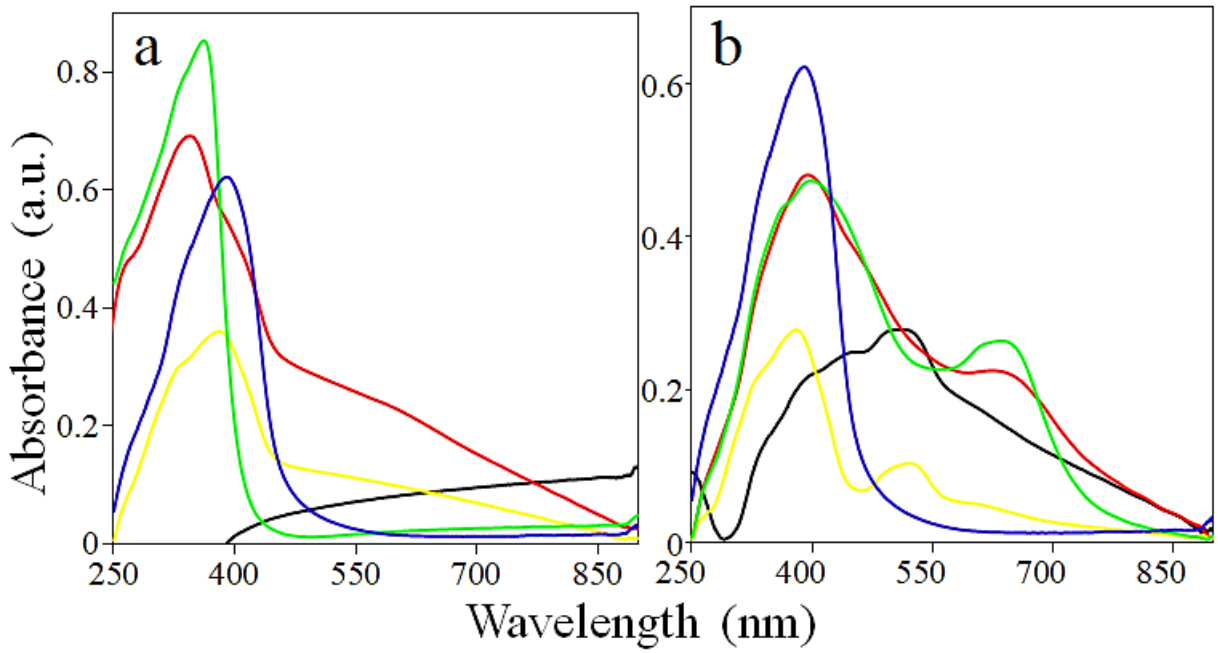

Figure 2.35: The UV–Vis absorption spectra of the a) ZnLDHs: ZnAl(2/1), ZnAl-CN-R, ZnAl-CN-I, ZnAl-750, g-C_3N_4 and b) ZnCoLDHs: ZnCoAl(2/1), ZnCoAl-CN-R, ZnCoAl-CN-I, ZnCoAl-750, g-C_3N_4 studied catalysts.

absorption band at 520 nm [208,222]. This is a good indication the ZnCoAl catalyst can absorb visible light, being a promising material in photocatalysis. Furthermore, according to Ulibarri [223] this band can be attributed to the $^4T_{1g}$ (F) → $^4T_{1g}$ (P) transition of the Co^{2+} cations which are octahedrally coordinated in the LDH layers. After calcination, for ZnCoAl-750, this band is shifted to 700 nm pointing out the formation of octahedral Co^{3+} after the thermal treatment at 750 °C [43]. Fresh g-C_3N_4 presents adsorption in the blue region of the visible spectrum, with two edges around 300 and 350 nm which can bet assigned to the n-π* transitions of the single electrons pair of the N atom of the triazine rings [214]. The introduction of the graphitic carbon nitride in the LDHs nanocomposites changes the initial absorption profile of the pristine LDHs. After reconstruction and impregnation, all the materials are able to adsorb visible light, property which can be assigned to the existence of the g-C_3N_4 in the structure of the nanohybrid. The capacity of the new materials to absorb visible light can be attributed to the strong interaction between graphitic carbon nitrate and LDHs [224].

The thermogravimetric measurements were realized in order to investigate the thermal stability and the composition of the as-synthesized materials. The thermogravimetric curves illustrated in figure 2.36 show three important mass losses, which are characteristic for layered double hydroxides [225]. The first mass loss (ZnAl(2/1) - 13 % and ZnCoAl(2/1) – 14.7) occurs from 50 to 215 ºC and it might be assigned to the evaporation of physisorbed water molecules from the surface of the catalyst. The next loss in the temperature range 200-450 °C is corresponding to the dehydroxylation of the lamella and the LDH anion removal placed

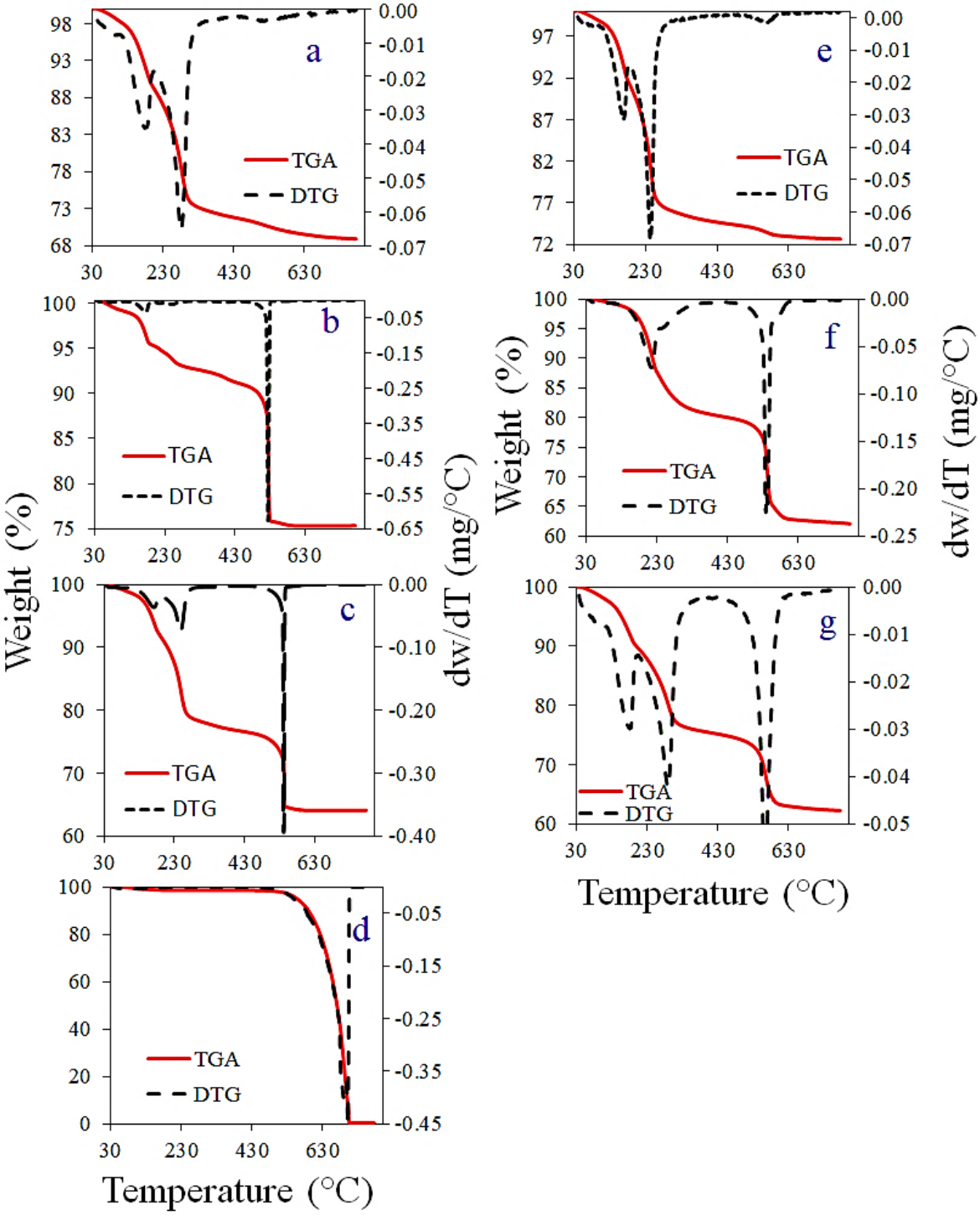

Figure 2.36: TG-DTG curves for: a) ZnAl(3/1), b) ZnAl-CN-R, c) ZnAl-CN-I d) g-C_3N_4, e) ZnGa(3/1), f) ZnGa-CN-R, g) ZnGa-CN-I .

in the interlayer space. The weight loss for this event is equal to 13.4 % for ZnAl(2/1) and 15.1 % for ZnCoAl(2/1). Besides, smaller losses are noticed in the DTG curves of ZnAl(2/1) and ZnCoAl(2/1) within the range 550-700 °C with corresponding weight losses equal to 3.4 %, and 3.7 %, respectively. These might be correlated with the crystallization of the mixed oxides and spinel phases. The presence of g-C_3N_4 in hybrids structure can also be proved by the TGA-DTG analysis. The LDHs-CN nanocomposites present the removal of the physisorbed water (between 13-15 %), the lamella dehydroxylation, the decomposition of the carbonate anion (between 7-10 %) and the collapse of the LDH structure (4 %) approximately in the same temperature range as for the fresh LDHs. However, a supplementary weight loss between 8-10 % takes place in the range of 490-600 °C for all hybrids. This loss can be assigned to the presence of g-C_3N_4 in the new hybrids. g-C_3N_4 is thermally inert until 530 °C. After this temperature, its oxidation starts and a mass loss of ~50 % can be identified up to 670 °C [221]. Thus, the increase of the mass loss in the temperature range of 490-600 °C can be directly attributed to the LDHs hybridization with g-C_3N_4.

b) Synthesis and physico-chemical characterization of ZnAl(3/1)LDH, ZnGa(3/1)LDH, their derived mixed oxides and their formulations with g-C_3N_4.

Synthesis

ZnAl(3/1) and ZnGa(3/1) layered double hydroxides were prepared by the co-precipitation method at constant pH [3]. So, ZnAl (Zn^{2+}/Al^{3+}= 3/1) was prepared by the slow addition of an aqueous solution containing 0.15 moles of $Zn(NO_3)_2.6H_2O$ (Sigma Aldrich, ≥99%) and 0.05 moles of $Al(NO_3)_3.9H_2O$ (Sigma Aldrich, ≥99%), to an aqueous solution of 1 M $NaOH/Na_2CO_3$ in such a way that the pH remains constant at a value of 9 during precipitation. For the drop by drop addition of the solutions was used an automatic titration system (see figure 2.31). For the synthesis of ZnGa (Zn^{2+}/Ga^{3+}= 3/1) was used a similar protocol, except that, in this case, the salts solution contained 0.06 moles of $Zn(NO_3)_2*6H_2O$ (Sigma Aldrich, ≥99%) and 0.02 moles $Ga(NO_3)_3*9H_2O$ (Sigma Aldrich, ≥99%).The resulting precipitates were stirred for 24 h at 55°C. The final materials were recovered by filtration, washed several times with bidistilled water, dried at 90 ^{0}C and denoted as ZnAl(3/1) and ZnGa(3/1).

The hybrid composites between the as-synthesized ZnAl(3/1) and ZnGa(3/1) and the graphitic carbon nitride (g-C_3N_4) were prepared via reconstruction method, as well as via impregnation route. Thus, 1.25g of ZnAl(3/1) or ZnGa(3/1) calcined at 550°C for 7 h was added, when their temperature decreased 480 °C, to an aqueous solutions containing 0.1 g of g-C_3N_4, and kept under vigorous stirring for 24 h at room temperature. The pH after 4 h was 6.5 and it was adjusted at 9 by adding NaOH, 1N. The obtained solids were washed with bidistiled water, recovered by centrifugation, and dried at 90 ^{0}C. The obtained materials were denoted as ZnAl-CN-R, and ZnGa-CN-R, respectively. Secondly, when the impregnation method was

used, the same quantities of LDHs supports and g-C_3N_4 used for reconstruction were separately dispersed in a 1:1 solution of ethanol:water, sonicated for 1 h, then both solutions were mixed together for 48 h under magnetic stirring at room temperature and under argon atmosphere (see figure 2.37). The obtained samples were centrifuged, dried at 80 ºC and denoted as ZnAl-CN-I, and ZnGa-CN-I, respectively. The derived mixtures of mixed oxides were obtained by calcination of fresh ZnAl(3/1), ZnGa(3/1) layered double hydroxides at 750ºC for 7 hours. They were denoted ZnAl-750, ZnGa-750.

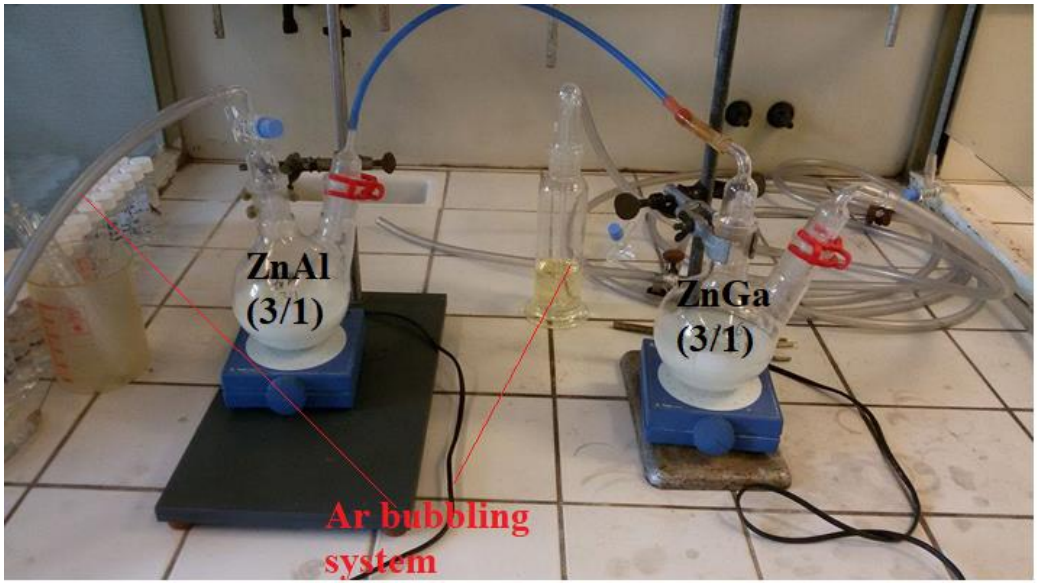

Figure 2.37: Reconstruction/ impregnation under inert atmosphere.

Physico-chemical characterization

The samples structure was investigated using X-ray Diffraction analysis. The XRD data expressed in figure 2.38 present the characteristic lamellar structure of the anionic clays for all the LDH meterials, with intense basal diffraction peaks around 11.7 ^{0}, 23.6 ^{0}, 34.7 ^{0}, indexed as (003), (006), (012) planes, and less intense diffraction nonbasal peaks around 39.3 ^{0}, 49.6 ^{0}, 60.6 ^{0}, which are typical to (015), (018), (110) planes [3]. The peaks are sharp and intense, suggesting a good crystallinity of the sample. Small quantities of ZnO were present in the reconstructed samples, which might be a consequence of a partial recover of the hydrotalcite structure. The pure g-C_3N_4 has two peaks at 27.2° and 13.2°, indexed to (100) and (002) diffraction planes, being characteristic for the conjugated aromatic system [103]. The presence of g-C_3N_4 can be confirmed with XRD measurements only in case of the reconstructed sample, for which a peak at 27.3° was observed. After the thermal treatment at 750 °C, the specific lamellar structure collapse and a mixed oxide mixture is formed, containing ZnO (^) and $ZnAl_2O_4$ (*) or $ZnGa_2O_4$ (*). The lattice parameters, the crystals size and the M^{2+}/M^{3+} based on

the EDX measurement are given in table 2.6. According with the (003) diffraction angle, the interlayer space is occupied by CO_3^{2-}.

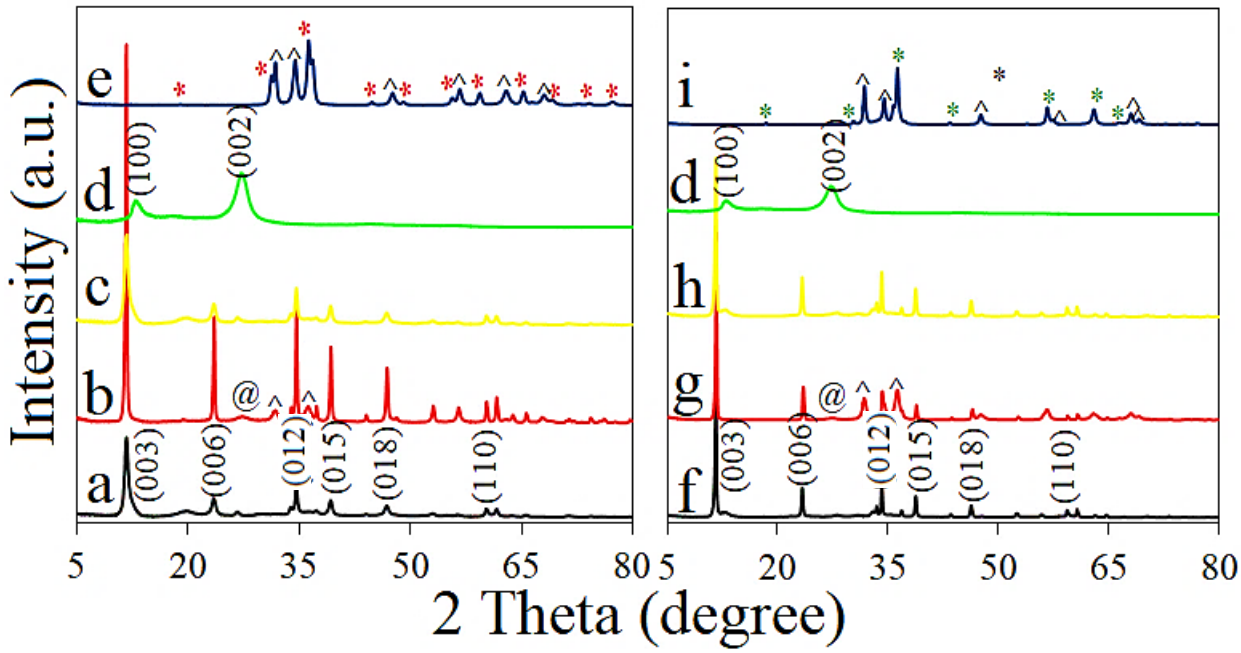

Figure 2.38: XRD pattern for: a) ZnAl(3/1), b) ZnAl-CN-R, c) ZnAl-CN-I, d) g-C_3N_4, e) ZnA-750, f) ZnGa(3/1), g) ZnAl-CN-R, h) ZnAl-CN-I, i) ZnGa-750; (*) $ZnAl_2O_4$, (*)$ZnGa_2O_4$; (^) ZnO, (@) g-C_3N_4..

Table 2 6: Chemical composition and lattice parameters for the studied catalysts.

Sample	*M^{2+}/M^3	**Crystal size (nm)	Lattice parameters (Å)	
			a	*c*
ZnAl(3/1)	2.5	14	3.068	22.65
ZnAl-CN-I	2.3	12.5	3.066	22.68
ZnAl-CN-R	2.2	32.4	3.066	22.65
ZnGa(3/1)	3.1	42.2	3.112	22.86
ZnGa-CN-I	2.9	31.5	3.114	22.86
ZnGa-CN-R	3	40	3.110	22.68

* the molar ratio obtained by EDX; the initial M^{2+}/M^3 ratio from synthesis was equal with 2 for all the catalysts; **crystal size calculated with Scherrer equation; $a = 2d_{110}$ and $c = 3d_{003}$ are the unit lattice parameter.

The EDX mesurements presented in fugure 2.39 reveal that, beside the constituiend LDHs elements as Zn, Al, O, and Ga, the samples resulted after LDHs hybridisation with g-C_3N_4 contain also N, which is an idication of the g-C_3N_4 presence in the structure.

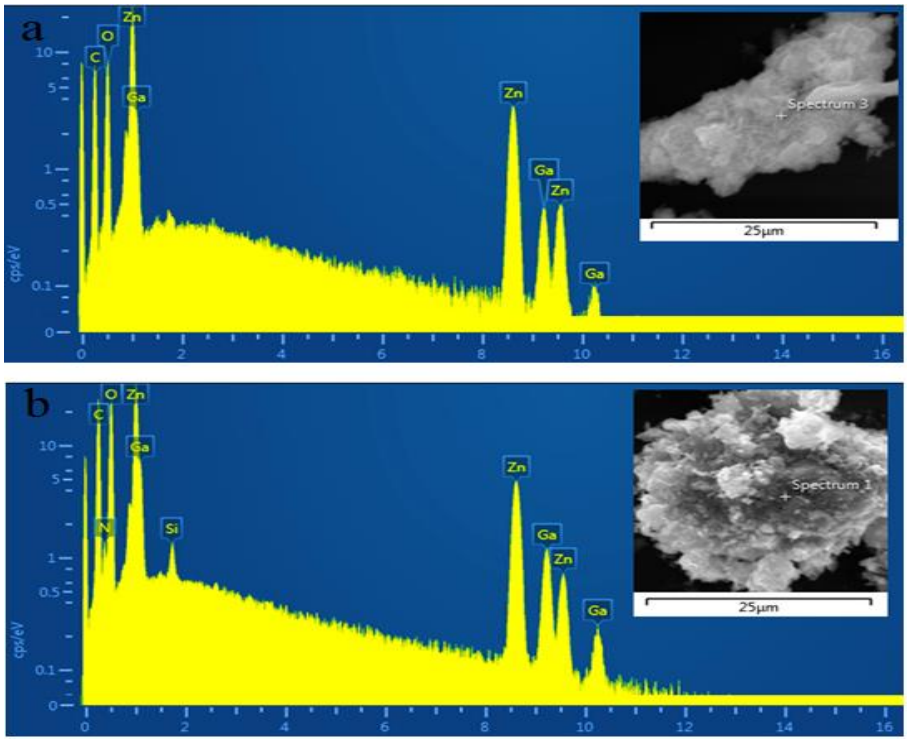

Figure 2.39: EXD spectra for a) ZnGa(3/1) and b) ZnGa-CN-R.

For more information, the DRIFT analyse was performed (figure 2.40). The spectra of the synthesized materials present the characteristic vibration bands of the hydrotalcite materials, with the presence of the vibration modes between 3000 – 3500 cm^{-1} attributed to the O-H hydroxyl groups from LDHs and the physisorbed water [1]; the vibration band which is characteristic to the interlayer water, H-O-H, appears as a small shoulder around 1640 cm^{-1}, but only in case of the ZnAl(3/1) and ZnGa(3/1) can be observed. For the hybrids, this vibration around 1640 cm^{-1} appears as a larger peak and it might include also the C=N vibration which has a particular peak around 1634 cm^{-1}. In the interlayer space are the CO_3^{2-} anions and their presence is confirmed by the two vibration band at 1360 cm^{-1} and at 1510 cm^{-1} corresponding to the symmetric and antisymmetric bending vibrations [220]. Between 800-400 cm^{-1} can be observed the typical modes for M-O and O-M-O bonds (M = Zn, Co, Al) [22]. The pure g-C_3N_4 has its characteristic vibration bands around 3200 cm^{-1} attributed to the stretching vibration of the N-H linkage, and between 1640 cm^{-1} - 1254 cm^{-1} assigned to the typical stretching vibrations modes of C=N and C-N heterocycles [216]. The absorption band at 810 cm^{-1} is characteristic to the vibration mode of the s-triazine ring [221]. The LDHs-CN hybrids present the characteristic vibration modes of graphitic carbon nitride.

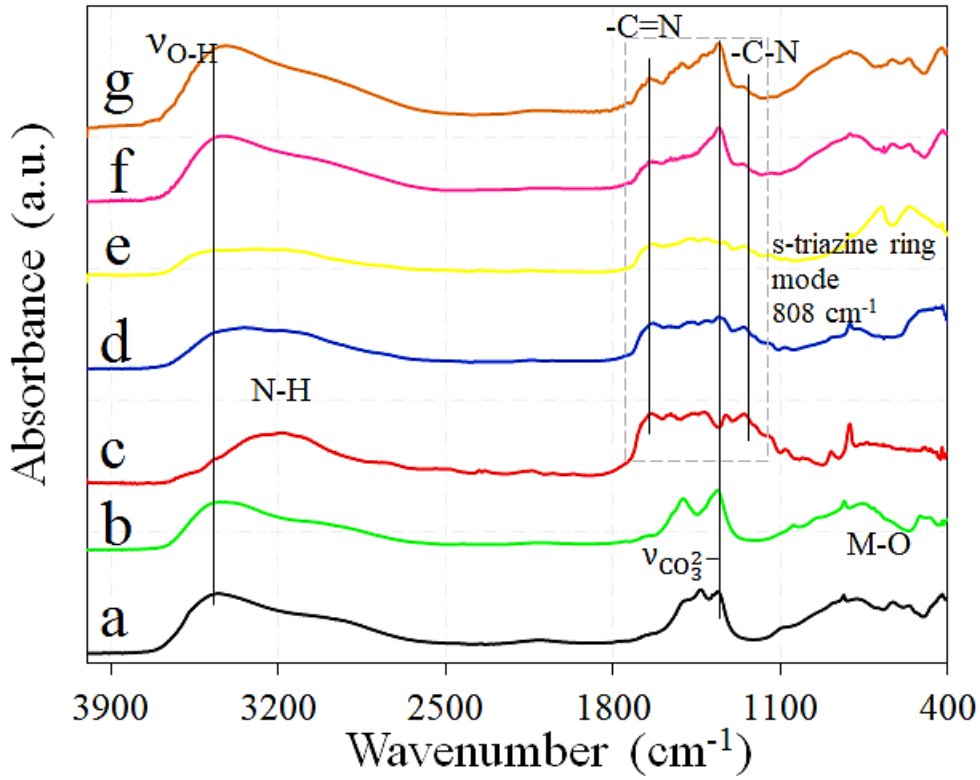

Figure 2.40: DRIFT spectra of a) ZnAl(3/1), b) ZnGa(3/1), c) g-C_3N_4, d) ZnAl-CN-R, e) ZnGa-CN-R, f) ZnAl-CN-I, g) ZnGa-CN-I.

The optical properties of LDHs materials were investigated by using UV-Vis diffuse reflectance spectroscopy (UV-DR). For this, the absorption spectra were recorded on a Thermo-electron evolution 500 (double beam), equipped with a UV-DR cell (RSA-UC-40) inside the UV-Vis apparatus and using white KBr standard as reflectance. In figure 2.41 are presented the UV-DR absorption spectra of ZnLDHs materials, their derived mixed oxides and their hybrids containing g-C_3N_4. The initial ZnAl(3/1) and ZnGa(3/1) present a small adsorption capacity in UV region, with an extension to the visible area of the spectrum. After the thermal treatment and the hybridization with g-C_3N_4, respectively, all the absorption spectra are sifted to the red region of the spectrum and also their ability to absorb UV light increases. During the calcination process at 750 °C, systems formed by metal oxides and spinel like phase are formed. Two shoulders around 220 and 265 nm can be assigned to the $ZnAl_2O_4$ or $ZnGa_2O_4$, while the edge from 360 nm can be attributed to ZnO. Fresh g-C_3N_4 presents adsorption in the blue region of the visible spectrum, with two edges around 300 and 350 nm which can be assigned to the n-π transitions of the single electrons pair of the N atom of the

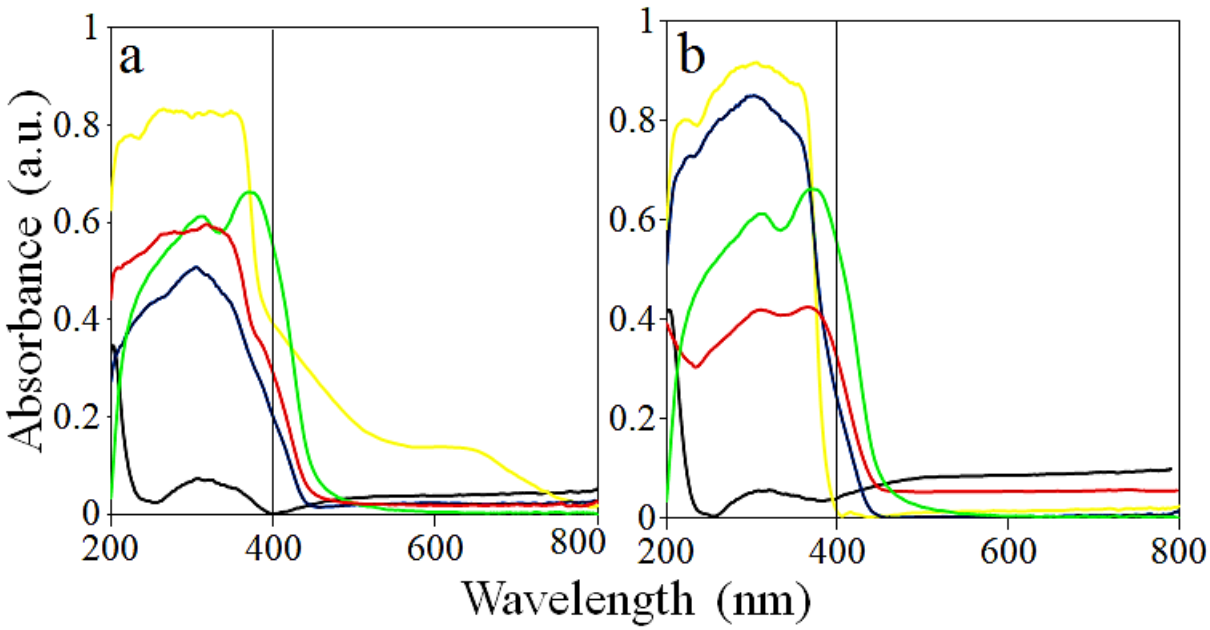

Figure 2.41: UV-DR absorption spectra for a) ZnAl(3/1)LDHs: ZnAl(3/1), ZnAl-CN-R, ZnAl-CN-I, ZnAl-750, $g\text{-}C_3N_4$ and b) ZnGa(3/1)LDHs: ZnGa(3/1), ZnGa-CN-R, ZnGa-CN-I, ZnGa-750, $g\text{-}C_3N_4$ studied catalysts.

triazine rings [214]. The presence of g-C3N4 into LDHs hybrids structures can be easily remarked by the presence on the absorption edge around 300 and 350 nm.

The presence of $g\text{-}C_3N_4$ in the LDHs hybrid, as well the thermal stability of the materials, was investigated by using the thermogravimetric analysis. From figure 2.42 might be observed that the ZnAl(3/1) and ZnGa(3/1) materials present three important mass losses [225]. The first event, assigned to the surface and interlayer water removal, takes place between 100-180 °C for ZnAl(3/1) and 100-170 °C for ZnGa(3/1) and it presents a mass loss of 10% and 7%, respectively. A temperature increase between 180-270 °C for ZnAl(3/1) and 170-245 °C for ZnGa(3/1) leads to the layers dehydroxylation and, with a weight losses of 14 % and 15.5 %. Further increase of temperature till 600 °C and 575 °C will produce the next mass loss of 6 % for ZnAl(3/1) and 4 % for ZnGa(3/1) attributed to the anion removal of the interlayer space. The DTG curves present a peak around 600 °C, 575 °C, which shows a phase change, with metal oxide and spinel formation. For the hybrids materials, the mass losses take place in almost the same temperature ranges and they are assigned to the same processes. However, an additional mass loss can be observed for the LDHs-CN (see figure 2.42 b-g), which can be attributed to de presence of $g\text{-}C_3N_4$ in the structure of the LDHs. It might be observed that graphitic carbon nitride (figure 2.42 d) has a good thermal stability until 530 °C. After this temperature, its oxidation take place with more than 50 % of mass loss till 700 °C [221]. A

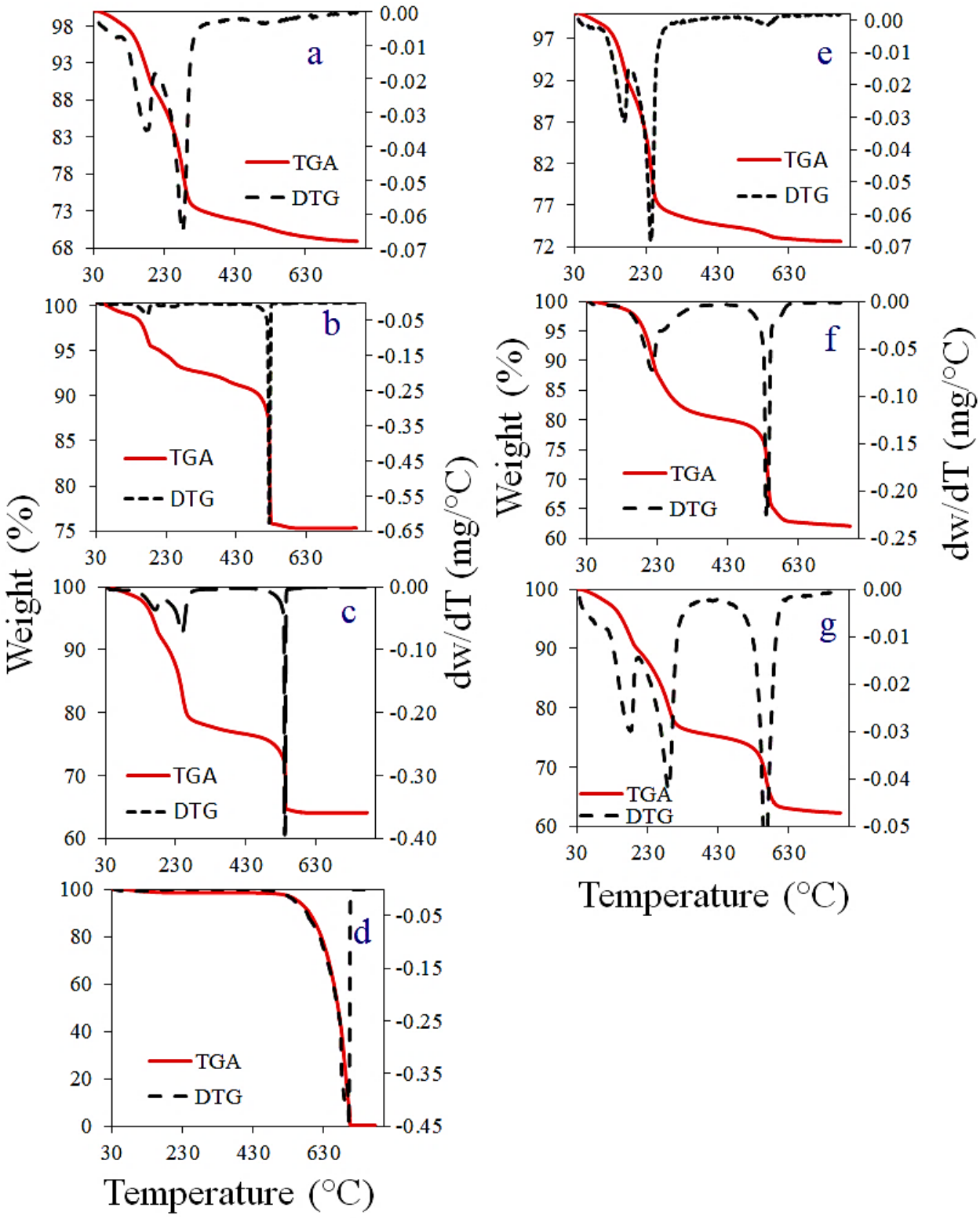

Figure 2.42**:** TG-DTG curves for: a) ZnAl(3/1), b) ZnAl-CN-R, c) ZnAl-CN-I d) g-C_3N_4, e) ZnGa(3/1), f) ZnGa-CN-R, g) ZnGa-CN-I.

weight loss between 25-38 % was observed for the hybrids, while for the fresh sample the maximum was 30 % obtained for ZnAl(3/1).

2.3.3. ZnLDHs, their derived mixed oxides and ZnLDHs-C_3N_4 formulations for solar photodegradation of diclofenac.

In this subchapter, ZnLDHs and ZnLDHs-CN obtained via different synthesis methods will be used in the solar photodegradation of diclofenac (DCF). The resulted degradation solutions were evalued by UV-Vis measurements performed with a Thermo-electron evolution 500 (double beam), for the measurements of liquids. Also, total organic carbon (TOC) measurements were performed at the beginning and at the end of the tests. TOC values were obtained by measuring the TC (total carbon) and the IC (inorganic carbon) and subtracting the IC concentration from the TC concentration. The TOC measurements were performed on a SHIMADZU TOC-Vcph instrument. In order to establish the degradation pathways, liquid chromatography quadrupole time-of-flight mass spectrometry was used (LC-QTOF MS). For the LC-QTOF MS measurements, the photodegradation solutions were injected into a Kinetex® XB-C18 column, using an Agilent 1290 chromatographic system. Data were analyzed by using a Mass-Hunter (Agilent, v B.06.00) and a Mass-Profiler Professional (Agilent, v 12.5), in both negative and positive mode. The photodegradation products were searched by using an untargeted approach: molecular features were extracted with the Molecular Feature Extractor algorithm (MFE, Agilent). The results were manually checked for mass accuracy to confirm the identification of each compound. LC-QTOF MS measurements were performed at Department of Pharmaceutical Sciences, University of Antwerpen, Belgium.

a) ZnAl(2/1)LDHs-C_3N_4 and ZnCoAl(2/1)LDHs-C_3N_4 formulations for solar photodegradation of diclofenac.

The synthesis and the characterization for this group of materials were presented in section 2.3.2. The photocatalytic experiments were carried out as described in the section 2.1. 25 mg/L DCF solution was solar photodegradated in presence of 1 g/L of different LDHs based catalysts. Additionally, for this group of catalysts, were performed also tests under UV and visible light. For this, it was used the same solar lamp equipped with block-filers able to stop the UV or the visible irradiation. The evolution in time of DCF degradation was monitored at 276 nm or in some cases at 236 nm, which is the maximum of absorption for the main photodegradation product.

➢ **Photocatalytic activity of the LDHs systems under solar irradiation**

The evolution in time for the processes initiated by solar irradiation, in presence of the as-prepared catalysts, is shown in figure 2.43. The blank test, realized by irradiating DFC

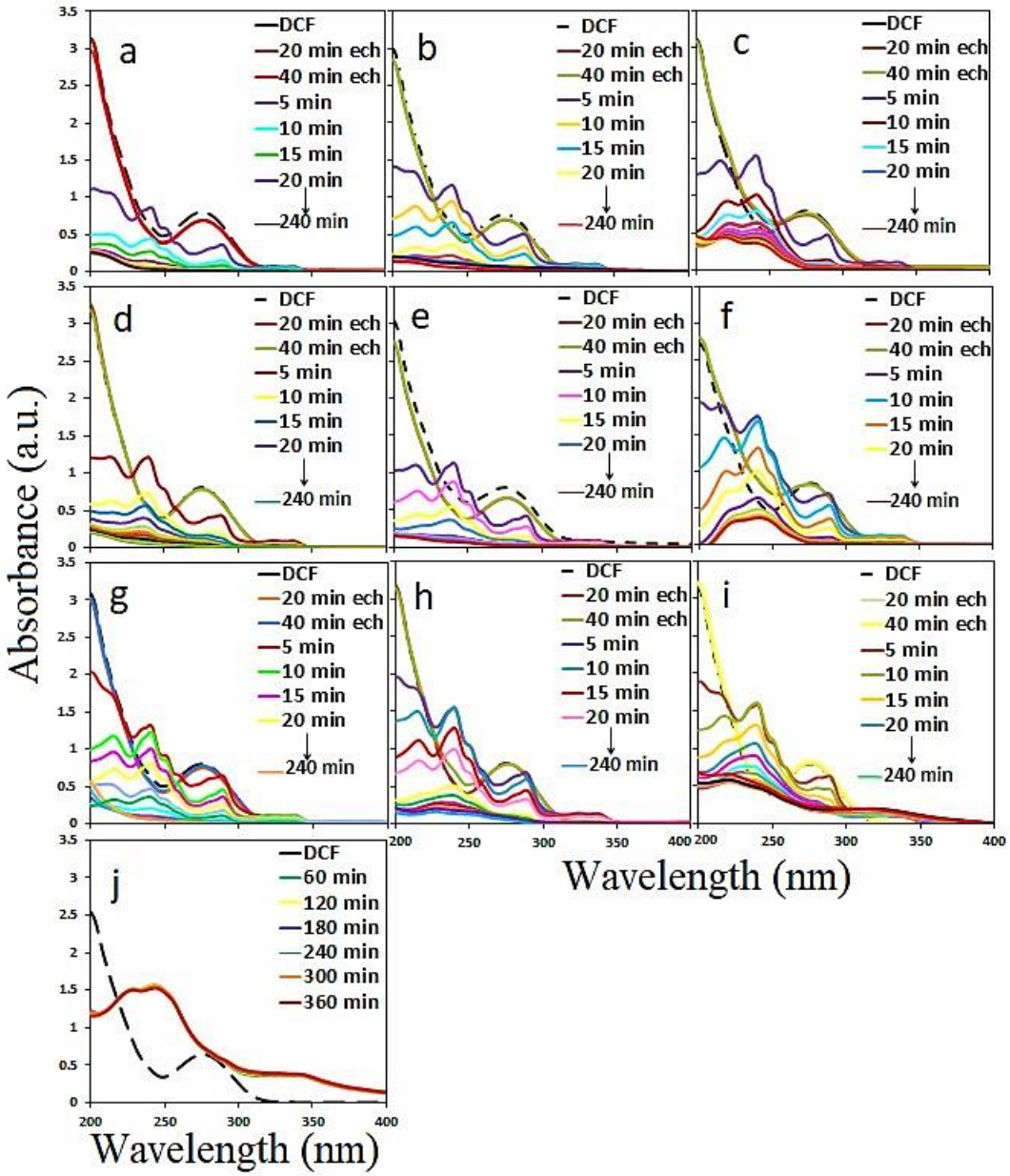

Figure 2.43: UV–Vis spectra of DCF photodegradation under solar irradiation and in the presence of the a) ZnAl(2/1), b) ZnAl-CN-I, c) ZnAl-CN-R, d) ZnCoAl(2/1), e) ZnCoAl-CN-I, f) ZnCoAl-CN-R, g) ZnAl-750, h) ZnCoAl-750, i) g-C_3N_4, j) blank.

solution, but without adding catalyst, indicate that a very stable product is formed immediately after the lamp is turned on (figure 2.43 – j). On the contrary, when the DFC solution is irradiated in the presence of catalyst, the photodegradation of DCF molecules occurs with the

rapid formation of chloro-carbazole Cz1 intermediary species [226]. It can be also observed from the UV-Vis profiles included in figure 2.43 that, during the photodegradation processes, different mechanisms are involved when using different photocatalysts, e. g. pristine LDHs, impregnated or reconstructed LDHs in the presence of g-C_3N_4 or their correspondent MMO, respectively. In all cases, the drug is first converted in many types of carbazoles followed by their partial or total decomposition depending of the involved photocatalyst. [168]. The photodegradation of DCF using the g-C_3N_4 (figure 2.43 i) and the reconstructed samples (figure 2.43 c and f) leads to the formation after approximately 80 minutes of reaction of stable products which might be related with those formed in case of the blank test (figure 2.43 c, f, i). For the rest of studied catalysts, e. g. LDHs (figure 2.43 a and d) and g-C_3N_4 impregnated LDHs (figure 2.43 b and e), the degradation process takes place continuously and, after 240 minutes of reaction, the spectral profiles attributed to the carbazol structures disappear.

Figure 2.44 presents the photocatalytic performances of the studied photocatalysts evaluated by UV-Vis and compared with the effective mineralization of the decomposition products evaluated by the TOC measurements. According to the UV-Vis results, the fresh samples and impregnated hybrids have the best activity, with a catalytic degradation efficiency of DCF more than 93 % from the initial concentration. However, it is interesting to note that

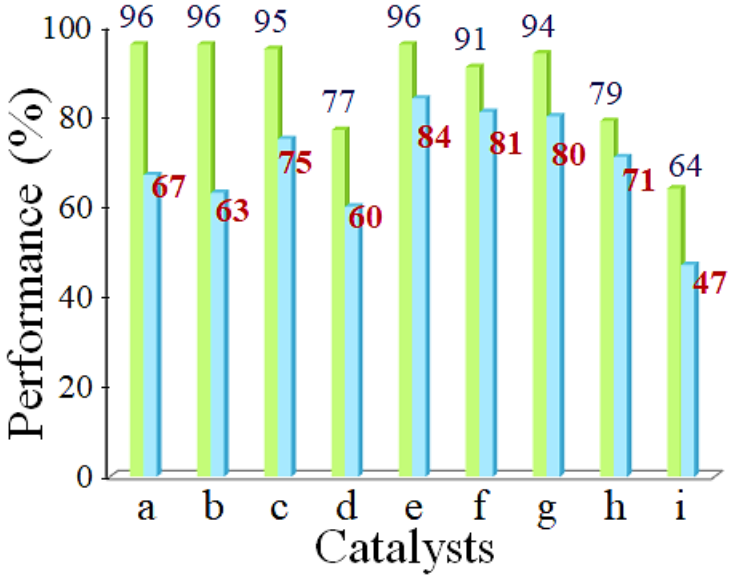

Figure 2.44: DCF solar photodegradation performance evaluated by - UV-Vis and - TOC for a) ZnAl(2/1), b) ZnAl-750, c) ZnAl-CN-I, d) ZnAl-CN-R, e) ZnCoAl(2/1), f) ZnCoAl-750, g) ZnCoAl-CN-I, h) ZnCoAl-CN-R, i) g-C_3N_4.

the TOC results indicate that the isomorphic substitution of Co^{II} within the layered network (the ZnCoAl sample) highly increases the TOC removal up to 84.1% as compared with the Co^{II} free layered network (the ZnAl sample) which might mineralize only 66.5 % of DFC in the same experimental conditions. Therefore, we might conclude that the introduction of Co^{II} in LDH structure improves the catalytic efficiency of the layered system. Furthermore, the

hybridization of the LDH matrices with g-C_3N_4 improves the DFC photo-mineralization degree from ~66%, as observed for the ZnAl(2/1) sample, up to ~75% for the ZnAl-CN-I sample. The presence of Co^{II} in the final hybrid material also proves to be beneficial, indicating an increase of mineralization degree up to ~80% (the case of hybrid formulation ZnCoAl-CN-I sample). When comparing the two routes for hybridization of LDHs with g-C_3N_4, e. g. impregnation or reconstruction respectively, it can be concluded that the use of the impregnation route leads to more active material as compared with the reconstruction method. These results might be well correlated with the characterization data which indicated that a very crystalline hybrid structure combining g-C_3N_4 and layered phase might be obtained via the impregnation route. Furthermore, when the reconstructed samples are used, the stable carbazolic intermediary product is formed after approximatively 80 minutes of reaction. The XRD profiles (figure 2.32 b and g) for these samples indicate the lack of reconstruction of the layered phase, the graphitic phase being the main contributing phase in these samples. As such, when used in a photocatalytic reaction, the behavior of these samples (figure 2.43 c and f) is similar with that of g-C_3N_4 (figure 2.43 i), when the formation of the intermediary carbazolic compound is observed. It can be concluded, that the presence of a crystalline LDH phase in the hybrid g-C_3N_4/LDH photocatalytic systems is directly influencing the photocatalytic mineralization pathway and degree of the DFC molecules.

Nayak *et al*. demonstrated that the quantity of C_3N_4 loaded on LDH can influence the photoresponsive activity of the formed complex. They proved that the activity increases proportionally with the amount of C_3N_4, and after a maximum, the activity of the complex start to decrease. So, in our hybrid samples, it is possible to have higher quantity of C_3N_4 and as a result of this, some of the active situs from the LDH surface become unavaible for the light excitation [224]. In this condition, the numbers of oxidative species decreases and because of this, the photocatalytic activity decreases also. As well, to sustain the previous affirmations, we can observe that the activity of impregnated samples is better than for the reconstructed one. From TG analysis we calculated the percentage of the C_3N_4 amount linked on LDH and we remarked that the quantity of graphene is bigger for the sample synthetized by impregnation.

For the best catalyst, ZnCoAl(2/1) four consecutive tests were performed in order to establish the reusability. The results indicate that after reusing the catalysts four times in the same conditions, it retains 68 % from its initial activity.

- **Photocatalytic activity of the LDHs systems under UV and visible light irradiation**

In order to investigate the influence of the UV or visible component of the sunlight, photocatalytic tests were carried out using blockfilters. Combined UV-Vis and TOC data were acquired in order to establish the photocatalytic performances of our materials. It was observed that the DFC photodegradation was insignificant when the samples were irradiated only by visible light, e. g. between 1-11%, the maximum being reached by ZnCoAl 750.

Under UV light, the degradation took place through different pathway and the carbazols products are not detected spectrophotometrically. The UV-Vis profiles (figure 2.45) of the resulting degradation components are matching with the initial profile corresponding to the initial DCF solution. However, we can also observe that the degradation pathway is different for the hybrids obtained via the reconstruction route. A possible explication for these new

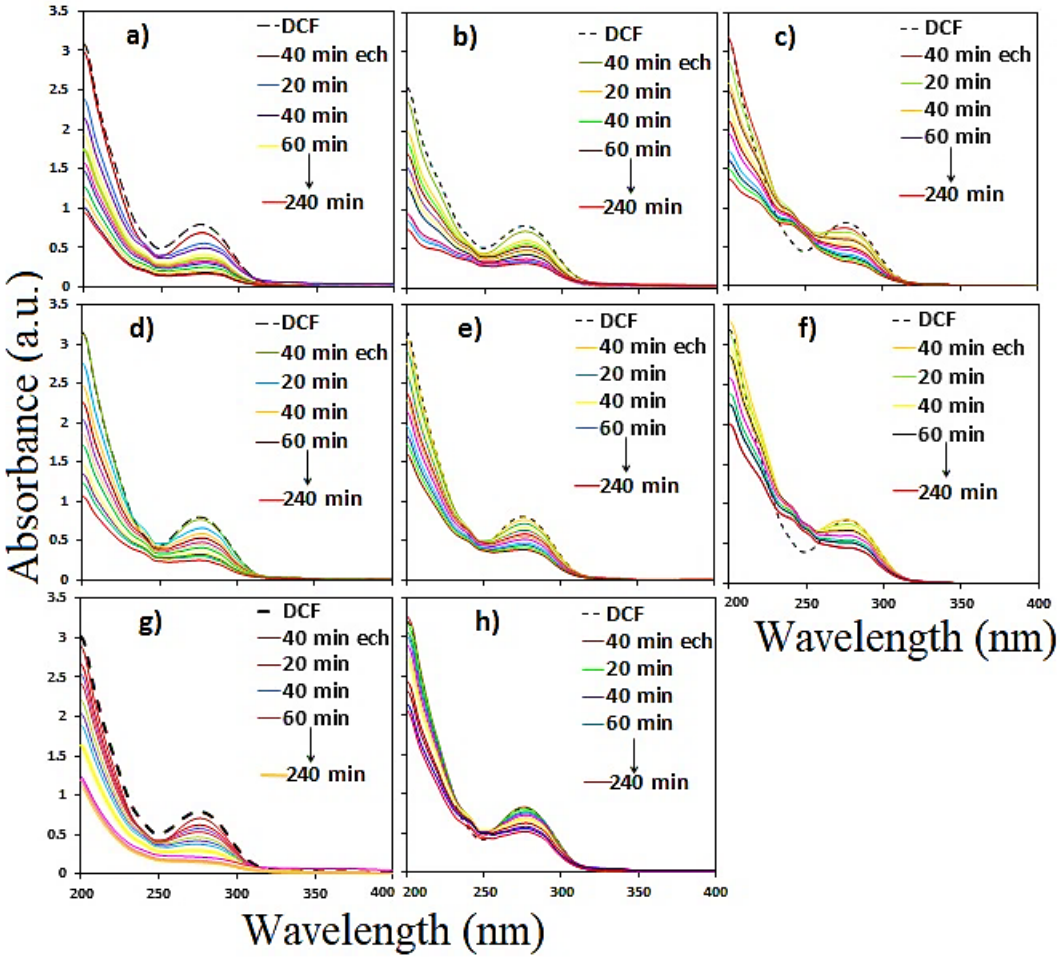

Figure 2.45: UV–Vis spectra of DCF photodegradation under UV irradiation and in the presence of the a) ZnAl(2/1), b) ZnAl-CN-I, c) ZnAl-CN-R, d) ZnCoAl(2/1), e) ZnCoAl-CN-I, f) ZnCoAl-CN-R, g) ZnAl-750, h) ZnCoAl-750.

mechanisms can be related with a slow conversion of DCF in carbazolic products. In this situation, in the system the concentration of DCF is always higher compared to the concentration of reaction products and for this reason the last ones, being in a small amount, they cannot be detected through UV-Vis measurements, but as will be further presented, they ca be detected by chromatographic measurements.

The results of the photoactivity studies (figure 2.46) show that under UV irradiation the most performant catalysts, according with TOC measurements, are the fresh samples and the

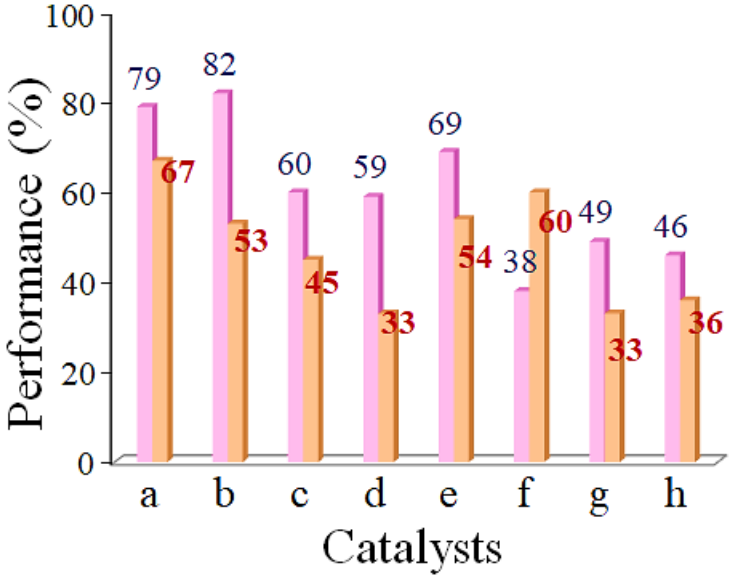

Figure 2.46: DCF UV photodegradation performance evaluated by - UV-Vis and - TOC for a) ZnAl(2/1), b) ZnAl-750, c) ZnAl-CN-I, d) ZnAl-CN-R, e) ZnCoAl(2/1), f) ZnCoAl-750, g) ZnCoAl-CN-I, h) ZnCoAl-CN-R.

calcined one. If we compare the performance for ZnAl and ZnCoAl obtained under UV irradiation with that obtained under solar light, we can see the contribution of Co in the enhancement of the ZnLDH photoactivity. ZnAl catalyst has the same activity under solar and UV irradiation (66.5 and 66.9 % TOC removed), but when Co is present in the structure, the capacity of the new material of absorbing visible light increases. In consequence, the performance enhances from 53.6 % to 84.1 %.

- **Mechanism of DCF photodegradation**

The photodegradation results revealed that the initial precursors have a good photoresponse and the introduction of g-C_3N_4 in LDHs matrix has not the beneficial effect that it was expected. In this context, a general photodegradation mechanism is proposed and it involves the formation of a complex between the LDHs and the DCF molecules. Based on the equations expressed below, the photodegradation takes place as a combination between between photosensitization (eq. 2.7-2.12) and photooxidation (eq. 2.13-2.17). Due to the presence on –OH groups on LDHs surface, the drug can be easily adsorbed and further excited

$$DCF + LDHs \rightarrow DCF/LDHs \quad (2.7)$$

$$DCF/LDHs + h\nu \rightarrow DCF^{\bullet}/LDHs \quad (2.8)$$

$$DCF^{\bullet}/LDHs \rightarrow DCF^{\bullet+} + LDHs(e_{CB}^{-}) \quad (2.9)$$

$$LDHs(e_{CB}^{-}) + O_2 \rightarrow O_2^{\bullet-} + LDHs \quad (2.10)$$

$$DCF^{\bullet+} \rightarrow products \quad (2.11)$$

$$DCF^{\bullet+} + O_2^{\bullet-} \rightarrow products \quad (2.12)$$

$$DCF/LDHs + h\nu \rightarrow DCF/LDHs\ (e_{CB}^{-} + h_{VB}^{+}) \quad (2.13)$$

$$DCF/LDHs\ (h_{VB}^{+}) + H_2O \rightarrow DCF/LDHs + OH^{\bullet} + H^{+} \quad (2.14)$$

$$OH^{\bullet} + DCF \rightarrow products \quad (2.15)$$

$$DCF/LDHs(e_{CB}^{-}) + O_2 \rightarrow DCF/LDHs + O^{\bullet-} \quad (2.16)$$

$$O^{\bullet-} + DCF \rightarrow products \quad (2.17)$$

by the absorbed photon. An electron transfer might occur between the excited DCF (DCF*) and the conduction band of the material, and in this way oxidative species are formed and further used in photodegradation. The DCF light sensitization and the material direct band excitation are also presented in figure 2.47 [209–211].

From the UV-Vis profiles can be noticed that the DCF is degraded via different pathways. However, because the UV-Vis spectra provide insufficient information for the

photodegradation mechanisms elucidation, the liquid chromatography quadrupole time-of-flight mass spectrometry was used (LC-QTOF MS) to complete the analyze. For this, four representative materials were chosen and tested in the solar DCF degradation. For each spectrophotometer measurement, LC-QTOF MS measurements were also performed and compared with the UV-Vis data. The LC-QTOF MS data indicate the formation of the degradation compounds and their gradual removal from the analyzed system. A partially quantification of the formed compounds was calculated as difference between the maximum reached LC-QTOF MS signal and the signal at the end of the 4 h of irradiation.

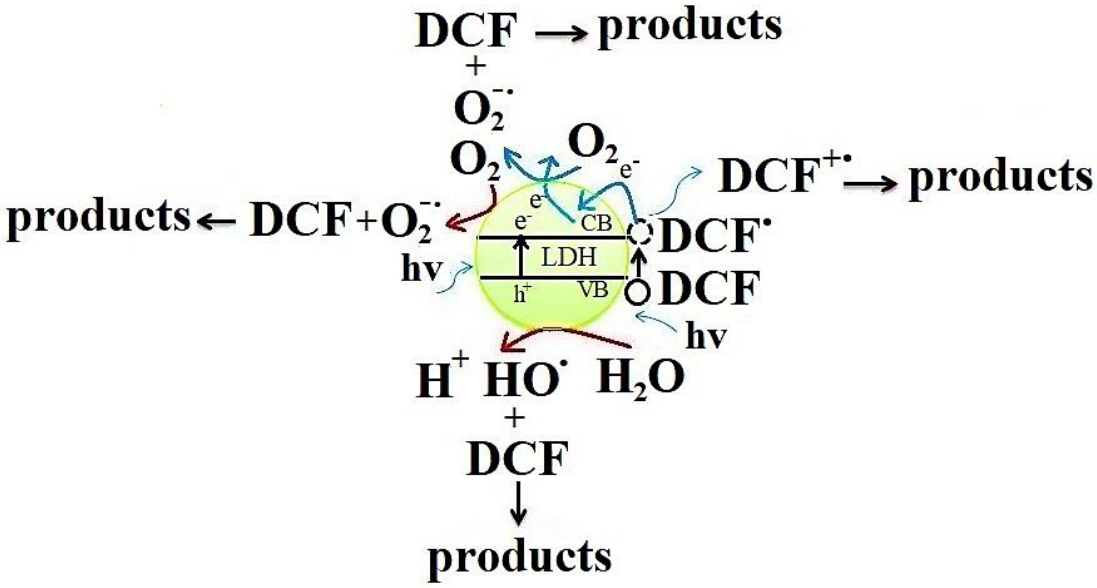

Figure 2.47: Proposed DCF photodegradation in presence of synthetized catalyst, involving both photosensitization and photooxidation.

- ***DCF photolysis (blank test)***

An important aspect in pollutants photodegradation is the final composition of the aqueous system. For this reason, one of the investigated photodegradation system was the DCF solar photolysis, in absence of a solid catalyst. It might be observed from figure 2.48 that during the irradiation process a significant number of stable compounds is obtained, and some of them are staying in the system till the end of the test. According with other studies made on the same subject, the resulted degradation solution has a higher toxicity compared with the one

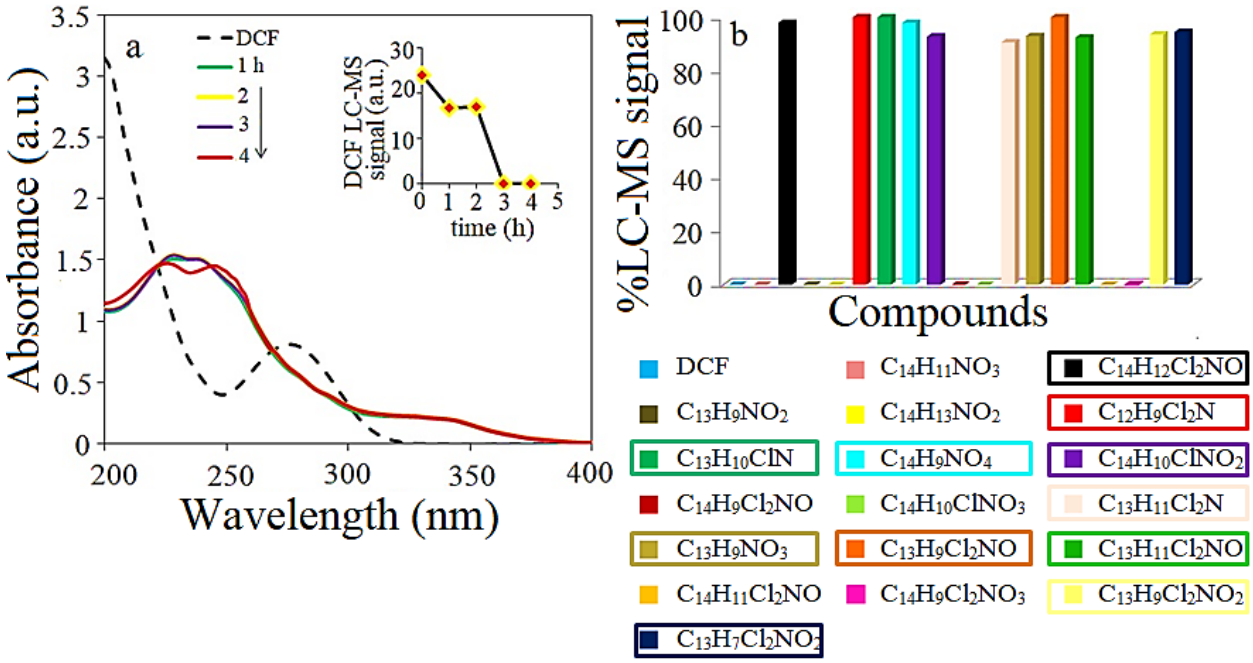

Figure 2.48: a) UV-Vis spectra profiles for DCF photolysis and b) the percentage LC-MS products signal after 4 hours of solar irradiation; insert: DCF LC-MS signal.

of the initial DCF solution [227,228]. For this reason, the design of robust materials able to total removal of harmful products is a subject intensely approached.

The proposed mechanism for the DCF photolysis is presented in figure 2.49. It involves two main alternative routes: the ring hydroxylation and the ring closure. These reactions can start with DCF decarboxylated intermediate C16, or with DCF. Via ring hydroxylation, compound C10 is firstly formed, and followed by its oxidation with C12 product formation. C12 will loss one water molecule and further oxidation will lead to quinine imine intermediate, C14 [228,229]. The second route can start also with DCF or product C16, and it involves the removal of a chloride atom, with ring closure, and with the formation of charbazole compounds [230,231]. Based on these two proposed photolysis routs, the main formed products are quinine imine structures (C6, C12, C13, C14) and carbazoles (C4, C5, C8, C9, C17, C18, C19) [231,232]. However, the chromatography data, apart from these primary compounds, other complex molecules were detected as well, and attributed to the pharmaceutical photolysis [201–204]. These compounds are a consequence of mono- or dechlorination of DCF (C1, C2) or of hydroxylation and oxidation of compound C16 (C20, C21). Because of the formation of stable products associated with carbazoles and quinine imines, the resulted compound mixture has a higher toxicity than that of the initial [226,228], the direct DCF solar degradation being a harmful process.

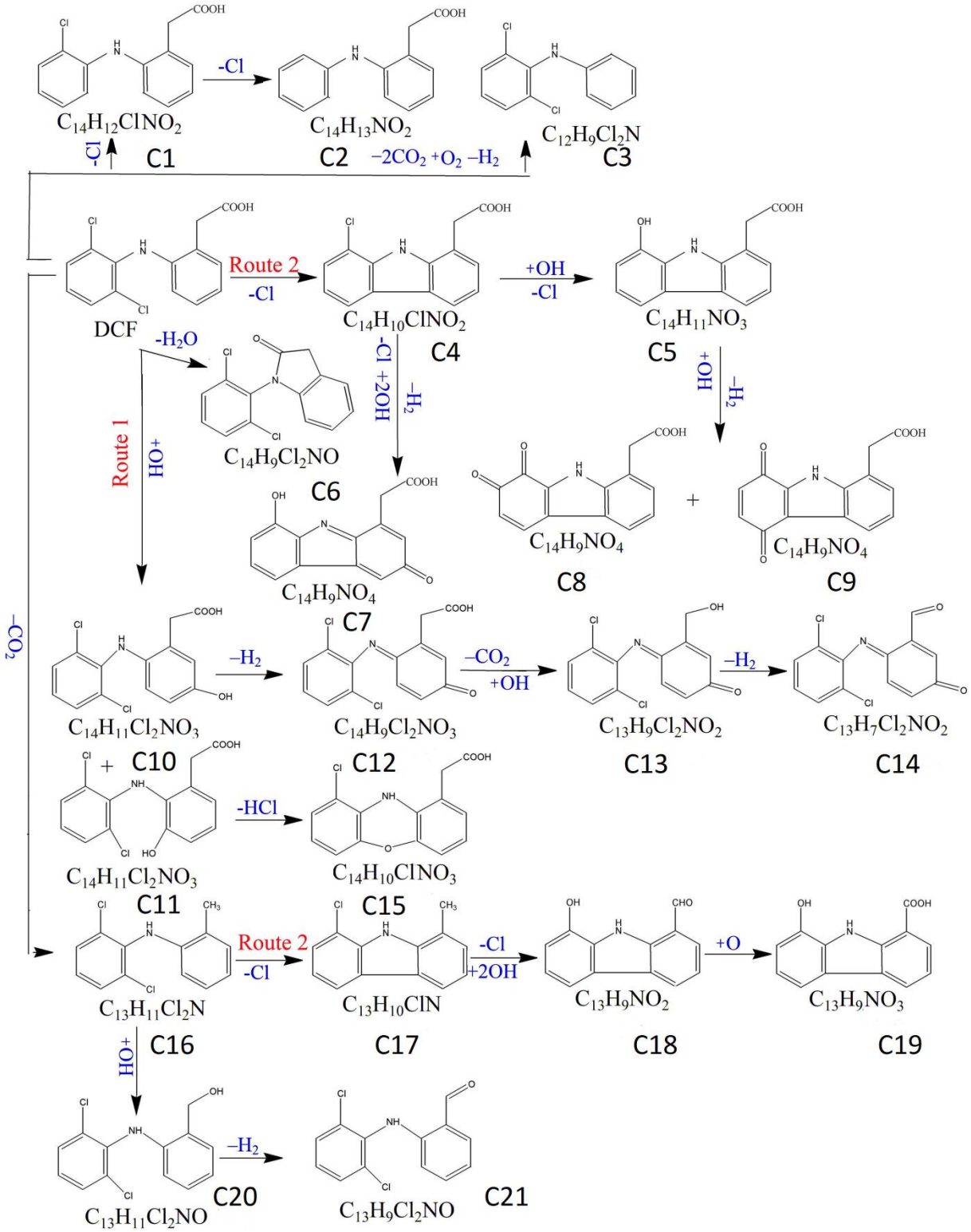

Figure 2.49: Proposed mechanism for solar photolysis of DCF (blank test).

- ***solar photodegradation of DCF in presence of ZnCoAl(2/1) catalyst***

When the catalysts are present in the system, they lead also to the formation of less stable products, which can be further decomposed. The best catalyst, ZnCoAl(2/1) was tested in the solar photodegradation of DCF. The UV-Vis and LC-QTOF MS measurements were performed and results are shown in figure 2.50. It might be observed from figure 2.50-b that the final solution has a less complex composition, compared with the one obtained in case of the blank test. The proposed mechanism of photodegradation using ZnCoAl is presented in figure 2.51. It involves the ring closure which can start with DCF or with compound C9, which is DCF decarboxilated intermediate. The reaction will lead to carbazoles compounds formation like C5, C6, C7, C8, C10 [233]. Furthermore, other complex compounds are formed as a result of the participation of DCF or of its photodegradation compounds at monochlorination, decarboxylation, hydroxylation or oxidation reactions [231,232]. Due to ZnCoAl(2/1) catalyst

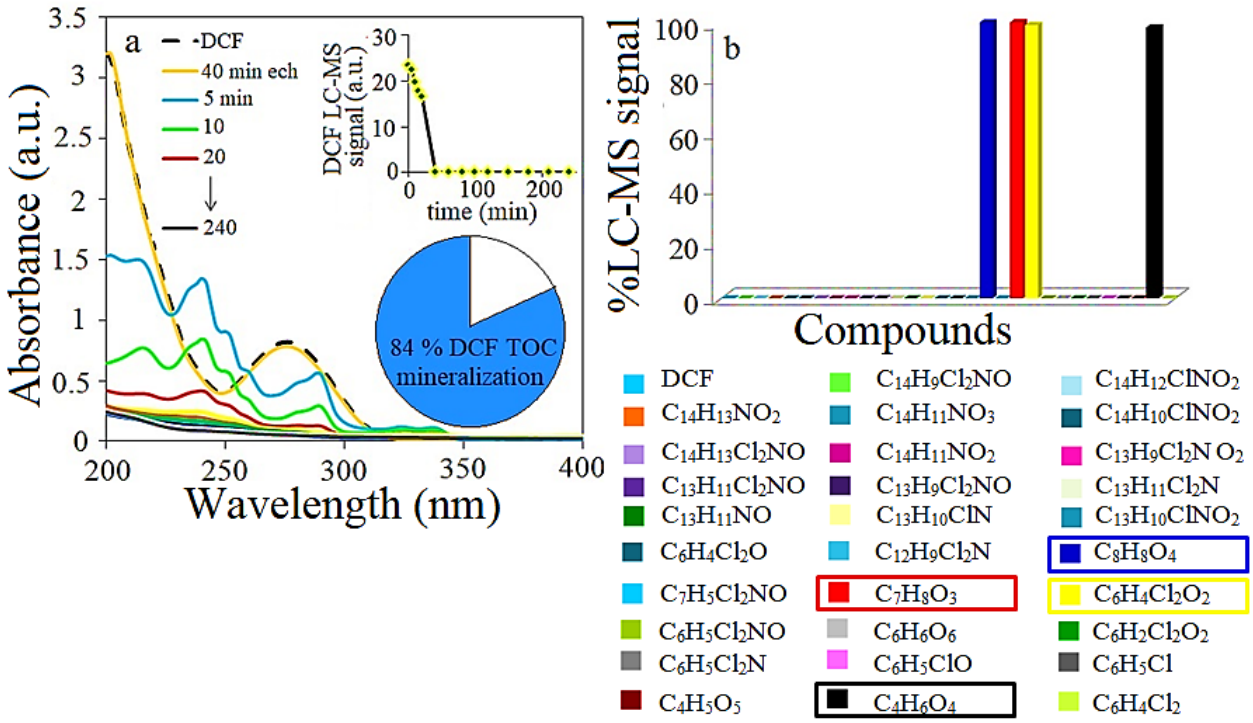

Figure 2.50: a) UV-Vis spectra profiles for DCF photodegradation initiated by ZnCoAl(2/1) catalyst and under solar irradiation; b) the percentage LC-MS products signal after 4 h of solar irradiation; insert: DCF LC-MS signal.

presence, two other consecutive pathways take place, involving the NH- cleavage and the ring opening, when smaller molecules are obtained and further transformed into CO_2 and HCl [229,232–234] These results demonstrate that the solid and the drug molecules interact with each other, resulting a new hybrid catalyst, a DCF-LDHs complex. The new complex, under light excitation, allows the charge transfer between DCF and LDHs. In this way the degradation

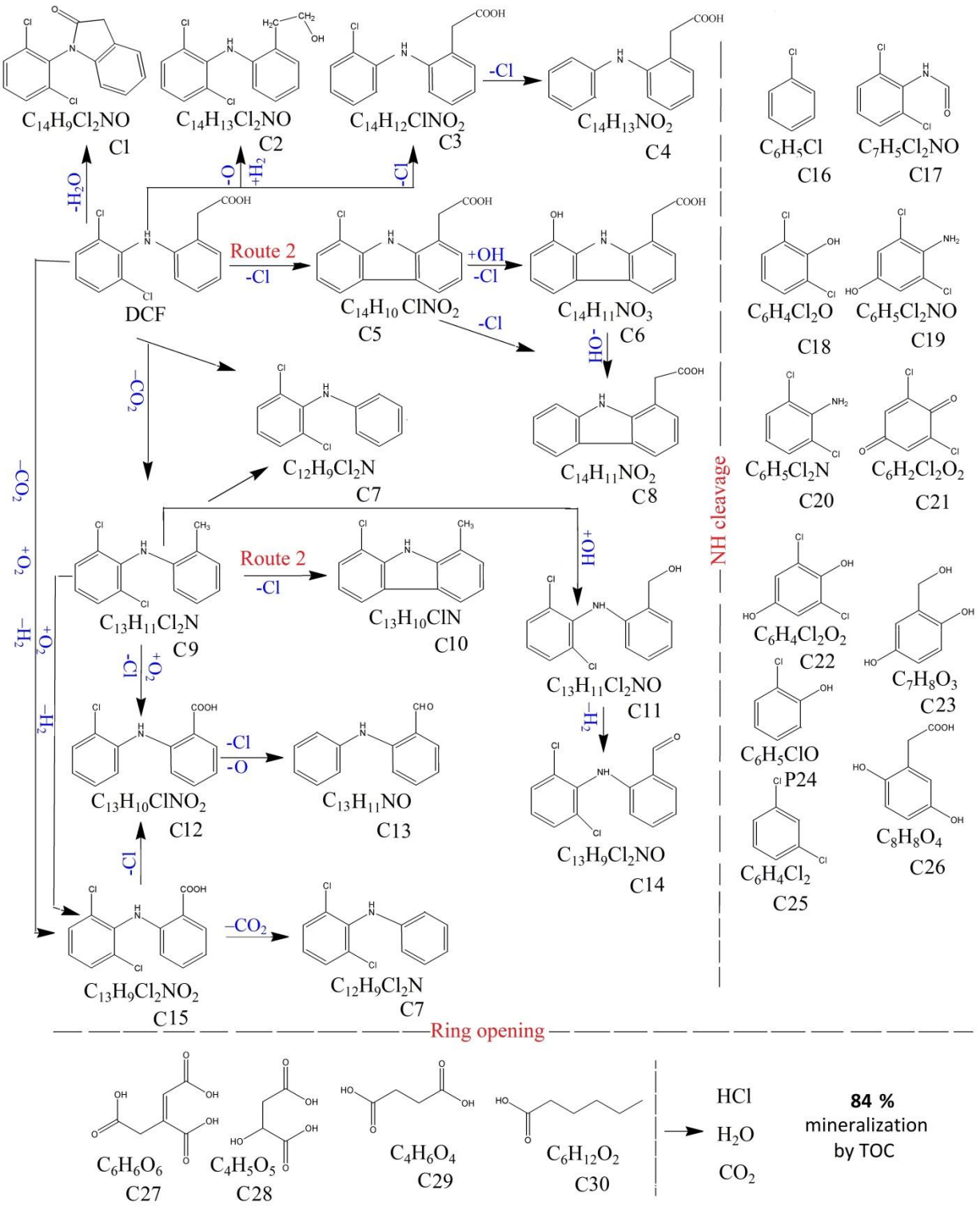

Figure 2.51: Proposed mechanism for solar photodegradation of DCF in presence of ZnCoAl(2/1) catalyst.

of drug take place like a combination between photosensitization and photo-oxidation, increasing the performance of the process [235–237]. The identity of the photodegradation compounds could show that some DCF molecules are interacting directly with the solar irradiation, while others are adsorbed on solid surface and converted in distinct molecules. However, all the resulted photolysis products might be the subject of supplementary interaction with the catalyst, being further photodegraded and mineralized.

- ***UV photodegradation of DCF in presence of ZnCoAl(2/1) catalyst***

To investigate the influence of irradiation type on the DCF photodegradation pathways, a photocatalytic test in presence of UV light and using ZnCoAl(2/1) catalyst was carried out. The chromatographic data presented in figure 2.52-b show that during the irradiation a significant number of stable compounds are formed. Additionally, both UV-Vis and LC-QTOF

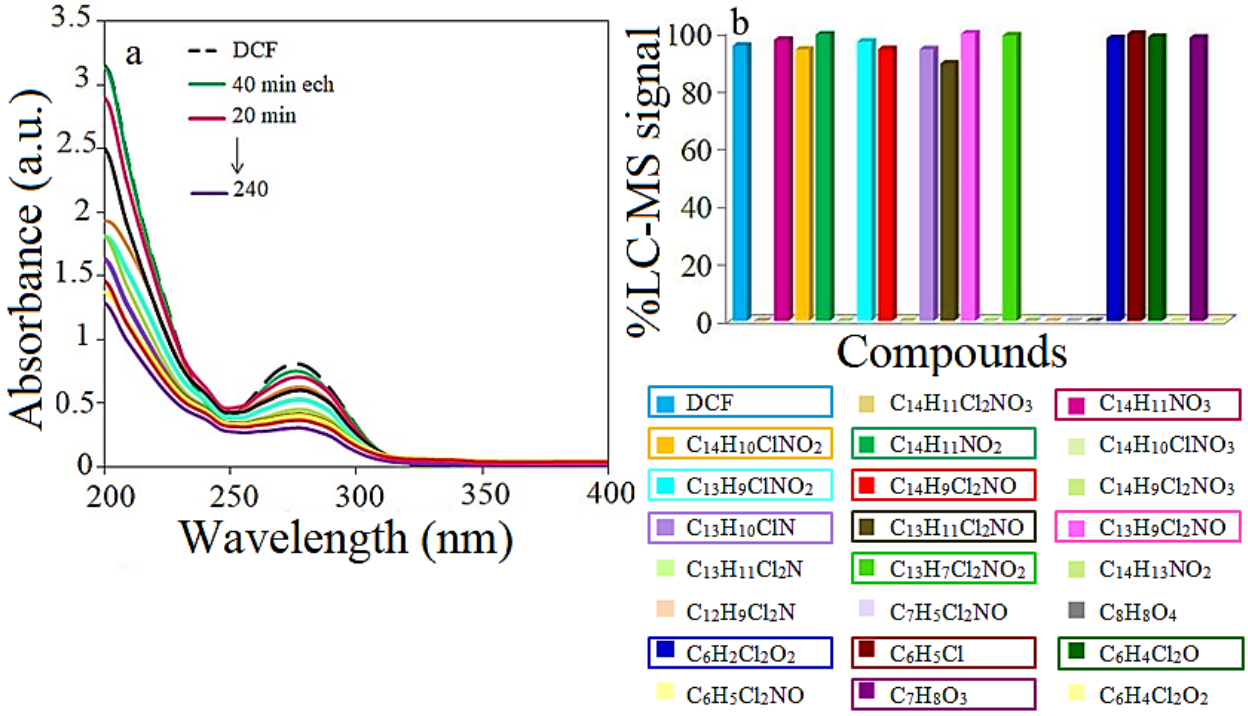

Figure 2.52: a) UV-Vis spectra profiles for DCF photodegradation initiated by ZnCoAl(2/1) catalyst and under UV irradiation; b) the percentage LC-MS products signal after 4 hours of solar irradiation; insert: DCF LC-MS signal.

MS measurements show that the DCF stays in the system till the end of the test (figure 2.52-a). However, even if the UV-Vis spectra do not present the characteristic profiles of the carbazolic intermediate, the chromatographic data reveal that these species are present in the solution.

The proposed degradation pathway (figure 2.53) involves the alternative hydroxylation and ring closure followed by NH- cleavage. As expected, the stable products identified as carbazoles (C1, C2, C4, C8) and quinine imine (C10, C14, C15) were detected, as a result of

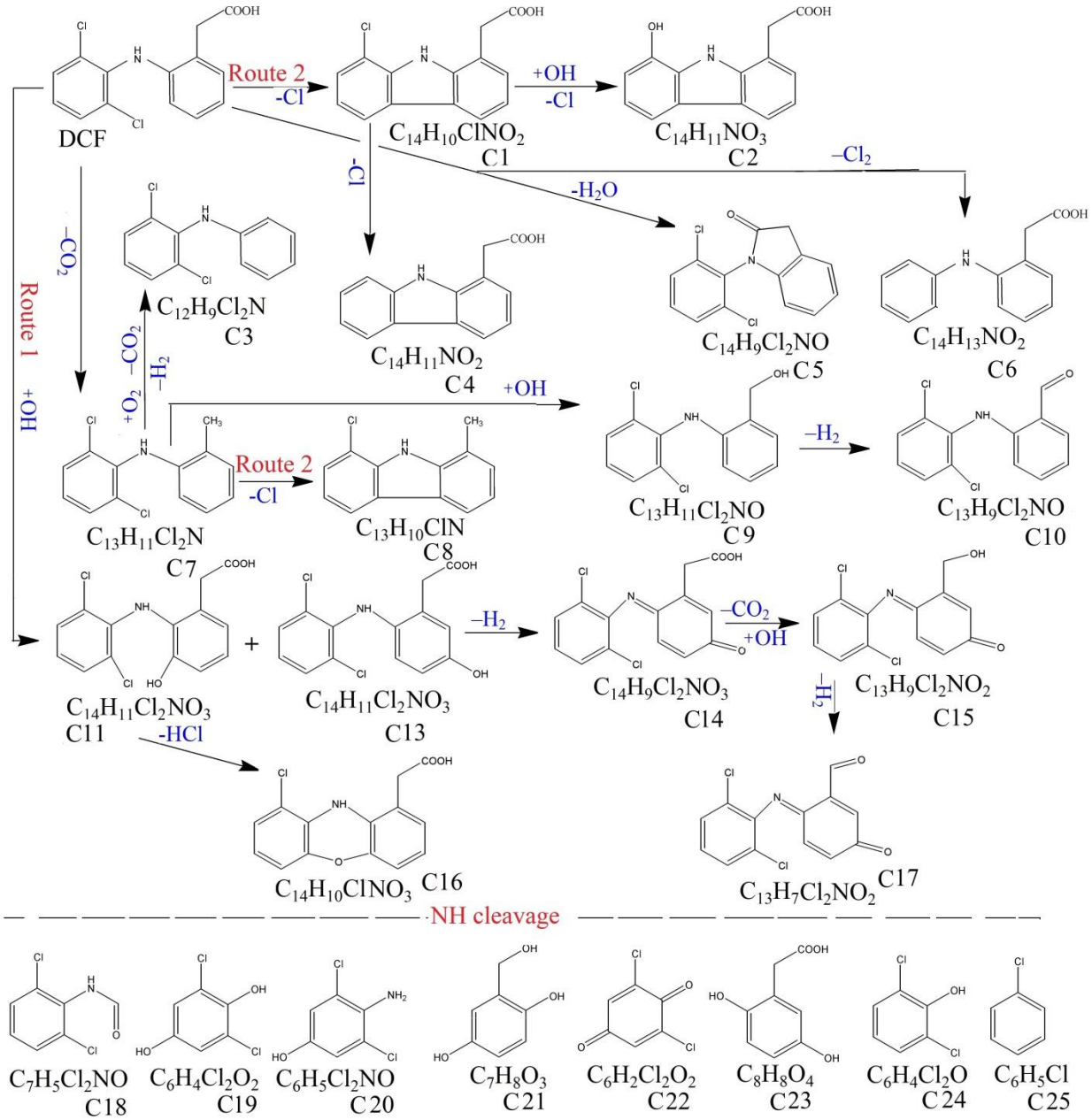

Figure 2.53: Proposed mechanism for DCF photodegradation under UV light and in presence of ZnCoAl(2/1) catalyst.

the mentioned reactions. However, in the same time, other less stable products were recorded in the system. Particularly, they present a fluctuant behavior, appearing and disappearing continuously from the solution. An explication of this phenomenon can be the slow and step by step continuously conversion of DCF in products and their further transformation in other compounds, which can make that at some sampling moments to be or not in the system. The final solution composition has commune compounds with the solution resulted in case of the DCF photolysis (see figure 2.48-b). Additionally, the final solution contains compounds as C1

($C_{14}H_{10}ClNO_2$) and C2 ($C_{14}H_{11}NO_3$), which based on the study made by S.K Alharby *et al.*, can increase the toxicity of the initial drug solution several times [226,227]. The TOC results for ZnCoAl(2/1) presented in the figures 2.44 and 2.46 clearly underline the importance of the visible component of the light in the photodegradation processes, leading to an increase of activity from 54 % (UV light) to 84 % (solar light).

- ***solar photodegradation of DCF in presence of ZnCoAl-CN-R catalyst***

This investigation was done in order to see how the presence of the g-C_3N_4 in LDHs structure affects the photodegradation pathway of DCF. According to the UV-Vis spectra profile (see figure 2.43 and 2.45), the DCF photodegradation takes place via four main mechanisms, which can be attributed as follows: to (1) the photolysis of DCF (figure 2.43-j), to (2) the DCF degradation under UV light (figure 2.45), (3) DCF degradation under solar light in presence of fresh, calcined and impregnated sample (figure 2.43 a, b, d, g, h), and in the end to (4) DCF degradation under solar light and in presence of g-C_3N_4 reconstructed sample (figure 2.45 c, f, i). In case of the reconstructed samples it was observed from the UV-Vis spectra that stable compounds are formed after 80 minutes of irradiation (figure 2.54). Based on the identity

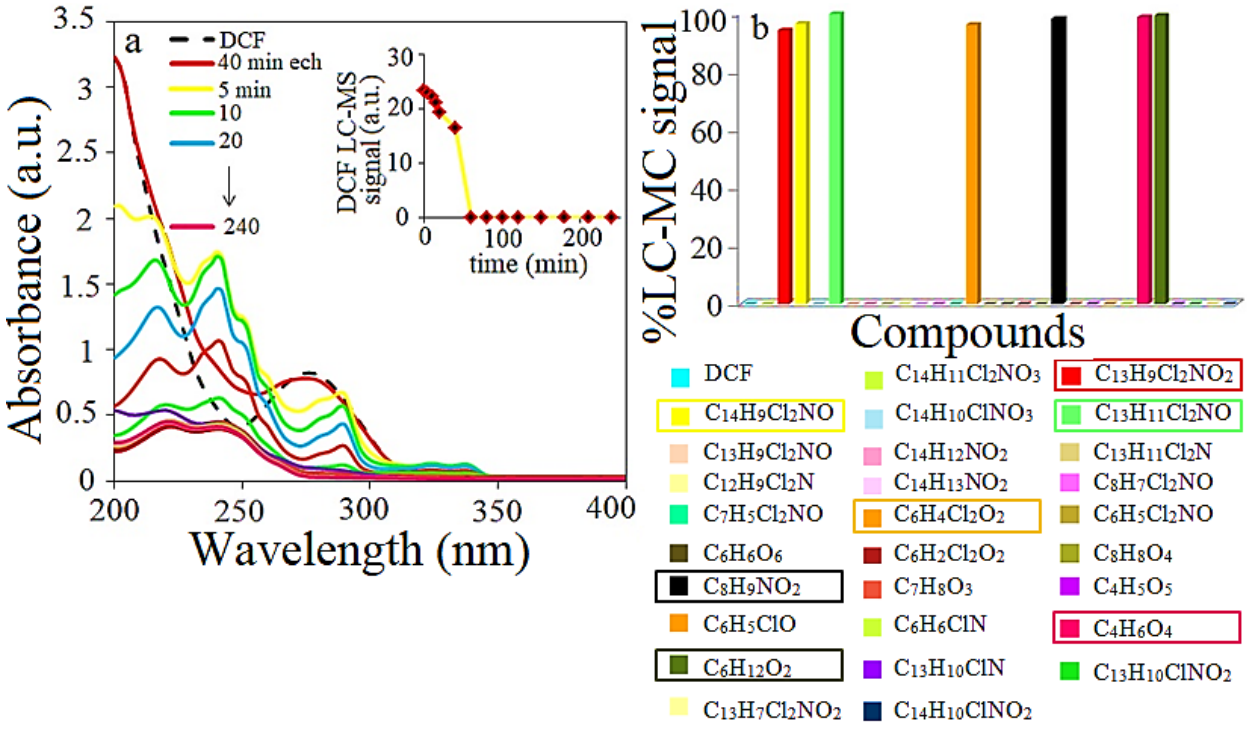

Figure 2.54: a) UV-Vis spectra profiles for DCF photodegradation initiated by ZnCoAl –CN-R catalyst under solar irradiation; b) the percentage LC-MS products signal after 4 hours of solar irradiation; insert: DCF LC-MS signal.

and the evolution of the identified compounds by using LC-QTOF MS measurements, the solar photodegradation mechanism (figure 2.55) might involve the alternative ring hydroxylation and

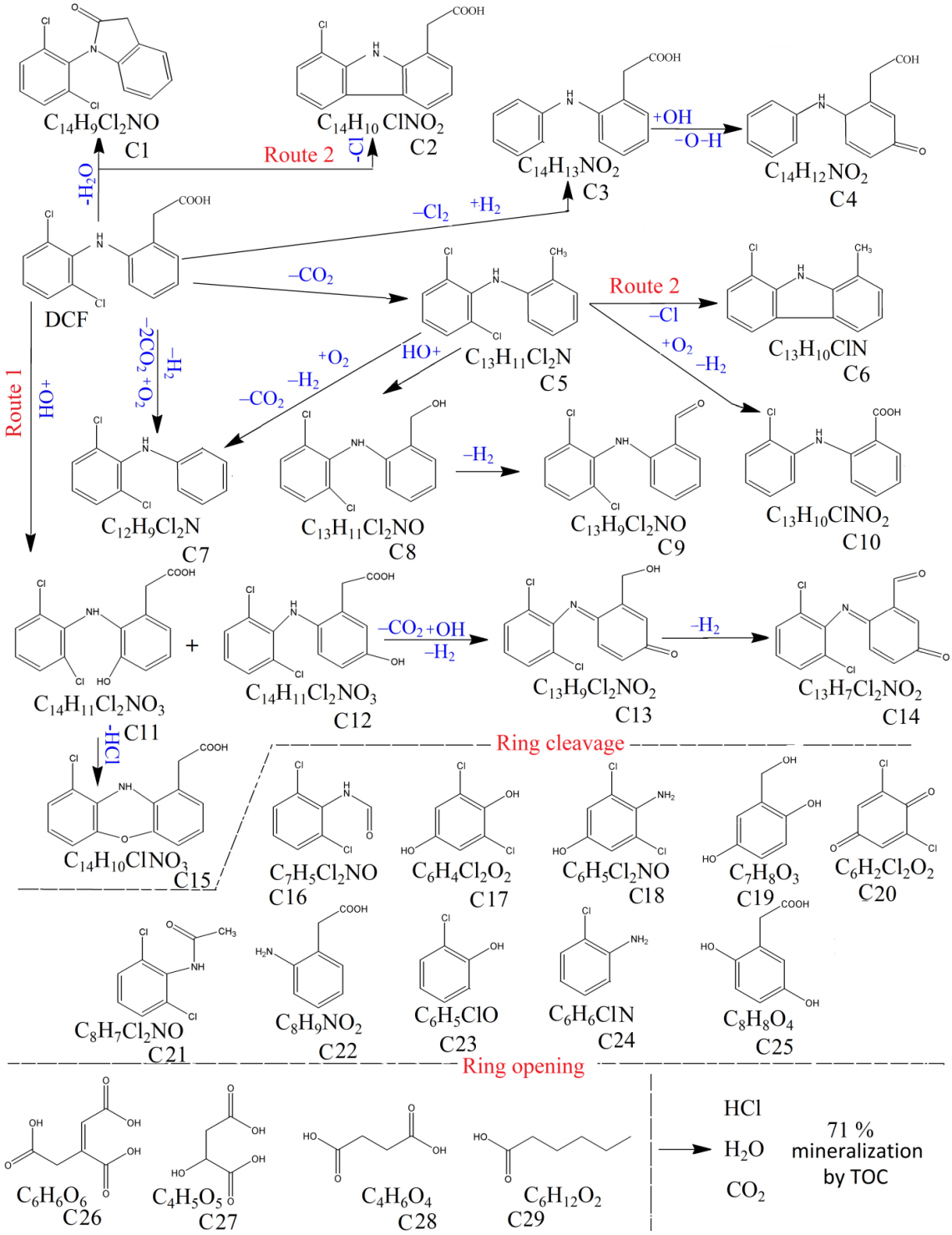

Figure 2.55: Proposed mechanism for DCF solar photodegradation in presence of ZnCoAl-CN-R catalyst.

ring closure, followed by the ring cleavage and ring opening (figure 2.55). The insert of figure 2.54-a shows that after 60 minutes of testing, all the DCF is converted into intermediates and after 4 h of irradiation, the mineralization degree is 71%. The LC-QTOF MS data (figure 2.54 b) reveal that in the final solution, three complex and stable photodegradation compounds (C1, C8, C13) are still present in the system. The presence of these three products is the main difference between pathways obtained for ZnCoAl(2/1) and ZnCoAl-CN-R catalysts during DCF solar photodegradation. For the drug decomposition using g-C_3H_4, the UV-Vis profiles are comparable with those of ZnLDH-CN-R. In these conditions, it can be affirmed that for the LDHs-CH reconstructed catalysts, the graphitic carbon nitride induces the photocatalytic reactions pathway.

- ***Investigation of the DCF-LDHs complex formation***

The general photodegradation mechanism which was proposed for these particular LDHs materials involves the formation of a complex between the LDH and DCF. DRIFT measurements were performed in order to investigate the complex formation on the LDH surface during the photocatalytic tests.

The DRIFT spectra of ZnCoAl(2/1) catalyst recorded before and after the photodegradation test under solar light and of DCF are shown in figure 2.56. It may be observed that the structure of the catalyst was not affected by the photocatalytic process. Only small changes occurs in the region between 1800 cm^{-1} and 1400 cm^{-1} (figure 2.56-A, b) which may be attributed to the –NH, -C=O, -C=C, -C-OH, and –C-Cl stretching vibrations of DFC molecules bonded to the catalyst layers.

In order to be able to discriminate between the absorption bands, the recovered catalysts were scanned using the initial samples as a background. In this way, we obtained only the additional peaks which are not assigned to the g-C_3N_4 or to the layered structure of the materials (figure 2.56 B). We can identify the stretching vibration of the -C=O groups from the carboxylic acid at 1739 cm^{-1}, while the peak at 1551cm^{-1} may be assigned to the stretching mode of the COO^- anions; as well, the corresponding vibration for C-OH in the carboxylic group appears in this case at 1231cm^{-1} [238]. The change of these absorption bands, with respect to the initial ones, can indicate a LDHs surface coordination with the participation of the carboxylic groups of the DFC molecules. Other vibration bands which appear in the subtracted spectrum are the stretching vibrations of C=C and C-H from the aromatic ring with the corresponding picks at 1464cm^{-1} and 1073cm^{-1} [239].

XRD measurements were also recorded on the recovered ZnCoAl catalyst in order to investigate the impact of the photocatalytic reactions on LDHs structure. The XRD pattern of the recovered ZnCoAl catalyst (figure 2.57) indicates the preservation of the layered features as well as the high crystallinity and therefore, a very stable structure.

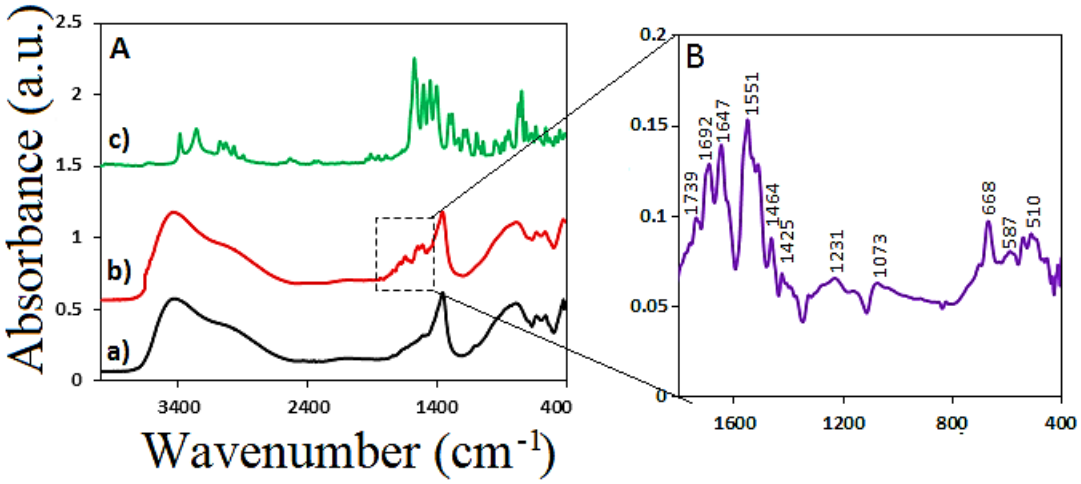

Figure 2.56: DRIFT spectra of A: a) ZnCoAl(2/1), b) ZnCoAl(2/1) recovered, c) DCF; B: the subtracted DRIFT spectrum region obtained by using the initial ZnCoAl catalyst as a background.

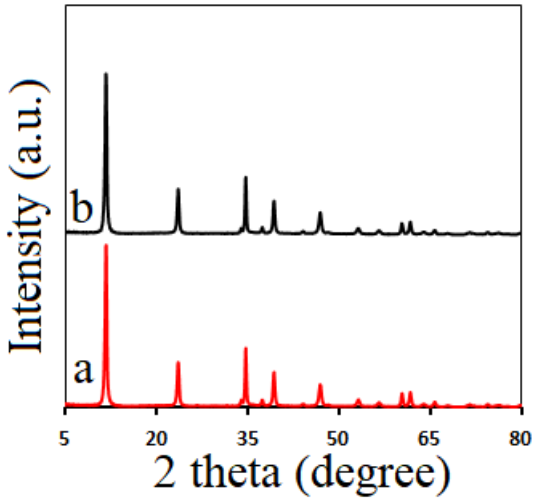

Figure 2.57**:** XRD patterns for ZnCoAl(2/1) and ZnCoAl(2/1) after the photocatalytic test**.**

These results indicate that the cobalt containing LDHs structures and their graphene hybrid formulations obtained via the impregnation route may be regarded as very promising photocatalysts for the mineralization of very stable drug molecules, such as diclofenac, in highly polluted pharmaceutical wastewaters.

b) ZnAl(3/1)LDHs-C_3N_4 and ZnGa(3/1)LDHs-C_3N_4 formulations for solar photodegradation of diclofenac.

The photocatalytic tests for this group of materials were carried out under solar irradiation as it was described in section 2.1. The photodegradation evolution was monitored by UV-Vis spectrometric measurements. The total organic carbon was also determinate.

The UV-Vis spectra profiles obtained for the degradation of DCF under solar irradiation and in presence of our catalysts are presented in figure 2.58. The blank test, which was made by using the simple solar irradiation of the DCF, shows the formation of stable compounds from the family of carbazoles (figure 2.58-j). On the contrary, when the LDHs catalysts are present in the system, oxidative species are formed and a fast conversion of the drug in different products was recorded by the spectrometric measurements. Further, the evolution of each photodegradation system is directly related to the catalyst type. Thus, a continuously degradation was observed for the fresh, calcined, impregnated samples and ZnAl-CN-R catalyst (figure 2.58 a-d, f-h). For these materials, according with spectrometric data, the main product is (8-chloro-9H-carbazol-1-yl) acetic acid, having an absorption peak at 236 nm. This peak is decreasing gradually in time till the end of the process. For the g-C_3N_4 and ZnGa-CN-R, after 80 minutes of testing, stable products are formed and the photodegradation processes take place slowly, with no significant increase of the DCF removal degree.

An interesting result was obtained in case of ZnGa(3/1) layered double hydroxides (figure 2.58-d), which leads to a total degradation and mineralization of DCF after 150 minutes of solar irradiation (figure 2.59 B- a). Taking this in consideration, and based on the weak ability of this material to absorb visible light, we consider that the drug molecules are degraded via photo - oxidation, with the implication of the catalyst and also via photosensitization, with the participation of light excited DCF adsorbed on catalyst surface (see eq. 2.7-2.17 and figure 2.47).

In figure 2.59 are presented the photocatalytic performances of the studied catalysts evaluated by UV-Vis and TOC measurements. It might be observed the all the catalysts have a high photo-response, with degradation and mineralization degree in a range of 64-100 %, 47-100%, respectively. Regarding the influence of the g-C_3N_4 presence on hybrid performance, only in case of ZnAl-CN-I was recorded an increase of activity, compared with its precursor, ZnAl(3/1), from 83 % mineralization, to 97 %. For the rest of catalysts, no beneficial effect was observed after the hybridization process. An explication can be a high quantity of graphitic carbon nitride, which might block the LDHs active sites. The UV-Vis spectra of ZnAl-CN-R, ZnGa-CN-I and ZnGa-CN-R presented in figure 2.41 show clearly the presence of a significant quantity of g-C_3N_4 into LDHs structure due to the absorption edge around 300 and 350 nm. On the contrary, for the ZnAl-CN-I, the UV-Vis spectra present a small shoulder around 350 nm which can be assigned to graphitic carbon. However, all the photocatalytic systems have a good photocatalytic performance.

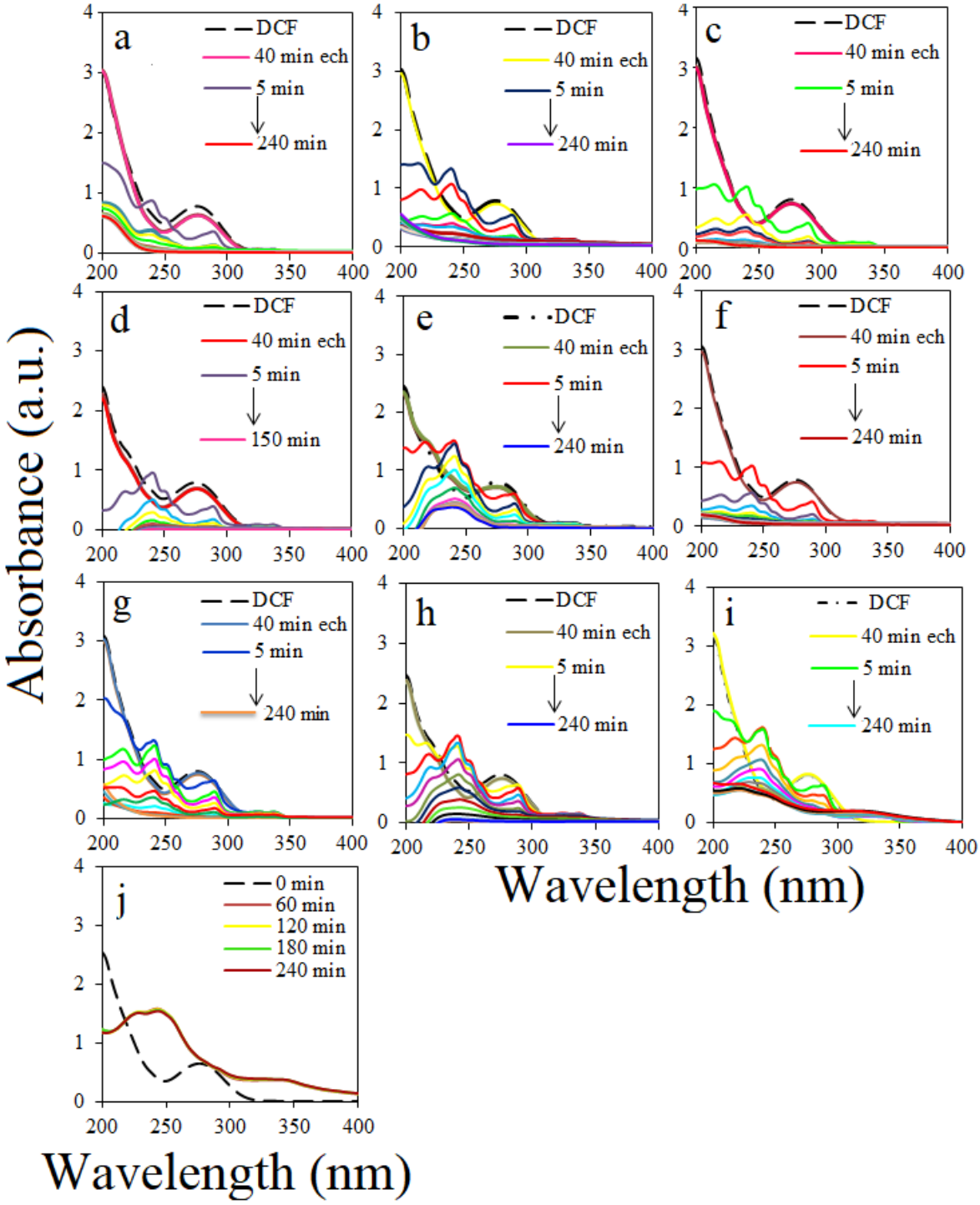

Figure 2.58: UV–Vis spectra of DCF photodegradation under solar irradiation and in the presence of the a) ZnAl(3/1), b) ZnAl-CN-R, c) ZnAl-CN-I, d) ZnGa(3/1), e) ZnGa-CN-R, f) ZnGa-CN-I, g) ZnAl-750, h) ZnGa-750, i) g-C_3N_4, j) blank.

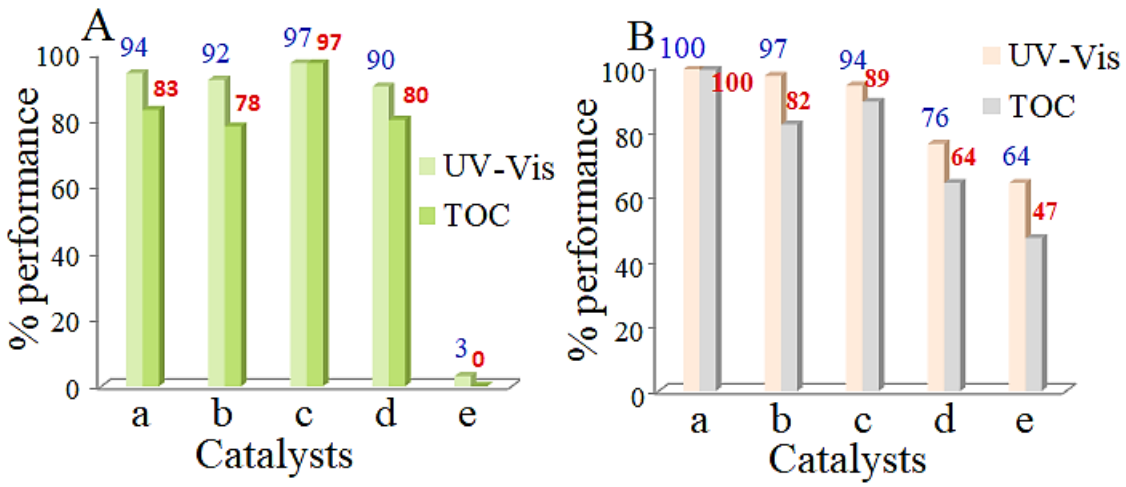

Figure 2.59: DCF photodegradation performance for A) ZnAlLDHs: a) ZnAl(3/1), b) ZnAl-750, c) ZnAl-CN-I, d) ZnAl-CN-R, e) blank; B) ZnGaLDHs: a) ZnGa(3/1), b) ZnGa-750, c) ZnGa-CN-I, d) ZnGa-CN-R, e) g-C_3N_4;.

The UV-Vis photodegradtion spectra profiles of DCF obtained for this group of materials are similar with those obtained for the group based on ZnAl(2/1)LDHs and ZnCoAlLDH(2/1) (see figure 2.43). Based on this, the degradation mechanisms of DCF should involve the same reaction as the ring hydroxylation, the ring closure, the NH- cleavage, and the ring opening, followed by the further degradation till total or partial mineralization. So, we assume that the pathway for the fresh, calcined, impregnated and ZnAl-CN-R, is similar with the one expressed in figure 2.51, while for g-C_3N_4 and ZnGa-CN-R is like the one presented in figure 2.55.

In this chapter DCF was solar photodegraded by using different novel LDHs materials hybridized with g-C_3N_4. Our results have shown that the majority of our composites are able to photodegrade and to mineralize between 64-100 %, 47-100 %, respectively. Several other studies were made on DCF degradation by using photooxidation processes. S. Salaeh *et al.* have used TiO_2/Fe zeolite to remove DCF (initial concentration 30 mg/L) in a photo-Fenton reaction, by using H_2O_2 and a 425 W Xe lamp. Their results indicated maximum TOC removal of 73 % in 180 minutes and 100 % drug conversion to products [233]. In a similar study, but this time using simple TiO_2, a DCF solution with the initial concentration of 15 mg/L, was totally mineralized in 2 h by using 0.2 g/L catalyst and 1500 W xenon lamp (6 times much powerful that the lamp used in our experiments) [240]. Y. He et al. immobilized TiO2 on sand and the resulted product was used in the solar photodegradation of 5 mg/L DCF solution. They used a Xe lamp, 55 W and 50 g/L catalyst. In 96 h of irradiation, the entire drug content was removed [241]. A promising catalysts type Ag_3PO_4/G-C_3N_4 has been prepared by W. Zhang et al. and used for the visible light DCF photodegradation. Their results have shown a total drug photodegradtion in 12 minutes (initial DCF 1 mg/L, catalyst concentration 0.1 g/L), by using a

catalyst with 30 % of Ag_3PO_4 content and a 300 W Xenon lamp. However, the TOC removal was only 43 %. This result is comparable with the one obtained in our study for the ZnGa(3/1) or ZnAl(2/1) catalysts, which are able to degrade more than 83 % in 20 minutes. Furthermore, in our study we used a ratio between the DCF/catalyst (mg/mg) of 1/40, while W. Zhang 1/100 [199].

2.4. Nanoparticles of In or Ga on ZnAlLDH and ZnGaLDH with a LDH Me^{2+}/Me^{3+} ratio=3/1 and their derived mixed oxides for solar photodegradation of phenol and p-nitrophenol.

2.4.1. Introduction

Oxides as In_2O_3 and Ga_2O_3 have been used in photocatalytic process for pollutants removal. A good photoresponse in the photodegradation of methyl orange and rhodamine B [242] was obtained by using In_2O_3 nano-cubes supported on carbon nanofibers. Both pollutants removal yield was about 80 % after 7 h or 8 h of irradiation, respectively. Furthermore, fipronil insecticide [243], methyl orange, rhodamine B, and benzoic acid [244] were UV photodegraded by using β-Ga_2O_3.

The photocatalytic performances of $ZnMe^{3+}$LDHs materials had been found to be useful in designing systems for solar energy conversion, and the idea of the doping LDHs with different materials was first approached by Garcia's group. Recently, our group has proven that supported nanoparticles as Ce_2O_3, AuNPs on ZnMeLDHs (Me = Al, Ti, Sn) present synergetic semiconducting properties and their photoresponses under light stimulation are over those of each separate component [33,34,178].

In this section will be presented the preparation, characterization and utilization of novel catalysts type InNPs or GaNPs on ZnAl(3/1) and ZnGa(3/1) in the solar photodegradation of p-nitrophenol and (phenol + p-nitrophenol) aqueous solutions.

2.4.2. Synthesis and physico-chemical characterization of ZnMeLDHs, their nanostructured assembles type In or Ga/ZnMeLDHs and their derived mixed oxides

Synthesis

The ZnAl(3/1) and ZnGa(3/1) materials were obtained by co-precipitation method, as it was presented in section 2.3.2-b. The hybrid formulation containing InNPs or GaNPs were obtained by using the reconstruction method (see figure 1.32). For this, 2.1 g of fresh ZnAl(3/1) or ZnGa(3/1) were calcined at 550 °C for 8 h and after they were added to a solution of 0.1M $Ga_2(SO_4)_3$*18H2O (Sigma Aldrich, ≥99%) or $In(C_2H_3O_2)_3$ (Sigma Aldrich, ≥99%). The resulted dispersions were mixed for 7 h at 20 °C, afterwards they have been recovered by centrifugation, and drayed at 80 °C. The catalysts were denoted as Ga/ZnAl, In/ZnAl, Ga/ZnGa and Ga/ZnGa. These reconstructed samples were further calcined at 750 °C and the obtained derived mixed oxides were denoted as In/ZnAl-Cal, Ga/ZnAl-Cal, In/ZnGa-Cal and Ga/ZnGa-Cal.

Physicoal-chemically characterization

The materials characterization was made by using the next instruments: the UV-Vis spectra were measured on a V650 JASCO spectrophotometer with an integrating sphere. X-ray patterns were obtained with a Shimadzu diffractometer operating in 2θ mode, between 5-80° The FTIR spectra were performed on a Perkin Elmer Spectrum spectrophotometer, in a range between 450-4000 cm-1, and at a resolution of 4 cm^{-1}. A Hitachi H900 transmission electron microscope coupled with an energy dispersive X-ray spectrometer was used to analyze the elemental composition of the samples. The surface chemical state was analyzed by using a Perkin Elmer Model 5500-MT X-ray photoelectron spectroscope, operating at 20 mA and 15 kV, and being equipped with a Mg Kα radiation.

For the LDHs materials and their reconstructed samples (figure 2.60) the XRD patterns

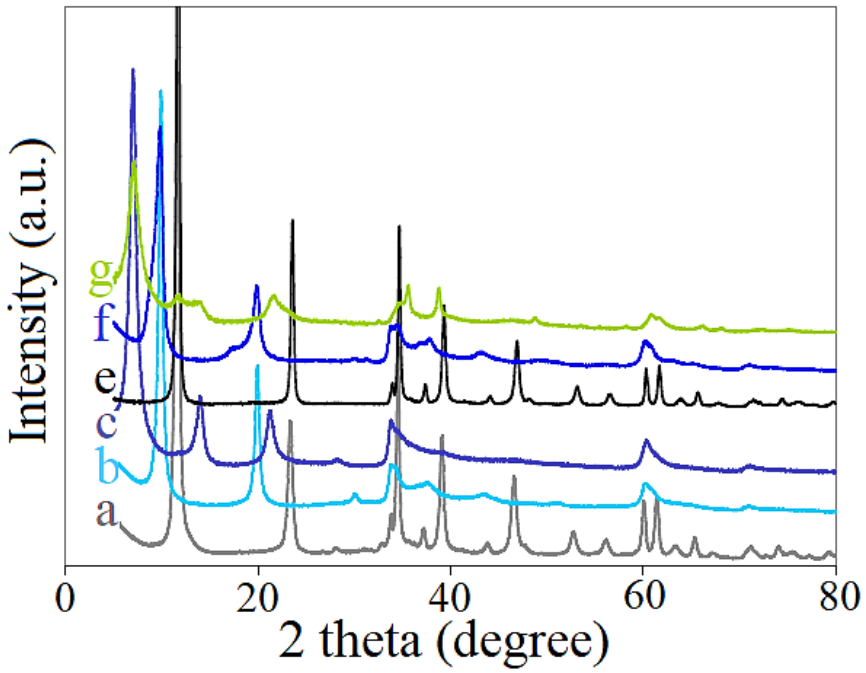

Figure 2.60: XRD patterns for a) ZnAl(3/1), b) Ga/ZnAl, c) In/ZnAl; e) ZnGa(3/1) f) Ga/ZnGa, g) In/ZnGa.

present a regular LDH structure defined by the typical diffraction peaks at 2θ = 11.8˚, 23.6˚, 34.9˚, 37.4˚, 39.5˚, 44.3˚, 47.1˚, 53.1˚, and 56.7˚ assigned to (003), (006), (009), (104), (015), (107), (018), (100), and (1/2 11) diffractions planes of the standard layered structure of LDHs [33]. Furthermore, after the reconstruction in aqueous solutions of $Ga_2(SO_4)_3$ and $In(C_2H_3O_2)_3$, the LDHs structure is totally recovered as proved by the edged and symmetric basal reflections of the ((003), (006), (009)) planes, even if it was observed a much wide and less intense reflections assigned for the non-basal ((012), (015) (018)) planes. This can point out a lower crystallinity and/or a particle size reduction of the crystallites for the LDH hybrids [245]. The presence of gallium or indium was not confirmed by using XRD measurements.

For the reconstruction samples, the (003) peak is much wider and it also shifted to lower 2θ values reflection e.g. 11.67° for ZnAl(3/1) and 11.7° for ZnGa(3/1) to 7.1° for In/ZnAl and 7.03° for In/ZnGa, while for Ga/ZnGa and Ga/ZnAl the values are 9.85° and 9.92°, respectively. This underlines that the reconstruction in $In(C_2H_3O_2)_3$ and $Ga_2(SO_4)_3$ water solution leads to an expanded LDHs structure. The shift of the (003) peaks is a clearly indication that the acetate and sulfate anions were successfully intercalated into the interlayers, which is also confirmed by the increase of interlayer distance (see table 2.7).

The LDHs lattice parameters *a* and *c* are also listed in Table 2.7. The replacement of Al^{3+} with Ga^{3+} cation produce no chance of the *a* lattice parameter, which gives information about the distance between the cation-cation form the LDHs lamella. For the rest of the sample, the *a* parameter suffers no significant value modification underlining that during the reconstruction, the initial order of the cations in the layer was recovered. The change of values

Table 2.7: Crystal size and lattice parameters for the studied catalysts.

				Lattice parameters (Å)	
Sample	***Crystal size (nm)**	**d (003)**	**d (110)**	***a***	***c***
ZnAl(3/1)	13	7.61	1.54	3.08	22.67
Ga/ZnAl	15	8.91	1.54	3.07	26.92
In/ZnA	9	12.56	1.53	3.06	37.32
ZnGa(3/1)	22	7.56	1.53	3.07	22.67
Ga/ZnGa	8	8.97	1.53	3.07	26.92
In/ZnGa	7	12.44	1.53	3.04	37.69

*crystal size calculated with Scherrer equation; $a = 2d_{110}$ and $c = 3d_{003}$ are the unit lattice parameter.
d(003) and d(110) were calculated with Bragg's law

for the *c* lattice parameter indicates that the acetate and sulfate anions have successfully replaced the carbonate anions from the initial ZnAl(3/1) and ZnGa(3/1) materials [246].

During the calcination at 750 °C the layered structure suffers successive changes, and the XRD spectra present a high complexity. For the ZnGa-Cal and Ga/ZnGa-Cal samples (figure 2.61), the main phase is the $ZnGa_2O_4$ spinel, presenting peaks at 30.4°, 35.7°, 43.4°, 54°, 57.4° and 63 ° assigned to (220), (311), (400), (422), (511), (440) planes [247]. ZnO is also present in the structure and it can be attributed to the 31.8°, 34.3° and 36.4° [124]. Furthermore, a peak around 19.6° can be assigned to β-Ga_2O_3 presence indexed as (201) [248].

The calcination of In/LDHs leads to less crystalline materials (see figure 2.62), formed also by spinels like phase and ZnO, while In_2O_3 is shown by the peaks at 21.6°, 30.8°, 33.5°, 37°, 45.6°, 51° and 61° [249].

The EDX measurements provided information about the elemental composition of the samples (see figure 2.63), which is listed in table 2.8. Because the Zn and Ga have near values of the binding energy (1.012 eV and 1.098 eV) [250], their corresponding peaks are not so well determined. For the In/ZnGa sample, In_2O_3 is the main phase, underlining that the indium oxide is a distinctive phase on the ZnAl(3/1) samples surface. This result is well correlated with XRD data which detected the indium oxide in cubic phase. For the reconstructed samples in gallium sulfate, it was noticed an increase of gallium content, probably due to the formation of $ZnGa_2O_4$, which has a high content of gallium.

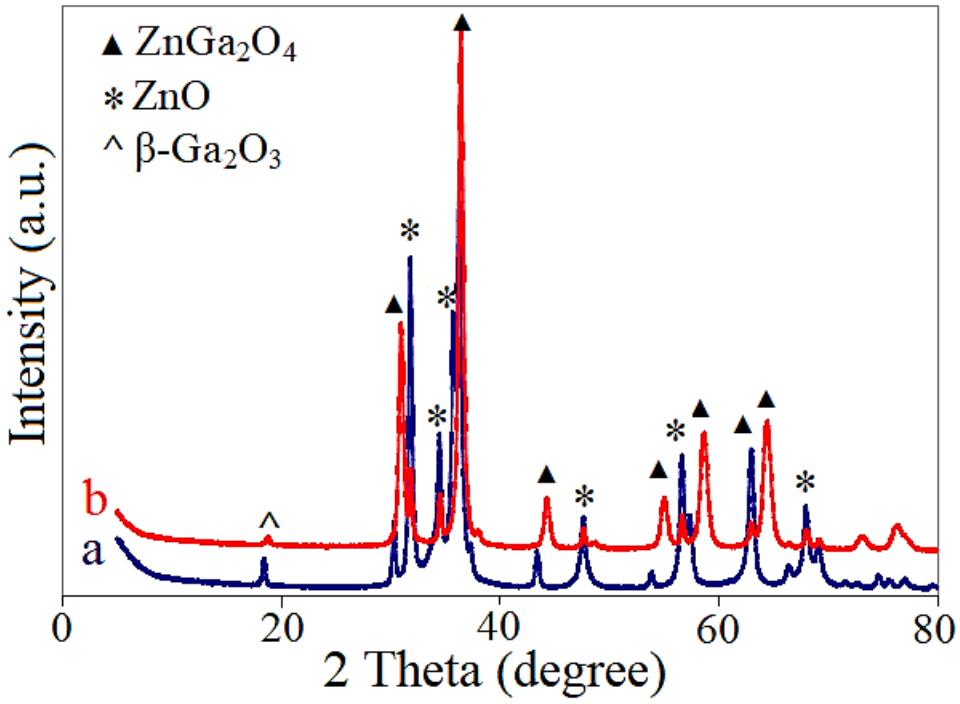

Figure 2.61: XRD patterns for a) ZnGa-Cal and b) Ga/ZnGa-Cal.

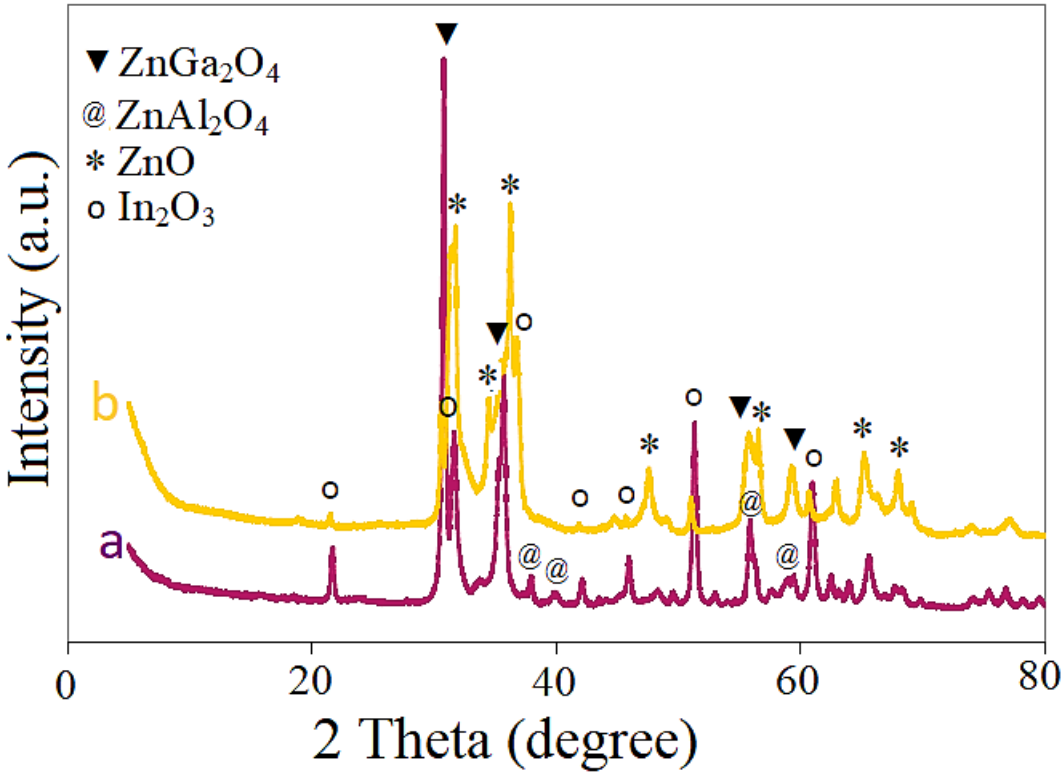

Figure 2.62: XRD spectra for a) In/ZnAl-Cal and b) In/ZnGa-Cal.

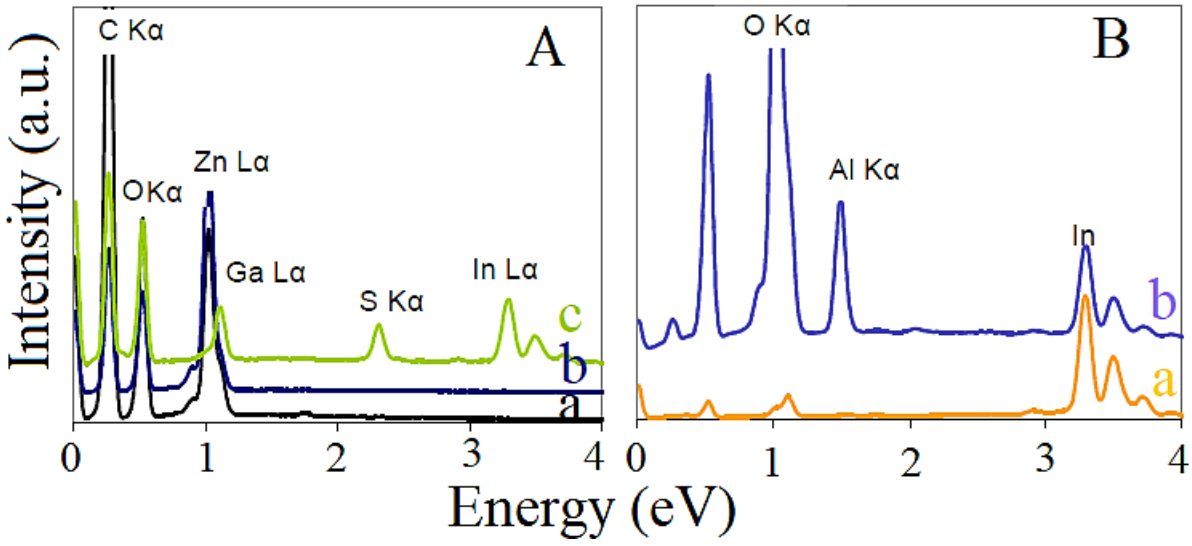

Figure 2.63: EXD spectra for A) a)ZnGa(3/1), b) ZnGa-Cal, c) In/ZnGa; B) a) In/ZnAl, b) In/ZnAl-Cal.

Table 2.8: Elemental composition based on EDX data for representative samples.

Sample	Zn	Ga	Al	In	S
ZnAl(3/1)	66	-	34	-	-
Ga/ZnAl	5	57	34	-	7
Ga/ZnAl-Cal	52	11	37	-	-
In/ZnAl	64	-	32	4	-
In/ZnAl-Cal	61	-	34	5	-
ZnGa(3/1)	68	32	-	-	-
ZnGa-Cal	77	23	-	-	-
Ga/ZnGa	47	44	-	-	9
Ga/ZnGa-Cal	57	43	-	-	-
In/ZnGa	61	35	-	4	-

The nature of the sample functional groups was investigated by using FTIR analysis. The FTIR spectrum (figure 2.64) presents the characteristic vibration bands of the layered double hydroxides with a broad absorption band around 3450 cm^{-1} associated with the O-H stretching of hydroxyl groups of LDHs from brucite-like layer and the physisorbed water [1]. It is followed by a broad shoulder at 3000 cm^{-1}, which is presented only in the spectrum of ZnAlLDH, and by an absorption peak at 1626 cm^{-1} assigned to H-O-H bending vibration of interlayer water molecules which are connected to the anions molecules through hydrogen bonds. The peaks corresponding to the M-O and O-M-O (M = Zn, Al, Ga), are observed between 800-400 cm^{-1} [22]. For the initial LDHs samples, obtained by co-precipitation, the interlayer anion is CO_3^{2-} with an intense peak at 1360 cm^{-1} and two small peaks at 833 cm^{-1} and 1505 cm^{-1} corresponding to the symmetric and antisymmetric bending vibrations [220]. After the reconstruction, in the structure of the new LDHs materials the presence of new anions can be observed. For the samples reconstructed in $In(C_2H_3O_2)_3$ aqueous solution it can be identified the presence of COO^- anions with two absorption bands at 1566 cm^{-1} and 1415 cm^{-1} corresponding to the antisymmetric and symmetric stretching modes and one at 1368 cm^{-1} which is assigned to the binding vibration corresponding to $–CH_3$ groups from the acetate ion [251]. In case of the samples reconstructed in $Ga_2(SO_4)_3$ it can be identified the vibration bands corresponding to interlayer SO_4^{2-} anions at 1112 cm^{-1}, 980 $cm^{-1}$and 672 cm^{-1} [35,252].

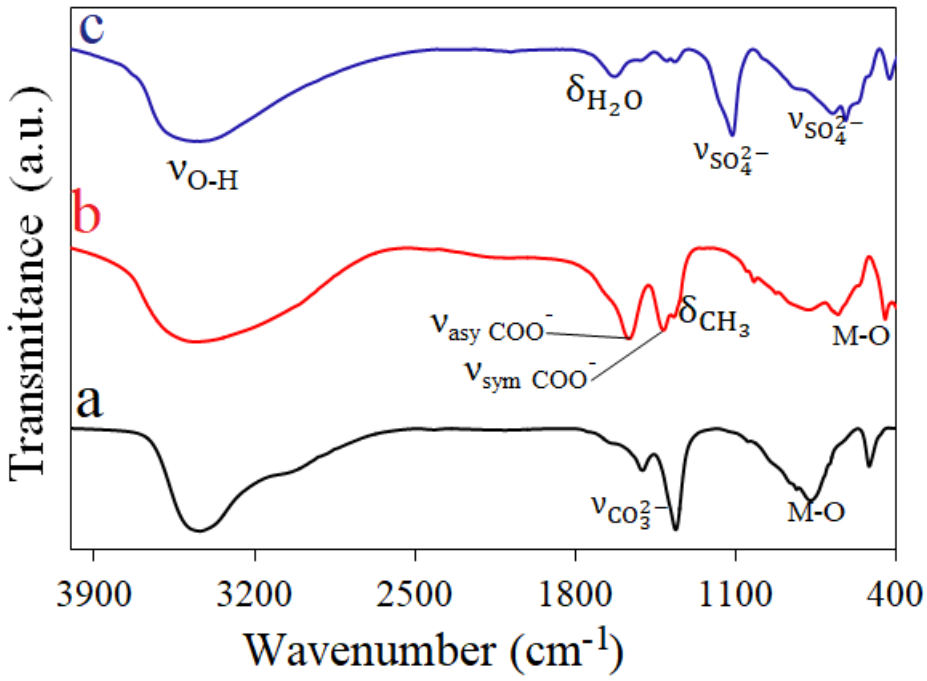

Figure 2.64**:** FTIR spectra a) ZnAl(3/1), b) In/ZnAl, c) Ga/ZnAl.

The surface state of the tested materials was investigated by XPS analyze. In figure 2.65 are presented the full XPS spectra of ZnGa-based samples and they demonstrate the existence of the Zn 2p, Ga 2p, and O 1s core levels. The insert presents the high resolution spectra of Ga $2p_{1/2}$ with the binding energy at 1145.1 eV which is an indication of the fact that on the LDH surface, gallium is in its oxide state, Ga_2O_3 [253]. The characteristic XPS spectra for the In/ZnGa and the typical pecks of Ga, In and O are shown in figure 2.66. Because the peaks for Ga 3d3/2 and Ga 2p1/2 are faintly asymmetrical they can be decovoluted in two, as presented in figure 2.66 b-c. The deconvoluted Ga 2p and Ga 3p peaks suggest that probably gallium is present in In/ZnGa as Ga^{3+} and probably as gallium metal or superoxide (Ga-O-Ga). The presence of In3d is indicated by the two symmetrical peaks at 445.33 and 452.91 eV, which underline that the indium is in its oxide state (figure 2.66-d). The O1s region from figure 2.66-e confirms the binding from gallium and indium oxide in the solids via a wide and asymmetrical peak in the 535-525 eV range. This peak can be deconvoluted in two peaks with a maximum at 531.96 and 530.78 eV assigned to Ga_2O_3 and In_2O_3, respectively [254]. In table 2.9 are presented the signals position for the studied samples.

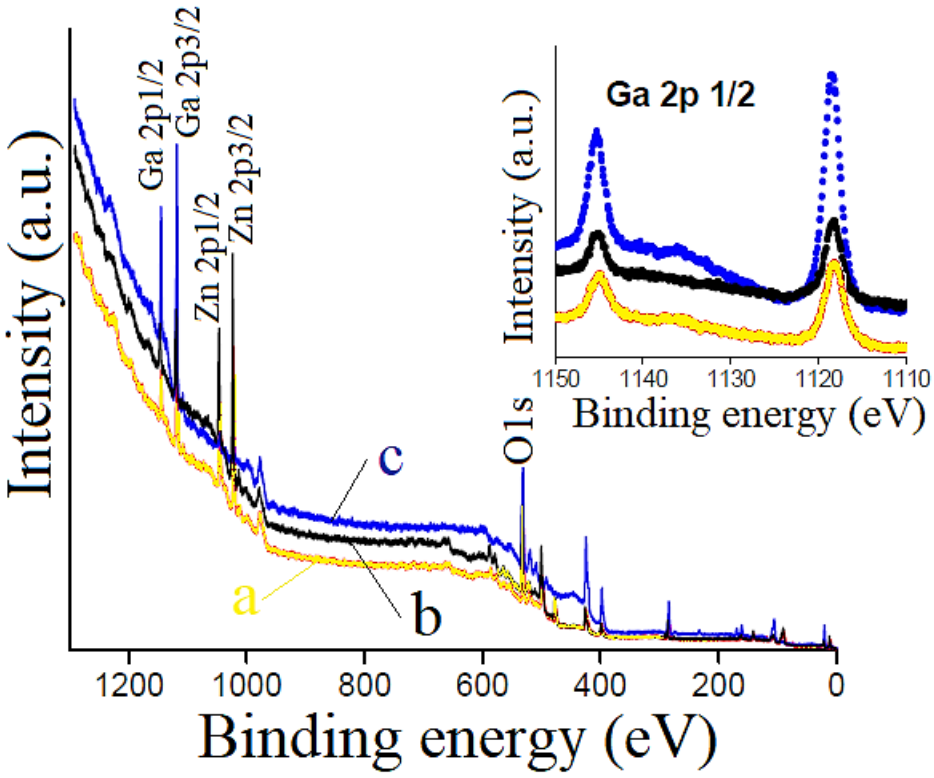

Figure 2.65: XPS spectra of a) Ga/ZnGa-Cal, b) ZnGa(3/1), c) Ga/ZnGa.

In case of the semiconductor materials an important information is the band gap value, which is the difference between the conduction and valence band energies. For the electron transfer from the valence band to the conduction band, the applied energy must be higher than the value of the semiconductor band gap. Generally, the band gap can be easily determined from the UV-Vis analysis, by extrapolating the linear region of the spectrum. Another way to obtain the band gap is to use the Tauc plot [255] which is a representation between $\alpha h\nu^n$ versus $h\nu$ (eq.2.18.):

$$\alpha h\nu = A(h\nu - Eg)^n \quad (2.18)$$

where :

- α is the absorption coefficient,
- h is Plank constant,
- n is dependent on the electronic transition and it can be 1/2, 3/2, 2, 3;
- A is the absorbance and
- ν is the light frequency.

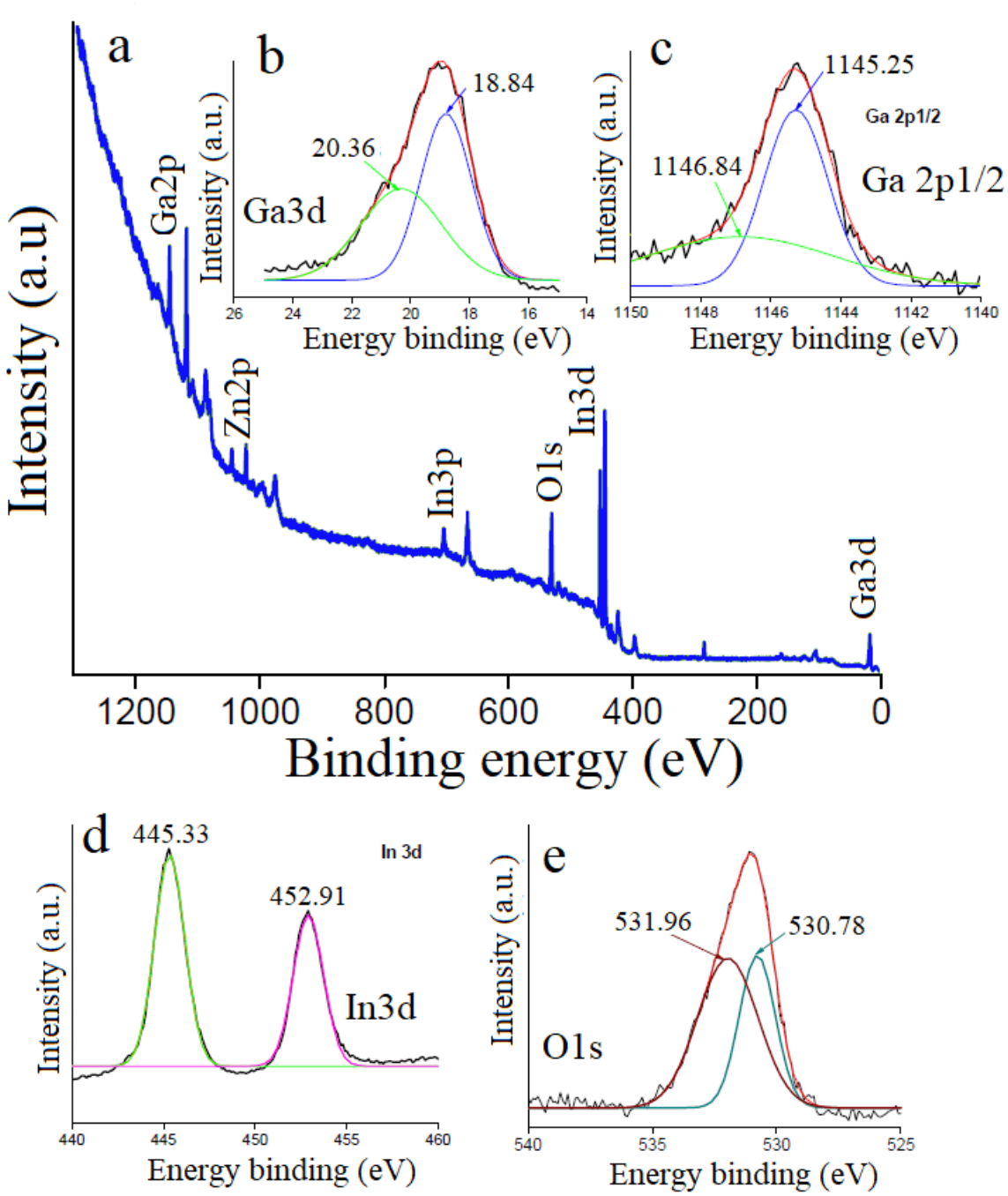

Figure 2.66: XPS spectra for a) In/ZnGa, and high resolution spectra for b) Ga3d, c) Ga2p1/2, d) In3d, e) O1s.

The UV-Vis spectra of the synthetized materials are given in figure 2.67, and the band gap values determined from Tauc plots are listed in table 2.10. The results show that the initial LDHs precursors, ZnAl(3/1) and ZnGa(3/1), can absorb only UV light with wavelengths lower

Table 2.9: XPS binding energies for gallium and oxygen.

Sample		Ga 2p1/2	Ga2p3/2	Ga2p3/2	O1s
ZnGa(3/1)		1145.2	1118.3	20.2	531.8
Ga/ZnGa		1145.3	1118.3	20.36	531.7
Ga/ZnGa-Cal		1145.0	1118.1	20.12	531.1
References	Oxide	1145	1117.4	20.4	531.96
[250,253,256]	Metal	1143		18.6	

Table 2.10: Band gap values for the studied materials.

Sample	Band gap, eV	Sample	Band gap, eV
ZnGa(3/1)	3.95	ZnAl(3/1)	3.57
Ga/ZnGa	2.83	Ga/ZnAl	2.92
Ga/ZnGa-Cal	2.75	Ga/ZnAl-Cal	2.84
In/ZnGa	2.92	In/ZnAl	3.1
In/ZnGa-Cal	2.81	In/ZnAl-Cal	2.74

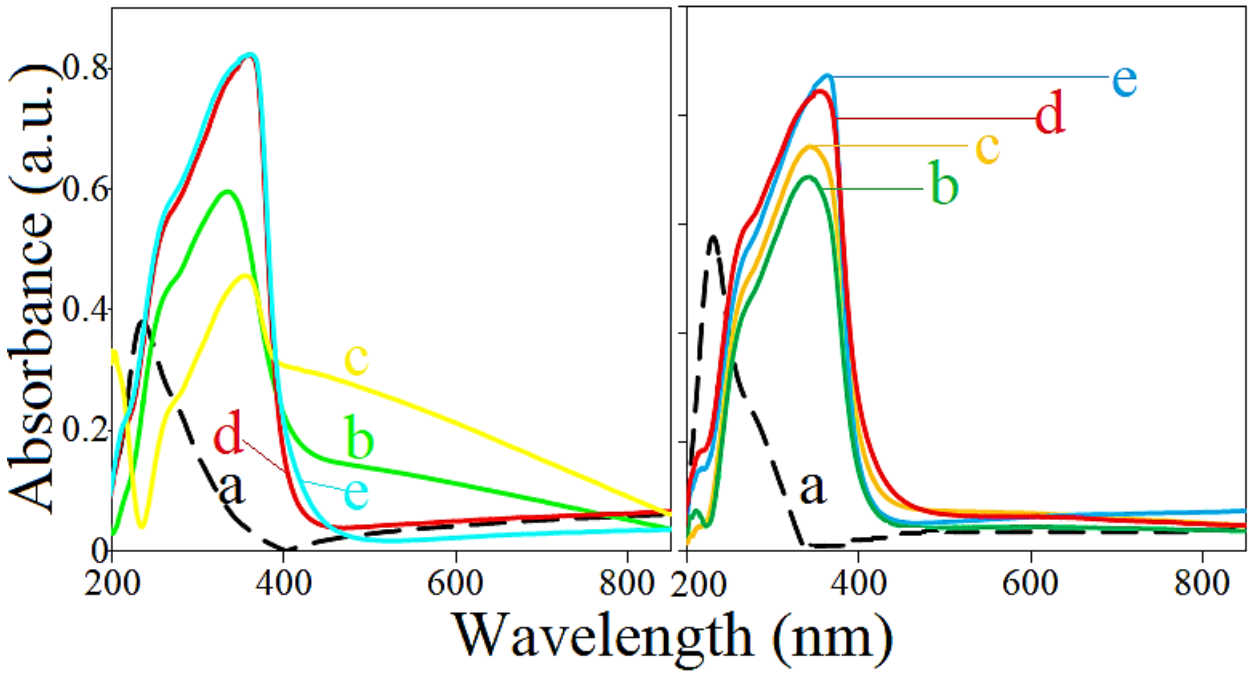

Figure 2.67: UV-Vis spectra for A) a) ZnAl(3/1), b) Ga/ZnAl, c) In/ZnAl, d)Ga/ZnAl-Cal, e) In/ZnAl-Cal; B)) a) ZnGa(3/1), b) Ga/ZnGa, c) In/ZnGa, d) Ga/ZnGa-Cal, e) In/ZnGa-Cal.

than 400 nm. After the reconstruction in presence of indium or galium, the initial band gaps of

ZnAl(3/1) and ZnGa(3/1) were changed from 3.57 and 3.95 eV to smaller values, indicating that the new materials can be activated also by the visible light, since the limit band gap between the UV and visible region is 3.1 eV. The changes of the absorption capacities in case of supported nanoparticles on larger surfaces can be an indication of the physicl phenomenon denoted as band –bending, and not necessary a modification of the initial band gap of the support. In this case, the changes of the UV-Vis spectra are a consequence of the supported nanoparticles absorption characteristics. In this context, a clear distinction between the band-gapping and band-binding is difficult to establish for the studied materials [257].

2.4.3. ZnAl(3/1)LDH, ZnGa(3/1)LDH, their nanostructured assembles type In or Ga/ZnAl(3/1)LDH and In or Ga/ZnGa(3/1)LDH and their derived mixed oxides for solar photodegradation of p-nitrophenol.

In this section are presented the photocatalytic performances of ZnAl(3/1), ZnGa(3/1) composites, their hybrid formulations with gallium and indium and their derived mixed oxides for the solar degradation of p-nitrophenol (p-nPh). The tests were carried out following the protocol presented at the begging of this chapter. The blank tests show no significant photolysis of the pollutant. During the adsorption-desorption equilibrium, it was observed that the initial absorption maximum of the p-nitrophenol was shifted from 317 nm to 400 nm, thus the photocatalytic degradation of the pollutant was monitored by UV-Vis measurements, following the evolution of the absorbance at 400 nm. From figure 2.68 and 2.69 can be observed that for all the catalysts based on ZnAl(3/1) and ZnGa(3/1) the absorbance decrease gradually in time till a maximum of 99.5 % degradation was obtained with the In/ZnAl-Cal sample. The parents materials are almost inactive, with less than 5 % of p-nPh photodegradation, while the materials resulted after the reconstruction in presence of Ga and In, and also their derived mixed oxides, present a significant enhancement of photoresponse, as presented in figure 2.68-f and 2.69-f.

The presence of gallium in the lamella induces an increase of activity for the NPs/ZnGaLDHs. Furthermore, the presence of indium on the LDHs surface is more beneficial for the activity than gallium, even if they have similar values of the band gap. This can be explained by a synergy between the absorption abilities and some structural characteristics of indium that make it more efficient. The photodegradation reactions follow a pseudo-first-order kinetic. The apparent constants rate (k_{app}) were determined from the slope of $-\ln(A/A_{max})$ vs t plots, where A value represents the normalized absorbance at 400 nm at different time intervals. The half-life time $t_{1/2} = 0.693/k_{app}$. The results are presented in figure 2.70 and table 2.11.

The data are in good concordance with the UV-Vis spectra evolution and the kinetic data show that p-nPh is most quickly degraded when the reaction is initiated by In/ZnAl-Cal. This evolution can be explained by the previous data which have shown that indium can stabilize the electron-hole pair of the material [258]. Nevertheless, the ZnGa-based materials,

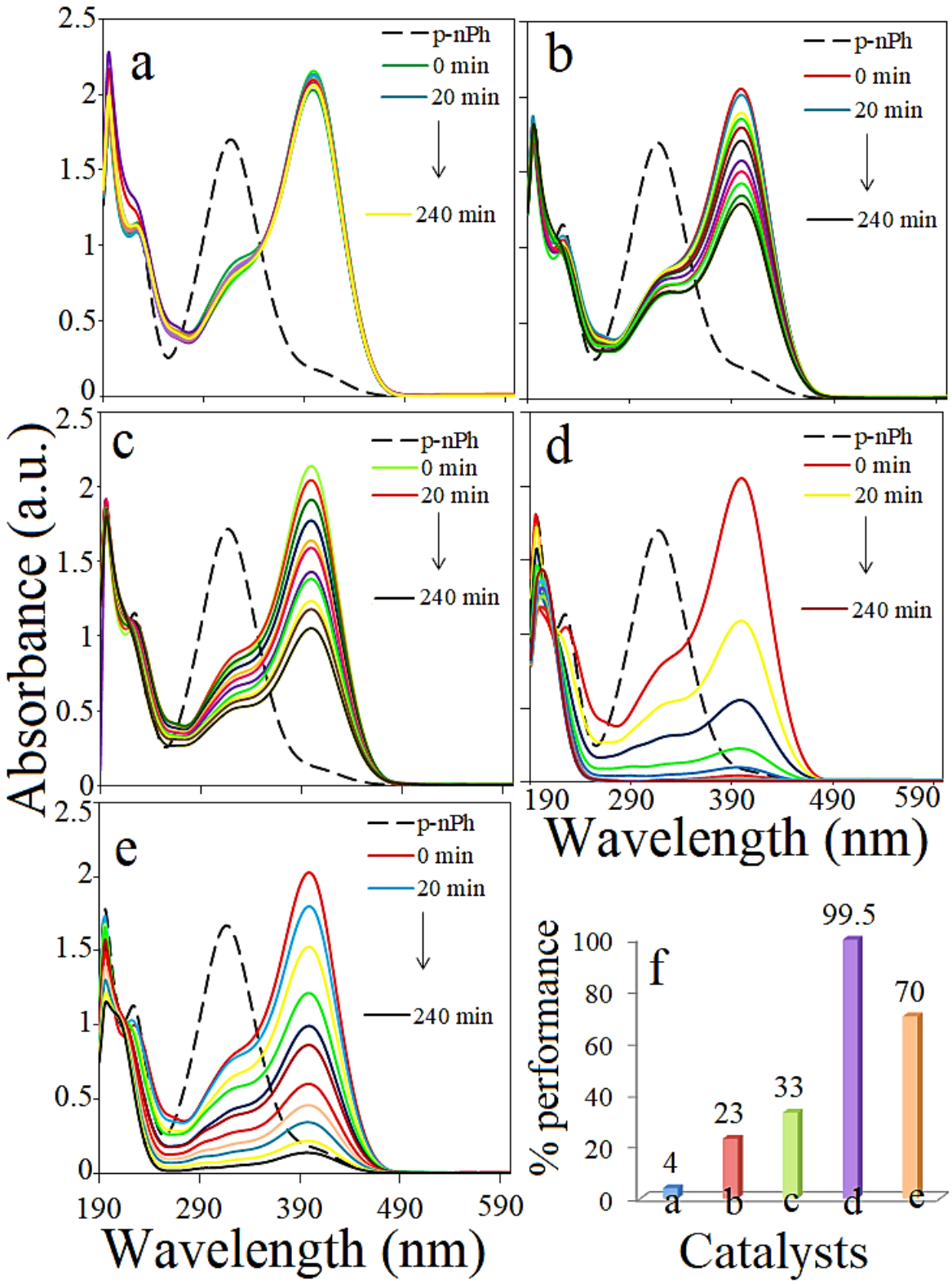

Figure 2.68: UV-Vis spectra of p-nPh for a) ZnAl(3/1), b) In/ZnAl, c) Ga/ZnAl, d) In/ZnAl-Cal, e) Ga/ZnAl-Cal, f) photocatalytic performance.

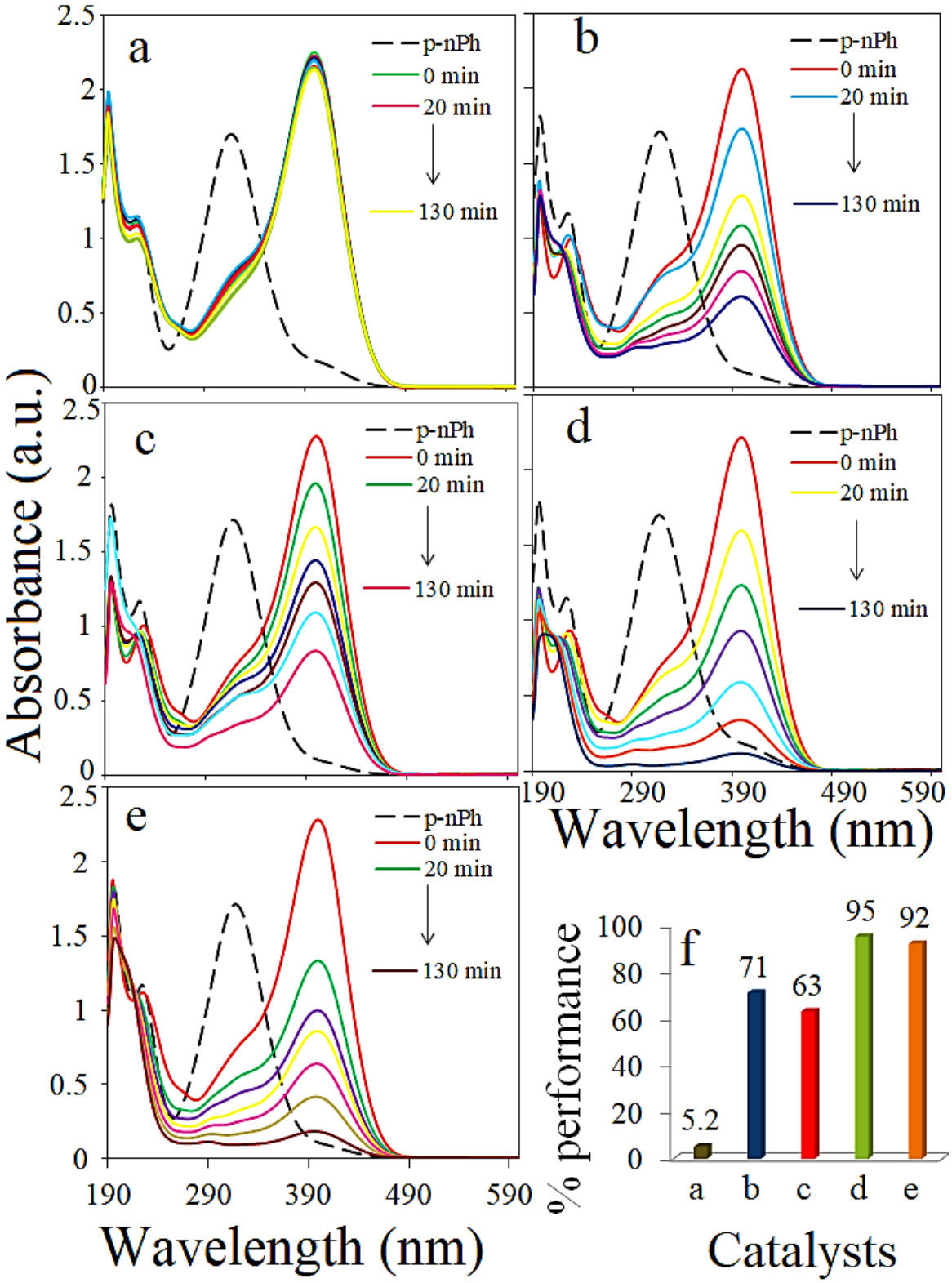

Figure 2.69: UV-Vis spectra of p-nPh for a) ZnGa(3/1), b) In/ZnGa, c) Ga/ZnGa, d) In/ZnGa-Cal, e) Ga/ZnGa-Cal, f) photocatalytic performance.

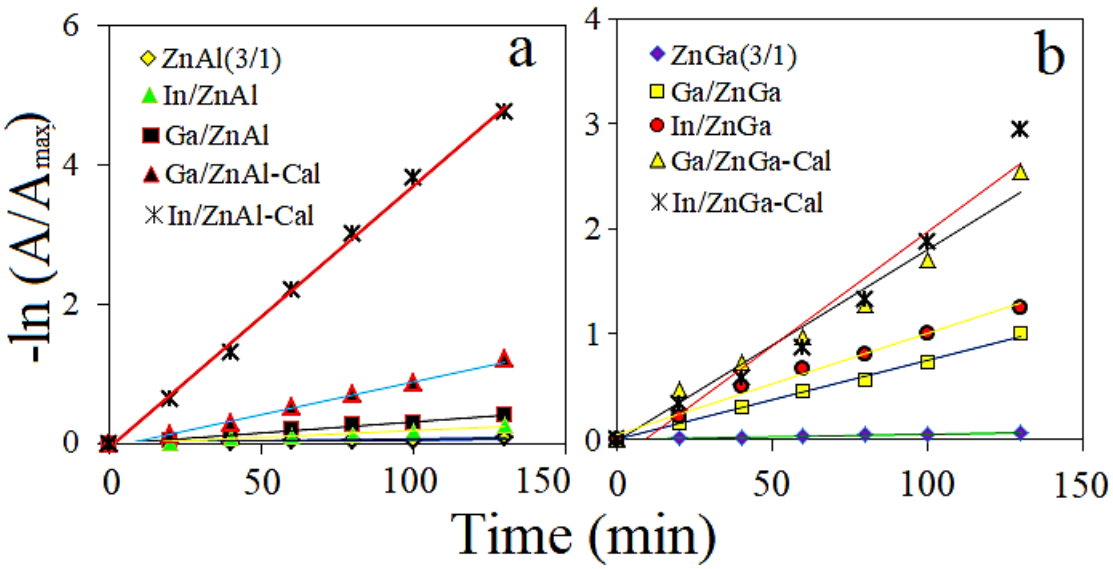

Figure 2.70: The natural logarithm of the normalized absorbance vs degradation time for p-nPh for a) ZnAl(3/1) materials and b) ZnGa(3/1) materials.

Table 2.11: Kinetic results for the photodegradation processes.

Sample	k_{app} (x 10^{-3} min^{-1})	$t_{1/2}$ (min)	Sample	k_{app} (x 10^{-3} min^{-1})	$t_{1/2}$ (min)
ZnGa(3/1)	0.4	1732	ZnAl(3/1)	0.5	1386
Ga/ZnGa	7.5	92	Ga/ZnAl	3.2	217
Ga/ZnGa-Cal	18	38	Ga/ZnAl-Cal	9.7	71
In/ZnGa	9.6	74	In/ZnAl	2.2	347
In/ZnGa-Cal	19.5	36	In/ZnAl-Cal	37.9	19

except ZnGa(3/1) and In/ZnGa-Cal, reached a double degradation rate compared with the ZnAl-based catalysts, in only 130 minutes of reaction.

In order to appreciate the mineralization degree and the decomposition products, TOC (Shimatzu analyser) and HPLC (SPD-20A Shimadzu) measurements were performed. For an accurate identification of the products, standard solution of benzoquinone, muconic acid, catechol and resorcinol were used. The TOC results, showed that the In/ZnAl-Cal can mineralize in 4 h 87 % of p-nPh, while the Ga/ZnAl-Cal only 60 %. The HPLC data confirmed that the hydroxyl radicals interact with p-nitrophenol, which lead via indirect p-nPh ring cleavage to hydroxylated phenolic compounds, as presented in figure 2.71.

In order to evaluate the catalyst stability, three consecutive tests were performed in the same experimental conditions, by using In/ZnAl-Cal. After each test, the catalyst was recovered, washed and reused. The results after three tests showed no loss of the initial activity.

Regarding other research on the same topic, in a recent study, Zhang and co-workers obtained derived mixed oxides starting with ZnNiAlLDH. They tested their materials for the

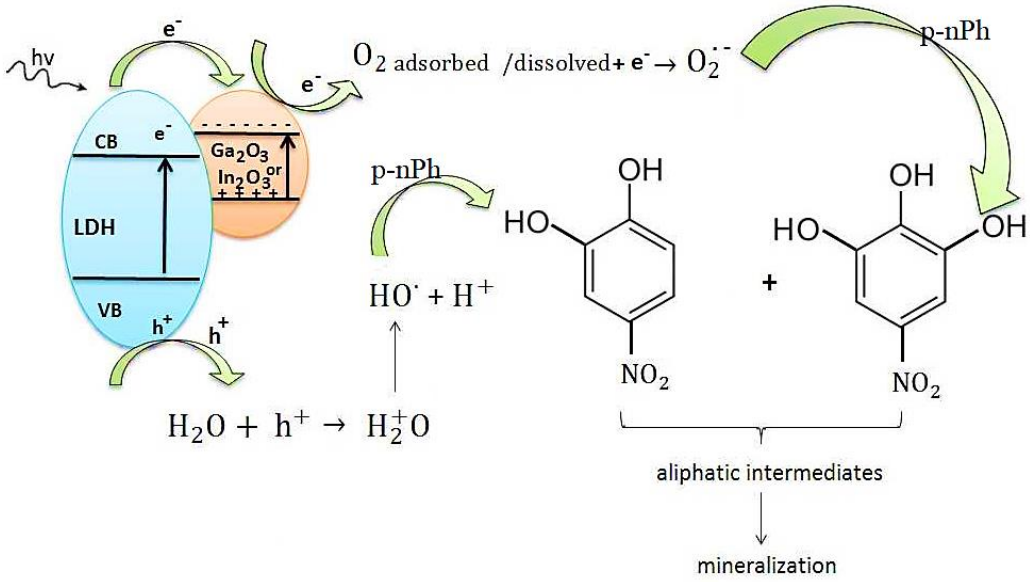

Figure 2.71: Proposed mechanism for the p-nPh solar photodegradation in presence of the studied catalysts.

visible light phorodegradation of a 10 mg/L p-nPh solution, using 1g/L catalyst. The irradiation was provided by a Xe lamp, 500 W. Their results have shown that in 180 minutes, the parent material, ZnNiAlLDH degrades 16.7 % of the initial concentration. Furthermore, the kinetic study revealed that the calcined LDH in a temperature range between 500-800 °C have $t_{1/2}$ between 46-325 min [259]. Compared with this study, our materials present better photo-response, taking in consideration that the pollutant concentration was 25mg/L, and the power of the lamp was 180 W. In another study realized on TiO_2, under UV light and using 14 mg/L pollutant and 4g/L catalyst, after 2 h of irradiation, only 90 % of the p-nNP was removed [197]. In this context, our materials can be considered as promising catalysts in the photodegrade of p-nPh.

2.4.4. ZnAl(3/1)LDH, the nanostructured assembles type In or Ga/ZnAl(3/1)LDHs and their derived mixed oxides for solar photodegradation of (phenol + p-nitrophenol) mixtures.

In this section are presented the photocatalytic performances of ZnAl(3/1)LDH, their hybrid formulations with gallium and indium and their derived mixed oxides for the solar degradation of a (p-nitrophenol + phenol) solution. The total concentration of the pollutant solution was 50 mg/L (25 mg p-nPh + 25 mg Ph), and the catalyst concentration was 1g/L. After the adsorption-desorption equilibrium, a shift from 317 nm to 400 nm was observed and it corresponds to the formation of the p-nitrophenolate anion [260]. The degradation was monitored by the absorbance evolution at 270 nm and 400 mn. In figure 2.72 are presented the

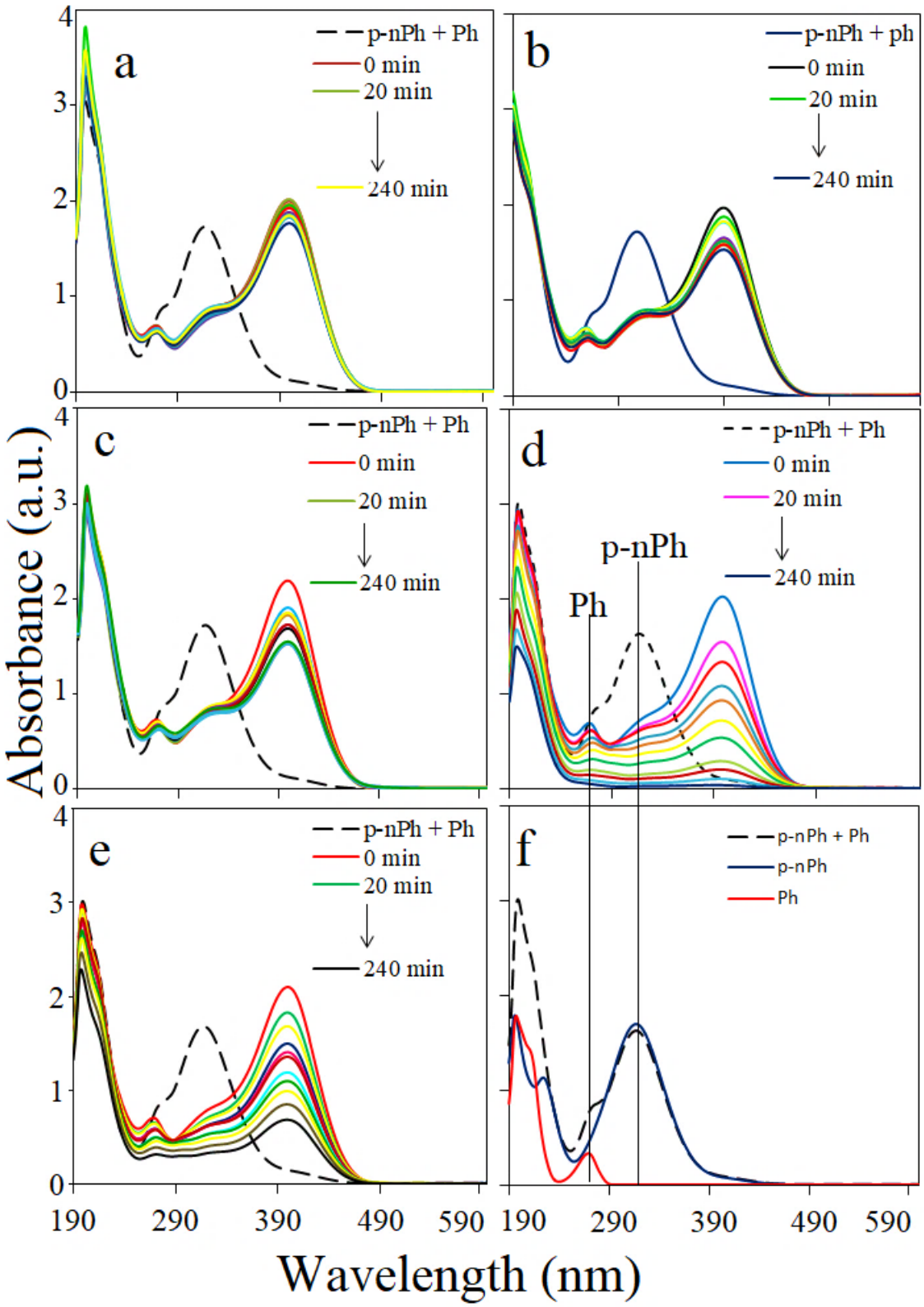

Figure 2.72: UV-Vis spectra of (p-nPh + Ph) for a) ZnAl(3/1), b) In/ZnAl, c) Ga/ZnAl, d) In/ZnAl-Cal, e) Ga/ZnAl-Cal, f) Ph, p-nPh and Ph + p-nPh spectra.

UV-Vis profiles for the studied catalysts. Also a correspondence between the UV-Vis spectra of 25 mg/L standard solutions of phenol, p-nitrophenol and (Ph + p-nPh) can be observed in figure 2.72 d, f. It might be observed that for all the catalysts the absorbance at 270 nm and 400 nm decrease during the time and the less performant catalyst is the parent ZnAl(3/1), with 4 % degradation of phenol and 7 % degradation of p-nPh (see figure 2.73). The most performant catalyst is In/ZnAl-Cal with a photocatalytic performance of 89 and 98 % of phenol, p-nitrophenol removal in 240 minutes.

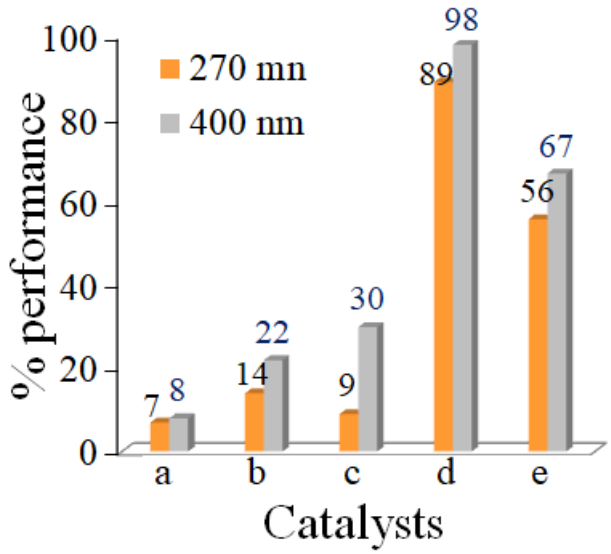

Figure 2.73: Photocatalytic performance for (p-nPh +Ph) solar photodegradation for a) ZnAl(3/1), b) In/ZnAl, c) Ga/ZnAl, d) In/ZnAl-Cal, e) Ga/ZnAl-Cal.

The photodegradation of the solution constituents follows a pseudo-first order reaction. In figure 2.74 is presented the dependence $-\ln(A/A_{max})$ and t. In table 2.12 are listed the k_{app} and the half-life time, $t_{1/2}$ calculated on the basis of the lines slopes.

The kinetic results show that the reconstruction in presence of indium and the thermal treatment at 750 °C leads to a catalyst, In/ZnAl-Cal, able to degrade more the 50% from the initial pollutants concentration in 60 minutes. The Ga/ZnAl-Cal have a half-life 10 times smaller for the degradation of p-nitrophenol and 7 times smaller for the degradation of phenol compared with that of ZnAl(3/1). For the In/ZnAl-Cal these values decrease considerably, compared with the parent material. Thus, the deposition of the metallic oxides on LDHs surface improves the catalytic efficiency of the layered systems. Furthermore, the semiconductor solid materials composed by a spinel phases homogenously dispersed in a metallic oxide phase have the highest photocatalytic performance for the decomposition of complex systems of pollutants.

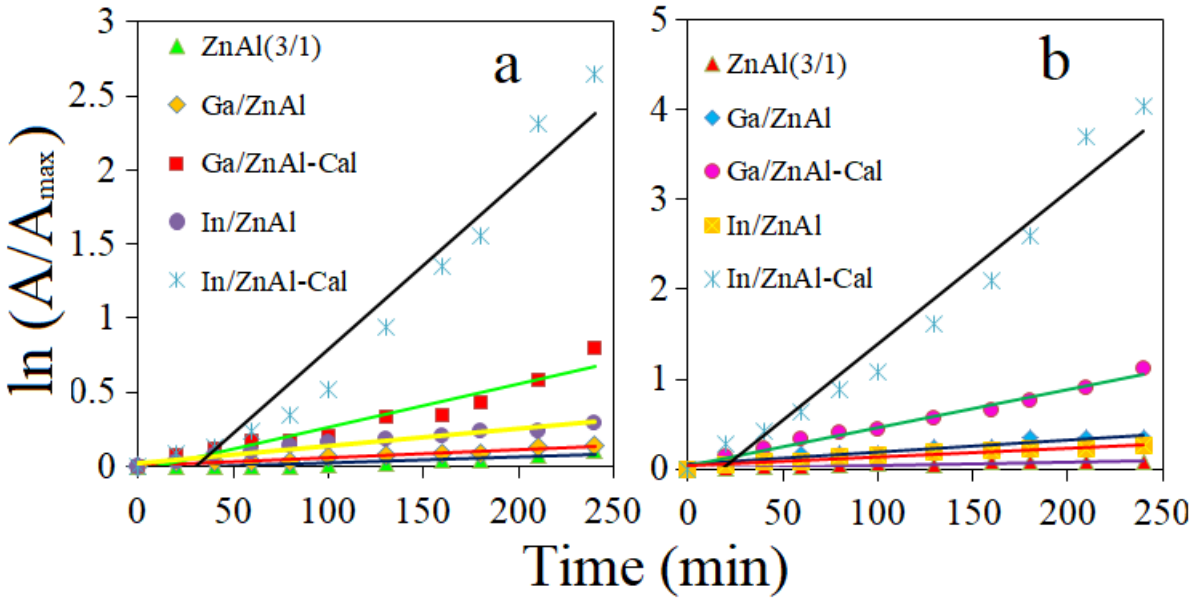

Figure 2.74: Natural logarithm of the normalized absorbance vs degradation time for a) Ph at 270 nm and b) p-nPh at 400 nm.

Table 2.12: Kinetic results of the photodegradation processes.

Sample	k_{app} (x 10^{-3} min^{-1}) for Ph	$t_{1/2}$ (min) for Ph	k_{app} (x 10^{-3} min^{-1}) for p-nPh	$t_{1/2}$ (min) for p-nPh
ZnAl(3/1)	0.4	1732	0.4	1732
Ga/ZnAl	0.5	1386	1.3	533
Ga/ZnAl-Cal	2.9	239	4.2	165
In/ZnAl	1.1	630	1	693
In/ZnAl-Cal	11.3	61	17	41

Based on the results expressed above, the materials based on Zn(Me=Al, Ga)LDHs and their reconstructed and calcined derivatives are excelent new materials able to be involved in water decontamination via photodegradation route, including also systems composed by one or more pollutants.

2.5. Conclusions

Chapter 2 has opened the original research part of this thesis. It presented the synthesis, the physico-chemical characterization of LDHs, NPs/LDHs and their derived mixed oxides, for further utilization in the solar photodegradation of organic pollutants. LDHs based materials are semiconductors and because of this property they can generate under irradiation reactive

species, which can be involved in the oxidation of organic pollutants. However, the ordinary LDHs composites, like ZnAlLDH or MgAlLDH have low photocatalytic performances because a phenomenon called recombination. To solve this problem, two protocols have been used: the fabrication of NPs/LDHs by approaching the reconstruction method, in presence or absence of UV-Vis light, or the synthesis of mixtures of mixed oxides (MMO), by applying a thermal treatment to a precursor LDH material.

Starting from this, subchapter 2.2 presented the fabrication protocols of nanoparticles of gold and silver on ZnAlLDH with a Me^{2+}/Me^{3+} ratio=2/1; 3/1; 4/1 and on ZnGaLDH with a Me^{2+}/Me^{3+} ratio=2/1. The obtained nanocomposites were used for the solar photodegradation of specific organic pollutants as phenol, achetophenone, p-nitrophenol.

The characterization techniques have shown that the obtained materials have a typical hydrotalcite structure, good crystallinity, and the presence of the Ag and Au in the structure was also confirmed.

The photodegradation of phenol under solar light and in presence of different gold containing LDHs revealed that the LDH reconstruction assisted by light can lead to performant materials, as for example Au/ZnAl(2/1)-R-3-Lg, which was able to degrade all the pollutant quantity in less than 4 hours. In a separate study, was demonstrated that formulations type Au/ZnAlLDHs with a $Me^{2+/}Me^{3+}$ ratio of 2/1; 4/1 can be capable to photo-decompose complex pollutant systems, as for example a solution containing phenol and p-nitrophenol (1/1,w/w). Furthermore, in this case, the performance of the materials increases with the increase of the Zn contain, while the thermal treatment at 750 °C leads also to an enhancement of materials activity.

The acetophenone decomposition was carried out by using different LDH materials type Au/ZnAlLDH, Au/ZnGaLDH and Ag/ZnGaLDH. The obtained results showed that the most performant nanocomposites are those containing gold, and also in this case the clays reconstructed under solar light presented a higher photo-response, compared with those obtained in absence of irradiation. All the investigated materials are able to solar photo-decompose more than 50 % of pollutant, while the best catalysts are capable to degrade all the acetophenone quantity in 130 minutes.

The next subchapter has presented the synthesis of novel and stable hybrid heterostructures based on ZnLDH (ZnAlLDH, ZnCoAlLDH and ZnGaLDH) with a $Me^{2+/}Me^{3+}$ ratio of 2/1; 3/1 and g-C_3N_4, obtained in a simple way and with a low cost by combining the co-precipitation method followed by structural reconstruction or impregnation fabrication steps. All the materials had hydrotalcite structure and the presence of the graphitic carbon nitride into the hybrid structure was confirmed. The obtained catalysts were used to solar photodegrade DCF. It has been demonstrated that between the catalyst and DCF a charge transfer complex is formed. During the photocatalytic tests carried out under solar and UV irradiation, the DCF is decomposed through different pathways. All the samples have shown a high photocatalytic response, and the best catalyst were ZnCoAlLDH(2/1), ZnAlLDH(3/1) and ZnGaLDH(3/1), with a photocatalytic performances of 84 %, 83 % and 100 % respectively,

according to the TOC measurements. From LDHs-CN hybrids, the ZnAl-CN-I samples (2/1 and 3/1) presented an activity improvement with respect to the fresh pristine ZnAlLDHs materials.

The last part of the second chapter approached the fabrication of nanocomposites type In/ZnAlLDH, In/ZnGaLDH, Ga/ZnAlLDH, Ga/ZnGaLDH and their derived mixed oxides for further utilization in the solar degradation of p-nittrophenol and a pollutants solution containing a mixture of phenol and p-nitrophenol. The materials physico-chemical analyses proved that the layered structure was recovered after the applied treatments (calcination and rehydration). Furthermore, the presence of indium and gallium oxide on the clay surface was confirmed. The photocatalytic results have shown that the thermal treatment of NPs/ZnLDHs materials leads to highly preformat nanocomposites able to remove more than 90 % of p-nitrophenol, the best catalyst being In/ZnGa-Cal, able to photodegrade 95 % of pollutant in 130 minutes. When used in a more complex pollutants solution, the obtained materials were efficient for both pollutant degradation, with a maximum of degradation obtained for the In/ZnGa-Cal hybrid, which was able to remove 89 % of phenol and 98 % of p-nitrophenol.

Considering all the photocatalytic result displayed in this chapter, can be concluded that the dispersion of different nanoparticles on a clay matrix has a beneficial effect for the photocatalytic performance of the final nanocomposite. Furthermore, the reconstruction under solar light favors the fabrication of materials where the gold is present in both Au^0 and Au^{3+} state and this can be an explanation for the high photocatalytic performance of these heterostrutures. Additionally, the thermal treatment and the increase of the Zn content in LDH matrix lead also to an enhancement of the photo-response of the resulted hybrids.

3. Biohybrid systems based on layered double hydroxides for catalytic purpose

One topic of this chaper is dedicated to the investigation of the ability of different formulation based on LDHs to act as supports for enzyme immobilisation. The study had involved the utilisation of ZnAlLDH based materials and Horseradis Peroxidase enzyme (HRP). The immobilisation was carried out via direct adsorption of the enzyme on the fresh or thermal actived LDH at 550 °C. The resulted materials were tested in specific enzymatic reactions. Another direction of study approched in this chapter was to investigate the activation of HRP and the regeneration of the NADH from NAD^+ by using solar irradiated AuNPs/LDH. For a better understanding, different sistems formed by free HRP and Au/ZnAlLDH based materials were tested in order to establish how the enzymatic solution can affects the material structure and which is the influence of the gold containig materials on the enzyme activity.

3.1. Generalities

Layered double hydroxides are materials which have been used many times for the immobilization of different enzymes [147,152,153]. These materials have good physico-chemical stability and they can work in a pH range of 5-9 [261,262]. Different studies revealed that the LDHs materials have a high biocompatibility and in presence of biomolecules, they act as s*oft* materials, without significant influence on their properties [67]. Furthermore, an approached direction for the immobilized enzymes is their utilization in biosensors design. For this reason, it has to be mentioned that the particular semiconducting property of LDH makes these anionic clays to be promising supports for the enzyme immobilization [150].

The enzyme immobilization on LDHs can be carried out via different techniques as direct protein adsorption, coprecipitation or rehydration. Since now, enzyme like tyrosinase [149], laccase [146], aminopeptidase [263], lactate dehydrogenase [147], yeast transketolase [153], fructose-6-phosphate aldolase [152], cellulase [145], peroxidase [155], superoxide dismutase [264], papain [265], phosphatase [144], dihydroxyacetone kinase, pyruvate kinase, triosephosphate isomerase [154] were immobilized on ZnAlLDH, MgAlLD, CoAlLDH, C-Dots/CoFeLDH, MgZnAlLDH and further the biohybrids were used in biosensing and enzymatic synthesis of different chemicals. The majority of these researches have reported that the enzyme immobilization on LDHs has no negative effects on the enzyme conformation or active site [266]. Contrariwise, other studies have shown that the enzyme can suffer some

structural changes or an improper orientation on the LDH surface during its immobilization [147]. Furthermore, the presence of some metals like nickel in the clay structure can lead to enzyme inhibition [149].

Horseradish Peroxidase (HRP) is an oxidoreductase which was used many times for phenolic substances (phenol, trichlorophenol, p-chlorophenols) degradation, in its free or immobilized form [161]. The enzyme needs an electron donor and a peroxide agent to become active. Usually, the peroxide is H_2O_2. When HRP is active, it catalyzes the polymerization of phenols, the resulted polymeric compound being insoluble in water is easy to separate [267] and further it can be valorized in precious metals recovery [268]. However, the permanently addition of H_2O_2, the ability of peroxide and of some reaction products to inhibit the enzyme are important inconveniences [269–272].

In this subchapter layered double hydroxides will be synthetized, characterized and further used to investigate their ability to imobilized the HRP enzyme. Furthermore, gold conteining materials derived from LDHs will be tested as potential vectors in HRP activation and NADH regeneration from NAD^+.

3.2. Horseradish Peroxidase (HRP) immobilization on LDHs materials.

3.2.1. Synthesis and physico-chemical characterization of LDHs and HRP-LDHs.

Synthesis

The layered double hydroxides abilities to immobilized enzymes were investigated for ZnAl(3/1)-based materials. Firstly, the parent ZnAl(3/1) material was obtained by using the co-precipitation method. For this, the slow precipitation of an aqueous solution of 0.15 moles of $Zn(NO_3)_2.6H_2O$ (Sigma Aldrich, ≥99%) and 0.05 moles of $Al(NO_3)_3.9H_2O$ (Sigma Aldrich, ≥99%), in the presence of a solution of 1 M $NaOH/Na_2CO_3$ was performed. The pH during the precipitation was kept constant at a value of 9. The resulted suspension was stirred for 24 h, afterwards it was washed several times with bidistilled water and dried at 60 °C and denoted ZnAl(3/1). Two hybrid formulations were obtained started from ZnAl(3/1) material. Thus, 1.5 g of fresh ZnAl(3/1) were calcined at 525 °C during 12 h and added to a 150 mL aqueous solution containing 0.15 g of gold acetate. The suspension was irradiated for 20 minutes with a solar lamp, 180 W, and further stirred for 24 h. Finally, the solid was recovered by centrifugation, dried at 60 °C and denoted Au/ZnAl. Furthermore, 1.25g of ZnAl(3/1) calcined at 550°C for 7 h was added, to an aqueous solutions containing 0.1 g of g-C_3N_4, and kept under vigorous stirring for 24 h at room temperature. The obtained solids were washed with bidistilled water, recovered by centrifugation, dried at 90 ºC and denoted ZnAl-CN.

The biohybrid materials were obtained by combining the synthetized materials with Horseradish Peroxidase. The peroxidase from *Horseradish*, 250 U/mg, type VI, EC 1.11.1.7 was purchased by Sigma-Aldrich Chemical Co. The HRP was immobilized on fresh ZnAl(3/1),

Au/ZnAl and ZnAl-CN materials, via direct adsorption. The reconstruction method was also used, when the ZnAl(3/1) and Au/ZnAl were firstly calcined at 550 °C and the cold metal oxides were rehydrated in HRP phosphate buffer solution [144]. Thus, in five glass tubs containing 60 mg of supports were added 5 mL of HRP solution, 200 µg HRP/mL prepared in phosphate buffer solution 0.1 M, pH=7. The suspensions were slowly stirred during 72 h. The immobilization was monitored by the evolution of the HRP absorbance at 403 nm. After the immobilization, the solids were removed by centrifugation, washed several times during 15 minutes with 5 mL of ultra-pure water and dried at the room temperature. The obtained samples were denoted as ZnAl-HRP, Au/ZnAl-HRP, ZnAl-550-HRP, Au/ZnAl-550-HRP, ZnAl-CN-HRP. In order to evaluate the immobilization efficiency, activity tests were made for the supernatant solutions resulted after the immobilization and washing cycles.

Physico-chemical characterization

The materials were characterized by using XRD, FTIR and TEM instruments. The XRD patterns were performed on a Bruker D8 Advance powder X-ray diffractometer equipped with Cu $K_{\alpha 1}$ radiation source (λ=0.1538 nm), operating at 40 kV and 40 mA and with a detector 1D Lynx eyes. The intensity data were collected over a 2θ range of 10-70 degree with a 0.014 degree step size using a counting time of 0.5 s per point. Crystalline phases were identified by comparison with the reference data from ICDD (international center of diffraction data) files. Infrared spectra (IR) were recorded using a PerkinElmer FTIR Spectrum 100 spectrometer. The TEM images were obtained using a Hitachi H-9000 NAR, 300 kV. The TEM was equipped with EDX detector.

The XRD analyze was performed in order to verify the crystallinity and the characteristic LDH structure for the synthetized materials. The X-ray diffractograms presented in figure 3.1 show that the co-precipitation and the reconstruction in gold acetate lead to a typical LDHs structure confirmed by sharp pecks at 2Θ = 11.7 °, 23.5 °, 34.6 °, 39.2 °, 46.9 °, 60.3 ° for ZnAl(3/1) and 11.6 °, 23.5 °, 34.6 °, 39.2 °, 46.7 °, 60.2 ° for Au/ZnAl, assigned to the (003), (006), (012), (015), (018) and (110) plans [3]. Beside the LDH phase, the Al_2O_3 (@) was observed on ZnAl(3/1) XRD spectra at 2Θ = 19.7 ° and 26.7 ° attributed to (113) and (012) plans [273]. The spectra of Au/ZnAl shows the presence of a small amount of ZnO (*) [179], and also of AuNPs (*), with diffraction pecks at 38.1 and 44.1 assigned to (111) and (200) plans [274]. During HRP immobilization on LDHs via direct adsorption it was observed that the layered hydrotalcite structure is preserved (see figure 3.1 A-b and B-b). Furthermore, the layered structure is recovered after calcined LDHs rehydration in enzyme solution, but the intercalation of the HRP between the lamellas is not confirmed. The XRD spectra for a ZnAl-550 and Au/ZnAl-550 reveal the formation of ZnO phase and the presence of AuNPs [179,274]. According with the (003) diffraction angle, the interlayer distance is 0.75 nm for ZnAl(3/1) and 0.76 for the rest of LDHs hybrids, underlining the presence of carbonate anions CO_3^{2-} in the interlayer region [3], being an additional indication that the enzyme was adsorbed on support surface, and not into the interlayer space.

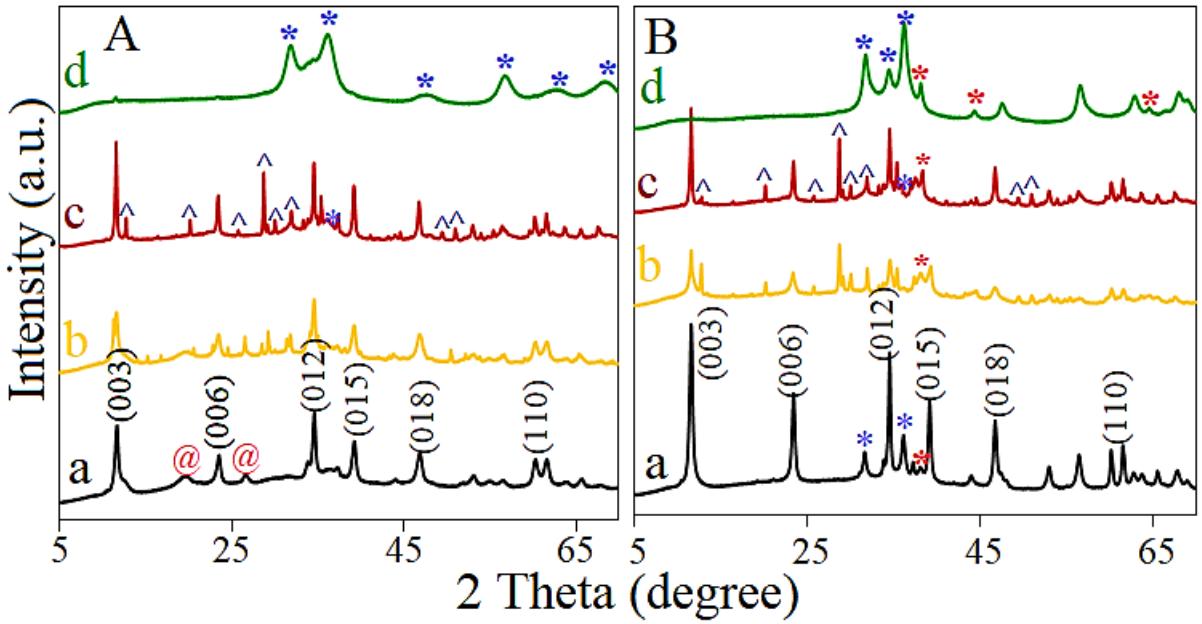

Figure 3.1: XRD patterns of A) a) ZnAl(3/1), b) ZnAl-HRP, c) ZnAl-550-HRP, d) ZnAl-550; B) a) Au/ZnAl, b) Au/ZnAl-HRP, c) Au/ZnAl-550-HRP, d) Au/ZnAl-550; (*) ZnO, (@) Al_2O_3, (*) Au, (^) $KZn(PO_4)$ H_2O.

For the LDHs-HRP biohybrids, the X-ray diffractograms show a small decrease of crystallinity and besides the typical diffraction signal attributed to the anionic clays, another crystalline phase was recorded (^). This new phase has a good match with the potassium zinc phosphate hydrate ($KZn(PO_4)$ H_2O), according with the reference data from ICDD files. The appearance of this new phase is a significative indication that the LDHs interact with enzymatic solution, more likely with the buffer constituents. Probably a solubilization of Zn^{2+} cations from the lamella takes place [275] and further they react with the potassium phosphate buffer. The formation of this new crystalline phase was also confirmed by the EDX measurements, which show that in the biohybrids structure, besides Zn, Al and Au, K and P are also present (see figure 3.2). The lattice parameters and the crystal size are listed in table 3.1. Also, the elemental composition, according to the EDX measurements is given in table 3.2.

The chemical composition listed in table 3.2 was calculated as an average between the EDX measurements performed in different areas of the samples.

The presence of the enzyme on the materials surface was further investigated by FTIR measurements. The FTIR spectra presented in figure 3.3 show the characteristic vibration bands of hydrotalcite materials which can be assigned to the O-H stretching of the lamella hydroxyl groups (3450 cm^{-1}), to the interlayer water which has an absorption peak at 1622 cm^{-1}, signal well defined only in case of ZnAl(3/1) material (see figure 3.3 A-a) and to the interlayer anion, which is for all the samples $\mathbf{CO_3^{2-}}$ with an intense peak at 1360 cm^{-1} [25]. Because of the reconstruction of calcined ZnAl(3/1) was performed in $Au(C_2H_3O_2)_3$, beside the carbonate

Table 3.1: Crystal size and lattice parameters for the studied materials.

		Lattice parameters (Å)	
Sample	***Crystal size (nm)**	***a***	***c***
ZnAl(3/1)	15	3.062	22.5
ZnAl-HRP	14	3.065	22.8
ZnAl-550-HRP	29	3.065	22.8
Au/ZnAl	18	3.067	22.8
Au/ZnAl-HRP	15	3.064	22.8
Au/ZnAl-550-HRP	28	3.067	22.8

*crystal size calculated with Scherrer equation;
$a = 2d_{110}$ and $c = 3d_{003}$ are the unit lattice parameter.

Table 3.2: Chemical composition of the samples according to EDX data.

	% O	**% Al**	**% Zn**	**% P**	**% K**	**% Au**
ZnAl(3/1)	55	10	35	0	0	0
ZnAl-HRP	56.4	5.8	27.8	8.5	3.4	0
ZnAL-550-HRP	54	8	30	5.7	2.9	0
Au/ZnAl	56.75	8.25	30	0	0	5.125
Au/ZnAl-HRP	56.5	3.9	26.5	10.6	5.125	0.375
Au/ZnAl-550-HRP	52.2	3.8	31.1	12.7	4.25	0.45

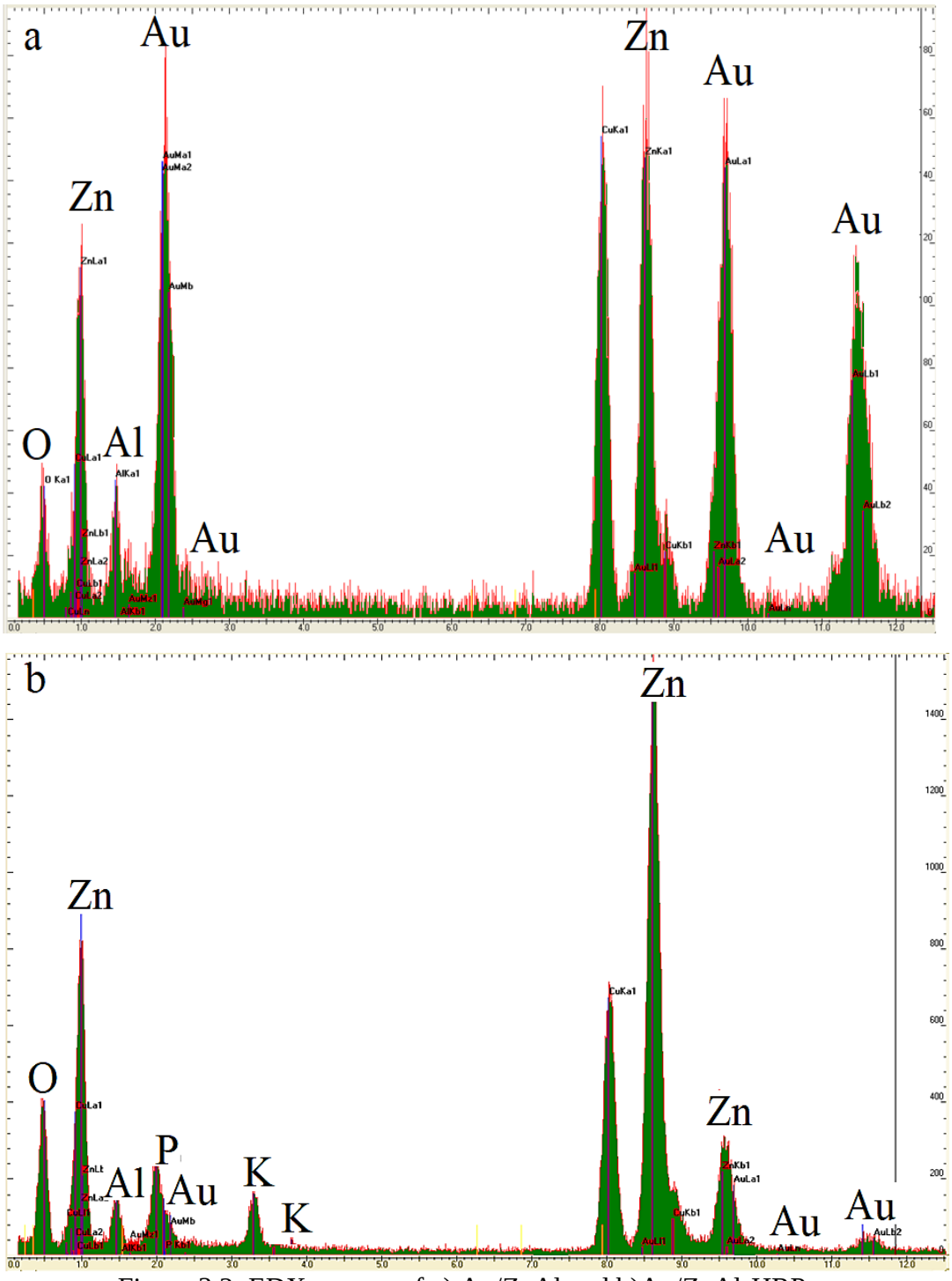

Figure 3.2: EDX spectra of a) Au/ZnAl and b)Au/ZnAl-HRP

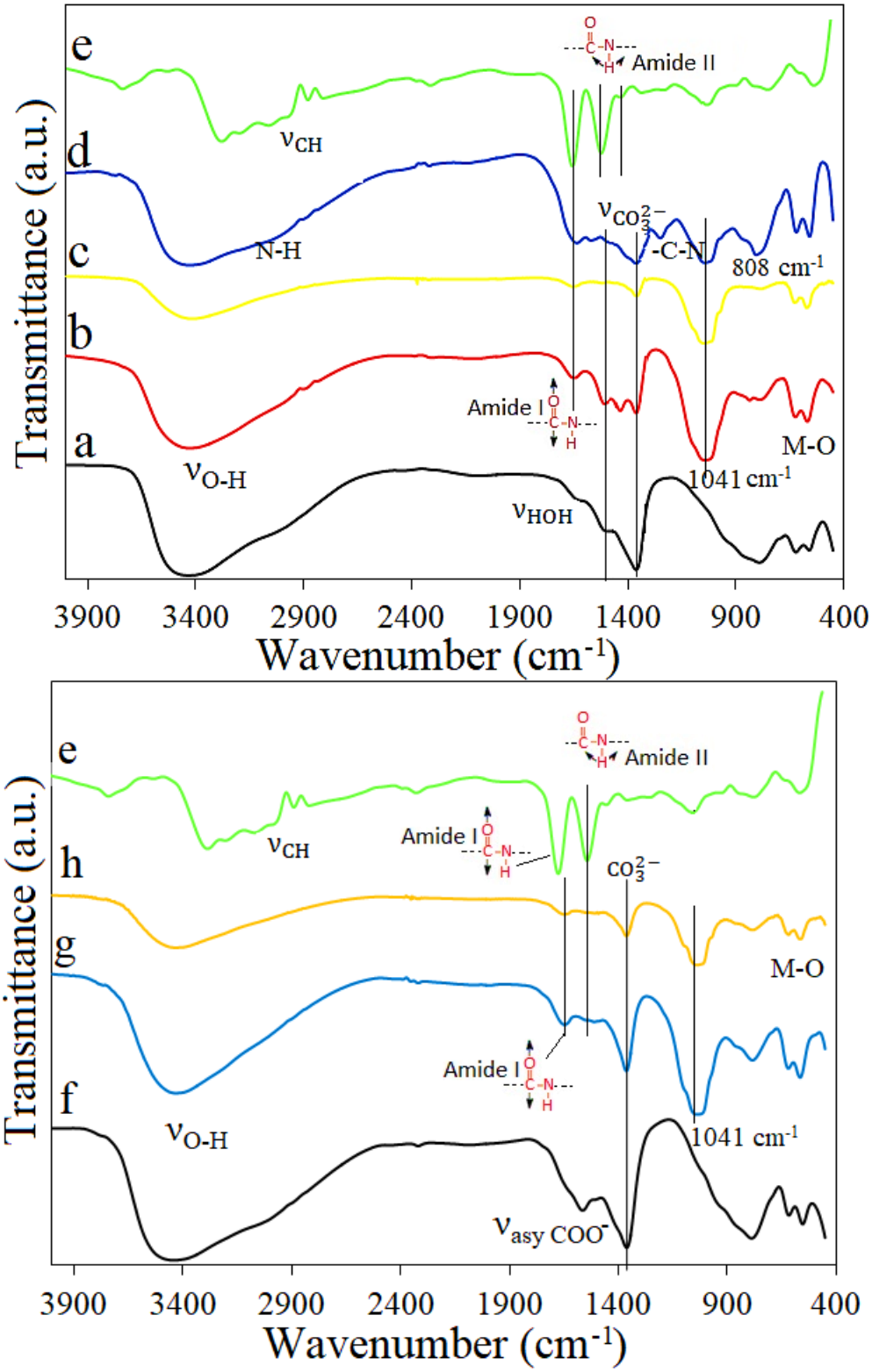

Figure 3.3: FTIR spectra for a) ZnAl(3/1), b) ZnAl-550-HRP, c) ZnAl-HRP, d) ZnAl-CN-HRP, e) HRP, f) Au/ZnAl, g) Au/ZnAl-550-HRP, h) Au/ZnAl-HRP.

anion, for the Au/ZnAl sample, a peak at 1564 cm^{-1} was identified and it might be assigned to the antisymmetric stretching modes of COO^- anions [251]. The spectrum of free HRP presents typical adsorption bands at 2976 and 2888 cm^{-1} which are characteristic for the C-H bound and 1665, 1535, 1446 cm^{-1} assigned to the amide I and amide II binding [276]. For the LDHs-HRP biohybrids, the FTIR spectra present some particularities which might be attributed to the enzyme presence on the material surface. The typical vibration bands which were observed for the free enzyme were identified for the LDHs-HRP materials, but with a small shift to lower wavelengths. This shift can be an indication of enzyme structural changes as denaturation or distortion of the structure. The g-C_3N_4 presence is indicated by the absorption peaks at 1573, 1250 and 808 cm^{-1} attributed to the vibration modes of C-N and of the triazine ring (see figure 3.3-d) [221]. An intense peak was recorded for all the biohybrids materials, around 1042 cm^{-1} and it is typical for the PO_4^{3-} anion vibration [277]. The presence of the PO_4^{3-} anion might be an indication for the formation of $KZn(PO_4)\ H_2O$ phase.

TEM analyses were further performed in order to verify the influence of the enzymatic solution on the LDHs morphology. The TEM images for the fresh ZnAl(3/1) LDH are given in figure 3.4 and they show the typical LDH morphology presented as large platelets with the size

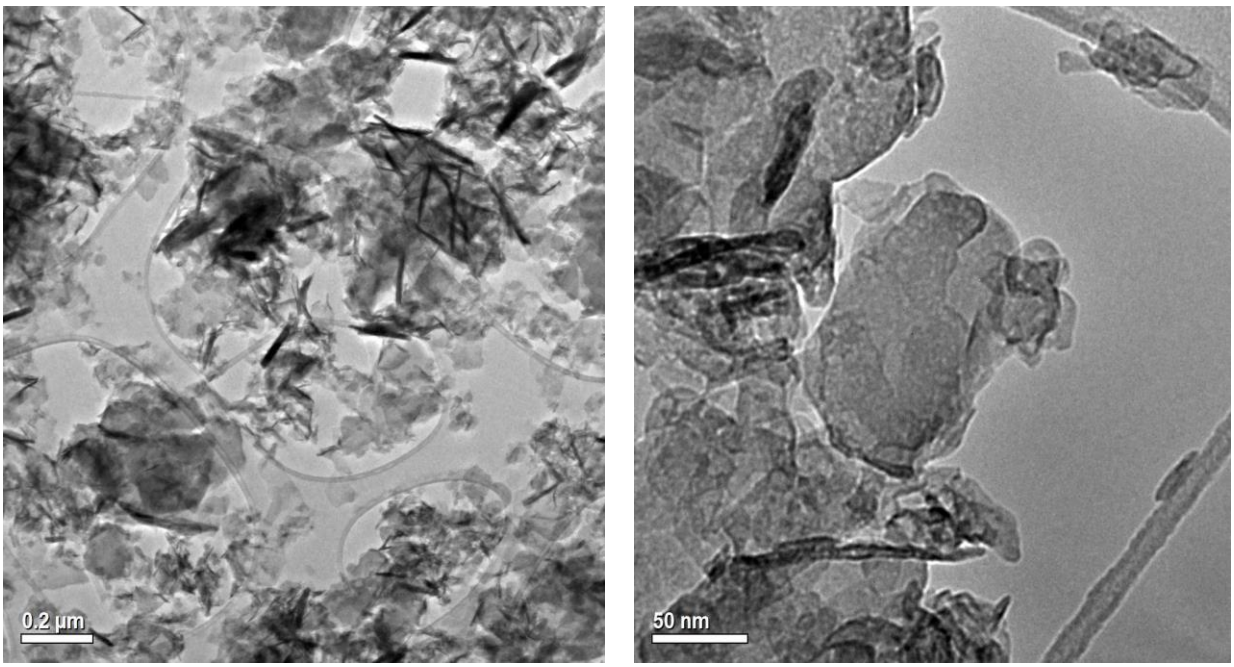

Figure 3.4: TEM images of ZnAl(3/1) at different magnifications.

between 250-500 nm, overlapping one on the other, giving rise to a non-uniform matrix [47]. After the reconstruction in $Au(C_2H_3O_2)_3$, gold nanoparticles were noticed on the LDH (see figure 3.5) as small darker spots on the large brighter LDH surface. It might be observed from figure 3.5-A that the LDH surface presents different areas which are distinctly populated

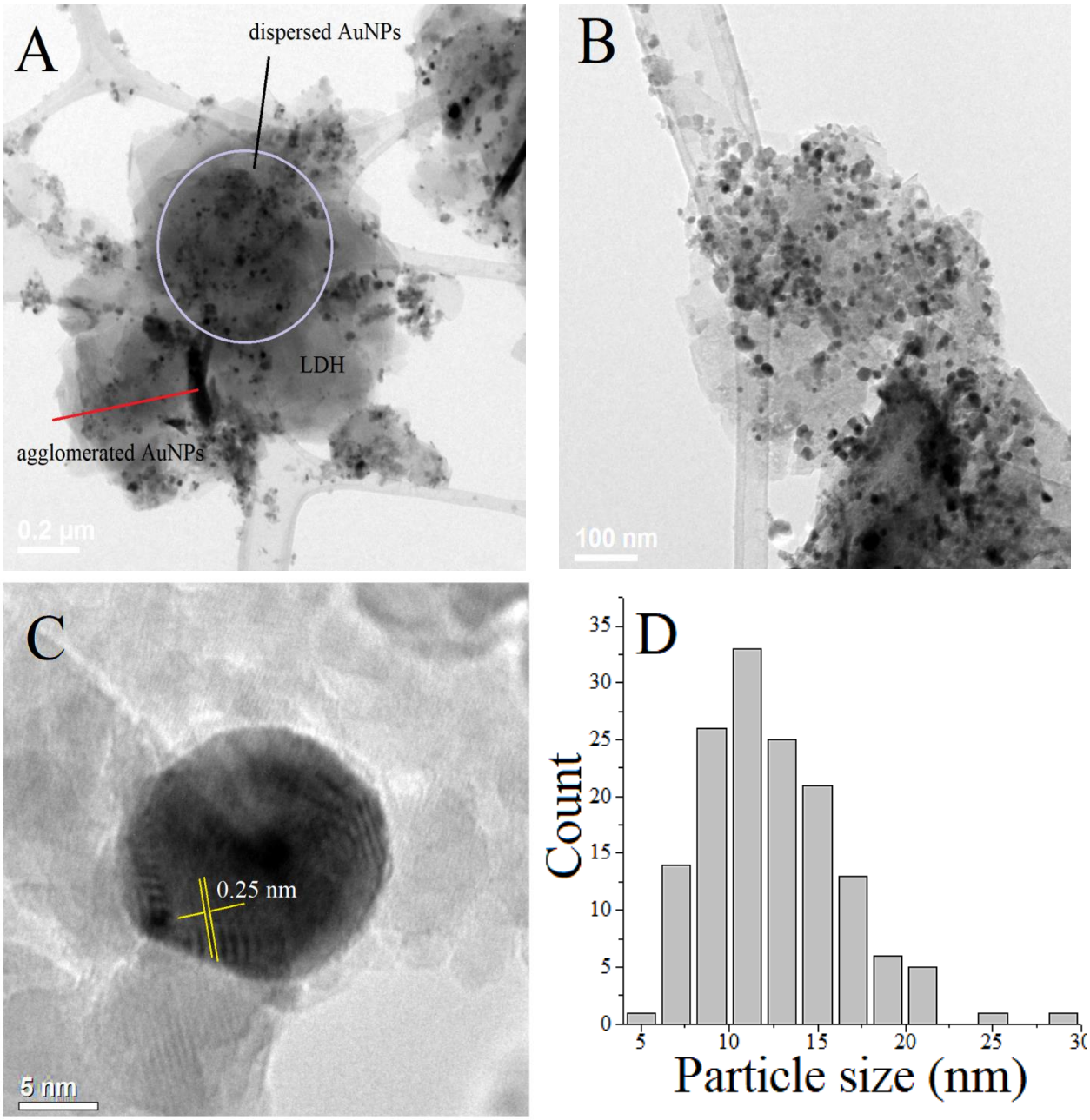

Figure 3.5: TEM images of Au/ZnAl at different magnifications (A and B), C) HRTEM of AuNP, D) the AuNPs size distribution on LDH surface based on figure 3.5-B.

with Au/NPs. So, areas with dispersed Au/NPs were detected, but also regions with agglomerated Au/NPs or with lower gold content. The size distribution of the AuNPs on ZnAl(3/1) LDH was determined by taking into consideration the TEM imagine presented in figure 3.5-B, and excluding the dark regions with a high amount of gold. According with the results shown in figure 3.5-D, on the clay surface, the AuNPs have diameters in a range on 5-30 nm, with a significant amount of particles between 10-15 nm. The HRTEM imagine presented

in figure 3.5-C confirms that the dark dots are Au/NPs based on the interplanar spacing of 0.25 nm attributed to the {111} planes of the face centered cubic gold [278].

After the thermal treatment at 550 °C the morphology of the initial LDHs changes as a result of lamella dehydroxilation and water, anion removal from the interlayer space. The EDX measurements confirm the presence of the ZnO and Au/NPs can be observed (see figure 3.6).

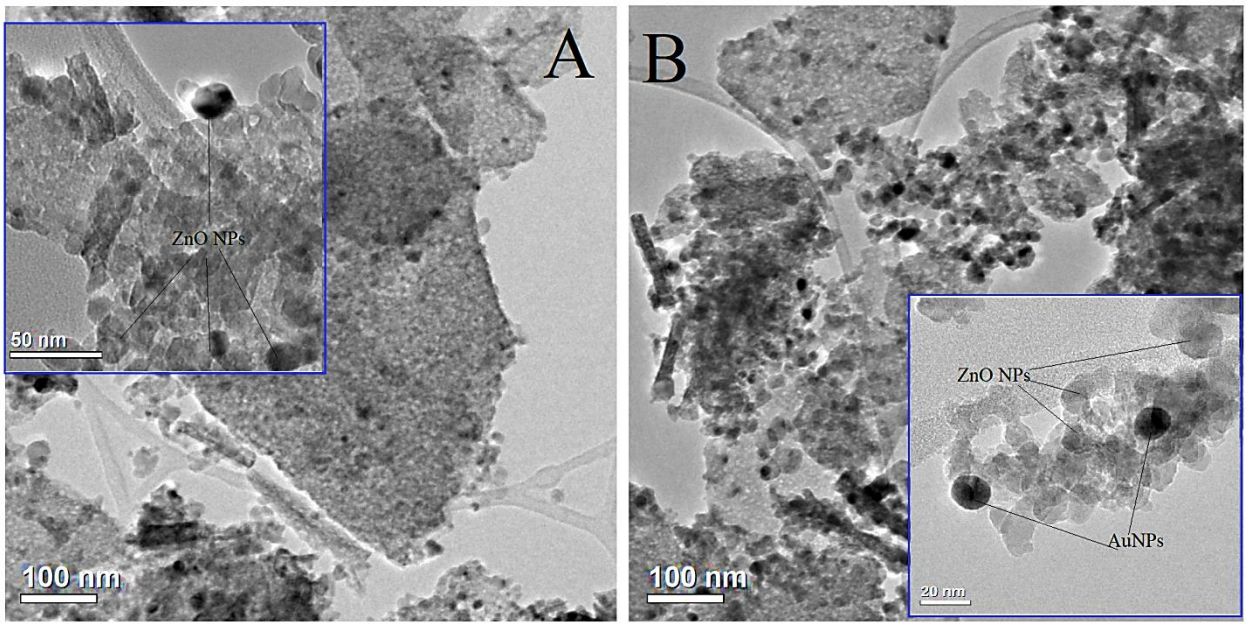

Figure 3.6: TEM images of A) ZnAl-550 and B) Au/ZnAl-550.

The immobilization process leads to modifications of the materials morphology as can be observed from figure 3.7. For all the LDH-HRP materials, after the immobilization, was observed that the new biohybrids present a more complex morphology compared with the ones discussed above. The LDHs characteristic aspect is difficult to be observed because the formation of dense aggregates on its surface (see figure 3.7 A-C), which might be assigned with the enzyme presence [153]. In case of gold containing biohybrids, the AuNPs are not so easy to be remarked, compared with Au/ZnAl nanocomposite (see figure 3.7 B).

A new phase was notice for all LDH-HRP biocomposites, and it appears as regular micrometric rectangles (see figure 3.7 A and C-F). The EDX measurements made for the biocomposites show that the areas of the materials which have different morphologies, have also different elemental composition. Thus, in function of the elemental composition, distinct phases can be identified. With this respect, might be pointed out that the well-defined micrometric rectangles have a significant content of P, O, Zn and K and only 1 % of Al. For this reason and taking into consideration the XRD data, we believe that these rectangles can be assigned to the potassium zinc phosphate hydrate. The small content of Al can be attributed to Al_2O_3 which was also identified in the XRD patterns. For the thin sheets (well spread out or wrinkled) the EDX data have shown that they have a small content of 1% of K and between 2-3

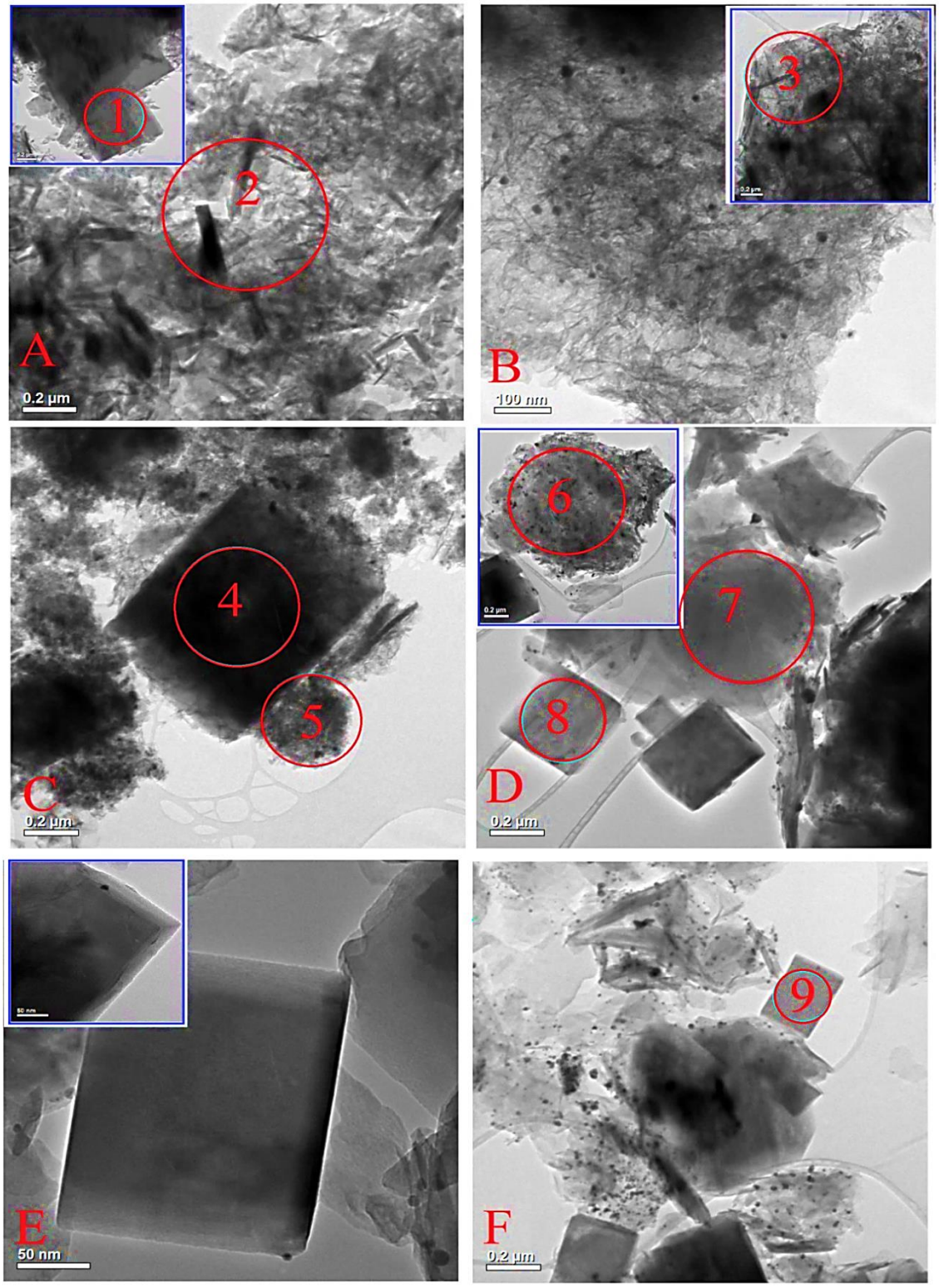

Figure 3.7: TEM images of A) ZnAl-HRP, B) and C) Au/ZnAl-550-HRP, D-F) Au/ZnAl-HRP.

% of P. Because these areas present morphologies closed to the ones of the initial materials, we concluded that they can be assigned to the LDH matrix. The red circles from the figure 3.7 are the areas where have been performed the EDX measurements. In table 3.3 are listed the elemental compositions for each area.

Table 3.3: EDX elemental composition for some particular areas of LDH-HRP.

Sample	EDX	% O	% Al	% Zn	% P	% K	% Au
ZnAl-HRP	1*	56	1	22	14	7	0
	2**	65	8	25	2	1	0
Au/ZnAl-550-HRP	3**	61	9	25	2	1	1
	4*	53	2	26	10	8	0
	5**	58	8	31	3	1	0
Au/ZnAl-HRP	6**	62	8	26	3	1	1
	7**	58	9	30	2	1	0.5
	8*	61	1	20	9	8	0.5
	9*	66	1	20	11	2	0

*$KZn(PO_4)\ H_2O$ morphology
** LDH morphology

It can be concluded that the materials analyses prove the obtaining of LDHs type materials. Furthermore, after the reconstruction in gold acetate, the LDHs structure was recovered and the gold was observed with TEM analyse as dispersed dark spots on the LDH surface. During the HRP immobilization on the ZnAl(3/1), Au/ ZnAl(3/1) and their derived mixed oxides, strongly interactions take place and the XRD and TEM images show the presence of an additional phase which was identified as $KZn(PO_4)\ H_2O$. The enzyme presence on the material surface was proved by FTIR measurements.

3.2.2. Determination of HRP quantity immobilized on the LDHs and LDHs-550 supports

An important step when working with immobilised enzymes is to determine the immobilization efficiency and the enzyme amount adsorbed on the support. With this respect, during the immobilization, the HRP UV-Vis spectra profiles were monitored at a maximum of 403 nm. The immobilization was considered to be finished when no modification of the HRP spectra profile was observed. It was remarked that the immobilization on the ZnAl-550 and Au/ZnAl-550 was faster than in case of uncalcined materials. An explanation of this fact can be the formation of pores during the calcination, when the anion and the water molecules are released from the material structure. Thus, during 24 h of contact all the enzyme was adsorbed on the thermal activated LDHs, while for the fresh and the reconstructed samples, the adsorption was performed during 72 h.

In order to have a good quantification of the quantity of bounded protein on the support, an activity standard curve was made for the free HRP. HRP is an enzyme which needs an electron donor for its utilization, and in this case H_2O_2 was used [161]. Also, ABTS (2,2'-azino-bis(3-ethylbenzothiazoline-6-sulphonic acid) (Sigma Aldrich, ≥98%), was used as a substrate. During the enzymatic tests, the ABTS oxidation was monitored, when a colored product with an absorption maximum at 415 nm is produced.

The first step was to find a correlation between the reduced ABTS and its oxidized form. So, in a total volume of 2400 µL, the H_2O_2 concentration was 200 µM, while the reduced ABTS concentration ($ABTS_{red}$) was varied (5, 7.5, 25, 37.5, 50 µM). To this mixture, 20 µL of HRP (200 µg/mL) was added. The excess of hydrogen peroxide was used to assure the total oxidation of ABTS. The reaction was monitored at 415 nm till a plateau was obtained. The standard curve of oxidized ABTS was obtained by making an average for all the points of the plateau (see figure 3.8-A). For each reduced ABTS concentration, the enzymatic tests were made three times, and the final value of the oxidized ABTS was an average between them. The standard error was also calculated for the correlation between the averages of the oxidized ABTS ($ABTS_{oxd}$) absorbance at plateau and the $ABTS_{red}$ concentration. Further, the free HRP activity standard curve was build. For this, to a total volume of 2400 µL phosphate buffer solution, with a concentration in $ABTS_{red}$ and H_2O_2 of 40 µM and 20 µM respectively, were added different quantities of HRP (0.001, 0.005, 0.05, 1, 2, 5, 10, 20 µg). The enzymatic tests were monitored at 415 nm for 10 minutes. Using the linear part of each obtained plot, the initial reaction velocities (V_i) were determined (V_i was cosiderated as the slope value of the line). The free HRP activity standard curve (figure 3.9) was obtained by representing the initial velocity in function of the corresponding enzyme quantity.

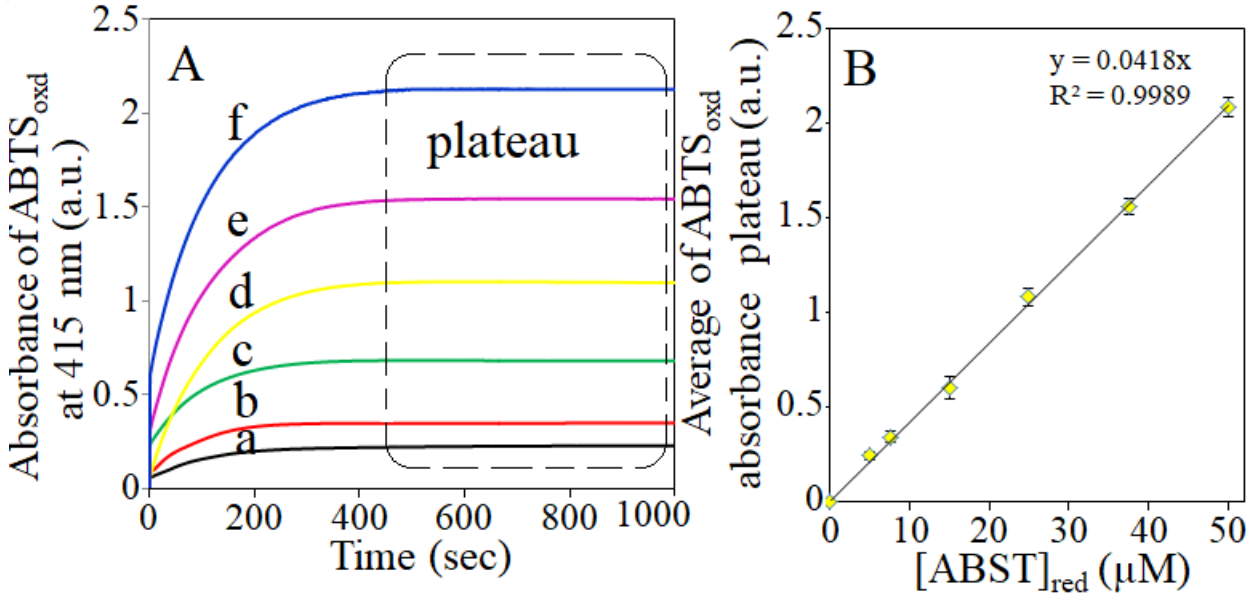

Figure 3.8: A) $ABTS_{red}$ oxidation reaction using free HRP and 200 µM of H_2O_2; a) 5 µM, b) 7.5 µM, 15 µM, 25 µM, 37.5 µM, 50 µM of ABTS; B) standard curve for $ABTS_{oxd.}$

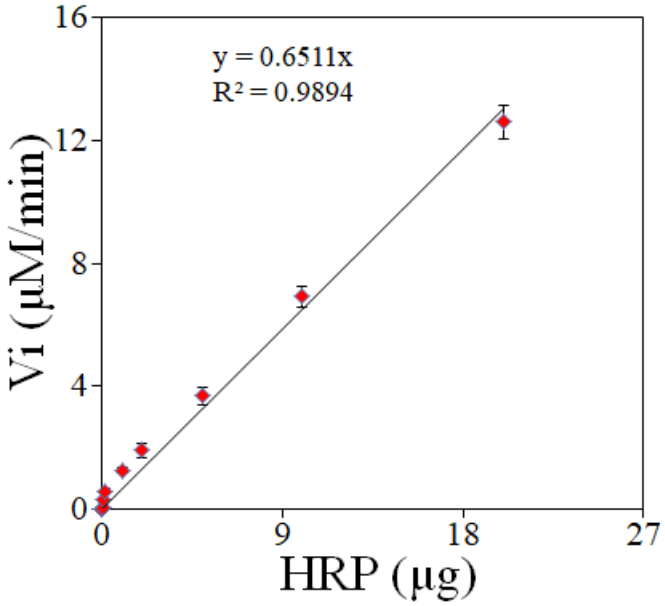

Figure 3.9: Activity standard curve for free HRP; 40 µM $ABTS_{red}$ and 20 µM of H_2O_2.

The obtained curve was used for the determination of enzyme quantity for particular solutions, as those resulted after the immobilization or after the support-enzyme washing. For this, in a 2400 µL phosphate buffer solution, with a concentration in $ABTS_{red}$ and H_2O_2 of 40 µM and 20 µM respectively, enzymatic solution were added and the reaction was performed. The resulted V_i was used to determine the enzyme quantity, which was used for the test. In figure 3.10 is presented the immobilization efficiency for the tested materials. It can be

observed that the thermal activated materials are able to immobilize almost all the enzyme quantity. The fresh materials, ZnAl(3/1) and Au/ZnAl have a small adsorption ability (see table 3.4).

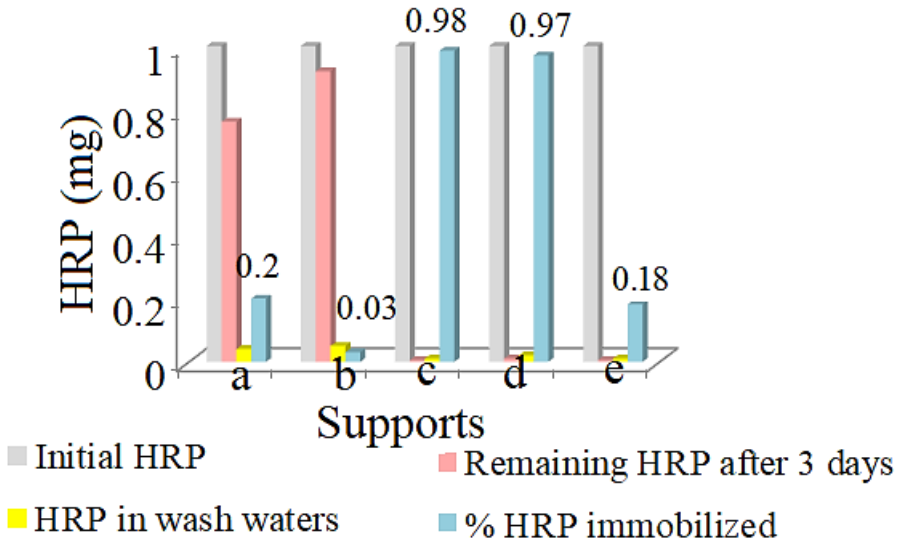

Figure 3.10: Quantification of HRP immobilization on a) ZnAl(3/1), b) Au/ZnAl, c) ZnAl-550, d) Au/ZnAl-550, e) ZnAl-CN.

During the washing it was remarked that only a small quantity of enzyme was released, this underlines that the interactions between the HRP and the support are strong [264]. In table 3.4 are listed the HRP amounts adsorbed on 1 mg of different supports. The highest adsorption capacity was obtained for the thermal active materials ZnAl-550 and Au/ZnAl-550. A similar result was obtained by J. Zhu et. al when they have immobilized acid phosphatase on calcine and fresh MgAlLDH. The thermal treated support at 500 had an enzyme immobilsation yield of 73, while the uncalcined sample reache only 59 % [144].

Table 3.4: HRP amount adsorbed on LDHs and LDHs-550 materials

Sample	**ZnAl(3/1)**	**Au/ZnAl**	**ZnAl-550**	**Au/ZnAl-550**	**ZnAl-CN**
Adsorbed HRP, µg/mg	3.5	0.5	16.5	16	3

3.2.3. Kinetic parameters determination for the free HRP and LDHs-HRP biohybrids.

For the determination of the kinetic parameters, V_{max} and K_M, enzymatic tests were performed in phosphate buffer solution, pH= 7 using a constant concentration of $ABTS_{red}$, (50 µM) and varying the H_2O_2 concentration in a range of 1.5-25 µM. To these solutions was added 1 µg of free HRP, or 5 mg of LDH-HRP, respectively. The reactions were monitored through the evolution of the absorbance at 415 nm. For the free enzyme, the reaction evolution was automatically monitored, while for the immobilized enzyme, samplings were performed at determined intervals of time, the solid was removed by centrifugation, and the supernatant was spectrophotometrically analyzed. The dependence f([$ABTS_{oxd}$] = t was plotted and the linear part of the plot was used to determine the initial velocity of the oxidation reaction. The obtained V_i were further used for the determination of the kinetic parameters, by using the graphical representation of Lineweaver-Burk equation. The tests were performed three times in the same conditions, and the results were presented as an average between them.

In figure 3.11 is presented the linear part of the $ABTS_{red}$ oxidation reactions in presence of HRP and different concentrations of H_2O_2 (a) and also the f($1/V_i$) = 1/[H_2O_2] plot. The tests were performed three times in the same experimental conditions. The reactions take place fast, and after 10 minutes the linear region was obtained for all the H_2O_2 concentrations.

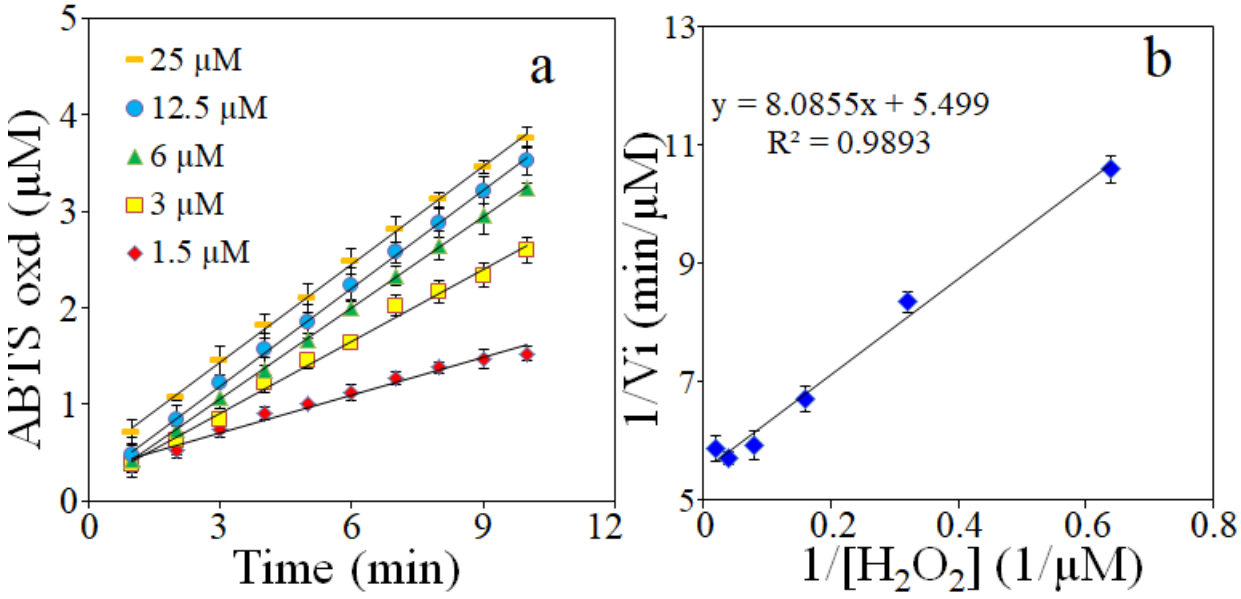

Figure 3.11: a) The kinetics of $ABTS_{red}$ oxidation reaction in presence of 1µg of HRP and of different concentrations of H_2O_2; b) graphical representation of Lineweaver-Burk equation.

For the immobilized HRP, it was observed that ZnAl-HRP, Au/ZnAl-HRP and Au/ZnAl-550-HRP have no enzymatic activity. An explanation of this behavior can be the small quantity of the enzyme on the support in case of ZnAl-HRP and Au/ZnAl-HRP.

However, the Au/ZnAl-550-HRP has a significant amount of enzyme on its surface and even so, no activity was noticed. Related to this, previous studies have shown that enzyme like catalase and peroxidase can be negatively affected by the AuNPs or ZnONPs [279,280]. In these conditions, the $ABTS_{red}$ oxidation reactions for the immobilized HRP were further performed only for the ZnAl-550-HRP and ZnAl-CN-HRP. The graphical representation of the reaction kinetics and the Lineweaver-Burk plot using ZnAl-550-HRP and ZnAl-CN-HRP are presented in figure 3.12. For the reaction using the immobilized enzyme was remarked a decrease of activity, compared with the free enzyme. The reactions take place slower and the

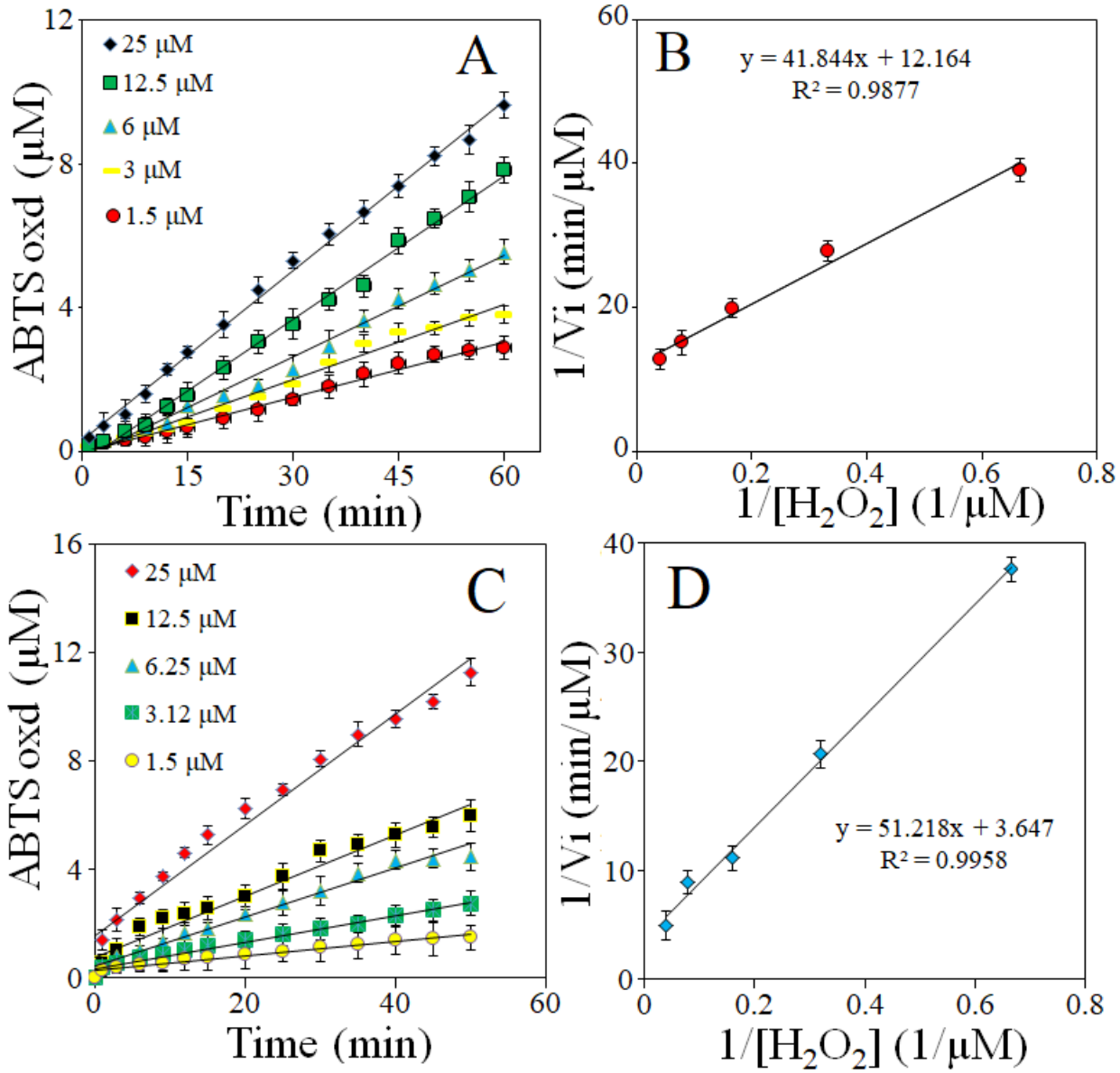

Figure 3.12: The kinetics of $ABTS_{red}$ oxidation reaction in presence of 5 mg of A) ZnAl-550-HRP and C) ZnAl-CN-HRP and different concentrations of H_2O_2; b) graphical representation of Lineweaver-Burk equation for B) ZnAl-HRP and D) ZnAl-CN-HRP.

linear part of the Michaelis-Menten graph was obtained after 60 minutes of reaction. An increase of activity vas observed in case of ZnAl-CN-HRP, compared with ZnAl-550-HRP. We believe that the functionalization of LDH with NH_2 provided by g-C_3N_4 made the enzyme to be more exposed to the substrates, and for this reason the biocatalytic activity of the material was enhanced. However, compared with the free enzyme, both biohybrids present a significant loss of activity. In table 3.5 are listed the kinetic parameters,V_{max} and K_M determined from each graphical representation of Lineweaver-Burk equation. Also, the specific maximal velocity was calculated as a ratio between the V_{max} and the quantity of the enzyme used in the biocatalytic reaction. A 10 time increase of the V_{max} was observed in case of the ZnAl-CN-HRP, compared to ZnAl-550-HRP. Based on the value of K_M, the enzyme affinity for the substrates decreases

Table 3.5: Kinetic parameters for the investigated materials

Enzymatic system	**K_M (µM)**	**V_{max} (µM/min)**	**V_{max} specific (µM/min/mg HRP)**
Free HRP	1.5	0.18	180
ZnAl-550-HRP	3.4	0.08	1
ZnAl-CN-HRP	14	0.27	18
ZnAl-HRP	Not quantifiable activity		
Au/ZnAl-HRP	Not quantifiable activity		
Au/ZnAl-550-HRP	Not quantifiable activity		

several times in case of the immobilized enzyme, as indicated by the increase of the K_M value. This behavior can be explained by some diffusional limitation of the substrates or by conformational enzyme changes. The catalysts characterizations have shown that the immobilized enzyme is placed in a very complex environment, with many crystalline phases, e.g. LDH, potassium zinc phosphate, ZnO. The FTIR analysis presented a small shift of the amide I vibration band which was reported as an indication of enzyme structural changes as denaturation or distortion of the structure. Furthermore, the decrease of activity can be an effect of an inappropriate binding of enzyme on the solid surface, when the active site of enzyme might be blocked [147]. The long time contact during the immobilization might also have a negative influence on the enzyme structure.

Studies made on HRP immobilization have shown that supports as cinnamic carbohydrate esters can decrease the enzyme affinity more that 50 % [281], while NH_2-modified Fe_3O_4/SiO_2 particles can maintain the initial affinity of the enzyme [282]. However in case of both mentioned studies, the enzyme affinity was smaller than in our case. Regarding

HRP immobilization on LDHs, it was successfully immobilized on ZnLDH, ZnNiLDH and mainly used in biosensors design [155,283–285].

In order to evaluate the performance of the HRP on the support, four consecutive tests were performed in the same experimental conditions. For this, after each test, the ZnAl-550-HRP biocatalyst was recovered, washed several times with ultra-pure water and after reused. The tests were performed by using 5 mg of ZnAl-550-HRP, and the $ABTS_{red}$ and H_2O_2 concentrations were 50 μM and 25 μM. The results have shown a very fast decrease of HRP activity. Thus, after four consecutive utilizations, the activity loss was 95 % (see figure 3.13).

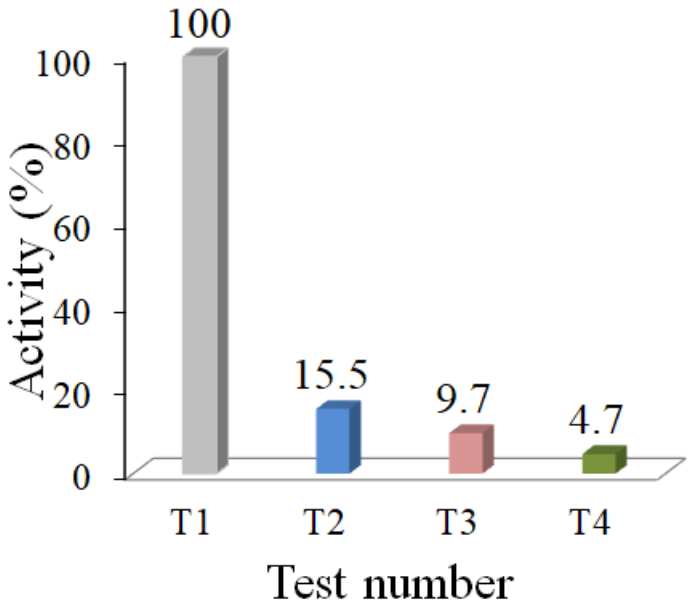

Figure 3.13: Residual activity of immobilized HRP obtained after 4 tests of $ABTS_{red}$ oxidation

This behavior could be associated to an enzymatic inhibition caused by substrate and/or reaction product [270]. Since the product has a similar structure to one of the substrates ($ABTS_{red}$), it can interact with the enzyme or the enzymatic complex. Diffusional limitations can also obstruct the diffusion of resulted product towards the solution and therefore it can remain inside the material, forming an unfavorable environment for the enzyme. As a result, the accessibility of the enzyme is decreased. The idea of enzyme leaching from LDH is not supported because during the 12 hours wash of ZnAl550-HRP with phosphate buffer, 0.1 M, pH 7, the enzyme release from ZnAl550-HRP material was insignificant to be correlated with this result.

3.3. Phenol degradation and photo-enzymatic degradation in presence of HRP-ZnAl(2/1)LDH biohybrid

Some organic pollutants, as phenols can be both photodegraded, by using a catalyst and a source of light [120], and biodegraded, by using an enzyme [161] or a microorganism [286]. In this context, the combination between the photo- and bio- degradation can be a solution for the removal of many pollutants in the same time or progressively, by using the cascade approach (step by step). For this reason, in this subchapter, LDH-HRP and LDH will be used for the degradation of phenol. So, phenolic solution will be solar photodegraded in presence of LDH, biodegraded in presence of HRP and LDH-HRP, and solar bio-photo-degraded by using LDH-HRP in presence of solar irradiation.

3.3.1. Synthesis and physico-chemical characterization of ZnAl(2/1)LDH and HRP-ZnAl(2/1)LDH

Synthesis

The ZnAl(2/1) material was obtained by using the co-precipitation method. So the slow precipitation of an aqueous solution of 0.1 moles of $Zn(NO_3)_2.6H_2O$ (Sigma Aldrich, ≥99%) and 0.05 moles of $Al(NO_3)_3.9H_2O$ (Sigma Aldrich, ≥99%), in the presence of a solution of 1 M $NaOH/Na_2CO_3$ was performed. The pH during the precipitation was kept constant at a value of 9. The resulted suspension was stirred for 20 h, afterwards it was washed several times with bidistlled water and dried at 80 °C and denoted ZnAl(2/1).

The biocatalyst as follows: firstly, the ZnAl(2/1) was thermal treated at 550 °C and 0.125 g of cold calcined material was added to 5 mL of phosphate buffer solution containing 40 μg of HRP. The immobilization evolution was monitored at 403 nm. When no changes on the spectrometric profiles were observed, the adsorption was considered to be finished. The solid was removed by centrifugation, washed during 30 minutes with ultrapure water and afterwards it was dried at room temperature and denoted as ZnAl-HRP. In order to determine the adsorbed amount of enzyme on support, enzymatic tests performed as described in section 3.2.2. No enzymatic activity was remarked in the wash waters, and it was considered that the all enzyme was adsorbed on the LDH.

Physico-chemical characterization

The XRD patterns of ZnAl(2/1) and ZnAl-HRP are given in figure 3.14. For both materials, the LDH characteristic structure is confirmed by sharp pecks at 2Θ = 11.7 °, 23.6 °,

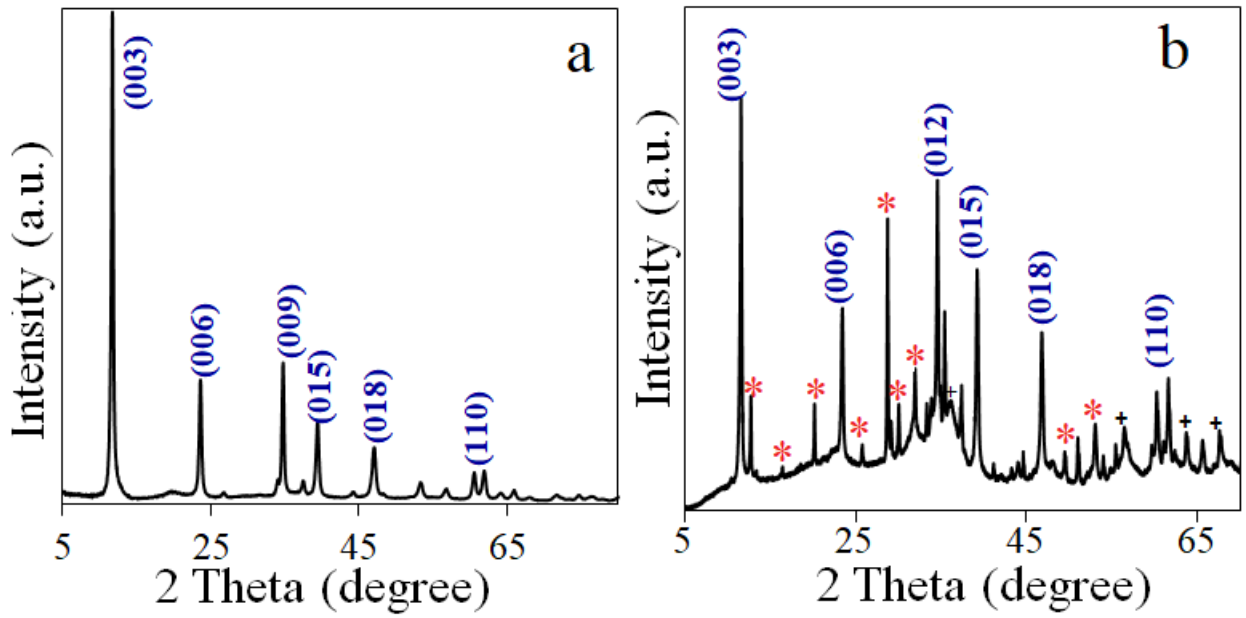

Figure 3.14: XRD patterns for a) ZnAl(2/1) and b) ZnAl-HRP; (*) $KZn(PO_4)$ H_2O; (+) ZnO.

34.7 °, 39.4 °, 47 °, 60.4 ° for ZnAl(2/1) and 11.6 °, 23.5 °, 34.6 °, 39.2 °, 46.7 °, 60.2 ° for ZnAl-HRP, assigned to the (003), (006), (012), (015), (018) and (110) plans [3]. In this case was also observed a new phase (*) in the structure of the ZnAl-HRP material with peaks at 2Θ = 12.75 °, 13.3 °, 16.4 °, 18.5 °, 20 °, 25.9 °, 28.7 °, 29.1 °, 30 °, 32 °, 49.5 °, 51 °, and it can be identified with $KZn(PO_4)$ H_2O. According with the value of the d_{003} = 0.75 nm for ZnAl(2/1) and 0.76 for ZnAl-HRP, the interlayer anion is CO_3^{2-} [3].

In table 3.6 are listed the lattice parameters and the crystal size of the synthetized materials. An increase of the *a* lattice parameter was remarked for the ZnAl-HRP. This might be an indication that a cation with a higher radius, as K (1.38 Å) had partially substituted the

Table 3.6: Crystal size and lattice parameters for the studied materials**.**

		Lattice parameters (Å)	
Sample	***Crystal size (nm)**	***a***	***c***
ZnAl(2/1)	15	3.051	22.56
ZnAl-HRP	14	3.067	22.8

*crystal size calculated with Scherrer equation;
$a = 2d_{110}$ and $c = 3d_{003}$ are the unit lattice parameter**.**

Zn^{2+} (0.74 Å) cation of the LDH. However, between K and Zn cation radius is difference of 0.64 Å, and the increase of the *a* parameter from 3.051 to 3.067 Å is not so high to be associated only to the partial substitution of Zn from the lattice. For this reason, we believe that a partial substitution of Al, whose ionic radius is 0.535 Å, with P which has a smaller ionic radius (0.38Å) might happen. Further, the enzyme presence on material surface was analyzed by using infrared spectroscopy (figure 3.15). It might be observed that, after the rehydration in phosphate buffer solution containing HRP, the LDH typical structure was recovered. The FTIR

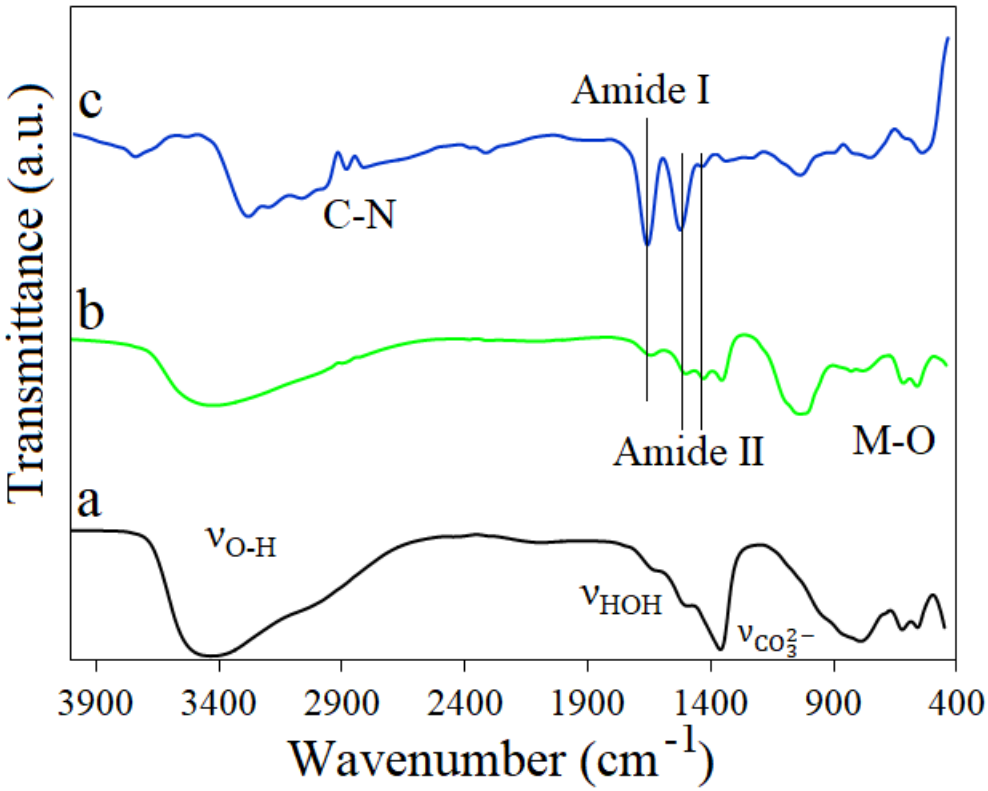

Figure 3.15: FTIR spectra of a) ZnAl(2/1), b) ZnAl-HRP, c) HRP

spectra present the characteristic vibration bands of the hydrotalcite materials, assigned to the presence of O-H groups on lamella, to the interlayer water and to the carbonate anion, with peaks around 3450 cm^{-1}, 1630 cm^{-1}, 1363 cm^{-1} respectively [3]. The enzyme presence is confirmed by the amide I vibration band at 1665 cm^{-1} and amide II vibration mode at 1357 and 1445 cm^{-1} [276]. Between 800-400 cm^{-1} can be observed the stretching vibration of M-O.

The optic properties were investigated by using UV-Vis spectroscopy analysis. The ZnAl(2/1) material presents an absorption peak in the UV region of the spectrum (see figure

3.16), while, after the HRP immobilization, the absorption profile of the initial material moves to the red region of the spectrum. An intense adsorption edge can be observed at 345 nm and it can be assigned to the ZnO presence in the ZnAl-HRP biocatalyst [225]. The UV-Vis spectrum of HRP was obtained by enzyme dilution in KBr. The enzyme presence on the LDH can be confirmed by the commune shoulder at 403 nm that can be remarked in case of HRP and ZnAl-HRP [287].

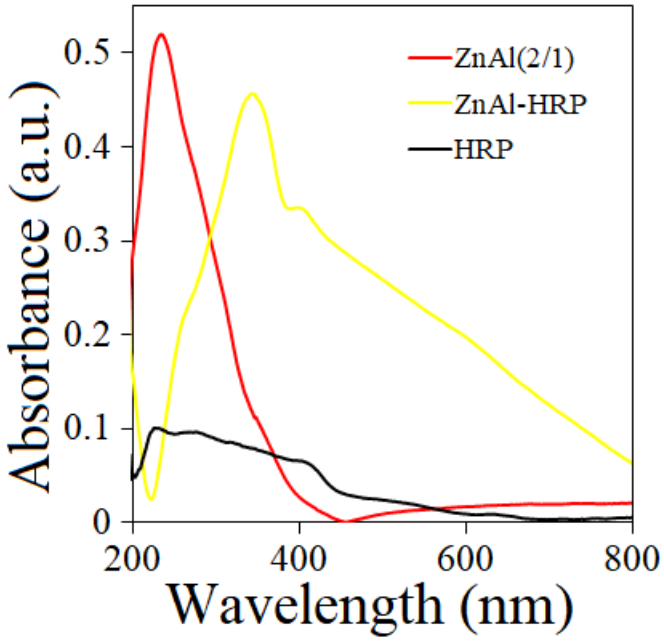

Figure 3.16: UV-Vis spectra of ZnAl(2/1), ZnAl-HRP, HRP.

TEM images from figure 3.17 show that ZnAl(2/1) has a morphology which is typical for LDHs materials, formed by large platelets overlapping one another [47]. After the immobilization, the material morphology becomes rather complex, with an association of LDH, enzyme and micrometric rectangles (see figure 3.17 C and D). Dark aggregates can be observed on TEM images and they might be attributed to the enzyme presence on the surface [153]. As for the first group of biohybrids, for this material, also the EDX measurements show that the rectangles have a small content of Al, being composed mainly from O, Zn, P and K. For this reason they have been assigned to the formation of a supplementary phase, which according to the XRD data it might be $KZn(PO_4)$ H_2O.

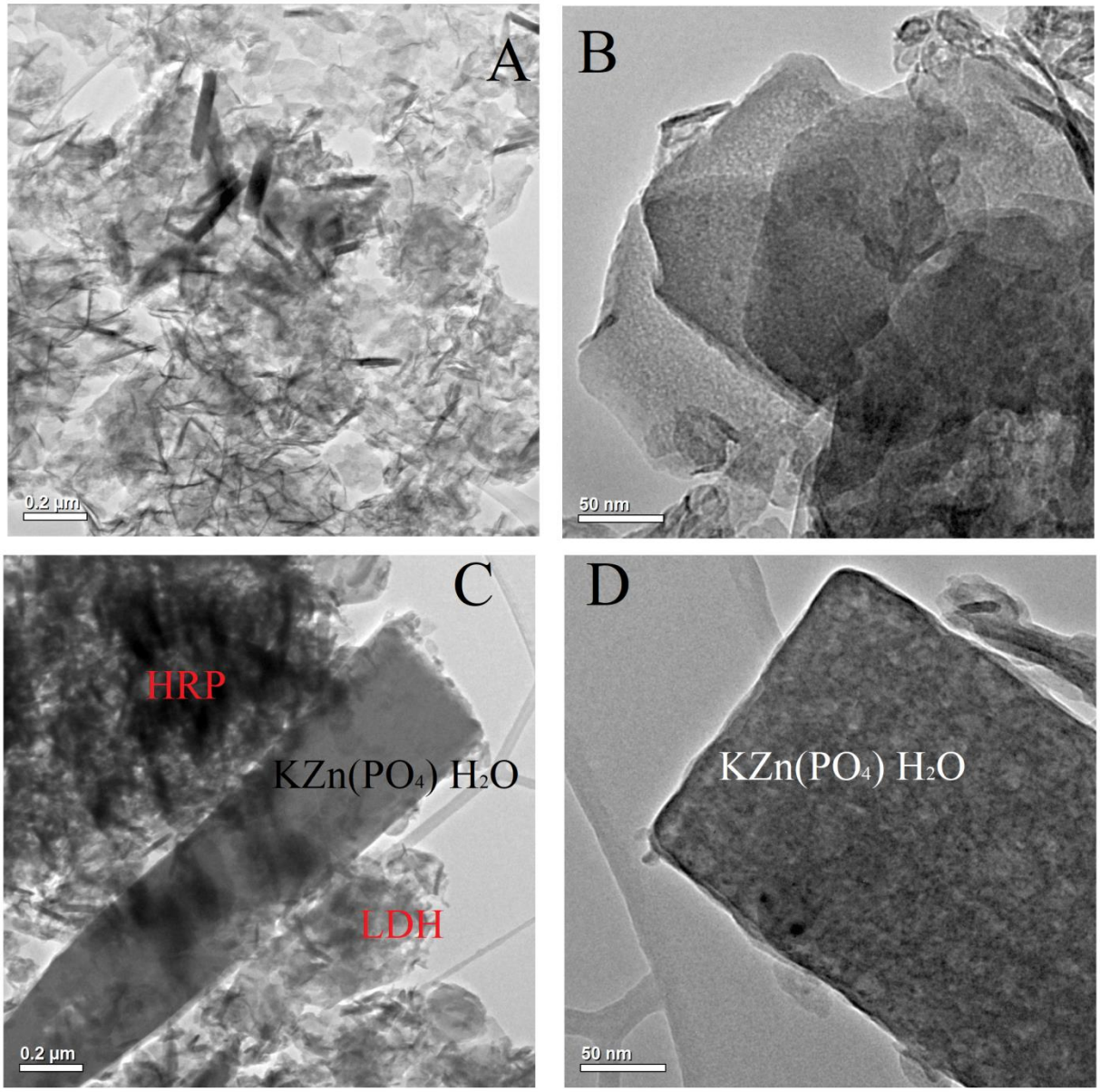

Figure 3.17: TEM images for A) and B) ZnAl(2/1) and C) and D) ZnAl-HRP.

3.3.2. Phenol removal via photodegradation, enzymatic and photo-enzymatic degradation in presence of ZnAl(2/1), HRP and ZnAl-HRP.

An attractive aspect in combining different techniques and for pollutants removal is the fact that some of them are able to degrade the pollutants via distinct pathways. This is the situation of phenols, which can be mineralized through photodegradation [120], but also they can be polymerized via enzymatic degradation [161], by using a specific enzymes class denoted oxidoreductase. Furthermore, these two methods could be combined simultaneously, following

a synergic effect between them for the removal of a particular class of pollutants, or they can be used in the same time or separately, following the degradation of different substances from the same system.

a) **Phenol removal via solar photodegradation in presence of ZnAl(2/1)**

The photocatalytic response corresponding to ZnAl(2/1) was tested for the solar photodegradation of phenol. Thus, 0.1 g of catalyst was dispersed in 100 mL phenol solution, 265 µM (1 g LDH/L phenol solution). Before starting the irradiation, the adsorption-desorption equilibrium of the pollutant on catalyst surface was performed, till no changes of the UV-Vis spectra were noticed. Afterwards, the firs sample was taken and the solar lamp (Unnasol US 800 solar simulator, 180 W) was turned on. The phenol photodegradation profile was monitored at 270 nm by measuring the UV-Vis absorption spectra with a Jasco V550 spectrophotometer.

The photocatalytic degradation of phenol under solar irradiation and in presence of ZnAl(2/1) is given in figure 3.18. The absorbance at 270 nm, corresponding to phenol,

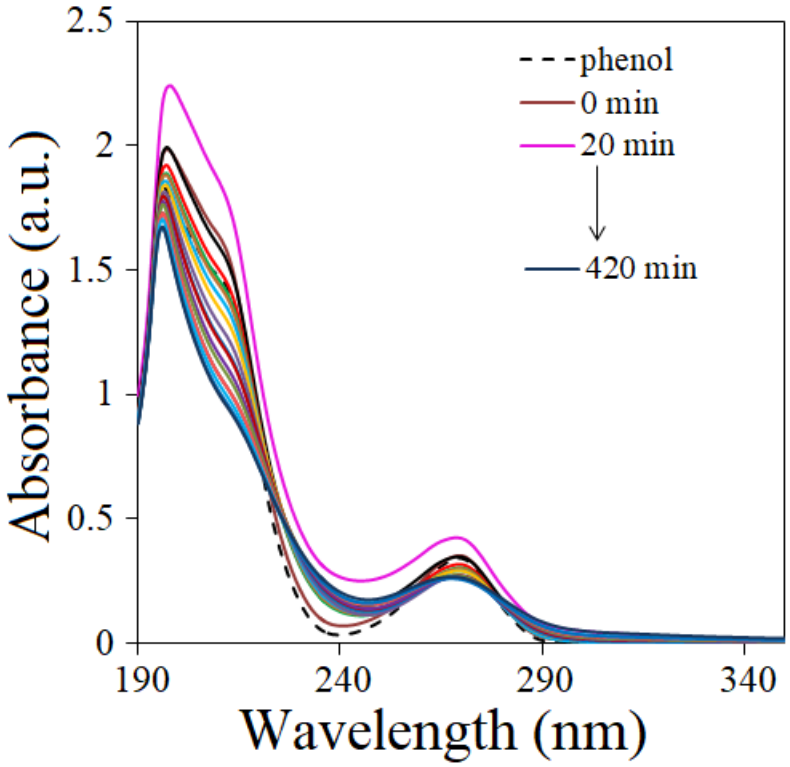

Figure 3.18: UV-Vis spectra profile for phenol solar photodegradation and using ZnAl(2/1) catalyst.

decreases slowly during the irradiation time, and after 7 h of testing, 20 % of phenol was removed from the system. The poor activity of this material is a consequence of its inability to absorb visible light. Furthermore, the band gap value of this material is 3.2 eV [225] and the

solar light is not a suitable source of energy to produce the required electron-holes pairs used further in photodegradation. Regarding the phenol photodegradation mechanism, our group was already investigated this reaction, which involves manly the photocatalytic conversion of phenol through three major stages: first, are formed instable phenoxy radicals, followed by a complex system containing catechol and benzoquinones formation. Further irradiation can convert the degradation products in biodegradable compounds as oxalic acid, malic acid, muconic acid and formic acid. In the end all this products are transformed into H_2O_2 and CO_2 [120,288].

b) Phenol removal via enzymatic biodegradation in presence of free HRP and ZnAl-HRP

The general mechanism of phenol photodegradation was discussed and approached many times in this thesis. However, the general reactions involved in the phenol polymerization, in presence of an oxidoreductase enzyme as HRP, needs to be also considered. In figure 3.19 are explained the main reactions which take place when phenols are enzymatically biodegraded.

Horseradish peroxidase is a heme enzyme containing in its structure an iron ion and for its utilization an electron donor is required. Generally this role is played by the H_2O_2 [289]. In presence of H_2O_2, the Fe (III) from the native HRP is oxidized to a compound I, which contains a Fe(IV) oxoferryl center [290]. Further, Compound I accepts in its active site a phenol molecule. In this way, a phenolic free radical is formed and released in the reaction medium. Another HRP compound is formed (II) and it will react with another molecule of phenol, returning the initial form of enzyme. The released aromatic free radicals, will interact with each other, and an insoluble polymeric product will be formed [291].

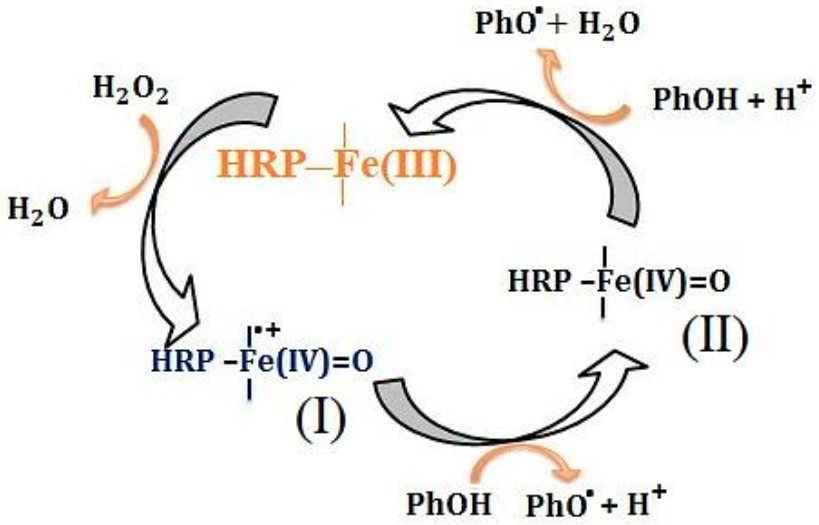

Figure 3.19: The enzymatic polymerization phenol (PhOH) in the presence of H_2O_2 and HRP.

The enzymatic experiments were performed in ultra-pure water, pH = 6.5. In a reaction volume of 25 mL, the H_2O_2 concentration was 750 µM and the phenol concentration was 265

µM. After the first sample was taken, 8 µg of free HRP were added to the solution. So, 20 µL of enzymatic solution (prepared in phosphate buffer, pH= 7) was added in case of free enzyme experiment (8 µg of free HRP), while for the supported enzyme test, 0.025 g of ZnAlLDH-HRP was used, containing approximately 8 µg of immobilized HRP. Each sample was centrifuged for solids removal (catalyst + precipitate). The supernatant was used to appreciate the phenol polymerization. It is important to be noted that the catalyst concentration in solution is for all the tests 1g/L. Also, the phenol concentration is the same, 265 µM (25 mg/L).

The UV-Vis spectra profiles of phenol obtained for its enzymatic biodegradation by using free HRP and ZnAl-HRP are given in figure 3.20. In case of free HRP experiments it was noticed that a new compound is obtained. In the first 5 minutes, the solution color modifies from colorless to a yellow tone (see figure 6.19 B) and on the UV-Vis profiles a new peak appears 399 nm. The evolution of this new peak was to increase fast in the first 5, afterwards it starts to decrease. Concomitant with the 399 nm absorbance decrease, a precipitate was formed. The precipitate amount enhances during the time (figure 3.20 B 1-6), and after 7 hours the solution is almost colorless. The total enzymatic biodegradation at the end of the test was 41 % from the initial concentration of phenol.

In presence of immobilized HRP, the polymerization reaction takes place, but it is much slower compared with the one of free enzyme (see figure 3.20 C). The intermediate product can be detected with the spectrophotometer after 130 minutes of reaction. The reaction has the same route like the free HRP: the peak at 399 nm increases till a maximum is reached, and then the decrease starts with the formation of polyphenol. During 7 h, 25 % from the initial phenol quantity were converted in products.

Similar studies showed that the HRP can be immobilized on TiO_2 [292], glass [293] and magnetic beads [267], and used successfully for the phenols removal. HRP covalent immobilized on graphene oxide-Fe_2O_3 composite degraded 95 % of phenol in presence of polyethylene glycol (PEG), while without PEG only 9 % of pollutant was degradated after 3 h of reaction [294]. Using HRP attached on aluminum-pillared clay, between 85 % -100 % of phenol was removed in 4 h by using PEG and immobilized HRP concentrations between 0.2-1 U/mL (the total volume reaction was 50 mL) [295]. Comparing our results with those mentioned above, we believe that the anionic clays can be promising supports for HRP immobilization and further utilization in hazardous substances removal. Even if a decrease of performance with about 50 % was observed after enzyme absorption on LDH, the immobilization and the enzymatic reactions were carried out free of other supplementary reagents, the process being greener and economic. Furthermore, the LDHs materials were poorly approached as supports for HRP immobilization and for further phenols degradation.

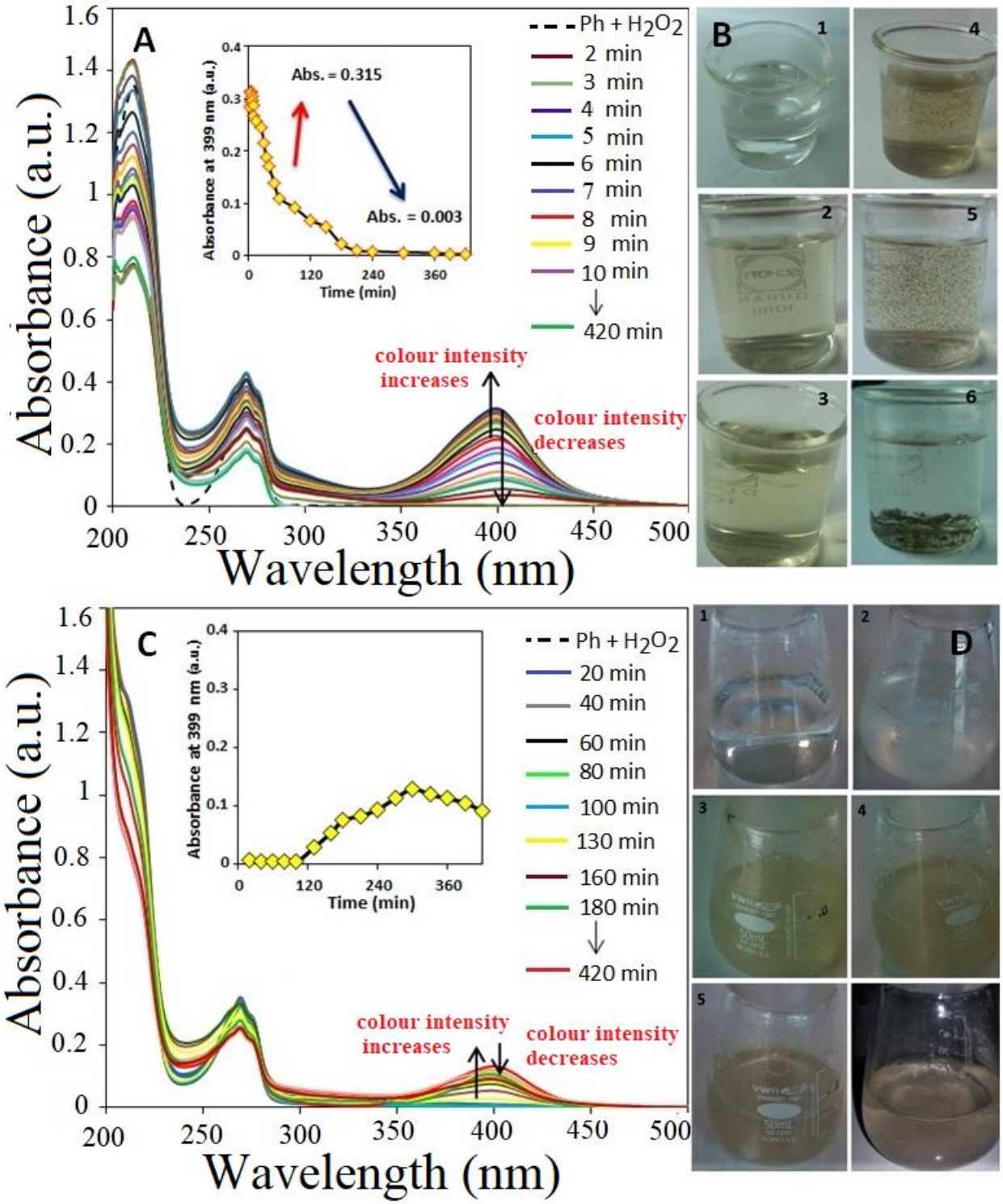

Figure 3.20: UV-Vis spectra of phenol enzymatic degradation in presence of A) HRP and C) ZnAl-HRP; B) Ph degradation with HRP 1) initial Ph; 2-3) Ph in the first 5'; 4) Ph after 20', 5) Ph after 7 h; 6) Ph sedimentation; D) Ph degradation with ZnAl-HRP 1) initial Ph; 2) Ph after ZnAl-HRP adding; 3-4) Ph after 180' and 300'; 5-6) Ph after 7h and after solid sedimentation.

c) **Phenol removal via photo-enzymatic degradation in presence ZnAl-HRP and solar light.**

Recently, efforts have been focused on heterogeneous catalytic processes obtained by combining biological systems with photocatalysis [286,296,297]. Photocatalysts based on TiO_2 and bacteria as *Geobacter sulfurreducens* [296], *Pseudomonas aeruginosa* ATCC27853 [286], *Methylibium, Runella, Pseudomonas* and *Comamonas* [297] have been previously raported for the photocatalytic-biodegradation of 4-clorphenol, phenol, tetracycline under UV, solar or visible light. Replacing the bacteria with enzymes can provide more stable end efficient systems since the enzymes are more active and easier to use [298]. Some researchers had degraded pollutants through separately photocatalytic and enzymatic degradation [299,300]. The cascade systems involving firstly a photochemical degradation followed by an enzymatic reaction [301,302] was also used for pollutants removal. However, the simultaneous photocatalytic-enzymatic degradation of efluents was poorly approched. J. Jia et al. have been reported for the first time the simultaneous utilization of immobilized laccase on porous glass and TiO_2 for the UV degradation of 2,4-diclorophenol [298]. Later, a catalysts containing glucose oxidase immobilized on TiO_2/polyurethane was used for the decolorization of acid orange 7 under UV light [303].

Since the redox enzyme operates similarly as photocatalysts, the main purpose of this study was to investigate if a biohybrid type ZnAl-HRP, formed from two elements able to degrade the same pollutant can be used together with total participation of both components.

The reaction system and the testing protocol were similar with those described in section 2.1, but in this case the reaction mixture contains the phenol (265 µM), the ZnAl-HRP (1g/L) and the H_2O_2 (750 µM), and it was mixed under solar irradiation during 7 h. The phenol concentration decreases slowly and after 130 minutes of irradiation, a new peak appears at 410 nm. In the zoomed area of figure 3.21 can be remarked that this peak has the same evolution, with an increase till a maximum value followed by a decrease. At the end of the test, 35 % of phenol was removed from its initial concentration.

In table 3.7 are presented the catalytic performances obtained for the phenol degradation by using different catalytic systems. After 7 h of irradiation, the ZnAl(2/1) degrades 20 % of phenol, while the ZnAl-HRP biohybrid removed 35 %. From figure 3.21 can be observed that the pollutant is degraded via both pathways: the cascade approach photodegradation and the enzymatic polymerization. These proceses are supported by the decrease of the absorbance at 270 nm, and also by the apparence of a peak at 410 nm, which can be attributed to the aromatic free radicals formation. Comparing the results obtained for the ZnAl-HRP without irradiation, can be concluded that the degradation of phenol under solar irradiation and using ZnAl-HRP is mainly a photodegradation process. Previous studies have shown that the enzyme activity can be drastically affected for the UV light [304]. Furthermore, the H_2O_2 can be also easily degraded by the light [305]. These two factors and the relatively high power of the solar lamp (180 W), could

explain the poor enzymatic activity of the ZnAl-HRP. However, this type of study, using a LDH-enzyme system, was for the first time approached now, form what we know, and it gives us important information about the system weakness, and it is a starting point for further investigations. For instance, the light intensity can be varied by modifying the distance between the light source and the degradation mixture, or visible light could be used. Additionally, highly photo responsive catalysts might be designed by doping the LDHs with different NPs, which can

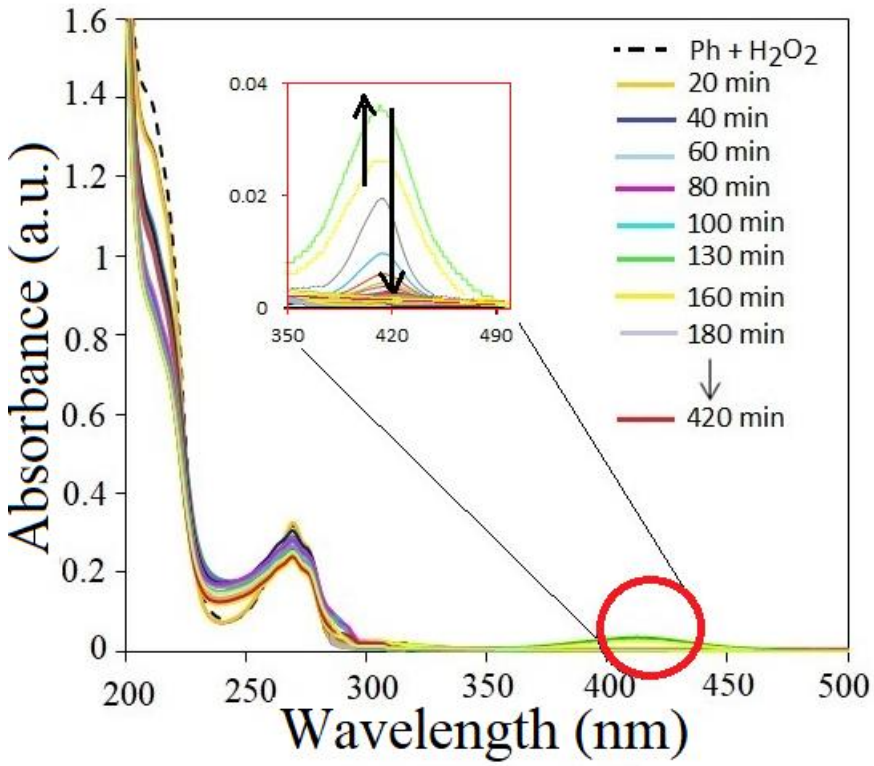

Figure 3.21: UV-Vis spectra of phenol photo-enzymatic degradation in presence ZnAl-HRP, solar irradiation and H_2O_2

Table 3.7: Catalytic performances in phenol degradation in presence of different catalytic systems.

	ZnAl(2/1) + h	**HRP**	**ZnAl-HRP**	**ZnAl-HRP + h**
% Phenol degradation	20	41	25	35
degradation type deducted	photodegradation	enzymatic polymerization	enzymatic polymerization	mainly photodegradation

be used to provide the oxidative agents that HRP needs for its activation. In this way, the H_2O_2 utilization could be avoided.

Another activity differences is also observed between the free enzyme, which is able to degrade 41 % of phenol, and the ZnAl-HRP which removes only 25 % of phenol. More likely, this difference could be explained by diffusional limitations of the substrate and products related to the HRP immobilized on the solid support. Furthermore, during the reaction, the solid amount issued from phenol polymerization can be adsorbed on LDH support, and this could decrease the availability of the enzyme active site. Some loss of ZnAl-HRP activity could also be a consequence of immobilization, when the enzyme might bound improperly on the LDH surface, or the enzyme structure is affected.

Figure 3.22 presents some perspective approaches which can be performed in order to remove different pollutants from the same system. Enzymes and LDHs can be combined in different ways leading to hybride catalysts or catalysis. For instance, the LDHs can be used simply as a support for the enzyme (a), and the resulted material can be further used in presence

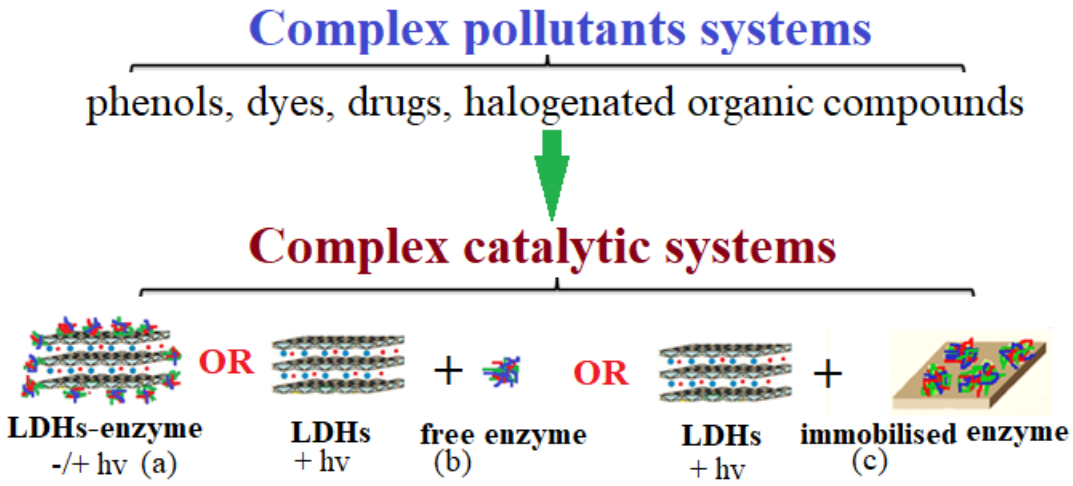

Figure 3.22: Catalytic systems design involving LDHs and enzyme for complex pollutant systems

or in absence of irradiation, in function of the pollutant system composition. When used under irradiation, the pollutants might be degradated via both enzymatic and photocatalytic patways. Free or immobilized enzyme can be also combined with LDHs (b and c). In this case, the photodegradation and the enzymatic degradation of the pollutants will take place in cascade mode, in function of the system particularities. For instance, the composition of the system can impose first the removal via photodegradtion of certain pollutant which may have a negative effect on the enzyme activity, followed by the enzymatic remediation.

3.4. Investigation of HRP - Au/ZnAlLDH systems

In chapter 3.2 was observed that after HRP immobilization on Au/ZnAl and Au/ZnAl-550 the resulted materials have no enzymatic activity. The materials characterization proved that the immobilized enzyme environment is quite complex, with many crystalline phases identified during different analyses. However, the same phases were observed for ZnAl-550-HRP material and in this case the HRP retains a part of its initial activity. For this reason, the investigation of HRP-Au/ZnAl systems was further investigated.

3.4.1. Synthesis and physico-chemical characterization of Au/ZnAlLDH.

The Au/ZnAl(3/1) layered double hydroxide synthesis and characterization were approached in subchapter 3.2.1.

3.4.2. HRP influence on AuNPs release from AuNPs/ZnAl(3/1)LDH

In order to determine how the enzymatic environment interacts with the Au/ZnAl material, different quantities of Au/ZnAl (2.25, 9, 22.5; 45 mg) were dispersed in 5 mL phosphate buffer solution containing 0.45 mg HRP. Thus, the ratio between HRP and Au/ZnAl was 1/5, 1/20, 1/50 and 1/100. During 5 days at determined time intervals, the solid was removed via centrifugation and the UV-Vis profiles and the enzymatic activity of the supernatant were monitored. For all the activity tests, 1 μL of supernatant was added to a 2.5 mL of buffer solution containing 40 μM $ABTS_{red}$ and 20 μM of H_2O_2. The HRP activity was determined from the linear part of the f([$ABTS_{oxd}$]) = t representation. In figure 3.23 are presented the UV-Vis profiles of HRP solutions after Au/ZnAl removal by centrifugation. The supernatant was spectrophotometrically analyzed in a range between 200-700 nm. It was noticed that the initial color of HRP solution changes from yellow-shade to different purple shades (see figure 3.23), when it is in contact with the Au/ZnAl. Also, when the color of supernatant starts to change, on the UV-Vis spectra (figure 3.23 a-d), peaks between 500-536 nm appears, which are assigned to AuNPs [274]. During the contact time, the peaks intensity attributed to AuNPs increase in supernatant, the wavelengths are moved more to the red region of the spectrum, while the purple color intensity increases. The enhancement of intensity is attributed to AuNPs release from the Au/ZnAlLDHs surface in the HRP solution [306], and the shift of AuNPs absorbance to longer wavelengths is assigned to the increase of the AuNPs diameter [307]. In case of the HRP:Au/ZnAlLDH = 1/100 system, the AuNPs resorption, togheter with a significant HRP adsorption on clay surface was observed, probably due to the higher Au/ZnAl quantity.

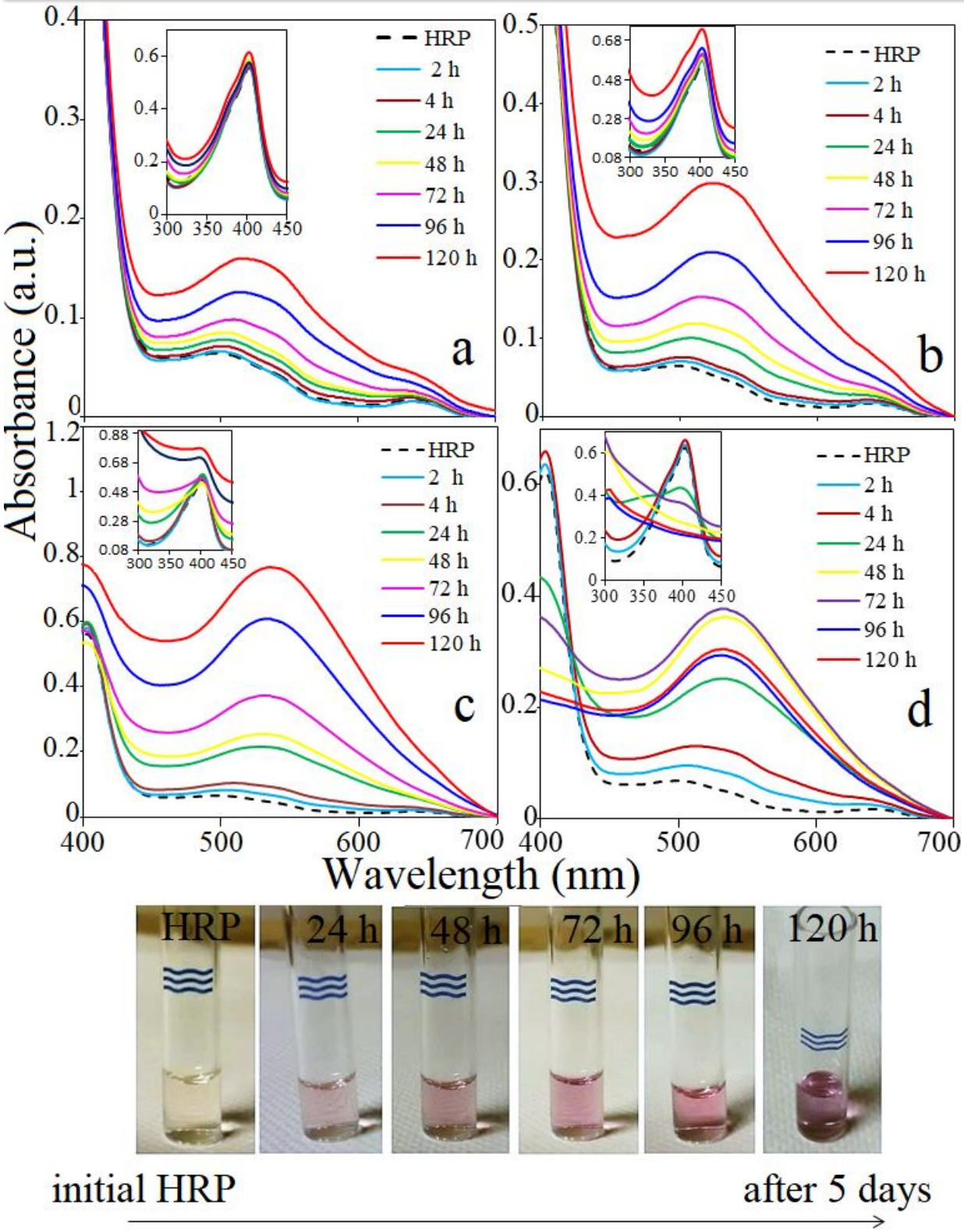

Figure 3.23: UV-Vis spectra profile evolution of HRP:Au/ZnAlLDH systems: a) 1/5, b) 1/20; c) 1/50, d) 1/100 and the color changes during 5 days of contact between HRP:Au/ZnAl = 1/20.

The UV-Vis spectrum of native HRP shows a peak around 280 nm characteristic to the proteins and another one at 403 nm assigned to the Soret band. The evolution in time these regions present a significand enhancement of the intensity during the contact, underlining an increase of the quantity of enzyme fixed on AuNPs [308].

As already mentioned, the HRP spectrometric profiles show a significant decrease of absorbance only when the enzyme:clay ratio was 1/100. However, when the activity of supernatant was determined and compared with the initial HRP activity, before its contact with the LDH, it was noticed that, except the system 1/5, the activity decreases in time, and the decrease could be directly correlated with the AuNPs quantity in solution (see figure 3.23 a-d and figure 3.24), since the enzyme adsorption on the support was insignificant. This might be an indication that the AuNPs might induce an enzyme inhibition [280], because of AuNPs binding to HRP active site [309].

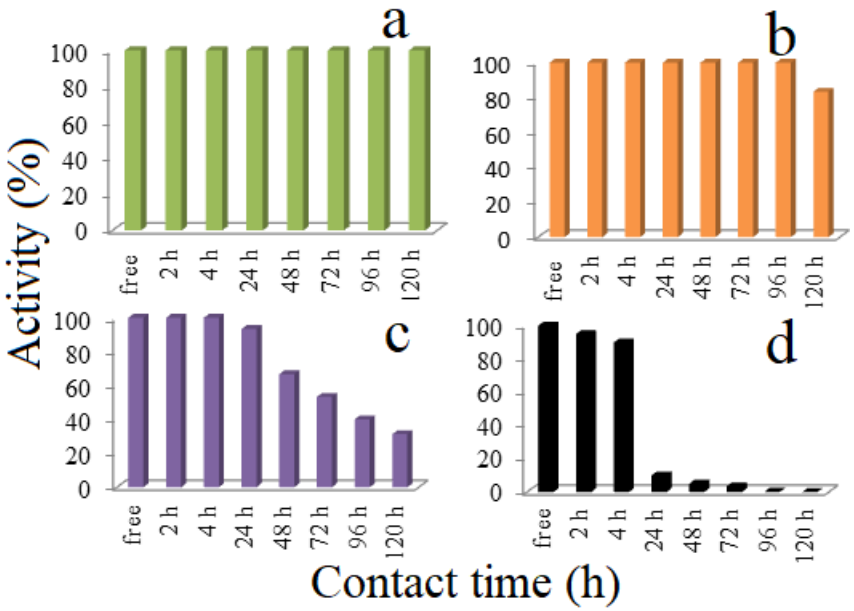

Figure 3.24: HRP activity evolution during 5 days of contact with different quantities of Au/ZnAlLDH: a) 1/5; b) 1/20, c) 1/50, d) 1/100.

When the pH was measured (table 3.8), an increase of its value from 7 to 10.5 was noticed during the 5 days of contact. For this reason, the enzyme activity decrease might be correlated also with the effect of the pH modification [310]. The pH value enhancement can be a quensequence of LDHs dispersion, but in the same time, the tendence to reach higer values as 10, migh underline a possible clay dissolution [275,311].

Table 3.8: HRP pH evolution during 5 days of contact with different quantities of Au/ZnAl.

		Time							
	HRP:Au/ZnAl	**initial**	**2h**	**4 h**	**24 h**	**48 h**	**72 h**	**96 h**	**120 h**
HRP solution pH	1/5	7	7	7	7.5	7.5	8	8	8
	1/20	7	7	7.5	7.5	8	8	8	9
	1/50	7	8	8	9	9	9.5	9.5	10
	1/100	7	7.5	7.5	8	9	9.5	10	10.5

a) **pH effect**

In order to establish if the pH increase can be related with AuNPs release in the solution, a HRP:ZnAl(3/1) = 1/50 system type was investigated for 5 days. The UV-Vis spectrum presented in figure 3.25 shows that the enzyme is adsorbed on LDHs surface in a proportion of 33 % from the initial peroxidase quantity. Furthermore, the supernatant solution activity decreases with 33 % compared with the initial enzyme performance, being in a good concordance with the quantity of enzyme adsorbed on support (see figure 3.25-b). The pH solution was at the end of the 5 days at a value of 7.5. This result shows that the gold nanoparticle presence in the enzymatic solution are able to influence the pH and the enzymatic activity. In the case of HRP:ZnAl(3/1) = 1/50 system the pH variation was small, and at pH around 7, 33 % of enzyme were immobilized. The systems containing gold have shown that an increase of pH leads to a low enzyme adsorption.

Taking this into consideration, and also the necessity to establish how the AuNPs affect the HRP performance, a new system HRP:Au/ZnAl = 1/50 was investigated, but in this case the pH was kept at a value of 7. For this, the pH was corrected with HCl, 2 M. From figure 3.26 it can be noticed that the adsorption capacity of the support is improved. Comparing the HRP:Au/ZnAl = 1/50 spectra at ph 7 with its corresponding image from figure 3.23-c, the effect of pH on the immobilization procedure and on the AuNPs release is evident, revealing that a value of pH equal with 7 favors the formation of strong electrostatic interactions between the positively charged lamella and negatively charged biomolecules [284]. Furthermore, when the pH is neutral, the intensity characteristic to AuNPs is half from the intensity of the AuNPs obtained from the initial test (see figure 3.23-c). It looks like the pH is an important parameter, which can be directly correlated with the adsorption of HRP, but also with AuNPs release.

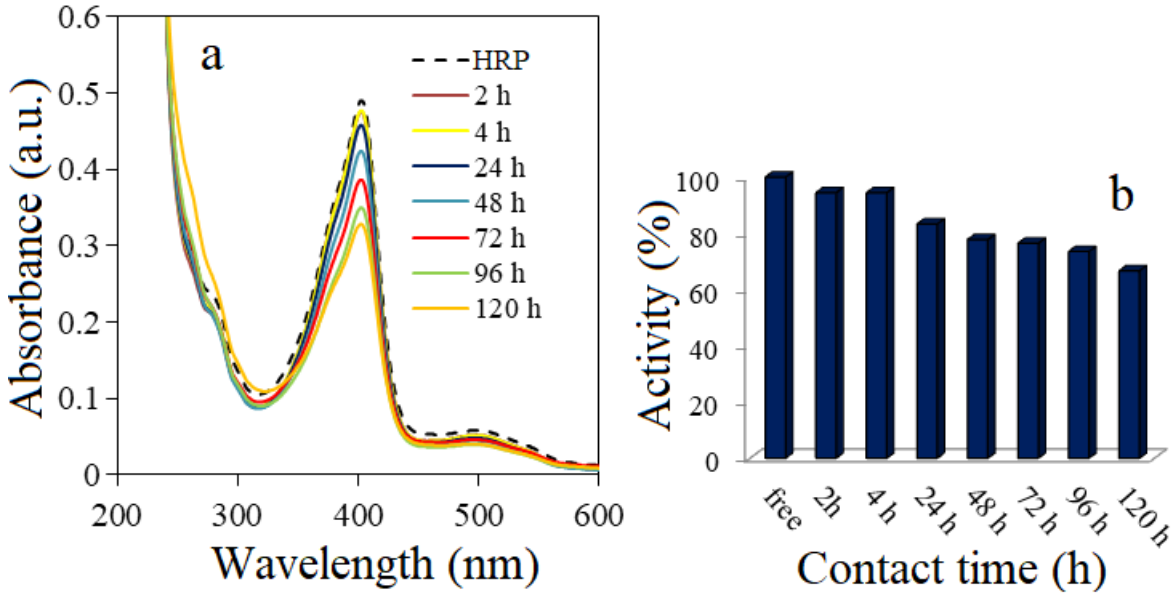

Figure 3.25: HRP UV-VIS spectra profiles (a) and activity evolution (b) during 5 days of contact with ZnAl(3/1); HRP:ZnAl(3/1) = 1/50.

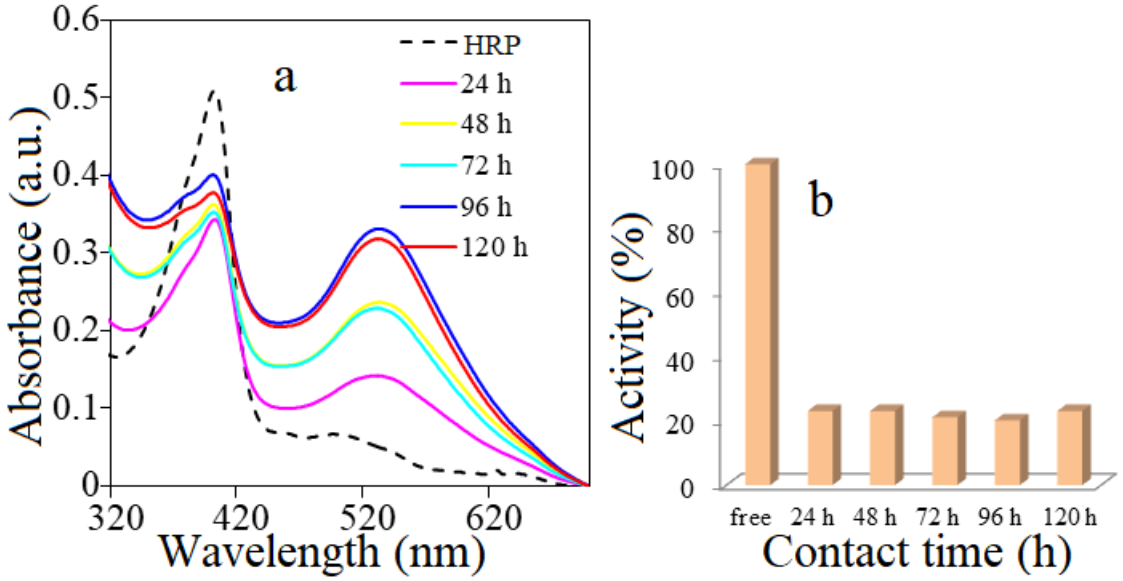

Figure 3.26: HRP UV-Vis spectra profiles (a) and activity evolution (b) during 5 days of contact with Au/ZnAl; HRP:Au/ZnAl = 1/50 and pH = 7.

In table 3.9 is presented the HRP activity loss in the supernatant for three representative systems, caused by HRP adsorption and AuNPs presence. According to the spectrum from figure 3.25, after 24 hours of contact, 32 % of HRP were adsorbed from the initial enzyme quantity and in solution 68 % of enzyme were remaining. However, the residual activity of the supernatant corresponding to the 24 h measurement shows that the activity is only 23 % from the initial one.

Table 3.9: HRP activity loss after 5 days in contact with different LDH supports.

	Activity loss (%)		
HRP:LDH systems = 1/50	HRP adsorption	AuNPs presence	Total activity loss (%)
HRP:ZnAl, pH = 7	33	-	33
HRP:Au/ZnAl, pH=7	32	45	77
HRP:Au/ZnAl, increasing pH	7	63	70

Thus, under constant pH conditions, the fast decrease of HRP activity for HRP:Au/ZnAl =1/50 cannot be correlated only with the adsorption, but also with an inhibition or denaturation of peroxidase because of the contact with AuNPs. Furthermore, in can be remarked that at pH=7, for the HRP:ZnAl = 1/50 and HRP:Au/ZnAl = 1/50 (see figures 3.25 and 3.26), the enzyme absorption on surface is 33 % and 32 % respectively. However, only for the system without gold, the enzyme activity in supernatant can be related with its immobilization. The system containing Au/ZnAl presents an additional 45 % enzyme loss, which can be attributed to the AuNPs presence. Comparing the last two systems from table 3.9, might be concluded that the pH increase induces a supplementary activity loss of 18 % (from 45 % to 63 %).

The obtained data show that a neutral pH imposes a smaller AuNPs release, while the progressively increase of pH implies the increase of AuNPs content in solution and consequently a rapid loss of HRP activity.

b) **Enzyme influence**

By now, it was remarked that the AuNPs have an influence on HRP activity. Furthermore, it was observed a release of gold from Au/LDH surface into the enzymatic solution. An important step at this point of the study is to establish if the gold release can be associated or not with the enzyme presence in the buffer solution. For this reason, the Au/ZnAl material was dispersed in 1 mL phosphate buffer, pH=7, 0.1 M. Another experiment was carried out by adding the Au/ZnAl nanocomosite to a catalase solution prepared in phosphate buffer, pH=7, 0.1 M. The second enzyme, catalase, was used in order to find out if the release of AuNPs from the LDH surface is dependent on enzyme type, or we can obtain the same effect by using other enzyems different from HRP. In figure 3.27 can be observed the UV-Vis spectra profiles of the investigated solutions. For the buffer solution, alternant desorption-adsorption of AuNPs from Au/ZnAl surface was noticed. The maximum AuNPs amount reached after 96 hours of contact is 18 times much smaller than for HRP:Au/ZnAl with a ratio of 1/50 (see figure 3.23 c). However, after 5 days, almost all the AuNPs are resorbed on support surface. The pH of the buffer solution increases till 9.5. In case of catalase solution, the AuNPs desorption was much intense if compared with buffer solution, but 6 times lower than HRP:Au/ZnAl (ratio of 1/50) system. These results show that whatever the enzyme, horseradish peroxidase or catalase, it

favors the AuNPs release form LDHs surface, probably through a gold-enzyme complex formation.

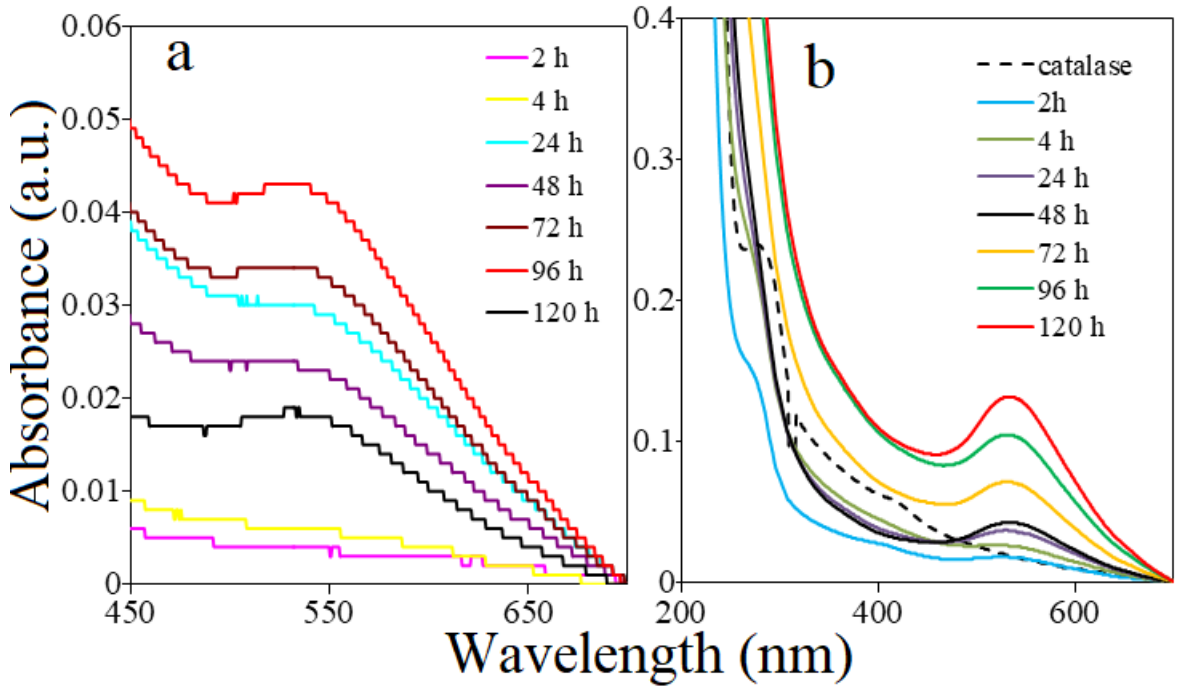

Figure 3.27: UV-Vis spectra profiles for Buffer:Au/ZnAl = 1:50 and catalase:Au/ZnAl = 1:50

c) **HRP-AuNPs complex formation**

The formation of gold – enzyme complexes was investigated by many scientists. Thus, enzyme like glucosidase, cellulase, pectinase, xylanase, phospholipase etc, were linked to colloidal gold nanoparticles via electrostatic interactions of negatively charged carboxylate groups of enzymes and used further in different applications [312]. A similar study, but starting from auric chloride solution which was contacted with HRP, showed the AuNPs formation, but in this case the enzyme activity was maintained [308]. During the research, the HRP was simply incubated in auric gold solution prepared in Tris-HCl buffer and the AuNPs synthesys was monitored by UV-Vis measurements. The authors had presumed that the retention of enzyme activity might be because of the nanoparticles and the enzyme had formed a linkuage via those animoacids which are not residues of the HRP active center. In another comunication, gold thioglucose had induced an inhibitory effect on selenium-glutathione peroxidase when used in presence of an excess of glutathione. It was concluded that the inhibition was caused by the interaction between the gold and the active site of the enzyme which might lead enzyme inactivation [309].

Regarding this particular situation when HRP is contacted with Au/ZnAlLDH, we propose a potential mechanism of AuNPs release during the contact between the system elements, which are explained in figure 3.28. Firstly, the enzyme comes in the proximity of the support. Here, a part of enzyme is adsorbed directly on layered double hydroxide matrix, another quantity of enzyme is adsorbed on AuNPs from clay surface. When attached, the AuNPs is fixed to the HRP active site and the new gold-enzyme complex is inactive [313]. The gold enzyme complex is continuously released in solution. Because after the HRP contact, the resulted solids are enzymatic inactive, it was assumed that after HRP adsorption on Au/LDH, it suffers conformational changes which affects its activity. In other words, the enzyme interaction

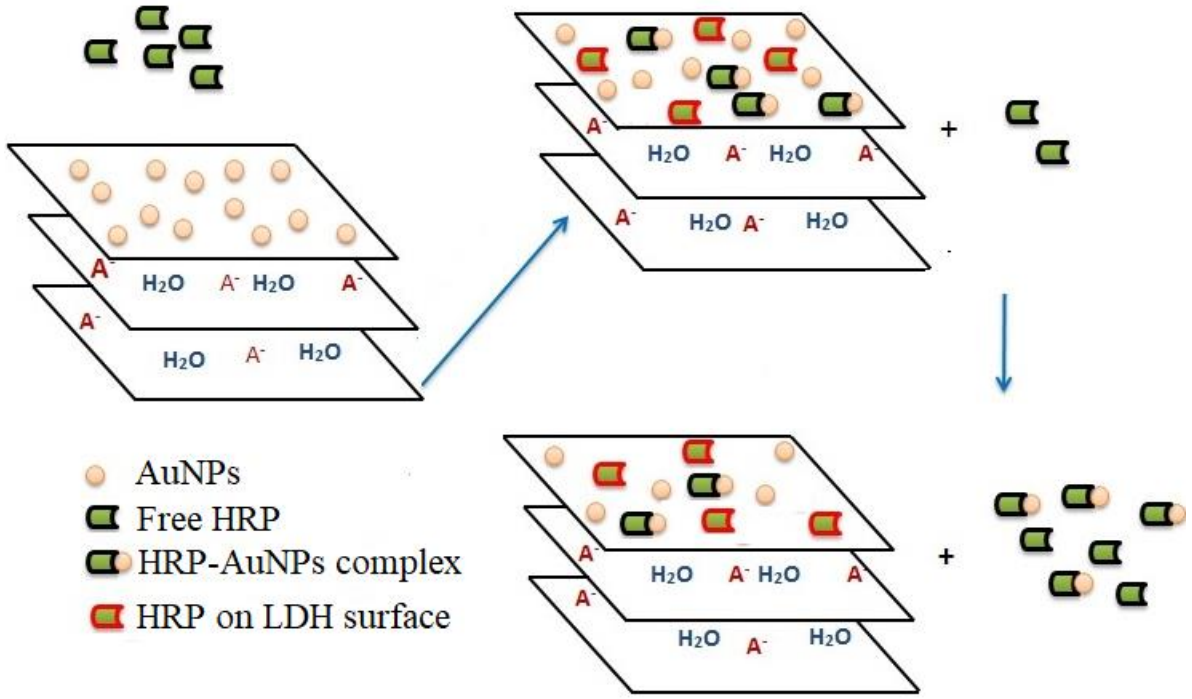

Figure 3.28: Proposed mechanism for AuNPs release with HRP-AuNPs complex formation.

with the AuNPs or the caly surface leads to its inactivation or distruction. Furthermore, considering the material features, we can affirm that some AuNPs from LDH surface are easier to be released into solution/ The TEM analysis of Au/ZnAl nanocomposite revealed that on LDHs surfaces, the AuNPs are dispersed or agglomerated. The agglomerated AuNPs are more suitable to link with the enzymes and to be released from the surface as a HRP-AuNPs complex.

d) **TEM surface analyze**

In order to see how the surface of the materials is affected by the long time contact with the enzyme, TEM analyses were performed. For this, after the 5 days of contact, the solids were removed, washed with ultra-pure water and dried at room temperature. The TEM analyses were made for the next systems: HRP:Au/ZnAl =1/50, Buffer:Au/ZnAl = 1/50, catalase:Au/ZnAl

=1/50 and HRP:Au/ZnAl = 1/50. The last sample was separated from the enzymatic system after one hour of contact. Furthermore, after 5 days of contact, the supernatant was collected for the HRP:Au/ZnAl and also analyzed to confirmed the AuNPs presence in the solution. The EDX measurements were made for representative regions of the solid samples and they revealed a decrease of gold content after the 5 day of contact, which might be assigned to the release of AuNPs from the matrix surface.

The TEM images (figure 3.29) present different morphologies for the same material, as it was previously observed in this chapter. The elemental analyses have proven the presence of micrometer rectangles (see figure 3.29 B, D, E), composted from O, Zn, P and K, the Al being in small percentages. These areas are assigned to the $KZn(PO_4)$ H_2O phase. There are also zones formed by O, Zn, Al and small amounts of P, K, which might be attributed to the layered double hydroxide phase, where a part of Al and Zn cations was substituted by P and K cations. The micrometer rectangles are observed also for the system Buffer:Au/ZnAl, and this is suggesting that their presence is not necessary depending on enzyme presence. However, for the system HRP:Au/ZnAl whose contact time was only one hour, the rectangles are not present and the surface look more like the one of the initial Au/ZnAl material. The rectangle morphology formation might be a function of the contact time between LDH and the phosphate buffer.

Besides these morphologies, the AuNPs were observed on LDHs surfaces, but the amount of the agglomerated AuNPs decreased. The surface presents a more dispersed gold on material surface, compared with the initial material (see figure 3.29 A, D and E). This can demonstrate that the agglomerated AuNPs are more suitable to bind the enzyme and to be released. The dispersed AuNPs, which intimately interact with the LDH surface, are more difficult to be unlinked from the surface. Furthermore, the EDX data support the TEM analyses, revealing an important decrease of gold content after the 5 days of contact. However, the decrease of gold is not significant for the system containing only buffer (see figure 3.29 B), being in good agreement with the UV-Vis profiles, which show that in presence of buffer, the gold release is not significant. Dark aggregates were observed on LDH and on the dispersed AuNPs (see figure 3.29 D and E-d) and they can be assigned with the enzyme presence.

The TEM imagine for the collected solution after five days of contact is presented in figure 3.29-F and it reveals that in solution AuNPs are present. The EXD shows that a small quantity of K is also present in the analyzed sample. The AuNPs diameters vary in a range of 3-29 nm and their shape is spherical for the smaller particles and oval for those with larger dimensions.

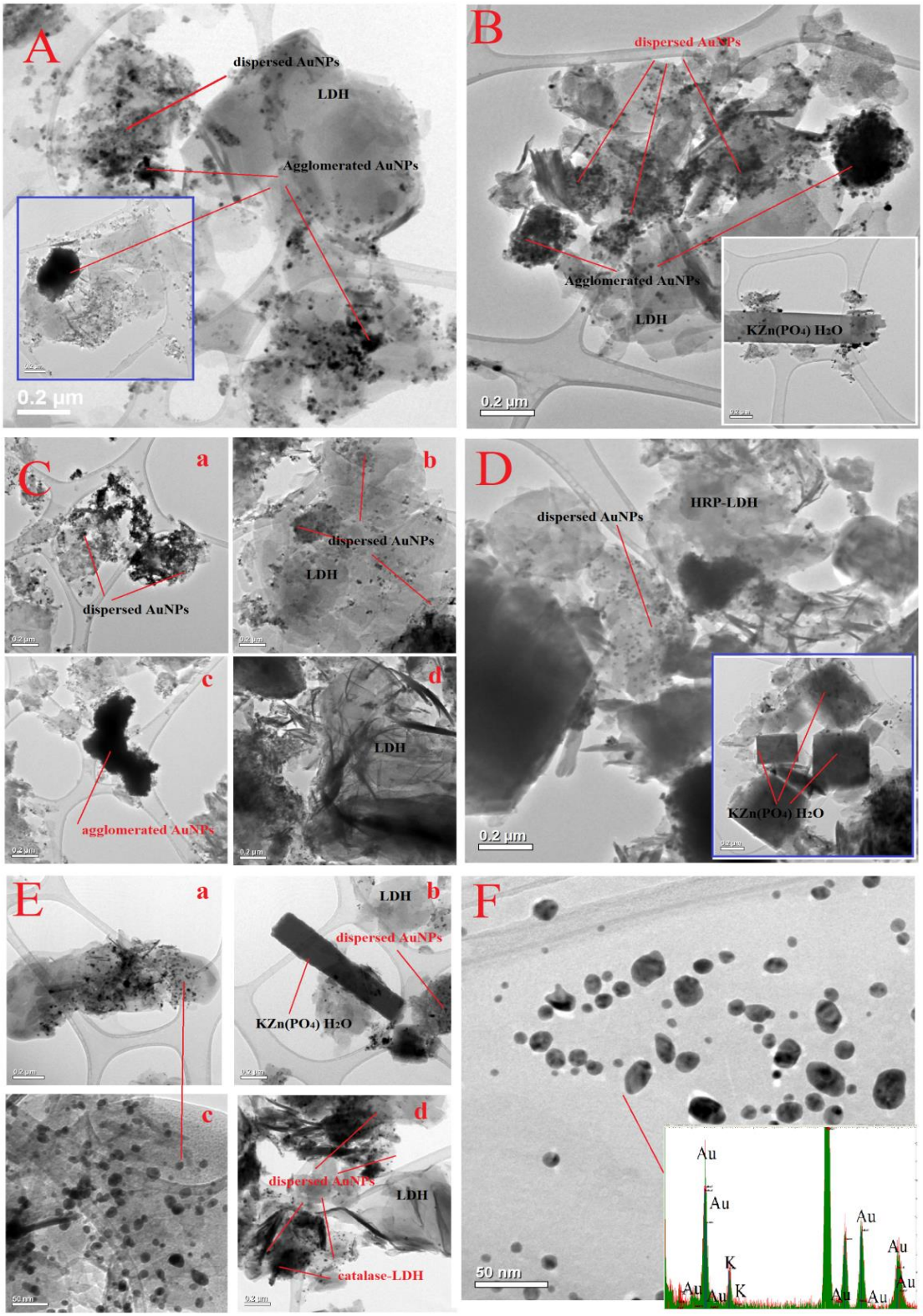

Figure 3.29: TEM images for A) Au/ZnAl, Buffer:Au/ZnAl; C) HRP-Au/ZnAl after 1 h of contact; D) HRP:Au/ZnAl; E) catalase: Au/ZnAl; F) AuNPs in collected solution after 5 days.

In this chapter we investigated systems formed by HRP and Au/ZnAl which were put in contact for 5 days. Both systems elements influence each other. The AuNPs presence on the LDH leads to enzyme activity loss, while the enzyme presence induces the release AuNPs from the clay surface. As far as we know, this is the first study which approaches the investigation of Au/LDH:enzyme systems. By now, was reported the synthesis of AuNPs or AgNPs by using different types of enzymes, usually starting with silver nitrate or auric chloride solution [314–319]. This study can be a start point for other investigations for NPs synthesis or their release from surfaces assisted by enzymes.

The negative effect that the AuNPs have on the HRP and catalase activity is a very interesting result which could be further approached in infections and cancer therapies. It is well known that the living cells have in their structure catalase and/or peroxidase [320]. These enzymes are very important because they protect the cells against the oxidative species, which can damage different macromolecules as DNA, proteins, lipids, which are important for the cellular activity. Inactivating these two enzymes, by targeting the Au/LDH to cancer cells or infections, the death of the cells can be induced, just because of the increase of the oxidative species. Furthermore, the AuNPs can be forward involved in processes with the same proposes after their release. An advantage of the LDH materials which makes them good candidates for this application is their biocompatibility. *In vivo* studies proved that the LDHs are highly tolerated by different organisms as that of the rabbits or mice [67].

3.5. HRP activation and NADH regeneration from NAD^+ by using ligth irradiated Au/ZnAl layered double hydroxide

3.5.1. HRP activation by Au/ZnAlLDH in presence of irradiation.

The layered double hydroxides are semiconductor materials able to generate redox agents when excited by appropriate energy sources (light, temperature). For this reason they were intensely approached in photocatalytic processes, when the reaction was initiated by a source of light [225]. On the other hand, oxidoreductase enzymes can be excellent biocatalyst for the oxidation of a variety of compounds. The horseradish peroxidase is a model enzyme which catalyze the oxidation of a wide number of phenolic derivatives. Generally, the HRP needs, beside the electron donor substrate, an oxidizing agent, and in the majority of the situation this role is played by the H_2O_2 [161,267]. However, the reaction is dependent on H_2O_2 and for this reason the constant addition of this regent is required. Furthermore, the longtime exposure of HRP to H_2O_2 will lead to enzyme irreversible denaturation [321].

It was believed that a photochemical reaction involving HRP and a source of irradiation can enhance the control of the enzymatic reaction, avoiding in the same time the utilization of hydrogen peroxide. Because the single HRP can not be activated only by the light, the design of a hybrid photochemical system is required. Regarding this, Soares *et al.* have been reported that

methylene blue (MB) can bind HRP and under light excitation the MB can act as a reducing agent for HRP [322]. Kamada *et al*. intercalated the HRP into the iron doped titanate layer (FT), and the light generated holes of FT were used to oxidize the HRP to its activated state. Another study was also approached, when the HRP was adsorbed on α-Fe_2O_3 and used for the photo-enzymatic oxidation of luminol. The reaction was initiated by visible light, without using hydrogen peroxide. The results show that the enzyme presence enhances the catalytic performance, and a synergic effect between photocatalysis and the enzymatic catalysis was observed [323].

Considering that the LDHs are semiconductors and based on the studies mentioned above, these materials could be also used for the HRP oxidation assisted by light. Furthermore, the anionic clays can be easly obtained, they do not require complicate experimental installations or conditions and their photocatalytic performances can be increased by their doping with different metals [120].

In the subchapter 3.3 we have investigated, during 5 days, the systems formed by HRP and Au/ZnAl. The results showed that the AuNPs presence. induced a drastically HRP activity loss. However, for the systems containing small amount of Au/ZnAl (e.g. HRP:LDH = 1/5, 1/20) the enzyme activity is maintained during the investigation without significant modification of activity. Furthermore, no significant enzyme adsorption was observed. Starting from this point, for the first time, we had reasons to believe that the LDHs can be coupled with HRP and used under irradiation, where the LDHs will act as a generator of oxidant species. However, the ordinary LDHs materials as ZnAlLDH or MgAlLDH have a low photoresponse, and for this reason the NPs/LDH can be used to increase the material light sensitivity.

For this study we used the Au/ZnAl material whose synthesis and characterization was presented in the subchapter 3.2.1. Thus, all the test were carried out in a total volume of 2500 μL of ABTS, 100 μM, prepared in phosphate buffer, 0.1 M, pH = 7. To this volume were added different quantities of Au/ZnAl (0.4, 1.2, 1.6 and 2 mg/mL). The experiments were made in absence or in presence of HRP. When the enzyme was present, 1 μg of HRP was added to the solution. The irradiation was provided by a deuterium lamp, 50 W at a wavelength of 400 nm. The reaction was monitored during 2 h by recording the UV-Vis spectra profile of the product. For this, the mixture was centrifugated and the supernatant was spectrophotometrically analyzed.

In figure 3.30 are presented the UV-Vis spectra profile for the $ABTS_{oxd}$ formation during the irradiation, with and without the presence of the peroxidase. It might be observed that the $ABTS_{red}$ can be oxidized only by light, in presence of Au/ZnAl (figure 3.29 a-d).This is possible because the redox species generated by the irradiated catalyst. The $ABTS_{red}$ oxidation is proportional with the Au/ZnAl quantity, the highest oxidation being obtained with 5 mg of catalyst.

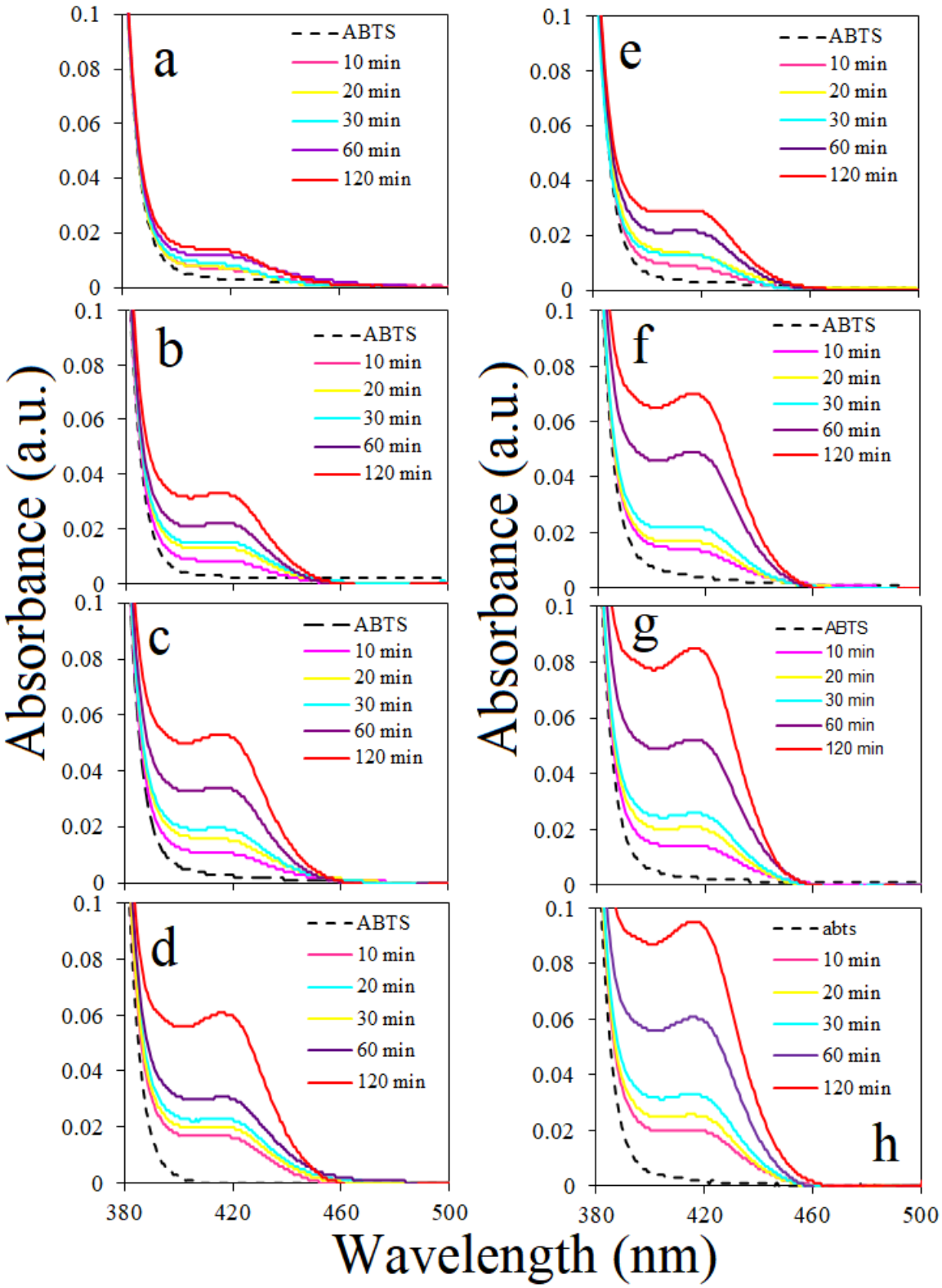

Figure 3.30: $ABTS_{oxd}$ UV-Vis spectra for a-d) 1-5 mg Au/ZnAl without HRP and in presence of UV irradiation and e-h) 1-5 mg Au/ZnAl with HRP and in presence of UV irradiation.

When the enzyme is present in solution, an increase of the product quantity is observed, as a result of HRP presence. Its contribution can be observed from the UV-Vis profiles expressed in figure 3.30 e-h. The $ABTS_{red}$ oxidation takes place as a combination between the photooxidation and the enzymatic oxidation initiated by light. Generally, the peroxidase can be activated by peroxides agents as H_2O_2 or ROOH, which are oxidizing agents. However, in absence of peroxides, the light generated holes of the Au/ZnAl layered double hydroxide can oxidize the enzyme, initiating the enzymatic reaction. Furthermore, the electrons and the holes can participate further in the oxidation reaction.

In figure 3.31 are presented the $[ABTS_{oxd}]$ *versus* t. The determination of the kinetic parameters was made on the basis of the data presented in figure 3.30. For the tests made without

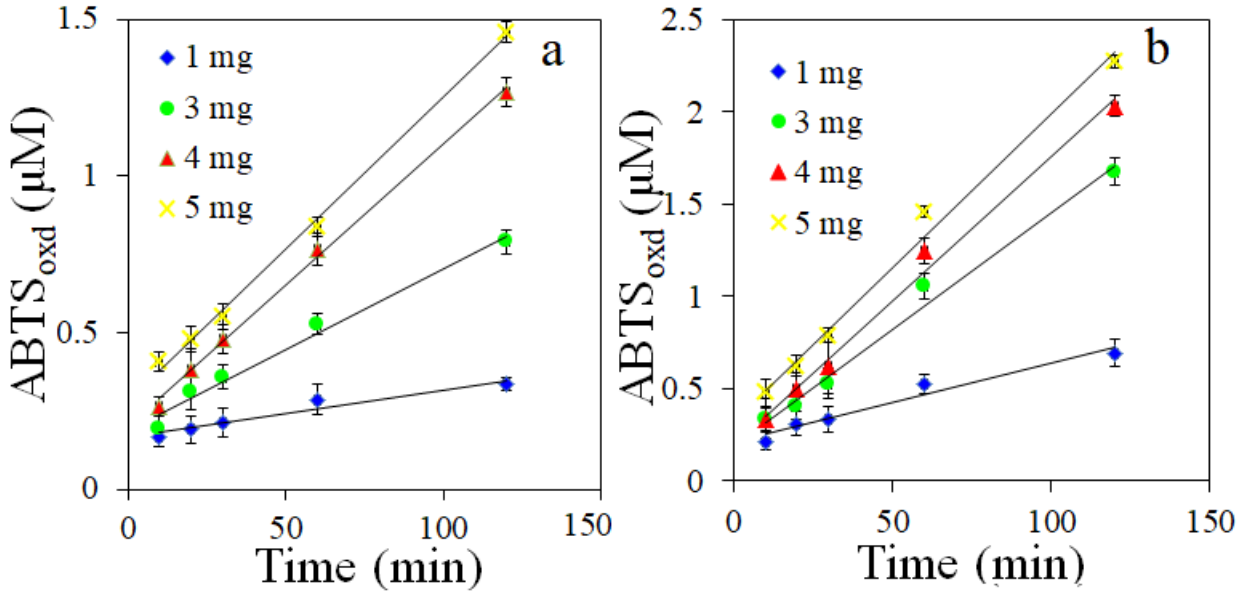

Figure 3.31: Evolution of $[ABTS_{oxd}]$ in function of Au/ZnAl quantity a) without HRP, b) with HRP.

enzyme, the reaction was considered as a pseudo-firs order reaction and the k_{app} was calculated from the representation of $-\ln([ABTS_{oxd}])$ vs *t.* For the reaction carried out in presence of HRP, the V_i was considered the slope of the each line. The $f(1/V_i) = 1/[Au/ZnAl]$ is presented in figure 3.32. The k_{app}, the $V_{max,}$ K_M and V_{max} specifiv are listed in table 3.10. Comparing the data listed in the table 3.10 with those from table 3.5, obtained for the free HRP, activated by H_2O_2, can be observed that the results are comparable. A 1.8 time decrease of the V_{max} and 6 time increase of $K_{M.}$ was obtained for the photo-activated HRP.

In order to be sure that the reactions take place only in presence or HRP, Au/ZnAl and light, control tests were made. For this in the next systems were investigated: $ABTS_{red}$ + HRP + hν; $ABTS_{red}$ + hν; dark + $ABTS_{red}$ + HRP. The results show no $ABTS_{red}$ oxidation. This is underlining that the HRP activation can be possible only in presence of Au/ZnAl irradiated. We also tested a system composed by HRP + ZnAl + hν. Neither in this situation no $ABTS_{oxd}$ was noticed. The result is pointing out that the LDH doping with AuNPs was mandatory in this case.

Comparing the kinetic resuts obtained by using Au/ZnAl as oxidizing agent (see table 3.10) with those obtained in case of H_2O_2 (see table 3.5), we can see that the data are comparable. Thus, we can conclude that the gold containing catalysts can be succesfuly used to replace the hydrogen peroxide, when the oxidoreductase enzyme are involved in the process. As far as we know, few studies have been made on the simultaneous photo-enzymatic catalysis and none of them had approached the utilization of immobilized HRP on LDHs for the photo-enzymatic degradation of phenol. For this reason, this study can represent a start point for designing processes for phenols photo-enzymatic degradation, by using photocatalysts and HRP, in absence of H_2O_2.

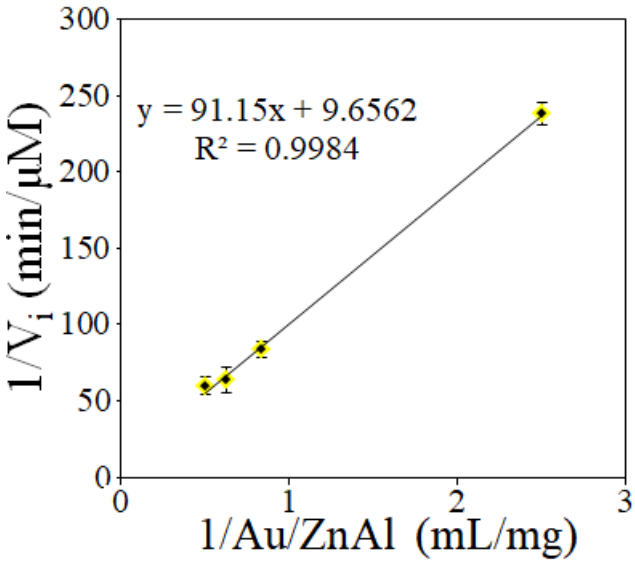

Figure 3.32: Graphical representation of Lineweaver-Burk equation.

Table 3.10: Kinetic results of the photo- and enzymatic $ABTS_{red}$ oxidation.

	Without HRP		**With HRP**	
Au/ZnAl (mg/mL)	k_{app} (x 10^{-3}/min)	V_{max} (μM/min)	K_M (μM)	V_{max} specific(μM/min/mg)
0.4	6.1	0.1	9.15	100
1.2	11.3			
1.6	13.3			
2	11.5			

3.5.2. NADH regeneration from NAD^+ in presence of solar irradiated Au/ZnAlLDH.

The oxidoreductases represent 25 % from the total number of enzymes. They are important biocatalysts used for the synthesis of valuable chemical and pharmaceutical products [324]. The main disadvantage of the majority of redox enzymes utilization is their dependence on a cofactor denoted nicotinamide adenine dinucleotide (NADH) or on its phosphorylated correspondent (NADHP).

Generally, when used, the NADH plays the role of a hydrogen donor, when the initial molecule is oxidized to NAD^+. Because 1 mole of NADH cost is approximatively \$3000, the reduction of NAD^+ to NADH is mandatory [324].

Traditionally, the nicotinamide adenine dinucleotide regeneration is carried out by using the enzymatic way, when two enzymes are coupled in order to regenerate the cofactor [324]. Thus, one enzyme is involved in the main reaction, while the other one is using a different substrate, which in presence of NAD^+ will be converted to a product, with the NADH formation. Some enzyme which can be used for the NADH regeneration can be alcohol dehydrogenase, hydrogenase, glucose dehydrogenase, glutamate dehydrogenase, formate dehydrogenase and others [324,325].

One particular model of the enzymatic regeneration is when one single enzyme is participating to both reduction and oxidation reactions. In this case, the enzyme (e.g. alcohol dehydrogenase) uses two substrates. The regeneration of the cofactor using biocatalysts comes with the advantages of low energy consumption, selectivity only for the NADH and high specific activity [324]. Because of the enzyme and substrate supplementary addition, this method is expensive. To avoid the enzymatic NADH regeneration, non-enzymatic NAD^+ reduction, like homogeneous and heterogeneous catalysis, photocatalysis, chemical and electrochemical catalysis were developed [324].

The utilization of irradiation and photo-responsive materials to regenerate the NADH is a promising direction. This topic has been approached in many studies. Typically, for this besides the light source and the catalyst, the system might contain also an electron donor and a mediator which facilitates the electron transfer. Usually the electron donor can be triethanolamine (TEOA) and the mediator $[Cp^*Rh(bpy)H_2O]^{2+}$ [324].

M. Aresta *et al*. photoregenerated the cofactor by using visible light, TiO_2 based catalysts and glycerol as an electron donor. Their results proved that the regeneration can take place and the water can play the role of the electron donor [326]. Organic semiconductors can be also used for this purpose. g-C_3N_4, in presence of $[Cp^*Rh(bpy)H_2O]^{2+}$ as a mediator can reduce almost 100 % the NAD^+ [325]. Recently, K.A. Brown efficiently regenerated the NADPH by using visible light and a combination between CdSe quantum dots and ferredoxin $NADP^+$-reductase [327]. PtNPs and Pt/Al_2O_3 catalysts were also investigated and the results have shown that both materials can convert more than 50 % of the initial NAD^+ concentration [324,328].

Layered double hydroxides were used many times in processes initiated by light [120,225,288]. However, as far as we know, they never has been approached to regenerate the

NADH from NAD^+. Since AuNPs [329], PtNPs [324,328] were successfully used in this application, we have reasons to believe that the NPs/LDHs can lead to promising results. The presence of the NPs on LDH surface can increase the life time of the photo induced charge carriers, and the photocatalytic performance is enhanced. Furthermore, in the previous subchapter it was proved that the irradiated Au/ZnAl can provide the oxidizing species required for HRP activation. Taking this into consideration, we propose an alternative material, Au/ZnAl(3/1) type, to be used for the solar photoregeneration of NADH.

For this study we used the Au/ZnAl material whose synthesis and characterization was presented in the subchapter 3.2.1. Because for this application the material optical properties are important, the UV-Vis measurement was performed for the solid Au/ZnAl catalyst. The analyze was performed with an UV-Vis Jasco V550 spectrophotometer with integration sphere.

The tests were carried out in a total volume of 10 mL of phosphate buffer, 0.1 M, with pH = 6, 7 and 8; the initial NAD^+ (Sigma Aldrich, ≥ 96.5 %) concentration was 70 μM and flavin mononucleotide (FMN) (Sigma Aldrich, ≥ 70 %), with the concentration of 30 μM was used as an electron mediator. To this mixture, 10 mg of Au/ZnAl were added. Before starting the irradiation, the suspension was stirred in the dark during 20 minutes. After this, the irradiation was started. During two hours samplings were done at determined intervals of time, the solid was centrifuged, and the supernatant was spectrometrically analyzed, following the peak at 340 nm which corresponds to NADH. The irradiation was provided by a solar simulator, 180 W.

A standard curve was made for NADH (Sigma Aldrich, ≥ 97 %). For this, a parent solution of NADH was firstly prepared, 100 μM, and by dilution smaller concentrations were obtained (5, 10, 20, 30, 40, 50, 80 μM).

The XRD analyze revealed that after the reconstruction the initial LDH structure of the material was recovered (see figure 3.1-B-a). The TEM images and the EDX spectrum proved that the AuNPs are present on the LDH surface, and the NPs dimensions are between 5-30 nm (see figure 3.5). From the UV-Vis spectra (figure 3.33) can be observed that the material has a strong capacity to absorb visible light, showing an absorption edge at 530 nm, which can be assigned to the gold presence on the layered double hydroxide surface.

The standard curve obtained for the NADH is presented in figure 3.34. With the help of this representation, the absorbance at 340 nm was converted in NADH concentration. During the adsorption desorption equilibrium a significant adsorption of NAD^+ and FMN was observed (see figure 3.35). When the irradiation was turned on, an increasing peak at 340 nm appeared and it was attributed to the regeneration of NADH from its oxidized form NAD^+. Pending two hours of irradiation, this peak absorbance increases progressively. Also an increase of the peak at 260 nm was remarked. Because NADH and NAD^+ have a peak at this wavelength (see figure 3.34 d) is difficult to discriminate between them. However, this peak increases during the time, which could suggest the regeneration of the cofactor.

The pH influence on the NAD^+ reduction shows that the decrease of the pH at 6 induces a decrease of the NADH regeneration yield also. An optimal pH was found to be at a value of 8, when almost all the initial NAD^+ was converted into NADH. Studies on the same subject have

revealed that the optimal pH for the NADH regeneration can be different in function of the catalyst type. However, good results were obtained in a range of pH between 7-9 [325,328,330].

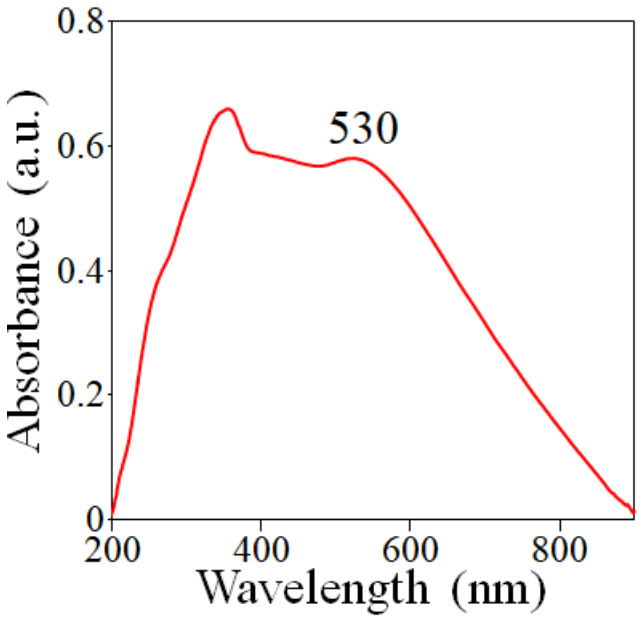

Figure 3.33: UV-Vis spectrum profile of Au/ZnAl catalyst.

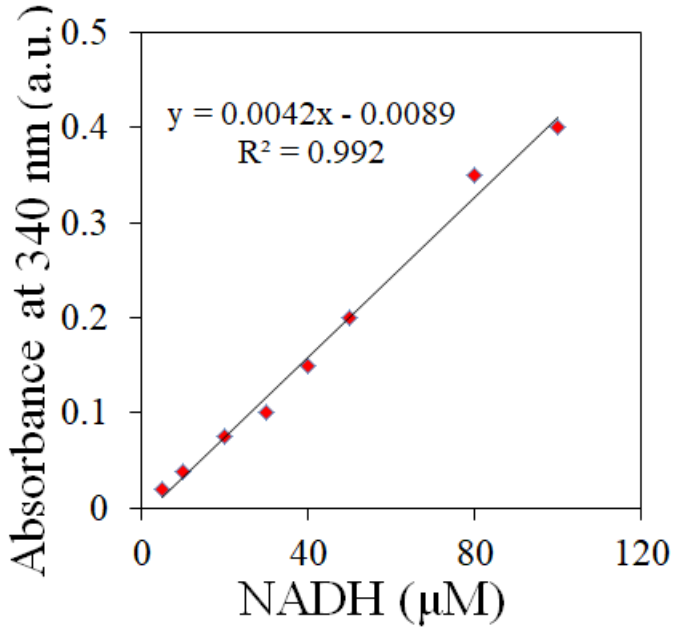

Figure 3.34: Standard curve of NADH in a range of 5-100 µM

Using the NADH standard curve, the NADH regeneration yield was calculated. From figure 3.36 can be observed that at a pH of 8, 99 % of NADH was regenerated, while at pH 6 only 15 %. Some control tests were also performed. For this, different components have been

removed from the mixture. It was observed that the presence of the Au/ZnAl and the flavin electron mediator are mandatory for the NAD^+ reduction. Furthermore, the test carried out by replacing the Au/ZnAl with the parent material, ZnAl(3/1)LDH had no performance for the photoconversion of the cofactor.

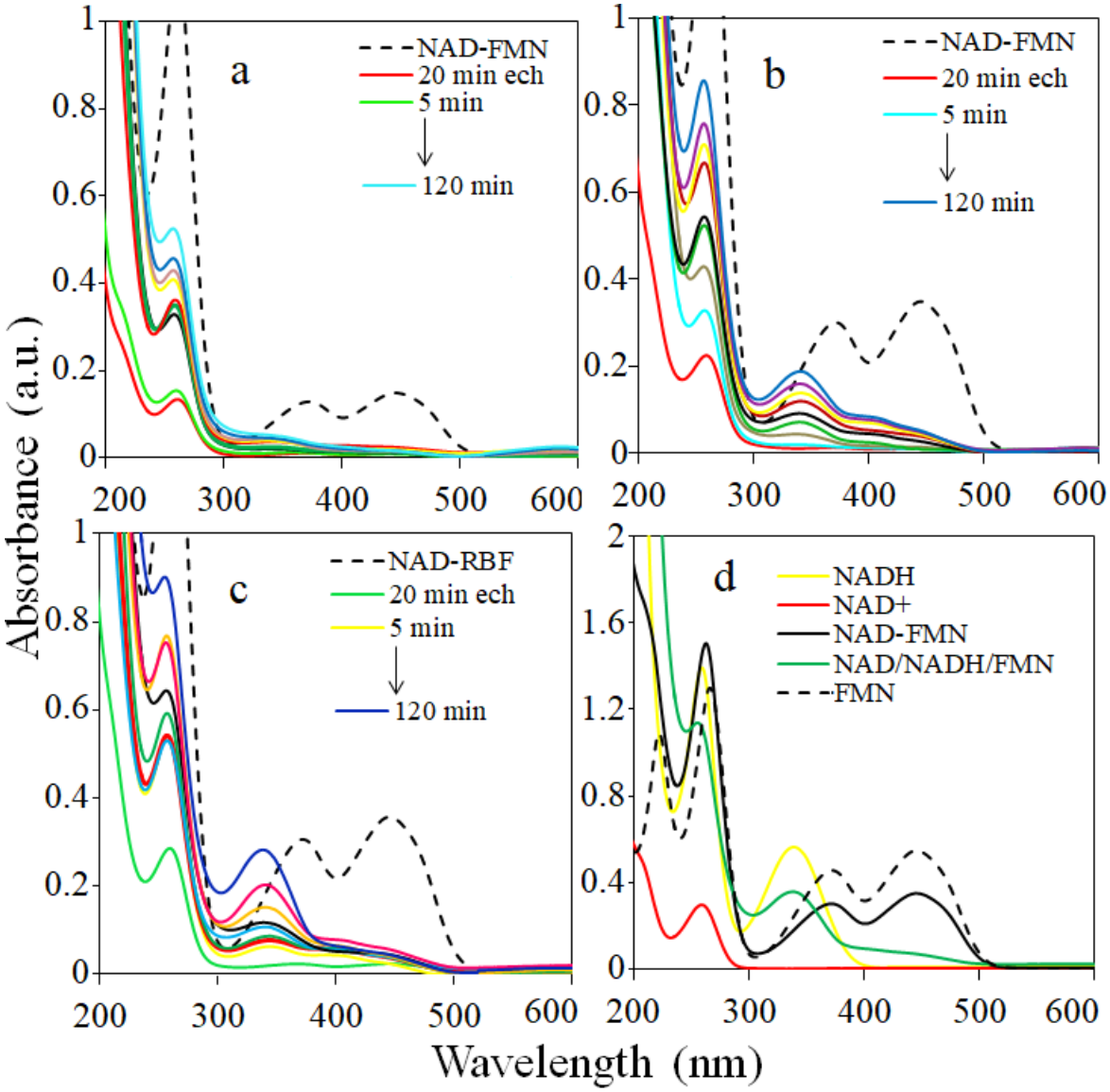

Figure 3.35: UV-Vis spectra profiles for the NADH regeneration for a) pH 6, b) pH 7, c) pH 8 and d) UV-Vis spectra for initial fresh solution of NADH, NAD^+, FMN, NADH-NAD^+-FMN and NAD^+-FMN.

The NADH regeneration was made in this study without any electron donor addition. Previous studies have shown that water can be an electron donor [331]. Generally, the presence of an electron donor is important because it can decrease the recombination rate of the catalyst and in this way the photocatalytic performance is enhanced. Furthermore, by supporting the

AuNPs on materials as LDH, the optical properties of the initial material were shifted to the red region of the spectrum, leading to an increase of the visible light absorption.

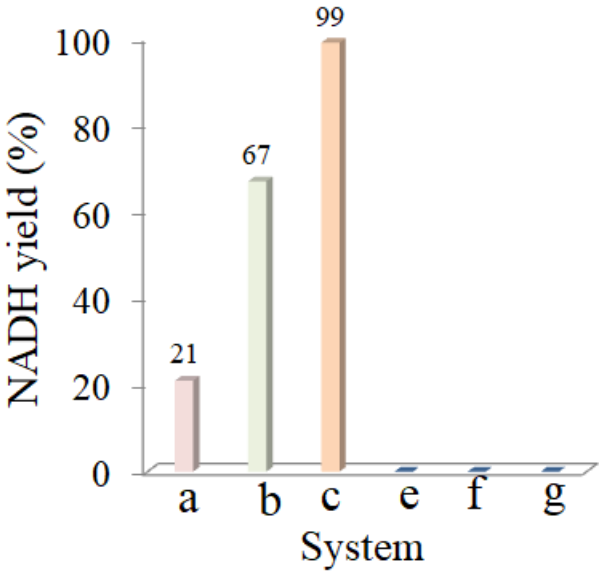

Figure 3.36: NADH regeneration performance at a) pH 6, b) pH 7, c) pH 8, e) using NAD^+ + FMN + hν; f) NAD^+ + Au/ZnAl + hν, g) ZnAl; initial NAD^+ was 70 μM; FMN, 30 μM, 1g/L catalyst.

The proposed mechanism for the NADH regeneration using solar light and Au/ZnAl layered double hydroxide nanocomposite is presented in figure 3.37. Under solar irradiation, electrons-holes pairs are formed as a result of catalyst interaction with light. The light induced holes from the valance band will form oxidizing species as a result of water oxidation, while the electrons from the LDH conduction band will be trapped by the AuNPs which are intimately contacted with the LDH surface. Here, the electrons can move freely at the nanoparticles surface and together with the generated H^+ species will participate to the reduction reaction of the FMN_{oxd}. In presence of NAD^+, the FMNH will be oxidized, while the first one will be reduced to NADH.

In this study we proved that the Au/ZnAl layered double hydroxide can be used in the regeneration of the NADH from NAD^+, using no electron donor. The FMN presence in the system was crucial for the regeneration process. Also, the catalyst and the irradiation source are mandatory. Studies on the same subject, where the NADH was regenerated by using photoresponsive materials, with or without the utilization of electron donors, have shown similar results [328,330]. However, our system had a superior performance compared with the doped or the simpleTiO_2 used by M. Aresta [326]. Approximatively 100 % NADH regeneration was obtained by using g-C_3N_4 semiconductor, in presence of electron donor and mediator [325].

Considering our results and the studies made till this moment, we believe that this study will be a starting point for other investigations involving layered double hydroxides and their hybrid formulation type NP/LDH, for the NADH regeneration.

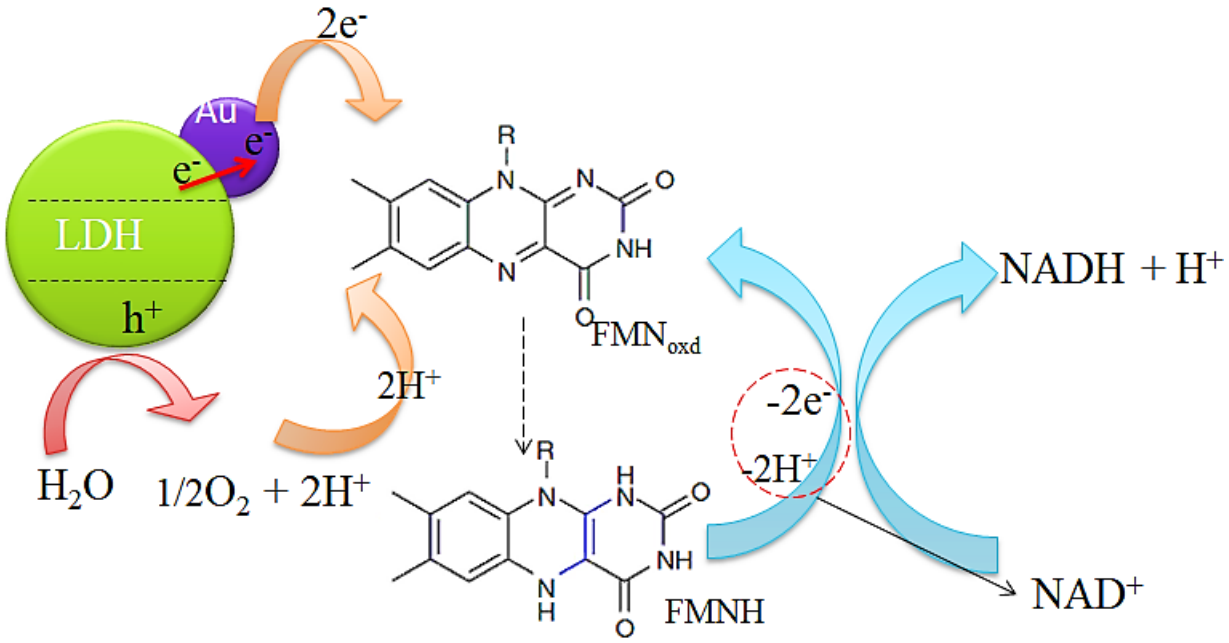

Figure 3.37: The proposed mechanism for the solar photoregeneration of NADH by using Au/ZnAl catalyst.

3.6. Conclusions

Chapter 3 has investigated the ability of LDHs based materials to immobilize the HRP enzyme for further utilization of the new bio conjugates in different applications. Thus, combining co-precipitation with reconstruction, three LDHs composites were fabricated: ZnAlLDH(3/1), Au/ZnAl and ZnAl-CN.

The enzyme was immobilized on ZnAlLDHs based composites and their calcined derivatives at 550 °C via direct adsorption. A high HRP adsorption was obtained for the calcined clay products, with almost the entire enzyme quantity attached to the inorganic support. The pysico-chemical characterization proved the presence of enzyme on the support and also the layered structure recovery, after metal oxide rehydration in HRP phosphate buffer solution. The enzymatic tests, made to evaluate the HRP activity before and after the immobilization, were carried out in presence of reduced ABTS, as a donor substrate, and H_2O_2 as an oxidation agent. The kinetic parameters have been determined by using the Michaelis Menten relation. The results have shown that the presence of gold in the structure of the resulted biocomposites (Au/ZnAl-550-HRP and Au/ZnAl-HRP) leads to total loss of enzyme activity. The best enzymatic performance was obtained for the ZnAl-CN-HRP biohybrid. However, this material activity is 10 times smaller than the one of the free HRP. This might underline that some diffusional limitation can take place, or/and the enzyme suffered conformational changes.

Another direction of study was to remove the phenol from an aqueous solution via different methods: through photodegradation by using ZnAlLDH, enzymatic degradation by using free HRP or ZnAl-HRP biohybrid and the photo-enzymatic degradation by using ZnAl-HRP and solar light. The LDH material was obtained via coprecipitation, while the biohybrid was synthetized through the direct enzyme adsorption on the calcined ZnAlLDH at 550 °C. It was observed that the immobilization process induced a decrease of enzyme efficiency with cca 50 % reported with the free HRP initial activity. Comparing the obtained results, the photo-enzymatic response of the ZnAl-HRP was up to 35 %, while the simple enzymatic degradation reached 25 %, and the photodegradation only 20%. This result underlines that in case of the photo-enzymatic system, the increase of the phenol removal is a consequence of the synergic effect between the enzymatic degradation initiated by the enzyme, and the photodegradation initiated by the solid catalyst and by the irradiation.

In a separate research, has been investigated the interaction of HRP with Au/ZnAl nanomaterial. The data has shown that the enzyme is able to facilitate the release of gold from the clay surface via an enzyme-gold complex formation. It has been observed that the gold release is dependent on clay quantity and enzyme solution pH. Furthermore, it was demonstrated that the HRP activity is drastically reduced in presence of the gold (from clay surface or from solution). Control tests performed in presence of catalase or in simple phosphate buffer, confirmed that the enzyme is the one which mediated the nanoparticles release.

Another study was analyzing the ability of Au/ZnAl material to generate, under irradiation, oxidative spices which might be further involved in the activation of HRP. The tests were carried out in absence of hydrogen peroxide (which generally plays the role of the oxidant agent in the reactions involving oxidoreductases enzymes) and using reduced ABTS as a donor substrate. To be able to evaluate correctly the involved processes, the ABTS oxidation was performed in presence or in absence of HRP. The reaction made in absence of enzyme was a first order reaction, while the one carried out in presence of HRP was evaluated with the Michaelis Menten relation. The resulted data confirmed that the light generated holes produced by the solar irradiated Au/ZnAl nanocomposite, can oxidize the HRP, initiating the enzymatic reaction. Furthermore, the kinetic parameters had close values with those obtained for the free enzyme.

Extremely important for some enzymatic reactions are a class of substances denoted cofactors. Very used cofactor molecules are nicotinamide adenine dinucleotide (NADH) or its phosphorylated correspondent (NADHP). However, an important issue in using cofactors is their costs. Because of this, the NADH (NADHP) regeneration is required, which usually is made by the utilization of specific enzymes, which are expensive materials. For this reason, in the last part of the third chapter was investigated the solar photo-regeneration the NADH from NAD^+ by using Au/ZnAl nanocomposite. As a mediator was used flavin mononucleotide (FMN). The study was made as a function of NAD^+ pH solution. Under irradiation and in presence of Au/ZnAl + FMN, a peak at 340 nm was observed, which corresponds to the NADH. The maximum NADH regeneration was obtained at a pH value of 8. Different control tests were also

performed. They have been proved that the cofactor regeneration can take place only if the system is containing Au/ZnAl + FMW + NAD^+ + hν.

4. Gold nanoparticles self-assembled on layered double hydroxides for hepatitis B virus inhibition

This chapter is dedicated to the investigation of LDH based materials behavior in presence of biological systems. A group of AuNPs/LDHs nanocomposites was fabricated combining the co-precipitation with reconstruction and used against Hepatitis B virus (HBV). In order to prove that our nanoarchitectonics have no effect over the normal cells, cytotoxicity tests have been performed by using uninfected HepG2.2.2.15 cells, which were treated with Au/LDHs. Their proliferation ability was monitored.

Hepatitis B is an important disease which causes more than 1 million deaths each year, in the entire world. Generally, the hepatitis B virus (HBV) can lead to cirrhosis, hepatocellular carcinoma and other health problems [332]. This virus is a member of the *Hepadnaviridae* family, presented as a spherical particle with a diameter of 42 nm [333] and with a circular DNA genome [334]. It was remarked that for the infected patients, besides the infectious particles, empty noninfectious subviral particles (SVP) are excessively secreted (1000-100.000-fold), forming smaller particles and filaments with a diameter of 25 nm, 22 nm respectively. The effect and the role of the subviral particles is not fully understood. Studies have shown that SVP can enhance the infection [335], others proved that in large quantities they can have an inhibitory effect [336].

The hepatitis B virus infection can be prevented by vaccination. However, for the chronic patients, the medication targeting the replication inhibition and the stimulation of the immune response, are deficient and they present also side effects during the treatment [337]. The shortage of the existent drugs, and the increasing number of HBV infections, require more studies in the direction of efficient materials synthesis for hepatitis B therapy [338]. Recent studies reveled that AgNPs can have an inhibition effect on the HBV, decreasing the quantity of the extracellular virions [339]. Furthermore, AuNPs utilization in anticancer therapies has demonstrated that these nanoparticles can be a promising tool for the medicine [340,341]. However, the combination of nanoparticles with different nanocomposites, in order to obtain non-toxic hybrids is a challenging approach [342]. Joining biocompatible supports with nanoparticles as AuNPs or AgNPs can lead to a synergy of their therapeutic properties and in this way the biospecificity and the activity can be enhanced [343]. When NPs are used for treating biological targets, an important aspect is their cytotoxic effect. The cytotoxicity is defined as the ability of a material to produce into the normal cells serious damages to important macromolecules or death [344].

Parameters as agglomeration susceptibility, texture, particle size and stability are influencing the NPs cytotoxicity [345].

A first challenge of NPs utilization in biological applications is their synthesis. In the most of the situations the final form of the NPs presents a high cytotoxicity because of the organic reagents used during their preparation. A meaningful example is the utilization of cetyltrimethylammonium bromide used in AuNPs synthesis, which by desorption from the nanoparticle surface, induces the cell death [346,347]. The stabilization agents as proteins, polymers, surfactants, citric acid, used to avoid the NPS aggregation, also can affect the interactions between the NPs and the biological material [348]. Taking into consideration that the utilization of organic compound has a direct influence on the efficiency of NPs in medical application, alternative synthesis methods are demanded. A very versatile technique to obtain NPs on a larger matrix, without the addition of other chemical products, is to use the self-assembly ability of LDHs materials [33,178,349]. Due to their low toxicity and a good biocompatibility, the anionic clays can be promising candidates for biomedical use [350,351].

In this section, a group of AuNPs/LDHs materials were synthetized, characterized and used for the first time in the HBV inhibition. The cytotoxicity effect and the antiviral activity of these materials were also investigated.

4.1. Synthesis and Physico-chemical characterization of ZnAl(2/1)LDH, MgAl(2/1)LDH, MgFeAl(2/1)LDH and their AuNPs/LDHs self-assemblies.

Synthesis

Layered double hydroxides ZnAl(2/1), MgAl(2/1) and MgFeAlLDH type were synthetized by using the coprecipitation method [3]. MgAl(2/1) was obtained by the drop by drop addition of a salts solution containing $Mg(NO_3)_2.6H_2O$ (Sigma Aldrich, ≥99%) and $Al(NO_3)_3.9H_2O$ (Sigma Aldrich, ≥99%), 1M to a Na_2CO_3 precipitation agent, $0.5*10^{-2}$M. The pH was kept constant at a value of 9.5 by adding NaOH, 0.1M. ZnAl(2/1) was prepared in the same way, but in this case the salt solution was containing $Zn(NO_3)_2.6H_2O$ (Sigma Aldrich, ≥99%) and $Al(NO_3)_3.9H_2O$, 1M. The precipitation was made at a constant pH = 9, using a Na_2CO_3/NaOH solution, 1M. MgFeAl (2/1) with the molar ratio $Mg^{2+}/Fe^{3+}/Al^{3+}$ = 2/0.5/0.5 was obtained as the first LDH, but in this case the salt solution was containing also $Fe_2(SO_4)_3$. The resulted dispersions were stirred during 20 h at 50 °C, the solids were recovered by filtration, washed many times with distilled water, and dried at 80 °C. They were denoted as MgAl(2/1), ZnAl(2/1) and MgFeAl(2/1).

The preparation of the Au/LDHs was made as following. 1 g of parent LDHs calcined at 500 °C for 7 h was added, under an energetic stirring, to a 150 mL solution of $Au(O_2CCH_3)_3$, 0.1

M. The dispersions were stirred during 7 h at 30 °C, separated by centrifugation and dried at 80 °C. The materials were denoted Au/MgAl, Au/ZnAl and Au/MgFeAl.

Physico-chemical characterization

TEM images were obtained by using a transmission electron microscope type Hitachi H900, working at an accelerating voltage of 200 kV. The X-ray photoelectron spectroscopy (XPS) was performed on a Perkin-Elmer Model 5500-MT instrument, equipped with Mg Kα radiation (1253.6 eV), working at 20 mA and 15 kV. Inductively coupled plasma (ICP) was used to determine the Au content in the materials. The samples crystallinity, purity and the structural characteristics were analyzed by using a XRD instrument type Shimadzu XRD 6100, with monochromatic light (λ=0.1541 nm), working at 30 mA and 40 kV, in a 2θ range from 4 to 70°. The UV-Vis spectra were recorded by using Jasco V550 apparatus with integration sphere.

The TEM images for the Au/LDHs materials are presented in figure 4.1. The figure 4.1-A

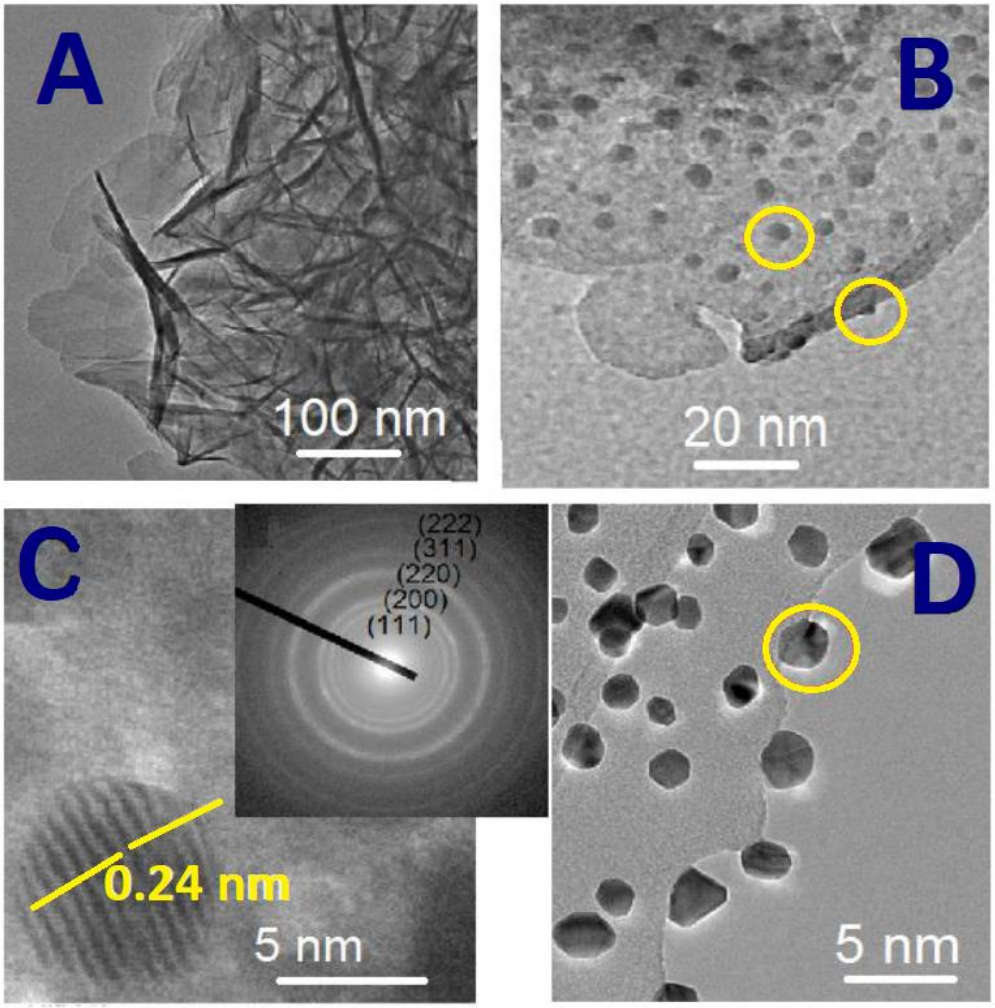

Figure 4.1: TEM images for: A) Au/ MgAl, B) Au/ZnAl, C) HRTEM image of Au/MgFeAl, D) Au/MgAl.

presents a typical LDH structure, with thin and large platelets, with a diameter of 150 nm [129,352]. The magnified images (see figure B and D) reveal that small particles, presented as dark dots, are dispersed on the LDHs surface. Their average size is 3.2 for Au/MgAl, 2.9 nm for Au/ZnAl and 3.7 nm for Au/MgFeAl, and the main nanoparticles have spherical shapes. No evidence of AuNPs unattached on the LDHs was observed, underlining that the nanoparticles were formed and stabilized only on the clay surface. The HRTEM imagine (see figure 4.1-C) reveals that the AuNPs are crystalline and also they show the lattice fringes, the interplanar spacing having a value of 0.24 nm, which is characteristic to the {111}planes of the fcc (face-centered cubic) Au (JCPDS, No. 04.0748). Additionally, the SAED pattern (selected area electron diffraction), presented in the insert of figure 4.1-C, shows the concentric diffraction rings, which can be assigned to the (111), (200), (220), (311) and (222) planes of Au [353].

The XPS spectra presented in figure 4.2 reveals the presence of AuNPs on LDHs surface,

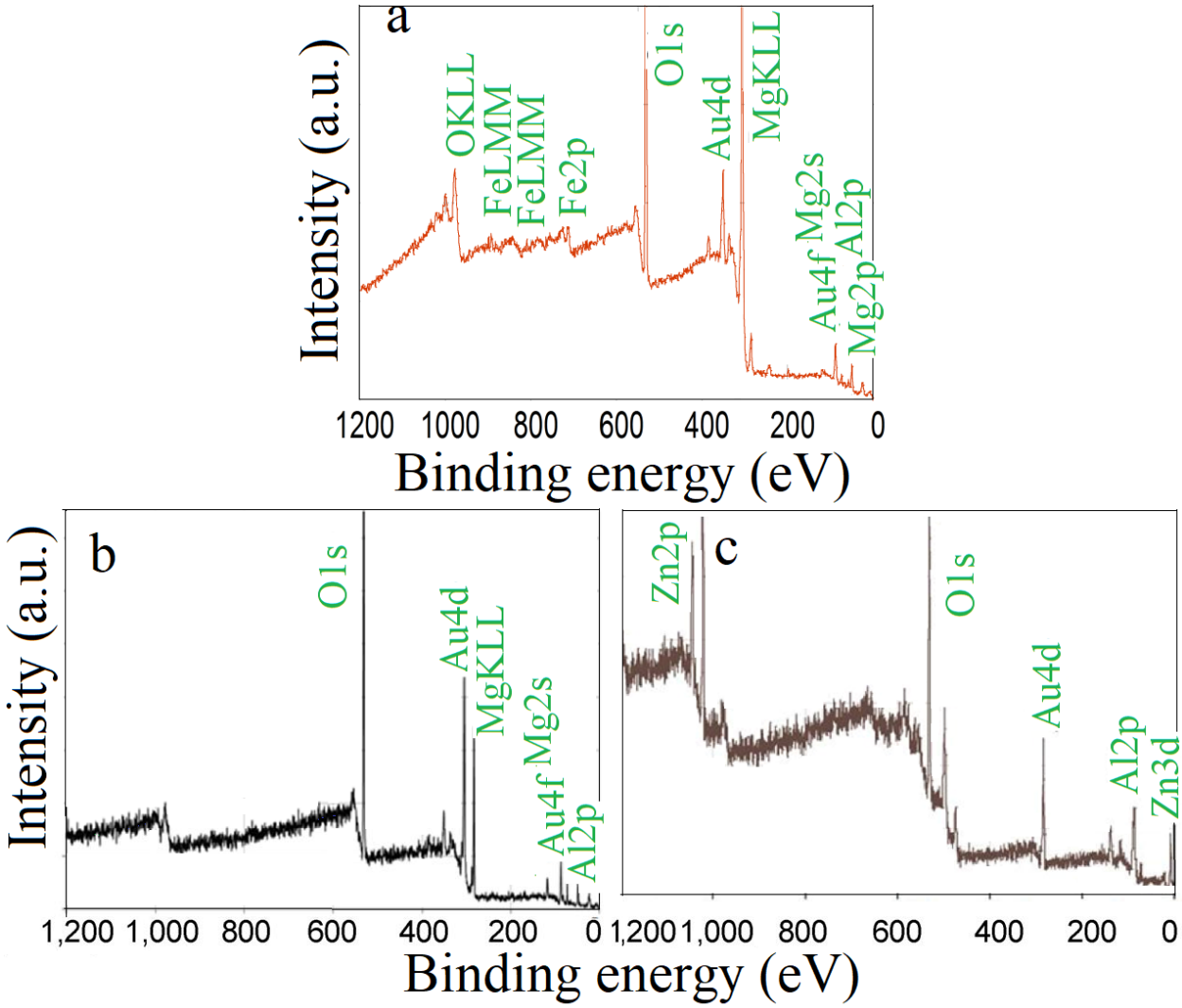

Figure 4.2: XPS patterns for a) Au/MgFeAl, b) Au/MgAl, c) Au/ZnAl.

with a gold content of cca. 4 %. The determined gold contents from XPS are in a good agreement with the ICP results (see table 4.1). In the XPS spectra (figure 4.2) can be observed that the surface elemental composition of the materials confirms the existence of Au, Mg, Al, and O for Au/MgAl; further, the Au/ZnAl material is composed by Au, Zn, Al and O, while for the Au/MgFeAl, the presence of Fe was also identified. The XPS results indicate that the AuNPs are intimately connected with the LDHs surface.

Table 4.1: Physico-chemical characterization of Au/LDHs.

		Au atomic ratio (%)	
Au/LDHs	**$D_{Au,}$ nm**	**ICP**	**XPS**
Au/MgAl	3.2	4.	3.7
Au/ZnAl	2.9	3.9	3.7
Au/MgFeAl	3.7	4.1	4

Further, the phase identity of the materials was analyzed by XRD measurements. The spectra of the Au/LDHs materials (see figure 4.3) present the typical hydrotalcite diffraction peaks, with symmetric and sharp basal reflection of the (003), (006) and (009) plans, and less intense reflection at (012), (015) and (018) of the non-basal plans [354,355]. Besides the LDHs characteristic peaks, a second phase can be observed (marked as #) for the Au/ZnAl and Au/MgFeAl, and it can be assigned to the presence of mixed oxides. This underlines a complete reconstruction for the Au/MgAl, and a partial reconstruction for the other two. The average crystallites size of the LDH matrix was calculated on basis of Debye-Scherrer equation [356], using the peaks assigned to (003) and (006) plans. The result revealed that the LDH matrix has dimensions around 150 nm which is in good concordance with TEM images. The interlayer space calculated on the basis of the (003) and (110) is 1.24 ± 0.1 nm, from where 0.48 nm is the width of the brucite lamella. This value is suggesting that the acetate anion was incorporated between the layers [357]. Because their small dimension and high degree of dispersion, the AuNPs were not detected by the XRD analyze [358]. It was proved that the thermal treatment of supported NPs on LDHs matrix can lead to the increase of the NPs dimensions as a consequence of their aggregation [347]. Because of this, the NPs were detected by the XRD measurements. Considering this, the thermal treatment at 750 °C was performed for the Au/LDHs materials. In figure 4.4 are presented the XRD patterns for the Au/LDHs-750. It reveals that the typical hydrotalcite structure is destroyed, leading to the formation of mixtures of mixed oxides whose composition is variating in function of the parent LDH composition. Furthermore, peaks which can be assigned to the presence of AuNPs were remarked at 2Θ = 38°, 44.3°, 64.5° and 77.4, matching with the diffraction rings of the (111), (200), (220) and (311) plans of the fcc (face centred cubic) gold [274]. Because the peak assigned to the (111) is more intense than the others, it might be assumed that it is the predominant orientation.

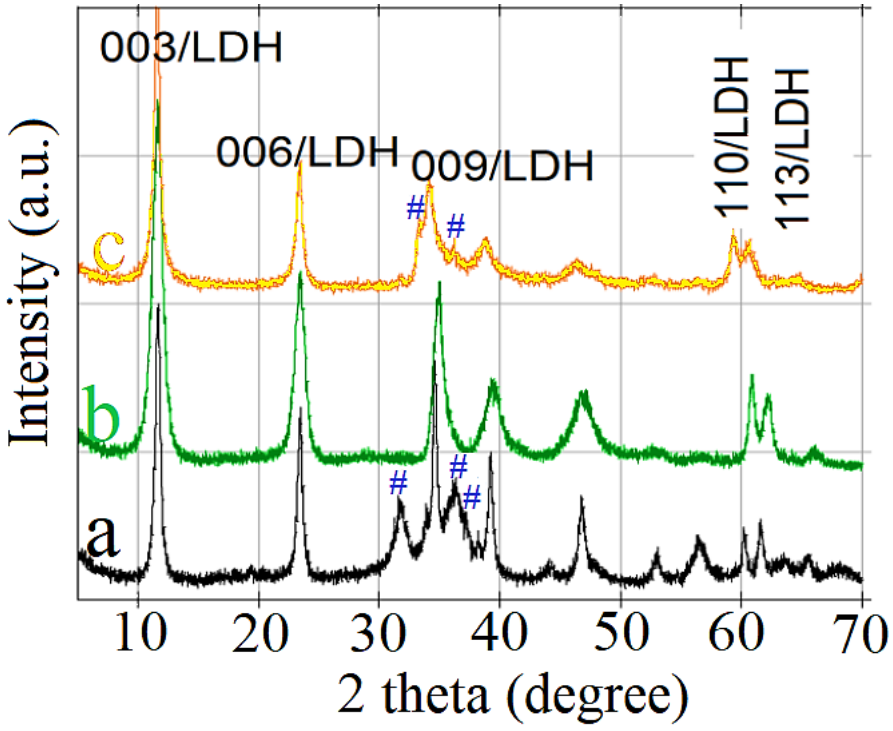

Figure 4.3: XRD patterns for the a) Au/ZnAl, b) Au/MgAl, c) Au/MgFeAl

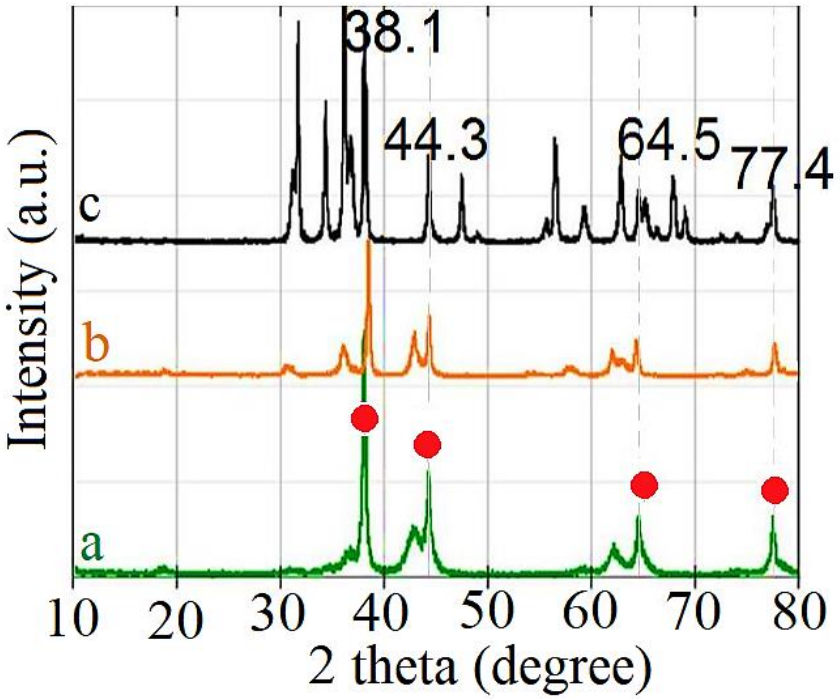

Figure 4.4: XRD patterns of a) Au/ZnAl-750, b) Au/MgAl-750, c) Au/MgFeAl-750.

In figure 4.5 can be observed the change of color of the parent LDHs after the reconstruction in gold acetate. According with these images, a broad and strong surface plasmon resonance (SPR) was observed on the UV-Vis spectra of the Au/LDHs nanocomposites (see figure 4.5-b). This is a clear evidence that the AuNPs are present on the clay surface. In the UV

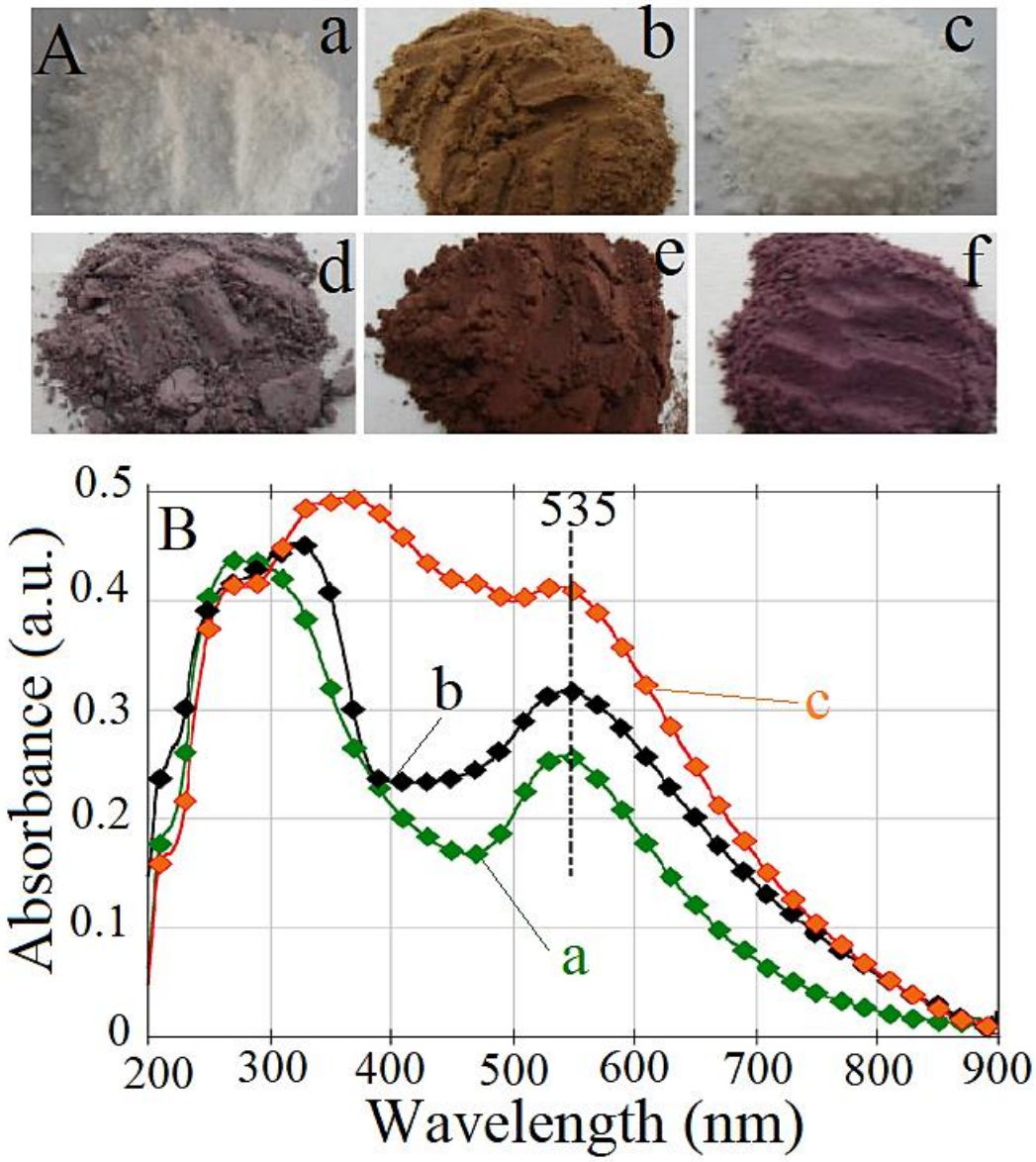

Figure 4.5: A) Images of a) ZnAl(2/1), b) MgFeAl, c) MgAl; B) UV-Vis spectra of a) Au/MgAl, b) Au/ZnAl, c) Au/MgFeAl.

region of the spectrum, all the samples present an intense absorption peak, which might be assigned to the LDHs network and the mixture of mixed oxides, already confirmed by the XRD analyses,. The absorption edge around 535 nm is a strong indication that the AuNPs are present in the metallic state. Even if the nanoparticles state is not influenced by the matrix composition,

the SPR intensity is. This affirmation is supported by the fact that the SPR can be influenced by factors as particles size, gold content and/or their surrounding environment [359,360]. Since the size and the gold contend are similar, the only parameter which is different is the clay composition.

4.2. Study on hepatitis B virus inhibition using Au/LDHs materials

All the studies from this section were carried out at the Department of Viral Glycoproteins, Institute of Biochemistry of the Romanian Academy, Bucharest, Romania.

A virus is an infectious agent which needs a host for its replication [361]. Generally, the HBV life-cycle (figure 4.6) starts when the virus passes by the cellular membrane of the hepatic cells and it releases inside of the nucleus the genetic material, the DNA and the RNA polymerase. Inside of nucleus, the DNA will organize itself in a circular manner, and the RNA

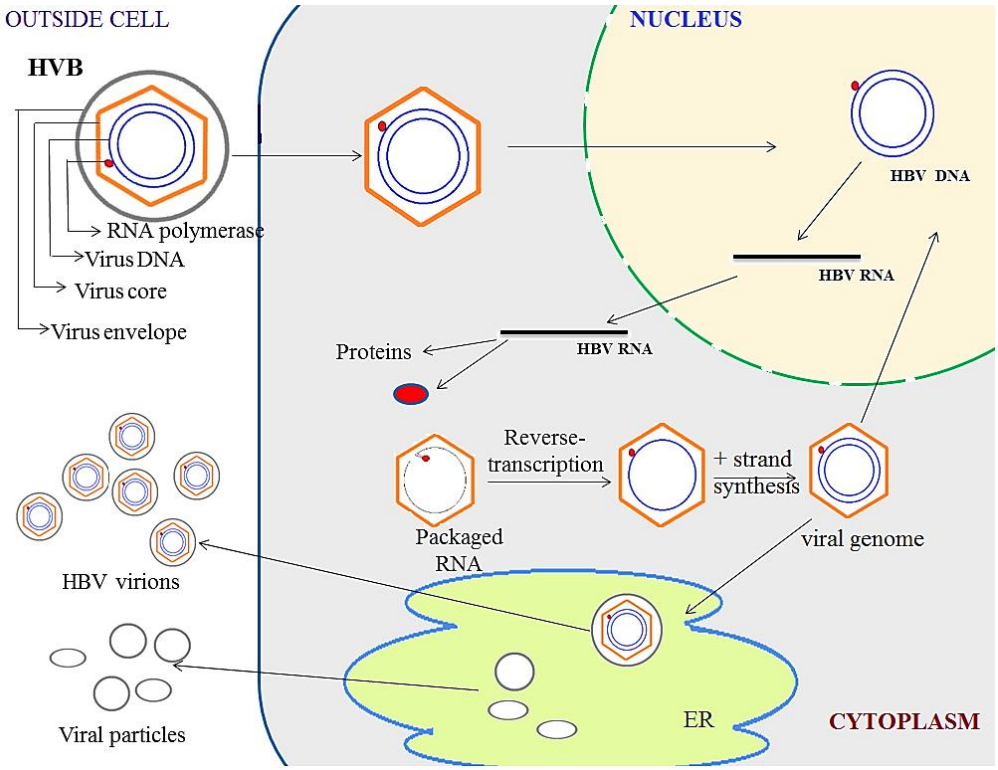

Figure 4.6: Hepatitis B virus (HBV) life-cycle.

polymerase will link on it. The RNA polymerase will produce further the viral RNA which will be transferred in the cytoplasm. In the cytoplasm, the RNA will produce structural proteins and also the DNA polymerase. These will participate to the revers transcription process. The reverse transcription starts with the encapsulation of the RNA and DNA polymerase in a protein membrane. Further, the circular DNA is produced and the viral genome is replicated. From this

point, the viral genome can be recycled to the nucleus or enveloped in the endoplasmic reticulum and secreted outside the cell, together with the subviral particles [336,361–363].

To study the antiviral effect of the previously synthetized Au/LDH materials, *in vitro* studies were carried out by using living mammalian cells. HepG2.2.2.15 is a commercial hepatic cell line, which was infected with HBV, by making stable transfection with two copies of the viral genome.

The cells were cultured in RPMI 1640 medium (Euroclone) supplemented with 10% of fetal bovine serum (FBS), antibiotics (50 μg/ml of streptomycin, 50units/ml of penicillin), and 2 mM of glutamine (GlutaMAX from Invitrogen). The HepG2.2.2.15 cells were seeded in monolayer conformation and the transfection was made by adding the viral genome in the culture medium. To make the selection of infected cells with HBV, 200 μg/ml of G418 (Gibco) was added to the medium. The hepatitis B virus has the DNA sequence which provides resistance to this antibiotic. Contrariwise, the HepG2.2.2.15 genome does not express the same tolerance to G418. The presence of HBV into the hepatic cells induces the resistance of the new created system against this antibiotic. In this way, the selection of the infected and non-infected hepatic cells can be made, the non-infected cells dying in the presence of the G418. All the cells that survive after this selection method are hosts of HBV, representing a new cell line that will be used in the following study.

Once the host was found, the HBV release its DNA into the nucleus of HepG2.2.2.15 cell. There the virus creates its own RNA required for synthesis of new specific proteins and DNA formation by revers transcription [336]. The enveloped viruses created in the host's cytoplasm are secreted outside the cell. In addition to the virions, other proteic non-infectious particles called subviral particles (SBV) are released externally of the host cell [335].

Before studying the antiviral effect of the AuNPs/LDHs assemblies, their biocompatibility was evaluated. The non-infected HepG2 cells were seeded in 96 well plates and incubated to different concentrations of Au/LDHs (15, 30, 60, 125 and 250 μg/ml). After 3 days were determined the viability and the proliferation capacity of the cells. The cellular proliferation is a normal bevaviour for the cells, showing their ability to divide. To do so, a colorimetric assay called MTS was added in the medium. It can detect the metabolic activity of the cell by targeting the NAD(P)H intracellular pool [364–366], MTS is bioreduced to formazan in the presence of dehydrogenase enzymes (figure 4.7). The formazan product was quantified by using a microplate reader (Mitras Berthold), measuring the absorbance at 550 nm. To evaluate the cytotoxic effect of the Au/LDHs, a control test was made in absence of nanoparticles. The results are presented as percentages calculated by reporting each proliferation to that obtained for the untreated cells (see figure 4.8). The HepG2.2.2.15 response to the different dosages of Au/LDHs showed that our nanocomposites behave as *soft* materials having no significant impact on the cells proliferation. However, in function of the matrix composition and solid concentration, a 16 % decrease was observed for the Au/MgFeAl, when the solid concentration was between 15-30 (see figure 4.8-a), while for the Au/ZnAl, a diminution of 20 % was remarked at a solid concentration of 250 μg/mL. For Au/MgAl the proliferation was 100 % for all the dosages. We also made the

same investigation using this time the parents LDHs clays. The results presented in figure 4.8- d-f show that the cytotoxic effect of the simple LDHs matrix is higher than the one for the hybrids type Au/LDHs.

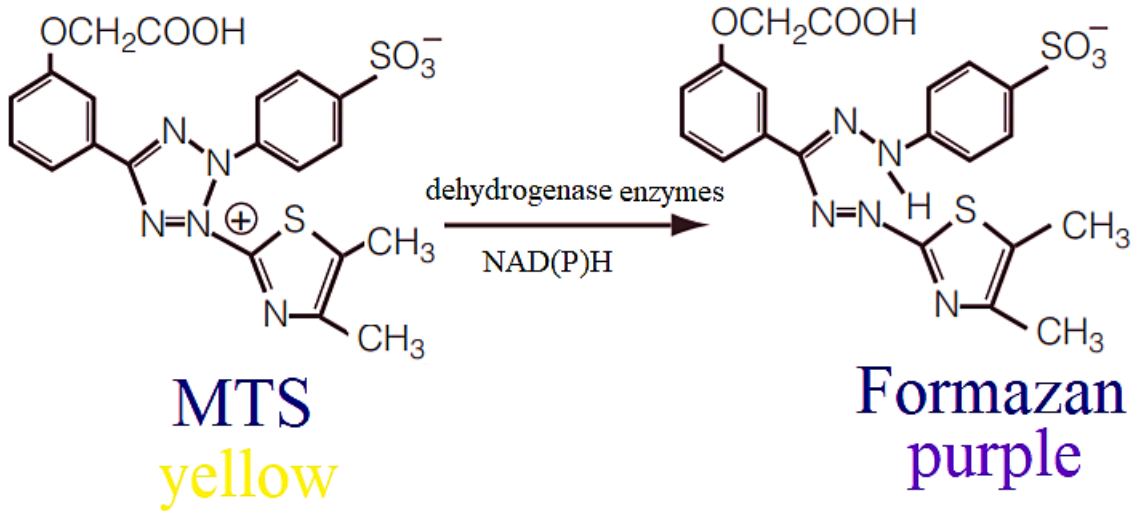

Figure 4.7: MTS conversion to formazan product in presence of the intracellular dehydrogenase enzyme.

Considering the obtained results, can be concluded that the Au/LDHs materials manifest a good biocompatibility for the mammalian cells, without creating damages and without affecting their proliferation capabilities. Starting from this point, we could further investigate the antiviral activity of the Au/LDHs. In a similar way as for the cytotoxicity tests, the host cells (hepatic cells infected with HBV) were exposed to different dosages of Au/LDHs (0, 15, 30, 60 and 125 μg/ml). After 3 days of incubation in presence of our nanocomposites, samples were taken, centrifuged and the supernatant was collected for further investigation. Because of the presence of HBV inside of the hepatic cells, we expect that the virus might secret viral and subviral particles, which will be expulsed in the extracellular medium. The encapsided HBV DNA from the supernatant was purified and quantified by real-time polymerase chain reaction (PCR) method. For this, was used the Maxima SYBR Green qPCR Master Mix (Fermentas), a kit containing the necessary reagents for DNA sequence amplification and primers. The primers were used to multiply a HBV specific section from the S gene: HBV3575-3854_rev, 5'-TGGCCCCCAATACCACATCATCC-3' and HBV3575-3854_for, 5'-TCCAGGATCCTCAACAACCAGCACG-3'. The PCR technique was performed on a Corbett Rotor Gene 6000 system. To determine the number of the viral genomes a standard curve was -designed by using known amounts of HBV DNA. The results expressed as percentages reported to the control test made in absence of nanoparticles are presented in figure 4.9 a-c. It was also investigated, in the same way, the inhibitory effect of the parent LDHs, and the results are shown in figure 4.9 d-f.

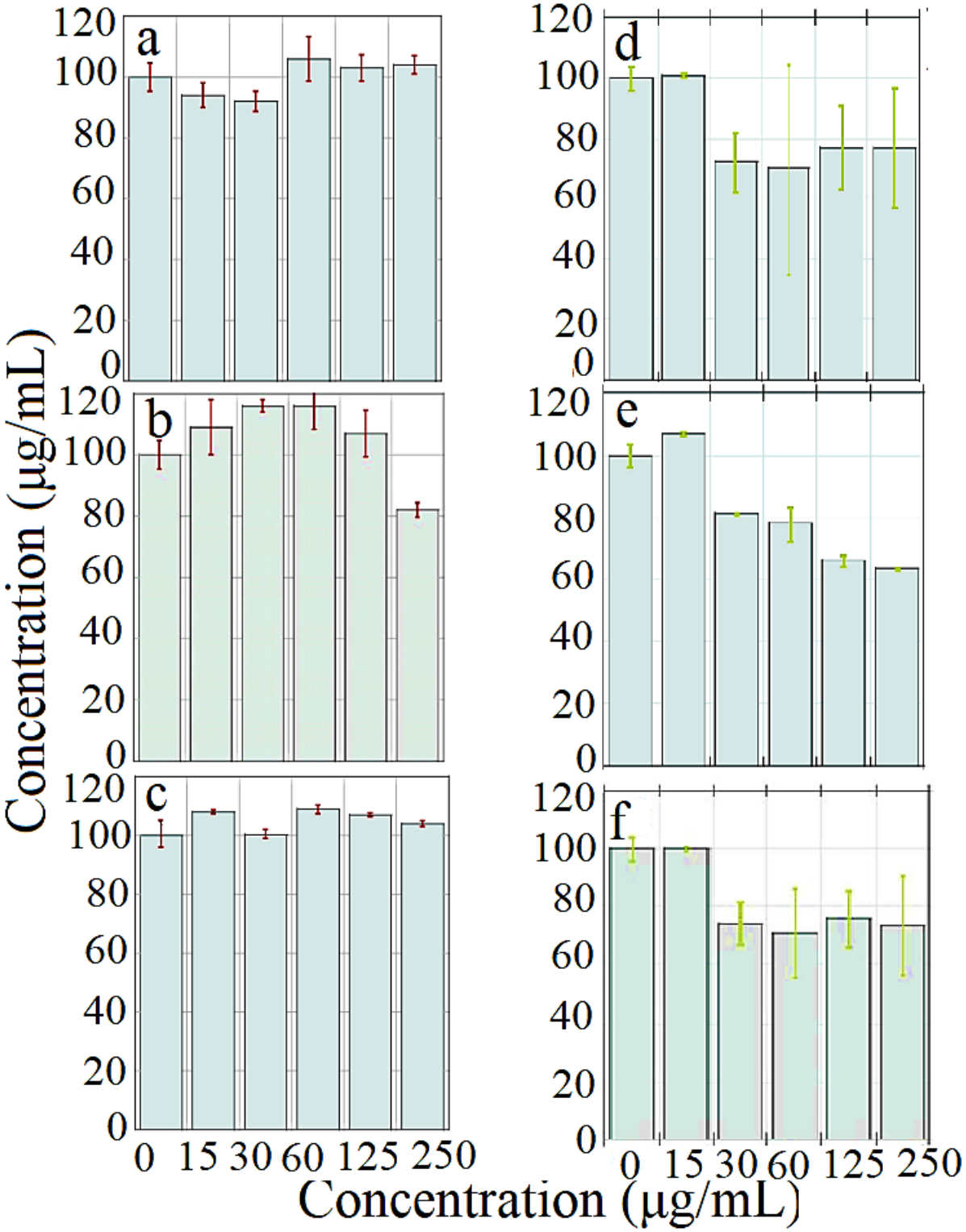

Figure 4.8: HepG2.2.2.15 cellular proliferation in presence of a) Au/MgFeAl, b) Au/ZnAl, c) Au/MgAl, d) MgFeAl, e) ZnAl, f) MgAl; 0 represents the control test.

From figure 4.9 a-c can be remarked that all the Au/LDHs hybrids have a significant antiviral effect, the Au/MgFeAl being the most efficient, with more than 90 % inhibition of the secreted viral particles. While Au/ZnAl inhibited the viral particles in dose-dependent way, for the Au/MgAl was observed that inhibition ability is higher at lower nanoparticles content, the antiviral effect decreasing with the increase of the Au/MgAl quantity. The materials analyses proved that the gold content is the same for all the sample; so, the distinct behavior in the HBV inhibition might be an effect of the different LDHs composition, which could influence the intracellular gold release from the Au/LDHs formulation. Considering this, we might assume that the Au release is higher for the Au/MgFeAl and Au/MgAl than for Au/ZnAl. For the parent LDHs (see figure 4.9 d-f) the antiviral effect was modest, even if the cytoxoxicity tests proved that the simple LDHs are more toxic for the hepatic cells than the Au/LDHs formulations.

The same supernatant obtained by centrifuging the treated HepG2.2.2.15 cells with Au/LDHs during 3 days, was used to determine the subviral particles (SVP) and the inhibitory effect of Au/LDHs on SVB (see figure 4.10). To do so, ELISA technique (enzyme-linked immunosorbent assay) and Monolisa HBs Ag Ultra kit (BioRad) were used. The quantification of SVP was made using a Mitras Berthold microplate reader. The results represent ratios of the sample's optical density divided to the cut-off value and converted to percentages by reporting to the control sample. The control represents serum collected from untreated cells. The results presented in figure 4.10 show that our Au/LDHs materials can inhibit the secretion of non-infectious particles, but they are not so efficient like in case of the inhibition of the viral particles. This behavior is underlining that the Au/LDHs are virus-specific. However, the Au/MgAl has shown inhibitory effect for both viral and subviral particles, suggesting that the clay composition have also an influence on the secretion. A similar study made by using 10 nm AuNPs, synthetized by sodium citrate reduction, showed a small efficiency in HBV inhibition. This might prove that the performance in the HBV inhibition cannot be assigned only to the AuNPs diameters and shape, but also to the LDH matrix. The clay can play an important role by facilitating the gold release and avoiding its agglomeration.

After establishing the antiviral effect of Au/LDHs systems to the extracellular HBV and SVP secretions, we want to determine if the intracellular HBV can be deactivated by our materials. To observe the inhibitory effect of Au/LDHs on the intracellular virus, was quantified the intracellular viral RNA, DNA and HBV envelope proteins, after treating the HBV host cells during 3 days with Au/LDHs. These investigations were carried out in order to obtain information about the mechanism of the HBV inhibition in presence of Au/LDHs.

The quantification of intracellular HBVs RNA was performed by reverse transcription real time PCR [361]. Using Invitrogen TRIzol reagent, the total RNA was extracted from treated or untreated (control) host HepG2.2.2.15 cells. The quantification was performed with a NanoDrop 2000 spectrophotometer (Thermo). Using Invitrogen Super Script III First Strand

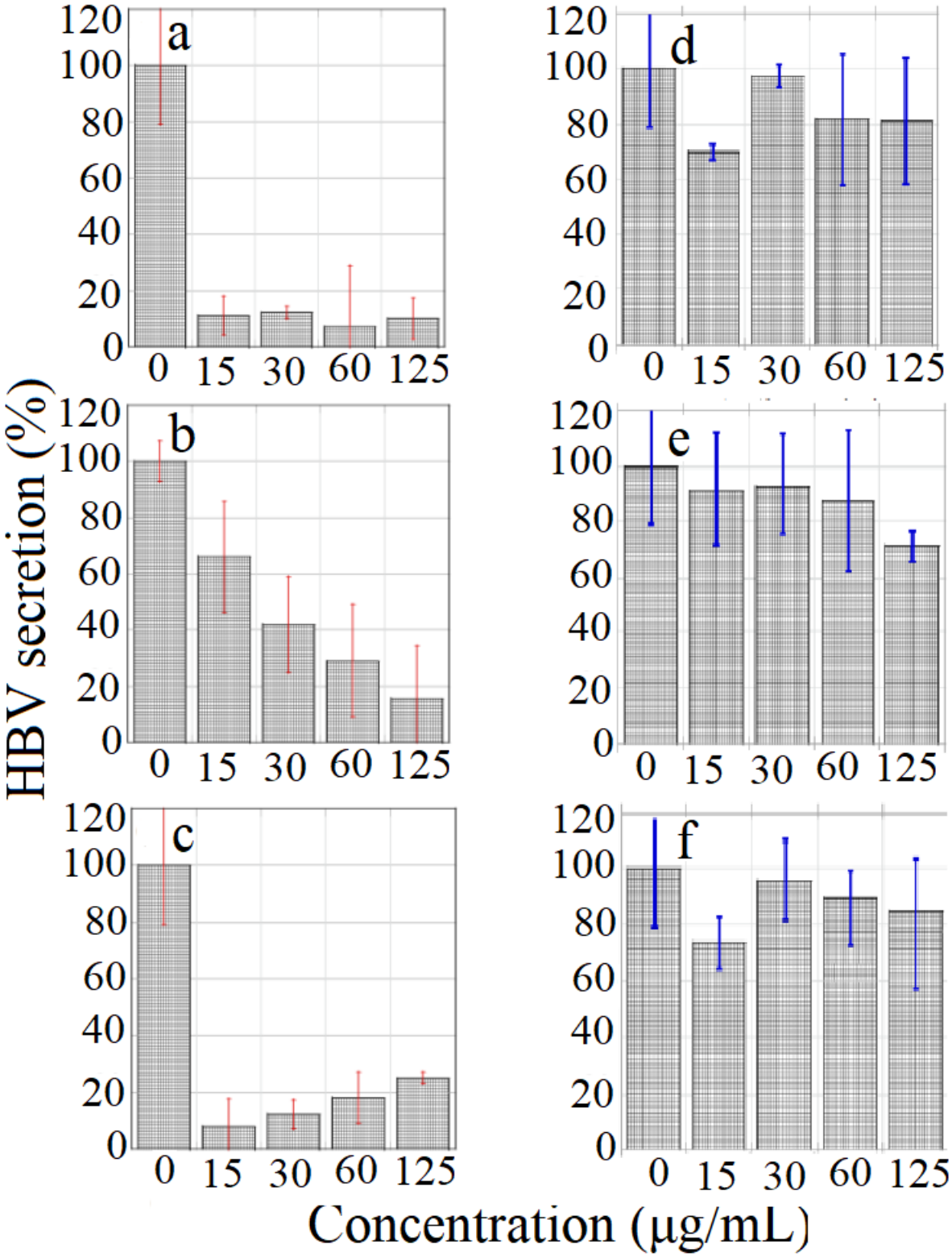

Figure 4.9: Antiviral effect of a) Au/MgFeAl, b) Au/ZnAl, c) Au/MgAl, d) MgFeAl, e) ZnAl, f) MgAl on the expression of HBV.

Synthesis kit, RNA was reverse transcribed, resulting DNA. The HBV specific DNA obtained in this way was quantified by real time PCR.

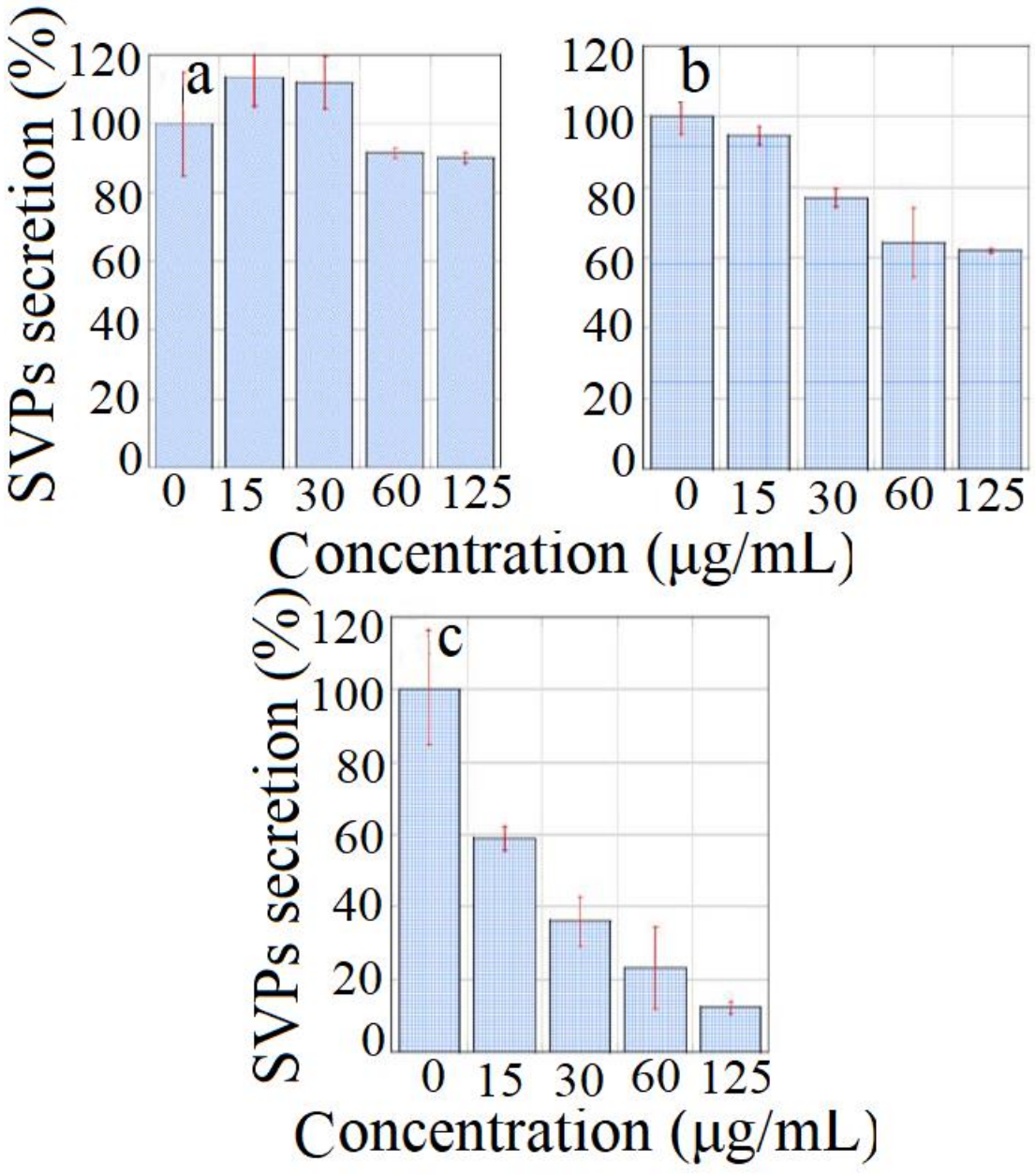

Figure 4.10: Inhibitory effect of a) Au/MgFeAl, b) Au/ZnAl, c) Au/MgAl on the expression of SVB.

The host HepG2.2.2.15 cells were counted under optical microscope. The same number of treated or untreated cells was lysed to extract the encapsulated viral DNA. The lysis solution was made in a buffer of 1M Tris-HCl at pH 8, 250 mM EDTA (Ethylenediaminetetraacetic acid) and 0.5% NP-40. The purified viral DNA was quantified by real time PCR.

The HBV envelope proteins were quantified by Western Blotting techniques [367]. To release the HBV envelope proteins from treated or untreated cells, the host's cellular membrane was lysed. The lysis buffer was made of 10mM Tris-HCl at pH 7.5, 2 mM EDTA, 150 mM NaCl, 0.5% TritonX-100 and a mixt of protease inhibitors purchased from Sigma Aldrich. After cell lysis and 10 minutes of centrifugation at 14000 x g, the supernatant was collected and used to determine the protein content by BCA (Bicinchoninic Acid) method (Pierce). The proteins were separated by sodium-dodecyl sulfate-polyacrylamide gel electrophoresis (SDS-PAGE) and transferred to nitrocellulose solid membrane using BioRad semi-dry blotter. The membrane was incubated successively with mouse anti-PreS1 (Santa Cruz), 1:1000 dilution a d HRP-labelled rabbit anti-mouse antibodies (Santa Cruz) 1:10000 dilution. The immune-detected viral proteins were visualized with ECL detection system (GE Healthcare).

The results of these investigations gave as information about the influence of the Au/LDHs materials on HBV activity inside the cells. Important steps like the viral proteins synthesis and assembly/ replication were followed after the host HepG2.2.2.15 was treated for 3 days with 125 µg/mL of Au/LDHs. Comparing the control, with the treated specimens, no significant changes were observed for the HBV transcripts (see figure 4.11 a). This is underlining that neither the RNA stability, neither the viral transcription were affected by the Au/LDHs.

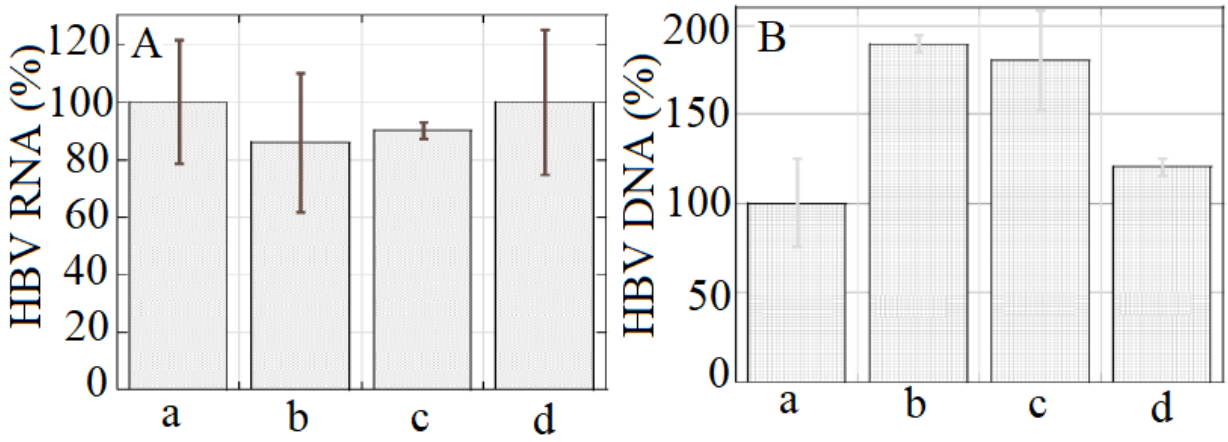

Figure 4.11: Intracellular analysis of A) HBV RNA and B) HBV DNA for a) control, b) Au/MgFeAl, c)Au/ZnAl, d)Au/MgAl.

Further, the virus DNA synthesis was investigated in both treated and untreated HepG2.2.2.15 cells. Interestingly, the HBV DNA was higher in presence of the Au/LDHs (see figure 4.11 B). Based on the significant inhibitory effect of our nanocomposites on the virus activity in the supernatant, this result can indicate that the viruses rather prefer to stay inside the cell, that to be secreted out, leading to an accumulation. The analysis of the L envelope proteins, which has an important role in the nucleocapsid envelopment, is supporting this hypothesis. Additionally, the Au/LDHs might induce an accumulation of both non-glycosylated (p) and glycosylated L isomers (figure 4.12). Since the viral RNA was the same for both treated and untreated cells, the remarked effect

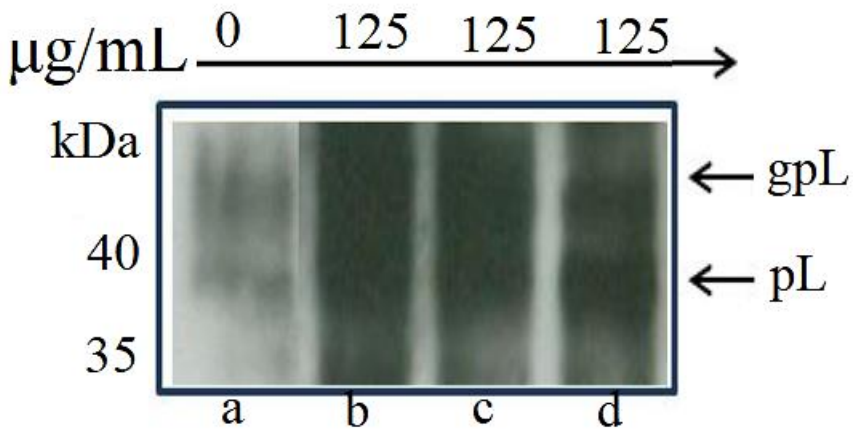

Figure 4.12: Western Blot results showing the glycosylated (gp) and non-glycosylated of the virus large envelope (L) protein isomers in a) untreated HepG2.2.2.15 cells and treated with b) Au/MgFeAl, c) Au/ZnAl, d) Au/MgAl. In kDa are represented the molecular protein weight.

suggests a strong retention of these proteins inside the hepatic cells, in presence of the Au/LDHs formulations. Till this point of the study we can affirm that the direct interactions take place between the nano-hybrids and the viral particles. However, further investigation has to be done to establish exactly the nature of these interactions.

The study presented in this section had approached for the first time the effect of gold containing LDHs on the proliferation of the hepatitis B virus. The data expressed above had shown that the investigated materials present an inhibitory effect on the HBV multiplication. Other studies involving LDHs based materials approached the utilization of these composite in applications as: drug delivery, anticancer and antytuberculosis formulations. Antimicrobial LDH materials and formulations containing noble nanoparticle were successful obtained and further tested against *P. aeruginosa, Escherichia coli, S. aureus, Saccharomyces cerevisiae* [67].

4.3. Conclusions

The interactions between LDHs based materials and the biological systems have been approached in chapter 4. LDHs materials type ZnAl(2/1), MgAl(2/1) and MgFeAl(2/1) were synthetized by using the co-precipitation method. Starting with these three materials, their correspondent nanocomposites type Au/LDH have been fabricated via reconstruction route. The physico-chemical characterization of the obtained materials had shown the hydrotalcite structure was achieved, while the gold presence on the reconstructed nanocomposites was also confirmed. The synthetized materials have been tested against the hepatitis B virus (HBV). Different tests have been processed in order to establish the behavior of the biological system in presence of LDH and Au/LDH materials. To do so, hepatic cells type HepG2.2.2.15 were transfected with

two copies of HBV genome, and further treated with different concentrations of LDHs hybrids, and the material toxicity and antiviral properties were monitored. The cytotoxicity data has shown that the LDHs based materials had no significant influence on the cells viability. Remarkably, the results of the antiviral activity of the Au/LDHs have shown that all the hybrid are able to inhibit the proliferation of HBV, Au/MgFeAl being the most efficient of all, with more than 90 % of virus inhibition. This result underline that the antiviral effect might be a function of clay composition, since the gold content on the clay surface was similar. The simple LDHs materials had a modest antiviral activity. Furthermore, it was remarked that the LDH matrices possessed a higher cytotoxic effect compared with their Au/LDH correspondents, suggesting a protective effect induced by the gold presence on the caly surface.

General conclusions and perspectives

The main purpose of the last chapter is to summarize and to give perspectives to the work expressed in this manuscript. In order to have a clear vision about the obtained results, an overview of the second part of the thesis has been presented. Forward, a short analyze of the most challenging topics was done and in the end some perspectives have been proposed, which may give new directions for the research.

General conclusions

The main objective of this project was to synthetize and to characterize a class of anionic composites denoted generally anionic clays or layered double hydroxides. Due to their unique properties, discussed in detail in the *State of the Art* section, these materials can be used in many areas of activity as biology, nanomedicine, catalysis, photocatalysis and others. Considering the recent studies which have been done regarding the layered double hydroxides, the aims of this research were also to design composite and nanocomposite based on LDH, able to be used in specific application as pollutant photodegradation under solar light, enzyme immobilization and their utilization under biological condition.

a) Synthesis of layered double hydroxides based materials

The starting point of this research was the synthesis of the parent clays by using the co-precipitation method; it involved the simultaneous addition of the precursor metal salts and the precipitation agents, keeping a constant pH. Because the nature and ratio the between the structural constituent cations play an important role for the final features of the material, LDHs with different composition were obtained: ZnAl (M^{2+}/M^{3+} = 2, 3, 4), ZnGa (M^{2+}/M^{3+} = 2, 3), ZnCoAl (2/1), MgAl(2/1), MgFeAl(2/1). The as prepared materials have been further used to obtain hybrid formulation type NP/LDHs (NP = Au, Ag, In, Ga) by using the reconstruction or impregnation methods. Furthermore, applying a thermal treatment to the LDHs composites, at a temperature value of 750 °C, mixtures of mixed oxide (MMO) have been prepared. The physico-chemical characterization confirmed the hydrotalcite structure of the materials, the presence of Au, Ag, In and Ga on clay surface and also the formation of MMO after calcination.

b) LDHs, NP/LDHs, MMO as photocatalysts in organic pollutant photodegradation

One of the main applications of the synthetized LDHs based materials was their utilization in the solar photodegradation of organic pollutants. Different classes of LDHs were used for the solar degradation of aqueous solution of phenol, p-nitorphenol, acetophenone and diclofenac. Remarkably efficient, when used for phenol degradation, was Au/ZnAl(2/1)-R-3-Lg nanocomposite able to total pollutant removal in less than 130 minutes. It is important to note that this material was reconstructed under solar light. As a consequence of this, the dispersed gold nanoparticles were found as Au^0 and Au^{3+}. The combination of these two chemical states of gold was assumed to be responsible to the increase of hybrid catalytic performance. The p-nitrophenol was easily solar photodegradated by In/ZnAl-Cal heterocomposite in 130 minute, while a solution containing phenol and p-nitrophenol was almost total decomposed by the same catalyst in 240 minutes. A very good result for the phenols mixtures solution was also obtained for the Au/ZnAl(1_0.12)-Lg-750 material. However, comparing the kinetic parameters (k_{app} and $t_{1/2}$), the In/ZnAl-Cal nanocomposites presented an increase of activity with 37 %. Nanocomposites type Au/ZnLDHs were used for the acetophenone removal. From all of the tested composites, four of them (Au/Zn4Al(2.1_0.1), Au/Zn4Al(2.1_0.2), Au/Zn4Al(0.1_0.12)-Lg, Au/ZnGa(2/1)) presented a pollutant removal between 98-100% reached after 130 minutes of irradiation. Considering the kinetic results, the solar reconstructed sample (Au/Zn4Al(0.1_0.12)-Lg) showed the highest photoresponse.

For the degradation of diclofenac, hybrid materials type ZnLDH-CN (CN = g-C_3N_4) were fabricated by combining the co-precipitation with the reconstruction and impregnation. The introduction of g-C_3N_4 had a beneficial effect only for the materials obtained via the impregnation route (ZnAl-CN-I and ZnGa-CN-I). Combining the UV-Vis and LC-MS data, it was revealed that the presence of g-C3N4 and also the synthesis route of the ZnLDH-CN hybrids had a direct influence on the photodegradation pathway. The most preformat catalyst was ZnGa(3/1) with a total diclofenac removal according to TOC data, in 150 minutes of solar irradiation.

To sum up, the photocatalytic performance of the ordinary LDHs materials was enhanced firstly by the introduction of NPs in their structure. Furthermore, it was observed that, the reconstruction under solar light, the calcination and the enhancement of the Zn content can lead to an increase of the final material photo-activity.

c) LDsH and NPs/LDHs for biocatalytic purpose

One direction of this research was to immobilize the Horseradish Peroxidase enzyme on ZnAlLDH, ZnAl-550, Au/ZnAl, Au/ZnAl-550 and ZnAl-CN. The results have shown a total enzyme adsorption on the 550 °C calcined materials, while the total reconstruction of the initial layered structure was achieved. However, the best enzyme activity, which was 10 times smaller than the one of the free HRP, was obtained for the ZnAl-CN-HRP material. It was assumed that this result might be due to the presence of the amino groups, which might link the enzyme and in this way it is more accessible to the substrate, and the diffusional limitations are reduced.

The materials containing gold had no enzymatic activity, underlining that the Au had a negative effect on the enzyme, more likely because to nanoparticles attachment to the active site of the enzyme.

Because the HRP is able to degrade the phenols, a comparative study on the enzymatic and the photocatalytic removal of phenol was made. Thus, ZnAlLDH, HRP and ZnAl-HRP materials were used for the pollutant removal. Furthermore, a new approach was introduced and the photo-enzymatic degradation of phenol was also performed. The results have shown that under solar light and in presence of H_2O_2, the ZnAl-HRP can participate with both its components: ZnAlLDH acted as a photocatalyst, while the HRP as a biocatalyst, removing the phenol via the enzymatic pathway. Even if the concept of a synergic effect was confirmed, a deeper investigation is required, since the photo-enzymatic response of the ZnAl-HRP was up to 35 %, while the simple enzymatic degradation reached 25 % (using ZnAl-HRP), and the photodegradation only 20%.

In a separate study, it was demonstrated that AuNPs can be released from Au/ZnAl nanocomposites, in presence of HRP enzyme. Furthermore, the negative effect of gold on the enzyme activity, makes this result to be particularly interesting for biomedical applications.

When working with oxidoreductases, the continuous addition of the oxidant agent can be an issue and might require special instrumentation. Additionally, in some cases, it was remarked that the H_2O_2 can have an inhibitory effect on the activity of the enzymes. For this reason, in a new study, the solar irradiated Au/ZnAl was used as an oxidant species generator for the HRP. The reaction performed in presence of Au/ZnAl, $ABTS_{red}$ and in absence of H_2O_2, confirmed that the enzyme can be activated by the irradiated Au/ZnAl, initiating further the ABTS substrate oxidation. Moreover, the kinetic parameters had close values with those obtained for the free enzyme. Considering this study, a new research was approached: the solar photo-regeneration the NADH from NAD^+ by using Au/ZnAl nanocomposite and flavin mononucleotide (FMN) as a mediator. The results have confirmed the formation of NADH under the specified condition, with a maximum of regeneration reached at pH = 8.

d) LDHs and NPs/LDHs for biomedical purpose

When used in presence of biological systems, is important to mention that the LDH materials behave as soft composites, are highly biocompatible, with minimal negative effect over the normal cells. For this reason, the anionic clays have been used many times as caries for different drugs and also because their antimicrobial, antitumor and anticancer therapy effect against different microorganisms and cells activity against. In this last section of this thesis, the interaction between Au/LDHs nanocomposites and the hepatitis B virus were studied. The resulted data have proven that the Au/LDHs materials have a minimal cytotoxic effect on the hepatic cells (HepG2.2.2.15), while the antiviral activity was remarked for all the hybrids, the best performances being obtained for Au/MgFeAl nanoarchitectonics. Furthermore, it was

noticed that the antiviral effect is a function of clay composition. Thus, it was concluded that the LDH composition might affect in the gold release from the clay surface.

Perspectives

The utilization of LDHs materials in the photodegradation of organic pollutant proved that formulations type NPs/LDHs can be extremely efficient. Thus, a new perspective for LDHs materials might be the transition for the laboratory scale to the pilot scale. It was proved that some hydrotalcite formulations are able to decompose a pollutant system composed by phenol and p-nitrophenol. In this context, an interesting approach might be to investigate the LDHs photocatalytic response in presence of real waste water collected from different industries. However, to consider LDHs as potential materials for real waste water decontamination, a feasibility study is required. To note that, the introduction of elements as Au, Ag, In, Ga makes the fabrication of these materials to be particularly expensive. However, to keep a high photocatalytic activity, but also to decrease de process costs, some compromises can be done. For instance, the catalyst concentration or the NPs particles quantity on LDHs support can be decreased, and as a consequence, the degradation time will increase.

Combining the enzymatic processes with the photocatalytic reactions, complex pollutant systems can be decomposed. The photo-enzymatic degradation of phenol by using ZnA-HRP was possible. However, the LDHs and oxidoreductases and can be combined in different ways leading to hybrid catalysts or catalysis. The pollutants can be degraded in cascade, when certain compounds are removed via photocatalysis, using LDHs, followed by the enzymatic degradation of the rest of the toxic substances. The LDHs can be used simply as a support for the enzyme, and the resulted material can be further used in presence or in absence of irradiation, in function of the pollutant system composition. When used under irradiation, the pollutants might be degraded via both enzymatic and photocatalytic pathways.

The design of a continuous NADH photo-regeneration during an enzymatic reaction would be an interesting continuation of the this study. Thus, during the enzymatic reaction, the cofactor will be oxidized to NAD^+, which will be further used under irradiation and in presence of Au/ZnAl for the NADH formation. The new formed cofactor molecules, will serve to the enzymatic reaction. In this case is mandatory be to use an irradiation source which will have no effects on the enzyme integrity, and studies on this direction might be requied.

Dissemination of the research results

Articles published in ISI journals

1. Elena-Florentina Grosu, Gabriela Carja, Renato Froidevaux, *Development of horseradish peroxidase/layered double hydroxide hybrid catalysis for phenol degradation*, Research on Chemical Intermediates (2018) doi.org/10.1007/s11164-018-3583-x789, (Springer), (IF =1.674).

2. Elena-Florentina Grosu, Gabriela Carja, Renato Froidevaux; *Horseradish Peroxidase-AuNP/LDH heterostructures: influence on nanogold release and enzyme activity*, Gold Bulletin, under review, minor revisions.

3. Gaku Mikami, Florentina Grosu, Shogo Kawamura, Yusuke Yoshida, Gabriela Carja, Yasuo Izumi, *Harnessing self-supported Au nanoparticles on layered doublehydroxides comprising Zn and Al for enhanced phenol decompositionunder solar light*, Applied Catalysis B: Environmental (2016) **199**:260–271 (Elsevier), (IF = 11,698).

4. Gabriela Carja, Elena Florentina Grosu, Mihaela Mureseanu, Doina Lutic, *A Family of Solar-Light Responsive Photocatalysts Obtained by $Zn^{2+}Me^{3+}$(Me=Al/Ga)LDHs Doped with Ga_2O_3 and In_2O_3 and their Derived Mixed Oxides: A Case Study of Phenol/4-Nitrophenol Decomposition*, Catalysis Science and Technology (2017) **7**:5402-5412 (Elsevier) (IF = 5.365).

5. Gabriela Carja, Elena Florentina Grosu, Catalina Petrarean, Norica Nichita, *Self-assemblies of plasmonic gold/layered double hydroxides with highly efficient antiviral effect against hepatitis B virus,* Nano Research (2015) **8**: 3512–3523 (Springer), (IF = 7.994).

Articles published in BDI journals and conference proceedings

1. Elena-Florentina Grosu, Gabriela Carja, *Iron based layered double hydroxide and its calcined derived as efficient photocatalyst in phenol removal*, Buletinul Institutului Politehnic from Iasi (2017) **63**:51-60, ISSN 0254-7104.

2. K. Katsumata, M. Puscasu, E. Seftel, E. F. Grosu, K. Ikeda, P. Cool, G. Carja, *Evolutions of self-assembled Bi_2O_3/LDHs nanostructures to mixtures of mixed oxides and their photocatalytic efficiency under UV and solar light*, Materials for energy, Efficienty and Sustainability: TechConnect Briefs (2015) 132-135, ISBN 978-1-4987-4728-8.

Oral communications and posters presented at international conferences

1. Elena-Florentina Grosu, Elena Seftel, Pegie Cool, Gabriela Carja, *Diclofenac removal from aqueous solution using ZnAlLDH and ZnCoAlLDH and their derived mixed oxides as highly efficient photocatalysts*, 3rd International Conference on Chemical Engineering – ICCE, November 9-11, 2016, Iasi, Romania (**Poster**)

2. Gabriela Carja, Mihaela Mureseanu, Elena-Florentina Grosu, Laura Dartu, Viorica Parvulescu, *Self-supported nanoparticles of gallium and indium on ZnMeLDHs (Me: Al, Ga) for efficient photocatalysis under solar irradiation*, European Materials Research Society, May 2-6, 2016, Lille, Franta (**Poster**).

3. Elena Grosu, Elena Seftel, Radu Ciocarlan, Myrjam Mertens, Gabriela Carja, Pegie Cool, *Diclofenac removal from aqueous solution using ZnAlLDH and ZnCoAlLDH and their derived mixed oxides as highly efficient photocatalysts*, Chemical Research in Flanders – CRF, October 24-26, 2016, Blankenberge, Belgia **(Poster).**

4. Gabriela Carja, Elena Florentina Grosu, Catalina Petrareanu, Norica Nichita, *Antiviral effect against hepatitis B virus of nanocomposites self-assemblies of plasmonic gold/layered doubles hydroxides*, 12th International Conference on Colloid and Surface Chemistry, ICCSC'2016, May 16-18, 2016 (**Oral Presentation**).

5. Elena Grosu, Ken-Ichi Katsumata, Kei Ikeda, Mihaela Vizitiu, Doina Sibiescu, Gabriela Carja, *Nanocomposites of Plasmonic Gold/Layered Double Hydroxides with Enhanced Photocatalytic Performances for Phenol Degradation*, 8th International Conference on Environmental Engineering and Management, September 9-12, 2015, Iasi, Romania (**Poster**).

6. K. Katsumata, M. Puscasu, E. Seftel, E. F. Grosu, K. Ikeda, P. Cool, G. Carja, *Evolutions of self-assembled Bi_2O_3/LDHs nanostructures to mixtures of mixed oxides and their photocatalytic effiecency under UV and solar light*, NanoTech: Advanced Materials and Applications, 14-17 June, 2015, Washington, US (**Poster**).

7. E. F. Grosu, L. E. Dartu, E. M. Seftel, G. Carja, *Nanostructured mixtures of mixed oxides derived from layered double hydroxides reconstructed in $Ga_2(SO_4)_3$ and $In(C_2H_3O_2)_3$ aqueous solutions for efficient, UV and solar-driven photocatalysis*, 2nd International Conference on Nanomaterials & Applications, 23-26 June, 2015, Maribor, Slovenia (**Oral Presentation**).

Oral communications and posters presented at national conferences

1. Elena-Florentina Grosu, Froidevaux Renato, Cârjă Gabriela, *Nanocomposites based on layered double hydroxide as novel materials for horseradish peroxidase enzyme immobilisation: A kinetic study*, TUIASI Doctoral School Conference, 23-24 May, 2018, Romania (**Oral Presentation**).

2. Elena Florentina Grosu, Magda Cornelia Puscasu, Vanesa Prevot, Gabriela Carja, *Hybrid formulations of layered double hydroxides for efficient UV and solar-driven photocatalysis*, The First Conference of Romanian Electron Microscopy Society, 7-8 May, 2015, Bucharest, Romania (**Oral Presentation**).

Scholarship programs

- 01/02/2018 - 01/04/2018 Erasmus+ Scolarship, *Studies on the interactions between enzymes/co-enzymes and layered double hydroxides (LDHs). Enzyme immobilization on LDHs*, Institute Charles VIOLLETTE –ProBioGEM, Lille University, Lille France.
- 01/09/2016 – 01/07/2017 Eiffel Scholarship Program of Excellence, *Studies on the properties and applications of biocomposites based on double lamellar hydroxides (LDHs) and their derived mixed oxides*, Institute Charles VIOLLETTE –ProBioGEM, Lille University, Lille France.
- 01/02/2016 – 01/08/2018 Erasmus+ Scolarship, *Designing LDH-Based Hybrid Nano Architectures and Their Applications in Photocatalysis*, Laboratory of Adsorption and Catalysis, Antwerp University, Antwerp (Belgium).

Dissemination of the Research Results

Research Project

- *Self-Assemblies of Nanoparticles of Metal Oxides-Layered Double Hydroxides as Novel Formulations for Photocatalytic Applications* – IDEI - PROIECTE DE CERCETARE EXPLORATORIE - PCE 2012-4-0057 (75/02.09.2013) – research assistant.

Bibliography

[1] M. Hadnadjev-Kostic, T. Vulic, R. Marinkovic-Neducin, *Adv. Powder Technol.* **25** (2014) 1624–1633.
[2] P. Nalawade, B. Aware, V.J. Kadam, R.S. Hirlekar, *Ind. Res.* **68** (2009) 267–272.
[3] A.V. F. Cavani, F. Trifirb, *Catal. Today*. **11** (1991) 173–301.
[4] S.J. Mills, A.G. Christy, J.-M.R. Génin, T. Kameda, F. Colombo, *Mineral. Mag.* **76** (2012) 1289–1336.
[5] D.G. Evans, R.C.T. Slade, Structural Aspects of Layered Double Hydroxides David, in: D.M.P. Mingos (Ed.), Structure and Bonding, Springer-Verlag Berlin Heidelberg, 2006: pp. 1–88.
[6] D. Basu, A. Das, K.W. Stöckelhuber, U. Wagenknecht, G. Heinrich, *Prog. Polym. Sci.* **39** (2014) 594–626.
[7] L.S. Heng, *Agency Sci. Technol. Res.* (2011) 2–3. https://phys.org/news/2011-03-layered-metallic-hydroxide-crystals-carbon.html
[8] A. de Roy, C. Forano, J. P. Besse, Layered double hydroxides: synthesis and post-synthesis modification, in V. Rives (Ed), *Layered double hydroxides: present and future*, Nova Science Publishers (2001) pp 1-41
[9] Y. Kuang, L. Zhao, S. Zhang, F. Zhang, M. Dong, S. Xu, *Materials* **3** (2010) 5220–5235.
[10] A. Vaccari, *Catal. Today*. **41** (1998) 53–71.
[11] H. Li, J. Ma, D.G. Evans, T. Zhou, F. Li, X. Duan, *Chem. Mater.* **1** (2006) 4405–4414.
[12] W.J.W. Kagunya, Z. Hassan, *Inorg. Chem.* **35** (1996) 5970-5974.
[13] L. Wang, F. Wang, L. Xu, *Ind. J. Chem*. **54** (2015) 607–612.
[14] R. Yang, Y. Gao, J. Wang, Q. Wang, *Dalt. Trans.* **43** (2014) 10317.
[15] N. Balsamo, S. Mendieta, M. Oliva, G. Eimer, M. Crivello, *Procedia Mater. Sci.* **1** (2012) 506–513.
[16] M.A. Woo, T.W. Kim, I.Y. Kim, S.J. Hwang, *Solid State Ionics*. **182** (2011) 91–97.
[17] X. Zhao, F. Zhang, S. Xu, D.G. Evans, X. Duan, *Chem. Mater.* **22** (2010) 3933–3942.
[18] W. Lv, Q. Mei, H. Fu, J. Xiao, M. Du, Q. Zheng, *J. Mater. Chem. A.* **5** (2017) 19079–19090.
[19] T. Xiao, Y. Tang, Z. Jia, D. Li, X. Hu, B. Li, L. Luo, *Nanotechnology*. **20** (2009) 475603–475610.
[20] A.C. Heredia, M.I. Oliva, B. Agñ, C.I. Zandalazini, S.G. Marchetti, E.R. Herrero, M.E. Crivello, *J. Magn. Magn. Mater.* **342** (2013) 38–46.
[21] Q. Li, L. Xing, X. Lu, N. Li, M. Xu, *Inorg. Chem. Commun.* **52** (2015) 46–49.
[22] A.A.A. Ahmed, Z.A. Talib, M.Z. Bin Hussein, *Appl. Clay Sci.* **56** (2012) 68–76.
[23] J.S. Valente, F. Tzompantzi, J. Prince, J.G.H. Cortez, R. Gomez, *Appl. Catal. B Environ.* **90** (2009) 330–338.
[24] B. Luo, R. Song, D. Jing, *Int. J. Hydrogen Energy*. **42** (2017) 23427–23436.
[25] Y. Zhu, R. Zhu, G. Zhu, M. Wang, Y. Chen, J. Zhu, Y. Xi, H. He, *Appl. Surf. Sci.* **433** (2018) 458–467.
[26] Z. Wang, Y. Song, J. Zou, L. Li, Y. Yu, L. Wu, *Catal. Sci. Technol.* **8** (2018) 268–275.
[27] Wikipedia, (n.d.). https://en.wikipedia.org/wiki/Transparency_and_translucency.
[28] G. Fan, F. Li, D.G. Evans, X. Duan, *Chem. Soc. Rev.* **43** (2014) 7040–7066.

Bibliography

[29] Y. Zhang, M.K. Ram, E.K. Stefanakos, D.Y. Goswami, *Surf. Coatings Technol.* **217** (2013) 119–123.

[30] G. Chen, S. Qian, X. Tu, X. Wei, J. Zou, L. Leng, S. Luo, *Appl. Surf. Sci.* **293** (2014) 345–351.

[31] K.I. Katsumata, K. Sakai, K. Ikeda, G. Carja, N. Matsushita, K. Okada, *Mater. Lett.* **107** (2013) 138–140.

[32] C. Gomes Silva, Y. Bouizi, V. Fornés, H. García, *J. Am. Chem. Soc.* **131** (2009) 13833–9.

[33] E.M. Seftel, M.C. Puscasu, M. Mertens, P. Cool, G. Carja, *Appl. Catal. B Environ.* **164** (2015) 251–260.

[34] E.M. Seftel, M.C. Puscasu, M. Mertens, P. Cool, G. Carja, *Applied Catal. B, Environ.* **150**–**151** (2014) 157–166.

[35] E.M. Seftel, M. Mertens, P. Cool, *Appl. Catal. B Environ.* **134**–**135** (2013) 274–285.

[36] A. Legrouri, M. Badreddine, A. Barroug, A. De Roy, J-P Basse, *J Mater Sci Lett.* **18** (1999) 1077–1079.

[37] Z. Gu, J.J. Athertonab, Z.P. Xu, *Chem. Commun.*, **51** (2015) 3024-3036.

[38] K. Abderrazek, N. Frini Srasra, E. Srasra, *J. Chinese Chem. Soc.* **64** (2017) 346–353.

[39] G.G.C. Arizaga, K.G. Satyanarayana, F. Wypych, *Solid State Ionics*. **178** (2007) 1143–1162.

[40] A. Chauhan, P. Chauhan, *J Anal. Bioanal. Tech.* **5** (2014) DOI: 10.4172/2155-9872.1000212.

[41] S.A Speakman, Basics of X-Ray Powder Diffraction, http://prism.mit.edu/xray/Basics%20of%20X-Ray%20Powder%20Diffraction.pdfS.A.

[42] B. Fultz, J. Howe , Diffraction and the X-Ray Powder, in Transmission Electron Microscopy and Diffractometry of Materials, Springer-Verlag Berlin Heidelberg, Heidelberg (2013) DOI 10.1007/978-3-642-29761-8_1

[43] B. Wiyantoko, P. Kurniawati, T.E. Purbaningtias, I. Fatimah, *Procedia Chem.* **17** (2015) 21–26.

[44] F.T.L. Muniz, M.A.R. Miranda, C. Morilla Dos Santos, J.M. Sasaki, *Acta Crystallogr. Sect. A Found. Adv.* **72** (2016) 385–390.

[45] P. Osiceanu, Metode de analiza a suprafetelor, interfetelor si straturilor subtiri : XPS (ESCA) – Auger, Bucuresti, 2009. http://www.icf.ro/individual/lab04/osiceanu/XPS_ESCA_book2009.pdf.

[46] Wikipedia, (n.d.). https://en.wikipedia.org/wiki/X-ray_photoelectron_spectroscopy.

[47] P. Roy Chowdhury, K.G. Bhattacharyya, *Dalt. Trans.* **44** (2015) 6809–6824.

[48] Wikipedia, (n.d.). https://en.wikipedia.org/wiki/Fourier-transform_infrared_spectroscopy

[49] D. Kumar, B. Singh, K. Bauddh, J. Korstad, Bio-oil and biodiesel as biofuels derived from microalgal oil and their characterization by using instrumental techniques, in: Singh (Ed.), *Algae and Environmental Sustainability*. Developments in Applied Phycology, Springer, New Delhi, (2015) 87-95.

[50] X. Liu, X. Zhao, Y. Zhu, F. Zhang, *Appl. Catal. B Environ.* **140**–**141** (2013) 241–248.

[51] L. Bulgariu, Controlul analitic al callitatii produselor, Politehnium, Iasi, 2013.

[52] https://www2.chemistry.msu.edu/faculty/reusch/virttxtjml/spectrpy/uv-Vis/uvspec.htm.

[53] B.W. David, C.C. Barry, Transmission Electron Microscopy, A textbook for Materiales Science, Springer, New York, 2009.

[54] S. Wischnitzer, Introduction to electron microscopy, Pergamon Press, New York, 1970.

[55] Wikipedia, (n.d.). https://en.wikipedia.org/wiki/Scanning_electron_microscope.

Bibliography

[56] https://www2.nau.edu/micro-analysis/wordpress/index.php/instrumentation/
[57] Y. Liu, J. Song, F. Jiao, J. Huang, *J. Mol. Struct.* **1064** (2014) 100–106.
[58] T. Chen, F. Zhang, Y. Zhu, *Catal. Letters*. **143** (2013) 206–218.
[59] X. Wang, C. Shang, G. Wu, X. Liu, H. Liu, *Catalysts*. **6** (2016) 101.
[60] Ivyroses, (n.d.). http://www.ivyroses.com/Biology/Techniques/How-does-a-Transmission-Electron-Microscope-work.php.
[61] Writeopinions, (n.d.). http://www.writeopinions.com/serial-block-face-scanning-electron-microscopy.
[62] C.A. Antonyraj, P. Koilraj, S. Kannan, *Chem. Commun.* **46** (2010) 1902.
[63] R. Li, Z. Hu, X. Shao, P. Cheng, S. Li, W. Yu, W. Lin, D. Yuan, *Sci. Rep.* **6** (2016) 1–9.
[64] Introduction to Energy Dispersive X-ray Spectrometry (EDS) http://cfamm.ucr.edu/documents/eds-intro.pdf
[65] R.K. Sahu, B.S. Mohanta, N.N. Das, *J. Phys. Chem. Solids*. **74** (2013) 1263–1270.
[66] N. Murasawa, H. Koseki, X.-R. Li, Y. Iwata, T. Sakamoto, *Int. J. Energy Eng.* **2** (2012) 242–252.
[67] B. Saifullah, M.Z.B. Hussein, *Int. J. Nanomedicine*. **10** (2015) 5609–5633.
[68] M. De Oliveira Melo, L.A. Silva, *J. Braz. Chem. Soc.* **22** (2011) 1399–1406.
[69] M. Shao, J. Han, M. Wei, D.G. Evans, X. Duan, *Chem. Eng. J.* **168** (2011) 519–524.
[70] A.S. Kim, J. Fahel, P. Durand, E. Andre, S. Kim, J. Fahel, P. Durand, E. André, C. Carteret, *Eur. J. Inorg. Chem.* (2017) 669–678. doi.org/10.1002/ejic.201601213
[71] X. Wang, P. Wu, Z. Huang, N. Zhu, J. Wu, P. Li, Z. Dang, *Appl. Clay Sci.* **95** (2014) 95–103.
[72] A. Mantilla, F. Tzompantzi, J.L. Fernández, J.A.I. Díaz Góngora, G. Mendoza, R. Gómez, *Catal. Today*. **148** (2010) 119–123.
[73] J. Ma, J. Ding, L. Yu, L. Li, Y. Kong, S. Komarneni, *Appl. Clay Sci.* **107** (2015) 85–89.
[74] Y. Zhao, S. Zhang, B. Li, H. Yan, S. He, L. Tian, W. Shi, J. Ma, M. Wei, D.G. Evans, X. Duan, *Chem. - A Eur. J.* **17** (2011) 13175–13181.
[75] S.J. Xia, F.X. Liu, Z.M. Ni, J.L. Xue, P.P. Qian, *J. Colloid Interface Sci.* **405** (2013) 195–200.
[76] Š. Paušová, J. Krýsa, J. Jirkovský, C. Forano, G. Mailhot, V. Prevot, *Appl. Catal. B Environ.* **170**–**171** (2015) 25–33.
[77] K. Hosni, O. Abdelkarim, N. Frini-Srasra, E. Srasra, *Korean J. Chem. Eng.* **32** (2014) 104–112.
[78] G. Mendoza-Damián, F. Tzompantzi, A. Mantilla, A. Barrera, L. Lartundo-Rojas, *J. Hazard. Mater.* **263** (2013) 67–72.
[79] B. Benalioua, M. Mansour, A. Bentouami, B. Boury, E.H. Elandaloussi, *J. Hazard. Mater.* **288** (2015) 158–167.
[80] V.R.R. Cunha, R.B. De Souza, A.M.C.R.P. Da Fonseca Martins, I.H.J. Koh, V.R.L. Constantino, *Sci. Rep.* **6** (2016) 1–10.
[81] F. Duda, M. Kieke, F. Waltz, M.E. Schweinefuß, M. Badar, P.P. Müller, K.H. Esser, T. Lenarz, P. Behrens, N.K. Prenzler, *J. Mater. Sci. Mater. Med.* **26** (2015) 1–8.
[82] L. Perioli, P. Mutascio, C. Pagano, *Pharm. Res.* **30** (2013) 156–166.
[83] M.A. Djebbi, Z. Bouaziz, A. Elabed, M. Sadiki, S. Elabed, P. Namour, N. Jaffrezic-Renault, A.B.H. Amara, *Int. J. Pharm.* **506** (2016) 438–448.
[84] H. Nabipour, M.H. Sadr, *J. Porous Mater.* **22** (2015) 447–454.
[85] D.A.F. Fontes, M.A.M. de Lyra, J.K.F. de Andrade, G.C.R. de Medeiros Schver, L.A.

Bibliography

Rolim, T.G. da Silva, J.L. Soares-Sobrinho, S. Alves-Júnior, P.J. Rolim-Neto, *J. Incl. Phenom. Macrocycl. Chem.* **85** (2016) 281–288.
[86] X. Gao, L. Chen, J. Xie, Y. Yin, T. Chang, Y. Duan, N. Jiang, *Mater. Sci. Eng. C*. **39** (2014) 56–60.
[87] R. Djaballah, A. Bentouami, A. Benhamou, B. Boury, E.H. Elandaloussi, *J. Alloys Compd.* **739** (2018) 559–567.
[88] A. Kuznetsova, P.M. Domingues, T. Silva, A. Almeida, M.L. Zheludkevich, J. Tedim, M.G.S. Ferreira, A. Cunha, *J Appl Microbiol.***122** (2017) 1207-1218.
[89] B. Saifullah, M.E. El Zowalaty, P. Arulselvan, S. Fakurazi, T.J. Webster, B.M. Geilich, M.Z. Hussein, *Int. J. Nanomedicine*. **11** (2016) 3225–3237.
[90] Y. Li, L. Tang, X. Ma, X. Wang, W. Zhou, D. Bai, *J. Phys. Chem. Solids*. **107** (2017) 62–67.
[91] X. Mei, S. Xu, T. Hu, L. Peng, R. Gao, R. Liang, M. Wei, D.G. Evans, X. Duan, *Nano Res.* **11** (2017) 195–205
[92] T. Xu, J. Zhang, H. Chi, F. Cao, *Acta Biomater.* **36** (2016) 152–163.
[93] E.R. Cernei, A. Maxim, D.C. Maxim, R.B. Mavru, G. Zegan, *Rev Chim.* **67** (2016) 1306-1308.
[94] F. Peng, D. Wang, H. Cao, X. Liu, *Mater. Lett.* **213** (2018) 383–386.
[95] S. Ray, S. Saha, B. Sa, J. Chakraborty, *Drug Deliv. Transl. Res.* **7** (2017) 259–275.
[96] Y.-X. Chen, R. Zhu, Z. Xu, Q.-F. Ke, C.-Q. Zhang, Y.-P. Guo, *J. Mater. Chem. B.* **5** (2017) 2245–2253.
[97] S. Senapati, R. Thakur, S.P. Verma, S. Duggal, D.P. Mishra, P. Das, T. Shripathi, M. Kumar, D. Rana, P. Maiti, *J. Control. Release*. **224** (2016) 186–198.
[98] H. Nakayama, A. Hatakeyama, M. Tsuhako, *Int. J. Pharm.* **393** (2010) 104–111.
[99] B. Balcomb, M. Singh, S. Singh, *ChemistryOpen*. **4** (2015) 137–145.
[100] S.M.N. Mohsin, M.Z. Hussein, S.H. Sarijo, S. Fakurazi, P. Arulselvan, Y.H. Taufiq-Yap, *Sci. Adv. Mater.* **6** (2014) 648–658.
[101] Y. Li, H.Y. Bi, G.W. Wang, N. Wang, C.X. Chen, Z.Z. Li, X.M. Fan, *J. Dispers. Sci. Technol.* **37** (2016) 366–373.
[102] M.F. De Almeida, C.R. Bellato, A.H. Mounteer, S.O. Ferreira, J.L. Milagres, L.D.L. Miranda, *Appl. Surf. Sci.* **357** (2015) 1765–1775.
[103] L. Zhang, M. Ou, H. Yao, Z. Li, D. Qu, F. Liu, J. Wang, J. Wang, Z. Li, *Electrochim. Acta*. **186** (2015) 292–301.
[104] S. Nayak, L. Mohapatra, K. Parida, *J. Mater. Chem. A.* **3** (2015) 18622–18635.
[105] J. Liu, G. Zhang, *Phys. Chem. Chem. Phys.* **16** (2014) 8178–8192.
[106] J. Memon, J. Sun, D. Meng, W. Ouyang, M.A. Memon, Y. Huang, S. Yan, J. Geng, *J. Mater. Chem. A.* **2** (2014) 5060.
[107] P.D. Marcato, N.V. Parizotto, D.S.T. Martinez, A.J. Paula, I.R. Ferreira, P.S. Melo, N. Durán, O.L. Alves, *J. Braz. Chem. Soc.* **24** (2013) 266–272.
[108] R. Lu, X. Xu, J. Chang, Y. Zhu, S. Xu, F. Zhang, *Appl. Catal. B Environ.* **111**–**112** (2012) 389–396.
[109] A. Ghiasi Moaser, R. Khoshnavazi, *New J. Chem.* **41** (2017) 9472–9481.
[110] D.B. Ingram, S. Linic, *J. Am. Chem. Soc.* (2011) **133** 5202–5205.
[111] J. Sun, Y. Zhang, J. Cheng, H. Fan, J. Zhu, X. Wang, S. Ai, *J. Mol. Catal. A Chem.* **382** (2014) 146–153.
[112] G. Huang, J. Chen, D. Wang, Y. Sun, L. Jiang, Y. Yu, J. Zhou, S. Ma, Y. Kang, *Mater.*

Bibliography

Lett. **173** (2016) 227–230.
[113] G. Carja, L. Dartu, K. Okada, E. Fortunato, *Chem. Eng. J.* **222** (2013) 60–66.
[114] E.M. Seftel, M. Niarchos, C. Mitropoulos, M. Mertens, E.F. Vansant, P. Cool, *Catal. Today*. **252** (2015) 120–127.
[115] S.J. Xia, F.X. Liu, Z.M. Ni, W. Shi, J.L. Xue, P.P. Qian, *Appl. Catal. B Environ.* **144** (2014) 570–579.
[116] T. Vulic, O. Rudic, S. Vucetic, D. Lazar, J. Ranogajec, *Cem. Concr. Compos.* **58** (2015) 50–58.
[117] S.P. Paredes, M.A. Valenzuela, G. Fetter, S.O. Flores, *J. Phys. Chem. Solids*. **72** (2011) 914–919.
[118] E.M. Seftel, E. Popovici, E. Beyers, M. Mertens, H.Y. Zhu, E.F. Vansant, P. Cool, *J. Nanosci. Nanotechnol.* **10** (2010) 1–7.
[119] Z. Huang, P. Wu, Y. Lu, X. Wang, N. Zhu, Z. Dang, *J. Hazard. Mater.* **246**–**247** (2013) 70–78.
[120] E.M. Seftel, M. Puscasu, M. Mertens, P. Cool, G. Carja, *Catal. Today*. **252** (2015) 7–13.
[121] G. Carja, Y. Kameshima, A. Nakajima, C. Dranca, K. Okada, *Int. J. Antimicrob. Agents*. **34** (2009) 534–539.
[122] W.-D. Zhang, Y.-M. Zheng, Y.-S. Xu, Y.-X. Yu, Q.-S. Shi, L. Liu, H. Peng, Y. Ouyang, *J. Nanosci. Nanotechnol.* **13** (2013) 409–416.
[123] Y. Kuthati, R.K. Kankala, C.H. Lee, *Appl. Clay Sci.* **112**–**113** (2015) 100–116.
[124] G.S. Thomas, P.V. Kamath, *Solid State Sci.* **8** (2006) 1181–1186.
[125] B. Hu, W. Liu, W. Gao, J. Han, H. Liu, L.A. Lucia, *Chem. Eng. J.* **277** (2015) 150–158.
[126] H. He, H. Kang, S. Ma, Y. Bai, X. Yang, *J. Colloid Interface Sci.* **343** (2010) 225–231.
[127] Q. Yang, S. Wang, F. Chen, K. Luo, J. Sun, C. Gong, F. Yao, X. Wang, J. Wu, X. Li, D. Wang, G. Zeng, *Catal. Commun.* **99** (2017) 15–19.
[128] X. Xiang, L. Xie, Z. Li, F. Li, *Chem. Eng. J.* **221** (2013) 222–229.
[129] V. Rives, M. del Arco, C. Martín, *Appl. Clay Sci.* **88**–**89** (2014) 239–269.
[130] D. Pan, H. Zhang, T. Fan, J. Chen, X. Duan, *Chem. Commun.* **47** (2011) 908–910.
[131] G. Mishra, B. Dash, S. Pandey, P.P. Mohanty, *J. Environ. Chem. Eng.* **1** (2013) 1124–1130.
[132] X. Bi, H. Zhang, L. Dou, *Pharmaceutics*. **6** (2014) 298–332.
[133] B. Brena, P. González-pombo, F. Batista-viera, Immobilization of Enzymes: A Literature Survey, in: J.M. Guisan (Ed.), *Immobilization of Enzymes and Cells*, *Methods in Molecular Biology*, 3rd ed., Springer science+Business Media, New York, (2013) pp. 15–31.
[134] P.A. Johnson, H.J. Park, A.J. Driscoll, Enzyme Nanoparticle Fabrication: Magnetic Nanoparticle Synthesis and Enzyme Immobilization, in: Shelley D. Minteer (Ed) *Enzyme Stabilization and Immobilization: Methods and Protocols*, Methods in Molecular Biology, Humana Press, Totowa, (2011) pp. 183–191.
[135] R.A. Messing, Introduction and General History of Immobilized Enzymes, in *Immobilized Enzymes for Industrial Reactors*, ACADEMIC PRESS, INC., 1975, pp 1-10
[136] D.W. Ball, J.W. Hill, R.J. Scott, Amino Acids, Proteins, and Enzymes, in: *Introduction to Chemistry: General, Organic, and Biological* (2012) pp. 1–24. https://2012books.lardbucket.org/books/introduction-to-chemistry-general-organic-and-biological/
[137] C. Oniscu, D. Cașcaval, Ingineria proceselor biotehnologice, in *Inginerie biochimică și*

Bibliography

biotehnologie, InterGlobal, Iași (2002).
[138] D.E. Koshland, *Angew. Chemie*. **106** (1994) 2468–2472.
[139] M. Yoshino, K. Murakami, *J. Enzyme Inhib. Med. Chem.* **24** (2009) 1288–1290.
[140] T. Sato, T. Tosa, Enzymes, immobilisation methods, in:, M.C. Flickinger (Ed) *Encyclopedia of Bioprocess Technology: Fermentation, Biocatalysis and Bioseparation,* John Wiley & Sons, INC (1999) pp. 1062–1064.
[141] J. Zdarta, A. Meyer, T. Jesionowski, M. Pinelo, *Catalysts*. **8** (2018) 92.
[142] N.R. Mohamad, N.H.C. Marzuki, N.A. Buang, F. Huyop, R.A. Wahab, *Biotechnol. Biotechnol. Equip.* **29** (2015) 205–220.
[143] W. Tischer, F. Wedekind, Immobilized Enzymes: Methods and Applications, **200** (1999) 95–126.
[144] J. Zhu, Q. Huang, M. Pigna, A. Violante, *Colloids Surfaces B Biointerfaces*. **77** (2010) 166–173.
[145] N. Zou, J. Plank, *J. Phys. Chem. Solids*. **76** (2015) 34–39.
[146] D.I.C. Córdova, R.M. Borges, G.G.C. Arizaga, F. Wypych, N. Krieger, *Quim. Nova*. **32** (2009) 1495–1499.
[147] M.A. Djebbi, M. Braiek, S. Hidouri, P. Namour, N. Jaffrezic-Renault, A. Ben Haj Amara, *J. Mol. Struct.* **1105** (2016) 381–388.
[148] Y. Ding, L. Liu, Y. Fang, X. Zhang, M. Lyu, S. Wang, *Nanomaterials*. **8** (2018) 173.
[149] A. Soussou, I. Gammoudi, F. Moroté, A. Kalboussi, T. Cohen-Bouhacina, C. Grauby-Heywang, Z.M. Baccar, *IEEE Sens. J.* **17** (2017) 4340–4348.
[150] D. Shan, S. Cosnier, C. Mousty, *Anal. Chem.* **75** (2003) 3872–3879.
[151] L. Fernández, I. Ledezma, C. Borrás, L.A. Martínez, H. Carrero, *Sensors Actuators, B Chem.* **182** (2013) 625–632.
[152] C. Guerard-Helaine, B. Legeret, C. Fernandes, V. Prevot, C. Forano, M. Lemaire, *New J. Chem.* **35** (2011) 776–779.
[153] K. Benaissi, V. Hélaine, V. Prévot, C. Forano, L. Hecquet, *Adv. Synth. Catal.* **353** (2011) 1497–1509.
[154] R. Mahdi, C. Guérard-Hélaine, V. Prévot, V. De Berardinis, C. Forano, M. Lemaire, *ChemCatChem*. **7** (2015) 3110–3115.
[155] Y. Wang, Z. Wang, Y. Rui, M. Li, *Biosens. Bioelectron.* **64** (2014) 57–62.
[156] W. Shi, M. Wei, L. Jin, C. Li, *J. Mol. Catal. B Enzym.* **47** (2007) 58–65.
[157] L. Ren, J. He, D.G. Evans, X. Duan, R. Ma, *J. Mol. Catal. - B Enzym.* **16** (2001) 65–71.
[158] World Water Assessement Programme, The United Nations World Water Development Raport: Water for the People, UNESCO Publishing, 2003.
[159] WHO/UNICEF Joint Monitoring Programme, Global water supply and sanitation assessment 2000 report, 2000. http://apps.who.int/iris/bitstream/handle/10665/42352/9241562021_eng.pdf?sequence=1&isAllowed=ydoiUNICEF.
[160] C. Hilton-Taylor, C.M. Pollock, J.S. Chanson, S.H. Butchart, T.E. Oldfield, V. Kataria, State of the world's species. Wildlife in a Changing World–An Analysis of the 2008 IUCN Red List of Threatened Species, IUCN, Gland, 2009.
[161] P. Kolhe, S. Ingle, N. Wagh, *Annu. Res. Rev. Biol.* **8** (2015) 1–15.
[162] Sigma-Aldrich, Phenol: Material Safty Data Sheet, 2004.S
[163] New Jersey Departament of Health, Hazardous Substance Fact Sheet, Acetophenone, 2009. https://web.doh.state.nj.us/rtkhsfs/factsheets.aspx

Bibliography

[164] Acetophenone: Hazard summary. https://www.epa.gov/sites/production/files/2016-09/documents/acetophenone.pdf

[165] M.L. Halmann, Photodegradation of water pollutants, CRC Press, 1995, pp 82, https://books.google.ro/books?id=xkqDymaQ7AcC&pg=PP3&hl=ro&source=gbs_selected_pages&cad=2#v=onepage&q&f=false

[166] Y. Wen, X. Jiang, *Plasma Chem. Plasma Process.* **20** (2000) 343–351.

[167] E. Muhr, O. Leicht, S.G. Sierra, M. Thanbichler, J. Heider, *Front. Microbiol.* **6** (2016) 1–12.

[168] B. Di Credico, I.R. Bellobono, M. D'Arienzo, D. Fumagalli, M. Redaelli, R. Scotti, F. Morazzoni, *Int. J. Photoenergy*. (2015) doi.org/10.1155/2015/919217

[169] C. Escapa, R.N. Coimbra, S. Paniagua, A.I. García, M. Otero, *Algal Res.* **18** (2016) 127–134.

[170] F. Cuklev, E. Kristiansson, J. Fick, N. Asker, L. Förlin, D.G.J. Larsson, *Environ. Toxicol. Chem.* **30** (2011) 2126–2134.

[171] A. Alshammari, V.N. Kalevaru, Supported Gold Nanoparticles as Promising Catalysts, in: N.K Mishra (Ed) *Catalytic Application of Nano-Gold Catalysts.* INTEC (2016) pp. 57–81. DOI: 10.5772/64394

[172] M. Haruta, N. Yamada, T. Kobayashi, S. Iijima, *J. Catal.* **115** (1989) 301–309.

[173] G.J. Hutchings, D.T. Grady, *Appl. Catal.* **17** (1985) 155–160.

[174] A. Corma, H. Garcia, *Chem. Soc. Rev.* **37** (2008) 2096–2126.

[175] J. Gong, *Chem. Rev.* **112** (2012), 2987–3054.

[176] S. Shuang, R. Lv, Z. Xie, Z. Zhang, *Sci. Rep.* **6** (2016) 26670.

[177] E. Di Fabrizio, W. Xie, N. Zabala, J. Aizpurua, P. Maioli, Y. Huang, *J. Phys.: Condens. Matter* **29** (2017) doi.org/10.1002/lpor.200810003.

[178] G. Carja, M. Birsanu, K. Okada, H. Garcia, *J. Mater. Chem. A.* **1** (2013) 9092–9098.

[179] Xiaofei Zhao, L. Wang, X. Xu, X. Lei, S. Xu, F. Zhang, *Am. Inst. Chem. Eng.* **58** (2012) 573–582.

[180] J.S. Valente, F. Tzompantzi, J. Prince, *Appl. Catal. B Environ.* **102** (2011) 276–285.

[181] H. Wei, J. Li, J. Yu, J. Zheng, H. Su, X. Wang, *Inorganica Chim. Acta*. **427** (2015) 33–40.

[182] F. Alzoubi, J. Al-Zouby, M. Alqadi, H.A. Alshboul, K. Aljarrah, *Chinese J. Phys.* **53** (2015) 1–9.

[183] D. Ghoneim, F.M. Hafez, N.A. Mohsen, *Int. J. Recent Res. Appl. Stud.* **12** (2012) 263.

[184] L. Wang, Y. Zhu, J.Q. Wang, F. Liu, J. Huang, X. Meng, J.M. Basset, Y. Han, F.S. Xiao, *Nat. Commun.* **6** (2015) 1–8.

[185] B.J. Kip, F.B.M. Duivenvoorden, D.C. Koningsberger, R. Prins, *J. Catal.* (1987) 10.1016/0021-9517(87)90005-4.

[186] G. V. Manohara, P. Vishnu Kamath, W. Milius, *J. Solid State Chem.* **196** (2012) 356–361.

[187] T. Tangkuaram, C. Ponchio, T. Kangkasomboon, P. Katikawong, W. Veerasai, *Biosens. Bioelectron.* **22** (2007) 2071–2078.

[188] W. Haiss, N.T.K. Thanh, J. Aveyard, D.G. Fernig, *Anal. Chem.* **79** (2007) 4215–4221.

[189] R Allmann, H.P. Jepsen, *Neues Jahrbuch fur Mineralogie, Monatshefte* (1969) 544–551.

[190] M. Kasithevar, M. Saravanan, P. Prakash, H. Kumar, M. Ovais, H. Barabadi, Z.K. Shinwari, *J. Interdiscip. Nanomedicine*. **2** (2017) 131–141.

[191] M. Wu, Y. Chang, T. Lin, *Jpn. J. Appl. Phys* **56** (2017) oi.org/10.7567/JJAP.56.04CJ01.

[192] M. Suárez-Quezada, G. Romero-Ortiz, V. Suárez, G. Morales-Mendoza, L. Lartundo-Rojas, E. Navarro-Cerón, F. Tzompantzi, S. Robles, R. Gómez, A. Mantilla, *Catal. Today*.

Bibliography

271 (2016) 213–219.
[193] R.R. Sheha, A.H. Harb, I. El, -T El-Sayed, A.S. Saleh, H.H. Someda, *4th Int. Conf. Radiat. Sci. Appl. 13-17/10/2014, Taba, E*gypt (2014) 151 -157.
[194] F. Chen, Q. Yang, C. Niu, X. Li, C. Zhang, G. Zeng, *RSC Adv.* **5** (2015) 63152–63164.
[195] S. Yu, J. Hu, J. Wang, *J. Hazard. Mater.* **177** (2010) 1061–1067.
[196] W. Zhai, F. Sun, W. Chen, Z. Pan, L. Zhang, S. Li, S. Feng, Y. Liao, W. Li, *Appl. Catal. A Gen.* **454** (2013) 59–65.
[197] S. Islam, S. Kumar Bormon, M. Nadim, K. Hossain, A. Habib, T. Selima Akhter Islam, *Am. J. Anal. Chem.* **5** (2014) 483–489.
[198] B. Zhao, G. Mele, I. Pio, J. Li, L. Palmisano, G. Vasapollo, *J. Hazard. Mater.* **176** (2010) 569–574.
[199] W. Zhang, L. Zhou, J. Shi, H. Deng, *Catalysts*. **8** (2018) 45.
[200] S. Soltan, H. Jafari, S. Afshar, O. Zabihi, *Water Sci. Technol.* **74** (2016) 1689–1697.
[201] E. Amereh, S. Afshar, *Mater. Chem. Phys.* **120** (2010) 356–360.
[202] S. Ahmad, A. Andeel, K. Yasin, *IOSR J. Appl. Chem.* **1** (2016) 1–4.
[203] Y. Ding, Y. Fan, X. Wei, D. Li, Y. Xiao, L. Jiang, *React. Kinet. Mech. Catal.* **118** (2016) 593–604.
[204] A.A. Khassin, I.I. Simentsova, A.N. Shmakov, N.V. Shtertser, O.A. Bulavchenko, S. V. Cherepanova, *Appl. Catal. A Gen.* **514** (2016) 114–125.
[205] K.Y. Ma, W.J. Zhao, J.P. Cheng, F. Liu, X. Bin Zhang, *J. Colloid Interface Sci.* **468** (2016) 238–246.
[206] Z. Li, Y. Wu, G. Lu, *Appl. Catal. B Environ.* **188** (2016) 56–64.
[207] J. Anton, J. Nebel, H. Song, C. Froese, P. Weide, H. Ruland, M. Muhler, S. Kaluza, *Appl. Catal. A Gen.* **505** (2015) 326–333.
[208] B. Wang, Y. Cai, W. Dong, C. Xia, W. Zhang, Y. Liu, M. Afzal, H. Wang, B. Zhu, *Sol. Energy Mater. Sol. Cells*. **157** (2016) 126–133.
[209] L. Yue, G. Li, F. Zhang, L. Chen, X. Li, X. Huang, *Appl. Catal. A Gen.* **512** (2016) 85–92.
[210] W. Ma, L. Wang, J. Xue, H. Cui, *J. Alloys Compd.* **662** (2016) 315–319.
[211] N.A.M. Barakat, *Appl. Catal. A Gen.* **451** (2013) 21–27.
[212] T. Li, X. Li, Z. Wang, H. Guo, Q. Hu, W. Peng, *Electrochim. Acta*. **191** (2016) 392–400.
[213] Y. Bao, K. Chen, *Nano-Micro Lett.* **8** (2016) 182–192.
[214] F. Dong, Z. Zhao, T. Xiong, Z. Ni, W. Zhang, Y. Sun, W.K. Ho, *ACS Appl. Mater. Interfaces*. **5** (2013) 11392–11401.
[215] W. Shan, Y. Hu, Z. Bai, M. Zheng, C. Wei, *Appl. Catal. B Environ.* **188** (2016) 1–12.
[216] K.C. Christoforidis, T. Montini, E. Bontempi, S. Zafeiratos, J.J.D. Jaén, P. Fornasiero, *Appl. Catal. B Environ.* **187** (2016) 171–180.
[217] Y. He, Y. Wang, L. Zhang, B. Teng, M. Fan, *Appl. Catal. B, Environ.* **168**–**169** (2015) 1–8.
[218] W. Li, C. Feng, S. Dai, J. Yue, F. Hua, H. Hou, *Appl. Catal. B Environ.* **168**–**169** (2015) 465–471.
[219] L. Zou, X. Xiang, M. Wei, F. Li, D.G. Evans, *Inorg. Chem.* **47** (2008) 1361–1369.
[220] N. Chubar, V. Gerda, O. Megantari, M. Mičušík, M. Omastova, K. Heister, P. Man, J. Fraissard, *Chem. Eng. J.* **234** (2013) 284–299.
[221] Y. Shi, Z. Gui, B. Yu, R.K.K. Yuen, B. Wang, Y. Hu, *Compos. Part B Eng.* **79** (2015) 277–284.
[222] J. Huo, H. Zeng, *Appl. Catal. B Environ.* **199** (2016) 342–349.

Bibliography

[223] M.A. Ulibarri, J.M. Fernández, F.M. Labajos, V. Rives, *Chem. Mater*.**3** (1991) 626-630.
[224] S. Nayak, L. Mohapatra, K. Parida, *J. Mater. Chem. A.* **3** (2015) 18622–18635.
[225] E.M. Seftel, E. Popovici, M. Mertens, K. De Witte, G. Van Tendeloo, P. Cool, E.F. Vansant, *Microporous Mesoporous Mater.* **113** (2008) 296–304.
[226] M. Qin, H. Yang, S. Chen, H. Xie, J. Guan, *Quim. Nova*. **35** (2012) 559–562.
[227] S.K. Alharbi, J. Kang, L.D. Nghiem, J.P. van de Merwe, F.D.L. Leusch, W.E. Price, *Process Saf. Environ. Prot.* **112** (2017) 222–234.
[228] M.S. Diniz, R. Salgado, V.J. Pereira, G. Carvalho, A. Oehmen, M.A.M. Reis, J.P. Noronha, *Sci. Total Environ.* **505** (2015) 282–289.
[229] J. Deng, Y. Shao, N. Gao, C. Tan, S. Zhou, X. Hu, *J. Hazard. Mater.* **262** (2013) 836–844.
[230] J. Eriksson, J. Svanfelt, L. Kronberg, *Photochem. Photobiol.* **86** (2010) 528–532.
[231] A. Agüera, L.A. Perez Estrada, I. Ferrer, E.M. Thurman, S. Malato, A.R. Fernandez-Alba, *J. Mass Spectrom.* **40** (2005) 908–915.
[232] R. Salgado, V.J. Pereira, G. Carvalho, R. Soeiro, V. Gaffney, C. Almeida, V.V. Cardoso, E. Ferreira, M.J. Benoliel, T.A. Ternes, A. Oehmen, M.A.M. Reis, J.P. Noronha, *J. Hazard. Mater.* **244**–**245** (2013) 516–527.
[233] S. Salaeh, D. Juretic Perisic, M. Biosic, H. Kusic, S. Babic, U. Lavrencic Stangar, D.D. Dionysiou, A. Loncaric Bozic, *Chem. Eng. J.* **304** (2016) 289–302.
[234] J. Hartmann, P. Bartels, U. Mau, M. Witter, W.V. Tümpling, J. Hofmann, E. Nietzschmann, *Chemosphere*. **70** (2008) 453–461.
[235] T.S. Anirudhan, P.L. Divya, J. Nima, S. Sandeep, *J. Colloid Interface Sci.* **434** (2014) 48–58.
[236] T.T. Le, M.S. Akhtar, D.M. Park, J.C. Lee, O.B. Yang, *Appl. Catal. B Environ.* **111**–**112** (2012) 397–401.
[237] J. Bandara, J.A. Mielczarski, J. Kiwi, *Langmuir*. **15** (1999) 7680–7687.
[238] T.D. Savić, Z. V. Šaponjić, M.I. Čomor, J.M. Nedeljković, M.D. Dramićanin, M.G. Nikolić, D.Ž. Veljković, S.D. Zarić, I.A. Janković, *Nanoscale*. **5** (2013) 7601–7612.
[239] K.D. Dobson, A. James McQuillan, *Spectrochim. Acta Part A.* **56** (2000) 557–565.
[240] P. Calza, V.A. Sakkas, C. Medana, C. Baiocchi, A. Dimou, E. Pelizzetti, T. Albanis, *Appl. Catal. B Environ.* **67** (2006) 197–205.
[241] Y. He, N.B. Sutton, H.H.H. Rjnaarts, A.A.M. Langenhoff, *Appl. Catal. B, Environ.* **182** (2015) 132-141.
[242] J. Mu, C. Shao, Z. Guo, M. Zhang, Z. Zhang, P. Zhang, B. Chen, Y. Liu, *J. Mater. Chem.* **22** (2012) 1786.
[243] H. Hidaka, T. Tsukamoto, Y. Mitsutsuka, T. Oyama, N. Serpone, *Photochem. Photobiol. Sci.* **14** (2015) 919–928.
[244] X. Li, X. Zhen, S. Meng, J. Xian, Y. Shao, X. Fu, D. Li, *Environ. Sci. Technol.* **7** (2013) 336-343.
[245] Z. Wang, B. Huang, Y. Dai, X. Qin, X. Zhang, P. Wang, H. Liu, J. Yu, *J. Phys. Chem. C*. **113** (2009) 4612–4617.
[246] E.M. Seftel, P. Cool, D. Lutic, *Mater. Sci. Eng. C*. **33** (2013) 5071–5078.
[247] X. Chen, H. Xue, Z. Li, L. Wu, X. Wang, X. Fu, *J. Phys. Chem. C*. **112** (2008) 20393–20397.
[248] W. Wei, Z. Qin, S. Fan, Z. Li, K. Shi, Q. Zhu, G. Zhang, *Nanoscale Res. Lett.* **7** (2012) 3–7.
[249] G. Liu, *Int. J. Electrochem. Sci.* **6** (2011) 2162–2170.

Bibliography

[250] Energy table for EDS analysis, available at: https://www.unamur.be/services /microscopie/sme-documents/Energy-20table-20for-20EDS-20analysis-1.pdf (accessed May 16th,2017).
[251] G. V. Manohara, P. Vishnu Kamath, W. Milius, *J. Solid State Chem.* **196** (2012) 356–361.
[252] R. Mostarih, A. de Roy, *J. Phys. Chem. Solids*. **67** (2006) 1058–1062.
[253] https://xpssimplified.com/periodictable.php
[254] D. Kim, P. Thissen, G. Viner, D.W. Lee, W. Choi, Y.J. Chabal, J.B. Lee, *ACS Appl. Mater. Interfaces*. **5** (2013) 179–185.
[255] J. Tauc, *Mater. Res. Bull.* **3** (1968) 37–46.
[256] R. Valdez, D.B. Grotjahn, D.K. Smith, J.M. Quintana, A. Olivas, *Int. J. Electrochem. Sci.* **10** (2015) 909–918.
[257] A. Murat, J.E. Medvedeva, *Phys. Rev. B - Condens. Matter Mater. Phys.* **86** (2012) 1–9.
[258] H. Peelaers, D. Steiauf, J.B. Varley, A. Janotti, C.G. Van De Walle, *Phys. Rev. B - Condens. Matter Mater. Phys.* **92** (2015) 1–6.
[259] G. Zhang, L. Hu, R. Zhao, R. Su, Q. Wang, P. Wang, *J. Photochem. Photobiol. A Chem.* **356** (2018) 633–641.
[260] A. Azetsu, H. Koga, A. Isogai, T. Kitaoka, *Catalysts*. **1** (2011) 83–96.
[261] J. Cai, Y. Zhang, Y. Qian, C. Shan, B. Pan, *Sci. Rep.* **8** (2018) 1–10.
[262] P. Nalawade, B. Aware, V.J. Kadam, R.S. Hirlekar, *J. Sci. Ind. Res. (India).* **68** (2009) 267–272.
[263] S.T. Frey, S.L. Guilmet, R.G. Egan. III, A. Bennett, S.R. Soltau, R.C. Holz, *ASC Appl Mater Interfaces*. **2** (2010) 2828–2832.
[264] M. Pavlovic, P. Rouster, I. Szilagyi, *Nanoscale*. **9** (2017) 369–379.
[265] N. Zou, J. Plank, *J. Phys. Chem. Solids*. **73** (2012) 1127–1130.
[266] D. Tonelli, E. Scavetta, M. Giorgetti, *Anal. Bioanal. Chem.* **405** (2013) 603–614.
[267] G. Bayramoğlu, M.Y. Arica, *J. Hazard. Mater.* **156** (2008) 148–155.
[268] H. Kawakita, *Sci. Technol.* **2** (2012) 25–29.
[269] M.B. Arnao, M. Acosta, J.A. Rio, F. Garcia-Canovas, *Biochim. Biophys. Acta*. **1041** (1990) 43-57.
[270] S. Dalal, M.N. Gupta, *Chemosphere*. **67** (2007) 741–747.
[271] S.J. Kim, B.K. Song, Y.J. Yoo, Y.H. Kim, *J. Korean Soc. Appl. Biol. Chem.* **57** (2014) 743–747.
[272] L. Mao, S. Luo, Q. Huang, J. Lu, *Sci. Rep.* **3** (2013) 1–7.
[273] C. Karunakaran, P. Anilkumar, P. Gomathisankar, *Chem. Cent. J.* **5** (2011) 31.
[274] Z. Wang, Y. Zhang, Q. Zhang, Y. Shen, D. Kuehner, *Green Chem.* **10** (2008) 907–909.
[275] M. Jobbágy, A.E. Regazzoni, *Appl. Clay Sci.* **51** (2011) 366–369.
[276] X. Liu, L. Luo, Y. Ding, Y. Xu, *Analyst*. **136** (2011) 696–701.
[277] A. Legrouri, M. Badreddine, A. Barroug, A. De Roy, J.P. Besse, *J. Mater. Sci. Lett.* **18** (1999) 1077–1079.
[278] A. Alshammari, A. Koeckritz, V.N. Kalevaru, A. Bagabas, A. Martin, *Appl Petrochem Res*. **2** (2012) 61–67.
[279] M. Ajdary, M. Negahdary, R. Chelongar, S. Zadeh, *Adv. Biomed. Res.* **4** (2015) 69.
[280] B. Morris, F, Behzad, *Biochem. Pharmacol. Open Access*. **3** (2014) 3–5. doi:10.4172/2167-0501.1000146
[281] R. Rojas, A.F. Jimenez-Kairuz, R.H. Manzo, C.E. Giacomelli, *Colloids Surfaces A Physicochem. Eng. Asp.* **463** (2014) 37–43.

Bibliography

[282] Q. Chang, H. Tang, *Molecules*. **19** (2014) 15768–15782.
[283] Z.M. Baccar, I. Hafaiedh, *Int. J. Electrochem.* **2011** (2011) 1–5.
[284] X. Chen, C. Fu, Y. Wang, W. Yang, D.G. Evans, *Biosens. Bioelectron.* **24** (2008) 356–361.
[285] D. Shan, S. Cosnier, C. Mousty, *Anal. Lett.* **36** (2003) 909–922.
[286] H. Hamdi, A. Namane, D. Hank, A. Hellal, *J. Mater. Environ. Sci.* **8** (2017) 3953–3961.
[287] A. Radoi, L. Dumitru, L. Barthelmebs, J.L. Marty, *Anal. Lett.* **42** (2009) 1187–1202.
[288] C.M. Puscasu, E.M. Seftel, M. Mertens, P. Cool, G. Carja, *J. Inorg. Organomet. Polym. Mater.* **25** (2015) 259–266.
[289] P.K. Patel, M.S. Mondal, S. Modi, D.V. Behere, *Biochim. Biophys. Acta - Protein Struct. Mol. Enzymol.* **1339** (1997) 79–87.
[290] N.C. Veitch, *Phytochemistry*. **65** (2004) 249–259.
[291] K.Q. Wilberg, D.G. Nnes, J. Rubio, *Brazilian J. Chem. Eng.* **17** (2000) 907-914
[292] J. Ai, W. Zhang, G. Liao, H. Xia, D. Wang, *RSC Adv.* **6** (2016) 38117–38123.
[293] J.L. Gómez, A. Bódalo, E. Gómez, J. Bastida, A.M. Hidalgo, M. Gómez, *Enzyme Microb. Technol.* **39** (2006) 1016–1022.
[294] Q. Chang, J. Huang, Y. Ding, H. Tang, *Molecules*. **21** (2016) 1044e .
[295] J. Cheng, S. Ming Yu, P. Zuo, *Water Res.* **40** (2006) 283–290.
[296] D. Zhou, S. Dong, J. Shi, X. Cui, D. Ki, C.I. Torres, B.E. Rittmann, *Chem. Eng. J.* **317** (2017) 882–889.
[297] H. Xiong, D. Zou, D. Zhou, S. Dong, J. Wang, B.E. Rittmann, *Chem. Eng. J.* **316** (2017) 7–14.
[298] J. Jia, S. Zhang, P. Wang, H. Wang, *J. Hazard. Mater.* **205**–**206** (2012) 150–155.
[299] R. Sarkhanpour, O. Tavakoli, M.H. Sarrafzadeh, H.R. Kariminia, *J. Environ. Sci. Heal. - Part A Toxic/Hazardous Subst. Environ. Eng.* **48** (2013) 300–307.
[300] P. Peralta-Zamora, A. Kunz, S.G. de Moraes, R. Pelegrini, P. de C. Moleiro, J. Reyes, N. Duran,*Chemosphere* **38** (1999) 835–852.
[301] L. Yin, Z. Shen, *Environ. Sci. Technol.* **44** (2010) 9117–9122.
[302] P. Peralta-Zamora, C.M. Pereira, E.R.L. Tiburtius, S.G. Moraes, M.A. Rosa, R.C. Minussi, N. Durán, *Chemosphere.* **42** (2003) 131–144.
[303] S. Shoabargh, A. Karimi, G. Dehghan, A. Khataee, *J. Ind. Eng. Chem.* **20** (2014) 3150–3156.
[304] A. Lante, F. Tinello, G. Lomolino, *Innov. Food Sci. Emerg. Technol.* **17** (2013) 130–134.
[305] F. Cataldo, *New Front. Chem.* **23** (2014) 99–110.
[306] X. Lv, J. Weng, *Sci. Rep.* **3** (2013) 1–10.
[307] A. Zuber, M. Purdey, E. Schartner, C. Forbes, B. Van Der Hoek, D. Giles, A. Abell, T. Monro, H. Ebendorff-Heidepriem, *Sensors Actuators, B Chem.* **227** (2016) 117–127.
[308] A. Mishra, P. Singh, M. Sardar, *Adv. Mater. Lett.* **6** (2015) 194–200.
[309] J. Chaudiere, A.L. Tappel, *J. Inorg. Biochem.* **20** (1984) 313–325.
[310] A.C. Osuji, S.O.O. Eze, E.E. Osayi, F.C. Chilaka, *Sci. World J.* **2014** (2014). doi.org/10.1155/2014/183163
[311] Y. Seida, Y. Nakano, *J. Chem. Eng. Japan*. **34** (2001) 906–911.
[312] M.A. Hayat, Colloidal gold: Principles, methods, and applications, Academic Press, New York, 1989.
[313] M. DeLuca, H. Lardy, R.L. Cross, Current topics in cellular Regulation, in R.W. Estabrook (Ed) Enzyme Catalysis and Control Current Topics in Cellular Regulation,

Bibliography

Academic Press (1984).
[314] L. Li, J. Weng, *Nanotechnology*. **21** (2010) 305603.
[315] K. Govindaraju, V. Kiruthiga, R. Manikandan, T. Ashokkumar, G. Singaravelu, *Mater. Lett.* **65** (2011) 256–259.
[316] H. Kawasaki, K. Hamaguchi, I. Osaka, R. Arakawa, *Adv. Funct. Mater.* **21** (2011) 3508–3515.
[317] P. Manivasagan, J. Venkatesan, K.H. Kang, K. Sivakumar, S.J. Park, S.K. Kim, *Int. J. Biol. Macromol.* **72** (2015) 71–78.
[318] M.A. Faramarzi, H. Forootanfar, *Colloids Surfaces B Biointerfaces*. **87** (2011) 23–27.
[319] R. Thapa, C. Bhagat, P. Shrestha, S. Awal, P. Dudhagara, *Ann. Clin. Microbiol. Antimicrob.* **16** (2017) 1–10.
[320] B. Halliwell, M.V. Clement, L.H. Long, *FEBS Lett.* **486** (2000) 10–13.
[321] K. Kamada, T. Nakamura, S. Tsukahara, *Chem. Mater.* **23** (2011) 2968–2972.
[322] V.A. Soares, D. Severino, H.C. Junqueira, I.L.S. Tersariol, C.S. Shida, M.S. Baptista, O.R. Nascimento, I.L. Nantes, *Photochem. Photobiol.* **83** (2007) 1254–1262.
[323] K. Kamada, N. Soh, *J. Asian Ceram. Soc.* **3** (2015) 18–21.
[324] X. Wang, T. Saba, H.H.P. Yiu, R.F. Howe, J.A. Anderson, J. Shi, *Chem.* **2** (2017) 621–654.
[325] J. Liu, M. Antonietti, *Energy Environ. Sci.* **6** (2013) 1486–1493.
[326] M. Aresta, A. Dibenedetto, T. Baran, A. Angelini, P. Łabuz, W. Macyk, *Beilstein J. Org. Chem.* **10** (2014) 2556–2565.
[327] K.A. Brown, M.B. Wilker, M. Boehm, H. Hamby, G. Dukovic, P.W. King, *ACS Catal.* **6** (2016) 2201–2204.
[328] J.H. Kim, Photocatalytic production method of oxidoreductase cofactors using pt nanoparticles, 2010. http://www.google.com/patents/WO2011108789A1.
[329] X. Huang, I.H. El-Sayed, X. Yi, M.A. El-Sayed, *J. Photochem. Photobiol. B Biol.* **81** (2005) 76–83.
[330] Y. zi Wang, Z. ping Zhao, R. li Zhou, W. fang Liu, *J. Mol. Catal. B Enzym.* **133** (2016) 188-193 .
[331] M. Mifsud, S. Gargiulo, S. Iborra, I.W.C.E. Arends, F. Hollmann, A. Corma, *Nat. Commun.* **5** (2014) 1–6.
[332] D.M. Parkin, *Lancet Onco*. **2** (2001) 533–543.
[333] B. Jiang, K. Himmelsbach, H. Ren, K. Boller, E. Hildt, *J. Virol.* **90** (2015) 3330–41.
[334] P. Arauz-Ruiz, H. Norder, B.H. Robertson, L.O. Magnius, *J. Gen. Virol.* **83** (2002) 2059–2073.
[335] N. Chai, H.E. Chang, E. Nicolas, Z. Han, M. Jarnik, J. Taylor, *J. Virol.* **82** (2008) 7812–7817.
[336] M. Bruns, S. Miska, S. Chassot, H. Will, *J. Virol.* **72** (1998) 1462–8.
[337] W. Yu, C. Goddard, E. Clearfield, C. Mills, T. Xiao, H. Guo, J.D. Morrey, N.E. Motter, K. Zhao, T.M. Block, A. Cuconati, X. Xu, *J. Med. Chem.* **54** (2011) 5660–5670.
[338] T.M. Block, R. Gish, H. Guo, A. Mehta, A. Cuconati, W. Thomas London, J.T. Guo, *Antiviral Res.* **98** (2013) 27–34.
[339] L. Lu, R.W.Y. Sun, R. Chen, C.K. Hui, C.M. Ho, J.M. Luk, G.K.K. Lau, C.M. Che, *Antivir. Ther.* **13** (2008) 252–262.
[340] F. Yang, C. Jin, S. Subedi, C.L. Lee, Q. Wang, Y. Jiang, J. Li, Y. Di, D. Fu, *Cancer Treat. Rev.* **38** (2012) 566–579.

Bibliography

[341] E.C. Dreaden, M.A. El-Sayed, *Acc. Chem. Res.* **45** (2012) 1854–1865.
[342] N. Leinskiw, V. Colvin, R. Drezek, *Small*. **4** (2008) 26–49.
[343] M. Thomas, A.M. Klibanov, *Proc. Natl. Acad. Sci.* **100** (2003) 9138–9143.
[344] M.A. MacKey, M.R.K. Ali, L.A. Austin, R.D. Near, M.A. El-Sayed, *J. Phys. Chem. B.* **118** (2014) 1319–1326.
[345] M.A. Mahmoud, M.A. El-Sayed, *J. Phys. Chem. Lett*. **4** (2013) 1541–1545.
[346] D. Goh, T. Gong, U.S. Dinish, K.K. Maiti, C.Y. Fu, K.T. Yong, M. Olivo, *Plasmonics*. **7** (2012) 595–601.
[347] X.D. Zhang, H.Y. Wu, D. Wu, Y.Y. Wang, J.H. Chang, Z. Bin Zhai, A.M. Meng, P.X. Liu, L.A. Zhang, F.Y. Fan, *Int. J. Nanomedicine*. **5** (2010) 771–781.
[348] J.A. Dahl, B.L.S. Maddux, J.E. Hutchison, *Chem. Rev.* **107** (2007) 2228–2269.
[349] S. Kawamura, M.C. Puscasu, Y. Yoshida, Y. Izumi, G. Carja, *Appl. Catal. A Gen.* **504** (2015) 238–247.
[350] K. Ariga, Q. Ji, M.J. Mcshane, Y.M. Lvov, A. Vinu, J.P. Hill, *Chem. Mater.* **24** (2012) 728−737.
[351] K. Ladewig, M. Niebert, Z.P. Xu, P.P. Gray, G.Q.M. Lu, *Biomaterials*. **31** (2010) 1821–1829.
[352] P.R. Chowdhury, K.G. Bhattacharyya, *Dalt. Trans.* **44** (2015) 6809–6824.
[353] J. He, T. Kunitake, *Chem. Mater.* **16** (2004) 2656–2661.
[354] V.A. Drits, A.S. Bookin, Crystal structure and X-Ray identificatio of layered double hydroxides, in: V. Rives (Ed) Layerd double hydroxides: Present and future, Nova Science Publishers, 2001: pp. 41–100.
[355] C. Alanis, R. Natividad, C. Barrera-Diaz, V. Martínez-Miranda, J. Prince, J.S. Valente, *Appl. Catal. B Environ.* **140**–**141** (2013) 546–551.
[356] B.D. Hall, D. Zanchet, D. Ugarte, *J. Appl. Crystallogr.* **33** (2000) 1335–1341.
[357] V. Prevot, V. Briois, J. Cellier, C. Forano, F. Leroux, *J. Phys. Chem. Solids*. **69** (2008) 1091–1094.
[358] A. Horváth, A. Beck, G. Stefler, T. Benkó, G. Sáfrán, Z. Varga, J. Gubicza, L Guczi, *J. Phys. Chem. C*. **115** (2011) 20388–20398.
[359] C. Zhou, J. Yu, Y. Qin, J. Zheng, *Nanoscale*. **4** (2012) 4228–4233.
[360] A. Mignani, B. Ballarin, M. Giorgetti, E. Scavetta, D. Tonelli, E. Boanini, V. Prevot, C. Mousty, A. Iadecola, *J. Phys. Chem. C*. **117** (2013) 16221–16230.
[361] C. Seeger, W.S. Mason, *Microbiol Mol Biol*. **64** (2000) 51–68.
[362] T.J. Huang, H. Chuang, Y.C. Liang, H.H. Lin, J.C. Horng, Y.C. Kuo, C.W. Chen, F.Y. Tsai, S.C. Yen, S.C. Chou, M.H. Hsu, *Eur. J. Med. Chem.* **90** (2015) 428–435.
[363] D. Grimm, R. Thimme, H.E. Blum, *Hepatol. Int.* **5** (2011) 644–653.
[364] T. Mosmann, *J. Immunol. Methods*. **65** (1983) 55–63.
[365] T. Bernas, J. Dobrucki, *Cytometry*. **47** (2002) 236–242.
[366] T.A. Berridge MV, *Arch Biochem Biophys*. **303** (1993) 474–82.
[367] T. Mahmood, P.C. Yang, *N. Am. J. Med. Sci.* **4** (2012) 429–434.